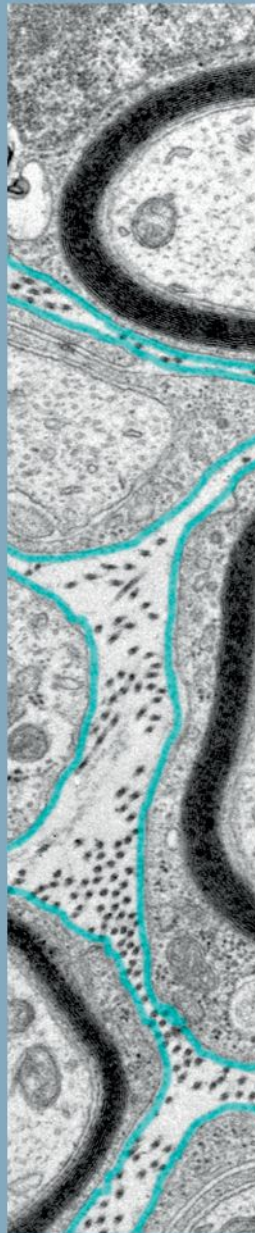


Neuron

Best of 2014/2015



A MAJOR LEAP FORWARD IN PHENOTYPING

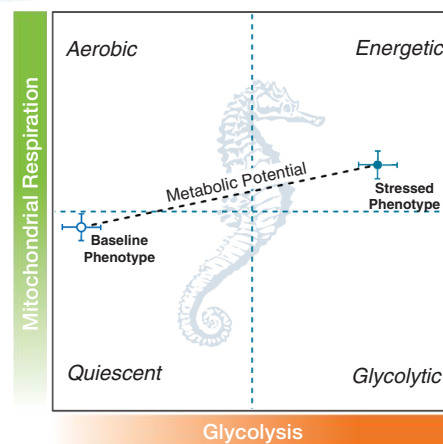
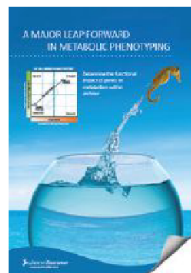
Determine the functional impact of genes on metabolism in an hour



XFp Cell Energy Phenotype Test Kit

Using as few as 15,000 live cells and an XFp Analyzer, the XF Cell Energy Phenotype Test identifies your cells' metabolic phenotype as well as their metabolic potential - the utilization of mitochondrial respiration and glycolysis.

Request a [FREE](#) poster and energy phenotype analysis of your cells at www.seahorsebio.com/pheno



Focused on antibodies for 40 years.
Not on advertising.



Bethyl Laboratories, Inc. has been dedicated to supporting scientific discovery through its qualified antibody products and custom antibody services since its founding in 1972.

Every antibody that Bethyl sells has been manufactured to exacting standards at its sole location in Montgomery, Texas, and has been validated in-house by Bethyl's team of scientists. Antibodies are tested across a range of applications including western blot, immunoprecipitation, immunohistochemistry, immunocytochemistry, ChIP, proximity ligation assay and ELISA.

Currently, Bethyl's portfolio consists of over 7,150 catalog products; offering close to 5,700 primary antibodies targeting over 2,700 proteins and 1,450 secondary antibodies raised against immunoglobulins from over 25 species. Trial sizes are available for over 4,000 antibodies targeting more than 2,350 protein targets. They are conveniently priced at \$50 and serve as an opportunity to discover for yourself why our antibodies are really good.

For really good antibodies, visit bethyl.com/trialsizes

Terms & Conditions: \$50 pricing for US customers only; international customers please contact your distributor for details. Trial sizes (catalog # ending in "-T") are not available for all antibodies and existing promotions or discounts do not apply.

© 2015 Bethyl Laboratories, Inc. All rights reserved.





Connecting Neuroscience and Immunology

Researchers are discovering increasing interconnections between the worlds of immunology and neuroscience. Immune cells that cross the blood brain barrier are gaining just as much importance as the microglia and protein aggregation mechanisms housed within the central nervous system.

With these newly emerging areas, scientists need dependable, high-quality reagents. Study both systems with BioLegend's comprehensive portfolio of immunology reagents and well-established former Covance neuroscience antibodies.

biolegend.com/neuroscience_products

15,000+ antibodies and reagents for:

- Immunohistochemistry
- Immunofluorescent Microscopy
- Western Blotting
- Bioassays
- Recombinant Proteins
- Flow Cytometry
- ELISAs
- Multiplex Assays
- Cell Separation Kits



Toll-Free Tel: (US & Canada): 1.877.BIOLEGEND (246.5343)

Tel: 858.768.5800

biolegend.com

08-0054-04

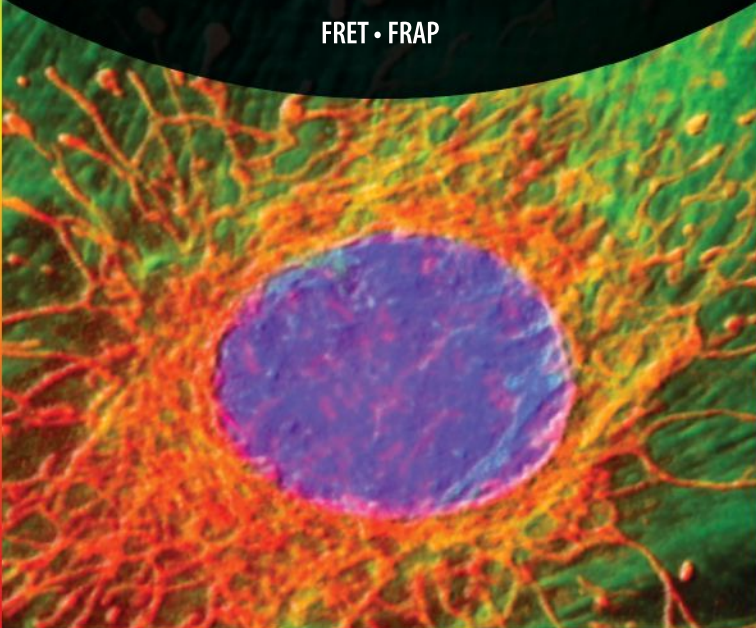
World-Class Quality | Superior Customer Support | Outstanding Value

**ADVANCED FLUORESCENCE
IMAGING SYSTEMS**

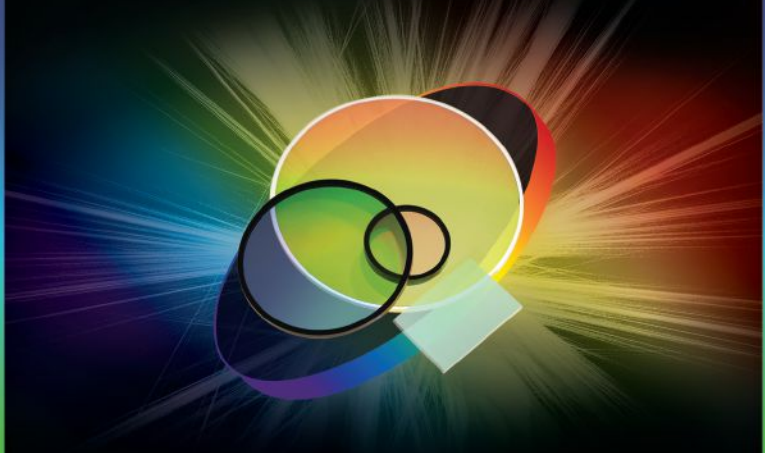


Imaging products from 89 North, Cairn Research
and CrestOptics create light re-engineered.

Confocal Imaging • Super-Resolution Imaging
High-Speed Ratiometric Imaging • Optogenetics • Photoactivation
Photoconversion • Simultaneous Multichannel Imaging
FRET • FRAP

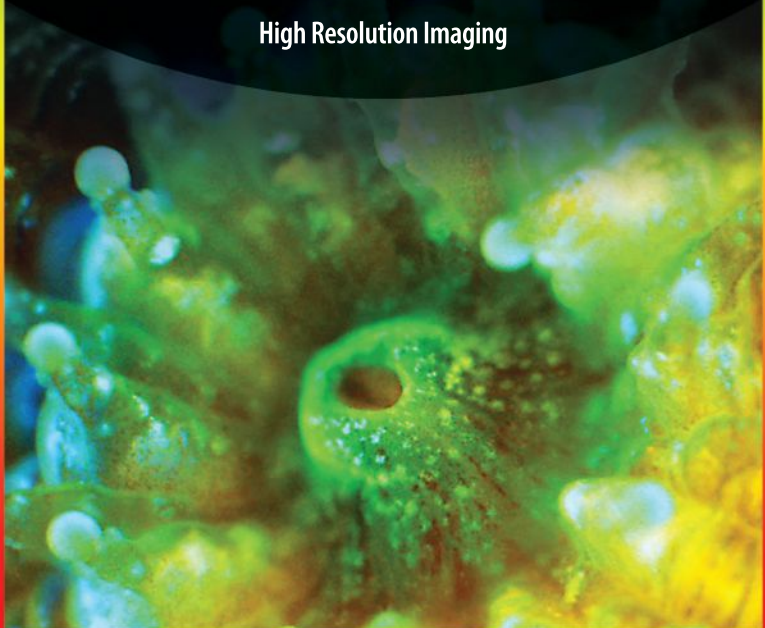


**DURABLE HIGH TRANSMISSION
SPUTTERED FILTERS FROM UV TO NIR**



From super-resolution to Raman spectroscopy,
Chroma filters give you more options.

Flow Cytometry • Machine Vision
Point-of-Care • Laser Applications
Raman • Fluorescence • Astronomy
High Resolution Imaging



Expect **MORE** from your Pooled RNAi Screens

MORE Potent

- shRNA-specific shERWOOD algorithm designs
- Optimized UltramiR scaffold increases shRNA processing
- Consistent knockdown from multiple shRNA per gene

MORE Specific

- microRNA-adapted shRNA
- Sequenced verified shRNA pools
- Equimolar pooling process for equal representation of shRNA in a pool

MORE Flexible

- *In vitro* or *in vivo* pool formats
- Plasmid DNA or lentiviral particles
- Choice of promoter allows screening in biologically relevant cells

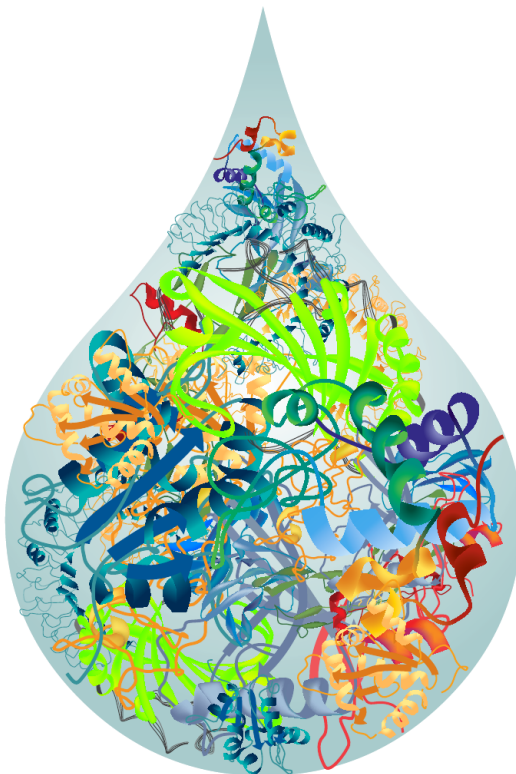
for **MORE** Confidence
in calling hits

Achieve superior RNAi screens with enhanced potency, sequence-verified shRNA pools and flexible delivery strategies. **shERWOOD-UltramiR lentiviral shRNA pooled screening libraries** are available targeting the human and mouse genome, epigenome, kinome, cancer metabolism, druggable and more. Catalog (Gene Ontology based) or Cusom (gene list, promoter, format and volume) are available. Need higher volumes of pooled viral particles? Contact us for more detail and volume based pricing.



Visit www.transomic.com/pooledscreening
for more details and to place your order.

Enabling Discovery Across the Genome



What's in Your Sample? Find Your Answers!



[rnsystems.com/
Immunoassays](https://rnsystems.com/Immunoassays)

Foreword



We are happy to present the latest edition in our annual *Best of Neuron* series. In this edition, we've looked back on the work we had the privilege to publish in the second half of 2014 and the first half of 2015 and put together this collection of resources, reports, and articles. We're extremely proud of all of the work found within the pages of *Neuron*, and choosing a "best of" list is always a challenge. We considered several factors when selecting articles for this edition. To ensure that our readers' voices were heard, we looked through our most highly downloaded articles (from publication on July 1, 2014 through June 30, 2015) to find those that captured the greatest interest from the community. We also wanted to represent the broad scope of *Neuron*, so inside you'll find articles touching on a wide range of topics, encapsulating the breadth of the journal's coverage.

This collection presents five NeuroResources, three short reports, and four full-length articles spanning the most exciting research of the last year. Included is a resource that is the first paper from the BRAIN initiative describing a new DREADD to silence neurons for multiplexed chemogenetic control of neural activity, a report demonstrating the discovery of small molecules that target repeat-containing RNA in C9ORF72 to block C9FTD/ALS-associated defects and reveal a potential biomarker for c9FTD/ALS, and an article that shows how states of curiosity in humans modulate hippocampus-dependent learning via dopaminergic circuitry.

We hope that you will enjoy reading this special collection. We'd like to thank all of our authors and reviewers: your contributions are what make *Neuron* great. Please be sure to check out the latest findings published in *Neuron* by visiting our homepage (www.cell.com/neuron) and signing up for our email alerts. And if you can't wait until next year's *Best of Neuron* edition to see what your colleagues find most exciting, stay on top of what they've been reading over the past 30 days at www.cell.com/neuron/mostread. Also be sure to visit www.cell.com to find other high-quality papers from all of our sister journals at Cell Press.

Finally, we are grateful for the generosity of our sponsors, who helped make this reprint collection possible, and we look forward to many more years of excellent neuroscience.

Neuron



For information for the Best of Series, please contact:

Jonathan Christison
Program Director, Best of Cell Press
e: jchristison@cell.com
p: 617-397-2893
t: @CellPressBiz

Dharmacon™

RNAi, Gene Expression, and Gene Editing



Specific, functional, and scalable

CRISPR-Cas9 gene editing

Simplify CRISPR-Cas9 gene editing with Dharmacon **predesigned CRISPR guide RNA reagents**. Selected by the **proprietary Dharmacon CRISPR RNA algorithm**, **these genome-wide products** are designed with unparalleled specificity checking, plus selection criteria trained and validated on functional knockout data. Now you can easily order specific, functional, predesigned CRISPR guide RNAs – without any time-consuming design steps or tedious cloning – for editing one gene or thousands.

Optimized tools for confident CRISPR-Cas9 genome engineering

gelifesciences.com/dharmacon

STUDY BIOENERGETICS

Assays Available for:

**Mitochondrial
Complexes I, II, III, IV, & V**

**Oxygen
Consumption Rate**

**Mitochondrial
Isolation**

**Citrate
Synthase Activity**

**Membrane
Potential**

Glycolysis



**BIOCHEMICALS • ASSAY KITS • ANTIBODIES
PROTEINS • RESEARCH SERVICES**

View our line of bioenergetics assay kits and other research tools at
www.caymanchem.com/bioenergetics

We make human cells.

We can't state it more simply: We manufacture human cells from induced pluripotent stem cells. Our highly pure iCell® and MyCell® products are consistent and reproducible from lot-to-lot, enabling you to focus on the biology . . . and what drives your research.

True Human Biology. Why use an animal or immortalized cell model as a proxy when a true human model, consistent across lots, is available? If you have a phenotype of interest, we can make iPSCs and terminal cells from your donors.

Highly Characterized. Highly Predictive. Our cells have the appropriate gene and protein expression and the relevant physiological response of the target cell type, with numerous peer-reviewed publications detailing their characterization and predictivity of human response.

MORE Cells. CDI provides more cells than other providers: 96-well capacity per vial. GUARANTEED.

**Any cell type.
Any genotype.
Any quantity.**



**CELLular
Dynamics
international**
a FUJIFILM company

You make:

safer medicines
discoveries
therapies
breakthroughs



Check out the iCell community of scientists who discuss the difference iCell products have made in their research:

www.cellulardynamics.com/community

Neuron

Best of 2014/2015

NeuroResources

Generation of Human Striatal Neurons by MicroRNA-Dependent Direct Conversion of Fibroblasts

Matheus B. Victor, Michelle Richner, Tracey O. Hermanstynne, Joseph L. Ransdell, Courtney Sobieski, Pan-Yue Deng, Vitaly A. Klyachko, Jeanne M. Nerbonne, and Andrew S. Yoo

A New DREADD Facilitates the Multiplexed Chemogenetic Interrogation of Behavior

Eyal Vardy, J. Elliott Robinson, Chia Li, Reid H.J. Olsen, Jeffrey F. DiBerto, Patrick M. Giguere, Flori M. Sassano, Xi-Ping Huang, Hu Zhu, Daniel J. Urban, Kate L. White, Joseph E. Rittiner, Nicole A. Crowley, Kristen E. Pleil, Christopher M. Mazzone, Philip D. Mosier, Juan Song, Thomas L. Kash, C.J. Malanga, Michael J. Krashes, and Bryan L. Roth

Epigenomic Signatures of Neuronal Diversity in the Mammalian Brain

Alisa Mo, Eran A. Mukamel, Fred P. Davis, Chongyuan Luo, Gilbert L. Henry, Serge Picard, Mark A. Urich, Joseph R. Nery, Terrence J. Sejnowski, Ryan Lister, Sean R. Eddy, Joseph R. Ecker, and Jeremy Nathans

Cell Lineage Analysis in Human Brain Using Endogenous Retroelements

Gilad D. Evrony, Eunjung Lee, Bhaven K. Mehta, Yuval Benjamini, Robert M. Johnson, Xuyu Cai, Lixing Yang, Psalm Haseley, Hillel S. Lehmann, Peter J. Park, and Christopher A. Walsh

Transgenic Mice for Intersectional Targeting of Neural Sensors and Effectors with High Specificity and Performance

Linda Madisen, Aleena R. Garner, Daisuke Shimaoka, Amy S. Chuong, Nathan C. Klapoetke, Lu Li, Alexander van der Bourg, Yusuke Niino, Ladan Egholf, Claudio Monetti, Hong Gu, Maya Mills, Adrian Cheng, Bosiljka Tasic, Thuc Nghi Nguyen, Susan M. Sunkin, Andrea Benucci, Andras Nagy, Atsushi Miyawaki, Fritjof Helmchen, Ruth M. Empson, Thomas Knöpfel, Edward S. Boyden, R. Clay Reid, Matteo Carandini, and Hongkui Zeng

Reports

Discovery of a Biomarker and Lead Small Molecules to Target r(GGGGCC)-Associated Defects in c9FTD/ALS

Zhaoming Su, Yongjie Zhang, Tania F. Gendron, Peter O. Bauer, Jeannie Chew, Wang-Yong Yang, Erik Fostvedt, Karen Jansen-West, Veronique V. Belzil, Pamela Desaro, Amelia Johnston, Karen Overstreet, Seok-Yoon Oh, Peter K. Todd, James D. Berry, Merit E. Cudkowicz, Bradley F. Boeve, Dennis Dickson, Mary Kay Floeter, Bryan J. Traynor, Claudia Morelli, Antonia Ratti, Vincenzo Silani, Rosa Rademakers, Robert H. Brown, Jeffrey D. Rothstein, Kevin B. Boylan, Leonard Petrucelli, and Matthew D. Disney

Cortical Representations Are Reinstated by the Hippocampus during Memory Retrieval

Kazumasa Z. Tanaka, Aleksandr Pevzner, Anahita B. Hamidi, Yuki Nakazawa, Jalina Graham, and Brian J. Wiltgen

Pupil Fluctuations Track Fast Switching of Cortical States during Quiet Wakefulness

Jacob Reimer, Emmanouil Froudarakis, Cathryn R. Cadwell, Dimitri Yatsenko, George H. Denfield, and Andreas S. Tolias

(continued)

Articles

Distinct Tau Prion Strains Propagate in Cells and Mice and Define Different Tauopathies

David W. Sanders, Sarah K. Kaufman, Sarah L. DeVos, Apurwa M. Sharma, Hilda Mirbaha, Aimin Li, Scarlett J. Barker, Alex C. Foley, Julian R. Thorpe, Louise C. Serpell, Timothy M. Miller, Lea T. Grinberg, William W. Seeley, and Marc I. Diamond

Loss of mTOR-Dependent Macroautophagy Causes Autistic-like Synaptic Pruning Deficits

Guomei Tang, Kathryn Gudsruk, Sheng-Han Kuo, Marisa L. Cotrina, Gorazd Rosoklija, Alexander Sosunov, Mark S. Sonders, Ellen Kanter, Candace Castagna, Ai Yamamoto, Zhenyu Yue, Ottavio Arancio, Bradley S. Peterson, Frances Champagne, Andrew J. Dwork, James Goldman, and David Sulzer

Increases in Functional Connectivity between Prefrontal Cortex and Striatum during Category Learning

Evan G. Antzoulatos and Earl K. Miller

States of Curiosity Modulate Hippocampus-Dependent Learning via the Dopaminergic Circuit

Matthias J. Gruber, Bernard D. Gelman, and Charan Ranganath



Are you still injecting?

Focus on your research instead, and let ALZET® Osmotic Pumps do the dosing for you.

ALZET pumps are a superior alternative to repetitive injections and other dosing methods that require frequent animal handling. These fully implantable pumps provide continuous and precise administration, for up to 6 weeks with a single pump, to unrestrained lab animals as small as mice. ALZET pumps are economical and easy to use by research personnel. Connection to a catheter enables direct delivery to vessels, cerebral ventricles, and other target sites. Learn more at alzet.com.

Now available: iPRECIO Pumps

- Programmable
- Refillable
- Implantable
- Small size for mice and rats

Learn more at www.alzet.com/iprecio



BAKER

Environments For Science™

From the moment when
the pieces fell into place,
and you saw the big picture,

through late nights reviewing literature,
designing procedures,
testing hypotheses —

nothing fell through the cracks,
because too much was at stake.

The work you did then
advanced your field,
and your career.

We are proud to have been there,
protecting your work, and you,
with the very best in air containment,
contamination control, and
controlled environment technology.

Now, as your work gives rise
to new discoveries —

**We can't wait to see
what you do next.**



bakerco.com

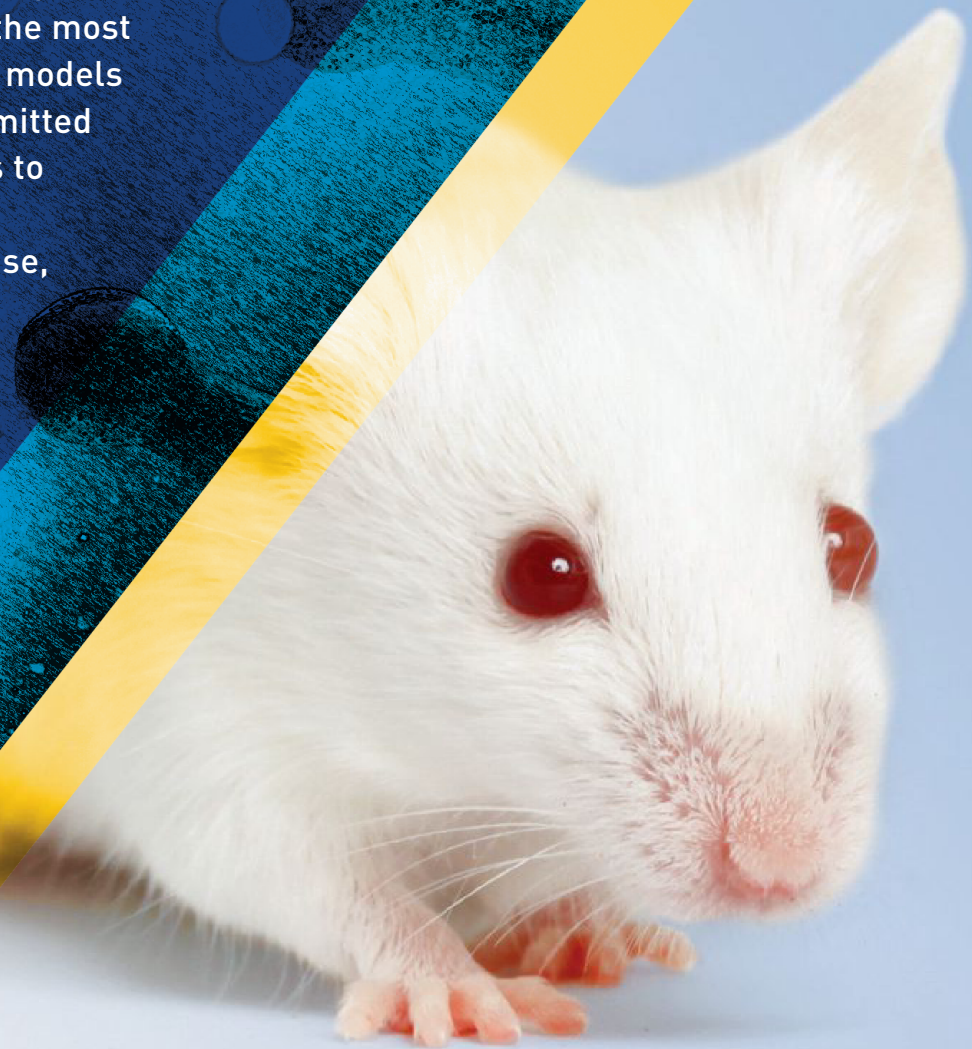
Biological Safety Cabinets • Clean Benches • Fume Hoods • CO₂ Incubators • Hypoxia & Anaerobic Workstations

ACCELERATING DRUG DISCOVERY

With ever-increasing precision, JAX[®] Mice, Clinical & Research Services offers definitive solutions for therapeutic development and efficacy evaluation. With the most innovative pre-clinical mouse models and applications, we are committed to providing you with the tools to propel science, delineate the mechanisms underlying disease, and enable efficacy testing of novel drugs.

To learn more visit:

jax.org



The Jackson
Laboratory

Knock Out Any Gene!



CRISPR/CAS 9 Genome Editing Kits

OriGene's system for genome disruption and gene replacement delivers pre-designed plasmids and all the vectors needed to knock out any human or mouse gene. Knockout is as simple as 1-2-3:

- 1 Search the gene symbol on origene.com and order
- 2 Follow the simple protocol for transfection and Puro selection
- 3 Validate the knockout

Kit Components Include:

- 2 guide RNA vectors to ensure efficient cleavage
- Donor vector with predesigned homologous arms
- Knockin GFP-Puro for selection
- Scramble gRNA as negative control included



Scan to view
CRISPR/Cas-9 Video

Come to OriGene,
the trusted molecular biology
expert, for your CRISPR needs.

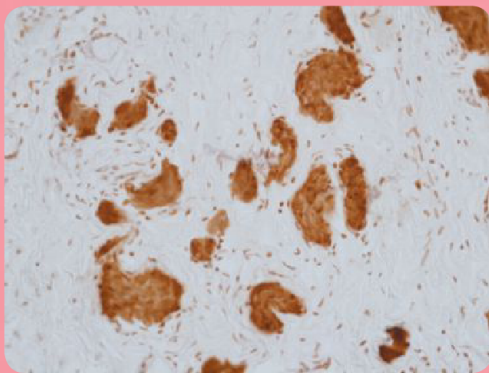


www.origene.com/CRISPR-CAS9



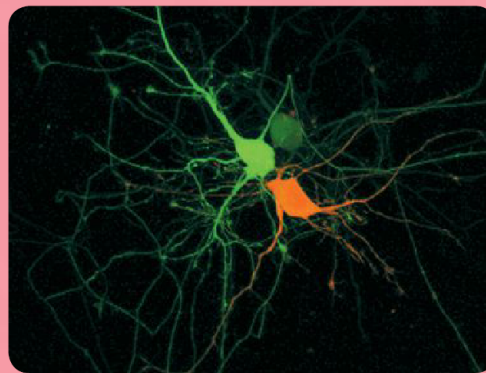
DISCOVERING SOLUTIONS TOGETHER

MBL International Corporation offers a wide range of antibodies, ELISA kits, and fluorescent vectors designed to support clinicians and researchers searching for the missing piece in neurodegenerative disease.



Submucosal hypertrophic nerve trunks in Hirschsprung's disease (x400)

Photo provided by Dr. Kobayashi Hiroyuki, Department of Pediatric Surgery, Juntendo University School of Medicine.



Kaede, a photoconvertible fluorescent protein, transfected neuron cells.

Red cell is irradiated with UV to convert fluorescence

Contact MBL International today to learn more about our other product listings to help you discover ways to make your science more efficient and effective.

mblintl.com
contact us: sales@mblintl.com

life.science.discovery.™

MBL[®]
International Corporation

The BMG LABTECH All Stars

Innovative, high-performance microplate readers for all assay needs



PHERAst[®] FS

The gold standard for High Throughput Screening. The PHERAst[®] FS is the ultimate multi-mode microplate reader, combining the highest sensitivity with the fastest read times in all microplate formats up to 3456-wells.

CLARIOstar[®]

The most sensitive monochromator-based microplate reader. Equipped with revolutionary LVF monochromators[™], it is the perfect reader for flexible assay development.

Omega series

Single and multi-mode filter-based plate readers. The perfect combination of flexibility and performance for life science applications.

SPECTROstar[®] Nano

Ultra-fast UV/Vis absorbance spectra in microplates and cuvettes.

Find all our microplate readers on www.bmglabtech.com



World-class innovation.
German engineering.
Local support.

250



BIO-RAD'S DROPLET DIGITAL™ PCR SYSTEMS

Over 250 Peer-Reviewed Droplet Digital PCR (ddPCR™) Publications*

From detection of rare mutations and cancer biomarkers to quantification of gene editing events and miniscule viral loads, the QX100™ and QX200™ Droplet Digital PCR Systems have been used to redefine the limits of absolute nucleic acid quantification. With over 250 peer-reviewed publications, ddPCR platforms have outperformed other digital PCR systems by several orders of magnitude. The third-generation QX200™ AutoDG™ System now brings automation and scalability to digital PCR.

Visit bio-rad.com/info/ddPCRelsevier for the publication list and to learn more.

* Based on PubMed data, July 2015.

BIO-RAD

Focused on antibodies for 40 years.
Not on advertising.

For really good antibodies, visit bethyl.com/trialsize



Generation of Human Striatal Neurons by MicroRNA-Dependent Direct Conversion of Fibroblasts

Matheus B. Victor,^{1,2,6} Michelle Richner,^{1,6} Tracey O. Hermanstynne,^{1,3} Joseph L. Ransdell,^{1,3} Courtney Sobieski,^{2,4} Pan-Yue Deng,⁵ Vitaly A. Klyachko,⁵ Jeanne M. Nerbonne,^{1,3} and Andrew S. Yoo^{1,*}

¹Department of Developmental Biology

²Program in Neuroscience

³Center for Cardiovascular Research

⁴Department of Psychiatry

Washington University School of Medicine, Saint Louis, MO 63110, USA

⁵Departments of Biomedical Engineering and Cell Biology and Physiology, CIMED, Washington University, Saint Louis, MO 63110, USA

⁶Co-first Authors

*Correspondence: yooa@wustl.edu

<http://dx.doi.org/10.1016/j.neuron.2014.10.016>

SUMMARY

The promise of using reprogrammed human neurons for disease modeling and regenerative medicine relies on the ability to induce patient-derived neurons with high efficiency and subtype specificity. We have previously shown that ectopic expression of brain-enriched microRNAs (miRNAs), miR-9/9* and miR-124 (miR-9/9*-124), promoted direct conversion of human fibroblasts into neurons. Here we show that coexpression of miR-9/9*-124 with transcription factors enriched in the developing striatum, BCL11B (also known as CTIP2), DLX1, DLX2, and MYT1L, can guide the conversion of human postnatal and adult fibroblasts into an enriched population of neurons analogous to striatal medium spiny neurons (MSNs). When transplanted in the mouse brain, the reprogrammed human cells persisted in situ for over 6 months, exhibited membrane properties equivalent to native MSNs, and extended projections to the anatomical targets of MSNs. These findings highlight the potential of exploiting the synergism between miR-9/9*-124 and transcription factors to generate specific neuronal subtypes.

INTRODUCTION

The generation of induced pluripotent stem cells (iPSCs) holds great promise for regenerative medicine and the study of human diseases (Takahashi and Yamanaka, 2006; Yu et al., 2007). Nevertheless, creating a reliable in vitro disease model based on deriving iPSCs from multiple human samples followed by differentiation into a specific cell subtype is a lengthy process, which can be further complicated by the variable and unpredictable nature across different iPSC lines (Hu et al., 2010). Moreover, reprogramming somatic cells to iPSCs has been shown

to reintroduce the embryonic state and therefore hinders the prospect of modeling late-onset disorders, although new methods are being developed that may overcome this barrier (Lapasset et al., 2011; Miller et al., 2013). Most importantly, current differentiation protocols often produce a population of cells with variable heterogeneity (Soldner and Jaenisch, 2012). Bypassing pluripotency and directly reprogramming readily accessible human tissues, such as skin, into neural cells may offer a fast and efficient approach to study neurological disorders (Caiazzo et al., 2011; Pang et al., 2011; Yoo et al., 2011). Although direct neuronal conversion may offer unique benefits, this approach is currently limited to a small number of protocols to specify neuronal subtypes using postnatal or adult human samples (Caiazzo et al., 2011; Liu et al., 2013; Ring et al., 2012; Son et al., 2011; Yoo et al., 2011).

MiR-9/9* and miR-124 are critical components of a genetic pathway that controls the assembly of neuron-specific, ATP-dependent chromatin remodeling complexes during neural development (Stahl et al., 2013; Yoo et al., 2009). In addition, these miRNAs have been shown to play key roles in the differentiation of neural progenitors to mature neurons by regulating the expression of antineural genes (Makeyev et al., 2007; Packer et al., 2008; Visvanathan et al., 2007; Xue et al., 2013). Ectopic expression of miR-9/9*-124 promotes the direct conversion of human adult fibroblasts toward neurons, a process greatly enhanced by coexpressing transcription factors, NeuroD2, ASCL1, and MYT1L, yielding a mixed population of excitatory and inhibitory neurons (Yoo et al., 2011). It remained unknown, nonetheless, whether the miR-9/9*-124-mediated neuronal conversion could yield a homogeneous population of a discrete neuronal subtype. Since the terminally differentiated state of neuronal subtypes can be instructed by transcription factors (Hobert, 2011), we hypothesized that transcription factors enriched in distinct brain regions could guide the miRNA-mediated neuronal reprogramming into a specific neuronal subtype.

In this study, we describe the identification of four transcription factors, CTIP2, DLX1, DLX2, and MYT1L (CDM), that synergize with miR-9/9*-124 to generate an enriched population of cells characteristic of striatal medium spiny neurons (MSNs), the

primary cell type affected in Huntington's disease (Albin et al., 1989). Importantly, this reprogramming relies on the activities of miR-9/9*-124, since CDM factors alone are ineffective for neuronal conversion. This combinatorial approach generates a large number of neurons with a gene expression profile analogous to primary human striatal cells microdissected from post-mortem brain sections. Furthermore, when transplanted into the mouse striatum, the reprogrammed neurons display functional properties similar to native MSNs. The high efficiency and specificity of our approach to directly derive human striatal MSNs will likely be advantageous in modeling disorders affecting MSNs such as Huntington's disease.

RESULTS

Enhancement of miR-9/9*-124-Mediated Reprogramming

We previously noticed that a large fraction of cells underwent cell death when transduced to express miR-9/9*-124 (Yoo et al., 2011). In an effort to optimize the miR-9/9*-124-mediated neuronal reprogramming, we tested if coexpression of an antiapoptotic gene would reduce the number of cells deaths during neuronal reprogramming. Previous studies have shown that abrogation of apoptosis could enhance neurogenesis (Sahay et al., 2011; Zhang et al., 2006) and that overexpression of an antiapoptotic gene *BCL2L1* (also known as *Bcl-xL*) suppressed programmed cell death (Alavian et al., 2011; Blömer et al., 1998). When we incorporated *Bcl-xL* into our lentiviral vector to be expressed with miR-9/9*-124 (Supplemental Experimental Procedures available online), we detected an increased number of surviving cells by over 40% and significantly improved the reprogramming efficiency (Figure S1). We utilized a doxycycline (Dox)-inducible promoter to temporarily regulate the expression of miR-9/9*-124 and *Bcl-xL*. Our characterization of the Dox-inducible promoter indicated that the transgene readily became inactive upon the removal of Dox within 3 days (Figure S2). We found that the continuous expression of miR-9/9*-124 for approximately 30 days was necessary for stable neuronal conversion as interrupting the transgene expression at day 15 resulted in a significant reduction in the neuronal conversion (Figure S2). Accordingly, in tissue culture as well as in experiments in vivo, we routinely withdrew Dox treatment after 30 days into reprogramming. Interestingly, we found that endogenous miR-9/9* and miR-124 were expressed after Dox removal by day 30 as the cells adopted a neuronal fate (Figure S2).

Identification of Transcription Factors to Specify Striatal Neurons

We focused on transcription factors expressed in the GABAergic MSNs of the striatum, a clinically relevant neuronal subtype affected in Huntington's disease (Albin et al., 1989). Striatum-enriched transcription factors were selected based on translational ribosome affinity purification data for DRD1- or DRD2-positive MSNs from the mouse striatum (Dougherty et al., 2010) and gene expression databases from Brainspan (<http://brainspan.org>) and Allen Brain Atlas (<http://human.brain-map.org/>). In order to identify transcription factors that would favor the MSN fate, we transduced human postnatal fibroblasts with lentivirus

to express miR-9/9*-124 and sixteen selected transcription factors individually and examined by immunostaining the number of MAP2-positive cells that were also positive for the neurotransmitter GABA and the dopamine- and cAMP-regulated neuronal phosphoprotein (DARPP-32), a well-documented marker of MSNs (Arlotta et al., 2008; Lobo et al., 2006; Ouimet and Greenard, 1990) (Figures 1A and S3). *BCL11B* (also known as *CTIP2*), a transcription factor critical for the differentiation of MSNs in vivo (Arlotta et al., 2008), was the only factor tested with miR-9/9*-124 to yield DARPP-32-positive neurons (Figure 1A). Furthermore, when miR-9/9*-124 were combined with *DLX1* and *DLX2*, previously shown to be important for terminal differentiation of MSNs (Anderson et al., 1997), we detected a large percentage of GABAergic neurons (72.3% of MAP2-positive cells) (Figure 1A). It is interesting to note that *MYT1L*, which has previously been used by our group and others to enhance direct neuronal reprogramming with other factors (Pang et al., 2011; Yoo et al., 2011), significantly increased the number of MAP2-positive cells when tested alone with miR-9/9*-124 (Figures 1A and S3). Importantly, single transcription factors tested without miR-9/9*-124 did not induce MAP2-positive cells (data not shown).

Immunostaining Analysis of Neuronal Markers

Based on our initial screening of individual transcription factors, we asked if the combination of *CTIP2*, *DLX1*, *DLX2* (*DLX1/2*), and *MYT1L* (collectively termed CDM) would synergize with miR-9/9*-124 to generate MSN-like cells (Figure 1A). We first determined if miR-9/9*-124 with CDM (miR-9/9*-124-CDM) would robustly generate neurons by examining the expression of general neuronal markers, MAP2, TUBB3 (also known as β -III tubulin), and NeuN (Figure 1B). Counting random fields of view revealed that approximately 90% of DAPI-positive cells were MAP2-positive ($n = 207$), 87% TUBB3-positive ($n = 328$), and 84% NeuN-positive ($n = 328$) at 5 weeks posttransduction (Figure 1C). The converted cells also expressed proteins important for neuronal function, including voltage-gated sodium channels (Figure 1D, left) and Synapsin 1 (Figure 1D, right). The neuronal conversion was dependent on miR-9/9*-124 as transducing human fibroblasts with CDM factors alone was ineffective in generating neurons (0.3% MAP2-positive, $n = 343$) (Figure 1E). Moreover, expression of CDM in human fibroblasts did not induce the expression of endogenous neural microRNAs such as miR-9/9*, miR-124, or miR-132 (Figure S4).

Detection of Markers of Medium Spiny Neurons

We found that the majority of the converted cells were GABAergic neurons (90% of MAP2-positive, $n = 474$) assayed by immunostaining for GABA (Figure 1F, top left, and S5, top, for larger overview) and GAD67 (Figures 1F, top right, and S5), without VGLUT1-positive (a marker for glutamatergic neurons) cells within the population of reprogrammed neurons (0.75% of MAP2-positive cells, $n = 400$; Figure S6). Furthermore, we found that a large fraction of converted neurons (70% of MAP2-positive, $n = 474$) expressed DARPP-32 (Figures 1G and S7 for view of GABAergic DARPP-32-positive cells) and expressed FOXP1 and *DLX5* (Figure 1F, bottom left and right, respectively; 1G for quantification; and S7 for larger fields of view), which are

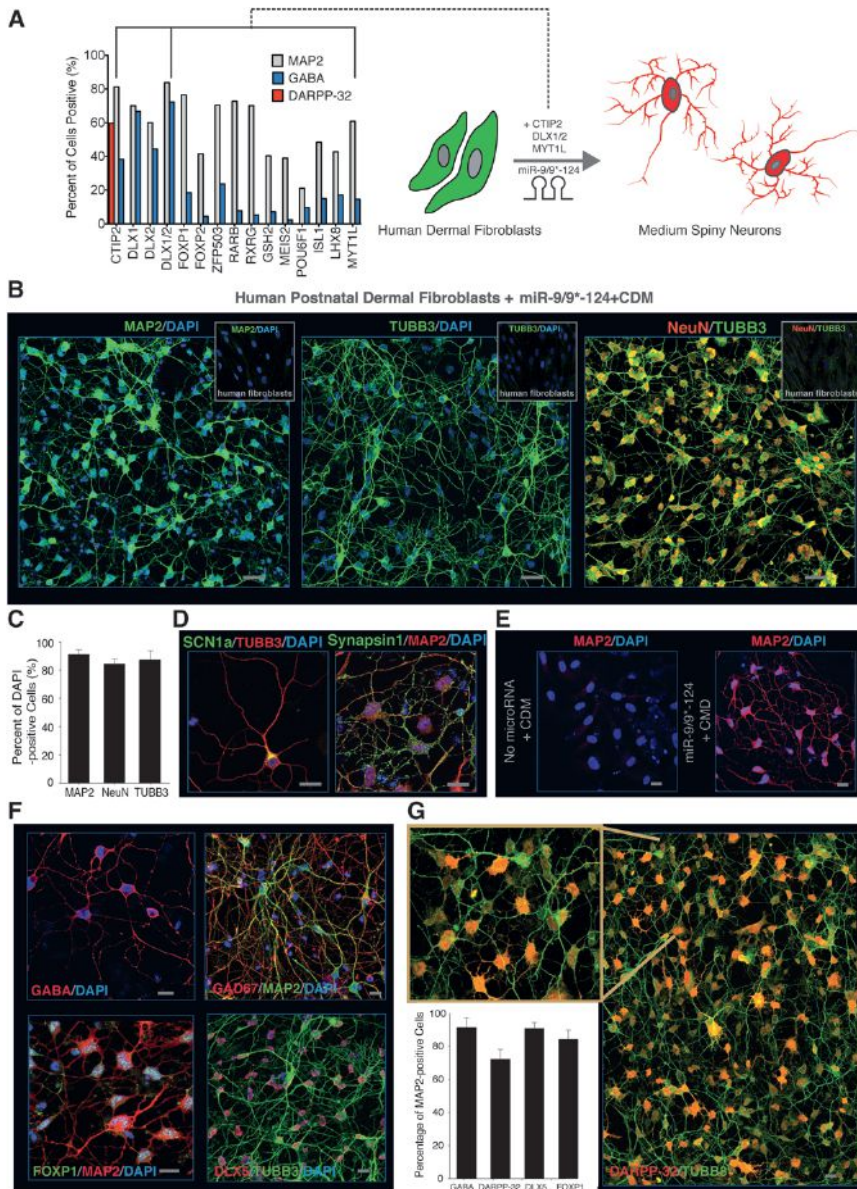


Figure 1. Neuronal Conversion of Human Fibroblasts by MicroRNAs and Striatal Factors

(A) Quantification by immunostaining of the synergistic effect of miRNAs and striatum-enriched factors represented by the percentage of human postnatal fibroblasts positive for MAP2, GABA, and DARPP-32 after 35 days of being transduced with miR-9/9*-124 in conjunction with striatum-enriched factors. On the right, diagram representing the ability of miR-9/9*-124 to generate striatal MSNs when combined with CTIP2, DLX1, DLX2, and MYT1L (CDM). (See Figure S3 for images of reprogrammed cells and other combinations attempted.)

(B) Expression of pan-neuronal markers, MAP2 (left), TUBB3 (middle), and NeuN (right) after neuronal conversion of human postnatal dermal fibroblasts with miR-9/9*-124 combined with transcription factors CDM. Larger scale views. Scale bar, 20 μ m.

(C) Quantification of MAP2-, NeuN-, and TUBB3-positive cells for DAPI signals from randomly picked fields of view. For MAP2 and TUBB3 quantification, only the cells with processes at least three times the length of the cell body were counted positive. MAP2: n = 207 cells; TUBB3: n = 328 cells; NeuN: n = 328 cells. The error bars are in SD.

(D) Expression of SCN1a and Synapsin 1 in miR-9/9*-124-CDM-converted cells. Scale bar, 20 μ m.

(E) Human postnatal fibroblasts transduced with CDM factors in the absence of miR-9/9*-124 did not generate neurons after 35 days, demonstrating the requirement of miR-9/9*-124 for neuronal conversion of human fibroblasts. Scale bar, 20 μ m.

(F and G) Expression of markers of GABAergic MSNs. GABA ([E], top left) and GAD67 ([E], top right). FOXP1 ([E], bottom left), DLX5 ([E], bottom right), and DARPP-32 (G) are proteins enriched in MSNs. The inset represents a magnified view of (G). The graph (in [G], bottom left) represents quantification of GABA, FOXP1, DLX5, and DARPP-32 expression in MAP2-positive cells. GABA: n = 474 cells; FOXP1: n = 232 cells; DLX5: n = 207 cells; DARPP-32: n = 260 cells. The error bars are in SD. Figures S5 and S7 provide larger overviews of these markers as well as GABAergic DARPP-32-positive cells and controls.

also highly expressed in MSNs (Desplats et al., 2006; Ferland et al., 2003; Stenman et al., 2003; Tamura et al., 2004). In addition, we found that the endogenous *DLX1* was also expressed in cells converted by miR-9/9*-124-CDM (Figure S8). Reprogramming human fibroblasts using miR-9/9*-124 with DLX1/2 and MYT1L but without CTIP2 yielded highly GABAergic neurons that were completely devoid of DARPP-32 expression (Figure S9).

Interestingly, overexpression of CTIP2 (*BCL11B*) has been shown to protect hematopoietic progenitor cells from apoptosis, partially through the activity of members of the BCL2 family, including Bcl-xL (Albu et al., 2007). We therefore tested if ectopically expressing CTIP2 would induce the expression of *Bcl-xL* but found no significant changes (Figure S4).

Single-Cell Gene Expression Profiling

To further characterize the converted cells, we performed multiplex gene expression analyses in single cells to determine the enrichment of neuronal subtypes. Single cells induced from postnatal human fibroblasts were collected at 5 weeks posttransduction and identified based on the expression of housekeeping genes, *GAPDH*, *RSP18*, and *HPRT1* (Figure 2A, left marked by green dendrogram; n = 76 cells). Consistent with our immunostaining data, we found that the majority of the induced cells were positive for gene products expressed in neurons including *MAP2*, *TUBB3*, and *MAPT*, as well as components of voltage-gated sodium channels (*SCN2A* and *SCN3A*), neural cell adhesion molecule (*NCAM1*), neuronal ankyrin (*ANK2*), brain-derived neurotrophic factor (*BDNF*), and the synapse-associated protein

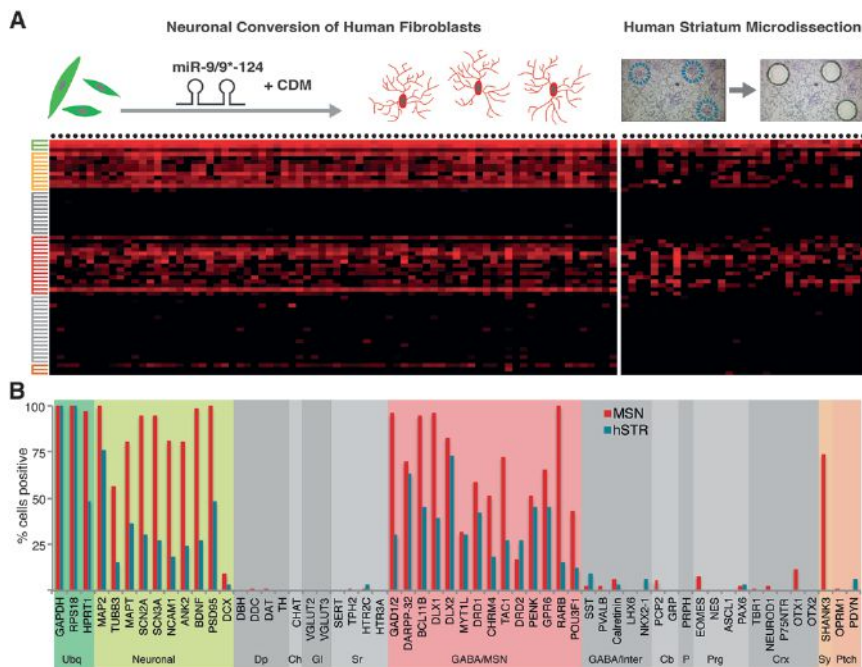


Figure 2. Single-Cell Gene Expression Analysis of Converted Cells and of Medium Spiny Neurons Microdissected from Human Adult Striatum

(A) Heatmap representation of multiplex qPCR of 76 converted cells (left) and 33 cells microdissected from postmortem human putamen sections (right). Each dot on top represents an individual cell and color-coded dendrograms denote genes of specific brain regions and cell types described in (B). Top illustrations represent the miR-9/9*-124-CDM-mediated neuronal conversion (left) and single-cell laser-microdissection of cresyl violet-stained human striatum sections (right).

(B) Quantification of percentages of converted cells and hMSNs for gene expression of specific neuronal types. Ubq: ubiquitous; Neuronal: genes generally expressed in neurons; Dp: dopaminergic; Ch: cholinergic; Gl: glutamatergic; Sr: serotonergic; GABA/MSN: GABAergic MSNs; GABA/Inter: GABAergic interneurons; Cb: cerebellum; P: peripheral nervous system; Prog: neural progenitors; Crx: cortical; Sy: presynaptic; Ptch: striatal patch. Figure S10 uses a pairwise comparison of these two sample groups to quantify the degree of similarity of gene expression profile.

PSD95 (also known as *DLG4*) (Figures 2A, left panel yellow dendrogram, and 2B, red bars). Interestingly, we did not detect the expression of doublecortin (*DCX*), a marker of immature, migratory neurons (Karl et al., 2005), suggestive of the maturity of the induced neurons. Importantly, miR-9/9*-124-CDM-induced cells were devoid of markers of dopaminergic neurons (*DBH*, *DDC*, *DAT*, and *TH*), cholinergic neurons (*CHAT*), glutamatergic neurons (*VGLUT2* and *VGLUT3*), and serotonergic neurons (*SERT*, *TPH2*, *HTR2C*, and *HTR3A*) (Figures 2A, left, gray dendrogram, and 2B). Instead, the majority of converted cells were positive for GABAergic markers (*GAD1/GAD2*) and *DARPP-32* (also known as *PPP1R1B*) in agreement with our immunostaining data. We also detected expression of genes associated with striatonigral (*DRD1*, *CHRM4*, and *TAC1*) and striatopallidal (*DRD2*, *PENK*, and *GPR6*) MSNs (Lobo et al., 2006) as well as transcription factors *RARB* and *POU3F1* (Figures 2A, left, red dendrogram, and 2B). *SHANK3*, which has been shown to be important for the synaptic function of MSNs (Peça et al., 2011), was also expressed in a high fraction of the converted cells. Interestingly, we did not detect expression of genes enriched in striatal patch neurons (*OPRM1* and *PDYN*) (Gong et al., 2003; Pert et al., 1976) in the converted cells. This suggests that the converted MSNs are likely to be of the striatal matrix (Figure 2B), which constitutes about 85% of the volume of the striatum (Johnston et al., 1990), consistent with the role of *DLX1/2* in specifying matrix neurons (Anderson et al., 1997).

Human Striatum Laser Microdissection

To compare the gene expression profile of the converted cells to primary striatal neurons in the human brain, we analyzed human striatal cells collected by laser capture microdissection (LCM) from human postmortem adult striatal sections using the same set of assay primers. Consistent with the notion that the striatum

is highly populated with MSNs (Gerfen, 1992), we detected that a large percentage of microdissected cells expressed *DARPP-32*. In addition, LCM samples expressed *CTIP2*, *DLX1*, *DLX2*, and *MYT1L*, and the overall gene expression profile was analogous to miR-9/9*-124-CDM-induced neurons (Figures 2A, right panel, and 2B, blue bars) (Figure S10 for pairwise comparison of LCM and reprogrammed MSNs). Importantly, miR-9/9*-124-CDM generated a homogenous population of MSNs, as we did not detect the expression of genes exclusive to striatal or cortical GABAergic interneurons (*SST*, *PVALB*, *Calretinin*, *LHX6*, and *NKX2-1*) (Marin et al., 2000; Tepper et al., 2010) (Figure 2). In both sets of data, genes enriched in the cerebellum (*PCP2* and *GRP*), peripheral nervous system (*PRPH*), neural progenitors (*EOMES*, *NES*, *ASCL1*, and *PAX6*), and in cortical neurons (*TBR1*, *NEUROD1*, *P75NTR*, *OTX1*, and *OTX2*) were also largely undetectable (Figure 2). Finally, a pairwise comparison of the expression of genes tested between the reprogrammed cells and microdissected human MSN (hMSN) indicated a strong correlation with a coefficient of determination (R squared) value of 0.77 (Figure S10). We also found miR-9/9* and miR-124 to be highly expressed in the human striatum (Figure S11), consistent with the expression of endogenous miR-9/9*-124 in converted MSNs (Figure S2).

Functional Properties of Reprogrammed hMSNs in Tissue Culture

The striatal circuitry is exceptionally intricate as it converges inputs from several brain regions with distinctive neurotransmitters, such as glutamatergic input from cortex and thalamus, dense dopaminergic innervation from substantia nigra, and local cholinergic and GABAergic inhibition (Graybiel et al., 1994). Many of these inputs have been shown to contribute to shaping the membrane properties and functional maturation of MSNs.

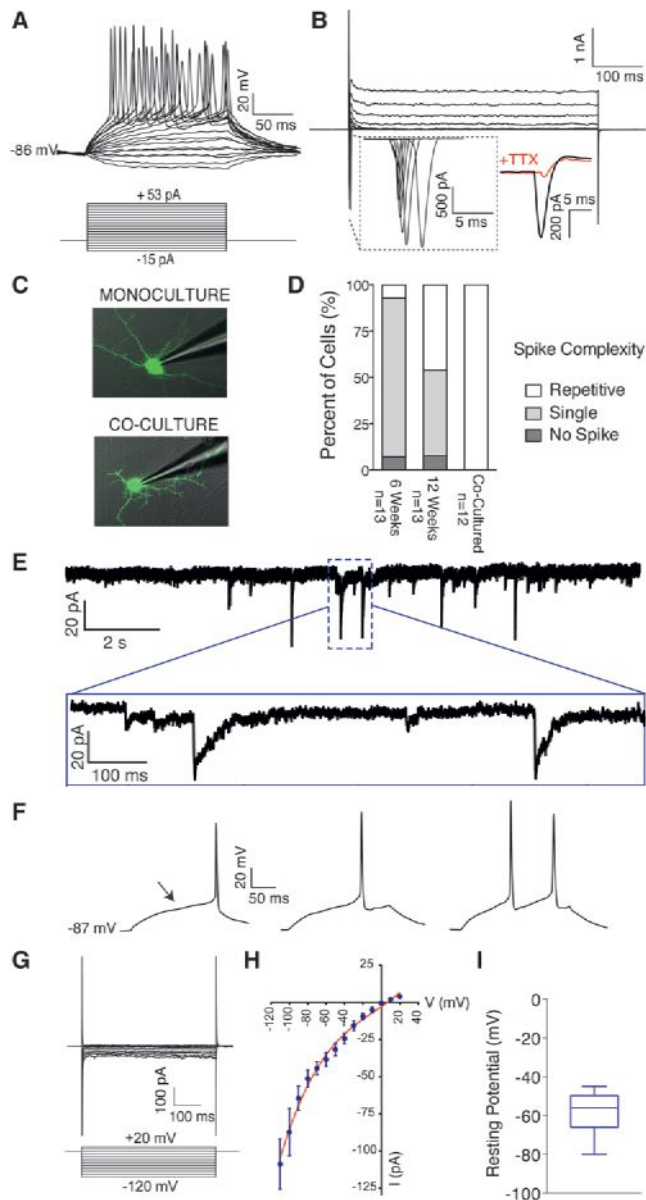


Figure 3. Electrophysiological Characteristics of Converted Medium Spiny Neurons in Tissue Culture

(A) Whole-cell current-clamp recording of MSNs converted from postnatal human fibroblasts. Converted human cells were cocultured with neonatal rat glia and displayed multiple APs in response to step current injections at 6 weeks posttransduction. All cells recorded ($n = 12$) fired APs in response to current injections.

(B) Representative traces of fast-inactivating inward currents recorded in voltage-clamp mode and blocked by 300 nM TTX. Voltage steps ranged from +10 to +70 mV.

(C and D) Increased complexity of AP spikes of converted cells when cocultured with glia. EGFP-tagged cells converted from postnatal fibroblasts were recorded at 6 or 12 weeks posttransduction. At 6 weeks, cells were recorded in the absence (monoculture) or presence of rat primary glia (coculture) (C). In monoculture, the majority of cells showed single spikes at 6 weeks posttransduction, whereas a larger percentage of cells recorded at 12 weeks generated repetitive APs. When cocultured with primary glia, all cells fired repetitively at 6 weeks (D). Intrinsic membrane properties are provided in Table S1.

For example, parvalbumin-expressing fast-spiking interneurons (PV-FSI) and neuropeptide-Y positive low-threshold spiking interneurons (NPY-LTS) have been shown to form synaptic connections with MSNs and regulate their firing activity (Do et al., 2012; Koós and Tepper, 1999). Therefore, MSNs can be distinguished *in vivo* not only due to their biochemical and anatomical differences but also by their intrinsic physiological properties. MSNs have been shown to rest at a hyperpolarized membrane potential (-80 mV to -90 mV), significant inwardly rectifying K^+ currents at or below resting membrane potentials, and a firing pattern with long delays to the initial action potential (AP) with little or no spike frequency accommodation (SFA) (Gertler et al., 2008; Venance and Glowinski, 2003). To examine the generic neuronal electrophysiological properties as well as MSN-specific properties in cells converted by miR-9/9*-124-CDM in tissue culture, we performed whole-cell patch-clamp recordings at 6 weeks posttransduction in converted cells cultured with rat primary glia. We found that all converted cells elicited multiple APs upon the injection of depolarizing currents (Figure 3A) and large fast-inactivating inward currents followed by outward potassium currents when evoked by a series of voltage steps (Figure 3B) (see Table S1 for intrinsic membrane properties) ($n = 12$). Inward currents were ablated upon local perfusion of tetrodotoxin (TTX) (300 nM), indicating that they were mediated via TTX-sensitive voltage-gated sodium channels (Figure 3B). To test the ability of converted cells to become electrically active in the absence of primary glia, we decided to investigate the membrane properties of our cells cultured in isolation (monoculture). Surprisingly, converted neurons were also capable of firing APs and displayed functional maturation over time in culture. Whereas the converted cells initially displayed modest APs at 6 weeks, a much more complex firing pattern with nearly 50% of the recorded cells firing repetitively was evident at 12 weeks posttransduction (shown in Figure 3D). In addition, converted cells displayed significantly larger peak amplitudes of inward currents at 12 weeks, correlated with increased excitability (see Figure S12 and Table S1 for additional traces and membrane properties). Since one of the major inputs impinging upon MSNs *in vivo* are excitatory glutamatergic afferents from the cerebral cortex (Kreitzer, 2009), we investigated if coculturing the converted cells with rat cortical neurons would lead to the formation of functional synapses. As seen by the synaptic currents (Figure 3E) (8 out of 13 total cells recorded), reprogrammed MSNs successfully mature into synaptically active neurons. In addition to determining that the reprogrammed cells are

(E) Representative trace of spontaneous postsynaptic currents from cocultured cells recorded at 12 weeks.

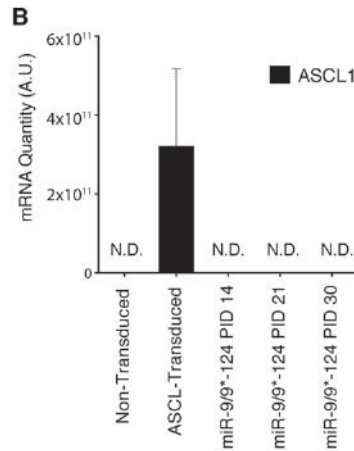
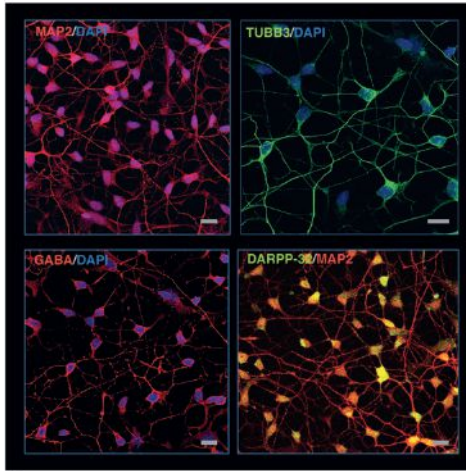
(F) Deconstructed traces from current-clamp recording shown in (A). The first spike event, followed by sequential steps is shown from left to right. Arrow denotes a latency to the initial spike characteristic of MSNs.

(G) Representative traces of inward rectifying currents generated from whole-cell voltage-clamp recording. Cells were stimulated with voltage steps ranging from -120 mV to +20 mV in 10 mV increments.

(H) Current levels at steady state were measured and plotted against holding voltage to generate an I-V curve fitted with a cubic spline curve (displayed in red) ($n = 7$).

(I) Resting membrane potentials of recorded cells ($n = 12$). Box and whisker plot is shown to represent the median as well as the greatest and lowest value.

A Human Adult Dermal Fibroblasts miR-9/9*-124 + CDM



C

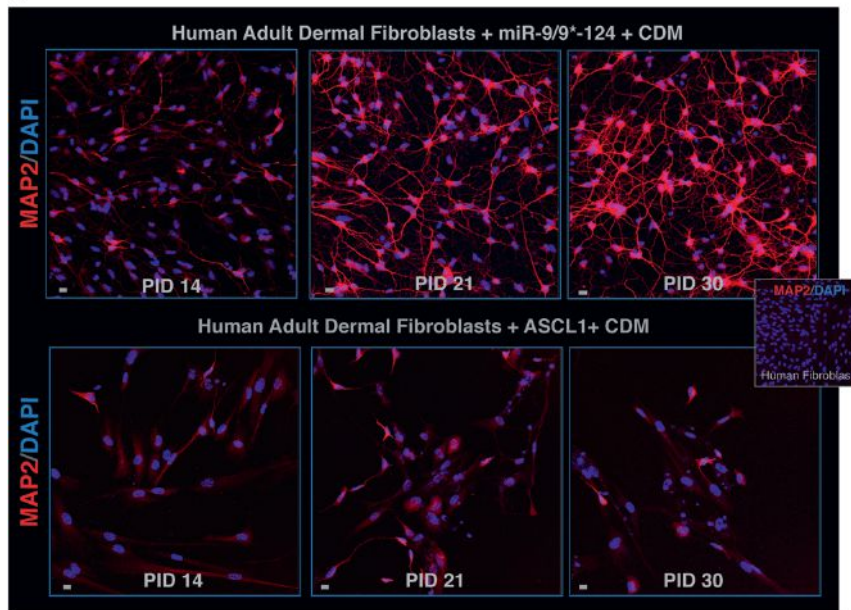


Figure 4. Conversion of Adult Human Fibroblasts Mediated by miR-9/9*-124 and Independent of ASCL1

(A) Expression of neuronal markers and markers of MSNs converted from adult human fibroblast (42 years old) transduced with miR-9/9*-124 + CDM. MAP2 (top left), TUBB3 (top right), GABA (bottom left), and DARPP-32 (bottom right).

(B) miR-9/9*-124-mediated neuronal reprogramming does not induce ASCL1 expression in human adult fibroblasts. miR-9/9*-124-expressing human adult fibroblasts were analyzed by qPCR at post-infection day (PID) 14, 21, and 30 for ASCL1 expression. As a positive control, a separate preparation of human fibroblasts was transduced with ASCL1 cDNA, and RNA was collected after 48 hr. N.D., not detected. Error bars = SEM.

(C) Testing whether ASCL1 could substitute miR-9/9*-124 for neuronal reprogramming of human adult fibroblasts. Human adult fibroblasts were transduced with either miR-9/9*-124 + CDM (top pictures) or ASCL1 + CDM (bottom pictures) and immunostained for MAP2 at PID 14, 21, and 30. Based on the observation that MAP2-positive neuronal cells were largely absent in ASCL1+CDM condition, miR-9/9*-124 is not interchangeable with ASCL1.

programming murine cells (Banito et al., 2009; Zhang et al., 2013). We asked whether the miR-9/9*-124-CDM-based approach could convert adult human fibroblasts into MSNs. We found that adult human dermal fibroblasts derived from a 42-year-old individual could be successfully converted into neurons with 82% of the cells being positive for MAP2 expression ($n = 405$ total cells) (representative image in Figure 4A). Consistent with the postnatal cells, the majority of adult cells were also GABAergic (86%, $n = 147$ total cells) and expressed DARPP-32 (77%, $n = 333$ total cells) (Figure 4A). In fact,

excitable, we also detected long delays to initial spike (Figure 3F) (6 out of 12 total cells recorded), a typical firing pattern of MSNs, whereas we only detected modest inward rectification (shown in Figure 3G and quantified in Figure 3H). We found that the degree of hyperpolarized resting membrane potential was minimal in tissue culture ($-58.35 \text{ mV} \pm 3.08$). The functional maturation of our cells from 6 to 12 weeks in monoculture (Figure S12) suggests that perhaps achieving a significantly hyperpolarized resting membrane potential requires longer culturing conditions. Consistently, MSNs from dissociated mouse striatal cultures have been shown to develop more negative membrane potentials with time in vitro (Lalchandani and Vicini, 2013).

Conversion of Adult Human Fibroblasts

Direct reprogramming of human postnatal and adult somatic cells into neurons has proved to be more challenging than re-

programming murine cells (Banito et al., 2009; Zhang et al., 2013). We asked whether the miR-9/9*-124-CDM-based approach could convert adult human fibroblasts into MSNs. We found that adult human dermal fibroblasts derived from a 42-year-old individual could be successfully converted into neurons with 82% of the cells being positive for MAP2 expression ($n = 405$ total cells) (representative image in Figure 4A). Consistent with the postnatal cells, the majority of adult cells were also GABAergic (86%, $n = 147$ total cells) and expressed DARPP-32 (77%, $n = 333$ total cells) (Figure 4A). In fact,

we found that miR-9/9*-124 could reprogram human fibroblasts from multiple individuals independent of the donor's age with a similar efficiency (Figure S3). The direct conversion of mouse fibroblasts into induced neurons has been reported with three transcription factors, BRN2, ASCL1, and MYT1L (Vierbuchen et al., 2010), while others have reprogrammed embryonic and fetal human fibroblasts with the same factors but supplemented with NeuroD1 (Pang et al., 2011; Son et al., 2011). Working solely with human postnatal fibroblasts, we showed that miR-9/9*-124 in combination with ASCL1, NEUROD2, and MYT1L successfully reprogrammed fibroblasts into functional neurons (Yoo et al., 2011). The role for ASCL1 in direct neuronal reprogramming (Caiazzo et al., 2011; Pang et al., 2011; Yoo et al., 2011) has recently been reported to be due in part to its activity as a pioneer transcription factor (Wapinski et al., 2013), and we asked if

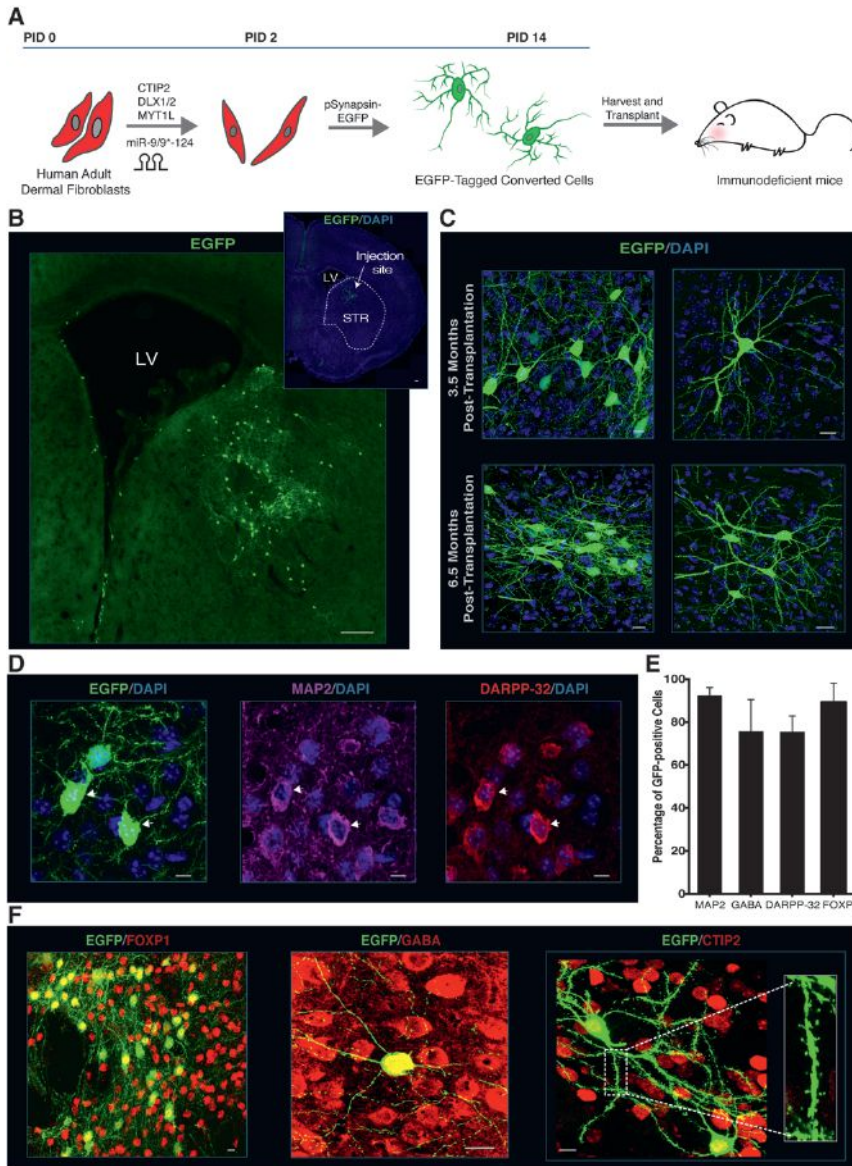


Figure 5. Engraftment and Long-Term Survival of Transplanted MSNs In Vivo

(A) A diagram illustrating our cell transplantation protocol. Human adult dermal fibroblasts were collected and cultured from a 22-year-old individual and transduced with lentivirus to express miR-9/9*-124 and CDM factors. At 2 days posttransduction, cells were transduced with additional lentivirus to label human cells with EGFP. At 2 weeks posttransduction, cells were harvested and transplanted into the striatum of NOD scid gamma immunodeficient mice.

(B) A low magnification of a coronal brain section showing transplanted human cells labeled with EGFP residing in the striatum. Scale bar, 80 μ m. The inset displays a reconstruction of the coronal brain section with DAPI in blue.

LV, Lateral ventricle. STR, Striatum.

(C) Low- and high-magnification views of EGFP-positive cells in situ for 3.5 and 6.5 months post-transplantation. Scale bar, 10 μ m.

(D) Expression of EGFP, MAP2, and DARPP-32. Arrows mark cells coexpressing all three markers. Scale bar, 10 μ m.

(E) Quantification of MAP2, GABA and DARPP-32, and FOXP1-positive cells for EGFP-expressing cells. MAP2: $n = 203$ cells; GABA: $n = 174$ cells; DARPP-32: $n = 173$ cells; FOXP1: $n = 173$ cells. Error bars are in SD.

(F) Expression of FOXP1, GABA, and CTIP2 in miR-9/9*-124-CDM. Inset highlights dendritic spines. Scale bar, 10 μ m.

miR-9/9*-124-mediated reprogramming involved the activity of ASCL1. We transduced human adult fibroblasts with miR-9/9*-124 to determine if *ASCL1* expression would be induced and found *ASCL1* expression to be undetectable upon the expression of miR-9/9*-124 at posttransduction days 14, 21, and 30 (Figure 4B). We also attempted to reprogram human adult fibroblasts into MSNs with CDM factors in conjunction with ASCL1. In comparison to miR-9/9*-124-CDM, ASCL1-CDM generated very few MAP2-positive cells that lacked neuronal morphologies (Figure 4C). Collectively, these findings indicate that miR-9/9*-124-mediated neuronal reprogramming is independent of the activity of ASCL1.

Functional Integration of Converted MSNs In Vivo

Next, we tested the ability of adult-derived cells to survive and differentiate in vivo by transplanting reprogrammed hMSNs

EGFP cells in mice even after 3.5 and 6.5 months, demonstrating the stable conversion and long-term survival of the reprogrammed cells (Figure 5C). EGFP-marked cells were 93% MAP2 positive ($n = 203$), 76% GABAergic ($n = 174$), 91% DARPP-32 positive ($n = 173$), and 91% FOXP1 positive ($n = 173$) (Figures 5D, 5E, and 5F). Moreover, transplanted cells exhibited dense dendritic spines (Figure 5F, right).

Membrane Properties of Converted MSNs In Vivo

We assessed the functional properties of reprogrammed hMSNs in vivo in comparison to native mouse MSNs (mMSNs) using whole-cell recordings in acute striatal slices at 112 DAT (Figure 6A). A total of 18 cells were targeted for recordings, including 11 non-EGFP mMSNs and 7 EGFP-positive hMSNs. Native mMSNs were identified and distinguished from striatal interneurons based on their characteristic membrane properties and AP

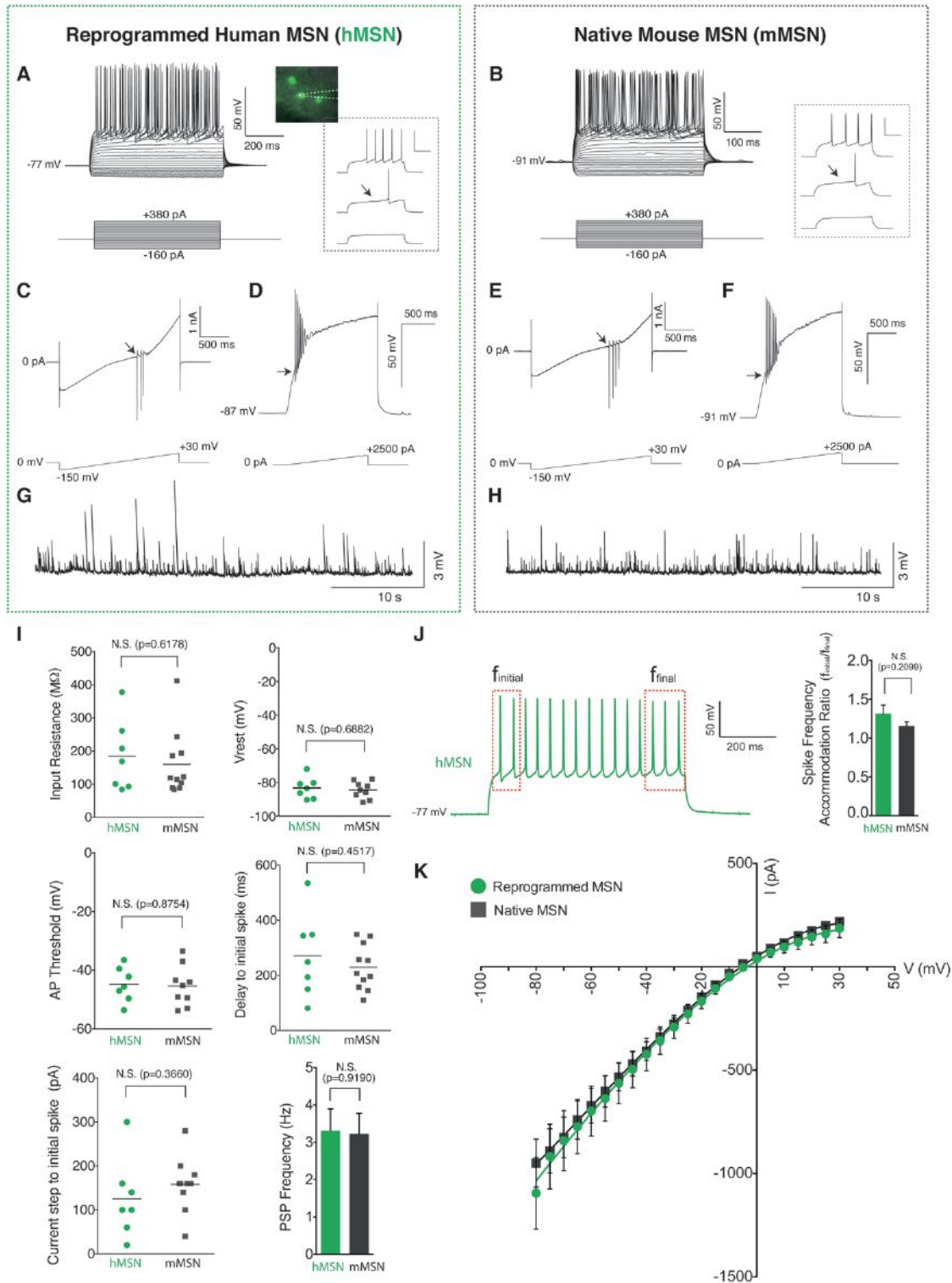


Figure 6. Functional Properties of Transplanted hMSNs in Comparison to mMSNs

(A and B) A total of 18 cells (7 EGFP-positive human cells and 11 non-EGFP mMSNs) were recorded from brains slices prepared at 16 weeks posttransplantation to compare membrane properties between reprogrammed human and mMSNs. AP trains were evoked by injecting current steps in EGFP-positive human cells (A) and mMSNs (B). The photograph depicts a representative image of whole-cell recording from an EGFP-positive cell in a striatal slice. Insets on the right show deconstructed traces of the first AP recorded, progressing from bottom to top. The arrows shown in the insets demonstrate delay to the initial spike, characteristic of MSNs. All 18 recorded cells were capable of generating repetitive APs.

(legend continued on next page)

firing patterns (Tepper et al., 2010). We found that all cells we examined (hMSNs and mMSNs) were able to fire AP trains when evoked by current steps and displayed long delays to initial AP spike (shown in the inset of Figures 6A and 6B and quantified in Figure 6I). Strong inward rectification, also characteristic of MSNs, was observed by an injection of voltage-ramp (Figure 6C for hMSNs and Figure 6E for mMSNs). The corresponding current-voltage relationship (I-V curve) was also identical between hMSNs and mMSNs (Figure 6K). Furthermore, we examined the AP threshold using a current-ramp protocol (Figure 6D for hMSNs and Figure 6F for mMSNs) and found no significant difference between the two cell types (Figure 6I). We then assessed whether transplanted cells were able to incorporate into local circuits by examining spontaneous postsynaptic potentials (sPSPs), which represent the network activity of surrounding neurons that form functional synapses onto hMSNs. As shown by the representative traces in Figures 6G and 6H, sPSPs were readily detected in all hMSNs (7 out of 7) and mMSNs (11 out of 11) with no significant difference in the sPSP frequency (Figure 6I), providing further evidence that transplanted cells could integrate into functional circuits *in vivo*. Additionally, we found that the resting membrane potentials of hMSNs were hyperpolarized ($-83.29 \text{ mV} \pm 2.40$) in hMSNs, similar to native mMSNs ($-85.20 \text{ mV} \pm 1.67$) (Figure 6I). We quantified the SFA ratio by calculating the frequency of the first spike (F_{initial}) in relation to the frequency of the average of the last two spike intervals (F_{final}), as previously reported (Venance and Glowinski, 2003). We found that both hMSNs and mMSNs displayed little to no spike accommodation with SFA values close to 1 (Figure 6J). Essentially, all membrane properties characteristic of MSNs that we analyzed were similar between transplanted and native MSNs during *ex vivo* recordings (Figure 6I).

Formation of Axonal Projections by Transplanted MSNs

Striatal MSNs give rise to projections terminating in two distinct nuclei within the basal ganglia, the globus pallidus and the substantia nigra, and these pair of nuclei in turn forms the two major striatal output systems (Gerfen, 1992). We therefore investigated whether transplanted hMSNs could extend projections into these distal targets of endogenous MSNs. Remarkably, we found EGFP-positive projections extending from the injection site in the dorsal striatum to the substantia nigra (six out of six brains analyzed at 56–64 DAT) with axon terminals also visible in the globus pallidus (Figure 7A). This finding signifies not only that reprogrammed hMSNs are capable of long distance axonal outgrowth but also that they recognize and follow axonal guid-

ance cues intrinsic to striatal projection neurons. Interestingly, although transplanted hMSNs are mostly confined within 1 mm of the injection site (Figure 7B), we observed that a small number of cells (4.7%; $n = 2,770$ cells) could be found beyond the striatal boundary (Figure 7C). Due to the required transduction of multiple lentiviral vectors, we suspected that cells adopting positions outside the striatum lacked the expression of one or more factors. We found that while the vast majority of our EGFP-positive cells residing within the striatum expressed CTIP2, the occasional EGFP-positive cells found outside the striatum mostly lacked the expression of CTIP2 (92.3% $n = 332$) (Figure 7C). Since CTIP2 is highly expressed in the striatum as seen by immunostaining (Figure 7D), this finding may suggest that expression of CTIP2 may be important for determining migratory boundaries for cells destined to become MSNs within the developing striatum.

DISCUSSION

In this study, we describe a method to directly convert human postnatal and adult fibroblasts into a highly enriched population of striatal MSNs, the main cell type affected in Huntington's disease. We find that our direct reprogramming approach offers an unprecedented technological advance in time and homogeneity of generating DARPP-32-positive neurons in comparison to cells derived from iPSCs (HD iPSC Consortium, 2012; Zhang et al., 2010). In addition, we show that the reprogrammed cells have an analogous gene expression profile to primary hMSNs captured by laser microdissection and, when transplanted into the murine striatum, can functionally integrate into the local circuit, persist *in situ* for over 6 months, and send projections to correct anatomical targets. In previous studies, directly reprogrammed human neurons exhibited decreased competence for synapse formation, which hampered their use in disease modeling and made differentiating iPSCs or embryonic stem cells into neurons more appealing (Zhang et al., 2013). In our current study, we present evidence that miRNA-dependent direct reprogramming generates functional neurons readily capable to form synapses *in vivo*. Lastly, our results demonstrate that miR-9/9*-124-CDM-mediated derivation of MSNs from human skin fibroblasts is efficient and consistent in multiple samples from postnatal to adult individuals.

The authenticity of our converted MSNs is likely due to the combinatorial code for gene expression generated by miR-9/9*-124-CDM, which resembles the endogenous cell differentiation program of MSNs. We paid particular attention to factors that could be instructive in defining different stages of the striatal

(C–F) Voltage ramp protocol from -150 mV to $+30 \text{ mV}$ shows inward rectification at hyperpolarized membrane potentials and outward currents as cells become depolarized in reprogrammed human cells (C) and mMSNs (E). Large inward currents can be seen as the cell reaches AP threshold (arrows). AP threshold was measured by assessing APs occurring with steady-state current injections in reprogrammed hMSNs (D) and mMSNs (F). Arrows demonstrate the onset of APs. (G and H) Representative traces of sPSPs recorded from transplanted human cells (G) and mMSNs (H). Seven out of seven EGFP-positive cells, and all mMSNs, displayed spontaneous PSPs. sPSP frequencies are quantified in the last graph of (I).

(I) Comparative analyses of active and passive membrane properties between hMSNs and mMSNs. Similar membrane properties were observed in all quantified properties, including input resistance, resting membrane potential (V_{rest}), AP threshold, delay time to initial spikes, current steps to initial spike, and PSP frequencies shown in (G) and (H). Individual data points are presented to show the degree of deviation from the mean. Histogram shown as mean \pm SEM. N.S., not significant by student t test.

(J) A representative AP trace from a hMSN illustrating the frequency ratio ($f_{\text{initial}}/f_{\text{final}}$) to determine SFAs, quantified at 40 pA above AP threshold. Histogram on the right shows no significant difference between hMSNs and mMSNs. Data presented as mean \pm SEM.

(K) I-V curves for hMSNs in green and mMSNs in gray, demonstrating large inward rectifications at hyperpolarized membrane potentials for both cases.

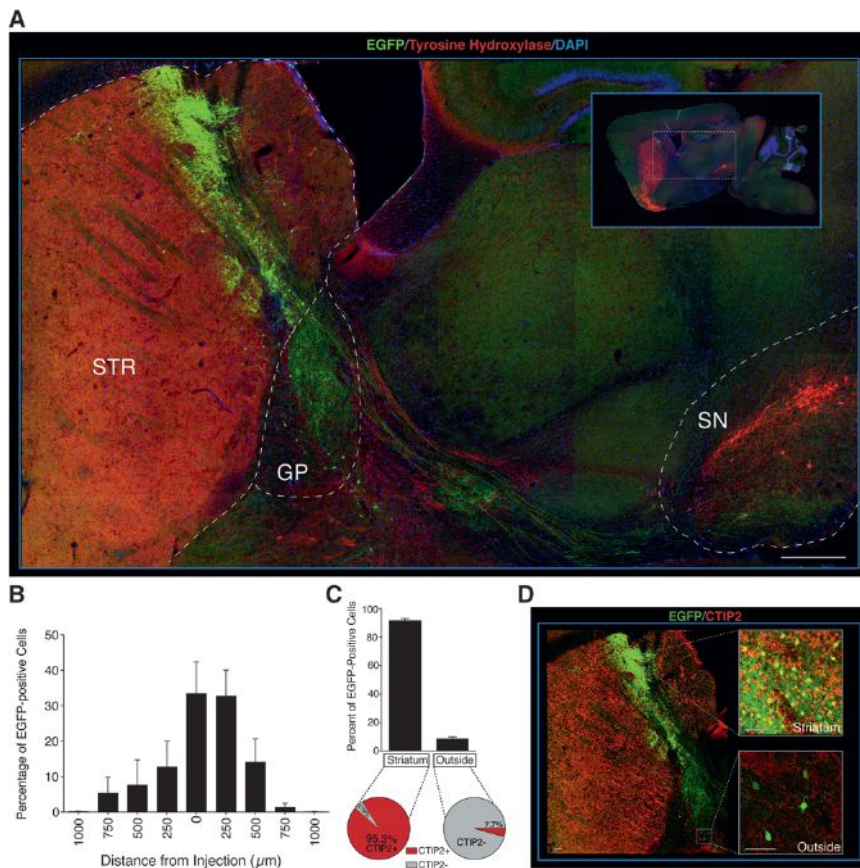


Figure 7. Establishment and Targeting of Axonal Projections by Transplanted HMSNs

(A) Midsagittal brain section immunostained with tyrosine hydroxylase in red labeling cell bodies in the substantia nigra (SN) and its dense innervation of the striatum (STR). EGFP-positive cells and dendrites can be seen dispersed throughout the dorsal striatum with projections extending to globus pallidus (GP) and substantia nigra (SN) in green. Scale bar, 300 μm .

(B) Quantification of cell migration in the medial-lateral axis from the injection site represented in the histogram as 0 μm . $n = 3$ animals with a total of 2,770 cells counted.

(C and D) The vast majority of EGFP-positive cells were confined within the striatum (95.3%), while a small population of cells was found beyond the striatal boundary ($n = 2,770$ cells counted for striatum versus outside) (C). While the vast majority of the EGFP-positive cells within the striatum were CTIP2 positive, nearly all the EGFP-positive cells found outside of the striatum lacked the expression of CTIP2 (quantified in the gray arc of the pie chart in [C] and pictured in [D]). $n = 332$ cells. Scale bar, 30 μm . Error bars = SEM.

cell lineage. For example, the expression of DLX1/2 in the absence of ASCL1 is known to form GABAergic neurons that originate from the same birthplace as MSNs, the ganglionic eminence of the ventral forebrain (Letinic et al., 2002). Later, as MSNs migrate away from the ganglionic eminence into the striatum, CTIP2 begins to be expressed and is maintained at high levels throughout adulthood (Arlotta et al., 2008). Similarly, the cells undergoing neuronal reprogramming were likely poised to a neuronal state by miR-9/9*-124 and MYT1L and refined to adopt a fate analogous to MSNs by the instruction of DLX1/2 and CTIP2. This process can be compared to a recent proposal that the attainment of a stable neuronal cell identity occurs in progressive steps in which a common neuronal identity is established first, and only after the initiation of refinement programs, a neuron becomes terminally differentiated (Fishell and Heintz, 2013). Similarly, we postulate that miR-9/9*-124 drives human fibroblasts into a neuronal state that can be further modulated by the instruction of lineage-specific fate determinants. This miR-9/9*-124-induced neuronal state can be characterized by (I) induction of proliferative cells to become post-mitotic, (II) acquisition of neuronal morphology, (III) induction of broadly expressed neuronal markers (MAP2, TUBB3, and NeuN) lacking markers of neuronal subtypes, (IV) induction of compositional changes in the neuron-specific BAF (nBAF) chromatin remodeling complexes (Staahl et al., 2013; Yoo et al., 2009), and lastly, (V) suppression of factors that antagonize the expression of neuron-specific genes, such as the RE1-silencing transcription

factor (REST/NRSF) and PTBP1 (Boutz et al., 2007; Conaco et al., 2006; Makeyev et al., 2007; Packer et al., 2008; Xue et al., 2013). In our current study, the overexpression of CDM was only capable of generating neurons when coexpressed with miR-9/9*-124, suggesting that these miRNAs promote a neuronal state permissive for the activity of terminal fate determinants. We postulate that this neuronal state may be, at least partially, due to the ability of miR-9/9*-124 to alter the chromatin landscape of non-neuronal cells during neural induction. Namely, miR-9/9* and miR-124 have been shown to regulate the activity of REST/NRSF complex (Packer et al., 2008; Visvanathan et al., 2007), which blocks the expression of neuronal genes in non-neuronal cells by recruiting and assembling a multimeric repressor complex composed of epigenetic regulatory factors (Ballas and Mandel, 2005). Therefore, the ectopic expression of miR-9/9*, which directly suppresses REST/NRSF, and miR-124, which targets the antineural factors PTBP1 and SCP1, results in activation of neuronal genes (Makeyev et al., 2007; Packer et al., 2008; Visvanathan et al., 2007). Importantly, miR-9/9*-124 orchestrate the switch of subunits of BAF chromatin remodeling complexes to promote a nBAF complex, an evolutionarily conserved process crucial for postmitotic neural development and dendritic morphogenesis (Yoo et al., 2009). It is interesting to note that REST-mediated neuronal gene repression has been demonstrated to be dependent on the activity of the BAF chromatin-remodeling complexes (Battaglioli et al., 2002). Even more intriguingly, CTIP2 (BCL11B) has recently been found to be a dedicated and stable subunit of the BAF complex (Kadoch et al., 2013). The ectopic expression of miR-9/9*-124 in conjunction with CTIP2 therefore is likely to shape the activity of the BAF complex and could potentially

explain our robust reprogramming toward a DARPP-32-positive cell fate, although this remains speculative. Collectively, the changes mediated by miR-9/9*-124 poise the cell to adopt a neurogenic state that can be influenced by lineage-specific transcription factors to guide neuronal conversion toward specific subtypes, as demonstrated in our study.

Moreover, we observed that several individual transcription factors besides CDM factors could robustly generate MAP2-positive human cells with miR-9/9*-124, although the subtype identity of these neurons are yet to be determined (Figure S3). This finding raises the possibility of simply fine-tuning the composition of additional transcription factors to generate various neuronal subtypes. Since our current study suggests that miR-9/9*-124-mediated reprogramming is independent of ASCL1, miR-9/9*-124-based reprogramming may be beneficial for inducing neuronal subtypes that do not contain ASCL1 in their endogenous differentiation program. Alternatively, ASCL1 may be combined with miR-9/9*-124 to derive neuronal subtypes where ASCL1 is involved in terminal differentiation. In summary, our study utilizing the neurogenic activities of microRNAs and transcription factors demonstrates an important step toward generating human neurons of a specific neuronal subtype, an experimental approach of extreme importance when studying neurological diseases affecting specific neuronal subtypes and brain regions.

EXPERIMENTAL PROCEDURES

Cell Culture

Lentiviral preparation of a Dox-responsive synthetic cluster of miR-9/9* and miR-124 (Yoo et al., 2011), as well as transcription factors cloned downstream of the EF1 α promoter, was used to transduce human postnatal or adult fibroblasts (ATCC and ScienCell). The following cell line was obtained from the NIGMS Human Genetic Cell Repository at the Coriell Institute for Medical Research: GM02171 and used for data shown in Figures 5 and S3 (C). Typically, infected human fibroblasts were maintained in fibroblast media for 2 days with Dox before replating onto coated coverslips. Cells were then selected with appropriate antibiotics in neuronal media (ScienCell) supplemented with valproic acid (1 mM), dibutyryl cAMP (200 μ M), BDNF (10 ng/ml), NT-3 (10 ng/ml), and RA (1 μ M). Dox was replenished every 2 days and media were changed every 4 days. A detailed reprogramming protocol is available in Supplemental Experimental Procedures.

Immunofluorescence

Cells were fixed using 4% paraformaldehyde or combined with 0.2% glutaraldehyde (both from Electron Microscopy Sciences) for 20 min at room temperature (RT) followed by permeabilization with 0.2% Triton X-100 for 10 min. One percent goat or donkey serum was used for blocking followed by incubation of primary antibodies overnight at 4°C. Secondary antibodies conjugated to Alexa-488, -594, or -647 were applied for 1 hr at RT. Detailed list of antibodies used and the procedure for immunohistochemistry analysis can be found in the Supplemental Experimental Procedures.

Single-Cell Quantitative PCR

Reprogrammed postnatal cells were harvested and single cells were collected by FACS sorting 5 weeks posttransduction. Deidentified human striatal sections from postmortem autopsy samples were obtained in accordance with the guideline of HRPO of Washington University School of Medicine. Postmortem single cells stained with cresyl violet were laser dissected from striatal putamen tissue sections of an 89-year-old individual. Samples were used for reverse-transcription and gene expression analysis using Fluidigm Dynamic arrays (see Supplemental Experimental Procedures).

Cell Harvesting and Transplantation

Reprogrammed cells were typically transduced with a Synapsin promoter-EGFP lentivirus at reprogramming day 2 and harvested for transplantation studies at reprogramming day 14. Adherent cell cultures were mechanically dissociated and concentrated by centrifugation (4 min at 1,000 RPM). Concentrated cell suspensions ($\sim 10^4$ cells/ μ l) were loaded into a 5 μ l Hamilton syringe (26 s/2/2 Gauge/Length/Point) and 2 μ l injected into the right striatum of NSG mice (P0 to P1).

Animals

Mice were maintained in standard housing conditions with food and water provided ad libitum. All procedures followed the guidelines of the Washington University's Institutional Animal Care and Use Committee (IACUC) and the Animal Studies Committee (ASC).

Electrophysiology, Slice Preparation, and Recordings

Detailed methods and description of the composition of internal and external solutions used for ex vivo recording can be found in the Supplemental Experimental Procedures.

SUPPLEMENTAL INFORMATION

Supplemental Information includes twelve figures, two tables, and Supplemental Experimental Procedures and can be found with this article online at <http://dx.doi.org/10.1016/j.neuron.2014.10.016>.

AUTHOR CONTRIBUTIONS

M.B.V., M.R., and A.S.Y. generated the hypotheses, designed experiments and wrote the manuscript. M.R. performed reprogramming experiments. M.B.V. generated data in Figures 3–7 and supplemental figures. C.S. generated data shown in Figure 3. A.S.Y. and M.R. generated data shown in Figure 2. J.M.N., T.O.H., and J.L.R. generated data in Figure 6. P.Y.D. and V.A.K. piloted in vivo electrophysiology experiments.

ACKNOWLEDGMENTS

We thank S. Dahiya and C. Huh for providing human striatum sections and performing laser microdissections and A. Soleiman for technical assistance. We thank J.D. Surmeier, S. Zakharenko, S. Mennerick, L. Solica-Krezel, and D. Abernathy for helpful suggestions with the manuscript; the Genome Technology Access Center in the Department of Genetics at Washington University School of Medicine for help with single-cell analysis; J. Ho and J. Richner for help with FACS sorting; and J. Dougherty for TRAP data analysis. M.B.V. is supported by the National Science Foundation Graduate Research Fellowship (DGE-1143954). C.S. is supported by the fellowship from Cognitive, Computational and Systems Neuroscience Pathway (T32N5023547) and a grant from NIH, MH078823. J.M.N. is supported by the National Institute of General Medical Sciences (R01 GM104991) and the National Heart Lung and Blood Institute (T.O.H. is supported by T32 HL007275). A.S.Y. is supported by NIH Director's Innovator Award (DP2) and awards from the Mallinckrodt Jr. Foundation, Ellison Medical Foundation, and Presidential Early Career Award for Scientists and Engineers.

Accepted: October 6, 2014

Published: October 22, 2014

REFERENCES

- Alavian, K.N., Li, H., Collis, L., Bonanni, L., Zeng, L., Sacchetti, S., Lazrove, E., Nabili, P., Flaherty, B., Graham, M., et al. (2011). Bcl-xL regulates metabolic efficiency of neurons through interaction with the mitochondrial F1FO ATP synthase. *Nat. Cell Biol.* 13, 1224–1233.
- Albin, R.L., Young, A.B., and Penney, J.B. (1989). The functional anatomy of basal ganglia disorders. *Trends Neurosci.* 12, 366–375.

- Albu, D.I., Feng, D., Bhattacharya, D., Jenkins, N.A., Copeland, N.G., Liu, P., and Avram, D. (2007). BCL11B is required for positive selection and survival of double-positive thymocytes. *J. Exp. Med.* *204*, 3003–3015.
- Anderson, S.A., Qiu, M., Bulfone, A., Eisenstat, D.D., Meneses, J., Pedersen, R., and Rubenstein, J.L. (1997). Mutations of the homeobox genes *Dlx-1* and *Dlx-2* disrupt the striatal subventricular zone and differentiation of late born striatal neurons. *Neuron* *19*, 27–37.
- Arlotta, P., Molyneaux, B.J., Jabaudon, D., Yoshida, Y., and Macklis, J.D. (2008). *Ctip2* controls the differentiation of medium spiny neurons and the establishment of the cellular architecture of the striatum. *J. Neurosci.* *28*, 622–632.
- Ballas, N., and Mandel, G. (2005). The many faces of REST oversee epigenetic programming of neuronal genes. *Curr. Opin. Neurobiol.* *15*, 500–506.
- Banito, A., Rashid, S.T., Acosta, J.C., Li, S., Pereira, C.F., Geti, I., Pinho, S., Silva, J.C., Azuara, V., Walsh, M., et al. (2009). Senescence impairs successful reprogramming to pluripotent stem cells. *Genes Dev.* *23*, 2134–2139.
- Battaglioli, E., Andrés, M.E., Rose, D.W., Chenoweth, J.G., Rosenfeld, M.G., Anderson, M.E., and Mandel, G. (2002). REST repression of neuronal genes requires components of the hSWI.SNF complex. *J. Biol. Chem.* *277*, 41038–41045.
- Blömer, U., Kafri, T., Randolph-Moore, L., Verma, I.M., and Gage, F.H. (1998). Bcl-xL protects adult septal cholinergic neurons from axotomized cell death. *Proc. Natl. Acad. Sci. USA* *95*, 2603–2608.
- Boutz, P.L., Stoilov, P., Li, Q., Lin, C.H., Chawla, G., Ostrow, K., Shiue, L., Ares, M., Jr., and Black, D.L. (2007). A post-transcriptional regulatory switch in poly-pyrimidine tract-binding proteins reprograms alternative splicing in developing neurons. *Genes Dev.* *21*, 1636–1652.
- Caiazzo, M., Dell'Anno, M.T., Dvoretzkova, E., Lazarevic, D., Taverna, S., Leo, D., Sotnikova, T.D., Menegon, A., Roncaglia, P., Colciago, G., et al. (2011). Direct generation of functional dopaminergic neurons from mouse and human fibroblasts. *Nature* *476*, 224–227.
- Conaco, C., Otto, S., Han, J.J., and Mandel, G. (2006). Reciprocal actions of REST and a microRNA promote neuronal identity. *Proc. Natl. Acad. Sci. USA* *103*, 2422–2427.
- HD iPSC Consortium (2012). Induced pluripotent stem cells from patients with Huntington's disease show CAG-repeat-expansion-associated phenotypes. *Cell Stem Cell* *11*, 264–278.
- Desplats, P.A., Kass, K.E., Gilmarin, T., Stanwood, G.D., Woodward, E.L., Head, S.R., Sutcliffe, J.G., and Thomas, E.A. (2006). Selective deficits in the expression of striatal-enriched mRNAs in Huntington's disease. *J. Neurochem.* *96*, 743–757.
- Do, J., Kim, J.I., Bakes, J., Lee, K., and Kaang, B.K. (2012). Functional roles of neurotransmitters and neuromodulators in the dorsal striatum. *Learn. Mem.* *20*, 21–28.
- Dougherty, J.D., Schmidt, E.F., Nakajima, M., and Heintz, N. (2010). Analytical approaches to RNA profiling data for the identification of genes enriched in specific cells. *Nucleic Acids Res.* *38*, 4218–4230.
- Ferland, R.J., Cherry, T.J., Preware, P.O., Morrissey, E.E., and Walsh, C.A. (2003). Characterization of *Foxp2* and *Foxp1* mRNA and protein in the developing and mature brain. *J. Comp. Neurol.* *460*, 266–279.
- Fishell, G., and Heintz, N. (2013). The neuron identity problem: form meets function. *Neuron* *80*, 602–612.
- Gerfen, C.R. (1992). The neostriatal mosaic: multiple levels of compartmental organization in the basal ganglia. *Annu. Rev. Neurosci.* *15*, 285–320.
- Gertler, T.S., Chan, C.S., and Surmeier, D.J. (2008). Dichotomous anatomical properties of adult striatal medium spiny neurons. *J. Neurosci.* *28*, 10814–10824.
- Gong, S., Zheng, C., Doughty, M.L., Losos, K., Didkovsky, N., Schambra, U.B., Nowak, N.J., Joyner, A., Leblanc, G., Hatten, M.E., and Heintz, N. (2003). A gene expression atlas of the central nervous system based on bacterial artificial chromosomes. *Nature* *425*, 917–925.
- Graybiel, A.M., Aosaki, T., Flaherty, A.W., and Kimura, M. (1994). The basal ganglia and adaptive motor control. *Science* *265*, 1826–1831.
- Hobert, O. (2011). Regulation of terminal differentiation programs in the nervous system. *Annu. Rev. Cell Dev. Biol.* *27*, 681–696.
- Hu, B.Y., Weick, J.P., Yu, J., Ma, L.X., Zhang, X.Q., Thomson, J.A., and Zhang, S.C. (2010). Neural differentiation of human induced pluripotent stem cells follows developmental principles but with variable potency. *Proc. Natl. Acad. Sci. USA* *107*, 4335–4340.
- Johnston, J.G., Gerfen, C.R., Haber, S.N., and van der Kooy, D. (1990). Mechanisms of striatal pattern formation: conservation of mammalian compartmentalization. *Brain Res. Dev. Brain Res.* *57*, 93–102.
- Kadoch, C., Hargreaves, D.C., Hodges, C., Elias, L., Ho, L., Ranish, J., and Crabtree, G.R. (2013). Proteomic and bioinformatic analysis of mammalian SWI/SNF complexes identifies extensive roles in human malignancy. *Nat. Genet.* *45*, 592–601.
- Karl, C., Couillard-Despres, S., Prang, P., Munding, M., Kilb, W., Brigadski, T., Plötz, S., Mages, W., Luhmann, H., Winkler, J., et al. (2005). Neuronal precursor-specific activity of a human doublecortin regulatory sequence. *J. Neurochem.* *92*, 264–282.
- Koós, T., and Tepper, J.M. (1999). Inhibitory control of neostriatal projection neurons by GABAergic interneurons. *Nat. Neurosci.* *2*, 467–472.
- Kreitzer, A.C. (2009). Physiology and pharmacology of striatal neurons. *Annu. Rev. Neurosci.* *32*, 127–147.
- Laichandani, R.R., and Vicini, S. (2013). Inhibitory collaterals in genetically identified medium spiny neurons in mouse primary corticostriatal cultures. *Physiol. Rep.* Published online November 24, 2013. <http://dx.doi.org/10.1002/phy2.164>.
- Lapasset, L., Milhavel, O., Prieur, A., Besnard, E., Babled, A., Ait-Hamou, N., Leschik, J., Pellestor, F., Ramirez, J.M., De Vos, J., et al. (2011). Rejuvenating senescent and centenarian human cells by reprogramming through the pluripotent state. *Genes Dev.* *25*, 2248–2253.
- Letinic, K., Zoncu, R., and Rakic, P. (2002). Origin of GABAergic neurons in the human neocortex. *Nature* *417*, 645–649.
- Liu, M.L., Zang, T., Zou, Y., Chang, J.C., Gibson, J.R., Huber, K.M., and Zhang, C.L. (2013). Small molecules enable neurogenin 2 to efficiently convert human fibroblasts into cholinergic neurons. *Nat. Commun.* *4*, <http://dx.doi.org/10.1038/ncomms3183>.
- Lobo, M.K., Karsten, S.L., Gray, M., Geschwind, D.H., and Yang, X.W. (2006). FACS-array profiling of striatal projection neuron subtypes in juvenile and adult mouse brains. *Nat. Neurosci.* *9*, 443–452.
- Makeyev, E.V., Zhang, J., Carrasco, M.A., and Maniatis, T. (2007). The MicroRNA miR-124 promotes neuronal differentiation by triggering brain-specific alternative pre-mRNA splicing. *Mol. Cell* *27*, 435–448.
- Marin, O., Anderson, S.A., and Rubenstein, J.L. (2000). Origin and molecular specification of striatal interneurons. *J. Neurosci.* *20*, 6063–6076.
- Miller, J.D., Ganat, Y.M., Kishinevsky, S., Bowman, R.L., Liu, B., Tu, E.Y., Mandal, P.K., Vera, E., Shim, J.W., Kriks, S., et al. (2013). Human iPSC-based modeling of late-onset disease via progerin-induced aging. *Cell Stem Cell* *13*, 691–705.
- Ouimet, C.C., and Greengard, P. (1990). Distribution of DARPP-32 in the basal ganglia: an electron microscopic study. *J. Neurocytol.* *19*, 39–52.
- Packer, A.N., Xing, Y., Harper, S.Q., Jones, L., and Davidson, B.L. (2008). The bifunctional microRNA miR-9/miR-9* regulates REST and CoREST and is downregulated in Huntington's disease. *J. Neurosci.* *28*, 14341–14346.
- Pang, Z.P., Yang, N., Vierbuchen, T., Ostermeier, A., Fuentes, D.R., Yang, T.Q., Citri, A., Sebastiano, V., Marro, S., Südhof, T.C., and Wernig, M. (2011). Induction of human neuronal cells by defined transcription factors. *Nature* *476*, 220–223.
- Peça, J., Feliciano, C., Ting, J.T., Wang, W., Wells, M.F., Venkatraman, T.N., Lascola, C.D., Fu, Z., and Feng, G. (2011). Shank3 mutant mice display autistic-like behaviours and striatal dysfunction. *Nature* *472*, 437–442.
- Pert, C.B., Kuhar, M.J., and Snyder, S.H. (1976). Opiate receptor: autoradiographic localization in rat brain. *Proc. Natl. Acad. Sci. USA* *73*, 3729–3733.

- Ring, K.L., Tong, L.M., Balestra, M.E., Javier, R., Andrews-Zwilling, Y., Li, G., Walker, D., Zhang, W.R., Kreitzer, A.C., and Huang, Y. (2012). Direct reprogramming of mouse and human fibroblasts into multipotent neural stem cells with a single factor. *Cell Stem Cell* *11*, 100–109.
- Sahay, A., Scobie, K.N., Hill, A.S., O'Carroll, C.M., Kheirbek, M.A., Burghardt, N.S., Fenton, A.A., Dranovsky, A., and Hen, R. (2011). Increasing adult hippocampal neurogenesis is sufficient to improve pattern separation. *Nature* *472*, 466–470.
- Soldner, F., and Jaenisch, R. (2012). Medicine. iPSC disease modeling. *Science* *338*, 1155–1156.
- Son, E.Y., Ichida, J.K., Wainger, B.J., Toma, J.S., Rafuse, V.F., Woolf, C.J., and Eggan, K. (2011). Conversion of mouse and human fibroblasts into functional spinal motor neurons. *Cell Stem Cell* *9*, 205–218.
- Staahl, B.T., Tang, J., Wu, W., Sun, A., Gitler, A.D., Yoo, A.S., and Crabtree, G.R. (2013). Kinetic analysis of npBAF to nBAF switching reveals exchange of SS18 with CREST and integration with neural developmental pathways. *J. Neurosci.* *33*, 10348–10361.
- Stenman, J., Toresson, H., and Campbell, K. (2003). Identification of two distinct progenitor populations in the lateral ganglionic eminence: implications for striatal and olfactory bulb neurogenesis. *J. Neurosci.* *23*, 167–174.
- Takahashi, K., and Yamanaka, S. (2006). Induction of pluripotent stem cells from mouse embryonic and adult fibroblast cultures by defined factors. *Cell* *126*, 663–676.
- Tamura, S., Morikawa, Y., Iwanishi, H., Hisaoka, T., and Senba, E. (2004). Foxp1 gene expression in projection neurons of the mouse striatum. *Neuroscience* *124*, 261–267.
- Tepper, J.M., Tecuapetla, F., Koos, T., and Ibanez-Sandoval, O. (2010). Heterogeneity and diversity of striatal GABAergic interneurons. *Front. Neuroanat.* *4*, <http://dx.doi.org/10.3389/fnana.2010.00150>.
- Venance, L., and Glowinski, J. (2003). Heterogeneity of spike frequency adaptation among medium spiny neurons from the rat striatum. *Neuroscience* *122*, 77–92.
- Vierbuchen, T., Ostermeier, A., Pang, Z.P., Kokubu, Y., Südhof, T.C., and Wernig, M. (2010). Direct conversion of fibroblasts to functional neurons by defined factors. *Nature* *463*, 1035–1041.
- Visvanathan, J., Lee, S., Lee, B., Lee, J.W., and Lee, S.K. (2007). The microRNA miR-124 antagonizes the anti-neural REST/SCP1 pathway during embryonic CNS development. *Genes Dev.* *21*, 744–749.
- Wapinski, O.L., Vierbuchen, T., Qu, K., Lee, Q.Y., Chanda, S., Fuentes, D.R., Giresi, P.G., Ng, Y.H., Marro, S., Neff, N.F., et al. (2013). Hierarchical mechanisms for direct reprogramming of fibroblasts to neurons. *Cell* *155*, 621–635.
- Xue, Y., Ouyang, K., Huang, J., Zhou, Y., Ouyang, H., Li, H., Wang, G., Wu, Q., Wei, C., Bi, Y., et al. (2013). Direct conversion of fibroblasts to neurons by reprogramming PTB-regulated microRNA circuits. *Cell* *152*, 82–96.
- Yoo, A.S., Staahl, B.T., Chen, L., and Crabtree, G.R. (2009). MicroRNA-mediated switching of chromatin-remodelling complexes in neural development. *Nature* *460*, 642–646.
- Yoo, A.S., Sun, A.X., Li, L., Shcheglovitov, A., Portmann, T., Li, Y., Lee-Messer, C., Dolmetsch, R.E., Tsien, R.W., and Crabtree, G.R. (2011). MicroRNA-mediated conversion of human fibroblasts to neurons. *Nature* *476*, 228–231.
- Yu, J., Vodyanik, M.A., Smuga-Otto, K., Antosiewicz-Bourget, J., Frane, J.L., Tian, S., Nie, J., Jonsdottir, G.A., Ruotti, V., Stewart, R., et al. (2007). Induced pluripotent stem cell lines derived from human somatic cells. *Science* *318*, 1917–1920.
- Zhang, R., Xue, Y.Y., Lu, S.D., Wang, Y., Zhang, L.M., Huang, Y.L., Signore, A.P., Chen, J., and Sun, F.Y. (2006). Bcl-2 enhances neurogenesis and inhibits apoptosis of newborn neurons in adult rat brain following a transient middle cerebral artery occlusion. *Neurobiol. Dis.* *24*, 345–356.
- Zhang, N., An, M.C., Montoro, D., and Ellerby, L.M. (2010). Characterization of Human Huntington's Disease Cell Model from Induced Pluripotent Stem Cells. *PLoS Curr.* *2*, RRRN1193.
- Zhang, Y., Pak, C., Han, Y., Ahlenius, H., Zhang, Z., Chanda, S., Marro, S., Patzke, C., Acuna, C., Covy, J., et al. (2013). Rapid single-step induction of functional neurons from human pluripotent stem cells. *Neuron* *78*, 785–798.

A New DREADD Facilitates the Multiplexed Chemogenetic Interrogation of Behavior

Eyal Vardy,^{1,8} J. Elliott Robinson,^{2,3,4,8} Chia Li,^{5,6,8} Reid H.J. Olsen,^{1,3} Jeffrey F. DiBerto,² Patrick M. Giguere,¹ Flori M. Sassano,¹ Xi-Ping Huang,¹ Hu Zhu,¹ Daniel J. Urban,¹ Kate L. White,¹ Joseph E. Rittiner,³ Nicole A. Crowley,^{1,3,4} Kristen E. Pleil,^{1,3,4} Christopher M. Mazzone,^{1,3,4} Philip D. Mosier,⁷ Juan Song,^{1,3} Thomas L. Kash,^{1,3,4} C.J. Malanga,^{2,3,4} Michael J. Krashes,^{5,6,*} and Bryan L. Roth^{1,3,*}

¹Department of Pharmacology and National Institute of Mental Health Psychoactive Drug Screening Program (NIMH PDSP)

²Neurology Department

University of North Carolina School of Medicine, Chapel Hill, NC 27514, USA

³Curriculum in Neurobiology

⁴Bowles Center for Alcohol Studies

University of North Carolina School of Medicine, Chapel Hill, NC 27599, USA

⁵Diabetes, Endocrinology, and Obesity Branch, National Institute of Diabetes and Digestive and Kidney Diseases, National Institutes of Health, Bethesda, MD 20892, USA

⁶National Institute of Drug Abuse, Baltimore, MD 21224, USA

⁷Department of Medicinal Chemistry, Virginia Commonwealth University School of Pharmacy, Richmond, VA 23298, USA

⁸Co-first author

*Correspondence: michael.krashes@nih.gov (M.J.K.), bryan_roth@med.unc.edu (B.L.R.)

<http://dx.doi.org/10.1016/j.neuron.2015.03.065>

SUMMARY

DREADDs are chemogenetic tools widely used to remotely control cellular signaling, neuronal activity, and behavior. Here we used a structure-based approach to develop a new G_i-coupled DREADD using the kappa-opioid receptor as a template (KORD) that is activated by the pharmacologically inert ligand salvinorin B (SALB). Activation of virally expressed KORD in several neuronal contexts robustly attenuated neuronal activity and modified behaviors. Additionally, co-expression of the KORD and the G_q-coupled M₃-DREADD within the same neuronal population facilitated the sequential and bidirectional remote control of behavior. The availability of DREADDs activated by different ligands provides enhanced opportunities for investigating diverse physiological systems using multiplexed chemogenetic actuators.

INTRODUCTION

Over the past several years, optogenetic and chemogenetic (Armbruster et al., 2007; Boyden et al., 2005) approaches have transformed neuroscience and other disciplines by facilitating the reversible, cell type-specific control of cellular signaling and electrical activity. As complementary technologies, opto- and chemogenetics have demonstrated robust utility for deconstructing the neuronal codes responsible for both simple and complex behaviors (Deisseroth, 2011; Sternson and Roth, 2014). The chemogenetic platform known as DREADDs (designer receptors exclusively activated by designer drugs) has proven to be extremely useful for interrogating cellular

signaling in cell types as diverse as glia (Aguilhon et al., 2013), pancreatic β -cells (Guettier et al., 2009; Jain et al., 2013), hepatocytes (Li et al., 2013), triple-negative breast cancer cells (Yagi et al., 2011), transformed fibroblasts (Vaqué et al., 2013), and induced pluripotent stem (iPS) cells (Dell'Anno et al., 2014).

Current DREADDs, activated by the inert clozapine metabolite clozapine-N-oxide (CNO), can silence (Armbruster et al., 2007) or enhance (Alexander et al., 2009) neuronal firing, and can modulate cellular signaling via G_i, G_q, G_s, or β -arrestin cascades (Guettier et al., 2009; Nakajima and Wess, 2012). However, the dependence of DREADD technology on the same inert ligand CNO limits its effectiveness for bidirectional and multiplexed chemogenetic control of neuronal and non-neuronal activity. Thus, the development of a new DREADD that can be activated by a distinct chemotype would represent a powerful new tool for neuroscientists and biologists in general.

The first chemogenetic tool based on a G protein-coupled receptor (GPCR) was developed by Strader and colleagues in 1991 (Strader et al., 1991). Since then, many orthologous receptor-ligand pairs have been developed (e.g., RASSLs, TRECs, neoceptors, and so on; Conklin et al., 2008), though with occasionally limited utility. Common problems associated with these first-generation chemogenetic tools included the following:

- (1) Many of the synthetic compounds that activate the modified receptors exhibit appreciable affinities and potencies for the native receptors. This nonselective activity limits their efficacy *in vivo* because of the need to employ knockout animals in order to avoid activation of endogenous receptors.
- (2) In some cases, ligand potency was too low to be useful for studies *in vivo*.
- (3) The selectivity profile of the ligands was typically unspecified (e.g., they may have activities at other unidentified cellular targets).

- (4) Many of the previously reported modified receptors had high basal signaling in vivo that obscures ligand-induced phenotypes (Rogan and Roth, 2011).

The recent development of engineered ligand-gated ion channels (PSAMs and PSEMs) overcomes many of these deficiencies (Magnus et al., 2011), although because PSAMs and PSEMs are ion channels, they have limited value in non-excitable cells.

Here we reveal the development of a new DREADD using the κ -opioid receptor (KOR) as a template that is activated by salvinorin B (SALB). Since SALB is an inactive, drug-like metabolite of the KOR-selective agonist salvinorin A (SALA) (Ansonoff et al., 2006; Roth et al., 2002), and because SALB has excellent CNS penetrability and pharmacokinetic properties in both rodents and non-human primates (Hooker et al., 2009), the SALB/KORD combination will be exceptionally suited for a variety of contexts. Additionally, the SALB/KORD pairing facilitates the multiplexed chemogenetic interrogation of GPCR signaling and behavior.

RESULTS

SALB Is Inert In Vivo

Previous preliminary studies showed that SALB is pharmacologically inert in vitro and in vivo (Ansonoff et al., 2006). To verify and extend these findings, we profiled SALB against a large number of CNS molecular targets using the resources of the National Institute of Mental Health Psychoactive Drug Screening Program as described in Besnard et al. (2012) and Keiser et al. (2009). SALB failed to show any activity except the previously reported low KOR [3 H]-diprenorphine radioligand binding affinity ($K_i = 2.95 \mu\text{M}$; Figure 1H). Importantly, SALB was also inactive at muscarinic receptor-based DREADDs (G_q , G_i , and G_s DREADDs; Figure S1). We found that SALB is a weak KOR agonist with an EC_{50} of 248 nM (Figure 1D; Table 1). Importantly, the potency of SALB is so weak that even after i.c.v. administration SALB failed to produce KOR-mediated anti-nociception, while SALA (its active precursor) was potently analgesic (Ansonoff et al., 2006).

Given both the weak potency of SALB at wild-type (WT) KOR and its inactivity when administered i.c.v., we reasoned that SALB will be inactive in vivo. To test this hypothesis, we used several behavioral assays to determine whether SALB can induce behavioral effects commonly associated with KOR agonists: analgesia, impairment of motor performance, and the production of anhedonic-like states. First, we measured the analgesic and ataxic effects of SALB and compared its activity with a metabolically stable SALA analog, MOM-ether SALB (MOM-B), using hot plate and rotarod assays, respectively. While 2.0 mg/kg MOM-B produced effects in both the hot plate and rotarod tests, administration of 10.0 mg/kg SALB did not alter performance relative to controls (Figures 1A and 1B). Subsequently, we used the curve-shift method of intracranial self-stimulation (ICSS) to detect reward-devaluing effects of SALB. While SALA (0.1–1.0 mg/kg) significantly elevated brain stimulation reward thresholds in C57BL/6J mice at all doses tested ($F_{3, 18} = 14.5$, $p < 0.001$; Figures 1C and S4), SALB (3.0–17.0 mg/kg) failed to significantly elevate thresholds up to

17.0 mg/kg s.c. Given that SALB is apparently inert in vivo, and because of its outstanding pharmacokinetic and CNS penetrability properties (Hooker et al., 2009), we predicted that SALB would represent a suitable ligand for a new DREADD.

Structure-Based Design of KORD

In order to develop a new DREADD, we initially hoped to evolve the human KOR (hKOR) to be responsive to SALB using our yeast-based directed molecular evolution approach (Armbruster et al., 2007; Dong et al., 2010). For these studies, hKOR was cloned into the yeast expression plasmid p416 and functionally expressed in a genetically modified strain of *S. cerevisiae*, which enables ligand-induced activation of heterologously expressed mammalian G_i -coupled GPCRs to engage the pheromone-signaling pathway, thereby promoting growth on selective media (Dong et al., 2010; Erlenbach et al., 2001; Noble et al., 2003). We created a library of mutant hKOR receptors by random mutagenesis, and screened them for activation by SALB. We were able to identify multiple mutants activated by SALB, although they all displayed high levels of constitutive activity, rendering them relatively useless for the studies we envisioned.

Therefore, we employed a rational approach to designing the KOR DREADD based on our recent crystallographic, mutagenesis, and molecular modeling studies of hKOR (Vardy et al., 2013; Wu et al., 2012). These studies showed that an alanine mutation at E297 at the extracellular end of TM6 (an important residue in KOR specificity determinant, in the so-called “address domain”; Larson et al., 2000) causes a 10-fold decrease in the affinity and potency of the endogenous peptide ligand dynorphin A (DYNA) without altering the affinity or potency of SALA (Vardy et al., 2013). Another residue, D138 in TM3, which belongs to the general opioid activation determinant, was also examined. This residue resides in the “message domain” of KOR (Portoghese, 1989; Vardy et al., 2013), and D138A mutations have been reported to nearly abolish the binding of all known KOR agonists without affecting the affinity or potency of SALA (Kane et al., 2006; Vardy et al., 2013). Furthermore, recent high-resolution crystal structures of related opioid receptors (Fenalti et al., 2014, 2015) implied that this residue is also essential for the interaction of other classes of opioids including opioid peptides and opioid antagonists. We reasoned, therefore, that changing the negative charge to a polar residue via a D138N mutation would further decrease the potency of endogenous peptide ligands and enhance the potency of SALB and SALA.

Indeed, the D138N mutation apparently abolished DYNA (1–13) agonist efficacy and potency and diminished peptide binding affinity while enhancing SALA and SALB affinities and potencies 10- to 30-fold (see Figures 1D and 1F–1H; Table 1). As a key requisite of DREADDs is the failure to be activated by endogenous neurotransmitters, we combined these two KOR mutants (e.g., D138N/E297A) and evaluated the resulting construct. Both the double D138N/E297A mutant and the single D138N mutant responded to SALB and SALA with greatly enhanced potencies compared to WT, while the E297A mutant alone had no effect on SALB agonist potency (Figure 1D). Critically, the single D138N mutant was not activated by any tested synthetic or endogenous peptide KOR ligands (Figure 1G; Table 1). Thus, in a screen of 21 endogenous opioids performed

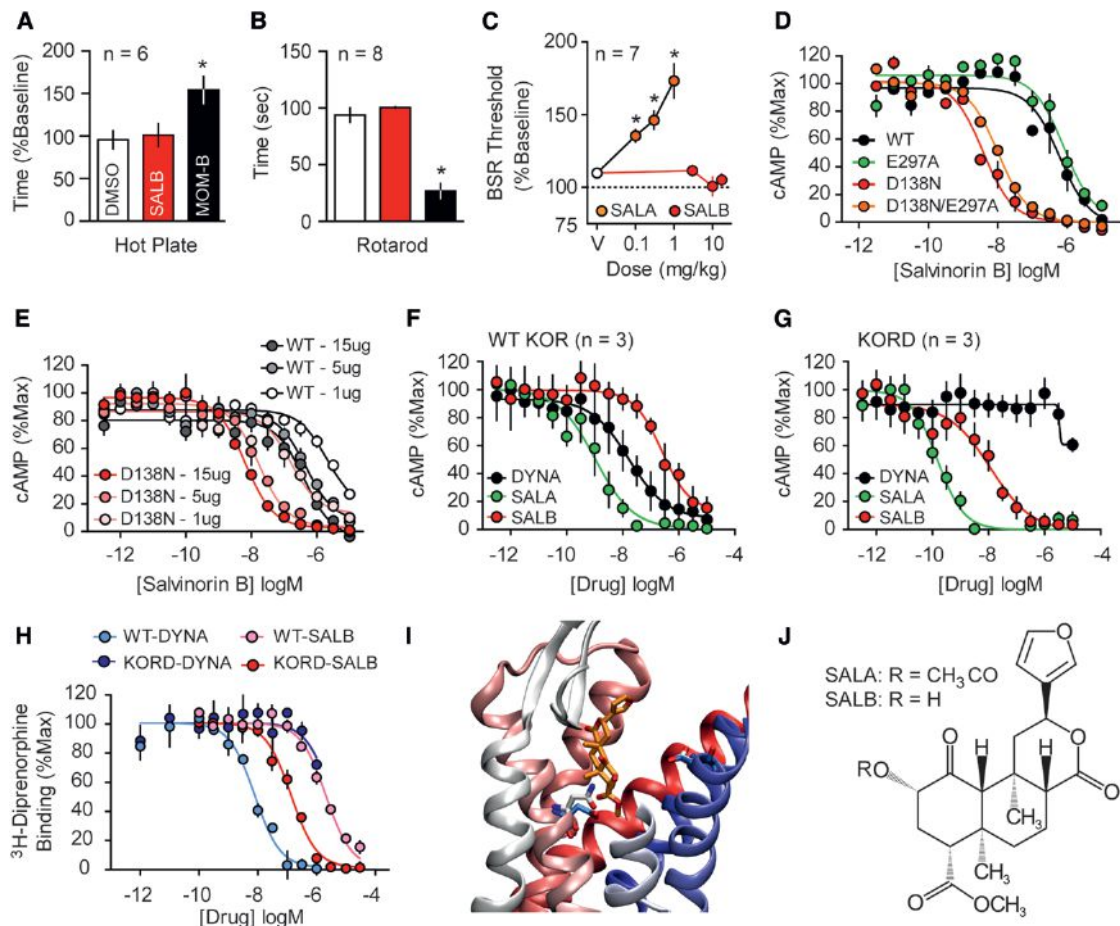


Figure 1. Rational Design and In Vitro Characterization of KORD

(A and B) SALB was initially validated as a DREADD ligand by demonstrating its apparent pharmacologic inertness in vivo using behavioral tests by comparing with MOM-SALB via (A) hot plate test and (B) impairment of motor performance using the rotarod test. In both tests SALB effects (red) were compared to vehicle (white) and a stabilized variant of SALA (MOM-SALB, black).

(C) The lack of production of a KOR-like anhedonic state was tested using ICSS and compared to the effects of SALA. Data represent mean \pm SEM of indicated number of separate experiments.

(D) We characterized the KORD comparing the G_i -mediated response of different KOR mutants and demonstrate an increased potency of SALB at D138N-containing mutants.

(E) The effect of receptor expression levels on SALB potency of WT KOR (gray) and KORD (red). As can be seen, DNA concentration is directly related in both WT-KOR and KORD to agonist potency yielding a right shift in potency of 1–2 orders of magnitude.

(F and G) Average G_i response of WT-KOR (F) and KORD (G) to classic KOR ligands dynorphin A (DYNA, black), SALA (green), and the inert compound SALB (red) is shown.

(H–J) (H) Competition binding isotherms of WT and KORD for DYNA (1–13) (pK_i values, 8.50 ± 0.12 and 5.79 ± 0.06 , respectively) and SALB (pK_i values, 5.53 ± 0.08 and 6.98 ± 0.13 , respectively). An examination of a model of KORD docked with SALB (I) suggests that the DREADD mutation (D138N) eliminates unfavorable interactions between D138 and SALB. In WT KOR, D138 is turned away from the ligand-binding site (cyan), while N138 in KORD (white) is interacting directly with the ligand. E297 in both models assumes the same conformation reflecting the fact that it has no effect on DREADD activity. Deacetylation at position 2 of SALA results in SALB (J). Asterisk indicates $p < 0.05$, and all values reported as mean \pm S.E.M.

at WT and the D138N mutants, no opioid peptide was found to have detectable agonist activity at the D138N mutant (Table 1; Figure 1G). As the D138N mutant is potently activated by the inactive drug SALB and apparently not activated by any tested endogenous peptide agonist, we chose it as our candidate DREADD and have dubbed it KORD (κ -opioid DREADD).

GPCR overexpression typically results in a large degree of receptor reserve thereby enhancing agonist potency. Thus, because a high level of receptor reserve can be easily achieved

for DREADDs via virally mediated transduction, receptor reserve could further enhance the apparent affinity, selectivity, and potency of SALB for the KORD. To test this notion, we transfected HEK293T cells with increasing concentrations of plasmids expressing either WT hKOR or the KORD (D138N hKOR), which resulted in varying levels of receptor expression. As predicted, increased receptor expression levels correlated with an increase in the apparent potency of SALB (Figure 1E). Significantly, the potency differences between cells expressing levels

Table 1. KORD Is Insensitive to Endogenous Opioid Peptides and Is Potently Activated by SALB

	hKOR			KORD		
	EC ₅₀ (nM)	pEC ₅₀ ± SEM	E _{max} (%)	EC ₅₀ (nM)	pEC ₅₀ ± SEM	E _{max} (%)
β-Endorphin (1–27) (β-Endor1–27) YGGFMTSEKSQTPLVLFKNAIKNAY	700 6.15 ± 0.22		100	NA		NA
β-Endorphin (1–31) (β-Endor1–31) YGGFMTSEKSQTPLVLFKNAIKNAYKKGE	706 6.15 ± 0.17		100	NA		NA
Leu-enkephalin (Leu-Enk) YGGFL	NA		NA	NA		NA
Met-enkephalin (Met-Enk) YGGFM	2,099 5.68 ± 0.12		79	NA		NA
Met-enkephalin-Arg-Phe (MERF) YGGFMRF	1,344 5.87 ± 0.14		99	NA		NA
Metorphamide YGGFMRRV-NH ₂	108 6.99 ± 0.07		97	NA		NA
BAM 12 YGGFMRRVGRPE	101 6.99 ± 0.07		99	NA		NA
BAM 18 YGGFMRRVGRPEWMDYQ	85 7.07 ± 0.09		97	NA		NA
BAM 22 YGGFMRRVGRPEWMDYQRYG	93 7.03 ± 0.07		95	NA		NA
Peptide E YGGFMRRVGRPEWMDYQRYGGFL	65 7.18 ± 0.07		95	NA		NA
Dynorphin A(1–6) (DynA1–6) YGGFLR	227 6.64 ± 0.24		86	NA		NA
Dynorphin A(1–7) (DynA1–7) YGGFLRR	107 6.97 ± 0.04		97	NA		NA
Dynorphin A(1–8) (DynA1–8) YGGFLRRI	122 6.91 ± 0.06		94	NA		NA
Dynorphin A(1–9) (DynA1–9) TGGFLRRIR	127 6.89 ± 0.07		93	NA		NA
Dynorphin A(1–13) (DynA1–13) YGGFLRRIRPKLK	19 7.71 ± 0.06		94	NA		NA
Dynorphin A(1–17) (DynA1–17) YGGFLRRIRPKLKWDNQ	13 7.87 ± 0.09		100	NA		NA
Dynorphin B(1–13) (DynB1–13) YGGFLRRQFKVVT	120 6.91 ± 0.08		100	NA		NA
Leumorphin YGGFLRRQFKVVTRSQEDPNAYEELFDV	21 97.68 ± 0.06		92	NA		NA
α-Neoendorphin (α-neo-End) YGGFLRKYPK	64 7.19 ± 0.07		95	NA		NA
Endomorphin-1 YPWF	NA		NA	NA		NA
Endomorphin-2 YPFF	NA		NA	NA		NA
Nociceptin FGGFTGARKSARKLANQ	1,007 5.99 ± 0.07		81	NA		NA
U69593	3.16 8.5 ± 0.1		100	> 10,000		NA
Salvinorin B (low expression)	2,045 5.68 ± 0.18		80	160 6.79 ± 0.13		94
Salvinorin B (high expression)	248 6.6 ± 0.1		100	11.8 7.98 ± 0.09		100
Salvinorin A (low expression)	19.8 7.71 ± 0.08		100	0.12 9.91 ± 0.08		100
Salvinorin A (high expression)	1.05 8.96 ± 0.08		100	0.04 10.35 ± 0.08		100

NA, no activation at 10 μM. Data represent mean EC₅₀ and mean pEC₅₀ ± SEM of n = 3 separate 16-point dose-response experiments each performed in triplicate. hKOR, human κ-opioid receptor; KORD, κ-opioid receptor DREADD.

of WT receptor (achieved using 1 μg DNA), which is at a level similar to endogenous brain expression, versus cells expressing high levels of the mutant receptor (achieved using 15 μg DNA), is close to 1,000-fold (Figure 1E). Thus, our rationally designed KORD greatly enhances hKOR sensitivity to SALB and simultaneously abolishes the agonist activity of a variety of endogenous and exogenous KOR agonists (Figure 1G; Table 1).

As constitutive activity is a potential confounding issue with respect to overexpressed chemogenetic and optogenetic tools, we next examined the constitutive activity of KORD compared to both a WT and a constitutively active KOR mutant (V108L). We found that the basal activity of KORD ($137 \pm 3.7 \times 10^5$ lumens/min; $n = 44$; $p > 0.05$ versus WT) was equivalent to WT ($134 \pm 3.2 \times 10^5$ lumens/min; $n = 48$) and less than the V108L constitutively active mutant ($94 \pm 3.7 \times 10^5$ lumens/min; $n = 50$; $p < 0.001$ versus WT), indicating that the KORD does not represent an apparently constitutively active mutant. Although the atomic mechanisms responsible for the increased affinity and potency for SALB are unknown, our modeling results suggest that it is likely due to the removal of an unfavorable desolvation cost associated with non-basic ligand binding to a charged aspartate (Asp) (Vardy et al., 2013). Indeed, our docking studies suggest that changing the Asp at this position to asparagine (Asn) results in an improved conformation for the Asn, decreases the energetic cost for desolvation, and thus increases affinity (see Figure 1I).

In Vivo Neuronal Validation of KORD

KORD Activation Induces Neuronal Hyperpolarization

To test the activity of the KORD in vivo, we used a standard Cre-recombinase-dependent adeno-associated virus (AAV), which enabled the targeting of KORD to specific neuronal populations in different Cre-driver mouse lines (Figure 2A). We verified effective transduction of KORD in a Cre-dependent manner in a variety of neurons, including the substantia nigra (SN) and the ventral tegmental area (VTA) of vesicular GABA transporter (VGAT)-*ires*-Cre mice (Figures 2B and 2C), the paraventricular hypothalamus (PVH) of single-minded1 (SIM1)-Cre mice (Baithasar et al., 2005), and the arcuate nucleus (ARC) of agouti-related peptide (AGRP)-*ires*-Cre mice (Tong et al., 2008) (Figures 3A, 3B, 3E, and 3F).

We next performed whole-cell patch clamp recordings in acutely prepared slices to test the ability of KORD to generate a SALB-induced hyperpolarization. Results were calculated as a shift from baseline resting membrane potential (RMP). In VTA/SN-VGAT-expressing (VTA/SN^{VGAT}) neurons transduced with KORD, bath application of SALB led to a robust and significant membrane potential hyperpolarization, while SALB had no effect on control (mCherry-transduced) neurons ($t_9 = 2.97$, $p < 0.05$; Figure 2D). To determine the generalizability of KORD-mediated hyperpolarization, we also evaluated SIM1-expressing neurons in the PVH (PVH^{SIM1}) and AgRP-expressing neurons in the ARC (ARC^{AgRP}). Upon bath application of SALB, both PVH^{SIM1} and ARC^{AgRP} neurons expressing KORD exhibited robust hyperpolarization, shifting -6.2 ± 2.1 mV and -10.1 ± 1.7 mV, respectively (PVH^{SIM1}, $t_5 = 2.99$, $p < 0.05$; ARC^{AgRP}, $t_4 = 5.94$, $p < 0.05$; Figures 3D and 3H). Next, we sought to determine if the KORD can act presynaptically to

inhibit neurotransmission by recording miniature inhibitory postsynaptic currents (mIPSCs) in VTA/SN neurons in the presence of SALB. In VGAT-*ires*-Cre mice with AAV-hSyn-DIO-KORD injected into the VTA/SN, SALB significantly reduced mIPSC frequency ($t_2 = 24.7$, $p < 0.001$; Figure 2E), but not amplitude ($t_2 = 2.45$, $p > 0.05$) compared to baseline, consistent with a presynaptic effect. SALB had no effect on mIPSCs in naive mice (frequency, $t_2 = 0.92$, $p > 0.05$; amplitude, $t_2 = 4.1$, $p > 0.05$). No differences in baseline mIPSC frequency were observed between AAV-hSyn-DIO-KORD-injected mice and naive mice (Figure 2E).

Peripheral SALB Administration Produces Robust Behavioral Responses

Given that SALB induced KORD-mediated hyperpolarization, we next tested whether the SALB-induced activation of KORD had functional consequences on three distinct neuronal populations: (1) VTA/SN^{VGAT}, (2) hypothalamic PVH^{SIM1}, and (3) hypothalamic ARC^{AgRP} (using VGAT-*ires*-Cre, SIM1-Cre, and AGRP-*ires*-Cre mice, respectively). Since previous studies have demonstrated that optogenetic modulation of VTA/SN^{VGAT} neurons can modify locomotion (van Zessen et al., 2012), we predicted that chemogenetic silencing via KORD of VTA/SN^{VGAT} neurons (Figures 2B and 2C) would increase locomotion. As expected, SALB produced a dose-dependent increase in locomotor activity ($F_{3, 21} = 19.1$, $p < 0.001$) (Figure 2F), while vehicle was without effect; post hoc testing revealed that the 1.0-, 3.0-, and 10.0-mg/kg SALB doses significantly enhanced locomotion. Importantly, mice expressing mCherry in the same neuronal population were unresponsive to SALB (Figure 4B).

Next, we evaluated KORD activity in a neural circuit known to be involved in feeding behavior. PVH^{SIM1} neurons (Figures 3A and 3B), which make up the vast majority of PVH cells, have been previously demonstrated to increase food intake when chemogenetically inhibited (Atasoy et al., 2012; Stachniak et al., 2014). Consistent with prior results obtained using hm4Di, SALB activation of KORD in PVH^{SIM1} neurons significantly increased feeding behavior compared to baseline (0.61 ± 0.04 g versus 0.06 ± 0.01 g; $t_6 = 11.8$, $p < 0.05$; Figure 3C), whereas WT control mice ($t_5 = 0.30$, $p < 0.05$) injected with the Cre-dependent KORD virus had no feeding effects in response to the administration of SALB.

As a final test, we evaluated the orexigenic ARC^{AgRP} neurons (Figures 3E and 3F), which have been shown to send inhibitory projections to the PVH and synapse onto a subpopulation of PVH^{SIM1} neurons (Krashes et al., 2014; Atasoy et al., 2012). Having established that activation of KORD hyperpolarizes PVH^{SIM1} neurons in vitro and increases food intake in vivo, we next tested KORD activation with SALB on the upstream inhibitory ARC^{AgRP} neurons (Figures 3G and S2). Following light cycle food restriction, food consumption was monitored during the first 60 min of the dark cycle, when mice normally eat and ARC^{AgRP} neural activity is high (Krashes et al., 2011). Compared to vehicle (0.59 ± 0.07 g), KORD inhibition of the hunger-promoting ARC^{AgRP} neurons resulted in significantly diminished levels of food intake (0.11 ± 0.03 g; $t_5 = 11.29$, $p < 0.05$). Importantly, SALB administration did not impact feeding responses in WT animals (vehicle, 0.52 ± 0.05 g; SALB, 0.55 ± 0.07 g).

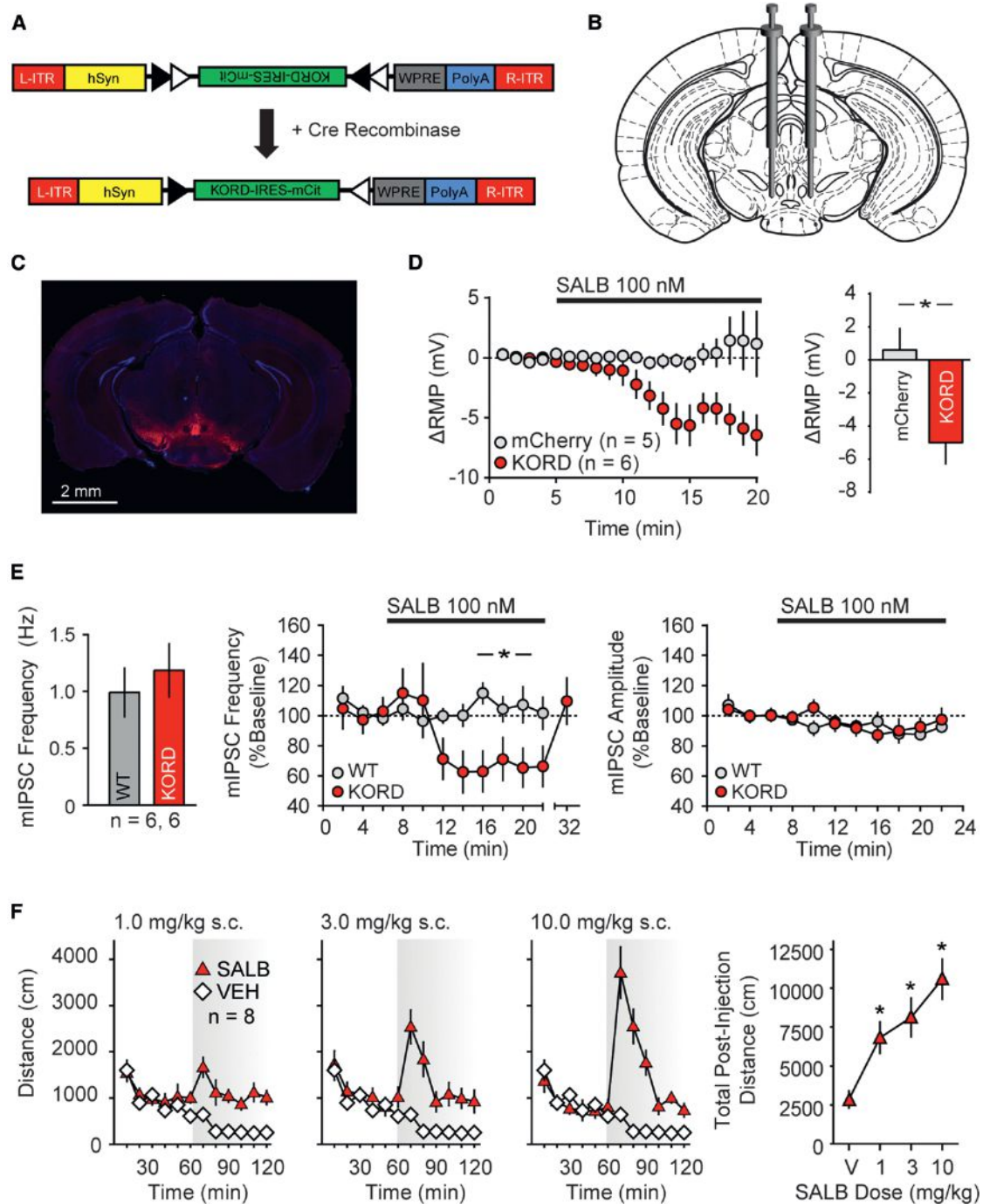


Figure 2. Validation of KORD In Vivo in VTA/SN^{VGAT} Neurons

(A) Schematic showing the AAV8 (hSyn-DIO-hKORD-IRES-mCIT-WPRE-PolyA-R-ITR) construct used and its recombination under the control of Cre-recombinase.

(B) Location for viral infusion of Cre-expressing VTA/SN^{VGAT} neurons.

(C) Representative low-power field of VTA/SN^{VGAT} neurons.

(D) Shift from baseline resting membrane potential (RMP) in VTA/SN^{VGAT} neurons transduced with KORD or mCherry (control) constructs.

(E) Baseline mIPSC frequency in non-KORD-expressing neurons in KORD-infected mice and control neurons from naive mice controls and the effects of SALB on miniature IPSC frequency and amplitude in uninfected VTA/SN^{VGAT} and naive control VTA/SN neurons.

(F) Locomotor responses for graded doses of SALB. Asterisk indicates $p < 0.05$, and all values reported as mean \pm S.E.M.

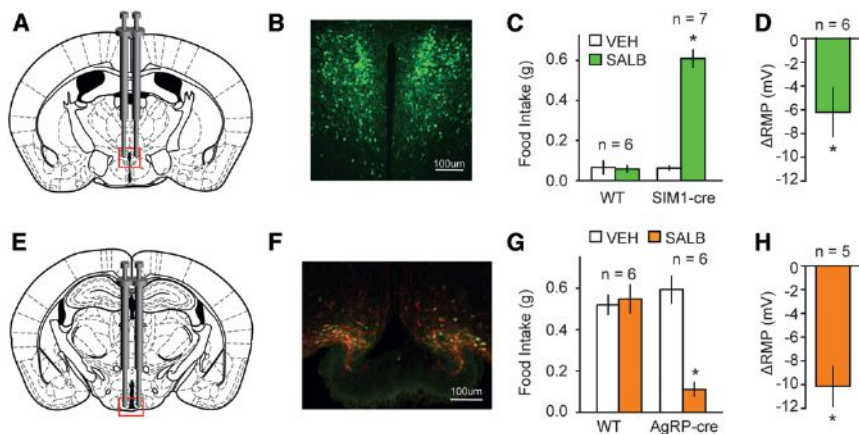


Figure 3. Validation of KORD In Vivo in PVH^{SIM1}- and ARC^{AgRP}-Expressing Neurons

(A) Location for viral infusion of PVH^{SIM1} Cre-expressing neurons. (B) Representative immunofluorescent photomicrographs demonstrating expression of mCitrine in virally transduced neurons. (C) Effects of SALB on food intake in AAV-hSyn-DIO-KORD-injected SIM1-Cre and WT mice. (D) Shift from baseline resting membrane potential (RMP) in KORD-transduced neurons in the PVH^{SIM1}. (E and F) Location of viral infusion and expression of mCitrine (green) and HA-hKORD (red) in ARC^{AgRP} neurons. (G) Suppression of food intake by SALB. (H) Shift from baseline RMP in KORD-transduced neurons in the ARC^{AgRP}. Asterisk indicates $p < 0.05$, and all values represent mean \pm S.E.M.

KORD Facilitates Chemogenetic Multiplexed Control of Behavior

One of our main goals for developing the KORD was to enable multiplexing experiments for either the simultaneous or sequential manipulation of neuronal pathways using a variety of chemo- and optogenetic platforms. To test whether two distinct DREADDs can reciprocally modulate neuronal activity and behavior in vivo, we transduced VTA/SN^{VGAT} neurons or hypothalamic ARC^{AgRP} neurons with both the inhibitory, G_i-coupled, SALB-activated KORD and the stimulatory, G_q-coupled, CNO-activated hM3Dq. We then tested for receptor expression and behavioral effects.

We found that locomotor activity could be bidirectionally modulated by KORD and hM3Dq in the same mouse. During different testing sessions, SALB (10.0 mg/kg) enhanced locomotor activity in mice that expressed both KORD and hM3Dq in VTA/SN^{VGAT} neurons compared to vehicle ($t_4 = 2.89$, $p = 0.04$; Figure 4B), and CNO (3.0 mg/kg) decreased locomotor activity ($t_4 = 5.44$, $p = 0.006$). When tested during the same session, CNO (3.0 mg/kg) produced significant locomotor depression ($t_4 = 3.28$, $p = 0.03$), while SALB (17.0 mg/kg) rescued the effects of CNO and significantly elevated locomotor activity when compared to vehicle ($t_4 = 3.44$, $p = 0.03$; Figures 4C and 4D). In these sessions, the onset of action of both CNO and SALB began influencing locomotor behavior within 10–20 min post-injection. Importantly, neither SALB (10.0 mg/kg; $t_5 = 1.93$, $p > 0.05$) nor CNO (3.0 mg/kg; $t_5 = 0.95$, $p > 0.05$) had any effect on locomotor activity in control mice expressing mCherry in VTA/SN^{VGAT} neurons (Figure 4B). Histologic analysis of VTA/SN^{VGAT} neurons showed that $87.7\% \pm 1.7\%$ of transduced neurons co-expressed both receptors with no significant difference in the transduction efficiency of either DREADD ($t_2 = 0.82$, $p > 0.05$; Figure S3). These results demonstrate for the first time that two different biologically inert designer ligands can produce robust behavioral changes in the same mouse, providing the first proof of concept for multiplexed chemogenetic control of behavior.

We next investigated the effectiveness of multiplex manipulation of behavior while transducing ARC^{AgRP} neurons with both the hM3Dq and KORD. As acute opto- and chemogenetic activation of ARC^{AgRP} neurons drives feeding behavior (Aponte

et al., 2011; Betley et al., 2013; Krashes et al., 2011), we attempted to reverse ARC^{AgRP} hM3Dq activation-induced feeding with simultaneous KORD inhibition. Importantly, for this experiment to work, extensive restraint of ARC^{AgRP} neuron activity is necessary to overcome the chemogenetically induced feeding response, given that only $\sim 10\%$ of ARC^{AgRP} neurons are required to drive the full magnitude of food intake (Aponte et al., 2011; Betley et al., 2013). Consistent with previous studies, CNO/hM3Dq-induced activation of ARC^{AgRP} neurons increased light cycle food intake (0.75 ± 0.03 g) significantly compared to saline baseline (0.04 ± 0.02 g; Time, $F_{6, 108} = 108.4$; Treatment, $F_{1, 18} = 10.6$; and Time \times Treatment, $F_{6, 108} = 4.5$; $F_{6, 108} = 62.1$, $p < 0.001$ for all; Figure 4E). However, co-administration of CNO and SALB significantly blunted feeding behavior (CNO versus CNO + SalB; Time, $F_{6, 108} = 80.9$; Treatment, $F_{1, 18} = 204.3$; and Time \times Treatment, $F_{6, 108} = 62.1$; $p < 0.001$ for all). Post hoc testing revealed a significant reduction of food intake similar to that observed during simultaneous optogenetic activation and hM4Di-mediated inhibition of ARC^{AgRP} neurons (Stachniak et al., 2014). Interestingly, these animals elevate their feeding rate in the next 2 hr (1–3 hr after ligand injection), reflecting both the transient action of SALB/KORD and persistent action of CNO/hM3Dq (Figure 4E).

DISCUSSION

Here we report the development of a new chemogenetic tool based on the KOR we have dubbed KORD (κ -opioid DREADD). We demonstrate that KORD can be used alone or in conjunction with other chemogenetic tools, thereby facilitating the multiplexed dissection of neural circuitry and behavior. As KORD is activated by SALB, it can be used in mice also expressing CNO-responsive DREADDs, allowing for the first time bidirectional chemogenetic manipulation of neural circuits. Although bidirectional control has only been demonstrated in the hypothalamus and VTA/SN, it is likely that this approach will work in other brain regions. The KORD could also be used together with other chemogenetic and optogenetic tools in order to provide higher-order multiplexed modulation of GPCR signaling in non-neuronal cells.

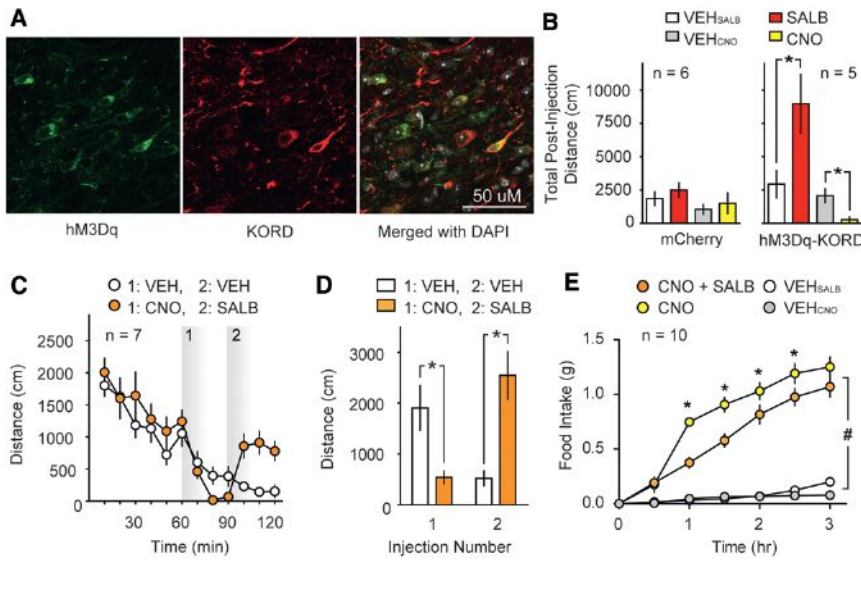


Figure 4. Multiplexed Bidirectional Chemo-genetic Control of Behavior

(A) Representative immunofluorescent confocal micrographs wherein hM3Dq and KORD were co-expressed in VTA/SN^{VGAT} neurons with co-localization data summarized in Figure S3.

(B) Comparison of the effects of CNO and SALB on spontaneous locomotor activity of dual DREADD-expressing mice (right panel; mice expressing both hM3Dq and KORD in VTA/SN^{VGAT} neurons) or control mice (mCherry; left panel). CNO inhibits spontaneous locomotor behavior, and SALB augments locomotor behavior on different testing days (right panel). CNO and SALB did not affect behavior in mice that expressed mCherry in the same brain region.

(C) Bidirectional manipulation of locomotor behavior: the locomotor activity of dual DREADD-expressing mice was inhibited by CNO (CNO injection at 60 min). The locomotor depression was reversed by SALB injection (SALB injection 30 min after CNO injection).

(D) Summary data of locomotor activity experiments using multiplexed DREADDs.

(E) Demonstration that SALB inhibits food intake induced by CNO-mediated activation of hM3Dq when both are expressed in ARC^{AgRP} neurons; these effects show transient effects of SALB versus the persistent effects of CNO. Asterisk indicates $p < 0.05$, and all values represent mean \pm S.E.M.

The kinetics of CNO on neuronal activation via hM3Dq have been demonstrated thoroughly by a large number of independent studies, with *in vivo* DREADD-mediated responses beginning 5–10 min after IP injection, and peak electrophysiological response occurring 45–50 min after injection (Alexander et al., 2009; Urban and Roth, 2015). It has also been reported by many labs that both the behavioral and electrophysiological effects of CNO-mediated DREADD activation can persist for several hours following a single injection in a manner predicted by its pharmacokinetic properties (Urban and Roth, 2015). By contrast, SALA and SALB concentrations in the rodent and primate brain increase within a few seconds following parenteral administration and then rapidly decline ($t_{1/2} = 10$ –15 min; Hooker et al., 2009). Likewise, the behavioral effects of SALB in KORD-expressing mice begin and peak shortly after injection, yielding a behavioral effect that lasts for approximately 1 hr with the doses administered here. As a prolonged activation of DREADDs by CNO may be a problem when studying rapidly modulated, short-term behaviors, the apparently brisk onset of the effects of SALB in KORD-expressing mice may prove valuable for such studies. Indeed, prior studies have demonstrated that SALB is cleared quickly from the brain, but has a slightly more prolonged plasma half-life (Hooker et al., 2009), and thus its pharmacokinetic properties may be better suited for studies in which relatively acute neuronal silencing is required, while CNO-based DREADDs (e.g., hM4Di) are useful where prolonged silencing is desired.

Given that SALB has some modest activity at KOR, it is possible that neurons with a high degree of receptor reserve could show responses to high systemically administered doses of SALB. Even though we have been unable to detect any pharmacological effect of SALB administration, it will be important to avoid using excessively high doses (e.g., > 10 mg/kg) and to test SALB in animals in which KORD has not been expressed. Addi-

tionally, because of the limited solubility of SALB, it will be important going forward to develop analogs of SALB which show improved water solubility.

Optogenetic and chemogenetic tools have revolutionized neuroscience research by facilitating the region- and cell type-specific manipulation of neuronal activity. Optogenetics provides inherent advantages with millisecond temporal resolution, although the hardware required for precise intracranial light delivery is not only invasive, but also cumbersome in comparison to the minimal requirements for chemogenetic manipulation. Chemogenetic control via DREADDs provides slower kinetics due to the systemic administration of CNO or SALB, but has demonstrated its ability to achieve the same functional mapping results with less invasive intervention (reviewed by Mahler et al., 2014; Stachniak et al., 2014; Urban and Roth, 2015). It is also possible to directly infuse CNO into specific brain structures to obtain a transient and focal DREADD activation. The newly developed KORD described here provides potentially greater temporal resolution compared to existing DREADDs, as SALB pharmacokinetics are relatively rapid; additionally, the KORD's effects are apparently robust. Finally, given the relative simplicity of multiplexing with bimodal control now easily achievable, the KORD will prove broadly useful for neuroscientists and other biologists.

EXPERIMENTAL PROCEDURES

Molecular Methods

Molecular Biology

Mutagenesis, radioligand binding, and functional assays were done exactly as described in Vardy et al. (2013).

Molecular Modeling

Molecular modeling of SALA and SALB in complex with the WT KOR was performed as previously described (Vardy et al., 2013). Modeling of SALA and SALB in complex with the KORD was achieved by *in silico* mutation of D138

to N in the respective WT KOR-ligand complexes, with subsequent energy minimization in SYBYL-X 2.1 (Tripos Force Field, Gasteiger-Hückel charges, distance-dependent dielectric constant = 4.0; non-bonded interaction cutoff = 8 Å; termination criterion = energy gradient < 0.05 kcal/(mol × Å) or 100,000 iterations).

Viral Production Methods

Virus Production

KORD (Table S2) in pcDNA 3.0 was cloned into a human synapsin (hSyn)-driven double-floxed pAAV vector derived from pAAV-HA-M4D-IRES-mCitrine. The pAAV-HA-KORD-IRES-mCitrine was then used for AAV9 production at the UNC Vector Core as described (Zhu et al., 2014).

Viral Infusion In Vivo

Mice were anesthetized with ketamine (120 mg/kg) and xylazine (18 mg/kg) (Sigma), and viral constructs (AAV-hSyn-DIO-HA-KOR DREADD, AAV-hSyn-mCherry, or AAV-hSyn-KOR DREADD + AAV-hSyn-hM3D) were stereotaxically injected bilaterally into the VTA/SN, or hypothalamic PVH or ARC (coordinates for VTA/SN: AP -3.1, ML ± 0.4, DV -5.0; coordinates for PVH: AP -0.65, ML ± 0.2, DV -4.7; coordinates for ARC: AP -1.5, ML ± 0.3, DV -5.7) using a 1.0- μ l Hamilton Neuros 7001 KH syringe at a volume of 300 nL/side, at a rate of 100 nL/min for the VTA/SN; 25 nL/side, at a rate of 50 nL/min for the PVH; and 200 nL/side, at a rate of 50 nL/min for the ARC. After surgery, mice were returned to their cages for 2–3 weeks of recovery before behavioral or electrophysiological testing.

Slide Preparation and Immunohistochemistry

Animals were deeply anesthetized with an overdose of ketamine (400 mg/kg) and xylazine (40 mg/kg) and transcardially perfused with PBS (4°C, pH 7.4) followed by 4% PFA in 0.1 M phosphate buffer (4°C, pH 7.4). Brains were post-fixed overnight in 4% PFA, and subsequently cryopreserved in 30% sucrose in 0.1 M phosphate buffer. For confocal image collection, tissue sections containing the VTA/SN were cut into 40- μ m sections using a sliding microtome (Leica SM2010 R) and stored in an ethylene glycol/sucrose-based cryoprotectant. For immunohistochemistry, tissue sections were washed in PBS (pH 7.4) three times, followed by 30 min of permeabilization in PBS with 0.3% Triton-X. Tissue sections were blocked in 5% normal donkey serum and PBS with 0.3% Triton-X for 1 hr, and incubated with 1:500 rabbit anti-HA (Cell Signaling, cat# 3724S, RRID: AB_1549585) and 1:500 mouse anti-mCherry (Abcam, cat# ab125096, RRID: AB_11133266) for 48 hr at 4°C. Subsequently, tissues were washed three times for 5 min in PBS with 0.3% Triton-X, and then incubated with Alexa 568 donkey anti-mouse and Alexa 647 donkey anti-rabbit secondary antibodies (1:250) for 24 hr at 4°C. Tissue sections were washed three times for 5 min in PBS with 0.3% Triton-X, followed by two 5-min washes with PBS (pH 7.4). A DAPI counterstain (300 nM) was applied in the first PBS wash step. Whole-tissue sections were imaged with an epifluorescent slide scanner at the UNC translational pathology lab. Confocal images of infected midbrain GABAergic neurons were taken using a Fluoview FV1000 with a 40 \times (NA 1.3) oil objective. To show co-expression of mCitrine and the HA-tagged KORD, the same staining protocol was observed, substituting an anti-GFP antibody recognizing mCitrine.

Quantification of Co-expression of M3-DREADD and KORDs

A total of three 40- μ m sections containing the VTA/SN were taken from brains of three mice who had received multiplexed DREADD injections. In each section, a z stack was collected in the VTA using a 40 \times oil objective (300 \times 300 μ m field of view). Co-expression of DREADDs was calculated by counting total transduced cells (either KOR or M3 positive) and calculating the relative percentages expressing KOR alone, M3 alone, or KOR/M3. Cell counts were averaged within each animal, and data were analyzed using a Student's paired t test.

Behavioral Studies

SALB Evaluation in Control Mice

The analgesic-like effect of KOR-specific drugs was determined measuring the heat sensitivity of mice in a hot plate assay as previously described (White et al., 2015). The effect of such drugs on balance and motor coordination was assessed by the rotarod test (White et al., 2015). KOR activation has been strongly related to anhedonia (Todtenkopf et al., 2004); the anhedonic effects

of KOR agonists were measured by ICSS in mice as previously described (Robinson et al., 2012). This operant behavioral method measures the value of electrical stimulation (brain stimulation reward or BSR) applied to the fibers of the medial forebrain bundle (MFB) at the level of the lateral hypothalamus and can be used to assess the reward-potentiating or reward-devaluing effects of drugs.

Animals

Adult (at least post-natal day 50) male and female Slc32a1^{tm2(cre)Lowl/J} (VGAT-ires-Cre; provided by Dr. Bradford Lowell, Harvard University) littermates were housed in a temperature- and humidity-controlled environment under a 12-hr light/dark cycle and had free access to food and water. All procedures were approved by the Institutional Animal Care and Use Committee (IACUC) of the University of North Carolina at Chapel Hill, the National Institute of Diabetes and Digestive and Kidney Diseases, or the National Institute on Drug Abuse, and were conducted according to the Guide for the Care and Use of Laboratory Animals (NIH publication no. 85-23, revised 2011).

Locomotor Studies

Locomotor activity was measured before and after treatment with vehicle (s.c. or i.p.), SALB (1.0–17.0 mg/kg s.c.), or CNO (i.p.) in 28 \times 28 cm plexiglass chambers containing two sets of 16 infrared photobeams (MedAssociates). Data were collected with software (MED-PC v4.1; MedAssociates) that calculated the total distance traveled (cm) by measuring the position of the mouse every 60 ms. During test sessions mice were placed into the center of the chamber, and locomotion was measured for 60 min. During single-drug exposure sessions, mice were removed from the chambers, injected with drug (SALB, 1–10.0 mg/kg; CNO, 3.0 mg/kg; or vehicle), and returned to the chamber for 60 min of testing. During two-drug exposure sessions, mice were removed from the chambers after a 60-min baseline, injected with vehicle or 3.0 mg/kg CNO, returned to apparatus for 30 min, removed, injected with 17.0 mg/kg SALB or vehicle, and returned to the chambers for an additional 30 min of testing. Mice were habituated to vehicle injections for 2 days before testing. SALB was dissolved in DMSO and injected subcutaneously (s.c.) through a 27-gauge needle at a volume of 1 μ L/g body weight using a Hamilton GASTIGHT 250- μ L syringe. CNO was dissolved in 10% DMSO in saline and injected i.p. through a 27-gauge needle at a volume of 10 μ L/g body weight. Drugs were administered in counterbalanced order using a within-subjects design. Drug effects were determined by the total distance traveled during the 60-min post-injection period or during each 30-min post-injection period. Dose effects were analyzed with repeated-measures ANOVA with post hoc Bonferroni t tests when $p < 0.05$. Individual drug determinations were compared to vehicle using paired t tests.

Mouse Handling for Feeding Studies

Mice (10- to 12-week-old males) were singly housed for at least 2.5 weeks following surgery and handled for 10 consecutive days before the assay to reduce stress response. Feeding studies were performed in home cages with ad libitum food access. Home cages were changed every day during food intake measurements to eliminate residual food crumbs in the bedding. CNO was administered at 1 mg per kg of body weight. Saline was delivered at the same volume as CNO to maintain consistency in the studies. SALB was administered at 10 mg/kg, dissolved in DMSO. DMSO was delivered at the same volume as SALB to maintain consistency. Mice with "missed" viral injections, incomplete "hits," or expression outside the area of interest were excluded from analysis after post hoc examination of mCherry and mCitrine expression.

Feeding Studies in SIM1-Cre Mice

During the light cycle, animals (*SIM1-cre*, $n = 7$; WT, $n = 6$) were injected with either DMSO (s.c.) or SALB (10 mg/kg; s.c.), and food intake was measured 1 hr after injection. A full trial consisted of assessing food intake from the study subjects after they received injections of DMSO on day 1 and SALB on day 2. Animals received a day "off" between trials before another trial was initiated. The food intake data from all days following DMSO/SALB injections were then averaged across four trials and combined for analysis.

Feeding Studies in AGRP-IRES-Cre Mice

Just before the onset of the dark cycle, animals (*AGRP-ires-cre*, $n = 6$; WT, $n = 6$) were injected with either DMSO (s.c.) or SALB (10 mg/kg; s.c.), and food intake was measured 1 hr after injection. A full trial consisted of assessing food intake from the study subjects after they received injections of DMSO

on day 1 and SalB on day 2. Animals received a day “off” between trials before another trial was initiated. The food intake data from all days following DMSO/SalB injections were then averaged across three trials and combined for analysis.

Feeding Studies with Multiplexed KOR and hM3Dq DREADD

During the light cycle, animals (*AGRP-ires-cre*, $n = 10$) were injected with saline (i.p.), CNO (1 mg/kg; i.p.), DMSO (s.c.), or CNO + SalB (10 mg/kg; s.c.), and food intake was monitored every 30 min for 3 hr after s.c. injection. A full trial consisted of assessing food intake from the study subjects after they received injections of saline on day 1, CNO on day 2, DMSO on day 3, and CNO + SalB on day 4. Animals received 3 days “off” between trials before another trial was initiated. The food intake data from all days were then averaged by condition across three trials and combined for analysis.

Whole-Cell Electrophysiology Experiments

The ability of KORD to generate a SALB-induced hyperpolarization was tested using whole-cell electrophysiology. Slices were checked for adequate expression of the target constructs via the mCitrine fluorescence, and those mice in which expression of constructs could not be identified were discarded. Using a potassium gluconate-based internal recording solution, whole-cell electrophysiological experiments were conducted in current-clamp at the RMP for each neuron. Following a 5-min stable baseline, 100 nM SALB was bath-applied for 10 min (VTA/SN^{VGAT}), 6 min (PVH^{SIM1}), or 7 min (ARC^{AgRP}) at a flow rate of 2 mL per minute. Average RMPs before and after the application of SALB were calculated, and results were presented as a shift from baseline RMP. Miniature IPSCs were recorded in the presence of tetrodotoxin (500 nM) and kynurenic acid (3 mM) to block AMPA and NMDA receptor-dependent postsynaptic currents. Neurons were held at -70 mV across all voltage-clamp recordings, and recording electrodes were filled with (in mM) 70 KCl, 65 potassium gluconate, 5 NaCl, 10 HEPES, 2 QX-314, 0.6 EGTA, 4 Na-ATP, 0.4 Na-GTP (pH 7.25), and 290–295 mOsm. After a 6-min stable baseline, SALB (100 nM) was bath-applied for 15 min, and recordings were continued during a 20-min washout period. mIPSCs were detected using ClampFit, and the frequency and amplitude of events were normalized to baseline.

SUPPLEMENTAL INFORMATION

Supplemental Information includes four figures and two tables and can be found with this article online at <http://dx.doi.org/10.1016/j.neuron.2015.03.065>.

AUTHOR CONTRIBUTIONS

E.V. and B.L.R. designed the strategy for creating KORD, which E.V. executed. E.V., J.E.R., and C.L. designed and executed the *in vivo* studies to validate KORD with supervision by B.L.R., C.J.M., and M.J.K. E.V., P.M.G., F.M.S., and X.-P.H. performed *in vitro* pharmacology with supervision by B.L.R.; R.H.J.O., H.Z., and D.J.U. performed stereotaxic viral injections with supervision by B.L.R.; R.H.J.O. performed immunofluorescent studies with supervision by J.S. and quantified images; K.L.W., H.Z., J.F.D., C.L., and J.E.R. performed behavioral studies with supervision by B.L.R., T.L.K., C.J.M., and M.J.K.; J.E.R. performed the initial yeast screen with supervision by B.L.R.; C.L., N.A.C., K.E.P., and C.M.M. performed electrophysiology studies with supervision by T.L.K. and M.J.K.; P.D.M. performed molecular modeling studies; E.V., J.E.R., C.L., M.J.K., and B.L.R. wrote the manuscript with assistance of all authors; and B.L.R. was responsible for the overall design and execution of these studies.

ACKNOWLEDGMENTS

This work was supported, in whole or in part, by the NIH BRAIN Initiative Grant UO1MH105892 (B.L.R. and T.L.K.) and by R01 DA017204 (B.L.R.), PO1DA035764 (B.L.R.), and the NIH-NIMH Psychoactive Drug Screening Program (B.L.R.) the Intramural Research Program of the NIH, The National Institute of Diabetes and Digestive and Kidney Diseases – NIDDK; DK075087, DK075089 (M.J.K.); and by R01AA019454, R00AA017668, NARSAD Young

Investigator Award, and U01AA020911 (T.L.K.); and F31AA02228001 (N.A.C.), R01 AA018335 (C.J.M.), and F30 AA021312 (J.E.R.).

Received: November 3, 2014

Revised: March 2, 2015

Accepted: March 29, 2015

Published: April 30, 2015

REFERENCES

- Agulhon, C., Boyt, K.M., Xie, A.X., Friocourt, F., Roth, B.L., and McCarthy, K.D. (2013). Modulation of the autonomic nervous system and behaviour by acute glial cell Gq protein-coupled receptor activation *in vivo*. *J. Physiol.* *591*, 5599–5609.
- Alexander, G.M., Rogan, S.C., Abbas, A.I., Armbruster, B.N., Pei, Y., Allen, J.A., Nonneman, R.J., Hartmann, J., Moy, S.S., Nicolelis, M.A., et al. (2009). Remote control of neuronal activity in transgenic mice expressing evolved G protein-coupled receptors. *Neuron* *63*, 27–39.
- Ansonoff, M.A., Zhang, J., Czyzyk, T., Rothman, R.B., Stewart, J., Xu, H., Zwiwony, J., Siebert, D.J., Yang, F., Roth, B.L., and Pintar, J.E. (2006). Antinociceptive and hypothermic effects of Salvinorin A are abolished in a novel strain of kappa-opioid receptor-1 knockout mice. *J. Pharmacol. Exp. Ther.* *318*, 641–648.
- Aponte, Y., Atasoy, D., and Sternson, S.M. (2011). AGRP neurons are sufficient to orchestrate feeding behavior rapidly and without training. *Nat. Neurosci.* *14*, 351–355.
- Armbruster, B.N., Li, X., Pausch, M.H., Herlitze, S., and Roth, B.L. (2007). Evolving the lock to fit the key to create a family of G protein-coupled receptors potentially activated by an inert ligand. *Proc. Natl. Acad. Sci. USA* *104*, 5163–5168.
- Atasoy, D., Betley, J.N., Su, H.H., and Sternson, S.M. (2012). Deconstruction of a neural circuit for hunger. *Nature* *488*, 172–177.
- Balthasar, N., Dalgaard, L.T., Lee, C.E., Yu, J., Funahashi, H., Williams, T., Ferreira, M., Tang, V., McGovern, R.A., Kenny, C.D., et al. (2005). Divergence of melanocortin pathways in the control of food intake and energy expenditure. *Cell* *123*, 493–505.
- Besnard, J., Ruda, G.F., Setola, V., Abecassis, K., Rodriguiz, R.M., Huang, X.P., Norval, S., Sassano, M.F., Shin, A.I., Webster, L.A., et al. (2012). Automated design of ligands to polypharmacological profiles. *Nature* *492*, 215–220.
- Betley, J.N., Cao, Z.F., Ritola, K.D., and Sternson, S.M. (2013). Parallel, redundant circuit organization for homeostatic control of feeding behavior. *Cell* *155*, 1337–1350.
- Boyden, E.S., Zhang, F., Bamberg, E., Nagel, G., and Deisseroth, K. (2005). Millisecond-timescale, genetically targeted optical control of neural activity. *Nat. Neurosci.* *8*, 1263–1268.
- Conklin, B.R., Hsiao, E.C., Claeysen, S., Dumuis, A., Srinivasan, S., Forsayeth, J.R., Guettier, J.M., Chang, W.C., Pei, Y., McCarthy, K.D., et al. (2008). Engineering GPCR signaling pathways with RASSLs. *Nat. Methods* *5*, 673–678.
- Deisseroth, K. (2011). Optogenetics. *Nat. Methods* *8*, 26–29.
- Dell’Anno, M.T., Caiazzo, M., Leo, D., Dvoretzskova, E., Medrihan, L., Colasante, G., Giannelli, S., Theka, I., Russo, G., Mus, L., et al. (2014). Remote control of induced dopaminergic neurons in parkinsonian rats. *J. Clin. Invest.* *124*, 3215–3229.
- Dong, S., Rogan, S.C., and Roth, B.L. (2010). Directed molecular evolution of DREADDs: a generic approach to creating next-generation RASSLs. *Nat. Protoc.* *5*, 561–573.
- Erlenbach, I., Kostenis, E., Schmidt, C., Hamdan, F.F., Pausch, M.H., and Wess, J. (2001). Functional expression of M(1), M(3) and M(5) muscarinic acetylcholine receptors in yeast. *J. Neurochem.* *77*, 1327–1337.
- Fenalti, G., Giguere, P.M., Katritch, V., Huang, X.P., Thompson, A.A., Cherezov, V., Roth, B.L., and Stevens, R.C. (2014). Molecular control of δ -opioid receptor signalling. *Nature* *506*, 191–196.

- Fenalti, G., Zatzepin, N.A., Betti, C., Giguere, P., Han, G.W., Ishchenko, A., Liu, W., Guillemy, K., Zhang, H., James, D., et al. (2015). Structural basis for bifunctional peptide recognition at human δ -opioid receptor. *Nat. Struct. Mol. Biol.* 22, 265–268.
- Guettier, J.M., Gautam, D., Scarselli, M., Ruiz de Azua, I., Li, J.H., Rosemond, E., Ma, X., Gonzalez, F.J., Armbruster, B.N., Lu, H., et al. (2009). A chemical-genetic approach to study G protein regulation of beta cell function in vivo. *Proc. Natl. Acad. Sci. USA* 106, 19197–19202.
- Hooker, J.M., Munro, T.A., Béguin, C., Alexoff, D., Shea, C., Xu, Y., and Cohen, B.M. (2009). Salvinorin A and derivatives: protection from metabolism does not prolong short-term, whole-brain residence. *Neuropharmacology* 57, 386–391.
- Jain, S., Ruiz de Azua, I., Lu, H., White, M.F., Guettier, J.M., and Wess, J. (2013). Chronic activation of a designer G(q)-coupled receptor improves β cell function. *J. Clin. Invest.* 123, 1750–1762.
- Kane, B.E., Nieto, M.J., McCurdy, C.R., and Ferguson, D.M. (2006). A unique binding epitope for salvinorin A, a non-nitrogenous kappa opioid receptor agonist. *FEBS J.* 273, 1966–1974.
- Keiser, M.J., Setola, V., Irwin, J.J., Laggner, C., Abbas, A.I., Hufeisen, S.J., Jensen, N.H., Kuijter, M.B., Matos, R.C., Tran, T.B., et al. (2009). Predicting new molecular targets for known drugs. *Nature* 462, 175–181.
- Krashes, M.J., Koda, S., Ye, C., Rogan, S.C., Adams, A.C., Cusher, D.S., Maratos-Flier, E., Roth, B.L., and Lowell, B.B. (2011). Rapid, reversible activation of AgRP neurons drives feeding behavior in mice. *J. Clin. Invest.* 121, 1424–1428.
- Krashes, M.J., Shah, B.P., Madara, J.C., Olson, D.P., Strohlic, D.E., Garfield, A.S., Vong, L., Pei, H., Watabe-Uchida, M., Uchida, N., et al. (2014). An excitatory paraventricular nucleus to AgRP neuron circuit that drives hunger. *Nature* 507, 238–242.
- Larson, D.L., Jones, R.M., Hjorth, S.A., Schwartz, T.W., and Portoghese, P.S. (2000). Binding of norbinaltorphimine (norBNI) congeners to wild-type and mutant mu and kappa opioid receptors: molecular recognition loci for the pharmacophore and address components of kappa antagonists. *J. Med. Chem.* 43, 1573–1576.
- Li, J.H., Jain, S., McMillin, S.M., Cui, Y., Gautam, D., Sakamoto, W., Lu, H., Jou, W., McGuinness, O.P., Gavrilo, O., and Wess, J. (2013). A novel experimental strategy to assess the metabolic effects of selective activation of a G(q)-coupled receptor in hepatocytes in vivo. *Endocrinology* 154, 3539–3551.
- Magnus, C.J., Lee, P.H., Atasoy, D., Su, H.H., Looger, L.L., and Sternson, S.M. (2011). Chemical and genetic engineering of selective ion channel-ligand interactions. *Science* 333, 1292–1296.
- Mahler, S.V., Vazey, E.M., Beckley, J.T., Keistler, C.R., McGlinchey, E.M., Kauffling, J., Wilson, S.P., Deisseroth, K., Woodward, J.J., and Aston-Jones, G. (2014). Designer receptors show role for ventral pallidum input to ventral tegmental area in cocaine seeking. *Nat. Neurosci.* 17, 577–585.
- Nakajima, K., and Wess, J. (2012). Design and functional characterization of a novel, arrestin-biased designer G protein-coupled receptor. *Mol. Pharmacol.* 82, 575–582.
- Noble, B., Kallal, L.A., Pausch, M.H., and Benovic, J.L. (2003). Development of a yeast bioassay to characterize G protein-coupled receptor kinases. Identification of an NH2-terminal region essential for receptor phosphorylation. *J. Biol. Chem.* 278, 47466–47476.
- Portoghese, P.S. (1989). Bivalent ligands and the message-address concept in the design of selective opioid receptor antagonists. *Trends Pharmacol. Sci.* 10, 230–235.
- Robinson, J.E., Fish, E.W., Krouse, M.C., Thorsell, A., Heilig, M., and Malanga, C.J. (2012). Potentiation of brain stimulation reward by morphine: effects of neurokinin-1 receptor antagonism. *Psychopharmacology (Berl.)* 220, 215–224.
- Rogan, S.C., and Roth, B.L. (2011). Remote control of neuronal signaling. *Pharmacol. Rev.* 63, 291–315.
- Roth, B.L., Baner, K., Westkaemper, R., Siebert, D., Rice, K.C., Steinberg, S., Ernsberger, P., and Rothman, R.B. (2002). Salvinorin A: a potent naturally occurring nonnitrogenous kappa opioid selective agonist. *Proc. Natl. Acad. Sci. USA* 99, 11934–11939.
- Stachniak, T.J., Ghosh, A., and Sternson, S.M. (2014). Chemogenetic synaptic silencing of neural circuits localizes a hypothalamus \rightarrow midbrain pathway for feeding behavior. *Neuron* 82, 797–808.
- Sternson, S.M., and Roth, B.L. (2014). Chemogenetic tools to interrogate brain functions. *Annu. Rev. Neurosci.* 37, 387–407.
- Strader, C.D., Gaffney, T., Sugg, E.E., Candelore, M.R., Keys, R., Patchett, A.A., and Dixon, R.A. (1991). Allele-specific activation of genetically engineered receptors. *J. Biol. Chem.* 266, 5–8.
- Todtenkopf, M.S., Marcus, J.F., Portoghese, P.S., and Carlezon, W.A., Jr. (2004). Effects of kappa-opioid receptor ligands on intracranial self-stimulation in rats. *Psychopharmacology (Berl.)* 172, 463–470.
- Tong, Q., Ye, C.P., Jones, J.E., Elmquist, J.K., and Lowell, B.B. (2008). Synaptic release of GABA by AgRP neurons is required for normal regulation of energy balance. *Nat. Neurosci.* 11, 998–1000.
- Urban, D.J., and Roth, B.L. (2015). DREADDs (designer receptors exclusively activated by designer drugs): chemogenetic tools with therapeutic utility. *Annu. Rev. Pharmacol. Toxicol.* 55, 399–417.
- van Zessen, R., Phillips, J.L., Budygin, E.A., and Stuber, G.D. (2012). Activation of VTA GABA neurons disrupts reward consumption. *Neuron* 73, 1184–1194.
- Vaqué, J.P., Dorsam, R.T., Feng, X., Iglesias-Bartolome, R., Forsthoefel, D.J., Chen, Q., Debant, A., Seeger, M.A., Ksander, B.R., Teramoto, H., and Gutkind, J.S. (2013). A genome-wide RNAi screen reveals a Trio-regulated Rho GTPase circuitry transducing mitogenic signals initiated by G protein-coupled receptors. *Mol. Cell* 49, 94–108.
- Vardy, E., Mosier, P.D., Frankowski, K.J., Wu, H., Katritch, V., Westkaemper, R.B., Aubé, J., Stevens, R.C., and Roth, B.L. (2013). Chemotype-selective modes of action of κ -opioid receptor agonists. *J. Biol. Chem.* 288, 34470–34483.
- White, K.L., Robinson, J.E., Zhu, H., DiBerto, J.F., Polepally, P.R., Zjawiony, J.K., Nichols, D.E., Malanga, C.J., and Roth, B.L. (2015). The G protein-biased κ -opioid receptor agonist RB-64 is analgesic with a unique spectrum of activities in vivo. *J. Pharmacol. Exp. Ther.* 352, 98–109.
- Wu, H., Wacker, D., Mileni, M., Katritch, V., Han, G.W., Vardy, E., Liu, W., Thompson, A.A., Huang, X.P., Carroll, F.I., et al. (2012). Structure of the human κ -opioid receptor in complex with JDTic. *Nature* 485, 327–332.
- Yagi, H., Tan, W., Dillenburg-Pilla, P., Armando, S., Amorphimoltham, P., Simaan, M., Weigert, R., Molinolo, A.A., Bouvier, M., and Gutkind, J.S. (2011). A synthetic biology approach reveals a CXCR4-G13-Rho signaling axis driving transendothelial migration of metastatic breast cancer cells. *Sci. Signal.* 4, ra60.
- Zhu, H., Pleil, K.E., Urban, D.J., Moy, S.S., Kash, T.L., and Roth, B.L. (2014). Chemogenetic inactivation of ventral hippocampal glutamatergic neurons disrupts consolidation of contextual fear memory. *Neuropsychopharmacology* 39, 1880–1892.

Epigenomic Signatures of Neuronal Diversity in the Mammalian Brain

Alisa Mo,^{1,2,11} Eran A. Mukamel,^{3,4,11} Fred P. Davis,^{5,11} Chongyuan Luo,^{6,11} Gilbert L. Henry,⁵ Serge Picard,⁵ Mark A. Urich,⁶ Joseph R. Nery,⁶ Terrence J. Sejnowski,^{3,7,8} Ryan Lister,^{6,9} Sean R. Eddy,⁵ Joseph R. Ecker,^{6,8,*} and Jeremy Nathans^{1,2,10,*}

¹Department of Molecular Biology and Genetics

²Department of Neuroscience

Johns Hopkins University School of Medicine, Baltimore, MD 21205, USA

³Computational Neurobiology Laboratory, The Salk Institute for Biological Studies, La Jolla, CA 92037, USA

⁴Department of Cognitive Science, University of California San Diego, La Jolla, CA 92037, USA

⁵Janelia Research Campus, Howard Hughes Medical Institute, Ashburn, VA 20147, USA

⁶Genomic Analysis Laboratory, The Salk Institute for Biological Studies, La Jolla, CA 92037, USA

⁷Division of Biological Sciences, University of California at San Diego, La Jolla, CA 92037, USA

⁸Howard Hughes Medical Institute, The Salk Institute for Biological Studies, La Jolla, CA 92037, USA

⁹The ARC Centre of Excellence in Plant Energy Biology, The University of Western Australia, Crawley, Western Australia 6009, Australia

¹⁰Howard Hughes Medical Institute, Johns Hopkins University School of Medicine, Baltimore, MD 21205, USA

¹¹Co-first author

*Correspondence: ecker@salk.edu (J.R.E.), jnathans@jhmi.edu (J.N.)

<http://dx.doi.org/10.1016/j.neuron.2015.05.018>

SUMMARY

Neuronal diversity is essential for mammalian brain function but poses a challenge to molecular profiling. To address the need for tools that facilitate cell-type-specific epigenomic studies, we developed the first affinity purification approach to isolate nuclei from genetically defined cell types in a mammal. We combine this technique with next-generation sequencing to show that three subtypes of neocortical neurons have highly distinctive epigenomic landscapes. Over 200,000 regions differ in chromatin accessibility and DNA methylation signatures characteristic of gene regulatory regions. By footprinting and motif analyses, these regions are predicted to bind distinct cohorts of neuron subtype-specific transcription factors. Neuronal epigenomes reflect both past and present gene expression, with DNA hypermethylation at developmentally critical genes appearing as a novel epigenomic signature in mature neurons. Taken together, our findings link the functional and transcriptional complexity of neurons to their underlying epigenomic diversity.

INTRODUCTION

In the mammalian brain, distinct types of neurons interact in intricate networks to govern thought, emotion, and behavior. Neurons can differ in their morphologies, synaptic connections, electrophysiological properties, neurotransmitter identities, and developmental histories. The balance of signaling across heterogeneous neurons is critical for healthy brain

function, and disruptions of genes that mediate this balance are implicated in neurological and psychiatric diseases (Sullivan et al., 2012).

Neuronal diversity arises partly through spatiotemporal regulation of gene expression by regulatory regions such as promoters and enhancers. These discrete regions of DNA can be identified using epigenomic signatures, which include accessible chromatin, active histone modifications, and low levels of DNA methylation (Bird, 2002; Heintzman et al., 2007; Stadler et al., 2011; Thurman et al., 2012). Neurons undergo extensive epigenomic changes during post-natal brain development, including de novo establishment of non-CG methylation (Lister et al., 2013; Xie et al., 2012). However, the genome-wide patterns of accessible chromatin and both CG and non-CG methylation in specific neuronal subpopulations are unknown. We reasoned that neuronal epigenomic landscapes should mirror neuronal diversity. Whereas gene expression analysis provides a snapshot of a neuron's molecular activity at a single point in time, the complementary epigenomic information captures gene regulatory mechanisms, developmental origins, and potential future responses induced by neuronal activity.

Cellular diversity is important for brain function, but it also poses a technical challenge for epigenomic studies. Cell-type-specific molecular profiling requires the isolation of targeted cell populations from complex tissues (Maze et al., 2014). Manual sorting (Sugino et al., 2006) and laser capture microdissection (Emmert-Buck et al., 1996) are useful for isolating small numbers of cells but do not provide enough material for epigenomic studies. Fluorescence-activated cell sorting (FACS) can isolate larger numbers of cells but may be challenging in tissues such as the adult brain, where cells are morphologically complex and densely interconnected. Although improvements have been made (Saxena et al., 2012), the neuronal dissociation process may also induce cellular stress

responses and perturb subsequent molecular profiles. Genetically directed strategies that isolate RNA from specific cell populations in mice (Doyle et al., 2008; Gay et al., 2013; Heiman et al., 2008; Sanz et al., 2009) have begun to chart transcriptional diversity across cell types but cannot profile epigenomic features unless combined with FACS (Mellén et al., 2012). Although nuclei can be isolated by FACS for epigenomic studies (Jiang et al., 2008), FACS-sorted nuclei are fragile and difficult to concentrate into the small volumes that are optimal for chromatin assays. An alternate approach is INTACT (isolation of nuclei tagged in specific cell types; Deal and Henikoff, 2010), which uses affinity purification to isolate tagged nuclei. Captured nuclei can be used for gene expression, epigenomic, and proteomic profiling (Amin et al., 2014; Henry et al., 2012; Steiner et al., 2012).

Here, we present the first application of INTACT in a mammalian organism and use it to address the cell-type-specific neuronal epigenome. Our approach uses the Cre-loxP system in mice to express a tagged nuclear membrane protein, allowing affinity purification of labeled nuclei from genetically defined cell populations. In this study, we applied INTACT to examine the core transcriptional and epigenomic features of three major functional classes of neocortical neurons: excitatory pyramidal neurons, Parvalbumin (PV)-expressing fast-spiking interneurons, and Vasoactive intestinal peptide (VIP)-expressing interneurons. 70%–85% of cortical neurons are excitatory. The remaining 15%–30% are inhibitory neurons, with approximately 40% expressing PV and 12% expressing VIP (Gelman and Marín, 2010; Rudy et al., 2011). Together, these mutually exclusive cell types represent both glutamatergic (excitatory) and GABAergic (inhibitory) signaling. Neocortical pyramidal neurons provide the long-range excitatory output of the brain, and inhibitory neurons modulate the rate and temporal structure of this network output (Molyneaux et al., 2007; Rudy et al., 2011). PV and VIP neurons have distinct computational roles as a result of differences in their firing patterns and synaptic connections (Kepecs and Fishell, 2014).

Several studies have identified genome-wide differences in gene expression across neuronal subpopulations (Doyle et al., 2008; Molyneaux et al., 2015; Sugino et al., 2006). However, neuron subtype-specific epigenomes remain largely unexplored. We find that among excitatory, PV, and VIP neurons, global epigenomic landscapes of DNA methylation and chromatin accessibility show widespread differences. These differences reflect distinct mechanisms of gene regulation, with candidate regulators identified using transcription factor (TF) footprinting and motif analyses. Integrating epigenomes together with expression profiles, we find intragenic non-CG methylation to be particularly salient for inferring neuronal gene expression. At TF genes with cell-type-specific developmental roles, we further identify a unique pattern of DNA hyper-methylation in adult neurons that is a long-lasting epigenomic signature of transient expression during brain development. Collectively, our results provide a comprehensive view of how distinct neuronal classes adopt unique epigenomic and gene regulatory configurations that reflect both mature neuronal function as well as developmental origin.

RESULTS

Mammalian INTACT Isolates Specific Populations of Neuronal Nuclei from the Brain

To generate a mouse line for affinity purification of labeled nuclei, we tagged the C terminus of mouse SUN1, a nuclear membrane protein, with two tandem copies of superfolder GFP and six copies of the Myc epitope (SUN1-sfGFP-Myc). We targeted *Sun1-sfGFP-myc* to the ubiquitously expressed *Rosa26* locus preceded by a CAG promoter and a *loxP-3x polyA-loxP* transcriptional roadblock (*R26-CAG-LSL-Sun1-sfGFP-myc*) (Figure 1A). Cells expressing Cre recombinase remove the roadblock and allow transcription of *Sun1-sfGFP-myc*. We first recombined *R26-CAG-LSL-Sun1-sfGFP-myc* in all cells using *Sox2-Cre*, a germline Cre driver (Figure S1A). *Sox2-Cre; R26-CAG-LSL-Sun1-sfGFP-myc* mice are healthy and fertile with no obvious phenotypic deficits, indicating that long-term expression of the fusion protein is well tolerated.

We expressed *Sun1-sfGFP-myc* in excitatory (Exc) neurons (*Camk2a-Cre*), PV interneurons (*PV-Cre*), and VIP interneurons (*VIP-Cre*) (Figure 1B and Table S1). Immunohistochemistry targeting GFP showed that the SUN1 fusion protein is localized to the nuclear periphery. Quantification of labeled nuclei together with neuronal markers (Figures 1B and S1B–S1G) indicated that each Cre driver predominantly recombines the targeted cell type. The pattern of labeling using anti-Myc is identical to anti-GFP (Figure S1H).

We next developed an affinity purification method to capture GFP+/Myc+ nuclei from fresh tissue homogenates (Figure 1C). Either anti-GFP or anti-Myc antibodies, together with Protein G-coated magnetic beads, can be used to isolate nuclei from both rare and common cell types with high yield and specificity. Examination of input versus affinity-purified (anti-GFP) nuclei (Figure 1D) by fluorescence microscopy showed that INTACT achieves >98% purity with >50% yield, even for cell types that represent only 1%–3% of the starting tissue (Figure 1E). Similar results were obtained using anti-Myc (95%–98% purity with 42%–65% yield, $n = 3$). To further assess the specificity of mouse INTACT, we performed flow cytometry on input and affinity purified (anti-Myc) nuclei from *VIP-Cre; R26-CAG-LSL-Sun1-sfGFP-myc* mice (Figure S1I). Flow cytometry showed that more than 99% of input nuclei (after step 2 in Figure 1C) were singlets, corresponding to well-isolated nuclei, and 1.5% of input nuclei were GFP+. In contrast, 98.9% of affinity purified nuclei were GFP+. Similar results were obtained using anti-GFP (Figure S1J). Therefore, both manual quantification and flow cytometry indicate that mouse INTACT isolates highly pure preparations of tagged nuclei.

INTACT RNA-Seq Captures Neuronal Subtype Markers

To assess patterns of gene expression and DNA methylation in distinct neuronal subtypes, we used RNA-seq to profile transcript abundance from INTACT-purified nuclei in adult mice, and we used MethylC-seq to generate single-base resolution methylome maps (Lister et al., 2008) from the same cell types, with the caveat that bisulfite sequencing does not differentiate between methylcytosine (mC) and hydroxymethylcytosine (hmC) (Figure 2A). RNA-seq profiles are highly similar across

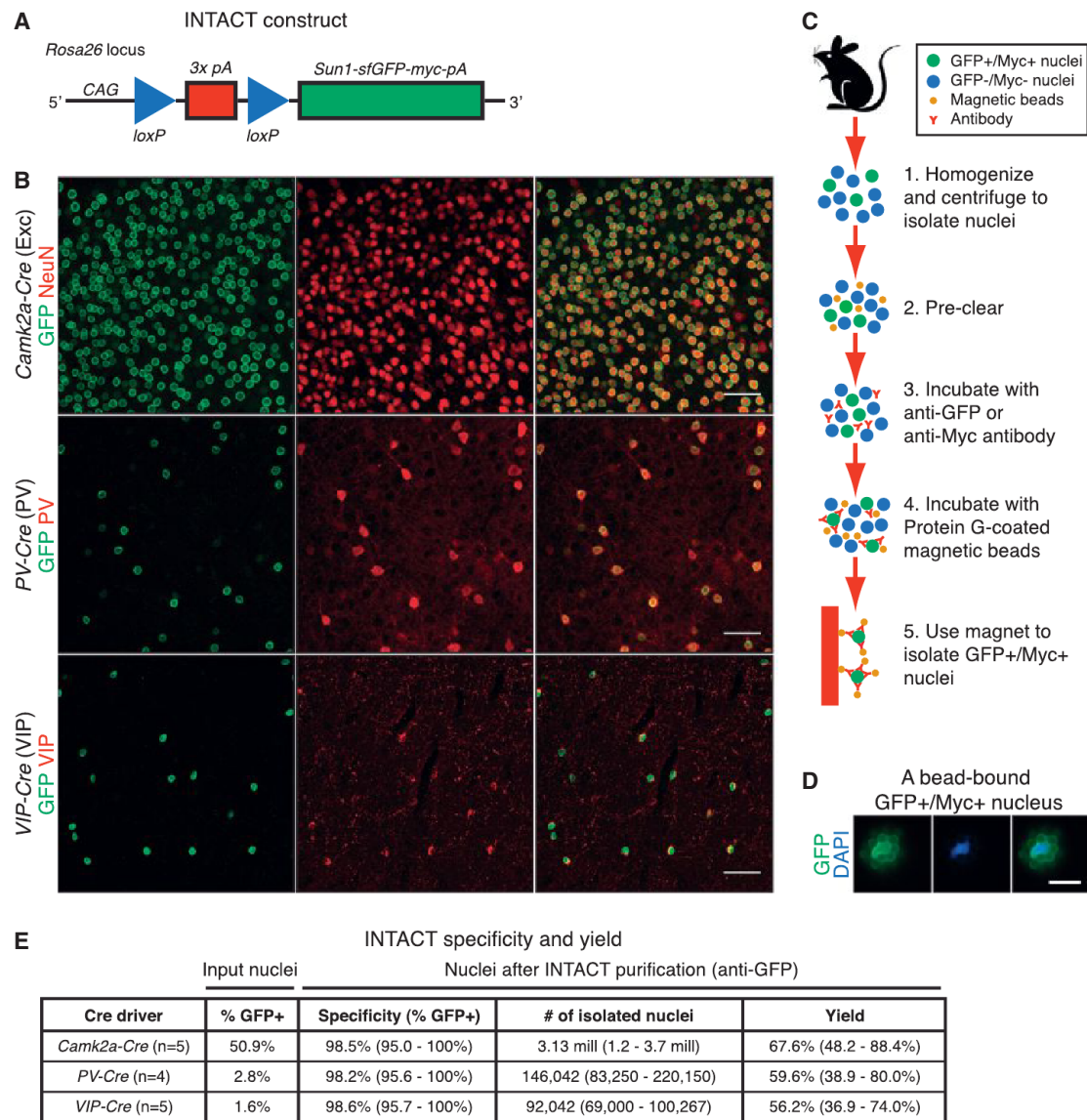


Figure 1. An Affinity Purification Method Isolates Cell-Type-Specific Nuclei in Mice

(A) Diagram of the INTACT knockin mouse construct. Cre-mediated excision of the transcription stop signals activates expression of the nuclear membrane tag (*Sun1-sfGFP-myc*) in the cell type of interest.

(B) Immunohistochemistry showing localization of SUN1-sfGFP-Myc in neocortical excitatory, PV, and VIP neurons in mice that carry *R26-CAG-LSL-Sun1-sfGFP-myc* together with a Cre driver. Scale bars, 50 μ m.

(C) Steps in the affinity purification method (INTACT).

(D) An example of a GFP+/Myc+ nucleus bound by Protein G-coated magnetic beads following INTACT purification and staining with DAPI. Scale bar, 10 μ m.

(E) For each experiment, INTACT purifications were performed with anti-GFP using pooled neocortices of two mice. Specificity of mouse INTACT: after INTACT purification, bead-bound nuclei were stained with DAPI, and the numbers of GFP+ versus GFP- nuclei were quantified by fluorescence microscopy (100–200 nuclei per experiment). Yield of mouse INTACT: the total number of input nuclei, the percentage of GFP+ nuclei in the input, and the total number of bead-bound nuclei after INTACT purification were quantified using fluorescence microscopy or a hemocytometer (100–200 nuclei per experiment). The yield was calculated based on the observed number of bead-bound nuclei versus the expected number from the input. For percentage of GFP+ nuclei in the input, the mean is shown. For quantities after INTACT purification, both the mean and ranges are shown. See also Figure S1.

replicates ($r = 0.98$) (Figures 2B, right panel, and S2A). A total of 4,095 genes show ≥ 2 -fold differential transcript abundance across neuronal subtypes, with over 2,000 between each pair of neurons (Table S2). Established subtype markers are enriched

in purified nuclei (e.g., *Slc17a7* and *Dkk3* in excitatory; *Pvalb* and *Lhx6* in PV; *Vip* and *Htr3a* in VIP), whereas markers of other lineages are depleted (Figure 2B, left three panels). The gene expression profile of INTACT-purified PV neurons is also

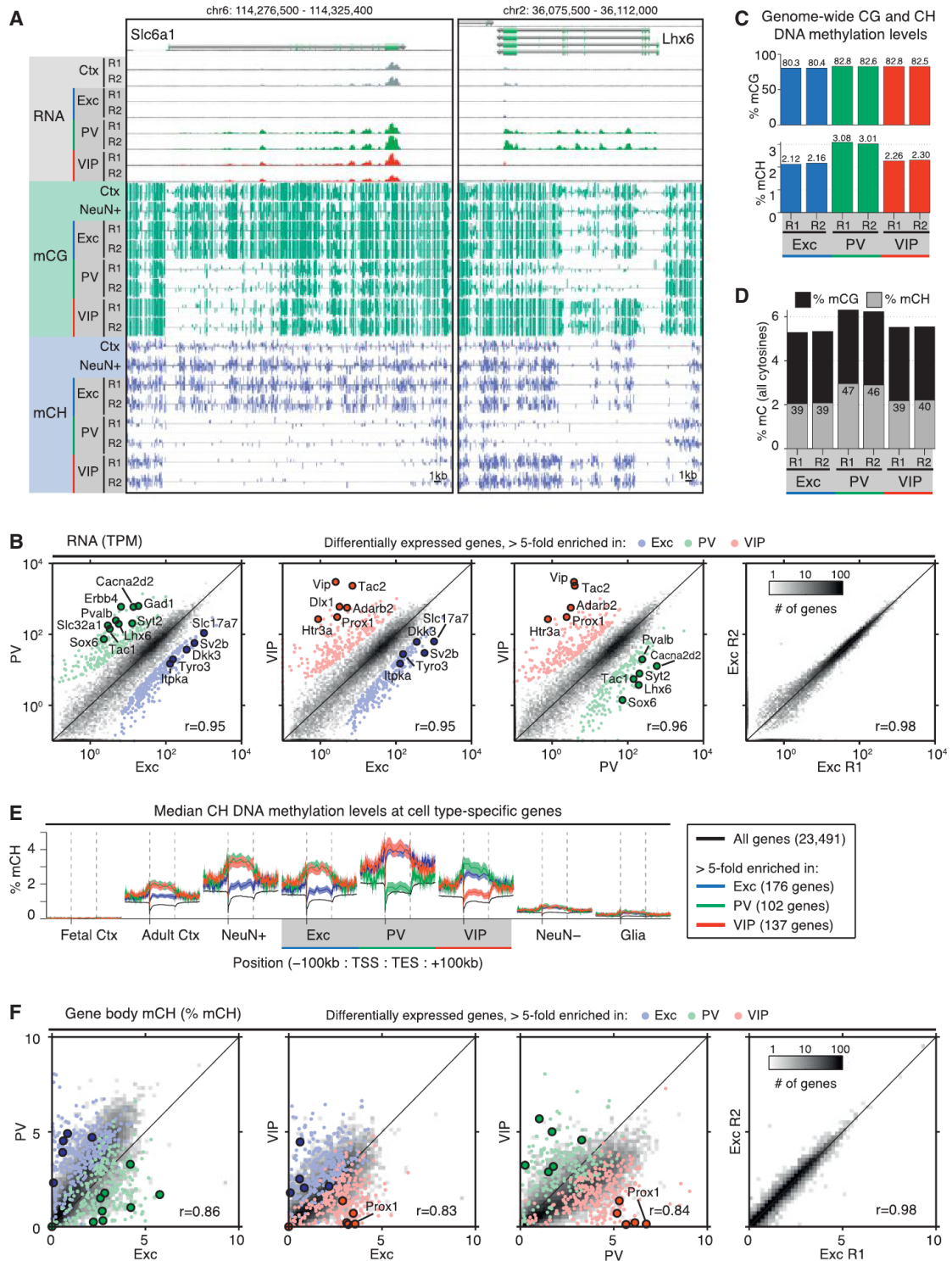


Figure 2. Widespread Differences in Gene Expression and DNA Methylation among Neuron Subtypes

(A) Browser representation of RNA-seq read density and DNA methylation in CG and non-CG contexts (mCG, mCH) at two genes. *Slc6a1* (GAT-1, left) is expressed primarily in inhibitory neurons. *Lhx6* (right) is PV neuron specific. Methylated CG (green) and CH (blue) positions are marked by upward (plus strand) and downward (minus strand) ticks. The height of each tick represents the percentage of methylation, ranging from 0% to 100%. NeuN+ and Ctx (cortex) adult mouse methylomes are from Lister et al. (2013). R1, replicate 1; R2, replicate 2.

(legend continued on next page)

consistent with RNA microarray data from manually sorted PV neurons (Figure S2B). We further used double fluorescent in situ hybridization to examine ten genes with previously unknown specificity in neocortical excitatory or PV neurons. Probe labeling for nine out of ten genes co-localized with the neuron type as predicted by RNA-seq and was excluded from other classes (Figure S2C), indicating that INTACT RNA-seq profiles identify novel patterns of gene expression.

Non-CG Methylation Is a Common Feature of Both Excitatory and Inhibitory Neurons, but Shows Widespread Differences in Genomic Distribution

In our MethylC-seq data, we observed substantial levels of DNA methylation in the non-CG context for all three neuronal populations (Figures 2A, 2C, and 2D). In most differentiated mammalian cells, DNA methylation is largely confined to the CG dinucleotide context. On the other hand, non-CG methylation (mCH, where H = A, C, or T) is a special feature of adult neurons but accumulates at much lower levels in adult glia and non-neuronal tissues (Lister et al., 2013; Xie et al., 2012). We find that mCH is most abundant in PV neurons (Figure 2C), where it constitutes nearly half (46%–47%) of the total methylcytosines (Figure 2D). Because mCH accumulates during the first weeks of post-natal development, coincident with the period of rapid synaptogenesis and long after excitatory and inhibitory lineages have diverged (Guo et al., 2014; Lister et al., 2013), these data suggest that a high level of non-CG methylation is a shared distinction of mature cortical neurons. Furthermore, because all three neuron subtypes share similar motif preferences for mCH, with CAC showing the highest methylation level (Figure S2D), it is likely that a common enzymatic mechanism (Gabel et al., 2015; Guo et al., 2014) is responsible for mCH deposition and maintenance in these neurons.

Both promoter and intragenic DNA methylation in CG and CH contexts inversely correlate with gene expression in the mammalian brain (Lister et al., 2013; Xie et al., 2012). However, a lack of cell-type specificity in existing in vivo datasets can complicate the interpretation at individual genes. For example, *Slc6a1* (GAT-1, primarily expressed in inhibitory neurons) and *Lhx6* (a PV-specific TF) appear to be both actively transcribed and highly methylated in samples of whole cortical tissue and in mixed neurons (NeuN+) (Figure 2A). Our datasets from INTACT-purified nuclei resolve these conflicting signals by showing that active gene expression and DNA methylation do not occur in the same cells but rather in distinct subpopulations. Using a list of highly specific genes from our RNA-seq data, we

find that both intragenic and promoter levels of CH (Figure 2E) and CG (Figure S2E) methylation are higher in the non-expressing cell type.

DNA methylation levels in gene bodies are highly variable across neuronal subtypes. As measured by pairwise Pearson correlations (Figures 2B, 2F, S2A, and S2F–S2H), gene body mCH levels are more divergent ($r = 0.83$ – 0.86) than both gene expression levels ($r = 0.95$ – 0.96 , $p = 0.003$, t test) and mCG levels ($r = 0.93$ – 0.94 , $p = 0.001$), whereas biological replicate signals are nearly identical for all features ($r \geq 0.97$). After normalization to adjust for the genome-wide average level of mCH, 8,662 genes (38%) show >50% difference in intragenic mCH in at least one pairwise comparison of cell types, versus 6.1% between biological replicates (Figure S2I, top). Certain genes display notably higher differences. For example, the VIP-specific TF *Prox1* has 23-fold higher mCH in excitatory neurons and 32-fold higher mCH in PV neurons compared to VIP neurons (Figure 2F). Variability in gene body CH methylation is paralleled by extensive differences at a global scale (Figure S2I, bottom). Genome-wide, 37% of all 5 kb bins show >50% difference in mCH between at least one pair of cell types, compared to only 3.8% between biological replicates.

Neuronal Regulatory DNA Is Predominantly Cell Type Specific

Localized regions of accessible chromatin and low levels of DNA methylation are well-established signatures of *cis*-regulatory elements such as promoters and enhancers (Neph et al., 2012; Stadler et al., 2011; Thurman et al., 2012). Therefore, we mapped the locations of putative gene regulatory regions in specific neuronal subtypes by systematically identifying these two features (Figures 3A and S3A). In excitatory neurons, we also profiled histone modifications using chromatin immunoprecipitation (ChIP) followed by sequencing to identify potential promoters (marked by H3K4me3), enhancers (H3K4me1 and H3K27ac), and Polycomb-associated repressed regions (H3K27me3). A limitation of our analysis is that we generally did not factor in sequence variation across mouse strains, which could potentially affect mapping to the C57BL/6 reference genome as well as levels of chromatin accessibility and DNA methylation (but see Supplemental Experimental Procedures).

We identified 322,452 discrete peaks of chromatin accessibility (median length 501 bp) in excitatory, PV, and VIP neurons using sub-nucleosomal (<100 bp) reads resulting from in vitro transposition of native chromatin by Tn5 transposase (ATAC-seq, Buenrostro et al., 2013) (Table S3). We find that most

(B) Pairwise comparisons of protein-coding gene expression measured by RNA-seq across cell types (left three panels) or between replicates (right panel). The most differentially expressed genes (>5-fold change) are shown as colored points, and selected cell-type-specific genes are labeled. r , Pearson correlation of $\log(\text{TPM}+0.1)$; TPM, transcripts per million.

(C) Percentage of MethylC-seq calls supporting methylation in the CG and CH contexts for each cell type on autosomes.

(D) Percentage of all MethylC-seq calls supporting methylation. The number in each bar indicates the percentage of all methylated cytosines on autosomes that occur in the CH context.

(E) Median ± 1 SEM of percentage of mCH within and surrounding gene bodies, showing an inverse correlation between expression and DNA methylation at differentially expressed genes identified from our RNA-seq data (>5-fold change for one cell type relative to both of the other cell types). TSS, transcription start site; TES, transcription end site; SEM, standard error of the mean.

(F) Pairwise comparisons of gene body percentage of mCH across cell types (left three panels) or between replicates (right panel). Colored dots correspond to the same genes shown in (B).

See also Figure S2.

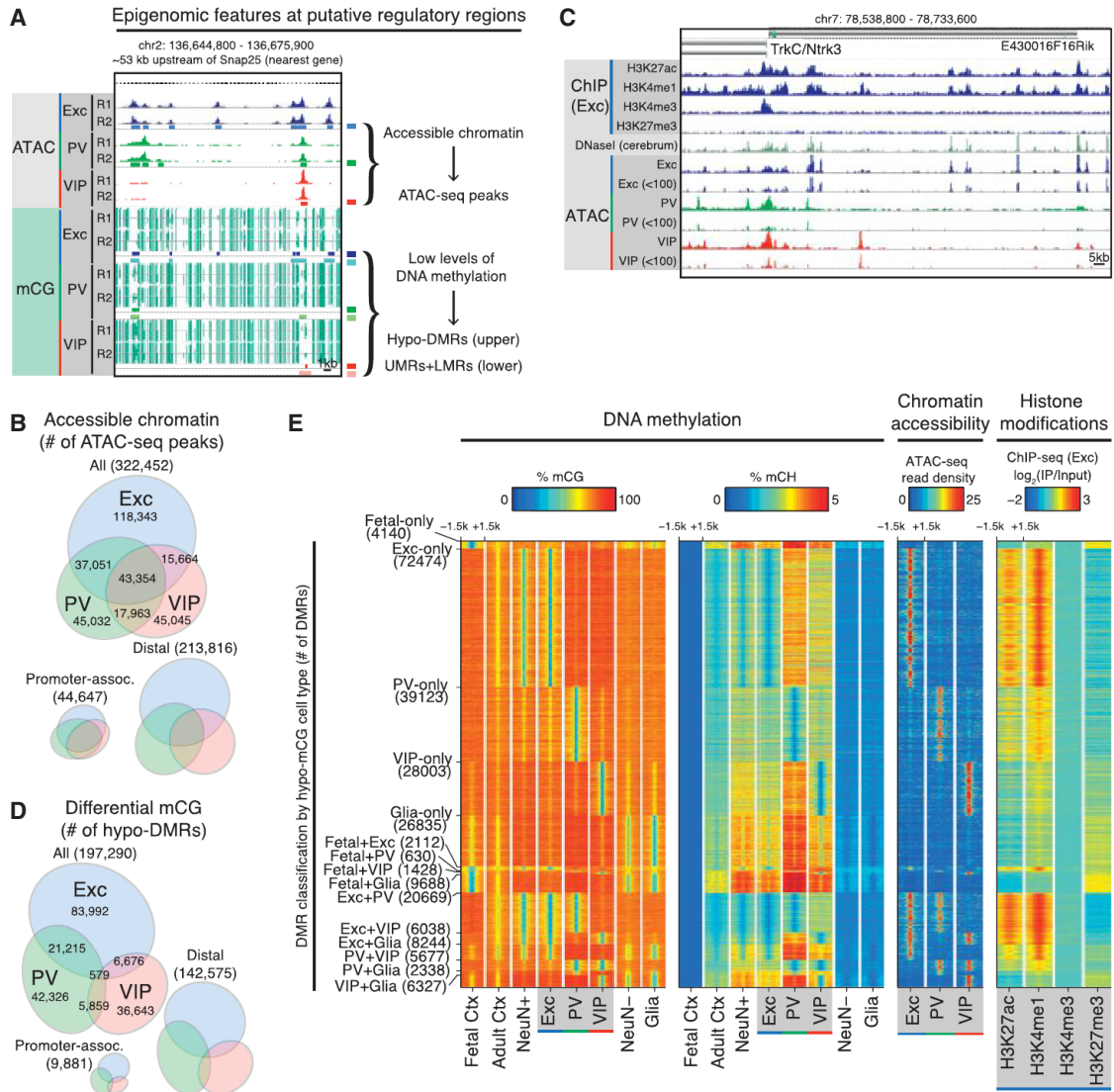


Figure 3. Epigenomic Marks Are Coordinated and Highly Cell Type Specific

(A) Examples of intergenic regulatory elements marked by accessible chromatin (peaks in ATAC-seq read density, upper tracks) and low levels of DNA methylation (hypo-DMRs and UMRs+LMRs, lower tracks) at an intergenic region ~53 kb upstream of *Snap25* (both the nearest gene and the nearest TSS). Locations of ATAC-seq peaks, hypo-DMRs, and UMRs+LMRs are shown below the corresponding raw data. R1, replicate 1; R2, replicate 2.

(B) Area-proportional Venn diagram showing the numbers of all cell-type-specific and shared ATAC-seq peaks across excitatory, PV, and VIP neurons (top). Area-proportional Venn diagrams showing that a greater fraction of promoter-associated peaks (within 2.5 kb of a TSS) are shared compared to distal peaks (>20 kb from a TSS), which are predominantly cell type specific (bottom).

(C) Browser representation of regulatory elements around *trkC/Ntrk3* marked by histone modifications in excitatory neurons, DNaseI hypersensitivity in whole cerebrum (from ENCODE), and peaks in ATAC-seq read density in excitatory, PV, and VIP neurons. For ATAC-seq, greater spatial resolution is achieved by using reads <100 bp in length (tracks labeled < 100).

(D) Area-proportional Venn diagram showing the numbers of DMRs identified to be hypo-methylated in excitatory, PV, and/or VIP neurons in a statistical comparison of CG methylation levels across five cell types. Two of these cell types, fetal cortex and glia, are not shown in the diagram. Most DMRs are distal to the TSS rather than promoter associated.

(E) Heatmap showing percentage of mCG plotted in 3 kb windows centered at DMRs hypo-methylated in one or two cell types (panel 1). At the same genomic regions, the following additional features were plotted: percentage of mCH (panel 2), chromatin accessibility (ATAC-seq reads) (panel 3), and histone modification ChIP-seq reads in excitatory neurons (panel 4). The number of DMRs in each category is shown in parentheses.

See also Figure S3.

regulatory elements in neuronal cells are cell type specific, including the large majority of distal regulatory elements (Figure 3B). In total, only 13.4% (43,354) of ATAC-seq peaks are

shared across all three neuronal subtypes. Compared to DNaseI-seq data from the whole cerebrum (Stamatoyannopoulos et al., 2012), nearly all (93%) shared ATAC-seq peaks are

also detected as cerebrum DNaseI-seq peaks (Figure 3C). In striking contrast, 62% of VIP-specific, 52% of PV-specific, and 31% of excitatory-specific ATAC-seq peaks are missed in the DNaseI-seq data, highlighting the advantage of INTACT profiling over whole-tissue analysis for identifying regulatory regions, particularly those unique to sparse cell types.

We next determined regions that differ in their levels of CG methylation across five cell populations: INTACT-purified excitatory, PV, and VIP neurons, plus fetal embryonic day 13 (E13) frontal cortex and adult S100b+ glia from Lister et al. (2013). We expected that including purified neurons would facilitate identification of differentially methylated regions (DMRs). Using a conservative statistical approach (Lister et al., 2013), we identified 251,301 DMRs with a median length of 275 bp (Table S3). Masking sequence variants across mouse strains did not substantially alter the DMR calling (see Supplemental Experimental Procedures). 112,462 of these DMRs are hypo-methylated (hypo-DMRs) in excitatory neurons. In keeping with our expectation, substitution of a mixed neuronal sample (NeuN+) with comparable sequencing coverage for the excitatory neuron sample results in 77,417 (68.8%) hypo-DMRs in NeuN+ neurons, despite the prevalence of excitatory neurons in this sample. The increased detection of DMRs using INTACT-purified excitatory neurons again demonstrates the power of cell-type-specific profiling for comprehensive identification of regulatory regions. To identify hypo-methylated regions that may not be differentially methylated across cell types, we segmented each methylome into unmethylated regions (UMRs) and low-methylated regions (LMRs) (Burger et al., 2013) (Table S3).

As expected from previous studies (Stadler et al., 2011), the majority of UMRs are located at promoters (66.3%–74.2% within 2.5 kb of a TSS), whereas most LMRs are potential distal regulatory elements (4.9%–6.2% within 2.5 kb of a TSS). For DMRs, the vast majority (93.8%) are also located more than 2.5 kb away from a TSS. Across DMRs that show hypo-methylation in at least one INTACT sample (Figure 3D), between 36,643 and 83,992 are hypo-methylated in a single neuron subtype. Recapitulating the division of ATAC-seq peaks (Figure 3B), excitatory neurons have the highest number of hypo-DMRs (Figure 3D), and remarkably, these are not shared with PV or VIP neurons. Taken together, these data extend previous profiling experiments in the brain, first by identifying hundreds of thousands of putative regulatory regions across three neuron subtypes, and then by classifying them into highly distinct sets in individual subtypes.

Cell-Type Specificity at Activity-Induced Transcription Factor Binding Sites

Because regions bound by activity-dependent TFs, as a whole, show constitutive DNA hypo-methylation (Guo et al., 2011) and chromatin accessibility (Malik et al., 2014), DMRs and differential ATAC-seq peaks could point to regulatory regions with cell-type-specific responses to induced neuronal activity. Therefore, we addressed the relationship between DMRs, differential ATAC-seq peaks, and activity-dependent TF binding in excitatory neurons, reasoning that our overall findings would also be applicable to the two inhibitory subpopulations that are not easily obtainable in quantities required for TF ChIP-seq. We examined activity-dependent TF binding profiles using previously published ChIP-

seq data from cortical cultures largely composed of immature excitatory neurons (Kim et al., 2010; Malik et al., 2014). The majority of activity-dependent binding sites for all TFs (58.2%–83.9%) overlap with excitatory neuron UMRs+LMRs (Figure S3B, left). However, only 1.4% of CREB and 10.8% of SRF binding sites overlap with excitatory neuron-specific hypo-DMRs, compared to 33.4%–40.3% of AP-1 (FOS, FOSB, JUNB) and NPAS4 binding sites ($p < 2 \times 10^{-38}$, Fisher's exact test [FET]). In particular, activity-dependent binding sites for AP-1 factors and NPAS4 in cortical cultures are enriched in excitatory hypo-DMRs and depleted in PV-, VIP-, and glia-specific hypo-DMRs (Figures S3B and S3C). These results are largely recapitulated by the ATAC-seq data. Our analysis suggests that excitatory neuron-specific hypo-DMRs and ATAC-seq peaks overlapping AP-1 and NPAS4 binding sites are a set of candidate regions that coordinate activity-dependent responses unique to excitatory neurons. Likewise, hypo-DMRs and differential ATAC-seq peaks in PV and VIP neurons provide a resource for identifying AP-1 and NPAS4 targets that orchestrate distinct activity-dependent responses in inhibitory neurons (Spiegel et al., 2014).

Neuronal Subtypes Show Coordinated Epigenomic Differences

Epigenomic marks carry information about cell function, via their correlation with gene expression and gene regulatory regions, as well as cell development (Bird, 2002; Hon et al., 2013; Stadler et al., 2011; Thurman et al., 2012). Therefore, we first assessed whether the epigenomic marks were well correlated with each other and then quantified their relationships across cell types and developmental stages.

Cell-type-specific hypo-methylation in the CG context is coordinated with hypo-methylation in the CH context (Figures 3E, left two panels, and S3D) and increased chromatin accessibility (Figure 3E, third panel). Excitatory neuron hypo-DMRs are also enriched for histone modifications associated with active enhancers (H3K4me1 and H3K27ac) but not promoters (H3K4me3) (Figure 3E, right panel). Similarly, ATAC-seq levels in excitatory neurons are correlated with both H3K4me1 and H3K27ac at enhancers (Figure S3E) but demarcate TF binding sites with greater spatial resolution (Figure 3E, third panel versus right panel). Overlapping features derived from multiple assays (Figure S3F) provide convergent evidence for identifying candidate regulatory regions, and both raw and processed data can be explored via a web-based browser (http://neomorph.salk.edu/mm_intact/).

We quantified the epigenomic relationships across cell types in several ways: by the similarity of DNA methylation patterns in 500 bp bins genome-wide (Figure S4A) and at ATAC-seq peaks (Figures 4A and S4B), and by the similarity of Tn5 insertion densities (Figure 4B) at ATAC-seq peaks. As expected, excitatory and NeuN+ neurons are strongly correlated using DNA methylation signal at both genomic bins and ATAC-seq peaks (Pearson $r \sim 0.9$), and hierarchical clustering groups excitatory neurons with NeuN+ neurons. PV and VIP neurons cluster together, in line with their functional roles as inhibitory neurons. In contrast, excitatory and VIP neurons show the lowest similarity across INTACT-purified cell types. Unexpectedly, CG methylation levels in fetal brain and in glia correlate more strongly

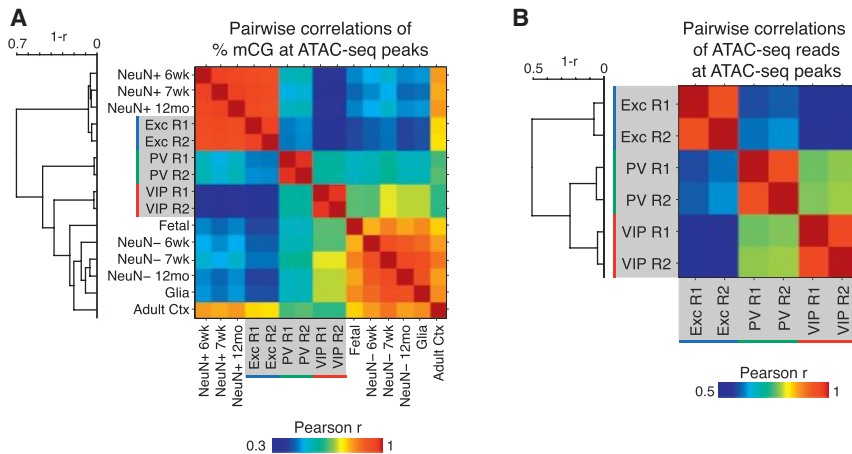


Figure 4. Relationships across Cell Types and Development via Epigenomic Marks

Matrices showing pairwise Pearson correlations for percentage of mCG (A) and ATAC-seq read densities (B) at ATAC-seq peaks. Dendrograms show hierarchical clustering using complete linkage and 1-Pearson correlation as the metric. See also Figure S4.

with VIP neurons than with excitatory or PV neurons. At ATAC-seq peaks (Figures 4A and S4B), this similarity among VIP, fetal, and glial samples could suggest that more gene regulatory characteristics of immature or progenitor cells are retained by VIP neurons than by excitatory or PV neurons. Collectively, our data demonstrates that DNA methylation and chromatin features reveal a coordinated, hierarchical organization of mature cortical cell types that is reflected across much of the genome.

Distinct Sets of DNA Binding Factors Act at Putative Neuron Subtype-Specific Regulatory Regions

We next sought to characterize the DNA binding TFs that are responsible for these unique neuronal regulatory landscapes. Our RNA-seq analysis identified 267 differentially expressed TFs (Table S2). These include TFs that play well-known regulatory roles in the development of each cell type (e.g., *Lhx6* in PV interneurons and *Prox1* in VIP interneurons) (Kessar et al., 2014) as well as many other TFs with unknown neuronal functions.

TF binding enhances chromatin accessibility, but the central region of binding is protected from the activity of enzymes such as Tn5 transposase, resulting in a notch, or footprint, in the ATAC-seq profile (Buenrostro et al., 2013). In agreement with previous footprinting studies (Neph et al., 2012), we observe a range of footprint shapes for different TFs (Figure 5A). With the notable exceptions of CTCF and ZFP410, footprinted sites in a cell are generally associated with reduced regional DNA methylation levels (Figure S5A).

We applied footprint analysis of ATAC-seq datasets to infer TF binding at cell-type-specific regulatory regions and combined it with complementary analysis of DNA binding sequence motifs enriched at hypo-DMRs. We focused on footprints and motifs of moderately to highly expressed TFs (TPM \geq 30) and identified 68 TFs that may regulate cell-type-specific gene expression (Figure 5B and Table S4). Overall, both our footprint and motif predictions converge on similar sets of enriched and depleted TFs. These sets encompass both well-established and novel TFs. In excitatory neurons, both footprint and motif predictions show overrepresentation of *Egr*, AP-1 family members, *Neurod2*, *Rfx1/3/5*, and *Tbr1*. Two TF groups potentially linked to PV neuron development, *Mafb/g* and *Mef2a/c/d* (Kessar et al., 2014), are among those enriched in PV-specific footprints and

hypo-DMRs (Figure 5B) as well as PV hypo-DMRs shared with both excitatory and VIP neurons (Figure S5B). Studies of MEF2 have largely focused on its role in excitatory neurons (Rashid et al., 2014); here, both footprinting and motif analyses suggest a critical function for MEF2 in PV neurons at PV-specific regulatory regions. Interestingly, VIP neuron footprints and DMRs are enriched for TFs best known for their developmental roles (e.g., *Dlx*, *Pou*, and *Sox* family members; *Arx* and *Vax2*) (Kessar et al., 2014), an extension of our previous observation that VIP methylomes share common patterns with fetal and glial methylomes. Motifs for these TFs are also enriched at fetal and glial hypo-DMRs, including those that are shared with VIP neurons (Figure S5B).

TFs control complex cellular processes by forming networks of mutual regulation, yet differences in TF regulatory networks between neuron types are largely unknown. We examined regulatory interactions among TFs by building networks of predicted cell-type-specific TF regulation, as well as a pan-neuronal regulatory network (Figures 5C and 5D; Table S4). These networks recover a number of previously implicated TF-TF regulatory interactions and suggest novel interactions. For example, our prediction that MEF2D targets *Dlx6* in PV neurons parallels the requirement of a homolog, MEF2C, for *Dlx6* expression in branchial arches (Verzi et al., 2007).

To explore the potential contribution of ATAC-seq peaks and footprints to the regulation of nearby gene expression, we examined their coverages around the TSS of highly cell-type-specific genes. Differentially expressed genes display an increased density of cell-type-specific footprints centered around the TSS (Figure 5E) and are significantly enriched for cell-type-specific ATAC-seq peaks (Figure 5F). When we examined pan-neuronal genes (Hobert et al., 2010) such as *Pclo*, *Rims1*, *Cdh2*, and *Grip1* (Figure S5C), we noted that they were also surrounded by an array of ATAC-seq peaks, many of which were present exclusively in one neuron class. Indeed, we find that cell-type-specific ATAC-seq peaks are moderately enriched around the TSS of pan-neuronal genes (Figure 5F), highlighting the potential for these regions to shape neuronal identity by regulating both cell-type-specific and pan-neuronal programs of gene expression.

Among DNA Methylation and Chromatin Accessibility Features, Non-CG Methylation Best Correlates with RNA Abundance

Genome-wide, we find a strong inverse correlation between RNA abundance and DNA methylation around the TSS, as well as a

positive correlation between RNA abundance and ATAC-seq signals (Figure 6A). For both mCG and mCH, the inverse correlation extends throughout the gene body, with a peak ~ 1 –2 kb downstream of the TSS. At differentially expressed genes, mCH is significantly more correlated with expression (Spearman $r = -0.50$) than mCG ($r = -0.34$; $p = 0.0063$, t test using the three cell types as samples) or ATAC-seq insertion density ($r = 0.25$; $p = 5.4 \times 10^{-4}$). A generalized linear model with a sparseness-promoting regularization (LASSO) using mCG, mCH, and ATAC-seq features (Table S5) further identifies gene body mCH as the most informative feature for inferring RNA abundance (Figures S6A and S6B).

Our finding that the strongest correlation between RNA levels and mCG occurs ~ 1 –2 kb downstream of the TSS agrees with recent findings in medulloblastoma cell lines (Hovestadt et al., 2014) and in human cardiomyocytes (Gilsbach et al., 2014). Our results extend this observation to mCH and show that mCH, an epigenetic modification abundant across diverse classes of neocortical neurons, is better correlated with gene abundances measured by RNA-seq. Future studies using more direct measures of gene transcription are warranted to complement these findings.

Gene Clusters Based on Intragenic Non-CG Methylation Share Gene Expression, Chromatin, and Functional Organization

As described above, non-CG methylation within the gene body is inversely correlated with gene expression. Yet, this epigenomic feature may display greater divergence across neuron types than their transcriptional configurations (Figures 2B and 2F), suggesting that it contains additional information related to cell-type-specific differences. To explore this idea, we used an unbiased clustering approach to group genes by their patterns of intragenic mCH, followed by an integrative analysis of gene expression, chromatin accessibility, and gene ontology. 23,023 genes were grouped into 25 clusters by their levels of intragenic mCH, normalized by the level in the flanking region (Figures 6B–6E and S6C). Approximately half of these genes share similar patterns of mCH across neurons, including hyper-methylated genes with low expression levels (clusters 2, 6; 13.5% of genes) and hypo-methylated genes with moderate to high expression (clusters 3–5, 7, and 8; 40%). The latter category is not enriched for differentially expressed genes (Figure 6D) but is enriched for cell-type-specific ATAC-seq peaks (Figure 6E). By gene ontology (GO) analysis (Huang et al., 2009) (Table S5), genes in these clusters tend to be enriched for general cellular processes, for example, transcription (GO: 0006350) and RNA binding (GO: 0003723).

The remaining half of genes captures the spectrum of intragenic CH methylation across neuronal populations by clustering into groups showing neuron subtype-specific hyper- and hypo-mCH. Clusters 10–18 (23.6% of genes) are hyper-methylated at CH sites in one or more cell types and are expressed at relatively low levels. Clusters 19–25 (17.8% of genes) are hypo-methylated in specific cell types and are generally expressed at higher levels, with hypo-methylation occurring together with increased expression (e.g., Cluster 22 enriched for PV > Exc and VIP genes). These clusters are enriched for both differentially

expressed genes and accessible chromatin. Although genes that are exclusively expressed in only one or two cell types are grouped in clusters 19–25, a subset of pan-neuronal genes that differ in their expression levels across neuronal subtypes are also grouped here (e.g., *Cdh2*, *Grip1*, *Bsn*). These clusters also contain pan-neuronal genes that do not meet our threshold for differential expression (e.g., *Anks1b*), an example of the ability of intragenic mCH to parse the neuronal transcriptome into finer patterns.

Several clusters with cell-type-specific hypo-methylation are enriched for neuronal GO categories, for example, postsynaptic density (GO: 0014069: 6.7-fold enrichment, $q = 0.035$, cluster 19) and synapse (GO: 0045202: 2.6-fold, $q = 0.033$, cluster 20; 2.9-fold, $q = 2.8 \times 10^{-4}$, cluster 21). Neuron subtype-specific differences in intragenic mCH may be especially relevant in light of recent evidence that MeCP2 binding to mCA represses transcription of long neuronal genes (Gabel et al., 2015). The enrichment of neuronal GO categories at these clusters suggests that cell-type-specific expression levels of genes with neuronal functions may partly be a consequence of differences in levels of intragenic mCH.

Non-CG Methylation Is Lowest at the Nucleosome Center and Increases at Linker Regions

In addition to its variations with gene expression, we asked whether mCH levels also differed relative to chromatin features such as nucleosome positioning. We estimated nucleosome locations using ATAC-seq and found that coherently phased modulation of mCH is evident over approximately 1 kb (~ 5 nucleosomes), decreasing by up to 9.5% at the nucleosome center and increasing by 11.1% in neighboring linkers (Figure 6F). mCG levels display a similar but weaker modulation (<2%) (Figure S6D). Our results support earlier studies in the CG context (Teif et al., 2014) and extend the link between nucleosome positioning and DNA methylation in mammalian cells to the non-CG context.

Identification of Distinct Classes of Large Hypo-methylated Regions

We further sought to identify multi-kilobase regions of low DNA methylation in our datasets. Hypo-DMRs are not randomly distributed in the genome but instead show a bimodal distribution of inter-DMR distances (Figure 7A). Closely spaced hypo-DMRs may represent fragments of larger hypo-methylated features. Therefore, we merged neuron subtype-specific hypo-DMRs located within 1 kb of each other and defined those exceeding 2 kb in length as “large hypo-DMRs” (Figure 7B, left). We also observed another category of large hypo-methylated domains that are consistent with previously described DNA methylation valleys (DMVs) or canyons (Jeong et al., 2014; Xie et al., 2013) (Figure 7B; see Supplemental Experimental Procedures).

Although both are multi-kilobase hypo-methylated regions, large hypo-DMRs and DMVs occupy distinct genomic locations (Figure S7A). Compared to large hypo-DMRs, DMVs have higher overlap across cell types (Figure S7A) and more extreme lengths (Figure S7B), extending up to 104 kb compared to large hypo-DMRs, which extend to 32 kb. Consistent with their higher GC content (Figure S7C) and lower levels of CG methylation

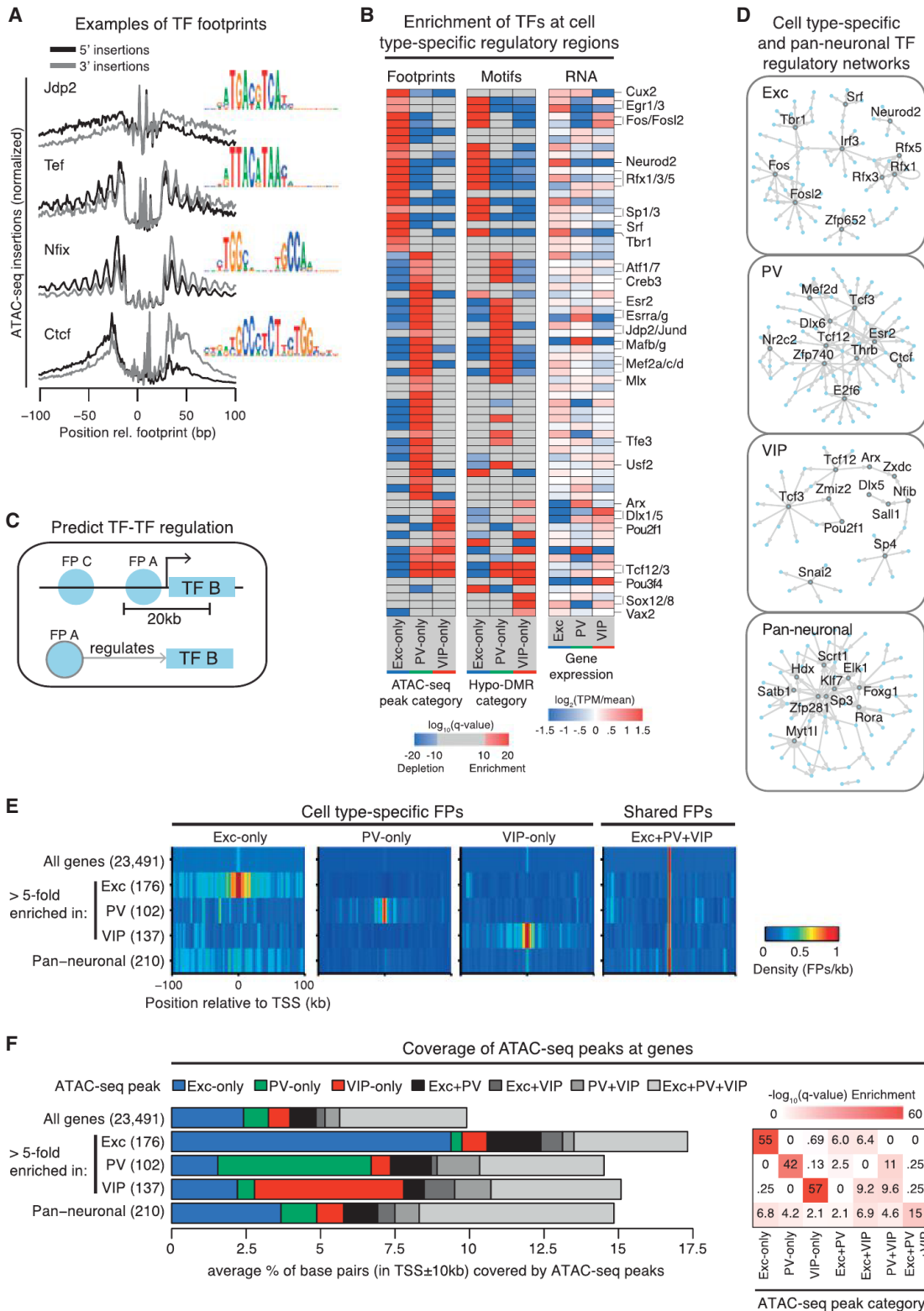


Figure 5. Neuronal Subtypes Are Associated with Distinct Patterns of TF Binding

(A) The average density of ATAC-seq read endpoints (Tn5 transposase insertions) within ± 100 bp relative to the estimated locations of footprints for four example TFs, showing characteristic footprint structures. Each footprint profile is normalized by the maximum over the profiled region. Inset: position weight matrix showing sequence motifs at the footprint center.

(legend continued on next page)

(Figure S7D), most DMVs (85%–94%) overlap CpG islands. In contrast, only 1%–9% of large hypo-DMRs overlap CpG islands. Furthermore, DMVs straddle the TSS, whereas large hypo-DMRs are enriched downstream of the TSS (Figure S7E).

To better characterize different classes of hypo-methylated regions, we took advantage of our histone modification data in excitatory neurons. Large hypo-DMRs show higher levels of histone modifications associated with active enhancers, H3K27Ac and H3K4me1, compared to DMRs <2 kb (Figure 7C, left). Excitatory DMVs display a bimodal distribution for H3K4me3 and H3K27me3 and can be divided as H3K4me3+ (Figure 7B, left) versus H3K27me3+ (Figure 7B, right). As expected, H3K27me3+ DMVs are depleted for ATAC-seq reads and overlap genes with low expression (Figure 7C, middle and right). Large hypo-DMRs and H3K4me3+, but not H3K27me3+, DMVs are enriched for differentially expressed genes (Figure 7D). In fact, the bimodal distribution of H3K4me3 and H3K27me3 levels in DMVs suggests that these domains can be associated with either active or repressed genes, and the two histone modifications partition DMVs into functionally distinct categories (Figures S7F and S7G).

Hyper-methylation at Cell-Type-Specific Transcription Factor Genes Preserves a Trace of Early Developmental Expression

DMVs are highly overlapping across adult cell types and fetal cortex (Figure S7A), in line with previous evidence (Xie et al., 2013) suggesting they may be established early during development and subsequently maintained. To address whether these regions are dynamically modified during development, we compared the boundaries of fetal DMVs between fetal and adult cells. Genome-wide, 51%–67% of fetal DMVs remain as DMVs in adult neurons and glia but gain methylcytosines, resulting in a contraction of DMV length as the brain matures (median decrease = 747 bp; $p < 2 \times 10^{-18}$, Wilcoxon rank sum).

We further focused our analysis on fetal DMVs overlapping genes. Fetal DMVs are highly enriched for TF genes (Figure S7G), and 75 out of 77 fetal DMVs associated with a list of candidate developmental TFs (Visel et al., 2013) are shorter in at least one adult cell type (Figure S7H). To identify the DMVs that display the most significant developmental mCG gains, we compared mCG levels across fetal and adult cells in the interior of fetal DMVs; to avoid the possible confound of intragenic DNA methylation, we used the DMV interior upstream of the TSS (Figure 7E). This analysis identified 454 genes (66%; FET, $q < 0.01$) that exhibit significantly increased mCG in at least one adult cell type versus fetal cortex; 210 genes (31%) have more than a 5-fold increase (Table S6).

When we examined these 210 genes, we noted that several code for critical TFs known to shape neuronal subtype identity and are predominantly expressed in neural progenitor cells and immature precursors; furthermore, the highest mCG fold change generally occurs in the cell type where the gene is active in development but downregulated in the adult (Table S6). For example, *Neurog2* is highly expressed during embryonic development in the common progenitors of cortical excitatory neurons and many glial cells, but it is not expressed in these cells in the adult brain nor at any time during inhibitory neuron development (Sommer et al., 1996; Wang et al., 2013). Our DNA methylation data shows that *Neurog2* lies within a DMV in all cells except excitatory neurons and glia, where the region is hyper-methylated (Figure 7F, left). In contrast, *Nkx2-1* is specifically expressed in the medial ganglionic eminence (MGE), the birthplace of cortical PV neurons (DeFelipe et al., 2013). Immature cortical PV neurons switch off *Nkx2-1* soon after leaving the MGE in order to direct their migration to the cortex; neurons that maintain *Nkx2-1* expression instead travel to the striatum (Nóbrega-Pereira et al., 2008). An extended (>15 kb) DMV covers *Nkx2-1* in fetal cortex, excitatory neurons, VIP neurons, and glia, yet this DMV is only ~6.5 kb in PV neurons (Figure 7F, right). Similar findings are seen at DMVs overlapping *Dlx2*, *Pax6*, *Vax1*, and *Gsx2* (Figures S7I and S7J).

At these TF loci, the methylomes of adult neurons contain a signature of past gene expression. In contrast to the rest of the genome, hyper-methylation, rather than hypo-methylation, marks the relevant cell-type-specific genes. In contrast to vestigial enhancers (Hon et al., 2013), this epigenetic trace of the neuron's development arises from the gain of cell-type-specific hyper-methylation rather than the retention of hypo-methylation. We further asked what fraction of this hyper-methylation is a result of hmC rather than mC. For DMVs at *Neurog2* and *Pax6*, we find that adult frontal cortex hmCG levels from TAB-seq (Lister et al., 2013) are approximately 10% of excitatory neuron MethylC-seq signals at CG sites. Because we lack matched hmC data from purified excitatory neurons, the precise contribution of hmCG is difficult to assess, although we believe from this comparison that the majority of the hyper-methylation originates from mCG. Furthermore, at non-CG sites in these two DMVs, we find that essentially all of the observed hyper-methylation originates from mCH, consistent with evidence that hydroxymethylation occurs nearly exclusively in the CG context (Yu et al., 2012).

DISCUSSION

This study introduces the INTACT system in mice, the first method to affinity purify nuclei from genetically defined cell types

(B) Heatmaps showing the enrichment (red) and depletion (blue) of footprints in cell-type-specific ATAC-seq peaks (left) or motifs in hypo-DMRs (middle). The relative TF expression level across excitatory, PV, and VIP neurons is also shown (right). Selected TFs are labeled; the full matrix can be found in Table S4.

(C) Schematic for assessing TF-TF interactions by detecting footprints of one TF (FP A) in a 20 kb window around the TSS of a second TF (TF B); footprints located farther away (FP C) are not predicted to interact.

(D) Networks of TF interactions predicted by the method shown in (C) using cell-type-specific and pan-neuronal footprints. Full networks can be found in Table S4.

(E) Heatmaps showing the average density of cell-type-specific and pan-neuronal footprints within a TSS \pm 100 kb window for each category of genes.

(F) Barplot showing the average percentage of base pairs within a TSS \pm 10 kb window that overlaps each ATAC-seq peak category, for each category of genes (left). Heatmap showing an enrichment of cell-type-specific peaks at both cell-type-specific and pan-neuronal genes (right). Pan-neuronal genes are from Hobert et al. (2010); q from one-sided Wilcoxon rank-sum test with Benjamini-Hochberg FDR correction.

See also Figure S5.

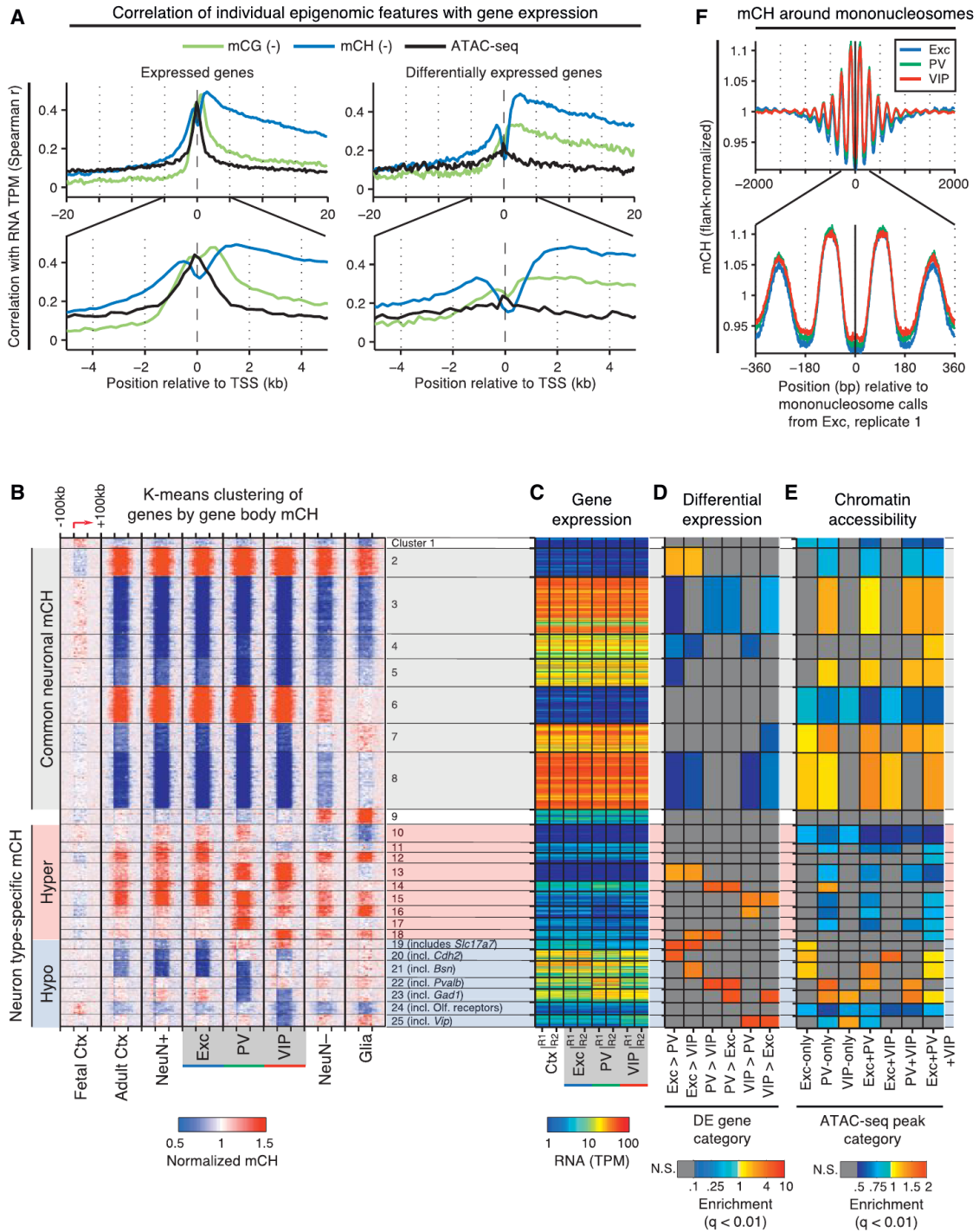


Figure 6. Integrative Analysis of DNA Methylation, Gene Expression, and Chromatin Features

(A) Spearman correlations of three epigenomic features (CG DNA methylation, CH DNA methylation, and ATAC-seq read density) with RNA expression level around the TSS of autosomal expressed (TPM > 0.1) genes (left) and differentially expressed genes (right). The signs of the correlations for mCG and mCH are negative, as these features inversely correlate with gene expression.

(B–E) Protein-coding genes were clustered by k-means based on patterns of intragenic mCH. For each cluster (1–25), the following features are plotted: mCH level within each gene body and flanking 100 kb (B); mRNA abundance (C); enrichment or depletion for differentially expressed (DE) genes (D), and enrichment or depletion for cell-type-specific and shared ATAC-seq peaks within ± 10 kb of the TSS (E). mCH levels for each gene are normalized by the levels at distal flanking

(legend continued on next page)

in a mammal. INTACT efficiently isolates nuclei from both common and rare cell types, enabling us to examine the epigenomic organization of neocortical excitatory, PV, and VIP neurons with unprecedented cell-type-specific resolution. We find that the morphological and physiological diversity of neocortical neurons is paralleled by widespread differences in their underlying epigenomes. By using coordinated epigenomic marks to show that neocortical neurons adopt unique regulatory landscapes, our data add a new resource to existing catalogs of transcriptional diversity. We further identify candidate TFs acting at regulatory regions and demonstrate how epigenomic states of adult cells capture long-lasting attributes of neuronal identity, including patterns of past gene expression, current gene expression, and potential experience-dependent responses. In particular, we find a close relationship between intragenic non-CG methylation and differential gene expression. Furthermore, purified neuronal epigenomes reveal distinctive hyper-methylation patterns associated with developmentally transient expression of critical TFs that shape neuronal subtype identity.

Affinity Purification of Nuclei Facilitates Epigenomic Studies

INTACT is uniquely suited to investigating cell-type-specific epigenomes, an application that can be challenging with other purification methods. Genome-wide epigenomic assays generally require tens of thousands to millions of cells, which limit the utility of manual sorting for this purpose. Methods that involve cellular dissociation in the adult brain may be inefficient and induce stress responses that alter the cellular state. In contrast, INTACT couples rapid tissue lysis with gentle isolation of sufficient numbers of cell-type-specific nuclei for epigenomic studies. Whereas FACS-sorted cells or nuclei may be fragile and difficult to manipulate, the attachment of magnetic beads to nuclei in INTACT greatly simplifies buffer exchanges and volume reductions. Furthermore, unlike FACS or laser capture microdissection, INTACT requires no specialized instruments. INTACT is particularly well-suited for isolating rare cell types; cells constituting 1%–3% of the starting material can be enriched to >98% purity and subsequently used for MethylC-seq and ATAC-seq.

In this study, we have focused on cellular diversity in the healthy mammalian brain. INTACT can also be used to explore cell-type-specific epigenomics in mouse models of neurodegeneration, schizophrenia, autism, and other neuropsychiatric disorders or adapted for use in non-neuronal tissues. In addition to epigenomic studies, INTACT is an efficient method for isolating nuclear RNA from defined cell types that complements existing strategies for RNA profiling. We note that some degree of non-specific RNA contamination is intrinsic to affinity purification strategies, including INTACT. Nevertheless, we have shown that INTACT expression profiles recover known cell markers and can be used to discover novel markers.

Cell-Type-Specific Developmental Signatures Are Encoded in the Methylomes of Adult Cells

Mature neuronal diversity arises from a developmental odyssey. Whereas one class of large hypo-methylated regions (large hypo-DMRs) reflects the neuron's current transcriptional state, a second class (DNA methylation valleys [DMVs]) reveals patterns of past gene expression. We find that a subset of genes coding for TFs that establish neuronal identity, including *Neurog2*, *Nkx2-1*, *Dlx2*, *Pax6*, *Vax1*, and *Gsx2*, overlap with DMVs showing cell-type-specific hyper-methylation. At these genes, hyper-methylation at DMVs in the adult methylome provides a record of transient high TF expression during development, whereas the same genes are hypo-methylated in other cell types. We speculate that this pattern might arise if (1) these DMVs are initially marked by H3K27me3 in neural progenitors (Xie et al., 2013), (2) H3K27me3 is removed in a particular neuronal lineage to allow TF expression at the appropriate developmental time point, and (3) this removal simultaneously increases the accessibility of the region to DNA methyltransferases, whereas other cell types maintain an inaccessible chromatin state throughout development and into adulthood. Measuring gene expression in defined populations of immature cells can be challenging as they are intermixed and often do not express the terminal markers of adult neuronal subtypes. Our data suggest that developmental TF expression could be predicted from DNA methylation patterns in adult cells, providing an alternate approach to investigating cell-type-specific developmental history. Our results highlight this finding at several of the most critical neuronal TFs; however, future studies using matched developmental and adult datasets are necessary to further explore the temporal relationships across DNA methylation, gene expression, and chromatin.

Genome-wide Analyses Parse Neuronal Diversity

Neuronal cell types have been defined based on morphology, electrophysiology, connectivity, and, more recently, patterns of gene expression and regulation. Traditional approaches for investigating these features produce datasets of modest size and with a relatively small number of independent parameters, which limit the distinctions that can be made among neuronal cell types. As demonstrated here, genome-wide approaches generate large and information-rich datasets that reveal complex neuron subtype-specific patterns of transcript abundances, DNA methylation, and chromatin accessibility. Genome-wide information derived from these datasets can be used to parse neuronal subtypes into even finer divisions based on patterns of both gene expression and gene regulation, which in turn can be combined with transgenic approaches to label new subpopulations of neurons and enable their purification. The synergy between genetic engineering of experimental organisms, cell-type-specific purification, and genome-scale data analysis promises a new and comprehensive view of neuronal diversity in the mammalian brain.

regions (50–100 kb upstream and downstream of the gene body). For clusters with cell-type-specific hypo-methylation, an example gene or gene set is listed. TPM, transcripts per million; N.S., not significant (FET, $q < 0.01$).

(F) mCH levels are higher in the nucleosomal linker region and lower in the nucleosome core. mCH levels are normalized by the level at flanking regions (1–2 kb upstream and downstream of the nucleosome center).

See also Figure S6.

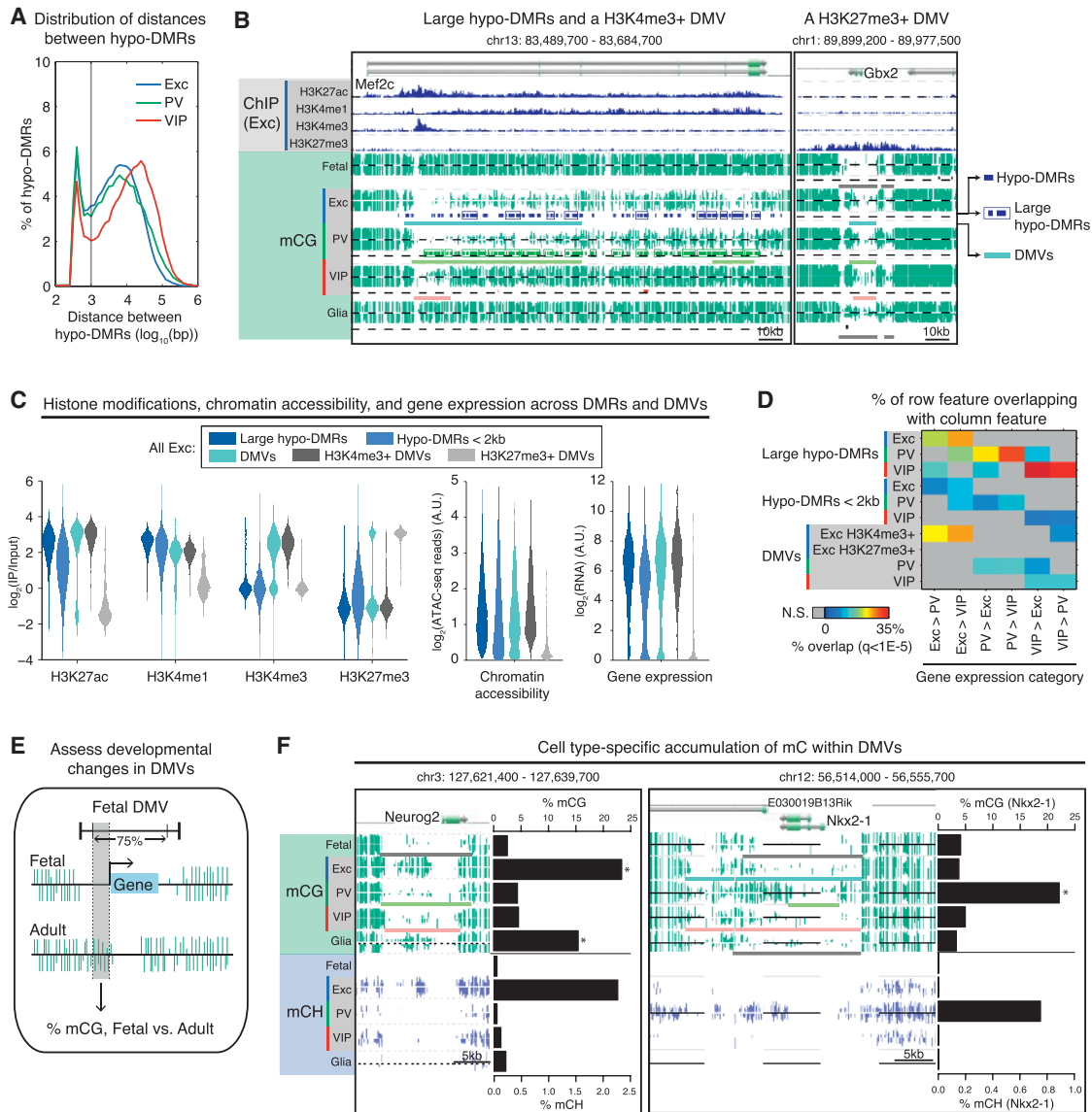


Figure 7. Large Domains of Low Methylation Link to Gene Expression, Including Unexpected Hyper-methylation at Developmental Genes

(A) Bimodal distribution of distances between hypo-DMRs in each cell type indicates that some hypo-DMRs are closely spaced (<1 kb separation) and form large blocks of differential methylation (“large hypo-DMRs”).

(B) Large hypo-DMRs and an H3K4me3+ DNA methylation valley (DMV) overlap *Mef2c* (left); an H3K27me3+ DMV overlaps *Gbx2* (right). As diagrammed for the excitatory neuron tracks, dark-colored bars indicate hypo-DMRs (top), boxes indicate hypo-DMRs that were grouped into large hypo-DMRs, and light-colored bars indicate DMVs (bottom).

(C) For excitatory neurons, violin plots show the distribution of histone modification enrichments (left), ATAC-seq read densities (middle), and gene expression levels (right) within large hypo-DMRs, hypo-DMRs < 2 kb, and DMVs. A.U., arbitrary units.

(D) Matrix showing the percentage of each row feature that overlaps with differentially expressed genes. Large hypo-DMRs and H3K4me3+ DMVs (in excitatory neurons) have higher enrichment for differentially expressed genes, compared to hypo-DMRs < 2 kb. H3K27me3+ DMVs (in excitatory neurons) are not enriched for differentially expressed genes at $q < 1 \times 10^{-5}$.

(E) Schematic for assessing the accumulation of CG methylation in each adult cell type (excitatory, PV, and VIP neurons, and glia) compared to fetal cortex, at fetal DMVs overlapping genes. See Table S6.

(F) DNA methylation levels for a region around *Neurog2* (left), an active TF in excitatory and many glial progenitors, and *Nkx2-1* (right), a transiently active TF in PV neuron development. See Table S6 for annotations and references. Barplots show percentage of mCG and percentage of mCH for each cell type in the region between dotted lines in (E). * $q < 1 \times 10^{-10}$ (mCG, adult cell type compared to fetal cortex, one-sided FET with Benjamini-Hochberg correction). In the browser representation, light-colored bars indicate DMVs.

See also Figure S7.

EXPERIMENTAL PROCEDURES

Further details can be found in the Supplemental Experimental Procedures.

Mouse INTACT

Animal procedures were conducted in accordance with the Institutional Animal Care and Use Committee guidelines of the Johns Hopkins Medical Institutions. The *R26-CAG-LSL-Sun1-sfGFP-Myc* knockin mouse was made according to standard procedures. GFP+/Myc+ nuclei from adult (8–11 weeks) mouse neocortex were isolated by affinity purification using anti-GFP or anti-Myc antibodies and protein G-coated magnetic beads.

RNA-Seq Library Generation

Nuclear RNA from INTACT-purified nuclei or whole neocortical nuclei was converted to cDNA and amplified with the Nugen Ovation RNA-seq System V2 (Nugen 7102). Libraries were sequenced using the Illumina HiSeq 2500.

MethylC-Seq Library Generation

Genomic DNA from INTACT-purified nuclei was fragmented, and MethylC-seq libraries were prepared. Libraries were sequenced using the Illumina HiSeq 2000.

ATAC-Seq Library Generation

50,000 bead-bound nuclei were transposed using Tn5 transposase (Illumina FC-121-1030) as previously described (Buenrostro et al., 2013). After 9–12 cycles of PCR amplification, libraries were sequenced on an Illumina HiSeq 2500.

ChIP-Seq Library Generation

INTACT-purified excitatory neuron nuclei were digested to mononucleosomes using micrococcal nuclease, followed by salt extraction of chromatin. After native ChIP and library construction, libraries were sequenced on an Illumina HiSeq 2500.

ACCESSION NUMBERS

The accession number for the raw and processed data files reported in this paper is GEO: GSE63137, and the data files are displayed via a web-based browser (http://neomorph.salk.edu/mm_intact/).

SUPPLEMENTAL INFORMATION

Supplemental Information includes Supplemental Experimental Procedures, seven figures, and six tables and can be found with this article online at <http://dx.doi.org/10.1016/j.neuron.2015.05.018>.

AUTHOR CONTRIBUTIONS

J.N., J.R.E., S.R.E., and T.J.S. designed and supervised the research. A.M. designed and generated the INTACT mouse, developed the affinity purification, and did nuclei isolations and related experiments. G.L.H. designed the Sun1 tag and constructed RNA-seq libraries. G.L.H. and S.P. constructed ATAC-seq libraries. A.M. and G.L.H. constructed ChIP-seq libraries. S.P. sequenced the RNA-seq, ChIP-seq, and ATAC-seq libraries. M.A.U. constructed MethylC-seq libraries. J.R.N. sequenced and mapped the MethylC-seq libraries. E.A.M., F.P.D., C.L., A.M., and R.L. analyzed data. A.M., E.A.M., and J.N. prepared the manuscript. F.P.D., C.L., J.R.E., S.R.E., G.L.H., and R.L. revised the manuscript.

ACKNOWLEDGMENTS

This work was supported by the Howard Hughes Medical Institute (J.R.E., S.R.E., J.N., and T.J.S.), 1-U01-MH105985 (J.R.E.), MSTP training grant (A.M.), and NIH/NINDS R00NS080911 (E.A.M.). J.N. and T.J.S. are Howard Hughes Medical Institute Investigators. J.R.E. is a Howard Hughes Medical Institute and Gordon and Betty Moore Investigator. We thank Hao Zhang at

the Johns Hopkins School of Public Health for flow cytometry. We thank Yu-peng He for comments and suggestions.

Received: January 15, 2015

Revised: April 14, 2015

Accepted: May 7, 2015

Published: June 17 2015

REFERENCES

- Amin, N.M., Greco, T.M., Kuchenbrod, L.M., Rigney, M.M., Chung, M.I., Wallingford, J.B., Cristea, I.M., and Conlon, F.L. (2014). Proteomic profiling of cardiac tissue by isolation of nuclei tagged in specific cell types (INTACT). *Development* *141*, 962–973.
- Bird, A. (2002). DNA methylation patterns and epigenetic memory. *Genes Dev.* *16*, 6–21.
- Buenrostro, J.D., Giresi, P.G., Zaba, L.C., Chang, H.Y., and Greenleaf, W.J. (2013). Transposition of native chromatin for fast and sensitive epigenomic profiling of open chromatin, DNA-binding proteins and nucleosome position. *Nat. Methods* *10*, 1213–1218.
- Burger, L., Gaidatzis, D., Schübeler, D., and Stadler, M.B. (2013). Identification of active regulatory regions from DNA methylation data. *Nucleic Acids Res.* *41*, e155.
- Deal, R.B., and Henikoff, S. (2010). A simple method for gene expression and chromatin profiling of individual cell types within a tissue. *Dev. Cell* *18*, 1030–1040.
- DeFelipe, J., López-Cruz, P.L., Benavides-Piccione, R., Bielza, C., Larrañaga, P., Anderson, S., Burkhalter, A., Cauli, B., Fairén, A., Feldmeyer, D., et al. (2013). New insights into the classification and nomenclature of cortical GABAergic interneurons. *Nat. Rev. Neurosci.* *14*, 202–216.
- Doyle, J.P., Dougherty, J.D., Heiman, M., Schmidt, E.F., Stevens, T.R., Ma, G., Bupp, S., Shrestha, P., Shah, R.D., Dougherty, M.L., et al. (2008). Application of a translational profiling approach for the comparative analysis of CNS cell types. *Cell* *135*, 749–762.
- Emmert-Buck, M.R., Bonner, R.F., Smith, P.D., Chuaqui, R.F., Zhuang, Z., Goldstein, S.R., Weiss, R.A., and Liotta, L.A. (1996). Laser capture microdissection. *Science* *274*, 998–1001.
- Gabel, H.W., Kinde, B., Stroud, H., Gilbert, C.S., Harmin, D.A., Kastan, N.R., Hemberg, M., Ebert, D.H., and Greenberg, M.E. (2015). Disruption of DNA-methylation-dependent long gene repression in Rett syndrome. *Nature*. <http://dx.doi.org/10.1038/nature14319>.
- Gay, L., Miller, M.R., Ventura, P.B., Devasthali, V., Vue, Z., Thompson, H.L., Temple, S., Zong, H., Cleary, M.D., Stankunas, K., and Doe, C.Q. (2013). Mouse TU tagging: a chemical/genetic intersectional method for purifying cell type-specific nascent RNA. *Genes Dev.* *27*, 98–115.
- Gelman, D.M., and Marin, O. (2010). Generation of interneuron diversity in the mouse cerebral cortex. *Eur. J. Neurosci.* *31*, 2136–2141.
- Giltsbach, R., Preissl, S., Grüning, B.A., Schnick, T., Burger, L., Benes, V., Würch, A., Bönisch, U., Günther, S., Backofen, R., et al. (2014). Dynamic DNA methylation orchestrates cardiomyocyte development, maturation and disease. *Nat. Commun.* *5*, 5288.
- Guo, J.U., Ma, D.K., Mo, H., Ball, M.P., Jang, M.H., Bonaguidi, M.A., Balazer, J.A., Eaves, H.L., Xie, B., Ford, E., et al. (2011). Neuronal activity modifies the DNA methylation landscape in the adult brain. *Nat. Neurosci.* *14*, 1345–1351.
- Guo, J.U., Su, Y., Shin, J.H., Shin, J., Li, H., Xie, B., Zhong, C., Hu, S., Le, T., Fan, G., et al. (2014). Distribution, recognition and regulation of non-CpG methylation in the adult mammalian brain. *Nat. Neurosci.* *17*, 215–222.
- Heiman, M., Schaefer, A., Gong, S., Peterson, J.D., Day, M., Ramsey, K.E., Suárez-Fariñas, M., Schwarz, C., Stephan, D.A., Surmeier, D.J., et al. (2008). A translational profiling approach for the molecular characterization of CNS cell types. *Cell* *135*, 738–748.
- Heintzman, N.D., Stuart, R.K., Hon, G., Fu, Y., Ching, C.W., Hawkins, R.D., Barrera, L.O., Van Calcar, S., Qu, C., Ching, K.A., et al. (2007). Distinct and

- predictive chromatin signatures of transcriptional promoters and enhancers in the human genome. *Nat. Genet.* 39, 311–318.
- Henry, G.L., Davis, F.P., Picard, S., and Eddy, S.R. (2012). Cell type-specific genomics of *Drosophila* neurons. *Nucleic Acids Res.* 40, 9691–9704.
- Hobert, O., Carrera, I., and Stefanakis, N. (2010). The molecular and gene regulatory signature of a neuron. *Trends Neurosci.* 33, 435–445.
- Hon, G.C., Rajagopal, N., Shen, Y., McCleary, D.F., Yue, F., Dang, M.D., and Ren, B. (2013). Epigenetic memory at embryonic enhancers identified in DNA methylation maps from adult mouse tissues. *Nat. Genet.* 45, 1198–1206.
- Hovestadt, V., Jones, D.T., Picelli, S., Wang, W., Kool, M., Northcott, P.A., Sultan, M., Stachurski, K., Ryzhova, M., Warnatz, H.J., et al. (2014). Decoding the regulatory landscape of medulloblastoma using DNA methylation sequencing. *Nature* 510, 537–541.
- Huang, W., Sherman, B.T., and Lempicki, R.A. (2009). Systematic and integrative analysis of large gene lists using DAVID bioinformatics resources. *Nat. Protoc.* 4, 44–57.
- Jeong, M., Sun, D., Luo, M., Huang, Y., Challen, G.A., Rodriguez, B., Zhang, X., Chavez, L., Wang, H., Hannah, R., et al. (2014). Large conserved domains of low DNA methylation maintained by Dnmt3a. *Nat. Genet.* 46, 17–23.
- Jiang, Y., Matevosian, A., Huang, H.S., Straubhaar, J., and Akbarian, S. (2008). Isolation of neuronal chromatin from brain tissue. *BMC Neurosci.* 9, 42.
- Kepecs, A., and Fishell, G. (2014). Interneuron cell types are fit to function. *Nature* 505, 318–326.
- Kessarlis, N., Magno, L., Rubin, A.N., and Oliveira, M.G. (2014). Genetic programs controlling cortical interneuron fate. *Curr. Opin. Neurobiol.* 26, 79–87.
- Kim, T.K., Hemberg, M., Gray, J.M., Costa, A.M., Bear, D.M., Wu, J., Harmin, D.A., Laptewicz, M., Barbara-Haley, K., Kuersten, S., et al. (2010). Widespread transcription at neuronal activity-regulated enhancers. *Nature* 465, 182–187.
- Lister, R., O'Malley, R.C., Tonti-Filippini, J., Gregory, B.D., Berry, C.C., Millar, A.H., and Ecker, J.R. (2008). Highly integrated single-base resolution maps of the epigenome in *Arabidopsis*. *Cell* 133, 523–536.
- Lister, R., Mukamel, E.A., Nery, J.R., Urich, M., Puddifoot, C.A., Johnson, N.D., Lucero, J., Huang, Y., Dwork, A.J., Schultz, M.D., et al. (2013). Global epigenomic reconfiguration during mammalian brain development. *Science* 341, 1237905.
- Malik, A.N., Vierbuchen, T., Hemberg, M., Rubin, A.A., Ling, E., Couch, C.H., Stroud, H., Spiegel, I., Farh, K.K., Harmin, D.A., and Greenberg, M.E. (2014). Genome-wide identification and characterization of functional neuronal activity-dependent enhancers. *Nat. Neurosci.* 17, 1330–1339.
- Maze, I., Shen, L., Zhang, B., Garcia, B.A., Shao, N., Mitchell, A., Sun, H., Akbarian, S., Allis, C.D., and Nestler, E.J. (2014). Analytical tools and current challenges in the modern era of neuroepigenomics. *Nat. Neurosci.* 17, 1476–1490.
- Mellén, M., Ayata, P., Dewell, S., Kriaucionis, S., and Heintz, N. (2012). MeCP2 binds to 5hmC enriched within active genes and accessible chromatin in the nervous system. *Cell* 151, 1417–1430.
- Molyneaux, B.J., Arlotta, P., Menezes, J.R., and Macklis, J.D. (2007). Neuronal subtype specification in the cerebral cortex. *Nat. Rev. Neurosci.* 8, 427–437.
- Molyneaux, B.J., Goff, L.A., Brettler, A.C., Chen, H.H., Brown, J.R., Hrvatin, S., Rinn, J.L., and Arlotta, P. (2015). DeCoN: genome-wide analysis of in vivo transcriptional dynamics during pyramidal neuron fate selection in neocortex. *Neuron* 85, 275–288.
- Neph, S., Vierstra, J., Stergachis, A.B., Reynolds, A.P., Haugen, E., Vernot, B., Thurman, R.E., John, S., Sandstrom, R., Johnson, A.K., et al. (2012). An expansive human regulatory lexicon encoded in transcription factor footprints. *Nature* 489, 83–90.
- Nóbrega-Pereira, S., Kessarlis, N., Du, T., Kimura, S., Anderson, S.A., and Marín, O. (2008). Postmitotic Nkx2-1 controls the migration of telencephalic interneurons by direct repression of guidance receptors. *Neuron* 59, 733–745.
- Rashid, A.J., Cole, C.J., and Josselyn, S.A. (2014). Emerging roles for MEF2 transcription factors in memory. *Genes Brain Behav.* 13, 118–125.
- Rudy, B., Fishell, G., Lee, S., and Hjerling-Leffler, J. (2011). Three groups of interneurons account for nearly 100% of neocortical GABAergic neurons. *Dev. Neurobiol.* 71, 45–61.
- Sanz, E., Yang, L., Su, T., Morris, D.R., McKnight, G.S., and Amieux, P.S. (2009). Cell-type-specific isolation of ribosome-associated mRNA from complex tissues. *Proc. Natl. Acad. Sci. USA* 106, 13939–13944.
- Saxena, A., Wagatsuma, A., Noro, Y., Kuji, T., Asaka-Oba, A., Watahiki, A., Gurnot, C., Fagiolini, M., Hensch, T.K., and Carninci, P. (2012). Trehalose-enhanced isolation of neuronal sub-types from adult mouse brain. *Biotechniques* 52, 381–385.
- Sommer, L., Ma, Q., and Anderson, D.J. (1996). neurogenins, a novel family of atonal-related bHLH transcription factors, are putative mammalian neuronal determination genes that reveal progenitor cell heterogeneity in the developing CNS and PNS. *Mol. Cell. Neurosci.* 8, 221–241.
- Spiegel, I., Mardinly, A.R., Gabel, H.W., Bazinet, J.E., Couch, C.H., Tzeng, C.P., Harmin, D.A., and Greenberg, M.E. (2014). Npas4 regulates excitatory-inhibitory balance within neural circuits through cell-type-specific gene programs. *Cell* 157, 1216–1229.
- Stadler, M.B., Murr, R., Burger, L., Ivanek, R., Lienert, F., Schöler, A., van Nimwegen, E., Wirbelauer, C., Oakeley, E.J., Gaidatzis, D., et al. (2011). DNA-binding factors shape the mouse methylome at distal regulatory regions. *Nature* 480, 490–495.
- Stamatoyannopoulos, J.A., Snyder, M., Hardison, R., Ren, B., Gingeras, T., Gilbert, D.M., Groudine, M., Bender, M., Kaul, R., Canfield, T., et al.; Mouse ENCODE Consortium (2012). An encyclopedia of mouse DNA elements (Mouse ENCODE). *Genome Biol.* 13, 418.
- Steiner, F.A., Talbert, P.B., Kasinathan, S., Deal, R.B., and Henikoff, S. (2012). Cell-type-specific nuclei purification from whole animals for genome-wide expression and chromatin profiling. *Genome Res.* 22, 766–777.
- Sugino, K., Hempel, C.M., Miller, M.N., Hattox, A.M., Shapiro, P., Wu, C., Huang, Z.J., and Nelson, S.B. (2006). Molecular taxonomy of major neuronal classes in the adult mouse forebrain. *Nat. Neurosci.* 9, 99–107.
- Sullivan, P.F., Daly, M.J., and O'Donovan, M. (2012). Genetic architectures of psychiatric disorders: the emerging picture and its implications. *Nat. Rev. Genet.* 13, 537–551.
- Teif, V.B., Beshnova, D.A., Vainshtein, Y., Marth, C., Mallm, J.P., Höfer, T., and Rippe, K. (2014). Nucleosome repositioning links DNA (de)methylation and differential CTCF binding during stem cell development. *Genome Res.* 24, 1285–1295.
- Thurman, R.E., Rynes, E., Humbert, R., Vierstra, J., Maurano, M.T., Haugen, E., Sheffield, N.C., Stergachis, A.B., Wang, H., Vernot, B., et al. (2012). The accessible chromatin landscape of the human genome. *Nature* 489, 75–82.
- Verzi, M.P., Agarwal, P., Brown, C., McCulley, D.J., Schwarz, J.J., and Black, B.L. (2007). The transcription factor MEF2C is required for craniofacial development. *Dev. Cell* 12, 645–652.
- Visel, A., Taher, L., Girgis, H., May, D., Golonzka, O., Hoch, R.V., McKinsey, G.L., Pattabiraman, K., Silberberg, S.N., Blow, M.J., et al. (2013). A high-resolution enhancer atlas of the developing telencephalon. *Cell* 152, 895–908.
- Wang, B., Long, J.E., Flandin, P., Pla, R., Waclaw, R.R., Campbell, K., and Rubenstein, J.L. (2013). Loss of Gsx1 and Gsx2 function rescues distinct phenotypes in *Dlx1/2* mutants. *J. Comp. Neurol.* 521, 1561–1584.
- Xie, W., Barr, C.L., Kim, A., Yue, F., Lee, A.Y., Eubanks, J., Dempster, E.L., and Ren, B. (2012). Base-resolution analyses of sequence and parent-of-origin dependent DNA methylation in the mouse genome. *Cell* 148, 816–831.
- Xie, W., Schultz, M.D., Lister, R., Hou, Z., Rajagopal, N., Ray, P., Whitaker, J.W., Tian, S., Hawkins, R.D., Leung, D., et al. (2013). Epigenomic analysis of multilineage differentiation of human embryonic stem cells. *Cell* 153, 1134–1148.
- Yu, M., Hon, G.C., Szulwach, K.E., Song, C.X., Zhang, L., Kim, A., Li, X., Dai, Q., Shen, Y., Park, B., et al. (2012). Base-resolution analysis of 5-hydroxymethylcytosine in the mammalian genome. *Cell* 149, 1368–1380.

Cell Lineage Analysis in Human Brain Using Endogenous Retroelements

Gilad D. Evrony,^{1,2,3,9} Eunjung Lee,^{4,5,9} Bhaven K. Mehta,^{1,2,3} Yuval Benjamini,⁶ Robert M. Johnson,⁷ Xuyu Cai,^{1,2,3,8} Lixing Yang,^{4,5} Psalm Haseley,^{4,5} Hillel S. Lehmann,^{1,2,3} Peter J. Park,^{4,5,10,*} and Christopher A. Walsh^{1,2,3,10,*}

¹Division of Genetics and Genomics, Manton Center for Orphan Disease Research, and Howard Hughes Medical Institute, Boston Children's Hospital, Boston, MA 02115, USA

²Departments of Neurology and Pediatrics, Harvard Medical School, Boston, MA 02115, USA

³Broad Institute of MIT and Harvard, Cambridge, MA 02142, USA

⁴Center for Biomedical Informatics, Harvard Medical School, Boston, MA 02115, USA

⁵Division of Genetics, Brigham and Women's Hospital, Boston, MA 02115, USA

⁶Department of Statistics, Stanford University, Stanford, CA 94305, USA

⁷NIH NeuroBioBank, University of Maryland, Baltimore, MD 21201, USA

⁸Present address: Illumina, Inc., 5200 Illumina Way, San Diego, CA 92122, USA

⁹Co-first author

¹⁰Co-senior author

*Correspondence: peter_park@hms.harvard.edu (P.J.P.), christopher.walsh@childrens.harvard.edu (C.A.W.)

<http://dx.doi.org/10.1016/j.neuron.2014.12.028>

SUMMARY

Somatic mutations occur during brain development and are increasingly implicated as a cause of neurogenetic disease. However, the patterns in which somatic mutations distribute in the human brain are unknown. We used high-coverage whole-genome sequencing of single neurons from a normal individual to identify spontaneous somatic mutations as clonal marks to track cell lineages in human brain. Somatic mutation analyses in >30 locations throughout the nervous system identified multiple lineages and sublineages of cells marked by different LINE-1 (L1) retrotransposition events and subsequent mutation of poly-A microsatellites within L1. One clone contained thousands of cells limited to the left middle frontal gyrus, whereas a second distinct clone contained millions of cells distributed over the entire left hemisphere. These patterns mirror known somatic mutation disorders of brain development and suggest that focally distributed mutations are also prevalent in normal brains. Single-cell analysis of somatic mutation enables tracing of cell lineage clones in human brain.

INTRODUCTION

Somatic mutations, occurring during or after the mitotic cell divisions that generate the body, cause not only cancer, but also diverse neurologic diseases, including cortical malformations, epilepsy, intellectual disability, and neurodegeneration (Poduri et al., 2013). Somatic mutations also remain an important, unexplored possible etiology of other neuropsychiatric diseases (Insel, 2014). In contrast to inherited mutations, somatic mutations cause disease depending not only on their effects on gene func-

tion, but also on the time, place, and cell lineage during development at which they occur (Frank, 2010). Therefore, pathogenic somatic mutations pose a challenge because of the variety of ways their effects are shaped by normal development. Systematic tracing of the patterns of distribution of clonally related cells in human brain has not been possible, relying instead on extrapolation from animal models and in vitro studies (Clowry et al., 2010). Knowledge of these patterns, in conjunction with systematic measurement of somatic mutation rates in the brain (Evrony et al., 2012; McConnell et al., 2013; Cai et al., 2014), is crucial to understand how somatic mutations might cause disease by impairing circuit function and their potential role in the large unexplained burden of neuropsychiatric disease.

Somatic mutations also present an opportunity to study the developmental processes that create the human brain. Marking all progeny of a specific cell or population of cells is a central tool of developmental biology, revealing patterns of progenitor proliferation, migration, and differentiation (Kretzschmar and Watt, 2012). Existing tools to mark cell lineages, such as retroviral tracers and genetic and fluorescent markers, have uncovered key aspects of brain development in model organisms (Franco and Müller, 2013; Marín and Müller, 2014) but are invasive and cannot be applied to human tissue in vivo. Somatic mutations, however, occur spontaneously and possess the key features required of lineage markers: (a) they are inherited by all descendant cells, and (b) they are not transferred between cells. Retrotransposon mutations in particular have been shown to occur in mouse brain in vivo (Muotri et al., 2005) and human neuronal progenitors in vitro (Coufal et al., 2009) and are detectable in human brain (Baillie et al., 2011; Evrony et al., 2012; Reilly et al., 2013). Retrotransposons also have unique sequence structures that make each insertion differentiable from other insertions (Goodier and Kazazian, 2008), enabling detection even at low mosaicism and suggesting they could be used as noninvasive cell lineage markers in human brain.

Here we show that single-neuron, high-coverage whole-genome sequencing (WGS), along with profiling of all active retrotransposon families and further single-molecule somatic

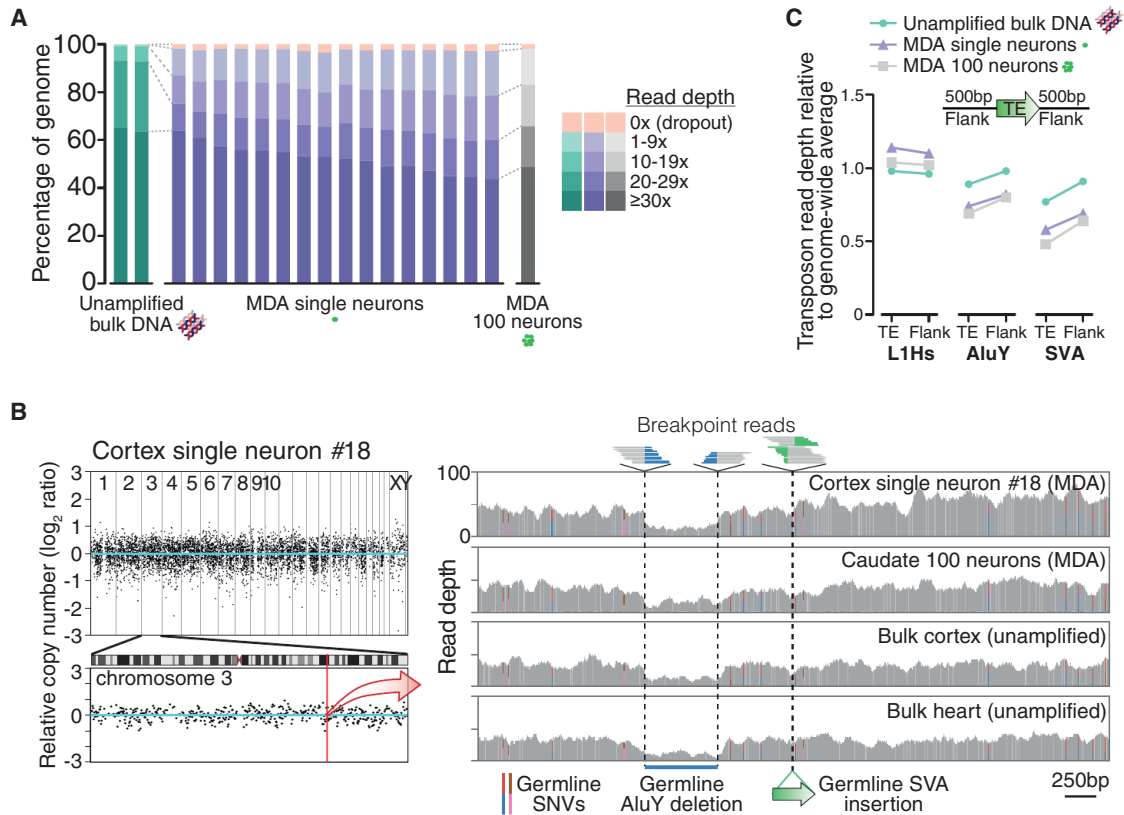


Figure 1. Single-Neuron WGS Genome Coverage

(A) Percentage of genome covered at specified read depths for all samples in this study.

(B) Representative genome-wide coverage plot of single neuron #18 in ~500 kb bins, with enlargement of chromosome 3 in which L1#2 was identified (Figure 2). See Figure S5 for plots of all samples. Right panel zoom of a 5 kb region (chr3: 147,605,344–147,610,345, hg19) shows single-neuron WGS simultaneous detection of three types of germline mutations, all concordant with 100-neuron and bulk samples: single nucleotide variants (SNVs, colored bars represent ratios of allele reads), a deletion (578 bp AluY and additional flanking sequence), and an SVA retrotransposon insertion. All mutations have been previously identified in public polymorphism databases.

(C) Average read depth of retrotransposon insertions annotated in the human genome reference and their 500 bp flanks, relative to the genome-wide average read depth. Relative read depths correlate with average GC content of each retrotransposon family (L1Hs: 42%; AluY: 54%; SVA: 63% GC content), due to GC amplification bias of MDA (see Table S2 and Note S1).

See also Figures S1–S9 and Tables S1 and S2.

mutation analyses, can identify and leverage somatic mutations as tags to identify unexpected spatial patterns of cell lineages in the human brain. Our data show a proof of principle that clonal patterns defined by somatic retroelement insertions and mutations of associated repeat sequences delineate patterns of lineage resembling those defined in animal models while enabling study of human-specific features, and suggest that deep analysis of the gamut of somatic mutations will allow a systematic reconstruction of key features of lineage patterns in the human brain.

RESULTS

High-Coverage Whole-Genome Sequencing of Single Neuronal Genomes

We selected 16 single neuronal genomes for high-coverage WGS from a population of large neuronal nuclei from the left middle frontal gyrus of the dorsolateral prefrontal cortex of a neuro-

logically normal individual (UMB1465). These genomes were amplified by multiple displacement amplification (MDA) (Dean et al., 2002) as part of a prior targeted study of LINE-1 (L1) retrotransposition (Evrony et al., 2012). WGS at a genome-wide average read depth of 42× achieved coverage of 98% ± 0.5% of the genome at ≥1× and 81% ± 2% at ≥10× read depth on average (±SD) across all single neurons (Figures 1A and 1B; Tables S1 and S2, available online), consistent with prior estimates of MDA locus dropout measured by targeted genotyping (Evrony et al., 2012) and WGS of MDA-amplified single cancer cells (Hou et al., 2012). Single neurons showed highly consistent sequencing quality, genome read alignment, and genome coverage (Figure S1; Tables S1 and S2). Sequencing and alignment metrics were generally similar to WGS of unamplified bulk DNA from cortex and heart, although as seen in prior single-cell studies (Evrony et al., 2012; Hou et al., 2012; Voet et al., 2013), MDA samples showed systematic and mostly correctable biases in genome coverage due to GC-sequence content (Figures 1C

and S2–S5; Table S2; Note S1). Compared to single cells amplified by the MALBAC method in a prior study (Zong et al., 2012), MDA achieves improved overall genome coverage, as well as more even amplification at smaller scales (<50 kb) necessary for reliable detection of sequence variants such as retrotransposon insertions (Figures S1, S6, and S7; Table S2; Note S1). On the other hand, MALBAC shows more even and reproducible coverage at larger scales (Figures S6 and S7; Note S1), consistent with its better performance in detecting large copy-number variants (Hou et al., 2013). Our high-coverage single-cell WGS dataset, the most extensive to date, provided an opportunity for additional detailed analyses of single-cell MDA performance, including in-depth investigation of genome coverage, GC-sequence bias, comparisons to other publicly available single-cell datasets, and MDA chimeras (stochastic false positive structural variants created during amplification). These comprehensive analyses are presented in Note S1 (see also Figures S1–S9; Tables S1 and S2) to aid future single-cell genomics research in understanding mechanisms of single-cell genome amplification and developing improved amplification methods (Blainey and Quake, 2014).

Somatic Retrotransposon Insertion Analysis with the Single-Cell Transposable Element Analyzer

We searched for somatic retrotransposon insertions deriving from all major active retrotransposon families (AluY, L1Hs, and SVA) using *scTea* (single-cell transposable element analyzer), a pipeline based on the *Tea* method originally developed for detection of somatic insertions in tumor samples (Lee et al., 2012b). *scTea* incorporates significant additional features and improvements for single-cell analysis, including identification of true insertions with high sensitivity and specificity (Figures 2A, 2B, S10, and S11; see Supplemental Experimental Procedures for details). *scTea* achieves sensitivity of 95%, 96%, and 86% in detection of AluY, L1Hs, and SVA insertions, respectively, that are absent from the human genome reference (nonreference insertions) in simulations generated from the only Sanger-sequenced diploid genome (HuRef) (Figure S10C). Specificity of AluY, L1Hs, and SVA bulk DNA insertion calls estimated by PCR and Sanger sequencing validation of 80 randomly selected insertion candidates from bulk DNA WGS of individual 1465 was 97%, 100%, and 100%, respectively (Table S3). In single-neuron genomes, *scTea* detected an average of 805 AluY, 131 L1Hs, and 17 SVA germline nonreference insertions (i.e., insertions also found in bulk samples of the individual), of which 708, 117, and 9, on average, were “known” insertions independently detected by prior population studies of retrotransposon polymorphism (Figure 2A). *scTea* achieved a single-neuron sensitivity of 74%, 79%, and 62% for AluY, L1Hs, and SVA, respectively, using the high-confidence known germline insertions of the individual as a reference (Figures S10D and S10E; see Supplemental Experimental Procedures for details).

Analysis of the 16 single-neuron genomes with *scTea* identified 18 somatic insertion candidates (Figure 2B; Table S3). The four highest-scoring candidates were two L1Hs insertions (each identified in two neurons: L1#1 in neurons 2 and 77 and L1#2 in neurons 6 and 18; Figures 2B–2D) and were the only candidates with convincing *in silico* evidence on manual review of WGS data (Table S3). Follow-up evaluation of all 18 candidates

by independent PCR assays validated only these four candidates. Remarkably, L1#1 was the same somatic insertion on chromosome 15 previously identified by targeted L1 insertion profiling (L1-IP) in the same two neurons (2 and 77) (Evrony et al., 2012). This represents important validation of L1-IP (Evrony et al., 2012) by an entirely independent sequencing method, dataset, and analysis pipeline.

Full-length cloning of L1#2 revealed that like L1#1, it showed all the hallmarks of a bona fide retrotransposition event (target site duplication [TSD] and poly-A tail), but also showed truncation, inversion, and a long 3' transduction (614 bp) identifying the source L1 on chromosome 13 (Figures 2E, 2F, S12A, and S12B; Table S3). The site of insertion was in an intergenic region far away from any obvious transcribed gene, strongly suggesting that this L1 does not alter the function of any nearby gene. Its long 3' transduction, which occurs infrequently during retrotransposition (<5% of insertions transduce >500 bp) (Goodier et al., 2000; Pickeral et al., 2000; Xing et al., 2006), is longer than the DNA fragments amplified by L1-IP, explaining why the insertion was not identified by L1-IP. Additional 3'-junction PCR (3' PCR) screening of a large set of single cells from the individual identified L1#2 in 13 of 587 single cortical neuron genomes, but not in 59 single caudate neuron genomes or 68 single cerebellar neuron genomes (Figures 2G, S12C, and S12D). Intriguingly, the source element for L1#2 on chromosome 13 was not active in previous *in vitro* assays (Brouha et al., 2003), suggesting that *in vivo* retrotransposon activity may differ from *in vitro* estimates and highlighting how single-cell studies can reveal *in vivo* activity of source elements. WGS analysis of single neurons was consistent with our previous targeted L1-IP (Evrony et al., 2012) and our prior estimate of low rates of L1 retrotransposition in the cerebral cortex (with 12/16 single neurons lacking validated insertions and two validated insertions each shared by two clonally related cells), and extends these results to find no evidence of Alu and SVA retrotransposition in the 16 sequenced single neurons from this normal individual. These results illustrate the advantage of single-cell WGS by its ability to analyze all retrotransposon families simultaneously and to recover somatic insertions that elude targeted sequencing approaches.

Tracing Spatial Distributions of Progenitor Lineages in Human Brain

A custom droplet digital PCR (ddPCR) assay with single-copy sensitivity (Figure S13) allowed quantification of the mosaicism (percentage of cells) and distribution of the two somatic L1s in unamplified (bulk) DNA extracted from frozen tissues from 32 regions across the left cerebral cortical hemisphere, left caudate, left cerebellum, and spinal cord (Figure S14; Table S4); the right hemisphere was formalin-fixed and therefore studied by a different nested PCR assay (see Supplemental Experimental Procedures). Remarkably, L1#1 was detected only in five adjacent locations in the left middle frontal gyrus of the cortex, spanning a region $\approx 2 \times 1$ cm in size and showing an average mosaicism of 0.09% (range: 0.04%–0.22%) (Figures 3, S14, and S15; Table S4). Absolute copy number quantification by ddPCR further estimated that at least 2,200 cells harbored L1#1 in our DNA samples, extrapolating to likely no more than 50,000 cells total in the cortex (see Supplemental Experimental Procedures).

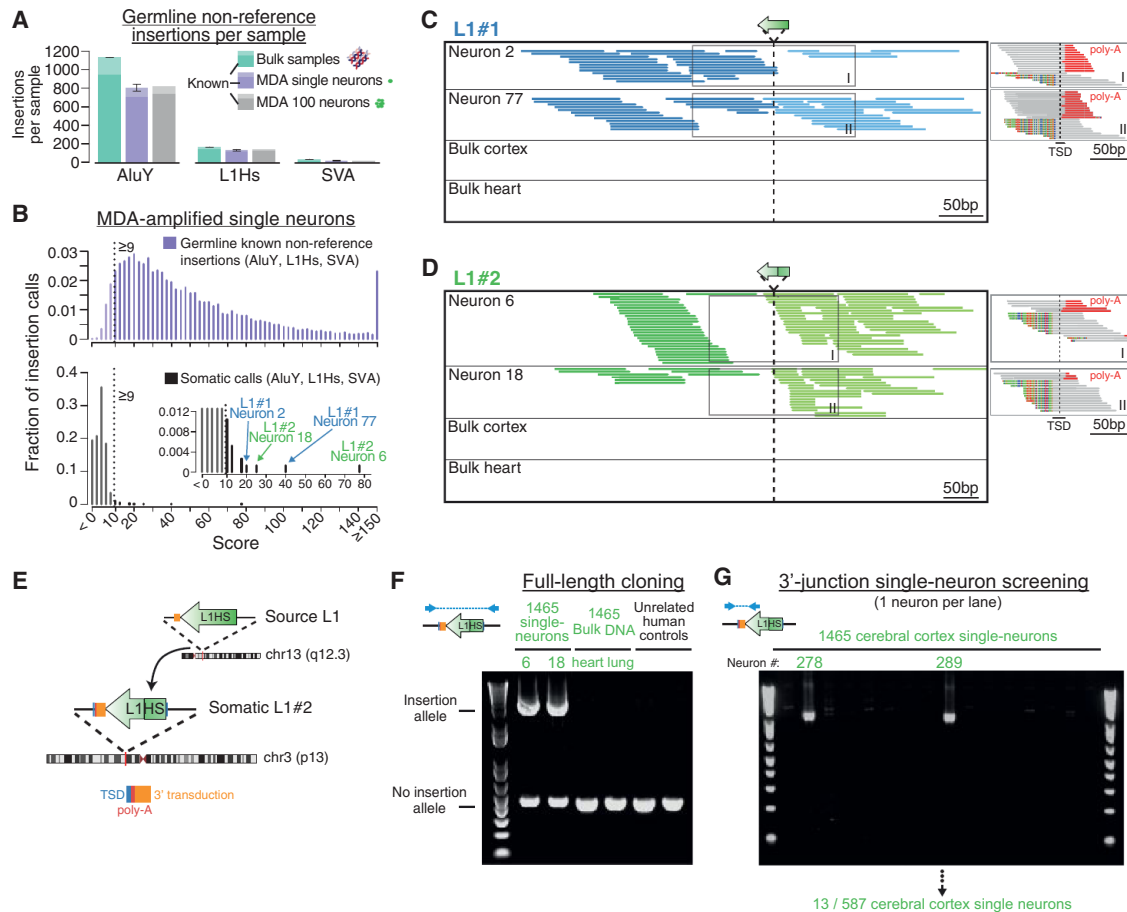


Figure 2. Single-Neuron WGS Analysis Identifies Somatic Retrotransposon Insertions

(A) Average number of germline nonreference insertions (i.e., present in either bulk cortex or heart) detected per sample with an *scTea*-calculated score ≥ 9 (see Supplemental Experimental Procedures for details on score calculation). Error bars, SD. The number of known insertions (reported in public databases and prior population studies of retrotransposon polymorphism) are shaded in a darker color.

(B) Score distribution of all AluY, L1Hs, and SVA germline known nonreference insertions (upper panel, $n = 13,849$ insertions) and somatic calls (lower panel, i.e., calls absent in bulk heart) detected across all 16 single neurons. Dashed line indicates score threshold ≥ 9 used to call somatic candidates, with bars below threshold drawn in a lighter color. Note the distribution of known insertions at higher scores compared to somatic calls at lower scores that arise from low-level MDA chimeras below threshold.

(C) Whole-genome sequencing reads detecting L1#1. Main panel shows fully aligned reads whose pairs aligned to L1, with darker and lighter colors indicating plus and minus orientations, respectively. Smaller panels on right show partially aligned (breakpoint) reads spanning the insertion breakpoint, detecting the TSD and poly-A tail. Mismatched bases relative to the human genome reference are colored.

(D) Whole-genome sequencing reads detecting L1#2. A few partially aligned reads distant from the insertion site are chimeras.

(E) Schematic of L1#2 and its source L1.

(F) Full-length PCR validation and cloning of L1#2.

(G) Representative gel from a 3' PCR screen for L1#2 in single neurons.

See also Figures S10–S12 and Table S3.

L1#1 was not detected in nonneuronal cells sorted from the left middle frontal gyrus, nor in multiple caudate, cerebellum, spinal cord, right cortex, heart, lung, and liver samples, illustrating the assay's specificity and ability to detect ultra-low mosaicism. The localized spatial distribution and very low mosaicism strongly suggest that the insertion marked a neocortical progenitor of the left middle frontal gyrus giving rise to mostly, if not exclusively, neurons.

In contrast to L1#1, L1#2 was detected in every sample of the left cerebral cortex and caudate nucleus tested, though at very low and highly variable mosaicism (cortex average 0.4%,

range 0.01%–1.7%) (Figures 3 and S15; Table S4). While it is not possible to estimate the total number of cells harboring L1#2 without assaying the entire brain, extrapolation from assayed regions suggests that L1#2's lineage encompasses tens to hundreds of millions of cells. L1#2 was also detected in sorted nonneuronal cells and at extremely low levels in left cerebellum, but not in formalin-fixed tissue of the right hemisphere, nor in spinal cord, heart, lung, or liver (Figures 3 and S15; Table S4), suggesting it mobilized considerably earlier in nervous system development than L1#1 and in a progenitor for both neurons and glia.

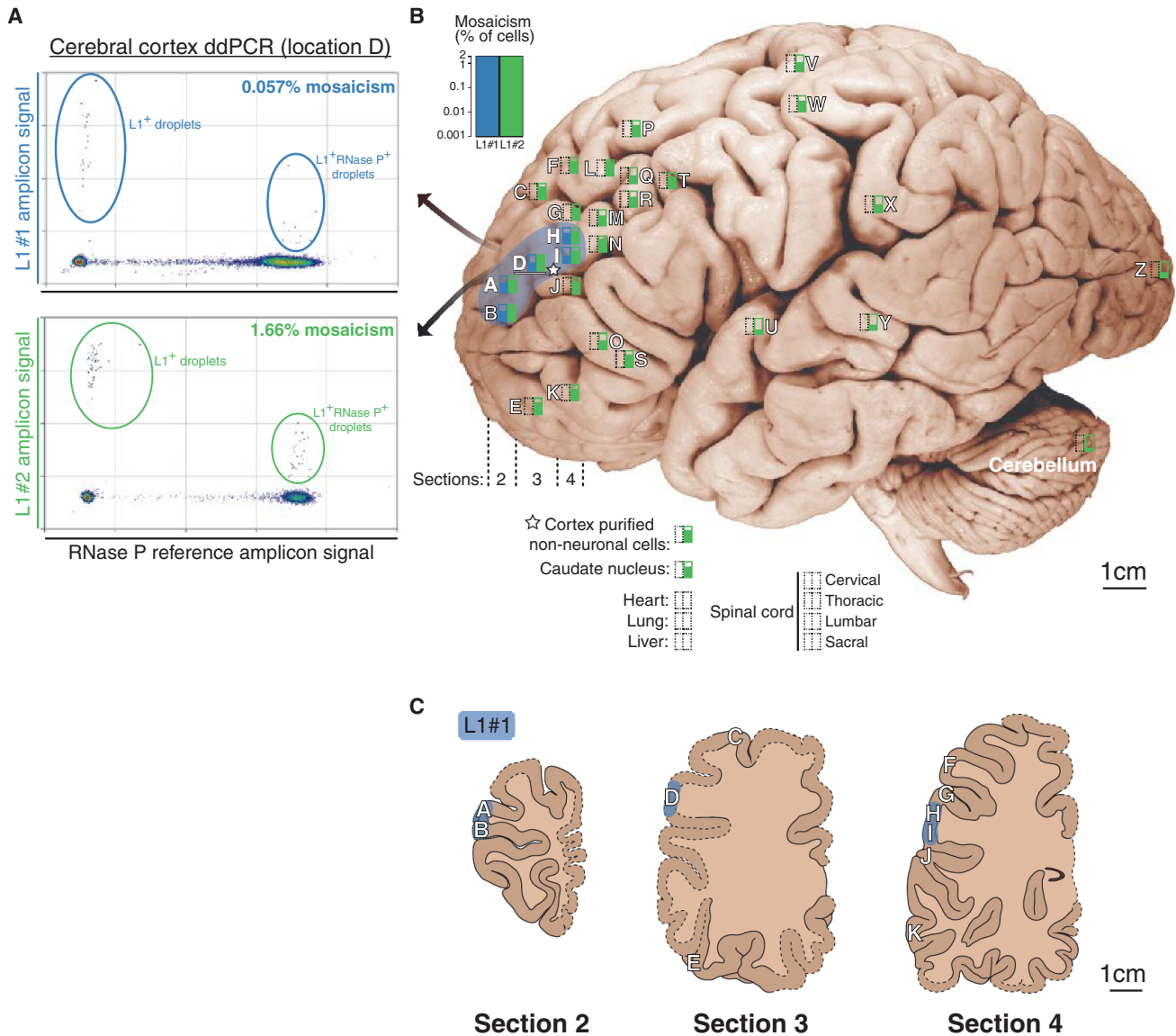


Figure 3. Mosaicism of Somatic L1 Insertions Measured by ddPCR

(A) Representative ddPCR plots of L1#1 and L1#2. L1⁺ droplets are plotted with larger points for better visualization. Reduced L1 signal in double-positive versus single-positive droplets is due to relatively higher PCR efficiency of *RNaseP* amplicons.

(B) Mosaicism levels measured in individual UMB1465, plotted on a representative brain, using logarithmic box plots to indicate level of mosaicism. Empty rectangles indicate no detection. Blue shading indicates the estimated distribution of L1#1 in the middle frontal gyrus. The 16 WGS single neurons were originally obtained from location D (underlined).

(C) Lucida tracings of cortex sections 2, 3, and 4 in which L1#1 was found, traced from photographs of sections. Dashed lines indicate regions that were not present in photographs of sections due to sampling prior to this study. Anatomy of these regions was extrapolated based on records of sampled locations, adjacent sections, photographs of right hemisphere formalin-fixed sections, and atlases of normal brain anatomy. Locations in which L1#1 was detected are highlighted in blue. See Figure S14 for diagrams of all sampled brain sections.

See also Figures S13–S15 and Table S4.

Poly-A Tails of Somatic Insertions Are Highly Mutable and Mark Sublineages

3' PCR validation data for L1#1 in neurons 2 and 77 suggested that the insertion was slightly different in size in each neuron (Figure 4A), which reflected unexpected secondary mutations in the poly-A tail of the L1 sequence. The difference in size was initially

surprising, as L1#1 was inherited by both neurons from a single event in a shared progenitor, as confirmed by identical breakpoints, TSD, and transduction sequences in both neurons (Evrony et al., 2012). Comparison of L1#1's sequence in the two neurons revealed that the poly-A tail, which was reverse transcribed into the genome from the original retrotransposon

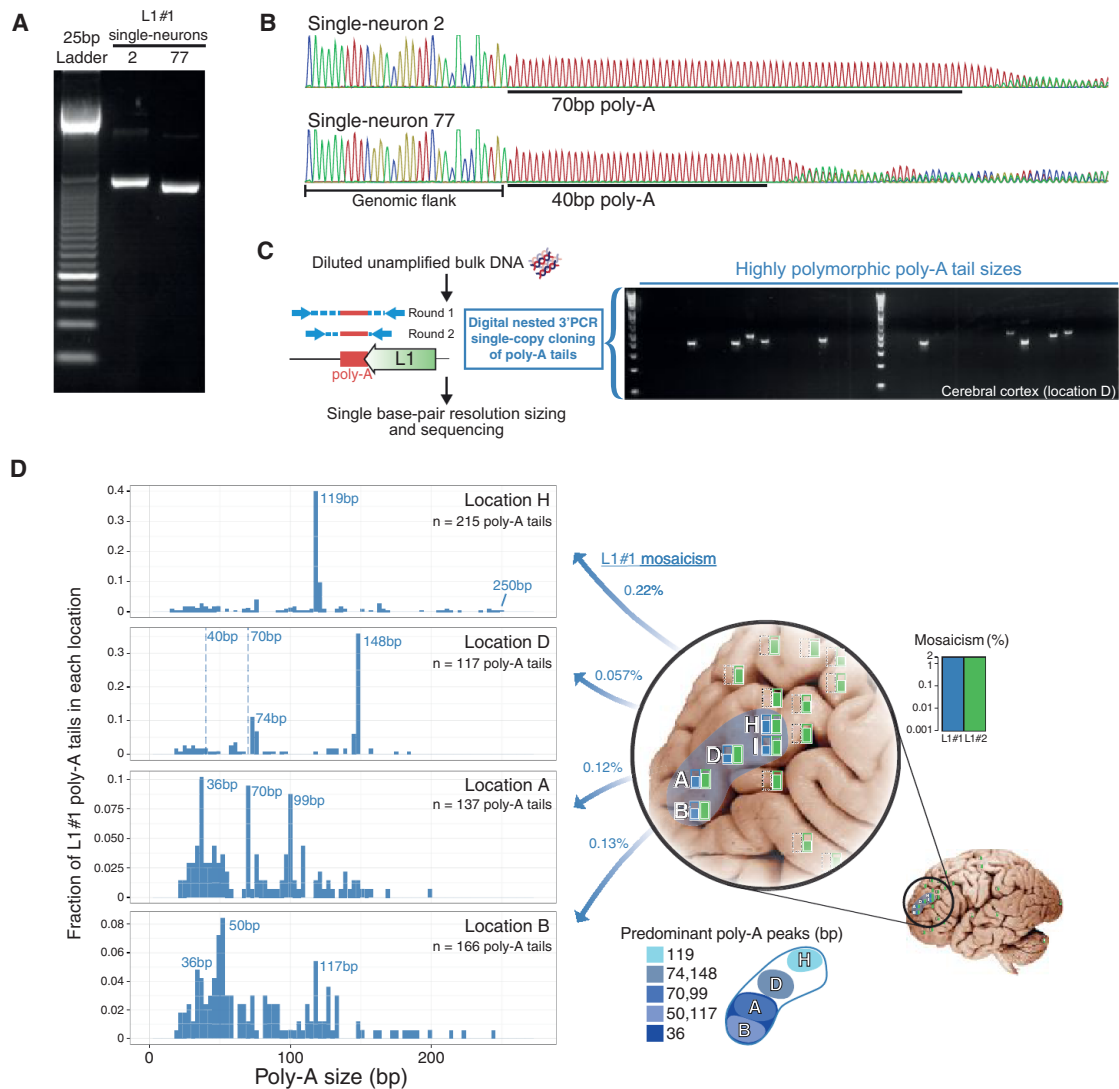


Figure 4. Somatic Retrotransposon Insertion Poly-A Tail Polymorphism Reveals Sublineages across Brain Regions

(A) L1#1 3' PCR products differ in size between single neurons 2 and 77.

(B) Sanger sequencing of L1#1 in single neurons 2 and 77 reveals poly-A tail polymorphism.

(C) Brief schematic of dnPCR single-copy cloning of poly-A tails directly from unamplified bulk DNA, and a representative gel showing highly polymorphic product sizes. Poly-A tail lengths were precisely measured by capillary electrophoresis.

(D) L1#1 poly-A tail size distributions (in 3 bp bins) obtained by dnPCR show peaks representing sublineages and marked variability within and between locations. Dashed lines mark poly-A tail sizes of single neurons 2 and 77 sorted from location D. Location I not shown, since, due to extremely low mosaicism, only four poly-A tails were cloned.

See also Figures S16–S19 and Table S5.

transcript's poly-A tail and shown before to be a highly mutable sequence element (Grandi et al., 2013), was longer in neuron 2 (70 bp) compared to neuron 77 (40 bp) (Figure 4B), fully accounting for the difference in insertion size. This suggested that the poly-A sequence of L1#1 underwent somatic mutation in descendant cells after the original insertion event. Using a digital nested 3'-junction PCR assay (dnPCR) with near 100% sensitivity and specificity in cloning single copies of L1#1's poly-A tail directly from unamplified bulk DNA (Figure S16A), we found

that the poly-A tail was highly polymorphic (Figure 4C), indicating that it mutated somatically many times.

Profiling the lengths of many L1#1 poly-A tails ($n = 639$) from locations where L1#1 was found revealed striking differences in poly-A size distributions between locations, including distinct peaks marking subset lineages of cells, as well as additional highly variable poly-A tail lengths at lower levels indicating frequent somatic mutation (Figure 4D; Table S5). Importantly, dnPCR of control poly-A tails of known lengths (Figure S16B)

and reproducibility of peaks across tissues (Figure S17) shows that dnPCR reliably measures poly-A tail lengths with precision up to ± 1 bp (see Supplemental Experimental Procedures for details). Overall, these results suggest that the poly-A tail of L1#1's originating retrotransposition event may have been >200 bp long (Figure 4D; and see Note S2 for further discussion) and that in subsequent descendant cells, *in vivo* somatic mutation generated widely varying poly-A lengths marking distinct sublineages— a striking example of nested somatic mutation. Moreover, the distinct distributions of poly-A tails in each location (Figure 4D) are consistent with migration of a subset of progenitors each with a different distribution of poly-A tails.

L1#2's poly-A tail showed less polymorphism. Only 1 of the 13 single neurons with the L1#2 insertion showed a large difference in poly-A size (Table S5), and dnPCR profiling of $>1,500$ poly-A tails across 12 locations in the cortex, caudate, and cerebellum showed some variability, though much less than L1#1 (Figure S17; Table S5). The different poly-A mutation rates of L1#1 and L1#2 may reflect a difference in poly-A size of the original insertion, regional genomic variability in mutation rates, timing of the insertion during development, or epigenetic effects on microsatellite and somatic mutation rates (Kim et al., 2013).

Notably, smaller clonal sets of cells carrying L1#1 with similar poly-A lengths appear to occupy smaller zones of the middle frontal gyrus (Figure 4D; Table S5). For example, cells carrying L1#1 marked by poly-A tails 118–120 bp in length (110/639 cells) were limited to location H of the middle frontal gyrus (104/110 = 95% of cells). Similarly, cells carrying 147–149 bp poly-A tails (46/639 cells) were found predominantly in location D (42/46 = 91% of cells), with the remaining cells in adjacent locations, while 99–100 bp poly-A tails (13/639 cells) were found predominantly in location A (12/13 = 92% of cells; 1/13 cells in adjacent location B). We interpret cells carrying the same poly-A length as sublineages, defined by poly-A mutations, that are offspring of the original progenitor in which L1#1 inserted. The distribution of these sublineages suggests that tangential dispersion becomes progressively restricted in later generations of neocortical progenitor lineages, though even these sublineages show remarkable intermingling with cells from distinct clonal origins. Larger scale single-cell analyses of somatic mutations will be necessary to study the generalizability of these patterns across different progenitor types and anatomic locations.

DISCUSSION

Here, we show how single-neuron WGS and in-depth characterization of somatic mutations can reveal spatial patterns of cell lineages in normal human brain. We were able to take advantage of somatic mutations for this purpose by our ability to definitively validate them and recover their full sequences from single neurons, a level of validation not routinely performed in single-cell studies. Although here we focused on somatic retrotransposition and the highly mutable poly-A microsatellites they create, potentially any type of somatic mutation that can similarly be definitively validated could be used for this purpose (Shapiro et al., 2013). Indeed, prior studies have found diverse types of somatic mutation in human brain, including copy-number variants (Cai et al., 2014; McConnell et al., 2013), point mutations (Poduri

et al., 2012), and other microsatellite polymorphisms (Gonitel et al., 2008). Since our single-neuron WGS captures most of the genome at high read depth, our methods may be extended to examine nearly all types of somatic mutation in one experiment. Further single-cell WGS studies of all classes of mutation simultaneously may achieve high-resolution tracing of lineages in human brain.

One limitation of retrotransposons for lineage tracing is our prior (Evrony et al., 2012) and current finding that, at least in the cerebral cortex, somatic insertions are relatively infrequent, being undetectable in 12/16 single-neuron genomes. Nonetheless, they offer important advantages as lineage markers relative to other mutation types: (a) they possess characteristic sequence signatures confirming they were created *in vivo* and not by MDA; (b) their breakpoints enable ultrasensitive assays; (c) each insertion is unique so that homoplasmy (occurrence of identical independent mutations) does not confound analysis. Spontaneous somatic retrotransposition as a tool to study brain development is compellingly analogous to classical retroviral labeling used to study cortical development in other mammals (Walsh and Cepko, 1992; Ware et al., 1999); in fact, retrotransposons and retroviruses are evolutionarily related (Eickbush and Jamburuthugoda, 2008). Identification of genetic backgrounds more permissive for retrotransposition (Muotri et al., 2010; Zhao et al., 2013), or individuals with a higher load of active elements, may identify brains with more spontaneously labeled lineages.

Notably, a recent study with a transgenic synthetic L1 mouse model found significant rates of somatic truncation of long (>100 bp) L1 poly-A tails (Grandi et al., 2013), consistent with our findings with endogenous human L1 elements. We also profiled single poly-A tails of a tumor-specific somatic L1 insertion we identified in a breast cancer (Figures S18A–S18C; Table S3) and found distinct poly-A size distributions in a metastasis of the cancer compared to the primary tumor (Figures S18D and S18E; Table S5), consistent with most of the metastasis deriving from likely one cell or at most a few cells. The significant somatic mutation of retrotransposon poly-A tails (see Note S2 for discussion) supports the potential of high-throughput microsatellite analysis for systematic lineage tracing (Naxerova et al., 2014; Shapiro et al., 2013).

The somatic mutations we studied exhibited distinct spatial patterns of mosaicism, resembling patterns of clonal dispersion previously seen only in animal models and suggesting that focal patches of somatic mutation are prevalent throughout normal brains. The detection of L1#1 only in the middle frontal gyrus suggests that it occurred in a neocortical progenitor relatively late in cortical development. Its isolation from a population of neurons with the largest nuclear size also suggests that it is likely present in pyramidal neurons (Evrony et al., 2012). Moreover, the focal spatial distributions of the L1#1 lineage and its sublineages imply radial ontogenetic units (Rakic, 2009). On the other hand, the dispersion of the L1#1 lineage at very low mosaicism ($\approx 0.1\%$) across at least 2 cm of cortex supports the existence of clonal heterogeneity among neocortical progenitor-derived cells within any given cortical column, consistent with lineage tracing studies in other mammals (Gao et al., 2014; Kriegstein and Noctor, 2004; Reid et al., 1997; Torii et al., 2009; Walsh and Cepko, 1988; Ware et al., 1999). Importantly, this implies

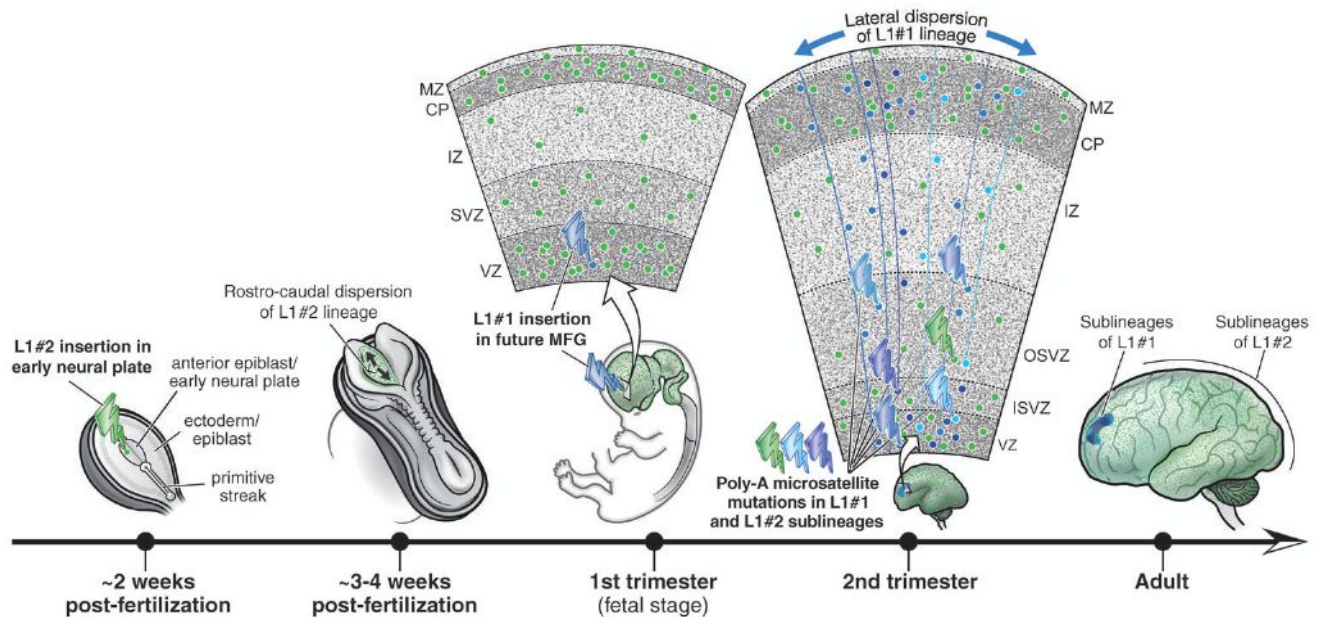


Figure 5. Developmental Model of Mutation Events and Lineages in This Study

L1#1 is illustrated as occurring in the first trimester, though its exact timing is unknown. MFG, middle frontal gyrus; VZ, ventricular zone; SVZ, subventricular zone; ISVZ, inner SVZ; OSVZ, outer SVZ; IZ, intermediate zone; CP, cortical plate; MZ, marginal zone.

additional complexity in the possible ways different somatic mutations may overlap spatially and interact to affect cortical circuits.

L1#2 marks a distinct lineage with a much wider geographic distribution than L1#1, suggesting it arose earlier in development. However, L1#2's low mosaicism (<2%) spanning the entire rostrocaudal length of the brain (from forebrain to hind-brain) implies surprising intermingling of clones in the early central nervous system (CNS). Remarkably, genetic fate-mapping of CNS clones in mouse (Mathis and Nicolas, 2000) revealed the same unexpected finding of significant rostrocaudal dispersion, with evidence suggesting that this results from intermixing along the rostrocaudal axis among the earliest CNS progenitors. Therefore, L1#2 likely inserted into one of the earliest progenitors of the CNS in the anterior (rostral) epiblast or early neural plate, prior to the transition to coherent growth when clonally related cells have more restricted rostrocaudal dispersion. It is possible that some L1#2-containing cells derived from ventral telencephalon progenitors, which give rise to interneurons that disperse across the cortex (Marín, 2013), though proving this would require new phenogenomic technologies combining single-cell genomics with broader single-cell phenotyping. In situ hybridization methods, such as High-Definition DNA Fluorescence In Situ Hybridization (HD-FISH), offer one possible route for phenogenomic study of somatic mutations (Bienko et al., 2013) to resolve cell-type, morphology, and layer distributions of cells within a lineage. However, attempts so far to detect somatic insertions shorter than 1 kb (such as the L1 transduction sequences available as targets in the current study) directly in brain tissue sections using this approach pose formidable challenges due to the sensitivity limits of current probe designs (M. Bienko, personal communication). We

provide a developmental model for the somatic mutation events we identified in Figure 5. Overall, these results illustrate how somatic mutations can yield important insight into clonal dispersion patterns in human brain development and point to the potential of future systematic study of large numbers of mutations and single cells to delineate lineages in the human nervous system.

The two L1 clones and smaller sublineages also match patterns of known somatic mutation disorders of human brain development and predict the existence of additional types of somatic lesions. Deleterious somatic mutations in mammalian target of rapamycin (mTOR) pathway genes cause hemimegalencephaly and show wide dispersion throughout an entire hemisphere (Poduri et al., 2012; Lee et al., 2012a), similar to L1#2, while focal cortical dysplasias, the most common cause of intractable epilepsy, are generally limited to smaller areas of cortex, remarkably similar to L1#1 (Poduri et al., 2013). Other deleterious mutations with such restricted distributions could potentially impact cortical areas strikingly unequally, affecting small regions of cortex (L1#1) or only one hemisphere (L1#2), providing a possible mechanism to generate selective and unpredictable disorders of cognition. Focal lesions of unknown etiology have been described in histology of brains of patients with autism spectrum disorder (Stoner et al., 2014); however, many autism brains do not have structural or radiographic findings. Focal mutation of genes involved in synaptic function, for example, may impair neuronal function locally without being structurally evident. Comprehensive single-cell sequencing and somatic mutation analyses across all cell types, brain regions, and time points in development will inform an understanding of normal human brain development and the role of somatic mutation in neuropsychiatric disease.

EXPERIMENTAL PROCEDURES

See Supplemental Experimental Procedures in the Supplemental Information for full method details.

Human Tissues and DNA Samples

Postmortem tissues from individual UMB1465 were obtained from the NIH NeuroBioBank at the University of Maryland. UMB1465 was a 17-year-old male and one of the individuals profiled in our previous single-neuron L1 insertion profiling (L1-IP) study (Evrony et al., 2012). All UMB1465 tissues were frozen and stored at -80°C without fixation within 4 hr of death, except for the right cerebral hemisphere, which was formalin-fixed. Coronal sections of the frozen left cerebral cortex were photographed before and after sampling. Sampled locations were mapped to a representative brain using measured section thicknesses and anatomy of gyri. Since an image of the complete brain of individual 1465 prior to sectioning was not available, sampled locations are illustrated on a representative brain image from the University of Wisconsin and Michigan State Comparative Mammalian Brain Collection (<http://brainmuseum.org>).

Bulk DNA was extracted from tissues with the QIAamp DNA Mini or QIAamp DNA FFPE Tissue kits (Qiagen). Genomes of the 16 cerebral cortex single-neuron samples and the caudate nucleus 100-neuron sample were amplified by MDA (Dean et al., 2002) as part of our previous targeted L1-IP study (Evrony et al., 2012). The 16 single neurons were originally sorted from location D of the left middle frontal gyrus. Unamplified bulk DNA from a breast cancer primary tumor, lymph node metastasis, and normal blood from an individual (ID: TCGA-E1-A15E) were obtained with permission from The Cancer Genome Atlas (TCGA) project.

Whole-Genome Sequencing and Read Alignment

Paired-end whole-genome sequencing libraries were prepared with the NEXTflex DNA Sequencing Kit (Bio Scientific) from 500 ng of DNA. Paired-end sequencing (100 bp \times 2 or 101 bp \times 2) was performed on HiSeq 2000 (Illumina) sequencers. High-coverage whole-genome sequencing data from prior studies of MALBAC-amplified single cancer cells (SW480 cancer cell line) (Zong et al., 2012) and MDA-amplified single lymphoblastoid cells (YH cell line) (Hou et al., 2012), and corresponding unamplified bulk DNA, were obtained from the NCBI Sequence Read Archive (SRA). High-coverage whole-genome sequencing data for breast cancer primary tumor, metastasis, and normal blood samples from individual TCGA-E1-A15E were obtained from CGHub. Sequencing reads were aligned to hs37d5 (1000 Genomes Project human genome reference based on the GRCh37 primary assembly) using bwa (Li and Durbin, 2009).

Single-Cell Analysis of Somatic Retrotransposition

Somatic retrotransposon insertion analysis was performed with *scTea* (Single-cell Transposable element analyzer). *scTea* is based on the *Tea* pipeline originally developed to detect somatic insertions of transposable elements in cancer genomes (Lee et al., 2012b), with additional significant modifications for single-neuron whole-genome analysis, including the following: (a) a scoring scheme assigning a score to each call, taking into account MDA and library preparation amplification noise; (b) improved handling of poly-A signals; (c) copy number genotyping of insertion calls; (d) local read assembly to detect transduced sequences; (e) a revised transposable element sequence library using only known active retrotransposon subfamilies; (f) rigorous sensitivity analyses to establish call criteria; and (g) specificity analyses using independent PCR validation.

Validation and Cloning of Retrotransposon Candidates

Validation of germline and somatic insertion candidates predicted by *scTea* was attempted by: (1) full-length PCR (FL-PCR) with genomic primers flanking the candidate (for Alu and L1 candidates) and (2) 3'-junction PCR (3' PCR) with a primer designed downstream of the 3' end of the candidate paired with an internal primer specific to the 3' sequence of the retrotransposon (for L1 and SVA candidates). Primer design and full-length cloning were performed as previously described (Evrony et al., 2012). Sequences of validation primers used for each candidate insertion can be found in Table S3. Positive validation reactions were confirmed by Sanger sequencing.

Droplet Digital PCR

Custom droplet digital PCR (ddPCR) assays for L1#1 and L1#2 were performed with the QX100 Droplet Digital PCR System (Bio-Rad). L1 assays were multiplexed with an assay for *RNaseP* serving as a genomic copy number reference for calculation of mosaicism. Multiple unrelated human control samples confirmed assay specificity (Table S4), and the presence or absence of L1#1 and L1#2 in unamplified bulk DNA from every location and tissue was independently verified by a bulk nested 3'-junction PCR (Figure S15).

Poly-A Tail Cloning and Sizing

Poly-A tail lengths of somatic retrotransposon insertions were measured using a digital nested 3' PCR approach (dnPCR) in which single copies of poly-A tails are cloned directly from unamplified bulk DNA, thereby avoiding potential MDA artifacts. Single-copy (digital) cloning by dnPCR also recovers the true poly-A tail distribution in tissues, which is not possible with bulk (nondigital) PCR, since PCR amplification efficiency varies with poly-A tail length (data not shown). dnPCR is performed by diluting DNA to a target retrotransposon insertion concentration of 0.3 copies/reaction based on the absolute concentration measured by ddPCR, such that there would be <5% chance that the diluted DNA input into a dnPCR reaction would contain >1 poly-A tail. A two-round nested PCR targeting the 3' junction (containing the poly-A tail) of the somatic retrotransposon insertion is then performed on the diluted DNA, using a FAM-labeled primer in the second-round PCR. dnPCR reactions are screened by agarose gel electrophoresis to identify reactions yielding a product. dnPCR products are then sized by capillary electrophoresis on 3130 or 3730 DNA Analyzers (Life Technologies) to obtain the poly-A tail length. A subset of positive dnPCR reactions from each tissue and location were Sanger sequenced (Genewiz) and confirmed that dnPCR amplifies the targeted retrotransposon insertion with 100% specificity (data not shown). dnPCR results across tissues show that dnPCR measures poly-A tails with a precision up to ± 1 bp across a wide range of poly-A tail sizes (see Supplemental Experimental Procedures for details).

ACCESSION NUMBERS

The NCBI Sequence Read Archive accession number for the single-neuron whole-genome sequencing data reported in this paper is SRP041470.

SUPPLEMENTAL INFORMATION

Supplemental Information includes Notes S1 and S2, Supplemental Experimental Procedures, 19 figures, and five tables and can be found with this article online at <http://dx.doi.org/10.1016/j.neuron.2014.12.028>.

AUTHOR CONTRIBUTIONS

G.D.E. and B.K.M. performed all wet-lab experiments, with input from X.C. and H.S.L. General and retrotransposition analyses of WGS data were performed by G.D.E. and E.L., respectively, with assistance from Y.B., L.Y., and P.H. Y.B. performed GC-content bias analyses. R.M.J. procured human tissues. G.D.E., E.L., P.J.P., and C.A.W. conceived and designed the project and wrote the manuscript.

ACKNOWLEDGMENTS

We thank Aldo Rozzo for logistical assistance, the Orchestra research computing team at Harvard Medical School for assistance with computing resources, Magda Bienko and Alexander van Oudenaarden for helpful discussions and pilot attempts to detect the somatic insertions in brain tissue using HD-FISH, Alexander Subtelny for assistance analyzing transcriptome poly-A length profiling data (Note S2), and Haig Kazazian and Tara Doucet for helpful discussions regarding activities of source retroelements. We also thank Kim Petro (Bio-Rad) for assistance with droplet digital PCR and Dick Bennett of the Boston Children's Hospital Molecular Biology core for assistance with capillary electrophoresis. Representative brain image in Figures 3B, 4D, and S14A was adapted with permission from the University of Wisconsin

and Michigan State Comparative Mammalian Brain Collections (<http://brainmuseum.org>), supported by the National Science Foundation. Figure 5 was illustrated by Ken Probst (Xavier Studio). Sequencing was performed with support of the Research Connection of Boston Children's Hospital. G.D.E. is supported by NIH MSTP grant T32GM007753 and the Louis Lange III Scholarship in Translational Research. E.L. is supported in part by the Eleanor and Miles Shore Fellowship. C.A.W. is supported by the Manton Center for Orphan Disease Research and grants from the NINDS (R01 NS079277 and R01 NS032457). C.A.W. is a Distinguished Investigator of the Paul G. Allen Family Foundation and an Investigator of the Howard Hughes Medical Institute.

Accepted: December 9, 2014

Published: January 7, 2015

REFERENCES

- Baillie, J.K., Barnett, M.W., Upton, K.R., Gerhardt, D.J., Richmond, T.A., De Sapio, F., Brennan, P.M., Rizzu, P., Smith, S., Fell, M., et al. (2011). Somatic retrotransposition alters the genetic landscape of the human brain. *Nature* **479**, 534–537.
- Bienko, M., Crosetto, N., Teytelman, L., Klemm, S., Itzkovitz, S., and van Oudenaarden, A. (2013). A versatile genome-scale PCR-based pipeline for high-definition DNA FISH. *Nat. Methods* **10**, 122–124.
- Blainey, P.C., and Quake, S.R. (2014). Dissecting genomic diversity, one cell at a time. *Nat. Methods* **11**, 19–21.
- Brouha, B., Schustak, J., Badge, R.M., Lutz-Prigge, S., Farley, A.H., Moran, J.V., and Kazazian, H.H., Jr. (2003). Hot L1s account for the bulk of retrotransposition in the human population. *Proc. Natl. Acad. Sci. USA* **100**, 5280–5285.
- Cai, X., Evrony, G.D., Lehmann, H.S., Elhosary, P.C., Mehta, B.K., Poduri, A., and Walsh, C.A. (2014). Single-cell, genome-wide sequencing identifies clonal somatic copy-number variation in the human brain. *Cell Rep.* **8**, 1280–1289.
- Clowry, G., Molnár, Z., and Rakic, P. (2010). Renewed focus on the developing human neocortex. *J. Anat.* **217**, 276–288.
- Coufal, N.G., Garcia-Perez, J.L., Peng, G.E., Yeo, G.W., Mu, Y., Lovci, M.T., Morell, M., O'Shea, K.S., Moran, J.V., and Gage, F.H. (2009). L1 retrotransposition in human neural progenitor cells. *Nature* **460**, 1127–1131.
- Dean, F.B., Hosono, S., Fang, L., Wu, X., Faruqi, A.F., Bray-Ward, P., Sun, Z., Zong, Q., Du, Y., Du, J., et al. (2002). Comprehensive human genome amplification using multiple displacement amplification. *Proc. Natl. Acad. Sci. USA* **99**, 5261–5266.
- Eickbush, T.H., and Jamburuthugoda, V.K. (2008). The diversity of retrotransposons and the properties of their reverse transcriptases. *Virus Res.* **134**, 221–234.
- Evrony, G.D., Cai, X., Lee, E., Hills, L.B., Elhosary, P.C., Lehmann, H.S., Parker, J.J., Atabay, K.D., Gilmore, E.C., Poduri, A., et al. (2012). Single-neuron sequencing analysis of L1 retrotransposition and somatic mutation in the human brain. *Cell* **151**, 483–496.
- Franco, S.J., and Müller, U. (2013). Shaping our minds: stem and progenitor cell diversity in the mammalian neocortex. *Neuron* **77**, 19–34.
- Frank, S.A. (2010). Evolution in health and medicine Sackler colloquium: Somatic evolutionary genomics: mutations during development cause highly variable genetic mosaicism with risk of cancer and neurodegeneration. *Proc. Natl. Acad. Sci. USA* **107** (1), 1725–1730.
- Gao, P., Postiglione, M.P., Krieger, T.G., Hernandez, L., Wang, C., Han, Z., Streicher, C., Papusheva, E., Insolera, R., Chugh, K., et al. (2014). Deterministic progenitor behavior and unitary production of neurons in the neocortex. *Cell* **159**, 775–788.
- Gonitel, R., Moffitt, H., Sathasivam, K., Woodman, B., Detloff, P.J., Faull, R.L., and Bates, G.P. (2008). DNA instability in postmitotic neurons. *Proc. Natl. Acad. Sci. USA* **105**, 3467–3472.
- Goodier, J.L., and Kazazian, H.H., Jr. (2008). Retrotransposons revisited: the restraint and rehabilitation of parasites. *Cell* **135**, 23–35.
- Goodier, J.L., Ostertag, E.M., and Kazazian, H.H., Jr. (2000). Transduction of 3'-flanking sequences is common in L1 retrotransposition. *Hum. Mol. Genet.* **9**, 653–657.
- Grandi, F.C., Rosser, J.M., and An, W. (2013). LINE-1-derived poly(A) microsatellites undergo rapid shortening and create somatic and germline mosaicism in mice. *Mol. Biol. Evol.* **30**, 503–512.
- Hou, Y., Song, L., Zhu, P., Zhang, B., Tao, Y., Xu, X., Li, F., Wu, K., Liang, J., Shao, D., et al. (2012). Single-cell exome sequencing and monoclonal evolution of a JAK2-negative myeloproliferative neoplasm. *Cell* **148**, 873–885.
- Hou, Y., Fan, W., Yan, L., Li, R., Lian, Y., Huang, J., Li, J., Xu, L., Tang, F., Xie, X.S., and Qiao, J. (2013). Genome analyses of single human oocytes. *Cell* **155**, 1492–1506.
- Insel, T.R. (2014). Brain somatic mutations: the dark matter of psychiatric genetics? *Mol. Psychiatry* **19**, 156–158.
- Kim, T.M., Laird, P.W., and Park, P.J. (2013). The landscape of microsatellite instability in colorectal and endometrial cancer genomes. *Cell* **155**, 858–868.
- Kretzschmar, K., and Watt, F.M. (2012). Lineage tracing. *Cell* **148**, 33–45.
- Kriegstein, A.R., and Noctor, S.C. (2004). Patterns of neuronal migration in the embryonic cortex. *Trends Neurosci.* **27**, 392–399.
- Lee, J.H., Huynh, M., Silhavy, J.L., Kim, S., Dixon-Salazar, T., Heiberg, A., Scott, E., Bafna, V., Hill, K.J., Collazo, A., et al. (2012a). De novo somatic mutations in components of the PI3K-AKT3-mTOR pathway cause hemimegalencephaly. *Nat. Genet.* **44**, 941–945.
- Lee, E., Iskow, R., Yang, L., Gokcumen, O., Haseley, P., Luquette, L.J., 3rd, Lohr, J.G., Harris, C.C., Ding, L., Wilson, R.K., et al.; Cancer Genome Atlas Research Network (2012b). Landscape of somatic retrotransposition in human cancers. *Science* **337**, 967–971.
- Li, H., and Durbin, R. (2009). Fast and accurate short read alignment with Burrows-Wheeler transform. *Bioinformatics* **25**, 1754–1760.
- Marín, O. (2013). Cellular and molecular mechanisms controlling the migration of neocortical interneurons. *Eur. J. Neurosci.* **38**, 2019–2029.
- Marín, O., and Müller, U. (2014). Lineage origins of GABAergic versus glutamatergic neurons in the neocortex. *Curr. Opin. Neurobiol.* **26**, 132–141.
- Mathis, L., and Nicolas, J.F. (2000). Different clonal dispersion in the rostral and caudal mouse central nervous system. *Development* **127**, 1277–1290.
- McConnell, M.J., Lindberg, M.R., Brennand, K.J., Piper, J.C., Voet, T., Cowing-Zitron, C., Shumilina, S., Lasken, R.S., Vermeesch, J.R., Hall, I.M., and Gage, F.H. (2013). Mosaic copy number variation in human neurons. *Science* **342**, 632–637.
- Muotri, A.R., Chu, V.T., Marchetto, M.C.N., Deng, W., Moran, J.V., and Gage, F.H. (2005). Somatic mosaicism in neuronal precursor cells mediated by L1 retrotransposition. *Nature* **435**, 903–910.
- Muotri, A.R., Marchetto, M.C., Coufal, N.G., Oefner, R., Yeo, G., Nakashima, K., and Gage, F.H. (2010). L1 retrotransposition in neurons is modulated by MeCP2. *Nature* **468**, 443–446.
- Naxerova, K., Brachtel, E., Salk, J.J., Seese, A.M., Power, K., Abbasi, B., Snuderl, M., Chiang, S., Kasif, S., and Jain, R.K. (2014). Hypermutable DNA chronicles the evolution of human colon cancer. *Proc. Natl. Acad. Sci. USA* **111**, E1889–E1898.
- Pickeral, O.K., Makatowski, W., Boguski, M.S., and Boeke, J.D. (2000). Frequent human genomic DNA transduction driven by LINE-1 retrotransposition. *Genome Res.* **10**, 411–415.
- Poduri, A., Evrony, G.D., Cai, X., Elhosary, P.C., Beroukhi, R., Lehtinen, M.K., Hills, L.B., Heinzen, E.L., Hill, A., Hill, R.S., et al. (2012). Somatic activation of AKT3 causes hemispheric developmental brain malformations. *Neuron* **74**, 41–48.
- Poduri, A., Evrony, G.D., Cai, X., and Walsh, C.A. (2013). Somatic mutation, genomic variation, and neurological disease. *Science* **341**, 1237758.
- Rakic, P. (2009). Evolution of the neocortex: a perspective from developmental biology. *Nat. Rev. Neurosci.* **10**, 724–735.

- Reid, C.B., Tavazoie, S.F., and Walsh, C.A. (1997). Clonal dispersion and evidence for asymmetric cell division in ferret cortex. *Development* 124, 2441–2450.
- Reilly, M.T., Faulkner, G.J., Dubnau, J., Ponomarev, I., and Gage, F.H. (2013). The role of transposable elements in health and diseases of the central nervous system. *J. Neurosci.* 33, 17577–17586.
- Shapiro, E., Biezuner, T., and Linnarsson, S. (2013). Single-cell sequencing-based technologies will revolutionize whole-organism science. *Nat. Rev. Genet.* 14, 618–630.
- Stoner, R., Chow, M.L., Boyle, M.P., Sunkin, S.M., Mouton, P.R., Roy, S., Wynshaw-Boris, A., Colamarino, S.A., Lein, E.S., and Courchesne, E. (2014). Patches of disorganization in the neocortex of children with autism. *N. Engl. J. Med.* 370, 1209–1219.
- Torii, M., Hashimoto-Torii, K., Levitt, P., and Rakic, P. (2009). Integration of neuronal clones in the radial cortical columns by EphA and ephrin-A signalling. *Nature* 461, 524–528.
- Voet, T., Kumar, P., Van Loo, P., Cooke, S.L., Marshall, J., Lin, M.L., Zamani Esteki, M., Van der Aa, N., Mateiu, L., McBride, D.J., et al. (2013). Single-cell paired-end genome sequencing reveals structural variation per cell cycle. *Nucleic Acids Res.* 41, 6119–6138.
- Walsh, C., and Cepko, C.L. (1988). Clonally related cortical cells show several migration patterns. *Science* 241, 1342–1345.
- Walsh, C., and Cepko, C.L. (1992). Widespread dispersion of neuronal clones across functional regions of the cerebral cortex. *Science* 255, 434–440.
- Ware, M.L., Tavazoie, S.F., Reid, C.B., and Walsh, C.A. (1999). Coexistence of widespread clones and large radial clones in early embryonic ferret cortex. *Cereb. Cortex* 9, 636–645.
- Xing, J., Wang, H., Belancio, V.P., Cordaux, R., Deininger, P.L., and Batzer, M.A. (2006). Emergence of primate genes by retrotransposon-mediated sequence transduction. *Proc. Natl. Acad. Sci. USA* 103, 17608–17613.
- Zhao, K., Du, J., Han, X., Goodier, J.L., Li, P., Zhou, X., Wei, W., Evans, S.L., Li, L., Zhang, W., et al. (2013). Modulation of LINE-1 and Alu/SVA retrotransposition by Aicardi-Goutières syndrome-related SAMHD1. *Cell Rep.* 4, 1108–1115.
- Zong, C., Lu, S., Chapman, A.R., and Xie, X.S. (2012). Genome-wide detection of single-nucleotide and copy-number variations of a single human cell. *Science* 338, 1622–1626.

Transgenic Mice for Intersectional Targeting of Neural Sensors and Effectors with High Specificity and Performance

Linda Madisen,¹ Aleena R. Garner,¹ Daisuke Shimaoka,² Amy S. Chuong,³ Nathan C. Klapoetke,³ Lu Li,¹ Alexander van der Bourg,⁴ Yusuke Niino,⁵ Ladan Egolf,⁴ Claudio Monetti,⁶ Hong Gu,¹ Maya Mills,¹ Adrian Cheng,¹ Bosiljka Tasic,¹ Thuc Nghi Nguyen,¹ Susan M. Sunkin,¹ Andrea Benucci,^{2,5} Andras Nagy,⁶ Atsushi Miyawaki,⁵ Fritjof Helmchen,⁴ Ruth M. Empson,⁷ Thomas Knöpfel,⁸ Edward S. Boyden,³ R. Clay Reid,¹ Matteo Carandini,² and Hongkui Zeng^{1,*}

¹Allen Institute for Brain Science, 551 N 34th Street, Seattle, WA 98103, USA

²UCL Institute of Ophthalmology, University College London, 11-43 Bath Street, London, EC1V 9EL, UK

³MIT Media Lab and McGovern Institute, Massachusetts Institute of Technology, 20 Ames Street, Cambridge, MA 02139, USA

⁴Brain Research Institute, University of Zurich, Winterthurerstrasse 190, CH-8057 Zurich, Switzerland

⁵Brain Science Institute, RIKEN, 2-1 Hirosawa, Wako-city, Saitama 351-0198, Japan

⁶Lunenfeld-Tanenbaum Research Institute, Mount Sinai Hospital, 600 University Avenue, Toronto, ON M5G 1X5, Canada

⁷Department of Physiology, Brain Health Research Centre, University of Otago, PO Box 913, Dunedin 9054, New Zealand

⁸The Division of Brain Sciences, Department of Medicine, Imperial College London, 160 DuCane Road, London, W12 0NN, UK

*Correspondence: hongkuiz@alleninstitute.org

<http://dx.doi.org/10.1016/j.neuron.2015.02.022>

SUMMARY

An increasingly powerful approach for studying brain circuits relies on targeting genetically encoded sensors and effectors to specific cell types. However, current approaches for this are still limited in functionality and specificity. Here we utilize several intersectional strategies to generate multiple transgenic mouse lines expressing high levels of novel genetic tools with high specificity. We developed driver and double reporter mouse lines and viral vectors using the Cre/Flp and Cre/Dre double recombinase systems and established a new, retargetable genomic locus, TIGRE, which allowed the generation of a large set of Cre/tTA-dependent reporter lines expressing fluorescent proteins, genetically encoded calcium, voltage, or glutamate indicators, and optogenetic effectors, all at substantially higher levels than before. High functionality was shown in example mouse lines for GCaMP6, YCX2.60, VSFP Butterfly 1.2, and Jaws. These novel transgenic lines greatly expand the ability to monitor and manipulate neuronal activities with increased specificity.

INTRODUCTION

The brain comprises a large number of neuronal and non-neuronal cell types, whose connections and interactions are fundamental to its function. To observe and manipulate their activities selectively, the best available approach is genetic targeting of protein-based sensors and effectors to specific cell types (Huang and Zeng, 2013). In mice, the Cre/lox recombina-

tion system is the most widely used approach to access specific cell types, utilizing gene promoters or loci with specific expression patterns (Gerfen et al., 2013; Gong et al., 2007; Madisen et al., 2010; Taniguchi et al., 2011). However, cell populations defined by Cre driver lines are often heterogeneous, encompassing multiple brain regions and/or multiple cell types (Harris et al., 2014). Fundamentally, cell types are rarely defined by single genes, but rather by intersectional expression of multiple genes. Thus, it is imperative to develop intersectional genetic targeting approaches, combining regulatory elements from two or more genes to increase specificity of transgene expression. Important efforts have been made to develop transgenic intersectional approaches, most successfully with the combination of Cre and Flp site-specific recombinases (SSRs) (Dymecki and Kim, 2007; Dymecki et al., 2010; Kranz et al., 2010; Ray et al., 2011; Robertson et al., 2013). However, thus far, intersectional approaches have not been widely used in functional studies, due to the limited number of validated transgenic tools available.

The ongoing development of increasingly effective sensors and effectors offers extraordinary opportunities for studies of neuronal interactions and functions (Fenno et al., 2011; Huang and Zeng, 2013; Knöpfel, 2012). One issue with the practical utility of these tools is that they require high-level expression in cell populations of interest. Such high levels of expression can be obtained with techniques that result in high transgene copy numbers in individual cells, such as in utero electroporation and adeno-associated virus (AAV) infection. However, these approaches have limitations, including invasive surgical delivery, incomplete coverage of the desired cell population, variable levels of expression in different cells, and, in the case of viruses, potential cytotoxicity associated with long-term viral infection and/or uncontrolled gene expression.

Transgenic mouse lines that express high and heritable patterns of genetic tools in specific cell populations provide an alternative that can overcome at least some of these limitations (Zeng

and Madisen, 2012; Zhao et al., 2011). We previously establish a standardized Cre-reporter system in which transgene expression was driven by a strong, ubiquitous CAG promoter targeted to the Rosa26 locus (Madisen et al., 2010; Muzumdar et al., 2007), expressing fluorescent proteins, calcium sensor GCaMP3, and optogenetic activator ChR2(H134R) and silencers Arch and eNpHR3.0 (Madisen et al., 2010, 2012; Zariwala et al., 2012). Although proved useful in many applications (Ackman et al., 2012; Haddad et al., 2013; Issa et al., 2014; Jackman et al., 2014; Kheirbek et al., 2013; Lee et al., 2014; Nguyen-Vu et al., 2013; Pi et al., 2013), we and others have also identified limitations in the sensitivity or functionality of these reporters in other situations.

Currently the only transgenic mouse approach demonstrated to reliably achieve AAV-like high-level expression is the use of the Thy1.2 promoter in randomly integrated transgenes (Arenkiel et al., 2007; Dana et al., 2014; Feng et al., 2000; Zhao et al., 2008), presumably with multiple copies at the insertion site. Although powerful in driving tool gene expression, this approach also has drawbacks. Expression of transgenes driven by the Thy1.2 promoter is strongly position dependent, necessitating a screen of multiple founder lines to find potentially useful ones. Furthermore, adding Cre-dependent control, e.g., a floxed-stop cassette, to a multi-copy transgene is problematic because Cre could then induce recombination both within and between the different copies, resulting in reduced transgene copy numbers and variability of transgene expression among different cells.

We therefore undertook a systematic evaluation of multiple approaches aiming at more specific and more robust transgene expression. To complement existing Cre driver lines, we focused on the intersection of Cre with another recombinase or with a transcriptional activator. In addition, we built and validated a new docking site in a permissive genomic locus, the TIGRE locus (Zeng et al., 2008), which supports repeated targeting. By introducing a tTA-based transcriptional amplification approach to the TIGRE locus, all reporter lines doubly regulated by Cre and tTA drove robust expression of sensors and effectors at levels substantially higher than those in comparable Rosa-CAG-based reporters. Functional characterization of lines carrying representative optical tools under Cre and tTA control demonstrates their enhanced efficiency for studies of neuronal activity, both *in vitro* and *in vivo*.

RESULTS

In our effort to improve upon current strategies for cell-type-specific transgene expression, we explored three strategies for intersectional control: (1) reporter expression that depends on two independent SSRs from the ubiquitous Rosa26 locus, (2) Cre-dependent reporter expression from an endogenous locus targeted because of its cell-type-specific expression pattern, (3) reporter expression dependent on Cre and the transcriptional transactivator tTA from another ubiquitous genomic locus, TIGRE. Since the third strategy resulted in the most strongly enhanced transgene expression, we created a series of TIGRE reporter lines that show high-level expression of novel calcium, voltage, and glutamate sensors and optogenetic effectors. The complete list of new intersectional transgenic mouse lines and

AAVs introduced in this paper (17 reporter lines, 4 driver lines, and 10 AAVs) is shown in Table 1. All other previously published mouse lines used in this study are listed in Table S1.

Dual-Recombinase Intersectional Strategies for Transgene Regulation Increase Specificity

An intersectional approach that has proven useful in transgenic studies is to use both Cre and Flp, expressed from separate driver lines using distinct regulatory sequences, to turn on a doubly controlled reporter allele (Dymecki et al., 2010). To incorporate this into our Rosa-CAG reporter system (Madisen et al., 2010) and to test additional recombinases such as Dre (Anastassiadis et al., 2009; Sauer and McDermott, 2004), we generated Cre/Flp or Cre/Dre double-dependent reporters, the Ai65(RCFL-tdT) line that contains FRT-stop-FRT (FRT: Flp recognition site) and LoxP-stop-LoxP double cassettes in front of tdTomato, and the Ai66(RCRL-tdT) line containing Rox-stop-Rox (Rox: Dre recognition site) and LoxP-stop-LoxP double cassettes (Figure 1A). We also generated driver lines expressing these recombinases in the *Pvalb* gene locus, *Pvalb*-2A-Flpe (Buchholz et al., 1998), *Pvalb*-2A-Flpo (Raymond and Soriano, 2007), and *Pvalb*-2A-Dre, through recombinase-mediated cassette exchange (RMCE) into our originally targeted *Pvalb*-2A-Cre line (Figure S1A). To evaluate the recombination efficiency and specificity, we generated triple transgenic (Tg) mice whose genealogy included a pan-GABAergic Cre line *Slc32a1*-IR-Cre (*Slc32a1* is also known as *VGAT*, a GABA vesicular transporter; IR stands for IRES [internal ribosome entry site]), one of the *Pvalb*-SSR lines, and Ai65 or Ai66 reporter.

Cre and Flp (both *Pvalb*-2A-Flpe and *Pvalb*-2A-Flpo) efficiently restricted transgene expression to cell populations with overlapping patterns of driver expression. In the *Slc32a1*-IR-Cre;*Pvalb*-2A-Flpo;Ai65(RCFL-tdT) triple Tg mouse, tdTomato expression was observed in a subset of cells in multiple areas, consistent with *Slc32a1*+/*Pvalb*+ expression pattern (Figure 1B). Reporter expression depended strictly on the presence of both Cre and Flp drivers (Figure S2A). Importantly, these triple Tg mice showed higher selectivity in expression than double Tg, *Pvalb*-2A-Cre;Ai14 mice, where Ai14 is a Rosa-CAG-based tdTomato reporter line (Madisen et al., 2010). In those mice, but not in the triple Tg mice, we found expression in cortical layer 5 pyramidal neurons and other non-interneuron cells, presumably arising from low-level or transient expression of the *Pvalb* gene (Figures S2B and S2C). Thus, the intersectional approach depending on two drivers provides increased specificity for targeting *Pvalb*+ GABAergic neurons.

We also combined Cre and Dre to produce an effective intersectional approach in *Slc32a1*-IR-Cre;*Pvalb*-2A-Dre;Ai66 (RCRL-tdT) triple Tg mice (Figure S3A). Control mice lacking Cre showed no reporter expression, but occasional tdTomato-positive cells in Cre+/*Dre*-/*Ai66*+ mice were observed. To further evaluate the Cre/Dre intersection, we generated another Dre-driver line, *Nr4a2*-SA-IR-Dre (*Nr4a2* is also known as *Nurr1*, a nuclear receptor with expression in dopamine neurons and in claustrum), and crossed it with *Emx1*-IR-Cre and Ai66. The resulting triple Tg mice showed specific, dense expression in claustrum and endopiriform nucleus (Figure 1C), consistent with adult brain areas known to express both *Emx1* and *Nr4a2*.

Table 1. Newly Generated Transgenic Mouse Lines and AAVs

Name ^a	Knockin Locus	Promoter Used	Expression Control	Gene Expressed	Function	JAX Stock Number
Ai65(RCFL-tdT)	Rosa26	CAG	Cre and Flp dependent	tdTomato	Fluorescent labeling	021875
Ai66(RCRL-tdT)	Rosa26	CAG	Cre and Dre dependent	tdTomato	Fluorescent labeling	021876
Ai57(RCFL-Jaws)	Rosa26	CAG	Cre and Flp dependent	Jaws-GFP-ER2	Optogenetic silencer	(not deposited)
Ai72(RCL-VSFPB)	Rosa26	CAG	Cre dependent	VSFP-Butterfly 1.2	Voltage indicator	(not deposited)
Ai87(RCL-iGluSnFR)	Rosa26	CAG	Cre dependent	iGluSnFR	Glutamate indicator	(not deposited)
Ai95(RCL-GCaMP6f)	Rosa26	CAG	Cre dependent	GCaMP6f	Calcium indicator	024105
Ai96(RCL-GCaMP6s)	Rosa26	CAG	Cre dependent	GCaMP6s	Calcium indicator	024106
Ai62(TITL-tdT)	TIGRE	TRE	Cre and tTA dependent	tdTomato	Fluorescent labeling	022731
Ai82(TITL-GFP)	TIGRE	TRE	Cre and tTA dependent	EGFP	Fluorescent labeling	023532
Ai79(TITL-Jaws)	TIGRE	TRE	Cre and tTA dependent	Jaws-GFP-ER2	Optogenetic silencer	023529
Ai93(TITL-GCaMP6f)	TIGRE	TRE	Cre and tTA dependent	GCaMP6f	Calcium indicator	024103
Ai94(TITL-GCaMP6s)	TIGRE	TRE	Cre and tTA dependent	GCaMP6s	Calcium indicator	024104
Ai92(TITL-YCX2.60)	TIGRE	TRE	Cre and tTA dependent	YCX2.60	Calcium indicator	In process
Ai78(TITL-VSFPB)	TIGRE	TRE	Cre and tTA dependent	VSFP-Butterfly 1.2	Voltage indicator	023528
Ai85(TITL-iGluSnFR)	TIGRE	TRE	Cre and tTA dependent	iGluSnFR	Glutamate indicator	In process
Snap25-LSL-2A-GFP	Snap25	Snap25	Pan-neuronal promoter, Cre dependent	EGFP	Fluorescent labeling	021879
Snap25-2A-GCaMP6s	Snap25	Snap25	Pan-neuronal promoter	GCaMP6s	Calcium indicator	025111
Pvalb-2A-Flpe	Pvalb	Pvalb	Driver line	Enhanced Flp	Recombination	021191
Pvalb-2A-Flpo	Pvalb	Pvalb	Driver line	Mammalianized Flp	Recombination	022730
Pvalb-2A-Dre	Pvalb	Pvalb	Driver line	Mammalianized Dre	Recombination	021190
Nr4a2-SA-IR-Dre	Nr4a2	Nr4a2	Driver line	Mammalianized Dre	Recombination	(not deposited)
AAV pmSyn1-EBFP-Cre-bGHpA	–	Mouse Syn1	Driver	EBFP-Cre	Recombination	–
AAV phSyn1-Dre-bGHpA	–	Human Syn1	Driver	Mammalianized Dre	Recombination	–
AAV phSyn1-Flpo-bGHpA	–	Human Syn1	Driver	Mammalianized Flp	Recombination	–
AAV phSyn1-Flpe-bGHpA	–	Human Syn1	Driver	Enhanced Flp	Recombination	–
AAV phSyn1-FSF-FLEX-ChR2(H134R)-EYFP-WPRE-bGHpA	–	Human Syn1	Cre and Flp dependent	ChR2(H134R)-EYFP	Optogenetic activator	–
AAV phSyn1-RSR-FLEX-ChR2(H134R)-EYFP-WPRE-bGHpA	–	Human Syn1	Cre and Dre dependent	ChR2(H134R)-EYFP	Optogenetic activator	–
AAV pCAG-FSF-FLEX-EGFP-WPRE-bGHpA	–	CAG	Cre and Flp dependent	EGFP	Fluorescent labeling	–
AAV pCAG-FLEX2-tTA2-WPRE-bGHpA	–	CAG	Cre-dependent driver	tTA2	Transcriptional activation	–
AAV pTRE-FLEX-EGFP-WPRE-bGHpA	–	TRE	Cre and tTA dependent	EGFP	Fluorescent labeling	–
AAV pTRE-FSF-FLEX-EGFP-WPRE-bGHpA	–	TRE	Cre, Flp and tTA dependent	EGFP	Fluorescent labeling	–

^aAcronyms: RCFL is Rosa26 – CAG promoter – FRT-STOP-FRT – LoxP-STOP-LoxP. RCRL is Rosa26 – CAG promoter – Rox-STOP-Rox – LoxP-STOP-LoxP. RCL is Rosa26 – CAG promoter – LoxP-STOP-LoxP. TITL is TIGRE – Insulators – TRE promoter – LoxP-STOP-LoxP. LSL is LoxP-STOP-LoxP. SA is Splice Acceptor. tdT is tdTomato. The 2A sequences used were F2A for Snap25-LSL-2A-GFP, and T2A for Snap25-2A-GCaMP6s, Pvalb-2A-Flpe, Pvalb-2A-Flpo, and Pvalb-2A-Dre.

Again, we observed no reporter expression in the absence of Cre but did detect sparse tdTomato-positive cells in Cre+/Dre-/Ai66+ mice (Figure S3B). This result suggests that while Dre specifically recombines Rox sites over Lox sites, Cre is slightly promiscuous toward Rox sites.

To complement our transgenic lines that incorporate dual recombinase control, we also generated a set of recombinant AAVs expressing Cre, Flpe, Flpo, and Dre drivers, as well as Cre/Flp and Cre/Dre doubly regulated reporters (Figures S4A–S4D). Consistent with previous reports (Fenno et al., 2014; Kranz

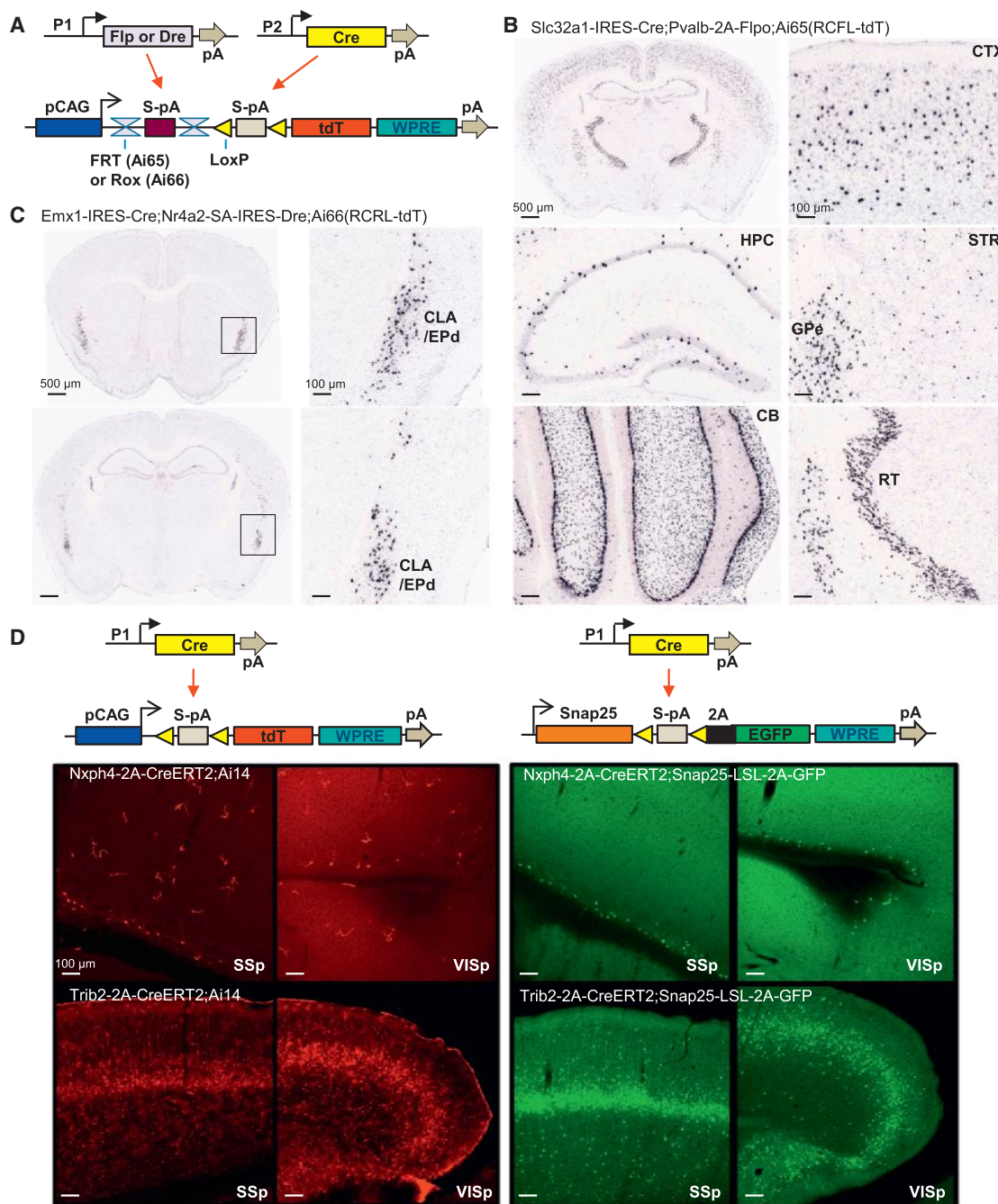


Figure 1. Intersectional Strategies Using Dual Recombinases or Cre Regulation of a Direct Neuronally Restricted Reporter

(A) Schematic diagram of intersectional control by either Cre/Flp or Cre/Dre recombinases, driven by different promoters (P1 or P2), on a doubly regulated reporter line: the Cre- and Flp-dependent Ai65(RCFL-tdT), or the Cre- and Dre-dependent Ai66(RCRL-tdT).

(B) ISH images of restricted tdTomato expression in *Slc32a1*^{+/+}*Pvalb*⁺ GABAergic neurons in the *Slc32a1*-IR-Cre;*Pvalb*-2A-Flpo;*Ai65*(RCFL-tdT) mouse. CTX, cortex; HPC, hippocampus; STR, striatum; GPe, globus pallidus, external segment; CB, cerebellum; RT, reticular nucleus of the thalamus.

(C) ISH images of restricted tdTomato expression in *Emx1*⁺/*Nr4a2*⁺ neurons in the claustrum (CLA) and endopiriform nucleus dorsal part (EPd) in the *Emx1*-IR-Cre;*Nr4a2*-SA-IRES-Dre;*Ai66*(RCRL-tdT) mouse.

(D) Direct neuronally restricted reporter gene expression by targeting Cre-dependent reporter gene to the pan-neuronal *Snap25* gene locus. TdTomato expression in cortex in both neuronal and non-neuronal cells of *Nxph4*-2A-CreERT2;*Ai14* and *Trib2*-2A-CreERT2;*Ai14* mice (left) compared with neuronally specific EGFP expression in *Nxph4*-2A-CreERT2;*Snap25*-LSL-2A-GFP and *Trib2*-2A-CreERT2;*Snap25*-LSL-2A-GFP mice (right). SSp, primary somatosensory cortex; VISp, primary visual cortex. (See also Figures S1–S4.)

et al., 2010), AAV-Flpo- and AAV-Dre-induced recombination comparable to AAV-Cre, whereas the recombination efficiency of AAV-Flpe was significantly lower. Flp and Dre viruses exhibited high specificity for FRT and Rox sites, respectively, whereas AAV-Cre recombined Rox sites at low frequency, with recombination most prevalent at the injection site, indicating increased promiscuity with high levels of Cre.

Direct Neuronally Restricted Reporter Gene Expression

To determine whether a simple intersectional strategy could restrict Cre-induced reporter expression to a specific cell type, we took advantage of the *Snap25* gene. *Snap25* encodes a synaptosome-associated protein. It is pan-neuronal and is among the most highly transcribed genes in the brain based on microarray data analysis (data not shown). We generated a *Snap25*-LSL-2A-GFP knockin line, where a floxed-stop cassette and T2A-linked EGFP reporter gene is targeted to the stop codon of *Snap25* (Figure 1D). We then assessed fluorescent reporter expression in double Tg mice containing Cre drivers, *Nxph4*-2A-CreERT2 or *Trib2*-2A-CreERT2, crossed to either Ai14 or *Snap25*-LSL-2A-GFP reporters.

In both sets of animals crossed to Ai14, we found both neuronal and non-neuronal expression (Figure 1D, left). In *Nxph4*-2A-CreERT2;Ai14 (*Nxph4* is neurexophilin 4), we observed sparse cortical layer 6b expression but also significant expression in small, possibly glial cells. Likewise, in *Trib2*-2A-CreERT2;Ai14 (*Trib2* is tribbles homolog 2), we saw enriched expression in layer 5a cortical neurons but also strong and widespread fluorescence in vasculature. When crossed to *Snap25*-LSL-2A-GFP; however, EGFP expression in both lines was restricted to neurons, thereby increasing uniformity in the labeled cell populations (Figure 1D, right). *Snap25*-LSL-2A-GFP also showed stronger GFP fluorescence than the Rosa-CAG based Ai3-EYFP reporter (Madisen et al., 2010) (data not shown).

The pan-neuronal expression strategy can also be employed to restrict the functionality of other genetic tools to facilitate more precise observation or manipulation of cell populations. To this end, we generated a *Snap25*-2A-GCaMP6s knockin line, which expresses a calcium indicator GCaMP6s (Chen et al., 2013) pan-neuronally and independently of any driver line (Table 1). This line can be used to monitor neuronal calcium activity throughout the brain (Michael Crair and H.Z., unpublished data), while being readily combined with Cre- or another driver-dependent, cell-type-specific genetic manipulation.

Cre/tTA-Dependent Reporters Targeted to the TIGRE Locus Are More Highly Expressed than Rosa-CAG Reporters

The tetracycline (Tet)-regulated expression system has been used in mice for inducible expression of genes from the TRE (tetracycline response element, also called tetO) promoter in response to tTA (Tet-Off) or rtTA (Tet-On) activation (Garner et al., 2012; Gossen and Bujard, 1992; Mayford et al., 1996; Reijmers et al., 2007; Urlinger et al., 2000). Previous work showed that TRE-driven genes targeted (via a retrovirus) to the mouse TIGRE locus, situated on chromosome 9 between the *AB124611* (HIDE1) and *Carm1* loci, could be expressed in most tissues in the presence of tTA (Zeng et al., 2008). However,

targeting of TRE-driven transgenic cassette to the Rosa26 locus resulted in silencing or mosaicism of the transgene expression (Tasic et al., 2012). To determine whether tTA/TRE can drive high-level expression in a defined locus, we created an expression platform in the TIGRE locus by homologous recombination. To establish feasibility, we first generated a tdTomato reporter allele, whose expression depends on both activation of the TRE promoter and Cre recombinase activity (Figure 2A). To prevent undesirable interactions with nearby chromatin, we flanked the reporter allele with two copies of the chicken β -globin HS4 insulator element (Chung et al., 1997; Gaszner and Felsenfeld, 2006) on each side. We named this new reporter line Ai62(TITL-tdT), to represent the TIGRE-Insulators-TRE promoter-LSL-tdTomato components.

To compare Ai62 with Ai14, we generated a series of double and triple Tg mice containing tdTomato-, Cre-, and/or tTA-expressing alleles and evaluated native fluorescence in brain sections (Figure 2B). We used three different tTA lines with our TIGRE mice: *Camk2a*-tTA (Mayford et al., 1996), *ROSA*:LNL:tTA (Wang et al., 2008), and *ROSA26*-ZtTA (Li et al., 2010) (Table S1), to test whether their varying tTA expression levels would influence the amount of reporter produced. *Camk2a*-tTA is restricted to forebrain excitatory neurons and striatal medium spiny neurons. The other two tTA lines are both targeted to the Rosa26 locus and contain floxed-stop cassettes and are thus presumed to have Cre-dependent ubiquitous expression. For a common Cre line, we used *Nr5a1*-Cre, which drives specific expression in cortical layer 4 neurons.

We observed robust tdTomato fluorescence in cortical layer 4 cells in all types of mice (Figure 2B). However, the fluorescence levels are different: lowest in *Nr5a1*-Cre;Ai14, followed by *Nr5a1*-Cre;*ROSA*:LNL:tTA;Ai62(TITL-tdT), then by *Nr5a1*-Cre;*ROSA26*-ZtTA;Ai62(TITL-tdT), and finally by *Nr5a1*-Cre;*Camk2a*-tTA;Ai62(TITL-tdT). Fluorescence-activated cell sorting (FACS) analysis of individual neurons isolated from cortical tissue of age-matched mice confirmed this result and revealed that tdTomato fluorescence per cell in each of the Ai62 triple Tg mice was 2- to 4-fold higher than that in Ai14 reporter cells (Figure S5). We tested specificity of expression of the TIGRE reporter Ai62 by generating mice that lacked either Cre or tTA. In these mice, we did not detect any fluorescence except for very weak fluorescence detected with *Camk2a*-tTA only. These results indicate that the Ai62 TIGRE reporter is tightly regulated (Figure 2C). Interestingly, we found that inclusion of the chromatin insulators is essential for high-level reporter expression, as a TIGRE reporter allele that lacks these insulators is poorly expressed in similar triple Tg animals (Figure 2D). The above comparison indicates that the TIGRE-targeted reporter is advantageous over Rosa26-CAG reporter in more robust transgene expression and the potential for additional specificity mediated through restricted tTA expression.

The new TIGRE allele differs from the Rosa26 allele in three key aspects: genomic location, use of the TRE promoter instead of the CAG promoter, and the flanking insulators. To begin to define which of these features contribute to the higher level of transgene expression apparent in Ai62 mice, we compared the expression of a pCAG-LSL-EGFP cassette that was targeted either to the TIGRE locus (with insulators) or to the Rosa26 locus (without insulators) in mouse ES cells (Figure S6). Following

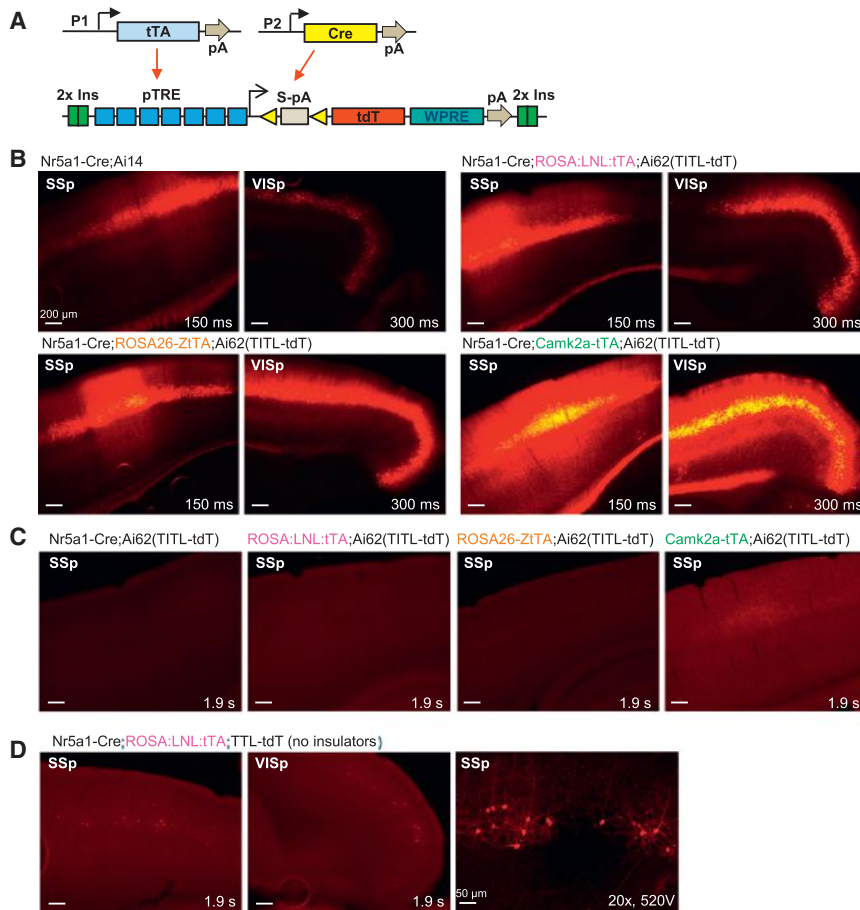


Figure 2. Cre- and tTA-Dependent Intersectional Strategy at the TIGRE Locus Produces Tightly Regulated and High-Level Expression

(A) Schematic diagram of intersectional control by Cre and tTA, driven by different promoters (P1 or P2), on a double reporter line based in the TIGRE locus, Ai62(TITL-tdT).

(B) Comparison of tdTomato fluorescence in four transgenic mouse lines carrying either Ai14 or Ai62 reporter alleles.

(C) No detectable tdTomato expression in the Cre+/tTA- control Nr5a1-Cre;Ai62(TITL-tdT) or in Cre-/tTA+ controls ROSA:LNL:tTA;Ai62(TITL-tdT) and ROSA26-ZtTA;Ai62(TITL-tdT). Very weak tdTomato fluorescence was seen in the barrel cortex and hippocampus of Camk2a-tTA;Ai62(TITL-tdT) control mice (Cre-/tTA+).

(D) Poor tdTomato expression in similar triple Tg mice with a TIGRE reporter (TTL-tdT) that lacks chromatin insulators (compare to B). Right: a higher-magnification confocal image of somatosensory cortex shows that the sparsely labeled cells are layer 4 neurons. For (B)–(D), exposure time for each epifluorescence image is shown for comparison. (See also Figures S4–S6.)

transient transfection of Cre into targeted clones to delete the stop cassettes, FACS analysis of two independent clones with each targeted locus showed comparable levels of EGFP fluorescence in all. Thus, we conclude that the difference in expression levels between Rosa26 and TIGRE mice is not simply due to the genomic location and the insulators; rather, it is more likely the result of the tTA/TRE-mediated transcriptional amplification (Iyer et al., 2001).

In addition to the transgenic reporter, we also generated AAV vectors to test the feasibility of Cre/tTA- and Cre/Fip/tTA-dependent regulation of virally encoded intersectional drivers and reporters. All reporters demonstrated the expected specificity of expression when paired with double or triple drivers, thereby further expanding the repertoire of viral tools that can be used for highly specific and versatile genetic control (Figures S4E–S4G).

New TIGRE Reporter Lines with Strong Expression of Sensors and Effectors

Based on the enhanced expression in Ai62, we proceeded to generate a series of TIGRE reporter lines carrying a variety of fluorescent sensors and optogenetic effectors (Table 1). This process was facilitated by our initial targeting strategy, which allows for subsequent rapid modification of the locus by RMCE (Figure S1B). In parallel, we generated Rosa26-based reporter

lines for some of the same genes, including calcium indicators GCaMP6f and GCaMP6s (Chen et al., 2013), voltage indicator VSFP-Butterfly 1.2 (VSFPB) (Akemann et al., 2012), glutamate sensor iGluSnFR (Marvin et al., 2013), and red-light optogenetic inhibitor Jaws (Chuong et al., 2014), for further direct comparison between the Rosa-CAG and TIGRE-TRE expression systems.

We evaluated native fluorescence expression by confocal microscopy using identical imaging parameters for pairs of age-matched reporter mice crossed to the same Cre lines (Figure 3). Although the fluorescence level varies among different proteins, in all cases the same protein was more highly expressed from the TIGRE allele than from the Rosa26 allele. In addition, GCaMP6s expression in the TIGRE allele Ai94 was not only stronger than the Rosa-CAG allele Ai96 (Figure 3B), but also stronger than the Snap25-2A-GCaMP6s line, which, like Ai96, showed no basal level fluorescence (data not shown).

We observed strong expression of reporter transgenes when combining TIGRE alleles with a variety of Cre drivers and either Camk2a-tTA or ROSA26-ZtTA (Figure 4). The EGFP reporter line (Ai82) exhibited superior cytoplasmic labeling (Figure 4A) over previous Rosa-CAG reporter Ai3 (Madisen et al., 2010) and Snap25-LSL-2A-GFP (Figure 1D). We saw strong expression and proper localization to the plasma membrane in lines expressing membrane proteins VSFPB (Ai78; Figure 4B) and Jaws (Ai79; Figure 4F). The calcium indicator YC2.60 (Ai92; Figure 4C) also displayed strong expression in both excitatory neurons and inhibitory interneurons. Likewise, cytoplasmic GCaMP6f (Ai93; Figure 4D) and GCaMP6s (Ai94; Figure 4E) were readily seen in cortical layer 4 and layer 2/3 excitatory neurons. In particular,

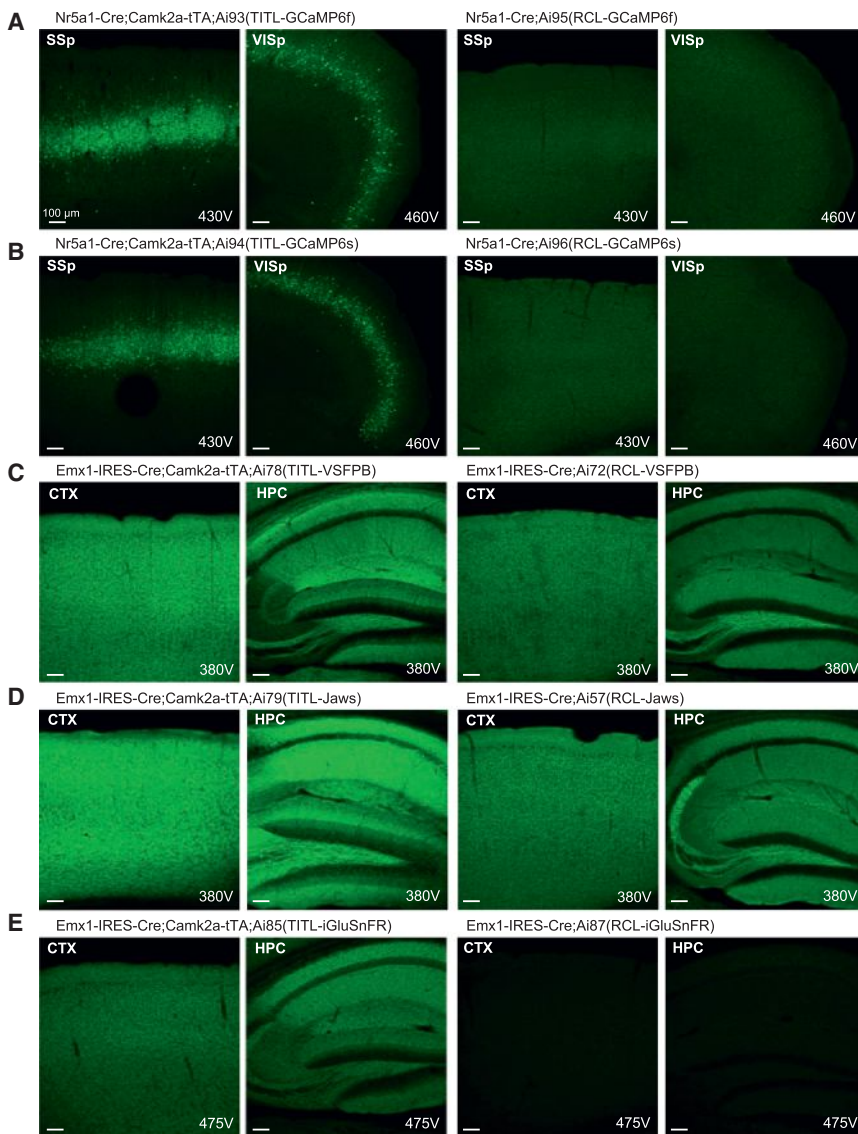


Figure 3. TIGRE Reporter Lines Have Higher-Level Transgene Expression than Rosa Reporter Lines in Multiple Direct Comparisons

Native fluorescence in each pair of lines was compared by confocal microscopy using identical imaging parameters. All images were taken under a 10× objective using 10% laser power, and the PMT gain (in voltage) is indicated on each image. Mouse names are shown above each set of images taken from the same mouse. Comparisons are shown for (A) GCaMP6f, (B) GCaMP6s, (C) VSFP-Butterfly 1.2, (D) Jaws-GFP-ER2, and (E) iGluSnFR. Ai57(RCL-Jaws) was created by crossing Ai57(RCFL-Jaws) with a Flp-deleter mouse, FLPeR, to delete the FSF cassette. (See also Figure S1.)

expressing cells either between different lines or across ages. When regulated by some more specific Cre drivers, however, we found that although general expression patterns are similar between Rosa26 and TIGRE reporters, variations can occur depending on which tTA line is used for activation, with ROSA26-ZtTA tending to drive expression in fewer cells compared to Ai14, especially in subcortical regions (Figures S7B–S7D). These findings indicate that the interplay between Cre, tTA, and reporter alleles among different cells in different mouse lines may not always be predictable, thus reporter expression needs to be carefully assessed in new lines to ensure their applicability.

Imaging of Membrane Voltage in TIGRE-VSFPB Mice

To evaluate the TIGRE lines in functional measurements of neural activity, we tested transgenic line Ai78, which delivers a highly sensitive, genetically encoded voltage indicator, the voltage-sensitive fluorescent protein VSFP-Butterfly 1.2 (Akemann et al., 2012). This indicator reveals strong voltage signals in mouse sensory cortex, both under anesthesia and in wakefulness (Akemann et al., 2012; Carandini et al., 2015; Scott et al., 2014). It exhibits voltage-dependent Förster resonance energy transfer (FRET) between a pair of green and red fluorophores: mCitrine (donor) and mKate2 (acceptor). By imaging both fluorophores and taking the ratio of their fluorescence, one can obtain a good estimate of the underlying membrane voltage.

To study the functionality of the indicator in vivo, we imaged hippocampal slices from triple Tg mice Rasgrf2-2A-dCre; Camk2a-tTA; Ai78 (TITL-VSFPB), which express the VSFP in the dentate granule cells of the hippocampus (Figure S8A). In these slices, a single shock to the perforant path evoked robust VSFP responses imaged over the dendritic field of dentate granule cells (Figure S8B). These responses could be observed both as increased acceptor signals and as decreased donor signals

long-term, sustained expression of GCaMP6f in the Ai93 brain did not result in nuclear invasion (Figure 4G). This result contrasts the common observation associated with viral infection of GCaMP in which transgene expression continues to rise and leads to unhealthy cells whose nuclei become filled with fluorescence within weeks. Thus, these stable transgenic lines may allow longer-term repeated experimentation within the same animal. Nonetheless, animals expressing these engineered, exogenous proteins should still be used cautiously and monitored for possible unexpected adverse effects.

To further compare gene expression patterns in Rosa26 and TIGRE reporter lines, we evaluated mRNA expression in multiple lines by in situ hybridization (ISH) (Figure S7). All lines examined exhibited widespread and high-density expression in cortex when under the control of Emx1-IR-Cre alone (for Rosa26 lines) or in combination with Camk2a-tTA or ROSA26-ZtTA (for TIGRE lines) (Figure S7A). There was no significant difference in the numbers of

(Akemann et al., 2012). We readily resolved VSFP transients above baseline noise in single sweeps (amplitude $\sim 3\text{--}4\times$ baseline noise, data not shown). Multiple stimulations ($5\times$) at 100 Hz increased the VSFP response amplitude. The increase was sub-linear, consistent with the temporal summation and well-known frequency-dependent depression of the synapses from medial perforant path to dentate granule cells (Petersen et al., 2013).

To address how well the indicator functions in vivo, we imaged a large portion of cerebral cortex on the left hemisphere (Figure 5A) of triple Tg mice *Rasgrf2-2A-dCre;Camk2a-tTA;Ai78* (TITL-VSFPB), where layer 2/3 pyramidal cells express the VSFP (Figure 4B). The cortex exhibited approximately uniform expression (Figure 5B, apparent variations in brightness are due largely to inhomogeneous illumination; see also Figure S8C). This wide pattern of expression allowed us to image distinct sensory regions responsive to somatosensory, visual, or auditory stimuli in head-fixed, awake mice (Figure 5C). Showing visual stimuli in different horizontal and vertical positions (Figures 5D and 5F) allowed us to obtain maps of retinotopy covering multiple visual areas (Figures 5E and 5G), including V1, LM, and AL (Wang and Burkhalter, 2007). Presenting tones of different frequencies (Figure 5H) yielded maps of tonotopy in at least two auditory areas (A1 and AAF) (Hackett et al., 2011) (Figure 5I).

To measure signal/noise (S/N) ratios of voltage signals, we drove specific regions of sensory cortex with a periodic stimulus, making their activity oscillate. We then imaged this oscillating activity and divided the amplitude of the oscillation observed during stimulation with that observed in the absence of stimuli (Benucci et al., 2007). In response to optimally placed visual stimuli, visual cortex gave S/N ratios of 11.8 in the example mouse (Figure 5J) and similar values in five other mice ($S/N = 12.1 \pm 2.7$ SEM). S/N ratios in these triple Tg mice were not statistically different ($p = 0.05$, Mann-Whitney test) from those seen in mice that expressed VSFP-Butterfly 1.2 following successful in utero electroporation ($S/N = 5.6 \pm 0.5$, $n = 3$ mice) (Carandini et al., 2015).

Visual cortex responded faithfully to the visual stimuli, following the 4 Hz neural oscillations caused by reversals in visual contrast (Figure 5J). Visual cortex, however, also responded to the onset of air puffs, whether they were delivered toward the whiskers (Figure 5K) or away from them (Figure 5L), indicating that these responses were due to the sound of the air puffs, and specifically by the first puff in the train. Such cross-modal interactions have been described previously (Iurilli et al., 2012), and in our data may be compounded by occasional blinks. In contrast, somatosensory cortex responded only to the air puffs delivered to the whiskers (Figure 5N) and not to visual stimuli or to the sounds of the air puffs (Figures 5M and 5O). Finally, auditory cortex responded approximately equally to air puffs, whether they were delivered toward or away from the whiskers (Figures 5Q and 5R) and did not respond to visual stimuli (Figure 5P). These data indicate that VSFPB expressed by the *Ai78* reporter is sufficiently sensitive to reliably and specifically record the membrane potential of neuronal populations, with fine temporal resolution.

In Vivo Recording of Calcium Signals in GCaMP6f and YCX2.60 Mice

GCaMP6 variants constitute the latest generation of genetically encoded calcium indicators (GECIs) (Chen et al., 2013) with

fundamentally improved sensitivity and performance over previous generations, e.g., GCaMP3 and GCaMP5. We conducted in vivo two-photon imaging (Andermann et al., 2011; Bonin et al., 2011) through a cranial window over visual cortex in head-fixed, running GCaMP6 reporter mice and were able to simultaneously image hundreds of neurons relatively deep in the cortex ($\sim 300\ \mu\text{m}$ below the pia surface, corresponding to visual cortical layer 4). Stimuli consisted of drifting sinusoidal gratings of five spatial frequencies (SFs), five temporal frequencies (TFs), and eight orientations (0° to 315° in 45° steps). In *Scnn1a-Tg3-Cre;Camk2a-tTA;Ai93*(TITL-GCaMP6f) triple Tg mice (Figures 6A–6C), GCaMP6f-labeled layer 4 neurons exhibited low baseline fluorescence in vivo (Figure 6A), while visual stimuli evoked responses with $\Delta F/F$ reaching 500% or higher (Figures 6A–6C). Visual responses selective for various orientations, SFs and TFs can be seen in different neurons (an example shown in Figure 6C).

Because of the low GCaMP6f fluorescence from the Rosa-CAG based *Ai95* line (Figure 3A), we investigated whether *Ai95* would still allow effective calcium imaging in comparison with *Ai93*. We measured neural activity from *Ai95* and *Ai93* under control of the pan-cortical driver *Emx1-IR-Cre*, i.e., in *Emx1-IR-Cre;Ai95*(RCL-GCaMP6f) (Figure 6D) and *Emx1-IR-Cre;Camk2a-tTA;Ai93*(TITL-GCaMP6f) (Figure 6E) mice. In both types of mice, robust fluorescent signal changes indicating neuronal activities were observed; however, signals were stronger in *Ai93* than in *Ai95* mice (compare bottom panels in Figures 6D and 6E). Additionally, the number of active neurons observable was significantly lower in *Ai95* mice compared to *Ai93* mice, especially deeper into the tissue (Figure 6F and Movies S1, S2, S3, and S4). Two-way ANOVA revealed a significant difference between genotypes, but not by depths and with no interaction (cells at $120\text{-}\mu\text{m}$ depth: *Ai95* 35 ± 5 , *Ai93* 102 ± 18 ; cells at $300\text{-}\mu\text{m}$ depth: *Ai95* 18 ± 5 , *Ai93* 129 ± 11 , $n = 3$ mice each, $p = 4.6 \times 10^{-5}$ between genotypes). In addition, activity-related signal flashes can also be easily seen in processes corresponding to dendrites and axons in *Ai93* mice (Movies S3 and S4). These results indicate that GCaMP6f expressed from both *Ai95* and *Ai93* mice yields signals responding to neuronal activities but that due to its higher expression level *Ai93* may be more capable of detecting weaker neuronal activities.

Ratiometric imaging using FRET-based calcium indicators, such as yellow cameleon (YC) indicators (Horikawa et al., 2010; Nagai et al., 2004; Yamada et al., 2011), is another approach that has the advantage of reduced sensitivity to motion artifacts and essentially permits quantification of calcium concentration levels. YCX2.60, a new version of YC indicator with an expanded dynamic range (Figure 7A), also displayed strong expression in both excitatory neurons and inhibitory interneurons (*Ai92*, Figure 4C). We performed two-photon calcium imaging in layer 2/3 of somatosensory cortex in *Rasgrf2-2A-dCre;Camk2a-tTA;Ai92*(TITL-YCX2.60) mice and observed spontaneous and sensory-evoked neuronal activity with high sensitivity (Figures 7B–7D), confirming the functionality of the *Ai92* mice.

Red Light-Mediated Optogenetic Inhibition in Jaws Mice

Jaws is the first red light drivable optogenetic inhibitor, engineered from *H. salinarum* (strain Shark) cruxhalorhodopin

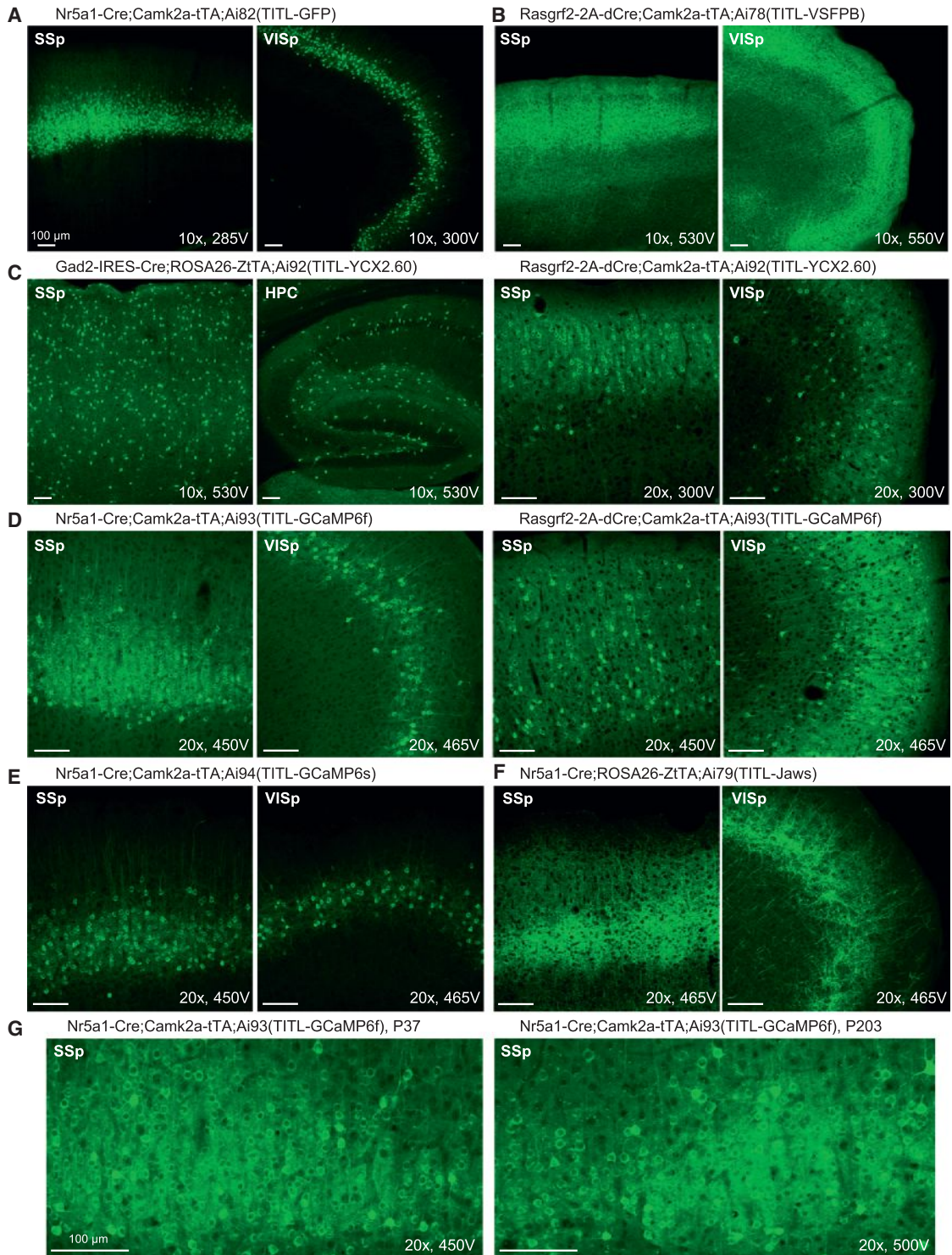


Figure 4. Strong Transgene Expression in all TIGRE-Based Reporter Lines, Driven by a Variety of Cre Lines Combined with Camk2a-tTA or ROSA26-ZiTA

Confocal images of native fluorescence are shown. All images were taken under a 10x or 20x objective using 10% laser power, and the PMT gain (in voltage) is indicated on each image for comparison.

(A) Very bright cytoplasmic GFP labeling of cortical layer 4 neurons in Nr5a1-Cre;Camk2a-tTA;Ai82(TITL-GFP) mouse.

(B) Bright membrane VSFP-Butterfly 1.2 labeling of cortical layer 2/3 neurons in Rasgrf2-2A-dCre;Camk2a-tTA;Ai78(TITL-VSFPB) mouse.

(legend continued on next page)

(Chuong et al., 2014). Compared with other photo-activated inhibitors such as eNpHR3.0, Arch, or ArchT, Jaws responds robustly to red light with high sensitivity, large photocurrent, and fast kinetics and thus enables better tissue penetrance and more effective optogenetic silencing of large volumes (Chuong et al., 2014). We compared the performance of a modified trafficking variant of Jaws, Jaws-GFP-ER2, expressed from the Rosa-CAG allele, i.e., *Emx1-IR-Cre;Ai57(RCL-Jaws)* mice (simplified as Ai57), and the TIGRE allele, i.e., *Emx1-IR-Cre;Camk2a-tTA;Ai79(TITL-Jaws)* mice (simplified as Ai79), via slice and in vivo electrophysiology, using virally expressed Jaws and Arch-expressing mice Ai35 as references (Chuong et al., 2014; Madisen et al., 2012) (Figure 8).

In brain slices, Jaws-expressing cells showed normal membrane properties ($n = 13$ cells in Ai57 mice, $n = 17$ in Ai79, $n = 12$ in Ai35, Figure S9A). Red light illumination (632 nm) induced strong hyperpolarizing currents in Jaws-expressing neurons in Ai79 mice and effectively blocked depolarization-induced spiking, whereas the light effect was small to moderate in Ai57 mice (Figures 8A–8C). Photocurrents were comparable between Ai79 and virally expressed Jaws at all irradiance levels tested but were significantly smaller in Ai57 cells (Figures 8D and 8E), consistent with the observation of stronger native fluorescence in Ai79 (Figure 3D). We also noticed that the Jaws-GFP-ER2 in Ai57 displayed lower protein fluorescence than the Arch-GFP-ER2 in the similar Rosa-CAG allele Ai35 (Figure S9C), possibly due to different protein properties (see Discussion below), but the low photocurrents generated were similar between the two (Figures 8D, 8E, and S9B).

Next, we assessed Jaws performance in vivo. We conducted extracellular recordings in the primary visual cortex of awake, head-fixed mice using glass pipettes and with a 200- μm optical fiber in place (Chuong et al., 2014). Due to the low photocurrents of Ai35 and Ai57 in slices, only Ai79 was tested in vivo. Ai79 showed strong red light (637 nm) induced suppression of spontaneous neuronal firing (Figures 8F and 8G; $n = 23$ units from 2 mice, $n = 3$ units showed no change). Light delivery through the fiber tip inhibited neuronal firing in a light intensity-dependent manner in these mice, comparable to the performance of virally expressed Jaws (Figure 8H).

DISCUSSION

We sought to develop transgenic strategies for intersectional control and to compare performance of these strategies under native conditions in the mouse brain. In addition to striving for high-level and highly specific expression of genetic tools, we aimed to generate standardized expression platforms, in a few defined genomic loci, that would allow rapid modification for

future improvements and applications. Such efforts are more laborious and time consuming than other in vivo approaches, such as random transgenesis or viral infection, but they can provide more definitive evaluations and more consistent platforms for incorporating additional genetic tools and expansion into other cell types.

For example, we observed significant, heritable variation in protein expression among the various sensors and effectors (Figures 3 and 4), despite their having the same configuration within the TIGRE or Rosa26 alleles. We think this variation is most likely due to intrinsic protein properties, as they originate from diverse non-mammalian species. Protein engineering, such as codon optimization and addition of membrane-targeting tags (Gradinaru et al., 2010), is essential for optimizing expression in the mammalian brain. However, since many of the proteins we worked with had already undergone such engineering, the observed variation suggests that intrinsic differences still exist. Therefore expression in mice as a stably integrated transgene is unpredictable and always needs to be examined experimentally in vivo. Our data indicate that while the Rosa-CAG approach could work well for some proteins with exceptional expressibility and/or functionality, e.g., in Ai14-tdTomato, Ai32-ChR2(H134R) (Madisen et al., 2012) as well as Ai95-GCaMP6f mice, our new TIGRE approach, with its much enhanced gene expression capability via tTA-assisted transcriptional amplification, will allow a wider spectrum of genetic tools to achieve functional levels and/or to perform better in stable transgenic settings. This amplification proves to be significant even in comparison with expression from transgenes targeting one of the brain's most highly expressed endogenous genes, *Snap25*.

On the other hand, in our effort to create more cell-type-specific tTA driver lines, we found that several knockin tTA driver lines we made exhibit no or low-level tTA-induced reporter expression (Table S2). This may be because the Tet-regulatory system is prone to epigenetic silencing (Tasic et al., 2012; Zhu et al., 2007). Further investigation and optimization will be needed to expand the repertoire of tTA drivers to take full advantage of the potential of TIGRE-based reporters. Nevertheless, our work validates the currently available Camk2a-tTA and ROSA26-ZtTA lines as effective components of a TIGRE-based approach in driving robust transgene expression.

We have established the TIGRE locus as a new permissive docking site for insertion of exogenous promoters and transgenes. This is significant since TRE-driven transgene cassettes are often silenced when inserted into the mouse genome randomly or even targeted to specific loci such as Rosa26 (B.T., L.M., and H.Z., unpublished data; see also Li et al., 2010; Tasic et al., 2012; Zhu et al., 2007). Our expression studies also showed that both TRE and CAG promoters worked well in

(C) Very bright cytoplasmic YCX2.60 labeling of interneurons in *Gad2-IR-Cre;ROSA26-ZtTA;Ai92(TITL-YCX2.60)* mouse and of cortical layer 2/3 neurons in *Rasgrf2-2A-dCre;Camk2a-tTA;Ai92(TITL-YCX2.60)* mouse.

(D) Bright cytoplasmic GCaMP6f labeling of cortical layer 4 neurons in *Nr5a1-Cre;Camk2a-tTA;Ai93(TITL-GCaMP6f)* mouse and of cortical layer 2/3 neurons in *Rasgrf2-2A-dCre;Camk2a-tTA;Ai93(TITL-GCaMP6f)* mouse.

(E) Bright cytoplasmic GCaMP6s labeling of cortical layer 4 neurons in *Nr5a1-Cre;Camk2a-tTA;Ai94(TITL-GCaMP6s)* mouse.

(F) Bright membrane Jaws-GFP-ER2 labeling of cortical layer 4 neurons in *Nr5a1-Cre;ROSA26-ZtTA;Ai79(TITL-Jaws)* mouse.

(G) Comparison of young and old Ai93 mice shows no or little nuclear invasion of transgene proteins with time. The ages (postnatal days) at which the mice were sacrificed are shown. (See also Figure S7.)

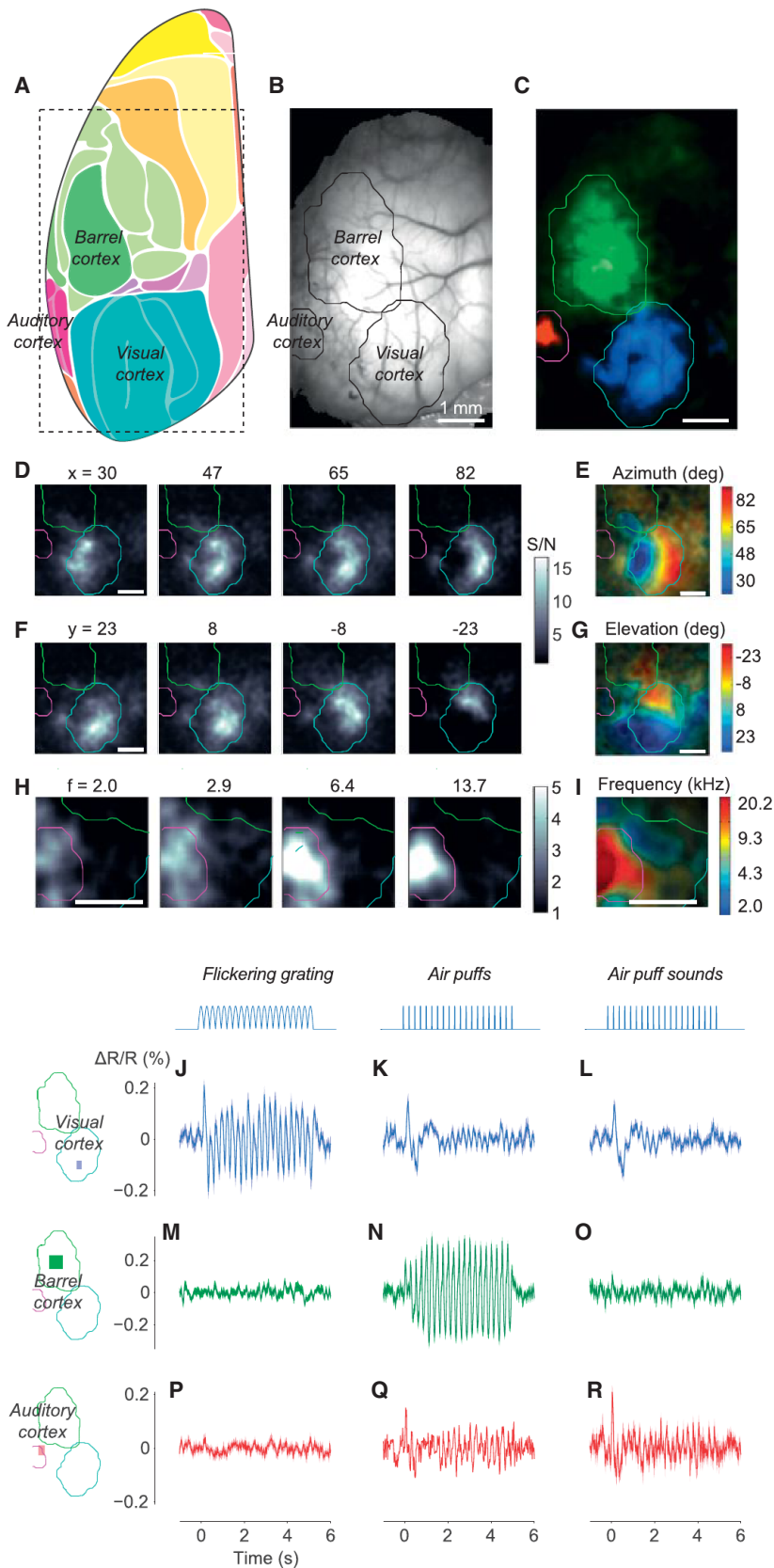


Figure 5. Wide-Field Imaging of Sensory Cortices of Ai78 Mice Expressing VSFP-Butterfly 1.2 in Cortical Layer 2/3 Excitatory Neurons

(A) Diagram showing mouse cortical regions observed from the top of the brain. Adopted and modified from Kirkcaldie (2012). The rectangle shows the approximate extent of our imaging area, which was angled at 30° relative to the vertical.

(B) Fluorescence of mCitrine imaged through the thinned skull.

(C) Maps of VSFP signals (acceptor-donor ratio) to auditory (red), somatosensory (green), and visual (blue) stimuli. Sensory regions are mapped as 4 Hz amplitude in response to 4 Hz train of tones, 4 Hz train of air puffs directed to whole whisker field, and 2 Hz flickering visual stimulus. Response amplitude was divided for each modality by amplitude measured in the absence of stimulation. The three maps came from experiments performed on different days, and the resulting maps were aligned based on the blood vessel pattern. Overlaid contour lines show the outlines of visual cortex, barrel cortex, and auditory cortex.

(D) Amplitude maps for 4 Hz responses to bars reversing in contrast at 2 Hz, presented at different horizontal positions (azimuths).

(E) The resulting maps of azimuth preference (retinotopy).

(F and G) Same as (D) and (E) for stimulus elevation (vertical position).

(H) Amplitude maps for 6 Hz responses to tones in 6 Hz trains, for different tone frequencies.

(I) The resulting maps of tone frequency preference (tonotopy).

(J–R) Unisensory and multisensory signals in visual cortex (J–L), barrel cortex (M–O), and auditory cortex (P–R). Stimuli were contrast-reversing visual gratings (J, M, and P), air puffs delivered to the whiskers (K, N, and Q), and (sham) air puffs delivered away from the whiskers to replicate the sound but not the somatosensory stimulation (L, O, and R). $\Delta R/R$ is calculated after normalization using data during the prestimulus period and high-pass filtering above 0.5 Hz. (See also Figure S8.)

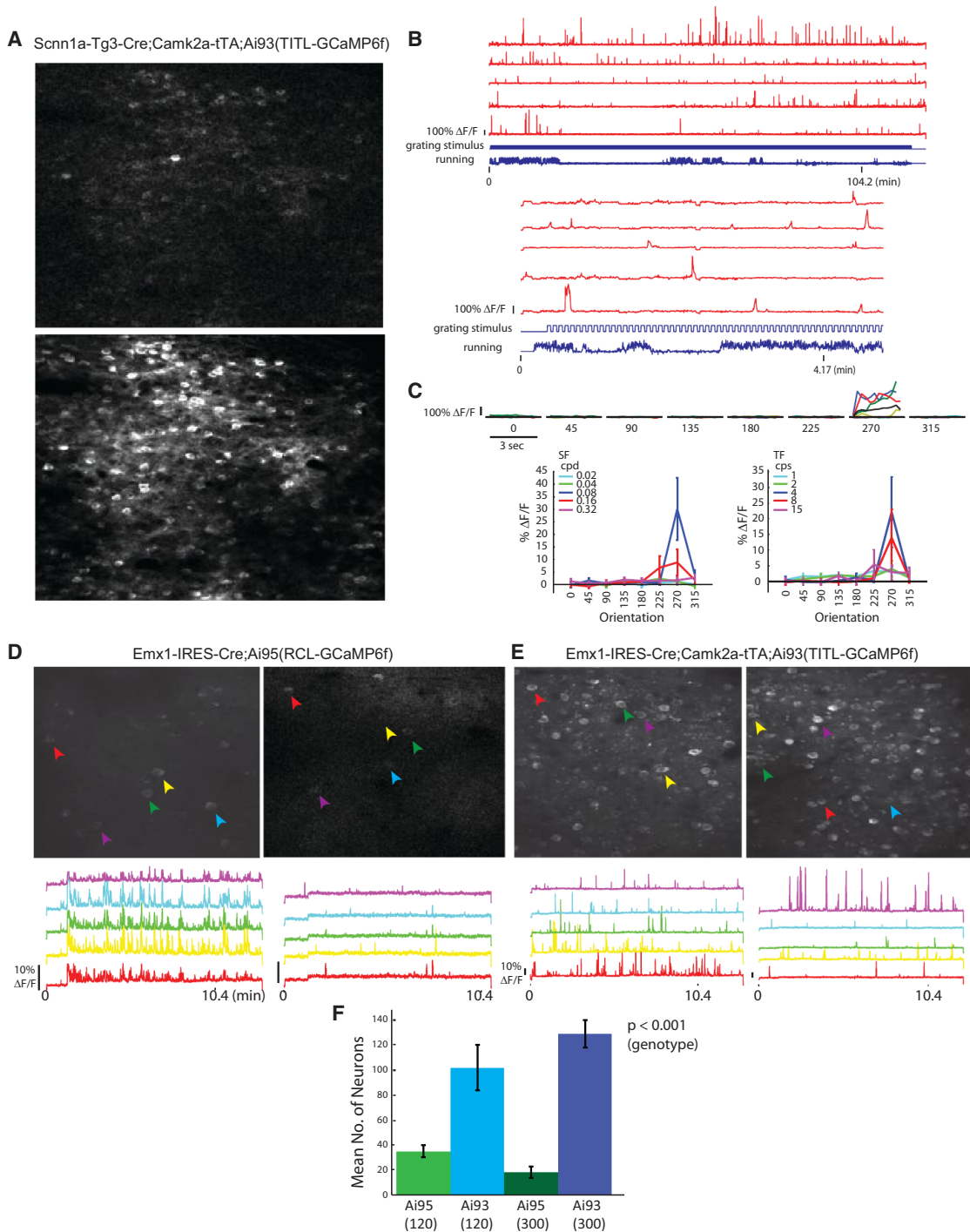


Figure 6. In Vivo Two-Photon Imaging of Calcium Signals in GCaMP6f Reporter Mice

(A–C) Calcium imaging in cortical layer 4 of Scnn1a-Tg3-Cre;Camk2a-tTA;Ai93(TITL-GCaMP6f) mice. (A) Images of baseline fluorescence with a single active cell (top) and Z projection (time series) of the same field of view showing all active cells (bottom). (B) Raw traces of five example neurons imaged during stimulus presentation. Top: the duration of the entire experiment. Bottom: the same five cells over a shorter timescale. The bottom cell trace is the cell analyzed for tuning properties shown in (C). (C) Visually evoked responses of an example cell. Top: peri-stimulus-time-histogram (PSTH) of the cell’s response at each stimulus orientation at optimal SF and TF. Colored lines represent individual trials and the black line represents the mean. Bottom left: mean response at each SF (averaged over all TFs) as a function of orientation. Bottom right: mean response at each TF (averaged over all SFs) as a function of orientation.

(legend continued on next page)

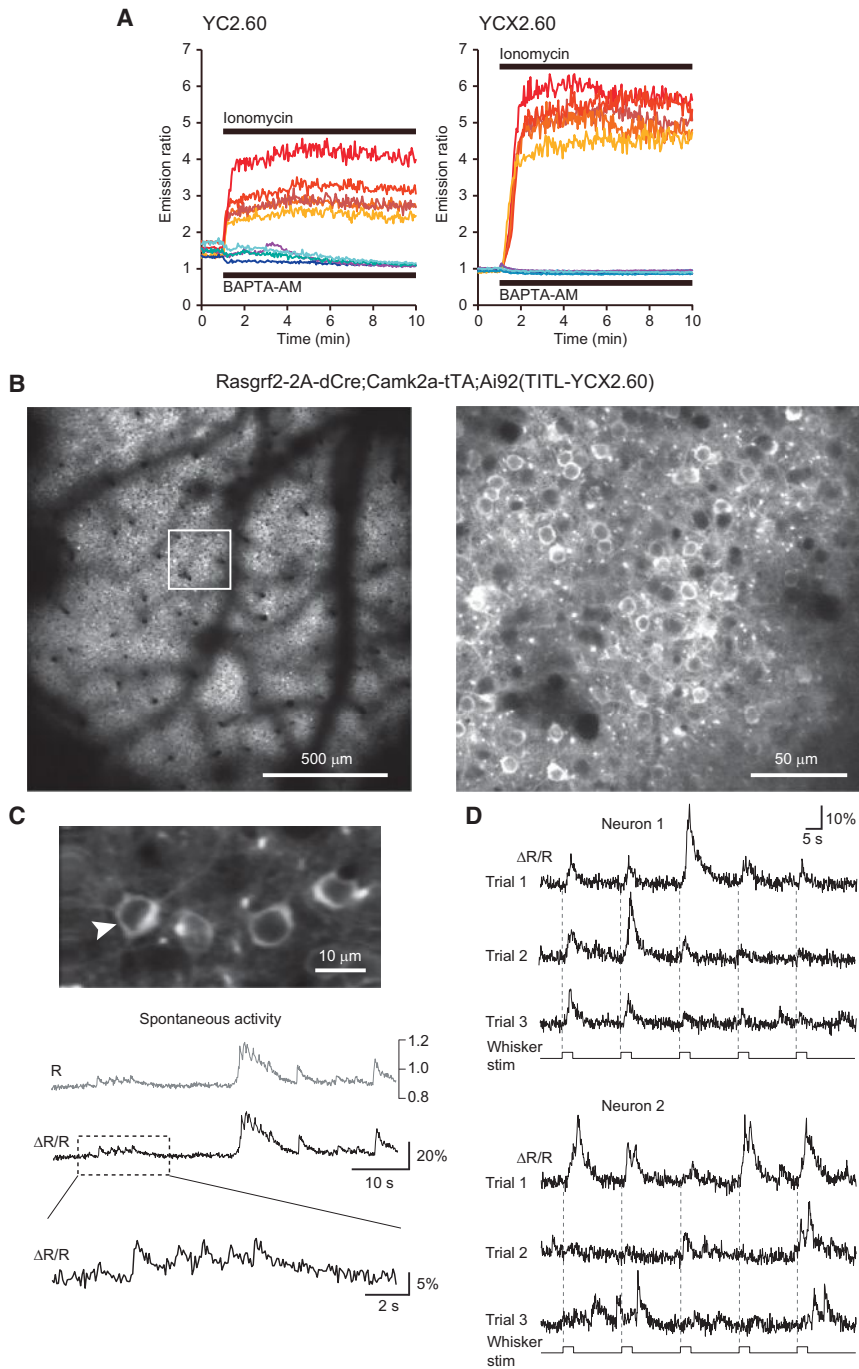


Figure 7. Calcium Measurements with Yellow Cameleon YCX2.60

(A) Responses in individual HeLa cells to ionomycin applied to saturate yellow cameleons (YCs) with calcium ($n = 5$) and to BAPTA-AM applied to deplete YCs of calcium ($n = 4$). The dynamic range of YCX2.60 is twice as large as that of YC2.60 ($R_{max}/R_{min} = 6.20$ versus 3.17). The apparent dissociation constants of YC2.60 and YCX2.60 for calcium were calculated as 80 nM and 220 nM, respectively (Y.N. and A.M., unpublished data).

(B–D) In vivo two-photon imaging of calcium signals in Rasgrf2-2A-dCre;Camk2a-tTA;Ai92(TITL-YCX2.60) mice. (B) Visualization of the uniform expression in layer 2/3 at 190- μ m depth within the cranial window 1 week after TMP induction (field of view size 1.7 \times 1.7 mm). Note the shadows from surface blood vessels. The image on the right is a magnified view of the boxed area in the left image, showing neuronal somata labeled with YCX2.60. (C) Representative 60 s example of spontaneous activity in the neuron marked with an arrow. Raw, unfiltered calcium transients are expressed once as YFP:CFP ratio R, which in principle can be calibrated in terms of absolute calcium concentration or as relative percentage change of the ratio R ($\Delta R/R$). The expanded view of the trace segment in the box highlights fast calcium transients presumably evoked by few or single action potentials. (D) Evoked activity in two example neurons following whisker stimulation. The principal whisker was repeatedly stimulated at 10 Hz for 2 s (onsets indicated with dashed lines). YCX2.60 $\Delta R/R$ traces are shown for two example layer 2/3 neuron for three trials, each comprising five stimulation periods. Note responses at stimulus onset, during stimulation, and at stimulus offset as well as spontaneous activity in between. Large calcium transients probably correspond to bursts of action potentials whereas small-amplitude transients may reflect occurrence of only few or single action potentials.

of enhancer elements or promoter variants. To facilitate repeated use of these expression platforms, we have built a cassette exchange mechanism into each, based on reconstitution of a split-hygromycin selectable marker (Figure S1). By doing so, the swapping of either alternative drivers in targeted lines or

TIGRE, suggesting that this locus can also serve as a docking site for insertion of other promoters and regulatory sequences. This could be particularly useful, for example, for the screening

new genetic tools in the TIGRE allele becomes a rapid and straightforward process, thereby extending the utility of these systems.

(D–F) Comparison of Emx1-IR-Cre;Ai95(RCL-GCaMP6f) and Emx1-IR-Cre;Camk2a-tTA;Ai93(TITL-GCaMP6f) mice at two imaging depths, 120 μ m and 300 μ m below the pia, corresponding to cortical layers 2/3 and 4, respectively. (D) Z projection of two-photon acquisition frames 120 μ m (left) and 300 μ m (right) below the pia of Ai95 mice. Raw traces of neural activity during \sim 10 min of visual stimulus presentation for five representative cells are shown below each image panel. (E) Same as (D) for Ai93 mice. (F) Mean number of cells from which activity could be observed during a 10 min imaging period at 120 μ m and 300 μ m depths within a 250 \times 150 μ m imaging area. All values represent mean \pm SEM (See also Movies S1, S2, S3, and S4).

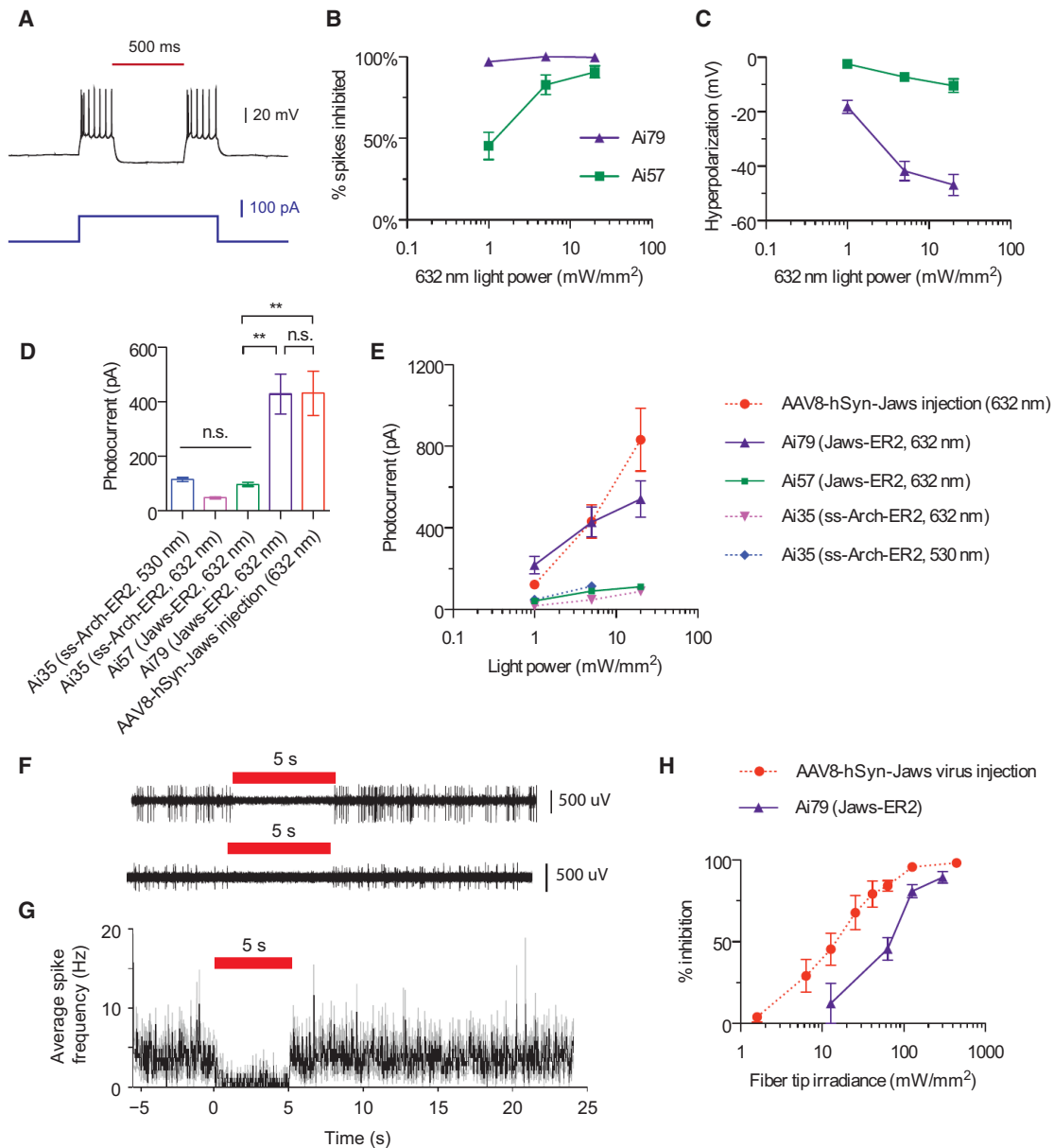


Figure 8. Optogenetic Inhibition of Neural Activity in Reporter Lines Expressing Jaws

(A) Representative current-clamp recording of a Jaws-expressing neuron from Ai79 undergoing optically evoked (632 nm, 5 mW/mm²) hyperpolarization in an acute cortical slice.

(B) Comparison of red light-induced inhibition of electrically evoked spiking in slices from Ai79 and Ai57 mice. Spiking was induced by a current injection of 1.5× the rheobase.

(C) Comparison of red light-induced hyperpolarization in slices from Ai79 and Ai57 mice.

(D) Comparison of red or green light (632 or 530 nm, 5 mW/mm²)-induced photocurrents in slices from Ai79, Ai57, Ai35, and AAV-Jaws virus-injected mice.

(E) Comparison of light-induced photocurrents in slices from Ai79, Ai57, Ai35, and AAV-Jaws virus-injected mice across different light intensities for red or green light.

(F and G) Representative extracellular recordings (F) in awake Ai79 mice demonstrate the in vivo inhibition of spontaneous firing activities (G) of Jaws-expressing neurons.

(H) Comparison of in vivo inhibition of spontaneous firing activities over a range of red light intensities between Ai79 and AAV-Jaws-injected mice. All values represent mean ± SEM. **p < 0.01; n.s., not significant. (See also Figure S9.)

Besides the intersectional strategies already shown here, we also tested additional recombinases B3 and KD and the Gal4/UAS transcriptional activation system but obtained undesirable

outcomes (see Table S2). However, there are still other approaches with unique merits that we have not tested, such as split-Cre (Casanova et al., 2003; Hirrlinger et al., 2009; Wang

et al., 2012) or the creation of Flp-, Dre-, or tTA-dependent Cre driver lines, which could be applied to the many existing floxed alleles. Developing these alternative intersectional approaches will further expand our capability in cell-type-specific control.

The validated transgenic strategies and new transgenic lines reported here will probably benefit a variety of applications. More Flpo, Dre, and tTA driver lines can be generated that, in conjunction with Cre driver lines, enable the targeting to highly specific cell types and populations. The dual-driver approaches allow for not only an “A and B” type of intersection, but also for other types of simultaneous differential control, such as “A or B” or “A not B” (Fenno et al., 2014; Huang and Zeng, 2013), when appropriate double reporter mice or viruses are developed. Even the low-level promiscuous recombination of Cre on Rox sites can be used to create extremely sparse labeling of individual cells by combining Rox-stop-Rox reporters with Cre drivers. An issue with using intersectional transgenic strategies is the laborious breeding involved in generating triple Tg mice. We found that both Rosa26 and TIGRE homozygous Tg mice are fertile, and because all these are knockin alleles, PCR-genotyping methods can be designed to distinguish wild-type, heterozygous, and homozygous alleles. So using homozygous alleles and/or double Tg × double Tg breeding schemes will increase breeding efficiency.

The collection of reporter lines should facilitate various ways of observing and manipulating cell-type functions, having advantage over viral expressions in large-area, uniform, and long-term monitoring and manipulation of neuronal activities. In particular, stable transgenic expression of GCaMP6f and GCaMP6s (Ai93-96 and Snap25-2A-GCaMP6s), YCX2.60 (Ai92), VSFPB (Ai78), and iGluSnFR (Ai85; Tim Murphy and H.Z., unpublished data) provides various options of imaging neuronal activity with increased sensitivity, complementing other recently reported transgenic lines PC::G5-tdT (Gee et al., 2014) and Thy1-GCaMP6 (Dana et al., 2014). These examples indicate that the TIGRE platform is suitable for expressing existing or new genetic tools and thus expanding the arsenal of genetic approaches to further our understanding of diverse biological systems.

EXPERIMENTAL PROCEDURES

All experimental procedures related to the use of mice were conducted according to NIH guidelines, the UK Animals Scientific Procedures Act (1986), the guidelines of the Veterinary Office of Switzerland, and the New Zealand Animal Welfare Act (1999). Experiments performed at the Allen Institute were approved by the Institutional Animal Care and Use Committee (IACUC) of the Allen Institute for Brain Science. Experiments performed at University College London were under personal and project licenses released by the Home Office following appropriate ethics review. Experiments performed at the University of Zurich were approved by the Cantonal Veterinary Office in Zurich. Additional details of experimental procedures are available in Supplemental Experimental Procedures online.

Transgenic Mice Generation and Expression Characterization

Transgenic mice were generated by inserting transgene cassettes into endogenous genomic loci via homologous recombination as previously described (Madisen et al., 2010) and, in many cases, subsequent Flp-mediated RMCE. Expression of the reporter genes was assessed by epifluorescence or laser-scanning confocal imaging of native fluorescence (without antibody staining),

by FACS of single-cell suspensions or by ISH. All ISH data can be found at the Transgenic Characterization database (<http://connectivity.brain-map.org/transgenic/search/basic>).

In Vitro and In Vivo Wide-Field Voltage Imaging

Hippocampal slice recording was done at room temperature. The dentate gyrus was imaged with a cooled CCD camera. In vivo imaging was done through thinned skull of head-fixed animal allowed to move freely on a spherical treadmill. Stimuli were trains of visual, somatosensory, or auditory stimuli, delivered to elicit periodic responses in cortex.

In Vivo Two-Photon Calcium Imaging

In visual cortex imaging experiments, the animal was allowed to move freely on a rotatable disc while head fixed. Visual stimuli consisted of drifting sinusoidal gratings with varying spatial frequencies, temporal frequencies, and orientations. In somatosensory cortex imaging experiments, mice were anesthetized and neuronal responses were measured in layer 2/3 upon mechanical stimulation of the identified principal whisker. Image data were acquired using custom-built two-photon microscopes with resonant and galvanometric scanners.

In Vitro and In Vivo Electrophysiology of Optogenetic Silencing

In vivo extracellular recordings were conducted in the visual cortex of awake, head-fixed mice using a glass microelectrode attached with a 200- μ m diameter optical fiber that is coupled to a 637-nm laser. Whole-cell patch-clamp recording in slice was carried out at 32°C with added Picrotoxin and kynurenic acid in ACSF to block GABAergic and glutamatergic synaptic transmission. Light pulses were delivered through the objective lens using a 530-nm LED or a 625-nm LED plus a 632 \pm 11 nm filter.

ACCESSION NUMBERS

The DDBJ/EMBL/GenBank accession number for the sequence of YCX2.60 reported in this paper is LC025957.

SUPPLEMENTAL INFORMATION

Supplemental Information includes Supplemental Experimental Procedures, nine figures, two tables, and four movies and can be found with this article online at <http://dx.doi.org/10.1016/j.neuron.2015.02.022>.

AUTHOR CONTRIBUTIONS

L.M. and H.Z. designed the transgenic strategies. L.M., H.G., and M.M. generated all new transgenic mouse lines except Nr4a2-SA-IR-Dre and some of the AAVs. C.M. and A.N. generated the Nr4a2-SA-IR-Dre mouse line. D.S., A.B., T.K., and M.C. conducted in vivo wide-field voltage imaging on Ai78 mice. R.M.E. conducted slice physiology on Ai78 mice. A.R.G., A.C., and R.C.R. conducted in vivo two-photon calcium imaging on Ai93 and Ai95 mice. A.v.d.B., L.E., and F.H. conducted in vivo two-photon calcium imaging on Ai92 mice. N.C.K., A.S.C., L.L., and E.S.B. conducted optogenetic silencing studies on Ai35, Ai57, and Ai79 mice. Y.N. and A.M. developed YCX2.60. B.T. and T.N.N. conducted FACS analysis and made some of the AAVs. S.M.S. provided project management for this work. L.M., A.R.G., D.S., A.S.C., L.L., R.M.E., T.K., M.C., and H.Z. were main contributors to data analysis and manuscript writing, with input from other co-authors.

ACKNOWLEDGMENTS

We are grateful to the Research and Development, Structured Science and Technology teams at the Allen Institute for their technical support in stereotaxic injections, mouse colony management, and ISH gene expression characterization. We thank Robert Hunter for coordinating transgenic mice production and Charu Reddy and Wolfgang Omlor for technical support. We thank Douglas Kim for providing the GCaMP6f and GCaMP6s constructs, Loren Looger for providing the iGluSnFR construct, Gary Felsenfeld for providing the chicken β -globin HS4 insulator element construct, Philippe

Soriano for providing the FLPo construct via Addgene, and Anton Maximov for providing the DHFR-Cre construct. This work was funded by the Allen Institute for Brain Science, NIH grant MH085500 to H.Z. and A.N., NIH grant DA028298 to H.Z., and Wellcome Trust grant 095669 to M.C. M.C. holds the GlaxoSmithKline / Fight for Sight Chair in Visual Neuroscience. The authors wish to thank the Allen Institute founders, Paul G. Allen and Jody Allen, for their vision, encouragement, and support.

Received: August 25, 2014

Revised: January 8, 2015

Accepted: February 11, 2015

Published: March 4, 2015

REFERENCES

- Ackman, J.B., Burbridge, T.J., and Crair, M.C. (2012). Retinal waves coordinate patterned activity throughout the developing visual system. *Nature* **490**, 219–225.
- Akemann, W., Mutoh, H., Perron, A., Park, Y.K., Iwamoto, Y., and Knöpfel, T. (2012). Imaging neural circuit dynamics with a voltage-sensitive fluorescent protein. *J. Neurophysiol.* **108**, 2323–2337.
- Anastasiadis, K., Fu, J., Patsch, C., Hu, S., Weidlich, S., Duerschke, K., Buchholz, F., Edenhofer, F., and Stewart, A.F. (2009). Dre recombinase, like Cre, is a highly efficient site-specific recombinase in *E. coli*, mammalian cells and mice. *Dis. Model. Mech.* **2**, 508–515.
- Andermann, M.L., Kerlin, A.M., Roumis, D.K., Glickfeld, L.L., and Reid, R.C. (2011). Functional specialization of mouse higher visual cortical areas. *Neuron* **72**, 1025–1039.
- Arenkiel, B.R., Peca, J., Davison, I.G., Feliciano, C., Deisseroth, K., Augustine, G.J., Ehlers, M.D., and Feng, G. (2007). In vivo light-induced activation of neural circuitry in transgenic mice expressing channelrhodopsin-2. *Neuron* **54**, 205–218.
- Benucci, A., Frazor, R.A., and Carandini, M. (2007). Standing waves and traveling waves distinguish two circuits in visual cortex. *Neuron* **55**, 103–117.
- Bonin, V., Histed, M.H., Yurgenson, S., and Reid, R.C. (2011). Local diversity and fine-scale organization of receptive fields in mouse visual cortex. *J. Neurosci.* **31**, 18506–18521.
- Buchholz, F., Angrand, P.O., and Stewart, A.F. (1998). Improved properties of FLP recombinase evolved by cycling mutagenesis. *Nat. Biotechnol.* **16**, 657–662.
- Carandini, M., Shimaoka, D., Rossi, L.F., Sato, T.K., Benucci, A., and Knöpfel, T. (2015). Imaging the awake visual cortex with a genetically encoded voltage indicator. *J. Neurosci.* **35**, 53–63.
- Casanova, E., Lemberger, T., Fehsenfeld, S., Mantamadiotis, T., and Schütz, G. (2003). Alpha complementation in the Cre recombinase enzyme. *Genesis* **37**, 25–29.
- Chen, T.W., Wardill, T.J., Sun, Y., Pulver, S.R., Renninger, S.L., Baohan, A., Schreiter, E.R., Kerr, R.A., Orger, M.B., Jayaraman, V., et al. (2013). Ultrasensitive fluorescent proteins for imaging neuronal activity. *Nature* **499**, 295–300.
- Chung, J.H., Bell, A.C., and Felsenfeld, G. (1997). Characterization of the chicken beta-globin insulator. *Proc. Natl. Acad. Sci. USA* **94**, 575–580.
- Chuong, A.S., Miri, M.L., Busskamp, V., Matthews, G.A., Acker, L.C., Sørensen, A.T., Young, A., Klapoetke, N.C., Henninger, M.A., Kodandaramaiah, S.B., et al. (2014). Noninvasive optical inhibition with a red-shifted microbial rhodopsin. *Nat. Neurosci.* **17**, 1123–1129.
- Dana, H., Chen, T.W., Hu, A., Shields, B.C., Guo, C., Looger, L.L., Kim, D.S., and Svoboda, K. (2014). Thy1-GCaMP6 transgenic mice for neuronal population imaging in vivo. *PLoS ONE* **9**, e108697.
- Dymecki, S.M., and Kim, J.C. (2007). Molecular neuroanatomy's "Three Gs": a primer. *Neuron* **54**, 17–34.
- Dymecki, S.M., Ray, R.S., and Kim, J.C. (2010). Mapping cell fate and function using recombinase-based intersectional strategies. *Methods Enzymol.* **477**, 183–213.
- Feng, G., Mellor, R.H., Bernstein, M., Keller-Peck, C., Nguyen, Q.T., Wallace, M., Nerbonne, J.M., Lichtman, J.W., and Sanes, J.R. (2000). Imaging neuronal subsets in transgenic mice expressing multiple spectral variants of GFP. *Neuron* **28**, 41–51.
- Fenko, L., Yizhar, O., and Deisseroth, K. (2011). The development and application of optogenetics. *Annu. Rev. Neurosci.* **34**, 389–412.
- Fenko, L.E., Mattis, J., Ramakrishnan, C., Hyun, M., Lee, S.Y., He, M., Tucciarone, J., Selimbeyoglu, A., Berndt, A., Grosenick, L., et al. (2014). Targeting cells with single vectors using multiple-feature Boolean logic. *Nat. Methods* **11**, 763–772.
- Garner, A.R., Rowland, D.C., Hwang, S.Y., Baumgaertel, K., Roth, B.L., Kentros, C., and Mayford, M. (2012). Generation of a synthetic memory trace. *Science* **335**, 1513–1516.
- Gaszner, M., and Felsenfeld, G. (2006). Insulators: exploiting transcriptional and epigenetic mechanisms. *Nat. Rev. Genet.* **7**, 703–713.
- Gee, J.M., Smith, N.A., Fernandez, F.R., Economo, M.N., Brunert, D., Rothermel, M., Morris, S.C., Talbot, A., Palumbos, S., Ichida, J.M., et al. (2014). Imaging activity in neurons and glia with a Polr2a-based and cre-dependent GCaMP5G-IR-tdTomato reporter mouse. *Neuron* **83**, 1058–1072.
- Gerfen, C.R., Paletzki, R., and Heintz, N. (2013). GENSAT BAC cre-recombinase driver lines to study the functional organization of cerebral cortical and basal ganglia circuits. *Neuron* **80**, 1368–1383.
- Gong, S., Doughty, M., Harbaugh, C.R., Cummins, A., Hatten, M.E., Heintz, N., and Gerfen, C.R. (2007). Targeting Cre recombinase to specific neuron populations with bacterial artificial chromosome constructs. *J. Neurosci.* **27**, 9817–9823.
- Gossen, M., and Bujard, H. (1992). Tight control of gene expression in mammalian cells by tetracycline-responsive promoters. *Proc. Natl. Acad. Sci. USA* **89**, 5547–5551.
- Gradinaru, V., Zhang, F., Ramakrishnan, C., Mattis, J., Prakash, R., Diester, I., Goshen, I., Thompson, K.R., and Deisseroth, K. (2010). Molecular and cellular approaches for diversifying and extending optogenetics. *Cell* **141**, 154–165.
- Hackett, T.A., Barkat, T.R., O'Brien, B.M., Hensch, T.K., and Polley, D.B. (2011). Linking topography to tonotopy in the mouse auditory thalamocortical circuit. *J. Neurosci.* **31**, 2983–2995.
- Haddad, R., Lanjuin, A., Madisen, L., Zeng, H., Murthy, V.N., and Uchida, N. (2013). Olfactory cortical neurons read out a relative time code in the olfactory bulb. *Nat. Neurosci.* **16**, 949–957.
- Harris, J.A., Hirokawa, K.E., Sorensen, S.A., Gu, H., Mills, M., Ng, L.L., Bohn, P., Mortrud, M., Ouellette, B., Kidney, J., et al. (2014). Anatomical characterization of Cre driver mice for neural circuit mapping and manipulation. *Front. Neural Circuits* **8**, 76.
- Hirrlinger, J., Scheller, A., Hirrlinger, P.G., Kellert, B., Tang, W., Wehr, M.C., Goebbels, S., Reichenbach, A., Sprengel, R., Rossner, M.J., and Kirchhoff, F. (2009). Split-cre complementation indicates coincident activity of different genes in vivo. *PLoS ONE* **4**, e4286.
- Horikawa, K., Yamada, Y., Matsuda, T., Kobayashi, K., Hashimoto, M., Matsuura, T., Miyawaki, A., Michikawa, T., Mikoshiba, K., and Nagai, T. (2010). Spontaneous network activity visualized by ultrasensitive Ca(2+) indicators, yellow Cameleon-Nano. *Nat. Methods* **7**, 729–732.
- Huang, Z.J., and Zeng, H. (2013). Genetic approaches to neural circuits in the mouse. *Annu. Rev. Neurosci.* **36**, 183–215.
- Issa, J.B., Haeffele, B.D., Agarwal, A., Bergles, D.E., Young, E.D., and Yue, D.T. (2014). Multiscale optical Ca2+ imaging of tonal organization in mouse auditory cortex. *Neuron* **83**, 944–959.
- Iurilli, G., Ghezzi, D., Olcese, U., Lassi, G., Nazzaro, C., Tonini, R., Tucci, V., Benfenati, F., and Medini, P. (2012). Sound-driven synaptic inhibition in primary visual cortex. *Neuron* **73**, 814–828.
- Iyer, M., Wu, L., Carey, M., Wang, Y., Smallwood, A., and Gambhir, S.S. (2001). Two-step transcriptional amplification as a method for imaging reporter gene expression using weak promoters. *Proc. Natl. Acad. Sci. USA* **98**, 14595–14600.

- Jackman, S.L., Beneduce, B.M., Drew, I.R., and Regehr, W.G. (2014). Achieving high-frequency optical control of synaptic transmission. *J. Neurosci.* *34*, 7704–7714.
- Kheirbek, M.A., Drew, L.J., Burghardt, N.S., Costantini, D.O., Tannenholz, L., Ahmari, S.E., Zeng, H., Fenton, A.A., and Hen, R. (2013). Differential control of learning and anxiety along the dorsoventral axis of the dentate gyrus. *Neuron* *77*, 955–968.
- Kirkcaldie, M.T.K. (2012). Neocortex. In *The Mouse Nervous System*, C. Watson, G. Paxinos, and L. Puelles, eds. (San Diego, CA: Academic Press), pp. 52–111.
- Knöpfel, T. (2012). Genetically encoded optical indicators for the analysis of neuronal circuits. *Nat. Rev. Neurosci.* *13*, 687–700.
- Kranz, A., Fu, J., Duerschke, K., Weidlich, S., Naumann, R., Stewart, A.F., and Anastasiadis, K. (2010). An improved Flp deleter mouse in C57Bl/6 based on F10 recombinase. *Genesis* *48*, 512–520.
- Lee, S.H., Marchionni, I., Bezaire, M., Varga, C., Danielson, N., Lovett-Barron, M., Losonczy, A., and Soltesz, I. (2014). Parvalbumin-positive basket cells differentiate among hippocampal pyramidal cells. *Neuron* *82*, 1129–1144.
- Li, L., Tasic, B., Micheva, K.D., Ivanov, V.M., Spletter, M.L., Smith, S.J., and Luo, L. (2010). Visualizing the distribution of synapses from individual neurons in the mouse brain. *PLoS ONE* *5*, e11503.
- Madisen, L., Zwingman, T.A., Sunkin, S.M., Oh, S.W., Zariwala, H.A., Gu, H., Ng, L.L., Palmiter, R.D., Hawrylycz, M.J., Jones, A.R., et al. (2010). A robust and high-throughput Cre reporting and characterization system for the whole mouse brain. *Nat. Neurosci.* *13*, 133–140.
- Madisen, L., Mao, T., Koch, H., Zhuo, J.M., Berenyi, A., Fujisawa, S., Hsu, Y.W., Garcia, A.J., 3rd, Gu, X., Zanella, S., et al. (2012). A toolbox of Cre-dependent optogenetic transgenic mice for light-induced activation and silencing. *Nat. Neurosci.* *15*, 793–802.
- Marvin, J.S., Borghuis, B.G., Tian, L., Cichon, J., Harnett, M.T., Akerboom, J., Gordus, A., Renninger, S.L., Chen, T.W., Bargmann, C.I., et al. (2013). An optimized fluorescent probe for visualizing glutamate neurotransmission. *Nat. Methods* *10*, 162–170.
- Mayford, M., Bach, M.E., Huang, Y.Y., Wang, L., Hawkins, R.D., and Kandel, E.R. (1996). Control of memory formation through regulated expression of a CaMKII transgene. *Science* *274*, 1678–1683.
- Muzumdar, M.D., Tasic, B., Miyamichi, K., Li, L., and Luo, L. (2007). A global double-fluorescent Cre reporter mouse. *Genesis* *45*, 593–605.
- Nagai, T., Yamada, S., Tominaga, T., Ichikawa, M., and Miyawaki, A. (2004). Expanded dynamic range of fluorescent indicators for Ca²⁺ by circularly permuted yellow fluorescent proteins. *Proc. Natl. Acad. Sci. USA* *101*, 10554–10559.
- Nguyen-Vu, T.D., Kimpo, R.R., Rinaldi, J.M., Kohli, A., Zeng, H., Deisseroth, K., and Raymond, J.L. (2013). Cerebellar Purkinje cell activity drives motor learning. *Nat. Neurosci.* *16*, 1734–1736.
- Petersen, R.P., Moradpour, F., Eadie, B.D., Shin, J.D., Kannangara, T.S., Delaney, K.R., and Christie, B.R. (2013). Electrophysiological identification of medial and lateral perforant path inputs to the dentate gyrus. *Neuroscience* *252*, 154–168.
- Pi, H.J., Hangya, B., Kvitsiani, D., Sanders, J.I., Huang, Z.J., and Kepecs, A. (2013). Cortical interneurons that specialize in disinhibitory control. *Nature* *503*, 521–524.
- Ray, R.S., Corcoran, A.E., Brust, R.D., Kim, J.C., Richerson, G.B., Nattie, E., and Dymecki, S.M. (2011). Impaired respiratory and body temperature control upon acute serotonergic neuron inhibition. *Science* *333*, 637–642.
- Raymond, C.S., and Soriano, P. (2007). High-efficiency FLP and PhiC31 site-specific recombination in mammalian cells. *PLoS ONE* *2*, e162.
- Reijmers, L.G., Perkins, B.L., Matsuo, N., and Mayford, M. (2007). Localization of a stable neural correlate of associative memory. *Science* *317*, 1230–1233.
- Robertson, S.D., Plummer, N.W., de Marchena, J., and Jensen, P. (2013). Developmental origins of central norepinephrine neuron diversity. *Nat. Neurosci.* *16*, 1016–1023.
- Sauer, B., and McDermott, J. (2004). DNA recombination with a heterospecific Cre homolog identified from comparison of the pac-c1 regions of P1-related phages. *Nucleic Acids Res.* *32*, 6086–6095.
- Scott, G., Fagerholm, E.D., Mutoh, H., Leech, R., Sharp, D.J., Shew, W.L., and Knöpfel, T. (2014). Voltage imaging of waking mouse cortex reveals emergence of critical neuronal dynamics. *J. Neurosci.* *34*, 16611–16620.
- Taniguchi, H., He, M., Wu, P., Kim, S., Paik, R., Sugino, K., Kvitsiani, D., Fu, Y., Lu, J., Lin, Y., et al. (2011). A resource of Cre driver lines for genetic targeting of GABAergic neurons in cerebral cortex. *Neuron* *71*, 995–1013.
- Tasic, B., Miyamichi, K., Hippenmeyer, S., Dani, V.S., Zeng, H., Joo, W., Zong, H., Chen-Tsai, Y., and Luo, L. (2012). Extensions of MADM (mosaic analysis with double markers) in mice. *PLoS ONE* *7*, e33332.
- Urlinger, S., Baron, U., Thellmann, M., Hasan, M.T., Bujard, H., and Hillen, W. (2000). Exploring the sequence space for tetracycline-dependent transcriptional activators: novel mutations yield expanded range and sensitivity. *Proc. Natl. Acad. Sci. USA* *97*, 7963–7968.
- Wang, Q., and Burkhalter, A. (2007). Area map of mouse visual cortex. *J. Comp. Neurol.* *502*, 339–357.
- Wang, L., Sharma, K., Deng, H.X., Siddique, T., Grisotti, G., Liu, E., and Roos, R.P. (2008). Restricted expression of mutant SOD1 in spinal motor neurons and interneurons induces motor neuron pathology. *Neurobiol. Dis.* *29*, 400–408.
- Wang, P., Chen, T., Sakurai, K., Han, B.X., He, Z., Feng, G., and Wang, F. (2012). Intersectional Cre driver lines generated using split-intein mediated split-Cre reconstitution. *Sci. Rep.* *2*, 497.
- Yamada, Y., Michikawa, T., Hashimoto, M., Horikawa, K., Nagai, T., Miyawaki, A., Häusser, M., and Mikoshiba, K. (2011). Quantitative comparison of genetically encoded Ca indicators in cortical pyramidal cells and cerebellar Purkinje cells. *Front. Cell. Neurosci.* *5*, 18.
- Zariwala, H.A., Borghuis, B.G., Hoogland, T.M., Madisen, L., Tian, L., De Zeeuw, C.I., Zeng, H., Looger, L.L., Svoboda, K., and Chen, T.W. (2012). A Cre-dependent GCaMP3 reporter mouse for neuronal imaging in vivo. *J. Neurosci.* *32*, 3131–3141.
- Zeng, H., and Madisen, L. (2012). Mouse transgenic approaches in optogenetics. *Prog. Brain Res.* *196*, 193–213.
- Zeng, H., Horie, K., Madisen, L., Pavlova, M.N., Gragerova, G., Rohde, A.D., Schimpf, B.A., Liang, Y., Ojala, E., Kramer, F., et al. (2008). An inducible and reversible mouse genetic rescue system. *PLoS Genet.* *4*, e1000069.
- Zhao, S., Cunha, C., Zhang, F., Liu, Q., Gloss, B., Deisseroth, K., Augustine, G.J., and Feng, G. (2008). Improved expression of halorhodopsin for light-induced silencing of neuronal activity. *Brain Cell Biol.* *36*, 141–154.
- Zhao, S., Ting, J.T., Atallah, H.E., Qiu, L., Tan, J., Gloss, B., Augustine, G.J., Deisseroth, K., Luo, M., Graybiel, A.M., and Feng, G. (2011). Cell type-specific channelrhodopsin-2 transgenic mice for optogenetic dissection of neural circuitry function. *Nat. Methods* *8*, 745–752.
- Zhu, P., Aller, M.I., Baron, U., Cambridge, S., Bausen, M., Herb, J., Sawinski, J., Cetin, A., Osten, P., Nelson, M.L., et al. (2007). Silencing and un-silencing of tetracycline-controlled genes in neurons. *PLoS ONE* *2*, e533.

Discovery of a Biomarker and Lead Small Molecules to Target r(GGGGCC)-Associated Defects in c9FTD/ALS

Zhaoming Su,^{1,13} Yongjie Zhang,^{2,13} Tania F. Gendron,^{2,13} Peter O. Bauer,^{2,13} Jeannie Chew,² Wang-Yong Yang,¹ Erik Fostvedt,¹ Karen Jansen-West,² Veronique V. Belzil,² Pamela Desaro,³ Amelia Johnston,³ Karen Overstreet,³ Seok-Yoon Oh,⁴ Peter K. Todd,⁴ James D. Berry,⁵ Merit E. Cudkowicz,⁵ Bradley F. Boeve,⁶ Dennis Dickson,² Mary Kay Floeter,⁷ Bryan J. Traynor,⁸ Claudia Morelli,⁹ Antonia Ratti,^{9,10} Vincenzo Silani,^{9,10} Rosa Rademakers,² Robert H. Brown,¹¹ Jeffrey D. Rothstein,¹² Kevin B. Boylan,³ Leonard Petrucelli,^{2,*} and Matthew D. Disney^{1,*}

¹Department of Chemistry, The Scripps Research Institute, Scripps Florida, 130 Scripps Way #3A1, Jupiter, FL 33458, USA

²Department of Neuroscience, Mayo Clinic, 4500 San Pablo Rd., Jacksonville, FL 32224, USA

³Department of Neurology, Mayo Clinic, 4500 San Pablo Rd., Jacksonville, FL 32224, USA

⁴Department of Neurology, University of Michigan, 1500 E. Medical Center Drive, Ann Arbor, MI 48109, USA

⁵Department of Neurology, Massachusetts General Hospital, Harvard Medical School, 15 Parkman Street, Boston, MA 02115, USA

⁶Department of Neurology, Mayo Clinic, 200 First Street SW, Rochester, MN 55905, USA

⁷Spasticity and Spinal Physiology Unit, National Institute of Neurological Disorders and Stroke, National Institutes of Health, Bethesda, MD 20892, USA

⁸Laboratory of Neurogenetics, National Institute on Aging, National Institutes of Health, Bethesda, MD 20892, USA

⁹Department of Neurology and Laboratory of Neuroscience, IRCCS Istituto Auxologico Italiano, Via Zucchi, 18, 20095 Cusano Milanino (Milan), Italy

¹⁰Department of Pathophysiology and Transplantation, “Dino Ferrari” Center, Università degli Studi di Milano, Via Sforza, 35, 20122, Milan, Italy

¹¹Department of Neurology, University of Massachusetts Medical School, Worcester, MA 01655, USA

¹²Department of Neurology, Brain Science Institute, Johns Hopkins University, 855 N Wolfe Street, Baltimore, MD 21205, USA

¹³Co-first author

*Correspondence: petrucelli.leonard@mayo.edu (L.P.), disney@scripps.edu (M.D.D.)

<http://dx.doi.org/10.1016/j.neuron.2014.07.041>

SUMMARY

A repeat expansion in *C9ORF72* causes frontotemporal dementia and amyotrophic lateral sclerosis (c9FTD/ALS). RNA of the expanded repeat (r(GGGGCC)_{exp}) forms nuclear foci or undergoes repeat-associated non-ATG (RAN) translation, producing “c9RAN proteins.” Since neutralizing r(GGGGCC)_{exp} could inhibit these potentially toxic events, we sought to identify small-molecule binders of r(GGGGCC)_{exp}. Chemical and enzymatic probing of r(GGGGCC)₈ indicate that it adopts a hairpin structure in equilibrium with a quadruplex structure. Using this model, bioactive small molecules targeting r(GGGGCC)_{exp} were designed and found to significantly inhibit RAN translation and foci formation in cultured cells expressing r(GGGGCC)₆₆ and neurons transdifferentiated from fibroblasts of repeat expansion carriers. Finally, we show that poly(GP) c9RAN proteins are specifically detected in c9ALS patient cerebrospinal fluid. Our findings highlight r(GGGGCC)_{exp}-binding small molecules as a possible c9FTD/ALS therapeutic and suggest that c9RAN proteins could potentially serve as a pharmacodynamic biomarker to assess efficacy of therapies that target r(GGGGCC)_{exp}.

INTRODUCTION

Frontotemporal dementia (FTD) and amyotrophic lateral sclerosis (ALS) are overlapping neurodegenerative diseases with no effective treatment. Success in developing a treatment will require a well-orchestrated effort that addresses multiple aspects of the drug discovery process, including target identification and validation, as well as the identification of biomarkers to assess efficacy of potential therapies in clinical trials. These endeavors have been hampered by an incomplete understanding of FTD and ALS pathogenesis. However, with the discovery that a GGGGCC repeat expansion in *C9ORF72* is the most common genetic cause of FTD and ALS (DeJesus-Hernandez et al., 2011; Renton et al., 2011), a new therapeutic target has come to light.

Two putative pathomechanisms of “c9FTD/ALS” involve RNA transcribed from the expansion. First, these transcripts (termed r(GGGGCC)_{exp}) may cause toxicity through the formation of nuclear RNA foci that sequester various RNA-binding proteins (for review, see Gendron et al., 2014). Second, r(GGGGCC)_{exp} undergoes repeat-associated non-ATG (RAN) translation, producing “c9RAN proteins” that form neuronal inclusions throughout the central nervous system (Ash et al., 2013; Mori et al., 2013b). Consequently, neutralizing or degrading r(GGGGCC)_{exp} holds promise as a therapeutic approach for c9FTD/ALS. Indeed, antisense oligonucleotides to *C9ORF72* transcripts suppress features associated with the repeat

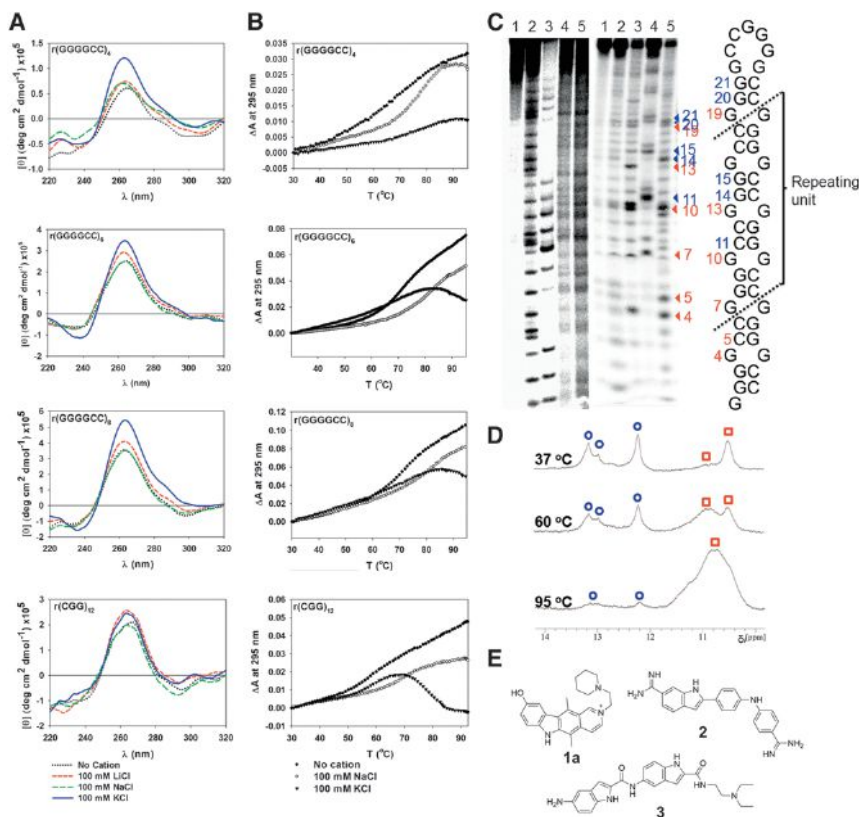


Figure 1. Probing r(GGGGCC)_n Secondary Structures

(A) CD spectra of r(GGGGCC)_{4,6,8} and r(CG)₁₂ in the presence of various monovalent cations.

(B) Optical melting curves for r(GGGGCC)_{4,6,8} and r(CG)₁₂ monitored at 295 nm. RNA samples (4 μM) were folded prior to recording CD spectra (20°C) and optical melting curves.

(C) DMS mapping data (left), enzymatic mapping data (middle), and predicted hairpin structure of r(GGGGCC)₈ using mapping restraints (right). DMS mapping lanes: 1, untreated RNA; 2, alkaline hydrolysis; 3, T1 digestion under denaturing conditions; 4, DMS modification in the presence of 185 mM Li⁺; 5, DMS modification in the presence of 185 mM K⁺. Enzymatic mapping lanes: 1, untreated RNA; 2, T1 digestion under denaturing conditions; 3, T1 digestion under native conditions; 4, V1 digestion in which base-paired nucleotides are cleaved; 5, S1 digestion in which all single-stranded nucleotides are cleaved.

(D) 1D ¹H NMR spectra of r(GGGGCC)₈ in the presence of 100 mM K⁺ annealed at 37°C, 60°C, or 95°C. Blue circles are imino proton resonances from G residues present as base pairs and red squares are imino proton resonances from non-canonically paired G residues.

(E) Structures of lead compounds 1a, 2, and 3 that bind to r(GGGGCC)₈. See also Figure S1.

expansion in human-induced pluripotent stem cell-derived neurons (Donnelly et al., 2013; Sareen et al., 2013). In light of pharmacological advantages, small molecules may offer an attractive option for targeting r(GGGGCC)_{exp}. Capitalizing on our findings that r(GGGGCC)_n adopts a hairpin structure in addition to a G-quadruplex one, we designed small molecules able to bind r(GGGGCC)_{exp} and to significantly decrease RAN translation and foci formation in cultured cells expressing r(GGGGCC)₆₆, and induced neurons (iNeurons) directly converted from fibroblasts of *C9ORF72* repeat expansion carriers. These findings indicate that designer small molecules targeting r(GGGGCC)_{exp} may prove promising as a c9FTD/ALS therapeutic. Furthermore, since we found that poly(GP) c9RAN proteins are detected in c9ALS cerebrospinal fluid (CSF), poly(GP) proteins may serve as a pharmacodynamic biomarker to assess efficacy of potential therapies that target r(GGGGCC)_{exp}.

RESULTS

r(GGGGCC)₈ Preserves a Hairpin Structure with Periodically Repeating 1 × 1 Nucleotide GG Internal Loops in Equilibrium with a G-Quadruplex

With the goal of designing small-molecule modulators of r(GGGGCC), we investigated its structure. Using evidence from gel mobility shift assays and spectroscopic methods, previous reports suggest that r(GGGGCC) forms intra- and intermolecular G-quadruplex structures (Fratta et al., 2012; Reddy et al., 2013), with another suggesting that r(GGGGCC) repeats

adopt both G-quadruplex and hairpin structures (Haeusler et al., 2014). To further probe the structure of r(GGGGCC), we completed spectroscopic (circular dichroism [CD] and optical melting), chemical (modification with dimethyl sulfate [DMS]), and enzymatic analyses (for a full description of our biophysical studies see the Supplemental Information available online). CD studies of r(GGGGCC)₄, r(GGGGCC)₆, and r(GGGGCC)₈ revealed that these RNAs probably fold into a G-quadruplex structure in the presence of K⁺ but not Na⁺, which promotes a hairpin structure (Figure 1A). We next studied the structures of r(GGGGCC) by optical melting, as G-quadruplexes have signature melting curves (large hypochromic transition of UV absorbance at 295 nm) (Mergny et al., 1998). In agreement with CD studies, optical melts completed in the presence of Na⁺ indicated that r(GGGGCC)₄, r(GGGGCC)₆, and r(GGGGCC)₈ form intramolecular hairpins. In contrast, optical melts completed in the presence of K⁺ indicate the presence of both hairpin and G-quadruplex structures (Figure 1B and Table S1).

The folding of r(GGGGCC)₈ was next examined using enzymatic and chemical mapping in the presence of Li⁺ or K⁺, the latter known to stabilize G-quadruplexes (Hardin et al., 1992). Enzymatic mapping revealed an alternating pattern of cleavage by enzymes that specifically cleave paired or noncanonically paired nucleotides (Figure 1C), suggesting that some populations form a hairpin structure. These findings were confirmed using the chemical modification reagent DMS.

We additionally explored the structure of r(GGGGCC)₈ by analyzing its 1D ¹H NMR spectra. At low annealing temperatures, the NMR spectra indicate that r(GGGGCC)₈ folds into a hairpin with noncanonically paired Gs in the stem (spectrum collected at 37°C; Figure 1D). As the annealing temperature increases, however, NMR peaks become broad, indicating increased population of a G-quadruplex. The existence of both conformations is not surprising as other studies have suggested RNAs that form quadruplexes can form alternative structures, including hairpins (Bugaut et al., 2012).

Identification of Small Molecules that Bind r(GGGGCC)_{exp}

Exploiting the findings above, we sought to identify small molecules that bind r(GGGGCC)_{exp} and determine whether they improve c9FTD/ALS-associated defects. It was reported that TMPyP4, a known G-quadruplex binder, binds r(GGGGCC)₈ in vitro (Zamiri et al., 2014). Although the bioactivity of TMPyP4 was not explored, these studies indicate that it is possible to identify small molecules that bind r(GGGGCC) repeats. We previously developed a strategy to design small molecules that bind an RNA target using information about RNA-small molecule interactions (Velagapudi et al., 2014). Small-molecule leads can be further optimized by chemical similarity searching, which identifies compounds that are chemically similar to the leads. We reported that small molecule **1a** binds 1 × 1 GG internal loops present in r(CG)_{exp} and improves fragile X-associated tremor/ataxia syndrome (FXTAS)-associated defects (Disney et al., 2012). Given the structural similarity between r(CG)_{exp} and r(GGGGCC)_{exp}, we hypothesized that **1a** and compounds chemically similar to it might bind r(GGGGCC)_{exp}. We collected 132 such small molecules and screened them for binding to r(GGGGCC)₈. Three lead compounds (**1a**, **2**, and **3**) were identified (Figures 1E and S1A; Table S2) and further characterized. Kinetic binding studies showed that **1a**, **2**, and **3** bind to r(GGGGCC)₈ with K_ds of 9.7, 10, and 16 μM, respectively, similar to those observed for r(CG)₁₂. In contrast, **1a**, **2**, and **3** bind more weakly to a hairpin with a fully paired stem, suggesting that the compounds are at least modestly selective (Figure S1B). We perturbed the equilibrium between hairpin and G-quadruplex structures by folding r(GGGGCC)₈ in the presence of an additional 100 mM NaCl (favors hairpin) or KCl (favors quadruplex). The observed K_ds for **1a** and **3** were 3- to 10-fold weaker in the presence of Na⁺ and K⁺, indicating that ionic strength affects binding. Of interest, the affinity of **2** for r(GGGGCC)₈ was not significantly affected by addition of Na⁺, but became > 6-fold weaker in K⁺. These results indicate that compound **2** recognizes the hairpin structure over the G-quadruplex (Figure S1B).

Given that small-molecule binders of r(GGGGCC)_{exp} may influence the thermodynamic stability of the RNA, which could in turn influence foci formation and RAN translation, optical melting was used to study whether compounds increase r(GGGGCC)₈ stability. While compound **3** did not significantly affect r(GGGGCC)₈'s stability or melting temperature, **1a** and **2** stabilized the RNA by 0.95 and 0.63 kcal/mol, respectively, and increased the T_m by 3.1 and 1.9°C, respectively (Figure S1C and Table S3).

Small-Molecule Binders of r(GGGGCC)_{exp} Inhibit RAN Translation and Foci Formation in (GGGGCC)₆₆-Expressing Cells

To determine whether compounds **1a**, **2**, and **3** bind r(GGGGCC)_{exp} in cells, we employed COS7 cells transfected to express 66 GGGGCC repeats with no upstream ATG and our previously reported strategy to identify small-molecule cellular targets. In this strategy, small molecules are conjugated to (1) a reactive module that forms a covalent cross-link with the target (chlorambucil; **CA**); and (2) biotin for facile isolation of small molecule-biomolecule adducts (Guan and Disney, 2013). First, a biotin-chlorambucil conjugate of **1a** was synthesized (**1a-CA-biotin**; Figure 2A, Figures S2A and S2B), added to (GGGGCC)₆₆-expressing cells, and allowed to react with its cellular targets. Biomolecule-small molecule adducts were then isolated with streptavidin-functionalized resin. qRT-PCR analysis of the isolated fractions showed an 80-fold enrichment of r(GGGGCC)₆₆ compared to 18S rRNA (normalized to untreated lysate; Figure 2B). To determine whether **1a**, **2**, and **3** bind r(GGGGCC)_{exp} directly, we completed a competitive profiling experiment by cotreating (GGGGCC)₆₆-expressing cells with **1a-CA-biotin** and the compound of interest. That is, the targets of **1a**, **2**, and **3** can be inferred by their depletion in pull-down fractions. Indeed, the amount of r(GGGGCC)₆₆ that forms an adduct with **1a-CA-biotin** was significantly depleted in the presence of each compound (Figure 2B).

Having established that all three compounds bind r(GGGGCC)₆₆, we evaluated their effect on RAN translation. While no evidence of RAN translation was seen in HEK293 cells expressing only 2 or 20 (GGGGCC) repeats, expression of (GGGGCC)₆₆ resulted in the synthesis of poly(GP) and poly(GA) proteins (Figure 2C), but not poly(GR) proteins (not shown). Compound **3** (100 μM, 24 hr) modestly inhibited synthesis of poly(GP) proteins but did not influence poly(GA) protein production (Figure 2D). In contrast, compounds **1a** and **2** significantly decreased both poly(GP) and poly(GA) protein levels (Figure 2D). Given that **1a** and **2** have similar effects on RAN translation and that **1a** also inhibits this event in iNeurons (shown below), we tested additional concentrations of **1a** and found that it affords a dose-dependent effect on RAN translation; statistically significant decreases in poly(GP) of 10%, 18%, and 47% were detected by immunoassay of lysates from (GGGGCC)₆₆-expressing cells treated with 25, 50, or 100 μM, respectively (Figure S2C).

In addition to the accumulation of c9RAN proteins, nuclear foci are detected in (GGGGCC)₆₆-expressing cells (Figure 2E). Consistent with their effect on RAN translation, compounds **1a** and **2**, but not **3**, significantly decreased the percentage of foci-positive cells (Figure 2F). This was probably caused by inhibition of foci formation, and not a result of impaired binding of the probe to r(GGGGCC)₆₆ in the presence of compound, given that conducting RNA FISH on fixed, nontreated (GGGGCC)₆₆-expressing cells with a probe coinubated with **1a** did not prevent detection of foci (Figure S2D).

Since the C9ORF72 repeat expansion is bidirectionally transcribed in c9FTD/ALS, and since antisense transcripts containing (CCCCGG) repeats are also RAN translated and form foci (Gendron et al., 2013; Mori et al., 2013a; Zu et al., 2013), we evaluated the effect of **1a** in r(CCCCGG)₆₆-expressing cells

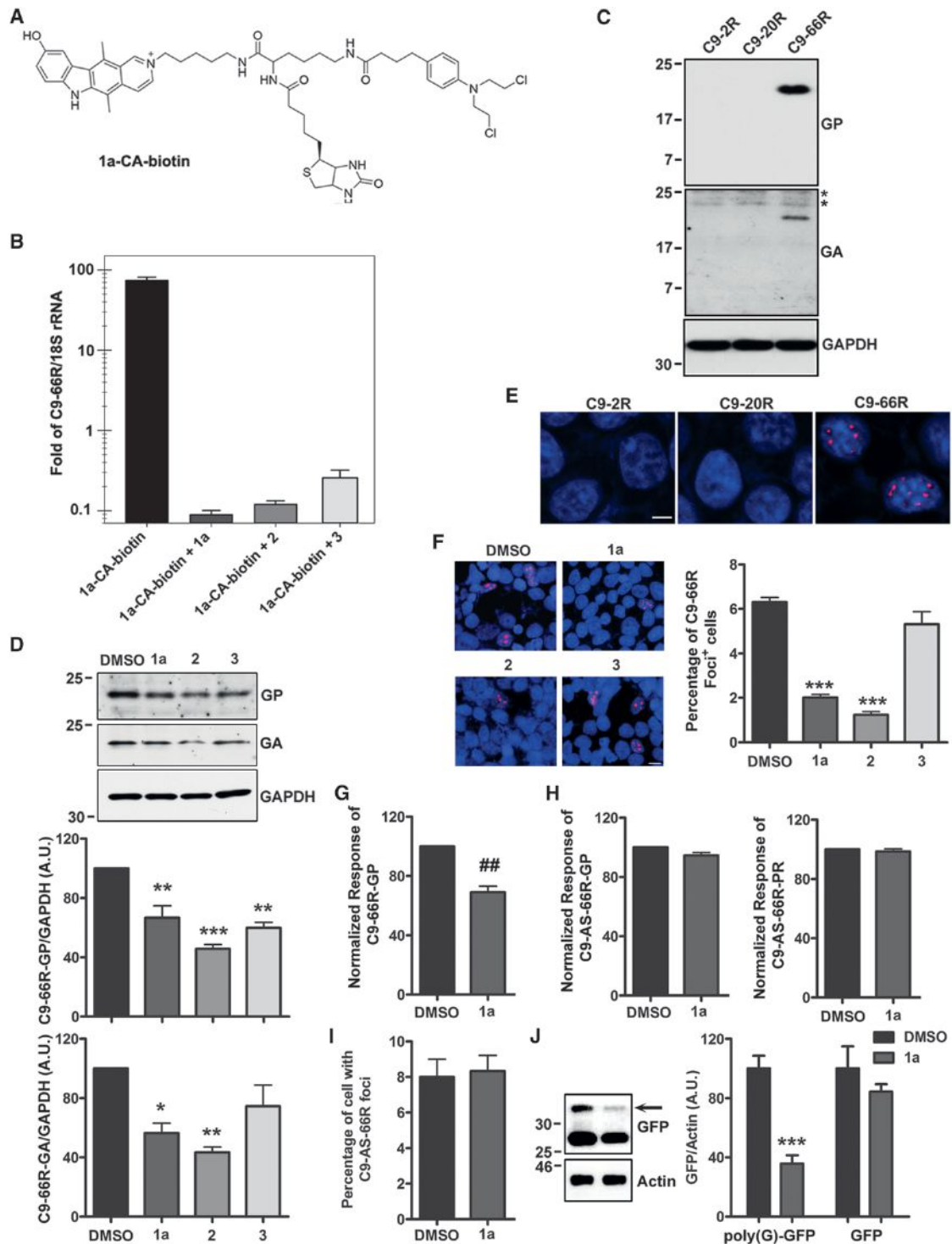


Figure 2. Small Molecules Targeting r(GGGGCC) Inhibit RAN Translation and Foci Formation in (GGGGCC)₆₆-Expressing Cells

(A) Structure of **1a-CA-biotin**; the chlorambucil moiety (**CA**) forms a covalent bond with the cellular target once the small molecule is bound. Biotin is used to isolate biomolecule-small molecule adducts from cells.

(B) Normalized enrichment of r(GGGGCC)₆₆ from biomolecules isolated with streptavidin beads as compared to 18S rRNA determined by qRT-PCR. Cells were treated with **1a-CA-biotin** alone or with **1a**, **2**, or **3** (competitive profiling). In competitive profiling experiments, the unreactive compound inhibits reaction of the target with **1a-CA-biotin** and thus the target is depleted in pull-down fractions. Data presented as mean ± SD (n = 2).

(legend continued on next page)

previously shown to express poly(PR) and poly(GP) proteins (Gendron et al., 2013). Whereas **1a** (100 μ M, 24 hr) significantly decreased poly(GP) proteins RAN translated from sense transcripts (Figure 2G), it had no effect on poly(GP) or poly(PR) proteins RAN translated from antisense r(CCCCGG)₆₆, as assessed by immunoassay (Figure 2H; see Figures S2E and S4A for assay validation). Likewise, no change in the percentage of cells bearing r(CCCCGG) foci was detected following **1a** treatment (Figure 2I). In contrast, we reported that **1a** does reduce foci in r(CGG)₆₀-expressing cells (Disney et al., 2012), and we show here that **1a** also inhibits RAN translation in cells expressing (CGG)₈₈ placed in the 5'-UTR of GFP, but does not affect downstream canonical translation (Figure 2J). These results confirm the structural similarity between r(CGG)_{exp} and r(GGGGCC)_{exp} in cells and the selectivity of **1a** toward this structure.

Small-Molecule Binders of r(GGGGCC) Inhibit RAN Translation and Foci Formation in (GGGGCC)_{exp}-Expressing iNeurons

To establish a more physiological disease cell model, fibroblasts with or without the *C9ORF72* repeat expansion were directly converted to a neuronal lineage by repressing polypyrimidine-tract-binding protein (PTB1), as recently described (Xue et al., 2013). PTB1 depletion caused fibroblasts to adopt a neuronal morphology with reduced soma size and neurite formation (Figures 3A, 3B, and S3A). These iNeurons expressed neuronal and synaptic markers, including MAP2, TUJ1, PSD95, Synapsin I, and Drebrin (Figures 3A and S3B). Nuclear foci, degraded by RNase A but resistant to DNase I (Figure S3C), were present in both *C9ORF72*+ fibroblasts (Figure S3D) and iNeurons (Figure 3C). Cytoplasmic poly(GP) inclusions, as well as poly(PR) inclusions, were also present in *C9ORF72*+ iNeurons (Figure 3C) but were not found in parental fibroblasts (Figure S3E). No foci or poly(GP) inclusions were detected in iNeurons lacking the expanded repeat (Figure 3C). Of importance, in three *C9ORF72*+ iNeuron lines, compound **1a** significantly decreased the percentage of cells with RNA foci (Figure 3D) and poly(GP) inclusions (Figures 3E and 3F), while having no effect on *C9ORF72* mRNA levels (Figure S3F). Consistent with findings in (GGGGCC)₆₆-expressing cells, a dose-dependent decrease in RAN translation of poly(GP) was observed in **1a**-treated *C9ORF72*+ iNeurons, but no change in poly(PR) expression, which is synthesized from the antisense transcript, was detected (Figure S3G). Due to toxicity associated with compound **2**

in iNeurons, it was not tested in this model. Taken together, our data indicate that our strategy to design small-molecule modulators of r(GGGGCC) led to the successful identification of a compound that mitigates abnormal events initiated by r(GGGGCC)_{exp}.

Poly(GP) Proteins Are Detected in c9ALS CSF

Our findings above indicate that r(GGGGCC)_{exp}-targeting small molecules can inhibit foci formation and RAN translation. Consequently, if c9RAN proteins are detected in CSF, they have the potential to serve as a measurable indicator of therapeutic efficacy. To test this notion, we developed a poly(GP) protein immunoassay (Figure S4A) and validated it as a sensitive means to measure endogenous poly(GP) using soluble fractions of frontal cortex tissues. As expected, poly(GP) was specifically detected in c9FTD/ALS samples (Figure S4B).

To test poly(GP) proteins as clinically relevant biomarkers, we evaluated whether they are detectable in CSF. We analyzed CSF from 14 c9ALS patients in comparison to CSF from 25 ALS patients without the *C9ORF72* mutation and 5 healthy subjects (see Table S4 for patient details). As shown in Figure 4A, poly(GP) proteins were detected only in c9ALS CSF. Using a (GP)₈ peptide standard curve, we estimate the median concentration of poly(GP) in c9ALS CSF to be 0.67 ng/ml (Figure S4C, Table S4). These exciting findings provide an important first step in identifying pharmacodynamic biomarkers for c9FTD/ALS (Figure 4B).

DISCUSSION

In the present study, we provide evidence that (1) r(GGGGCC)_{exp} adopts both hairpin and G-quadruplex structures—information important for the design of r(GGGGCC)-binding small molecules; (2) human fibroblasts can be directly converted to neurons that recapitulate salient features of disease; (3) small molecules that bind r(GGGGCC)_{exp} inhibit RAN translation and foci formation; and (4) c9RAN proteins are detectable in c9ALS CSF.

Recent studies show that r(GGGGCC) repeats forms G-quadruplexes (Fratta et al., 2012; Reddy et al., 2013), with another reporting they adopt both G-quadruplex and hairpin structures (Haeusler et al., 2014). In agreement with the latter, our chemical and enzymatic probing studies reveal that r(GGGGCC)₈ do form a hairpin structure. NMR studies suggest that the hairpin structure predominates at low refolding temperatures while the quadruplex predominates at higher ones. To understand the finer details of this equilibrium in cells, chemical mapping could

(C) Cells overexpressing 66 (GGGGCC) repeats (C9-66R), but not 2 (C9-2R) or 20 (C9-20R), express poly(GP) and poly(GA) proteins. Asterisks demark nonspecific bands.

(D) Western blot and densitometry of poly(GP) and poly(GA) proteins in (GGGGCC)₆₆-expressing cells treated with DMSO or compounds **1a**, **2**, or **3** (100 μ M, 24 hr). Data represent mean + SEM (n = 3).

(E) RNA foci (red) are detected in the nucleus (Hoechst; blue) of C9-66R cells.

(F) Evaluation of the percentage of foci-positive cells by RNA FISH posttreatment. Data represent mean + SEM in ten fields.

(G and H) Compound **1a** decreases RAN translation of poly(GP) proteins from sense (GGGGCC)₆₆ repeats in C9-66R cells (G) but does not influence levels of poly(GP) or poly(PR) proteins RAN translated from antisense (CCCGG)₆₆ repeats in C9-AS-66R cells (H), as assessed by GP and PR immunoassays. Data represent mean + SEM (n = 3 or 4).

(I) The percentage of r(CCCCGG)-containing foci in C9-AS-66R cells is not affected by **1a**.

(J) **1a** decreases RAN translation of poly(G) in cells expressing (CGG)₈₈ upstream of GFP. Data presented as mean + SEM (n = 3).

*p < 0.05, **p < 0.01, ***p < 0.001, as assessed by one-way ANOVA followed by Dunnett's Multiple Comparison Test. ##p < 0.01, as assessed by t test. See also Figure S2.

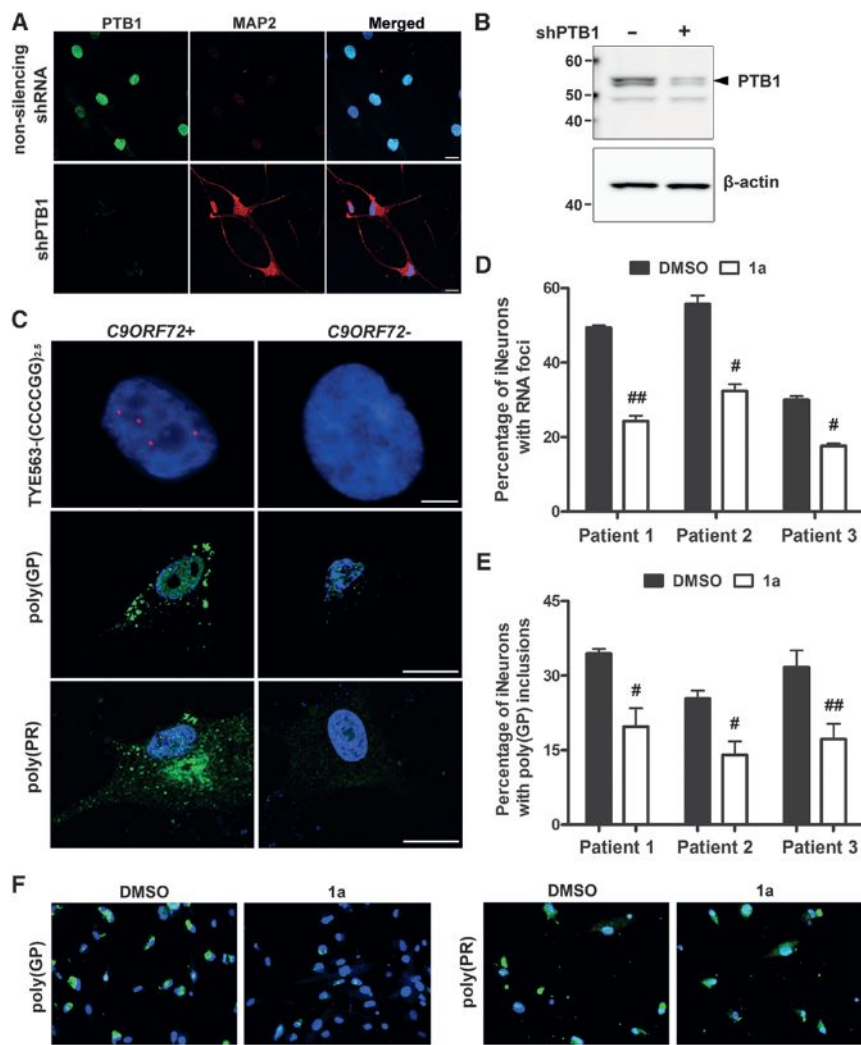


Figure 3. Small Molecules Targeting r(GGGGCC) Inhibit RAN Translation and Foci Formation in iNeurons with the C9ORF72 Expansion

(A) Immunofluorescence staining of fibroblasts transduced with nonsilencing shRNA or shPTB1 for PTB1 and the neuronal marker, MAP2. Scale bar, 20 μ m.

(B) PTB1 western blot analysis of fibroblasts transduced or not with shPTB1.

(C) RNA foci accumulate in iNeurons with the C9ORF72 repeat expansion (C9ORF72+) but not in iNeurons lacking the expansion (C9ORF72-), as assessed by RNA FISH. Immunofluorescence staining with anti-GP or anti-PR illustrates the accumulation of c9RAN proteins specifically in C9ORF72+ iNeurons. Scale bars, 5 μ m.

(D) Treatment of C9ORF72+ iNeurons with compound **1a** (2 μ M, 4 d) significantly decreased the percentage of cells with foci. For each iNeuron line, data reflects the average percentage of foci-positive cells + SEM in three separate fields.

(E and F) Compound **1a** significantly decreased the percentage of cells with anti-GP, but not anti-PR, immunoreactive inclusions (magnification: 20 \times). For each line, data represent the average percentage of inclusion-positive cells + SEM counted in nine wells of a 96-well plate. # p < 0.05, ## p < 0.01, as assessed by t test. See also Figure S3.

be completed as described in yeast (Wells et al., 2000), although readout using reverse transcriptase could be challenging. Alternatively, antibodies that recognize RNA quadruplexes could be employed (Lam et al., 2013).

We identified three compounds that bind r(GGGGCC) (**1a**, **2**, and **3**), two of which significantly inhibited RAN translation and foci formation in a novel r(GGGGCC)₆₆ cell model developed for the rapid screening of drugs. In addition, we found that **1a** inhibits RAN translation and foci formation in C9ORF72+ iNeurons. This report shows that adult human fibroblasts can be directly converted to neurons that mirror disease-specific defects and that these defects can be blocked by pharmacological manipulation. Of interest, RNA foci were observed in both C9ORF72+ fibroblasts and iNeurons, while poly(GP) and poly(PR) inclusions were observed in iNeurons but not fibroblasts. These findings are consistent with our observation that poly(GP) inclusions are restricted to neurons in c9FTD/ALS (Ash et al., 2013).

There are at least two mechanisms by which our small molecules may affect RAN translation. In the first model, their

binding to r(GGGGCC)_{exp} increases the thermodynamic stability of the RNA and is thus an impediment for ribosomal read-through of the transcript. Indeed, **1a** and **2** stabilize r(GGGGCC)₈ in vitro. In a second model, the binding of small molecules to the repeats impedes initiation of translation at these sites. In a similar fashion, the decrease in foci

observed upon treatment could result from the inability of **1a**- or **2**-bound r(GGGGCC)_{exp} to bind RBPs that promote foci formation.

As a pathological hallmark of c9FTD/ALS, and one that is influenced by r(GGGGCC)_{exp}-targeting small molecules, c9RAN proteins have potential to serve as clinically relevant biomarkers. Our discovery that poly(GP) is detectable specifically in c9ALS CSF could facilitate identification of C9ORF72 repeat expansion carriers in the course of diagnostic work-ups and pave the way in determining whether changes in c9RAN protein levels in CSF correlate with disease severity or progression. Of importance, CSF c9RAN proteins could serve as an enrollment stratification tool in clinical trials and a pharmacodynamic biomarker to assess efficacy of therapies that target r(GGGGCC)_{exp} (Figure 4B). While these critical questions are investigated, it should be kept in mind that the C9ORF72 expansion is bidirectionally transcribed (Gendron et al., 2013; Mori et al., 2013a; Zu et al., 2013); as such, therapeutics may have to target both r(GGGGCC)_{exp} and r(CCCCGG)_{exp}. Because poly(GP) proteins are produced by RAN translation of sense and antisense

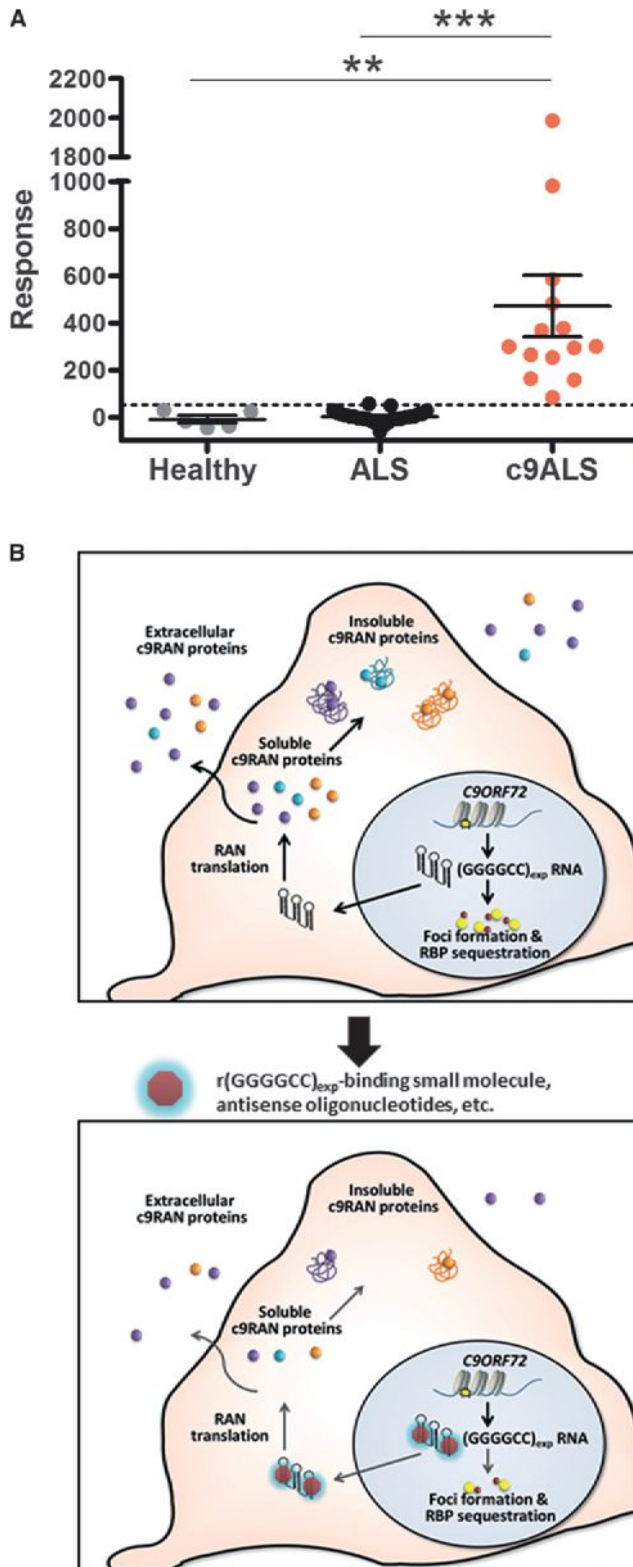


Figure 4. Poly(GP) Proteins Are Detected in c9ALS Cerebrospinal Fluid

(A) Poly(GP) expression in CSF from five healthy individuals, 25 ALS patients negative for the *C9ORF72* repeat expansion, and 14 c9ALS patients were

transcripts, poly(GP) immunoassays, such as the one described herein, could be of great use in testing therapeutics toward both r(GGGGCC)_{exp} and r(CCCCGG)_{exp}.

EXPERIMENTAL PROCEDURES

For ¹H NMR spectroscopy, r(GGGGCC)₈ (600 μM) was prepared in 10 mM Tris HCl, pH 7.4 and 100 mM KCl and annealed at the appropriate temperature for 5 min and allowed to cool to room temperature. After equilibration for 2 hr, NMR spectra were recorded at 10°C.

To identify RNA targets of **1a**, **2**, and **3**, COS7 cells expressing r(GGGGCC)₆₆ were treated with **1a-CA-Biotin** and compound of interest. Total RNA was extracted 24 hr later and incubated with streptavidin beads. cDNA was generated from bound RNA-**1a-CA-Biotin** adducts released from beads for quantitation of r(GGGGCC)₆₆ by qPCR. To detect products of RAN translation, lysates were prepared from (GGGGCC)_n-expressing HEK293 cells treated or not with compound for western blotting using anti-GP, anti-GA, or anti-GR antibodies. The effect of **1a** was also tested in cells expressing r(CGG)₈₈ embedded in the 5'-UTR of an open reading frame encoding GFP to allow detection of RAN-translated products by western blot using anti-GFP. Poly(GP) or poly(PR) expression in (GGGGCC)_n-expressing cells, human brain lysates, and CSF were evaluated by sandwich immunoassays. Foci in (GGGGCC)_n-expressing cells were visualized by RNA FISH using a Cy3-(GGCCCC)₄ probe.

Fibroblasts derived from patient skin samples were converted to iNeurons by transduction with pLKO.1 coding for shPTB1 (Xue et al., 2013). Poly(GP) and poly(PR) expression in iNeurons treated or not with **1a** were evaluated by immunofluorescence staining and foci were visualized by FISH using a locked nucleic acid probe (5'-TYE563-CCCCGGCCCCGGCCCC-3'). RNA extracted from iNeurons was utilized for qRT-PCR analysis of *C9ORF72* mRNA expression.

Data are presented as the mean ± SEM from a minimum of three experiments unless otherwise indicated. Statistical comparisons were made by Student's t test or ANOVA. Statistical significance was inferred at *p* < 0.05.

For more details on all methods, please see Supplemental Information.

SUPPLEMENTAL INFORMATION

Supplemental Information includes four figures, four tables, and Supplemental Experimental Procedures and can be found with this article online at <http://dx.doi.org/10.1016/j.neuron.2014.07.041>.

AUTHOR CONTRIBUTIONS

All co-first authors participated in the design of the study. Z.S. performed experiments relating to the determination of r(GGGGCC) secondary structure, the identification of small molecule binders of r(GGGGCC), and the evaluation of cellular targets of lead compounds. Y.Z. led studies developing and characterizing the (GGGGCC)₆₆-expressing cell model and testing the effect of compounds on foci formation and RAN translation in this model. T.F.G. developed immunoassays for the detection of poly(GP) and poly(PR) proteins, collaborated with Y.Z. in evaluating RAN translation in (GGGGCC)₆₆-expressing cells, assisted in the coordination of CSF sample collection, and assessed whether poly(GP) proteins are detectable in patient CSF. P.O.B. developed and characterized iNeurons directly converted from patient fibroblasts and

assessed by GP immunoassay. Response values correspond to the intensity of emitted light from which the background response was subtracted. Dashed line represents the limit of detection [LoD = LoB + 1.645(SD_{blank}); where LoB (limit of blank) = mean_{blank} + 1.645(SD_{blank})]. ***p* < 0.001, ****p* < 0.001 as assessed by one-way ANOVA followed by Tukey's Multiple Comparison Test. (B) Schematic representation of the effect of r(GGGGCC)_{exp}-targeting small molecules on foci formation and RAN translation, and the potential use of extracellular c9RAN proteins as a pharmacodynamic marker of treatment efficacy. See also Figure S4.

tested the effect of compounds on foci formation and RAN translation in this model.

ACKNOWLEDGMENTS

We are grateful to patients who donated CSF, skin samples, and postmortem tissue. We acknowledge Lillian Daugherty, Luc Pregent, and Mary Davis for technical support, Dr. Xiangming Kong for help with 1D ¹H NMR experiments. This work was supported by the National Institutes of Health (NIH)/National Institute on Aging (R01GM097455 [M.D.D.]; R01AG026251 [L.P.]); NIH/National Institute of Neurological Disorders and Stroke (R21NS074121 [K.B.B., T.F.G.], R21NS079807 [Y.Z.], R21NS084528 [L.P.], R01NS088689 [R.H.B., L.P.], R01NS063964 [L.P.]; R01NS077402 [L.P.]; R01NS050557 [R.H.B.]; ARRA Award RC2-NS070-342 [R.H.B.], P01NS084974 [L.P., D.D., R.R., K.B.B.]); National Institute of Environmental Health Services (R01 ES20395 [L.P.]); Department of Defense (ALSRP AL130125 [L.P., M.D.D.]); the Intramural Program of the NIH, the National Institute on Aging (Z01-AG000949-02 [B.J.T.]), and the National Institute of Neurological Disorders and Stroke (Z01 NS002976-16 to M.F.K. and B.J.T.); Mayo Clinic Foundation (L.P.); Mayo Clinic Center for Regenerative Medicine (P.O.B.), Mayo Clinic Center for Individualized Medicine (T.F.G., L.P., K.B.B.), ALS Association (K.B.B., P.O.B., L.P., T.F.G., Y.Z., and M.E.D.), Alzheimer's Association (Y.Z.), Robert Packard Center for ALS Research at Johns Hopkins (L.P., J.D.R.), Target ALS (L.P., M.D.D.), Canadian Institutes of Health Research (V.V.B.), Siragusa Foundation (V.V.B.), Robert and Clarice Smith & Abigail Van Buren Alzheimer's Disease Research Foundation (V.V.B.), Digiovanni Sundry Fund (M.E.D.), ATA (M.E.D.), Project ALS (R.H.B.), Angel Fund (R.H.B.), AriSLA cofinanced with support of '5x1000'-Healthcare research of the Italian Ministry of Health (grants EXOMEFALS 2009 [V.S.] and NOVALS 2012 [V.S.]), the Italian Ministry of Health (RF-2009-1473856 [C.M., A.R., V.S.]), and the European Commission (JNPD SOPHIA and STRENGTH [C.M., A.R., V.S.]). Z.S. and V.B. are Milton Safenowitz Postdoctoral Fellows funded by the ALS Association. W-Y.Y is a FRAXA Postdoctoral Fellow funded by FRAXA Research Foundation. Antibodies to c9RAN proteins have been licensed to a commercial entity. R.R. holds a patent on methods to screen for the hexanucleotide repeat expansion in the C9ORF72 gene.

Accepted: July 29, 2014

Published: August 14, 2014

REFERENCES

- Ash, P.E., Bieniek, K.F., Gendron, T.F., Caulfield, T., Lin, W.L., DeJesus-Hernandez, M., van Blitterswijk, M.M., Jansen-West, K., Paul, J.W., 3rd, Rademakers, R., et al. (2013). Unconventional translation of C9ORF72 GGGGCC expansion generates insoluble polypeptides specific to c9FTD/ALS. *Neuron* 77, 639–646.
- Bugaut, A., Murat, P., and Balasubramanian, S. (2012). An RNA hairpin to G-quadruplex conformational transition. *J. Am. Chem. Soc.* 134, 19953–19956.
- DeJesus-Hernandez, M., Mackenzie, I.R., Boeve, B.F., Boxer, A.L., Baker, M., Rutherford, N.J., Nicholson, A.M., Finch, N.A., Flynn, H., Adamson, J., et al. (2011). Expanded GGGGCC hexanucleotide repeat in noncoding region of C9ORF72 causes chromosome 9p-linked FTD and ALS. *Neuron* 72, 245–256.
- Disney, M.D., Liu, B., Yang, W.Y., Sellier, C., Tran, T., Charlet-Berguerand, N., and Childs-Disney, J.L. (2012). A small molecule that targets r(CGG)(exp) and improves defects in fragile X-associated tremor ataxia syndrome. *ACS Chem. Biol.* 7, 1711–1718.
- Donnelly, C.J., Zhang, P.W., Pham, J.T., Haeusler, A.R., Mistry, N.A., Vidsensky, S., Daley, E.L., Poth, E.M., Hoover, B., Fines, D.M., et al. (2013). RNA toxicity from the ALS/FTD C9ORF72 expansion is mitigated by antisense intervention. *Neuron* 80, 415–428.
- Fratia, P., Mizielinska, S., Nicoll, A.J., Zloh, M., Fisher, E.M., Parkinson, G., and Isaacs, A.M. (2012). C9orf72 hexanucleotide repeat associated with amyotrophic lateral sclerosis and frontotemporal dementia forms RNA G-quadruplexes. *Sci Rep* 2, 1016.
- Gendron, T.F., Bieniek, K.F., Zhang, Y.J., Jansen-West, K., Ash, P.E., Caulfield, T., Daugherty, L., Dunmore, J.H., Castanedes-Casey, M., Chew, J., et al. (2013). Antisense transcripts of the expanded C9ORF72 hexanucleotide repeat form nuclear RNA foci and undergo repeat-associated non-ATG translation in c9FTD/ALS. *Acta Neuropathol.* 126, 829–844.
- Gendron, T.F., Belzil, V.V., Zhang, Y.J., and Petrucelli, L. (2014). Mechanisms of toxicity in C9FTLD/ALS. *Acta Neuropathol.* 127, 359–376.
- Guan, L., and Disney, M.D. (2013). Covalent small-molecule-RNA complex formation enables cellular profiling of small-molecule-RNA interactions. *Angew. Chem. Int. Ed. Engl.* 52, 10010–10013.
- Haeusler, A.R., Donnelly, C.J., Periz, G., Simko, E.A., Shaw, P.G., Kim, M.S., Maragakis, N.J., Troncoso, J.C., Pandey, A., Sattler, R., et al. (2014). C9orf72 nucleotide repeat structures initiate molecular cascades of disease. *Nature* 507, 195–200.
- Hardin, C.C., Watson, T., Corregan, M., and Bailey, C. (1992). Cation-dependent transition between the quadruplex and Watson-Crick hairpin forms of d(CGCG3GCG). *Biochemistry* 31, 833–841.
- Lam, E.Y., Beraldi, D., Tannahill, D., and Balasubramanian, S. (2013). G-quadruplex structures are stable and detectable in human genomic DNA. *Nat Commun* 4, 1796.
- Mergny, J.L., Phan, A.T., and Lacroix, L. (1998). Following G-quartet formation by UV-spectroscopy. *FEBS Lett.* 435, 74–78.
- Mori, K., Arzberger, T., Grässer, F.A., Gijssels, I., May, S., Rentzsch, K., Weng, S.M., Schludi, M.H., van der Zee, J., Cruts, M., et al. (2013a). Bidirectional transcripts of the expanded C9orf72 hexanucleotide repeat are translated into aggregating dipeptide repeat proteins. *Acta Neuropathol.* 126, 881–893.
- Mori, K., Weng, S.M., Arzberger, T., May, S., Rentzsch, K., Kremmer, E., Schmid, B., Kretzschmar, H.A., Cruts, M., Van Broeckhoven, C., et al. (2013b). The C9orf72 GGGGCC repeat is translated into aggregating dipeptide-repeat proteins in FTD/ALS. *Science* 339, 1335–1338.
- Reddy, K., Zamiri, B., Stanley, S.Y., Macgregor, R.B., Jr., and Pearson, C.E. (2013). The disease-associated r(GGGGCC)_n repeat from the C9orf72 gene forms tract length-dependent uni- and multimolecular RNA G-quadruplex structures. *J. Biol. Chem.* 288, 9860–9866.
- Renton, A.E., Majounie, E., Waite, A., Simón-Sánchez, J., Rollinson, S., Gibbs, J.R., Schymick, J.C., Laaksovirta, H., van Swieten, J.C., Myllykangas, L., et al.; ITALSGEN Consortium (2011). A hexanucleotide repeat expansion in C9ORF72 is the cause of chromosome 9p21-linked ALS-FTD. *Neuron* 72, 257–268.
- Sareen, D., O'Rourke, J.G., Meera, P., Muhammad, A.K., Grant, S., Simpkinson, M., Bell, S., Carmona, S., Ornelas, L., Sahabian, A., et al. (2013). Targeting RNA Foci in iPSC-Derived Motor Neurons from ALS Patients with a C9ORF72 Repeat Expansion. *Sci. Transl. Med.* 5, 208ra149.
- Velagapudi, S.P., Gallo, S.M., and Disney, M.D. (2014). Sequence-based design of bioactive small molecules that target precursor microRNAs. *Nat. Chem. Biol.* 10, 291–297.
- Wells, S.E., Hughes, J.M., Igel, A.H., and Ares, M., Jr. (2000). Use of dimethyl sulfate to probe RNA structure in vivo. *Methods Enzymol.* 318, 479–493.
- Xue, Y., Ouyang, K., Huang, J., Zhou, Y., Ouyang, H., Li, H., Wang, G., Wu, Q., Wei, C., Bi, Y., et al. (2013). Direct conversion of fibroblasts to neurons by reprogramming PTB-regulated microRNA circuits. *Cell* 152, 82–96.
- Zamiri, B., Reddy, K., Macgregor, R.B., Jr., and Pearson, C.E. (2014). TMPyP4 porphyrin distorts RNA G-quadruplex structures of the disease-associated r(GGGGCC)_n repeat of the C9orf72 gene and blocks interaction of RNA-binding proteins. *J. Biol. Chem.* 289, 4653–4659.
- Zu, T., Liu, Y., Bañez-Coronel, M., Reid, T., Pletnikova, O., Lewis, J., Miller, T.M., Harms, M.B., Falchook, A.E., Subramony, S.H., et al. (2013). RAN proteins and RNA foci from antisense transcripts in C9ORF72 ALS and frontotemporal dementia. *Proc. Natl. Acad. Sci. USA* 110, E4968–E4977.

Cortical Representations Are Reinstated by the Hippocampus during Memory Retrieval

Kazumasa Z. Tanaka,^{1,2} Aleksandr Pevzner,² Anahita B. Hamidi,² Yuki Nakazawa,² Jalina Graham,² and Brian J. Wiltgen^{1,2,*}

¹Department of Psychology

²Center for Neuroscience

UC Davis, Davis, CA 95618, USA

*Correspondence: bjwiltgen@ucdavis.edu

<http://dx.doi.org/10.1016/j.neuron.2014.09.037>

SUMMARY

The hippocampus is assumed to retrieve memory by reinstating patterns of cortical activity that were observed during learning. To test this idea, we monitored the activity of individual cortical neurons while simultaneously inactivating the hippocampus. Neurons that were active during context fear conditioning were tagged with the long-lasting fluorescent protein H2B-GFP and the light-activated proton pump ArchT. These proteins allowed us to identify encoding neurons several days after learning and silence them with laser stimulation. When tagged CA1 cells were silenced, we found that memory retrieval was impaired and representations in the cortex (entorhinal, retrosplenial, perirhinal) and the amygdala could not be reactivated. Importantly, hippocampal inactivation did not alter the total amount of activity in most brain regions. Instead, it selectively prevented neurons that were active during learning from being reactivated during retrieval. These data provide functional evidence that the hippocampus reactivates specific memory representations during retrieval.

INTRODUCTION

Since patient H.M., researchers have known that the hippocampus is essential for memory (Scoville and Milner, 1957). This discovery was confirmed by animal studies showing that dysfunction in this area produces profound amnesia for spatial and contextual information (Kim and Fanselow, 1992; Morris et al., 1986). Despite these facts, it is still unknown why the hippocampus is so fundamental for memory. The dominant idea, based on the work of Marr, is that memory is retrieved when the hippocampus reinstates patterns of cortical activity that were observed during learning (Alvarez and Squire, 1994; Marr, 1971; Treves and Rolls, 1994). This idea is supported by spatial studies in rodents showing that learned sequences are replayed in the hippocampus and cortex after training (Ji and Wilson, 2007). Similar effects have been observed in human patients during free recall of episodic memories (Gelbard-Sagiv et al., 2008). However, it has yet to be determined whether cortical represen-

tations formed during learning are reinstated by the hippocampus during retrieval.

Recent studies have used *fos-tTA* reporter mice to tag active neurons in the hippocampus, cortex, and amygdala during context fear learning and show that they are reactivated several days later when memory is retrieved (Liu et al., 2012; Ramirez et al., 2013; Reijmers et al., 2007; Tayler et al., 2013). Similar to recording experiments, these data indicate that specific context representations are reactivated after learning. However, studies to date have not determined whether the hippocampus is responsible for reinstating memory representations in other structures as is widely assumed (Frankland and Bontempi, 2005). To examine this idea, we used *fos-tTA* mice to tag active CA1 neurons with the long-lasting fluorescent protein H2B-GFP and the light-activated proton pump archaerhodopsin (ArchT). These proteins allowed us to identify encoding neurons several days after learning and inactivate them with laser stimulation. When tagged CA1 neurons were silenced, we found that memory retrieval was impaired and representations in the cortex (entorhinal, retrosplenial, and perirhinal) and amygdala (central nucleus) could not be reactivated. These results provide direct evidence that the hippocampus is fundamental for memory because it reinstates patterns of activity that were originally present during learning.

RESULTS

Silencing Encoding Neurons in CA1

To identify and label active neurons, we used *fos-tTA* reporter mice that express the long-lasting fluorescent protein H2B-GFP. We previously found that $\approx 40\%$ of tagged neurons in the CA1 region of the hippocampus are reactivated when context fear memories are retrieved (Tayler et al., 2013). To selectively silence these cells, we engineered our reporter mice to express Cre recombinase under the control of the *tetO* promoter. In the absence of doxycycline (DOX), c-Fos activity leads to the expression of tTA, H2B-GFP, and Cre in these animals (Figure 1A). Previous studies showed that activity-dependent labeling in *fos-tTA* reporter mice largely recapitulates the expression of endogenous c-Fos in the hippocampus (Liu et al., 2012). To silence CA1 neurons that were active during learning, we infused an adeno-associated virus (AAV) that encodes a double-floxed inverted ArchT gene into the dorsal hippocampus (AAV-FLEX-ArchT) (Figure 1B). Once expressed, ArchT can be activated

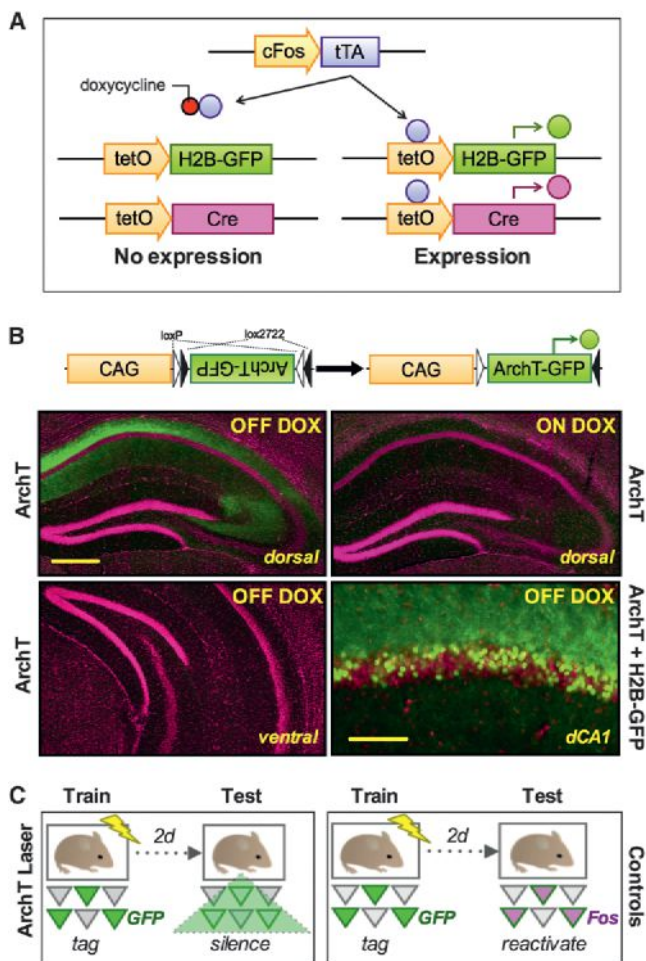


Figure 1. TetTag-Cre System

(A) Activation of the *c-fos* promoter drives the expression of H2B-GFP and Cre in a DOX-regulated manner. (B) *Fos-tTA/tetO-Cre* mice received infusions of AAV-FLEX-ArchT into the dorsal hippocampus and were fear conditioned off DOX. In these animals, Cre recombination in active neurons led to the expression of ArchT in the dorsal hippocampus (top left). Expression was not observed in the ventral hippocampus (bottom left) or in mice trained on DOX (top right). In *Fos-tTA/tetO-Cre/tetO-H2B-GFP* mice, fear conditioning led to the expression of ArchT and H2B-GFP in dorsal CA1 (bottom right). H2B-GFP (green) was expressed exclusively within the nucleus (magenta, DAPI), while ArchT (green) was expressed only in axons and dendrites. The scale bar represents 400 μm , or 100 μm on the bottom right panel. (C) Experimental procedure. Active CA1 neurons were tagged with H2B-GFP and ArchT during training (left). During testing, laser stimulation was delivered to silence tagged cells. In control animals (right), tagged cells were not inactivated during testing and should therefore be reactivated during testing. See also Figure S1.

with green light to produce robust silencing of neural activity (Han et al., 2011).

In our mice, Cre is expressed in active neurons and causes the ArchT gene to be inverted and expressed under the control of the constitutively active CAG promoter. Figure 1B (top left) shows the expression of ArchT in the dorsal hippocampus of *Fos-tTA/tetO-Cre* mice that underwent context fear conditioning off DOX. Expression was restricted to CA1 dendrites and axons

and was not observed in cell bodies. We estimated that ArchT was expressed in $\approx 1.05 \text{ mm}^3$ of tissue in the dorsal hippocampus (Figure S1 available online). Expression was not observed in the ventral hippocampus (bottom left). We also did not observe ArchT expression in mice that were fear conditioned on DOX (top right). Given that ArchT was selectively expressed in CA1 dendrites and axons, we used H2B-GFP to determine which cells were active during learning. Figure 1B (bottom right) shows the expression of H2B-GFP in cell nuclei and ArchT in fibers of *Fos-tTA/tetO-Cre/tetO-H2B-GFP* mice that were trained off DOX. Consistent with previous work, expression was observed almost exclusively in excitatory cells (Figure S2) (Liu et al., 2012; Reijmers et al., 2007; Tayler et al., 2013). Given their distinct localization, we could not determine the degree to which H2B-GFP and ArchT overlapped in CA1 neurons. However, the inactivation data presented in the next section provides direct evidence that ArchT is selectively expressed in H2B-GFP-positive cells. We also examined the expression of H2B-GFP in control mice ($n = 3$) that had DOX removed but were not trained. Consistent with previous work, these animals had significantly fewer H2B-GFP-positive neurons in CA1 (11%) than mice in the ArchT (28%) and No ArchT Laser (23%) groups (main effect of group, $F(2, 11) = 7.2$, $p < 0.05$; planned comparisons, Fisher's PLSD, p values < 0.05) (Tayler et al., 2013).

Reactivation of CA1 Neurons Is Required for Memory Retrieval

To inactivate ArchT-positive neurons during memory retrieval, we infused AAV-FLEX-ArchT into dorsal CA1 (dCA1) and implanted bilateral optic fibers in the same region. During context fear conditioning, DOX was removed to induce the selective expression of ArchT and H2B-GFP in active neurons (Figure 1C, left). After training, we administered high-concentration DOX to suppress additional expression of H2B-GFP and ArchT. A memory test was conducted 2 days later and green laser light (532 nm, 10mW) was delivered to both hippocampi to stimulate ArchT. We compared performance in the ArchT-Laser group to three control conditions. One group received laser stimulation but did not express ArchT (No ArchT-Laser). Another expressed ArchT but did not receive laser stimulation (ArchT-No Laser). The third control group did not express ArchT and did not receive laser stimulation (No ArchT-No Laser). In each of these groups, H2B-GFP-positive neurons should be intact during testing and express *c-Fos* when memory is retrieved (Figure 1C, right).

When tagged CA1 neurons were silenced, we found that memory retrieval was significantly impaired in the ArchT-Laser group relative to controls (Figure 2A; main effect of group $F(3, 19) = 5.15$, $p < 0.05$; planned comparisons, Fisher's PLSD, p values < 0.05). Freezing levels did not differ between any of the control groups (planned comparisons, Fisher's PLSD, p values > 0.05). These results provide functional evidence that memory retrieval requires the reactivation of previously engaged CA1 neurons. To determine the degree to which reactivation was disrupted, we quantified the expression of H2B-GFP and *c-Fos* 90 min after the memory test. As in our previous work, we compared the percentage of double-labeled neurons observed in dCA1 to that expected by chance alone (percent H2B-GFP \times percent *c-Fos*) (Tayler et al., 2013). We found a significant

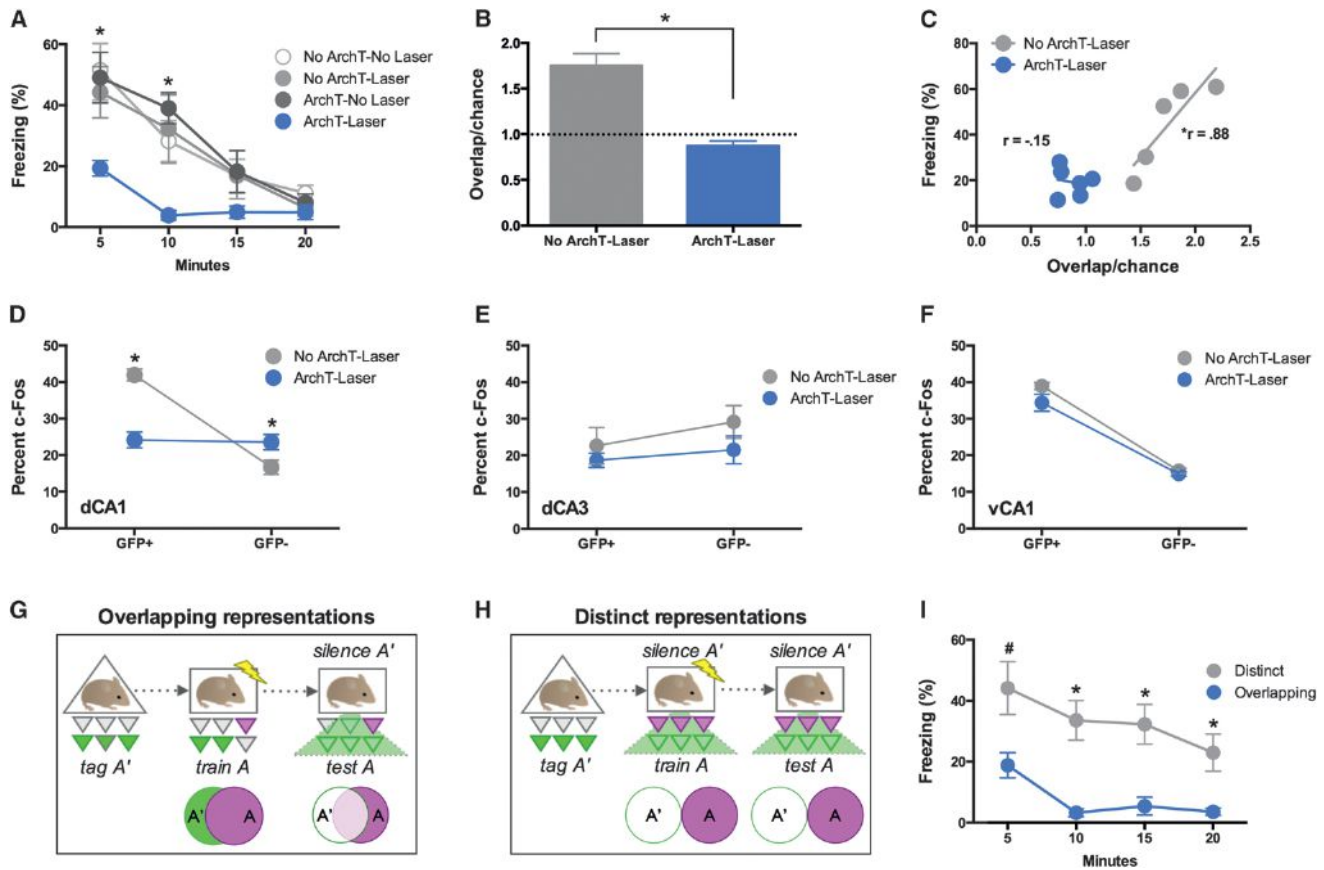


Figure 2. CA1 Silencing during Memory Retrieval

(A) During the memory test, ArchT-stimulated mice ($n = 6$) froze significantly less than the control groups (ArchT-No Laser $n = 6$; No ArchT-No Laser $n = 5$; No ArchT-No Laser $n = 6$). The control groups did not differ from one another. (B) The reactivation index (overlap/chance) was significantly reduced in the CA1 region of ArchT-Laser mice compared to the No ArchT-Laser group. (C) The amount of freezing was strongly correlated with the reactivation index ($r = 0.88$) in CA1 in the No ArchT-Laser group. This correlation was eliminated in ArchT-Laser mice ($r = -0.15$). (D) c-Fos activity was reduced in H2B-GFP-tagged neurons in the Arch-Laser group and increased in untagged neurons. (E and F) There was no effect on c-Fos expression in tagged or untagged neurons in (E) dCA3 or (F) vCA1. (G) Experimental procedure to silence overlapping context representations. Active neurons in dCA1 were tagged with ArchT during exposure to context A' (off DOX) (left). Two days later, animals were fear conditioned (on DOX) in context A, an environment whose representation overlaps with context A' (middle). Two days after training, mice were tested in context A, while tagged neurons were silenced (right). (H) Experimental procedure to silence distinct context representations. Active neurons in dCA1 were tagged with ArchT during exposure to context A' (off DOX) (left). Two days later, animals were fear conditioned (on DOX) in context A, while tagged neurons were silenced (middle). This manipulation should result in a distinct representation for context A that does not overlap with context A'. Two days after training, mice were tested in context A while tagged neurons were once again silenced (right). (I) When ArchT-labeled neurons were silenced, memory retrieval was selectively impaired in mice that had overlapping memory representations ($n = 5$) and had no effect in animals with distinct representations of context A and A' ($n = 9$). Values are represented as means \pm SEM, * $p \leq 0.05$, # $p = 0.06$. See also Figure S2.

reduction in double labeling (normalized to chance) in the ArchT-Laser group compared to that observed in No ArchT-Laser mice (Figure 2B; main effect of group $F(1,9) = 43.83$, $p < 0.05$). Reactivation of dCA1 neurons exceeded chance levels in No ArchT-Laser mice (paired t test, $p < 0.05$) but did not in the ArchT-Laser group (paired t test, $p > 0.05$). These results indicate that ArchT stimulation prevented the reactivation of dCA1 neurons during memory retrieval. Laser stimulation in the No-ArchT group did not appear to disrupt reactivation as the degree of overlap was nearly identical to that seen in nonstimulated control animals (Figure S2).

The amount of freezing observed during testing was strongly correlated with the degree of reactivation in the dCA1 region of

No ArchT-Laser mice (Figure 2C; $r = 0.88$, $p < 0.05$). This correlation was completely eliminated in the ArchT-Laser group ($r = -0.15$, $p > 0.05$). Expression levels of H2B-GFP (no effect of group, $F(1,9) = 2.18$, $p > 0.05$) and c-Fos (no effect of group, $F(1,9) = 1.21$, $p > 0.05$) in dCA1 were similar in both groups. However, as expected, c-Fos expression was selectively reduced in tagged neurons relative to untagged cells in ArchT-Laser animals (Figure 2D; group \times cell type interaction, $F(1,9) = 127.4$, $p < 0.05$). This result demonstrates that ArchT was selectively expressed in H2B-GFP-tagged neurons. Interestingly, c-Fos expression in the ArchT-Laser group was decreased in tagged cells (Fisher's PLSD, $p < 0.05$) and increased in untagged neurons (Fisher's PLSD, $p < 0.05$) compared to No ArchT-Laser

controls. This finding is consistent with the idea that active CA1 neurons can suppress the activity of neighboring cells (Hirase et al., 2001).

To determine the anatomical specificity of our manipulation, we also examined reactivation in dorsal CA3 (dCA3) and ventral CA1 (vCA1). We found that ArchT stimulation in dCA1 had no effect on c-Fos expression in H2B-GFP-positive or -negative neurons in dCA3 (Figure 2E; no effect of group $F(1, 9) = 1.51$, $p > 0.05$; no group \times cell type interaction $F < 1$) or vCA1 (Figure 2F; no effect of group $F(1, 9) = 4.07$, $p > 0.05$; no group \times cell type interaction $F(1, 9) = 1.5$, $p > 0.05$). These results indicate that ArchT-mediated silencing was restricted to neurons in the dorsal segment of CA1.

Our data suggest that a specific subset of dCA1 neurons mediate memory retrieval. However, an alternative possibility is that retrieval is impaired anytime hippocampal activity is disrupted (independent of which neurons are affected). To test this idea, we silenced dCA1 neurons that were either part of the trained context representation (overlapping) or orthogonal to it (distinct). If memory retrieval requires the reactivation of specific CA1 cells, then performance should only be impaired when an overlapping representation is silenced. Inactivation of a distinct context representation should have no effect. To test this idea, we trained mice in similar environments (A and A') that activate many of the same cells in dCA1 (Figure S3). Mice were first exposed to A' (off DOX), where active neurons were tagged with ArchT (Figure 2G). Two days later, animals were fear conditioned (on DOX) in context A. Neurons were not tagged during this session. Memory was then tested in context A while neurons from A' were silenced via ArchT stimulation. Given the significant overlap between these representations, we predicted that memory retrieval would be impaired. In a second procedure, we prevented overlap between context representations by inactivating A' neurons while mice were fear conditioned in A. Once again, active neurons were first tagged with ArchT in context A'. To prevent overlap, these cells were silenced during subsequent training in A (Figure 2H). Silencing A' cells during testing in this group should not alter the representation of context A and, as a result, memory should be intact.

Figure 2I shows the freezing levels during the context A memory test when ArchT-labeled neurons were silenced. As predicted, inactivating these cells impaired retrieval in mice that had overlapping context representations and had no effect on animals with distinct representations of A and A' (Figure 2I; main effect of group $F(1, 12) = 9.42$, $p < 0.05$). The amount of freezing in the Distinct memory group was comparable to that observed in the control groups shown in Figure 2A. An analysis of overlap in H2B-GFP-positive mice from each group suggests that ArchT stimulation silenced a similar number of tagged neurons in both conditions (Figure S3). Together, these data demonstrate that hippocampal inactivation impairs retrieval only when the same neurons that were active during encoding are silenced during retrieval.

CA1 Silencing Disrupts Reactivation of Cortical Representations

We next examined the assumption that the hippocampus reactivates cortical representations during memory retrieval. To do

this, we quantified the expression of H2B-GFP and c-Fos in regions that receive monosynaptic projections from dCA1: subiculum (SUB), lateral entorhinal cortex (LEC), perirhinal cortex (PER), and retrosplenial cortex (RSC) (Cenquizca and Swanson, 2007). We observed a large number of ArchT-labeled fibers in each of these regions (Figures 3A, 3D, and 3G). We used these fibers to trace the axons of tagged CA1 cells and examine activity in directly connected cortical regions. When dCA1 neurons were silenced, we found that the total amount of c-Fos expression in the SUB and RSC were unaltered (Figures 3B and 3E; no effect of group, SUB $F < 1$; RSC $F < 1$). However, there was a significant reduction in c-Fos expression in tagged neurons (Fisher's PLSD, $p < 0.05$) compared to untagged cells (Fisher's PLSD, $p > 0.05$) in the ArchT-Laser group (Figures 3C and 3F; significant group \times cell type interaction, SUB $F(1, 9) = 44.73$, $p < 0.05$; significant group \times cell type interaction RSC $F(1, 9) = 4.63$, $p = 0.05$). In LEC/PER, there was a slight reduction in the total amount of c-Fos expression (Figure 3H; main effect of group, $F(1, 9) = 6.54$, $p < 0.05$) that was observed in both tagged (Fisher's PLSD, $p < 0.05$) and untagged (Fisher's PLSD, $p < 0.05$) cells (Figure 3I). However, similar to the results in SUB and RSC, the size of this reduction was significantly larger in tagged neurons compared to untagged cells (significant group \times cell type interaction, $F(1, 9) = 16.83$, $p < 0.05$). Together, these data demonstrate that the hippocampus is fundamental for memory because it can restate patterns of cortical activity that were originally observed during learning.

CA1 Silencing Disrupts Reactivation in the Central but Not Basolateral Amygdala

In our final analyses, we examined activity in two regions of the amygdala that are known to be essential for context fear; the central nucleus (CeA) and the basolateral nucleus (BLA) (Figure 4A) (Maren, 2001). The CeA receives dense inputs from SUB, LEC, and PER and light inputs from vCA1 (Pitkänen et al., 2000). We found that ArchT stimulation in dCA1 did not affect the total amount of c-Fos expression in this region (Figure 4B; no effect of group, $F(1, 9) = 3.05$, $p > 0.05$). However, c-Fos expression in tagged neurons was significantly reduced (Fisher's PLSD, $p < 0.05$) compared to that observed in untagged cells (Fisher's PLSD, $p > 0.05$) (significant group \times cell type interaction, $F(1, 9) = 17.86$, $p < 0.05$) (Figure 4C). These data suggest that dCA1 modulates activity in the CeA via its projections to the SUB, LEC, and/or PER.

In contrast to the CeA, the BLA exhibited no change in overall levels of c-Fos (Figure 3E, top; no effect of group, $F(1, 8) = 0.34$, $p > 0.05$) or c-Fos expression in tagged (Figure 3E, bottom; Fisher's PLSD, $p > 0.05$) and untagged neurons (Fisher's PLSD, $p > 0.05$) (no group \times cell type interaction, $F(1, 9) = 1.4$, $p > 0.05$; no effect of group, $F < 1$) when dCA1 was silenced. This result is consistent with the fact that the BLA receives dense projections from vCA1, which exhibited normal reactivation in our experiments (Pitkänen et al., 2000). Together, these data suggest that dorsal and ventral CA1 can independently modulate the retrieval of context fear memories in the amygdala, a finding that is not predicted by traditional models (Wiltgen and Fanselow, 2003).

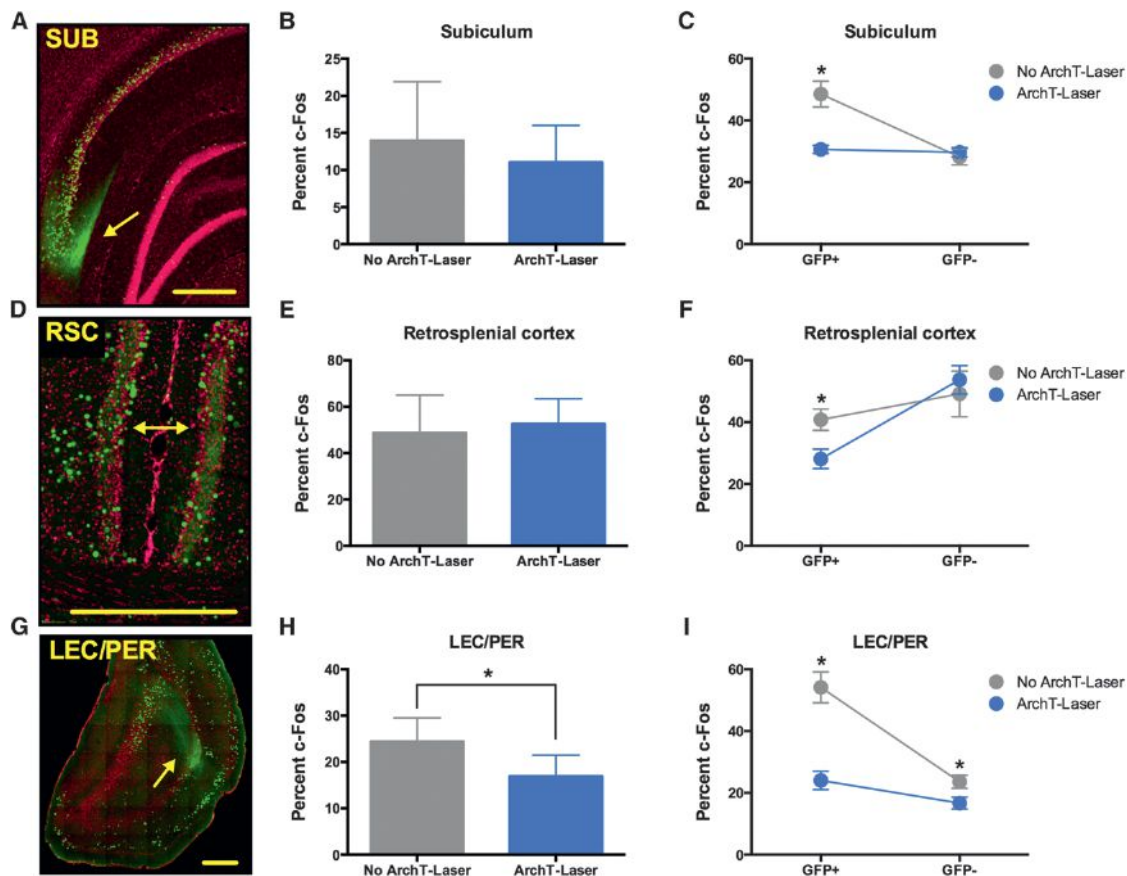


Figure 3. Effects of CA1 Silencing on Cortical Activity

Mice from the ArchT-Laser ($n = 6$) and No ArchT-Laser ($n = 5$) groups were used for these analyses. (A) ArchT fibers (green) from tagged dCA1 neurons terminating in SUB. H2B-GFP-expressing nucleus in green; DAPI-stained nucleus in magenta. (B) When dCA1 was silenced, there was no effect on total c-Fos expression in SUB. (C) c-Fos activity was selectively reduced in tagged neurons in SUB. (D) ArchT fibers (green) from tagged dCA1 neurons terminating in RSC. (E) When dCA1 was silenced, there was no effect on total c-Fos expression in RSC. (F) c-Fos activity was selectively reduced in tagged neurons in RSC. (G) ArchT fibers (green) from tagged dCA1 neurons terminating at the border of LEC/PER. (H) When dCA1 was silenced, there was a slight reduction in total c-Fos expression in LEC/PER. (I) There was a reduction in c-Fos activity in both tagged and untagged neurons LEC/PER. However, the magnitude of this reduction was significantly larger in H2B-GFP-tagged neurons. Values are represented as means \pm SEM, $*p \leq 0.05$. The scale bar represents 400 μ m. See also Figure S3.

DISCUSSION

The hippocampus is essential for retrieving spatial and contextual memories (Kim and Fanselow, 1992; Moser and Moser, 1998). It is thought to mediate this process by activating unique representations of the environment that were formed during learning. To test this idea, we combined *fos-tTA/tetO-Cre* mice with hippocampal infusions of AAV to induce ArchT expression in an activity-dependent manner. This allowed us to selectively silence CA1 neurons that were sufficiently active to drive the *c-fos* promoter. When these cells were inactivated with laser stimulation, mice were unable to retrieve a previously formed context fear memory. Silencing CA1 neurons that were not active during learning had no effect on retrieval. These results are consistent with the idea that specific ensembles of CA1 neurons are used to encode context memories (Guzowski et al., 1999).

The expression of immediate-early genes (IEGs) requires high-frequency activity that is sufficient to activate NMDARs (Steward

and Worley, 2001; Tayler et al., 2011). This type of activity is observed in the hippocampus when animals enter a place field (O'Keefe, 1978). Consistent with this idea, the number of neurons expressing IEGs after spatial exploration is similar to the number of place cells that are found in recording studies (Guzowski et al., 1999; Leutgeb et al., 2004). In addition, manipulations that alter the activity of place cells produce similar effects on IEG-labeled (e.g., *Arc*) neurons (Vazdarjanova and Guzowski, 2004). Given that gene expression in *fos-tTA* mice largely recapitulates endogenous c-Fos expression (Liu et al., 2012), it is likely that place cell activity played a major role in the induction of H2B-GFP, Cre, and ArchT in our experiments.

The current study also examined the idea that the hippocampus retrieves memory by reinstating patterns of cortical activity that were observed during learning. This assumption has been central to theories of hippocampal function for decades (Frankland and Bontempi, 2005). Previous work showed that hippocampal and cortical neurons are reactivated after learning during

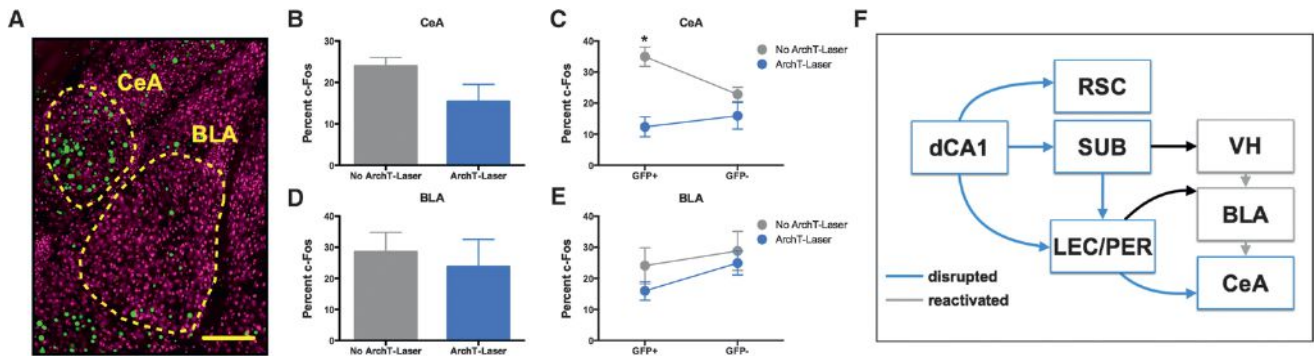


Figure 4. Effects of CA1 Silencing on Amygdala Activity

Mice from the ArchT-Laser ($n = 6$) and No ArchT-Laser ($n = 5$) groups were used for these analyses. (A) H2B-GFP expression in CeA and BLA. H2B-GFP-expressing nucleus in green; DAPI-stained nucleus in magenta. The scale bar represents 200 μm . (B) When dCA1 was silenced there was no effect on total c-Fos expression in CeA. (C) c-Fos activity was selectively reduced in tagged neurons in CeA. (D) When dCA1 was silenced there was no effect on total c-Fos expression in BLA. (E) There was no effect on c-Fos expression in tagged or untagged neurons in BLA. (F) Selective silencing of tagged dCA1 neurons disrupted reactivation in RSC, SUB, and LEC/PER. This manipulation also resulted in reduced reactivation in CeA, while activity in the BLA and vCA1 was unaltered. Values are represented as means \pm SEM, $^*p < 0.05$. See also Figure S4.

memory retrieval and sleep (Ji and Wilson, 2007; Tayler et al., 2013). However, these studies did not determine whether the hippocampus is required to induce reactivation in the cortex as is assumed by current models. To test this idea, we traced ArchT-labeled fibers from tagged dCA1 neurons to their targets in SUB, LEC, PER, and RSC. When CA1 neurons were silenced during retrieval, reactivation was disrupted in these regions (Figure 4F). Importantly, the disruption was selective; activity was normal in cortical neurons that were not engaged during learning (i.e., H2B-GFP-negative cells). Therefore, when dCA1 is prevented from retrieving a specific context memory, representations in connected cortical regions also cannot be reactivated. This finding implies that extrahippocampal inputs to these cortical areas cannot fully activate representations that were established during learning.

The fact that reactivation was reduced in the cortex while overall activity was maintained suggests that new cortical neurons came online during the retrieval test. We observed a similar effect in CA1 (Figures 2 and S3). These data suggest that memory retrieval depends on the reactivation of specific cells in the hippocampus and cortex. Our previous work (showing reactivation in the training context but not a distinct environment) is consistent with this finding (Tayler et al., 2013). Increased activity in new cortical cells may have been difficult to detect in our experiments because the number of H2B-GFP-negative neurons is quite large compared to that observed in CA1 (90%–95% in cortex versus 75%–80% in CA1) (Tayler et al., 2013). As a result, a large number of H2B-GFP-negative cells in the cortex would need to express c-Fos to significantly increase activity in this population.

In the current experiments, reactivation was only analyzed in cortical regions that contained ArchT-labeled fibers. These areas were quantified because they received direct projections from the tagged CA1 neurons that were silenced during retrieval. However, models of hippocampal function predict widespread disruption in the cortex when the hippocampus is compromised (Frankland and Bontempi, 2005). This assumption was difficult to assess because indirectly connected cortical regions did not

contain ArchT-labeled fibers. Given that only a portion of CA1 was silenced (Figure S1), nonlabeled regions probably contain areas that lost input from the hippocampus as well as areas that retained it. Therefore, in the absence of ArchT-labeled fibers, it is difficult to know where reactivation should be examined. Despite this fact, we did observe activity changes in amygdala nuclei that are indirectly connected to dCA1. We believe that this was the case because the CeA and BLA are relatively small and their role in context fear conditioning has been thoroughly described (Goossens and Maren, 2001).

Current models of fear conditioning assume that contextual information is relayed from the ventral hippocampus to the BLA, where it can be associated with aversive events (Maren and Fanselow, 1995). The CeA is typically viewed as an output structure that receives input from the BLA and induces fear responding via its projections to the midbrain (LeDoux, 2000) (but see Balleine and Killcross, 2006). However, the CeA also receives dense projections from the SUB, LEC, and PER that could influence fear responding (Pitkänen et al., 2000). Consistent with this idea, we found that silencing dCA1 neurons disrupted reactivation in each of these cortical regions and in the CeA (Figure 4F). Activity in vCA1 and the BLA were not affected. In contrast to traditional models, these data suggest that the dorsal hippocampus can modulate fear responding independent of the ventral hippocampus.

To summarize, three main discoveries were made in the current study. First, we found that a subset of dCA1 neurons (those that were engaged during learning) must be reactivated for context fear memories to be retrieved. This result provides functional evidence that specific CA1 ensembles are used to encode context memories. Second, we showed that silencing previously active CA1 neurons prevents reactivation in cortical regions that are known to be important for context memory. This result provides direct evidence that the hippocampus is fundamental for memory because it can reinstate patterns of cortical activity that were observed during learning. Third, we found that silencing dCA1 neurons did not affect activity in the ventral hippocampus or BLA but, instead, disrupted reactivation in CeA.

This result suggests that the dorsal hippocampus can modulate fear responding independent of the ventral hippocampus. Together, these data illustrate the utility of new genetic tools that can be used to answer fundamental questions about the hippocampus and memory, some of which have remained intractable for decades.

EXPERIMENTAL PROCEDURES

Subjects

Triple transgenic *fos-tTA/tetO-H2B-GFP/tetO-Cre* (TetTag-Cre) mice were generated by crossing heterozygous double transgenic mice expressing H2B-GFP under control of the tetO promoter (*tetO-H2B-GFP*) and a tetracycline-transactivator (tTA) protein under control of the *c-fos* promoter (*fos-tTA*) (Taylor et al., 2013) with heterozygous transgenic mice expressing Cre recombinase under control of the tetO promoter (*tetO-Cre*, JAX 006234). TetTag-Cre animals were maintained in a C57BL/6J background. B6/129 F1 hybrids were generated by breeding TetTag-Cre animals with 129S6 mice (Taconic). All of the mice used in the current experiments were F1 hybrids. All experiments were approved by the UC Davis, Institutional Animal Care and Use Committee (IACUC).

Surgery

At 8–12 weeks of age, mice received stereotaxic infusions of AAV and optic fiber implantation. Briefly, AAV2/5-CAG-FLEX-ArchT-GFP was microinjected bilaterally into the CA1 region of the dorsal hippocampus (anterioposterior [AP] -2.0 mm from bregma, mediolateral [ML] ± 1.5 mm, dorsoventral [DV] 1.5 mm). Optic fibers were constructed as previously described (Sparta et al., 2012) and implanted into the same stereotaxic coordinates.

Behavioral Experiments

TetTag-Cre mice were born and raised on low-concentration DOX chow (40 mg/kg, Harlan Laboratories). To label active neurons with H2B-GFP and ArchT, we removed DOX 3 days prior to fear conditioning in context A or exposure to context A'. After the conditioning/exposure session, mice were immediately given high-concentration DOX chow (1 g/kg, Harlan Laboratories) to suppress further H2B-GFP and Cre expression. Memory was assessed 2 days after conditioning by returning the mice to the training context for 30 min and measuring the freezing response. The automated Video Freeze System (Med Associates) was used to quantify freezing as previously described (Anagnostaras et al., 2010). Animals in the Laser groups received stimulation (532 nm, 10 mW) that was directed at dorsal CA1.

See Supplemental Information for detailed procedures.

Statistics

Group differences were analyzed with one-way ANOVAs or repeated-measure factorial ANOVAs followed by planned comparisons (Fisher's PLSD). The percentage of double-labeled neurons ([H2B-GFP and c-Fos/DAPI]) was compared to that expected by chance ([H2B-GFP/DAPI] \times [c-Fos/DAPI]) using paired t tests. Effects with *p* values ≤ 0.05 are reported as significant.

SUPPLEMENTAL INFORMATION

Supplemental Information includes Supplemental Experimental Procedures and three figures and can be found with this article online at <http://dx.doi.org/10.1016/j.neuron.2014.09.037>.

ACKNOWLEDGMENTS

We thank Charan Ranganath, Arne Ekstrom, and Andy Yonelinas for their helpful comments and E. Boyden and the University of North Carolina Vector Core for ArchT constructs. These experiments were supported by a Whitehall Research Grant and a McKnight Memory & Cognitive Disorders Award to B.J.W., a Nakajima Foundation Fellowship to K.Z.T., and an NSF graduate fellowship to A.B.H.

Accepted: September 25, 2014

Published: October 9, 2014

REFERENCES

- Alvarez, P., and Squire, L.R. (1994). Memory consolidation and the medial temporal lobe: a simple network model. *Proc. Natl. Acad. Sci. USA* *91*, 7041–7045.
- Anagnostaras, S.G., Wood, S.C., Shuman, T., Cai, D.J., Leduc, A.D., Zurn, K.R., Zurn, J.B., Sage, J.R., and Herrera, G.M. (2010). Automated assessment of pavlovian conditioned freezing and shock reactivity in mice using the video freeze system. *Front Behav Neurosci* *4*, 158.
- Balleine, B.W., and Killcross, S. (2006). Parallel incentive processing: an integrated view of amygdala function. *Trends Neurosci.* *29*, 272–279.
- Canquiza, L.A., and Swanson, L.W. (2007). Spatial organization of direct hippocampal field CA1 axonal projections to the rest of the cerebral cortex. *Brain Res. Brain Res. Rev.* *56*, 1–26.
- Frankland, P.W., and Bontempi, B. (2005). The organization of recent and remote memories. *Nat. Rev. Neurosci.* *6*, 119–130.
- Gelbard-Sagiv, H., Mukamel, R., Harel, M., Malach, R., and Fried, I. (2008). Internally generated reactivation of single neurons in human hippocampus during free recall. *Science* *322*, 96–101.
- Goosens, K.A., and Maren, S. (2001). Contextual and auditory fear conditioning are mediated by the lateral, basal, and central amygdaloid nuclei in rats. *Learn. Mem.* *8*, 148–155.
- Guzowski, J.F., McNaughton, B.L., Barnes, C.A., and Worley, P.F. (1999). Environment-specific expression of the immediate-early gene *Arc* in hippocampal neuronal ensembles. *Nat. Neurosci.* *2*, 1120–1124.
- Han, X., Chow, B.Y., Zhou, H., Klapoetke, N.C., Chuong, A., Rajimehr, R., Yang, A., Baratta, M.V., Winkle, J., Desimone, R., and Boyden, E.S. (2011). A high-light sensitivity optical neural silencer: development and application to optogenetic control of non-human primate cortex. *Front Syst Neurosci* *5*, 18.
- Hirase, H., Leinekugel, X., Czurkó, A., Csicsvari, J., and Buzsáki, G. (2001). Firing rates of hippocampal neurons are preserved during subsequent sleep episodes and modified by novel awake experience. *Proc. Natl. Acad. Sci. USA* *98*, 9386–9390.
- Ji, D., and Wilson, M.A. (2007). Coordinated memory replay in the visual cortex and hippocampus during sleep. *Nat. Neurosci.* *10*, 100–107.
- Kim, J.J., and Fanselow, M.S. (1992). Modality-specific retrograde amnesia of fear. *Science* *256*, 675–677.
- LeDoux, J.E. (2000). Emotion circuits in the brain. *Annu. Rev. Neurosci.* *23*, 155–184.
- Leutgeb, S., Leutgeb, J.K., Treves, A., Moser, M.B., and Moser, E.I. (2004). Distinct ensemble codes in hippocampal areas CA3 and CA1. *Science* *305*, 1295–1298.
- Liu, X., Ramirez, S., Pang, P.T., Puryear, C.B., Govindarajan, A., Deisseroth, K., and Tonegawa, S. (2012). Optogenetic stimulation of a hippocampal engram activates fear memory recall. *Nature* *484*, 381–385.
- Maren, S. (2001). Neurobiology of Pavlovian fear conditioning. *Annu. Rev. Neurosci.* *24*, 897–931.
- Maren, S., and Fanselow, M.S. (1995). Synaptic plasticity in the basolateral amygdala induced by hippocampal formation stimulation in vivo. *J. Neurosci.* *15*, 7548–7564.
- Marr, D. (1971). Simple memory: a theory for archicortex. *Philos. Trans. R. Soc. Lond. B Biol. Sci.* *262*, 23–81.
- Morris, R.G., Anderson, E., Lynch, G.S., and Baudry, M. (1986). Selective impairment of learning and blockade of long-term potentiation by an N-methyl-D-aspartate receptor antagonist, AP5. *Nature* *319*, 774–776.
- Moser, M.B., and Moser, E.I. (1998). Distributed encoding and retrieval of spatial memory in the hippocampus. *J. Neurosci.* *18*, 7535–7542.
- O'Keefe, J.N.L. (1978). *The Hippocampus as a Cognitive Map*. (Oxford: Oxford University Press).

- Pitkänen, A., Pikkarainen, M., Nurminen, N., and Ylinen, A. (2000). Reciprocal connections between the amygdala and the hippocampal formation, perirhinal cortex, and postrhinal cortex in rat. A review. *Ann. N Y Acad. Sci.* 911, 369–391.
- Ramirez, S., Liu, X., Lin, P.A., Suh, J., Pignatelli, M., Redondo, R.L., Ryan, T.J., and Tonegawa, S. (2013). Creating a false memory in the hippocampus. *Science* 341, 387–391.
- Reijmers, L.G., Perkins, B.L., Matsuo, N., and Mayford, M. (2007). Localization of a stable neural correlate of associative memory. *Science* 317, 1230–1233.
- Scoville, W.B., and Milner, B. (1957). Loss of recent memory after bilateral hippocampal lesions. *J. Neurol. Neurosurg. Psychiatry* 20, 11–21.
- Sparta, D.R., Stamatakis, A.M., Phillips, J.L., Hovelsø, N., van Zessen, R., and Stuber, G.D. (2012). Construction of implantable optical fibers for long-term optogenetic manipulation of neural circuits. *Nat. Protoc.* 7, 12–23.
- Steward, O., and Worley, P.F. (2001). Selective targeting of newly synthesized Arc mRNA to active synapses requires NMDA receptor activation. *Neuron* 30, 227–240.
- Taylor, K.K., Lowry, E., Tanaka, K., Levy, B., Reijmers, L., Mayford, M., and Wiltgen, B.J. (2011). Characterization of NMDAR-Independent Learning in the Hippocampus. *Front. Behav. Neurosci.* 5, 28.
- Taylor, K.K., Tanaka, K.Z., Reijmers, L.G., and Wiltgen, B.J. (2013). Reactivation of neural ensembles during the retrieval of recent and remote memory. *Curr. Biol.* 23, 99–106.
- Treves, A., and Rolls, E.T. (1994). Computational analysis of the role of the hippocampus in memory. *Hippocampus* 4, 374–391.
- Vazdarjanova, A., and Guzowski, J.F. (2004). Differences in hippocampal neuronal population responses to modifications of an environmental context: evidence for distinct, yet complementary, functions of CA3 and CA1 ensembles. *J. Neurosci.* 24, 6489–6496.
- Wiltgen, B.J., and Fanselow, M.J. (2003). A model of hippocampal-cortical-amygdala interactions based on contextual fear conditioning. In *The Neurobiology of Spatial Behaviour*, K. Jeffery, ed. (New York: Oxford University Press), pp. 83–103.

Pupil Fluctuations Track Fast Switching of Cortical States during Quiet Wakefulness

Jacob Reimer,^{1,*} Emmanouil Froudarakis,¹ Cathryn R. Cadwell,¹ Dimitri Yatsenko,¹ George H. Denfield,¹ and Andreas S. Tolias^{1,2,*}

¹Department of Neuroscience, Baylor College of Medicine, Houston, TX 77030, USA

²Department of Computational and Applied Mathematics, Rice University, Houston, TX 77005, USA

*Correspondence: jreimer@cns.bcm.edu (J.R.), atolias@cns.bcm.edu (A.S.T.)

<http://dx.doi.org/10.1016/j.neuron.2014.09.033>

SUMMARY

Neural responses are modulated by brain state, which varies with arousal, attention, and behavior. In mice, running and whisking desynchronize the cortex and enhance sensory responses, but the quiescent periods between bouts of exploratory behaviors have not been well studied. We found that these periods of “quiet wakefulness” were characterized by state fluctuations on a timescale of 1–2 s. Small fluctuations in pupil diameter tracked these state transitions in multiple cortical areas. During dilation, the intracellular membrane potential was desynchronized, sensory responses were enhanced, and population activity was less correlated. In contrast, constriction was characterized by increased low-frequency oscillations and higher ensemble correlations. Specific subtypes of cortical interneurons were differentially activated during dilation and constriction, consistent with their participation in the observed state changes. Pupillometry has been used to index attention and mental effort in humans, but the intracellular dynamics and differences in population activity underlying this phenomenon were previously unknown.

INTRODUCTION

Responses to external stimuli are strongly modulated by the brain's internal dynamics, which are organized around characteristic states that vary with arousal, attention, and behavioral context (Harris and Thiele, 2011; Iriki et al., 1996; Kahneman, 1973; Lee and Dan, 2012). Across multiple species, more active states are associated with cortical desynchronization, a reduction in the amplitude of low-frequency oscillations measured in EEG, LFP, or intracellular recordings. For example, primate cortex is more desynchronized during attentive states (Gould et al., 2011; Grent-t-Jong et al., 2011; Rohenkohl and Nobre, 2011) and in REM sleep compared to deeper sleep stages (Colten and Altevogt, 2006).

Nonprimate mammals also display a spectrum of cortical dynamics during waking periods, from more synchronized to more desynchronized states, and this internal variability modulates re-

sponses to external stimuli (Hei et al., 2014; Zhuang et al., 2014). Specifically, recent work in awake mice has revealed that the cortex is desynchronized during bouts of exploratory behavior, such as whisking (Crochet and Petersen, 2006; Poulet and Petersen, 2008) and running (Bennett et al., 2013; Niell and Stryker, 2010; Polack et al., 2013), compared to stationary periods. In mouse primary visual cortex (V1), this desynchronization is coupled with an enhancement of sensory responses (Fu et al., 2014; Froudarakis et al., 2014) and a reduction in detection thresholds (Bennett et al., 2013), and similar effects are seen in primary somatosensory cortex (area S1; Zagha et al., 2013).

Between bouts of activity, there are longer epochs of “quiet wakefulness,” periods of behavioral quiescence that have not been well studied. While previous reports have emphasized the average increase in low-frequency synchronous activity during quiet wakefulness, we observed second-to-second state fluctuations during these periods in both V1 and S1. Fast state fluctuations during quiet wakefulness were closely tracked by changes in pupil diameter. During dilation, we found that the cortex was desynchronized and more responsive to external stimuli, compared to constriction, when low-frequency oscillations were enhanced and ensemble correlations were increased. (In this study we always use “dilation” and “constriction” to refer to active dilating and constricting, and not the state of being dilated or constricted.) Furthermore, vasoactive intestinal peptide-expressing (VIP+) GABAergic interneurons and somatostatin-expressing (SOM+) interneurons were differentially modulated during dilation and constriction. These interneuron subtypes have recently been shown to participate in a canonical local circuit essential for the enhancement of visual responses during running (Fu et al., 2014), and our results suggest that this mechanism may be recapitulated in the state fluctuations that occur during quiet wakefulness.

RESULTS

Exploratory Behaviors Are Accompanied by Cortical Desynchronization and Pupil Dilation

We performed whole-cell patch-clamp recordings of layer 2/3 cortical neurons in awake mice ($n = 111$ total neurons from 38 animals) while monitoring treadmill motion, whisking behavior, eye movements, and pupil diameter (Figures 1A and 1B). All analyses in Figures 1, 2, and 3 were of spontaneous recordings, in order to avoid any confounding effects of visual stimuli. Periods of running, whisking, and eye movements usually occurred

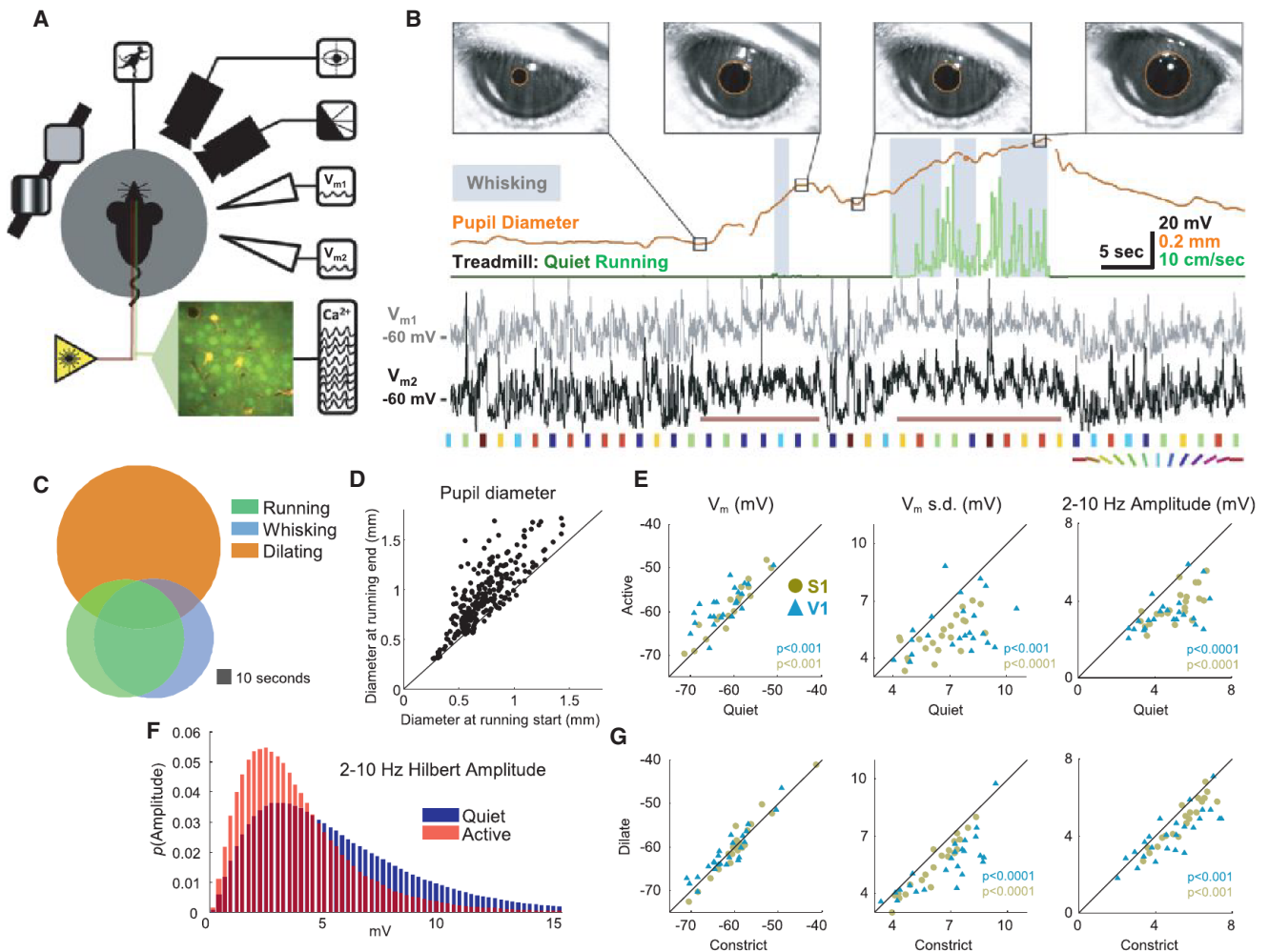


Figure 1. Pupil Diameter, Locomotion, and Whisking Correlate with Subthreshold Measures of Cortical State

(A) Schematic of simultaneous recordings showing mouse on spherical treadmill with eye and whisker cameras, single- or dual-patch pipettes, calcium imaging, and visual stimuli.

(B) Example treadmill activity (running periods in light green, see Supplemental Experimental Procedures), pupil diameter (orange), whisking (light blue background, see Supplemental Experimental Procedures), and V_m from two simultaneously patched cells (black and gray; depolarization around whisking and running epochs indicated with horizontal red lines). Colored patches below the voltage traces indicate presentations of oriented drifting gratings (Figure 4 only). Images of the eye are shown at the time points indicated in the pupil diameter trace, with pupil detection indicated by orange circles. Gaps in the pupil trace are due to blinks.

(C) Overlap of running, whisking, and pupil dilation episodes.

(D) Pupil size before and after running epochs.

(E) Changes in subthreshold membrane potential between quiet wakefulness and activity (running and whisking) without visual stimulation.

(F) Distribution of low-frequency amplitude during active behavior compared to quiet wakefulness.

(G) Changes in subthreshold membrane potential during dilating and constricting epochs of quiet wakefulness, also without visual stimuli. See also Figures S1 and S3 and Movie S1.

together (Figures 1C and S1; Movie S1), consistent with the idea that these behaviors are manifestations of a common exploratory state (Grant et al., 2012). Approximately 90% of these epochs were accompanied by an increase in pupil size (Figures 1B and 1D; mean increase in pupil diameter during running periods $202 \pm 11 \mu\text{m}$, mean \pm SEM; see Experimental Procedures).

Consistent with previous studies (Bennett et al., 2013; Crochet and Petersen, 2006; Niell and Stryker, 2010; Polack et al., 2013; Poulet and Petersen, 2008; Zagha et al., 2013), we found that during exploratory behaviors (running and/or whisking), the

membrane potential (V_m) in both S1 and V1 was desynchronized (red horizontal lines under example V1 recordings in Figure 1B). Relative to quiet wakefulness, V_m in these periods was depolarized (S1: $1.9 \pm 0.4 \text{ mV}$, $p < 0.001$; V1: $3.6 \pm 0.7 \text{ mV}$, $p < 0.001$) and less variable in V_m standard deviation, S1: $-1.4 \pm 0.2 \text{ mV}$, $p < 0.0001$; V1: $-1.7 \pm 0.4 \text{ mV}$, $p < 0.001$), and low-frequency oscillations were reduced (Hilbert amplitude of 2–10 Hz band-pass filtered V_m ; S1: $-1.4 \pm 0.2 \text{ mV}$, $p < 0.0001$; V1: $-1.3 \pm 0.2 \text{ mV}$, $p < 0.0001$; Figure 1E; mean difference \pm SEM; Wilcoxon signed-rank test for all comparisons). High-frequency

oscillations in the gamma range were also enhanced during activity compared to quiet wakefulness (Figure S1B), consistent with previous reports (Niell and Stryker, 2010).

During Quiet Epochs, Spontaneous Pupil Fluctuations Are a Sensitive Index of V_m Desynchronization

The large overlap in the amount of synchronous activity during active and quiet periods (Figure 1F) and the reliable increase in pupil size during the desynchronized periods associated with running and whisking led us to ask whether pupil dilation might also be associated with a desynchronized state during quiet wakefulness. To study quiet wakefulness, we excluded periods of running and whisking, and also saccades and blinks, which occurred rarely outside of active behaviors (less than one saccade per minute and less than one blink every 5 min; Figure S1A). We found that during quiet wakefulness, V_m variability was reduced during dilation versus constriction (change in V_m standard deviation, S1: -0.6 ± 0.08 mV, $p < 0.0001$; V1: -1.2 ± 0.2 mV, $p < 0.0001$). This effect could be explained primarily by a reduction in low-frequency oscillations (2–10 Hz Hilbert amplitude; S1: -0.56 ± 0.09 mV, $p < 0.001$; V1: -0.8 ± 0.2 mV, $p < 0.001$; Figure 1G; mean difference \pm SEM; Wilcoxon signed-rank test for all comparisons). A modest increase in V_m oscillations at higher (gamma) frequencies was also observed during dilation compared to constriction (Figure S1C). However, in contrast with the effects of running and whisking, mean V_m was not significantly different for dilation versus constriction.

Pupil fluctuations were much smaller and faster during quiet wakefulness than around bouts of exploratory behavior (Figures 2A–2C; Movies S1 and S2). The duration of individual dilation and constriction periods during quiet wakefulness varied, although in general dilation was faster than constriction (mean dilating duration 1.6 s, mean constricting duration 2.0 s; Figure S2). In order to characterize the time course of the change in synchronous activity relative to pupil fluctuations during quiet wakefulness, we binned the instantaneous 2–10 Hz Hilbert amplitude by the phase of the pupil trace at each time point, aligning multiple cycles of dilation and constriction to one canonical cycle. We found that the amplitude of low-frequency V_m oscillations reached a minimum toward the middle of the dilating phase and peaked during constriction (Figure 2D; plots are mean \pm SEM across cells). Overall, the average intracellular membrane potential was more desynchronized during dilation in both areas S1 and V1 (Figure 2E; S1 and V1, $p < 0.001$; paired t test; bars are mean change during dilation compared to constriction over cells, error bars are SEM; see also Figure S3). This relationship between cortical state and pupil fluctuations persisted even after removing occasional small postural adjustments or whisker twitches from our analysis and after habituating the mice to the treadmill for 30 min per day for 5 days prior to recording (Movie S1; Figure S4).

The robust link between pupil dilation and membrane potential desynchronization in area S1 argues against the possibility of a purely visual effect related to increased illumination of the retina. Although a small number of S1 cells (2/17) were weakly visually responsive (responsiveness generously defined as any significant change in V_m from baseline during a visual stimulus;

$\alpha = 0.05$, Wilcoxon signed-rank test), the majority of visually unresponsive S1 cells still showed a robust relationship between dilation and V_m desynchronization (10/15; Figure 2F). To further rule out the possibility that changes in the visual input alone were responsible for cortical desynchronization, we patched cells in V1 of 8-week- to 4-month-old FVB/NJ (FVB) mice. In these mice, the retinal ganglion cell layer undergoes severe degeneration by P21 (Chang et al., 2002). In contrast to wild-type mice, where most of the V1 cells were visually responsive (12/13), none of the patched cells (0/9) were visually responsive in FVB mice. Yet the relationship between pupil fluctuations and cortical state was also observed in these cells (Figures 2D–2F; $p < 0.05$ Wilcoxon signed-rank test; Figure 2E). We did not observe a significant difference in the effect across the three groups of cells (S1, V1, FVB; one-way ANOVA, $p = 0.53$).

To examine whether state changes were tracked more closely by dilation and constriction or by pupil diameter, we examined the correlation between V_m synchronization and the derivative and absolute size of the pupil (Figures 2G and 2H). We found that the amplitude of 2–10 Hz oscillations was more closely tracked by the derivative than diameter of the pupil (mean fraction of variance explained in a two-way ANOVA for each cell by derivative, 0.13; by diameter, 0.05; $p < 0.0001$, t test).

A Local Interneuron Circuit Participates in the State Changes Tracked by Pupil Fluctuation

Recently, Fu and colleagues found that VIP+ interneurons are activated during running, while SOM+ interneurons are inhibited (Fu et al., 2014), consistent with several recent studies showing that VIP+ cells directly inhibit SOM+ cells, producing a net disinhibition of nearby pyramidal neurons. Furthermore, Fu et al. demonstrated that this cortical circuit was both necessary and sufficient to produce the enhancement of visual responses observed during running.

We initially sought to replicate the effect of active behavior on these interneuron subtypes with targeted patch recordings of labeled VIP+ ($n = 6$) and SOM+ ($n = 30$) cells in V1. Consistent with Fu et al., 2014, VIP+ cells were robustly depolarized during running (4.6 ± 0.8 mV; $p < 0.05$ Wilcoxon signed-rank test; Figures 3B and 3C). However, the behavior of SOM+ cells was more complex. We found that our SOM+ Cre driver line (SST-IRES-Cre; Taniguchi et al., 2011) labeled a population of neurons that could be grouped into two distinct classes, which we call Type I and Type II. Type I SOM+ cells, which were the majority ($n = 21/30$), exhibited the characteristic low V_m variability described by Petersen and colleagues (Gentet et al., 2012), and these cells were inhibited during active epochs of running and whisking (-2.1 ± 0.47 mV; $p < 0.001$ Wilcoxon signed-rank test; Figures 3A and 3C; Figure S5). A smaller population of Type II-labeled SOM+ cells ($n = 7/30$) had intrinsic membrane properties more similar to VIP+ or PV+ cells, and these cells were depolarized during active epochs (3.5 ± 0.9 mV; $p < 0.01$ Wilcoxon signed-rank test; Figure S5). In many cases, we recorded from both types of labeled SOM+ cells in the same animal, and they were completely separable by a number of features, the simplest being the range of voltages spanned by V_m during recordings of spontaneous activity (Figure S5). Both

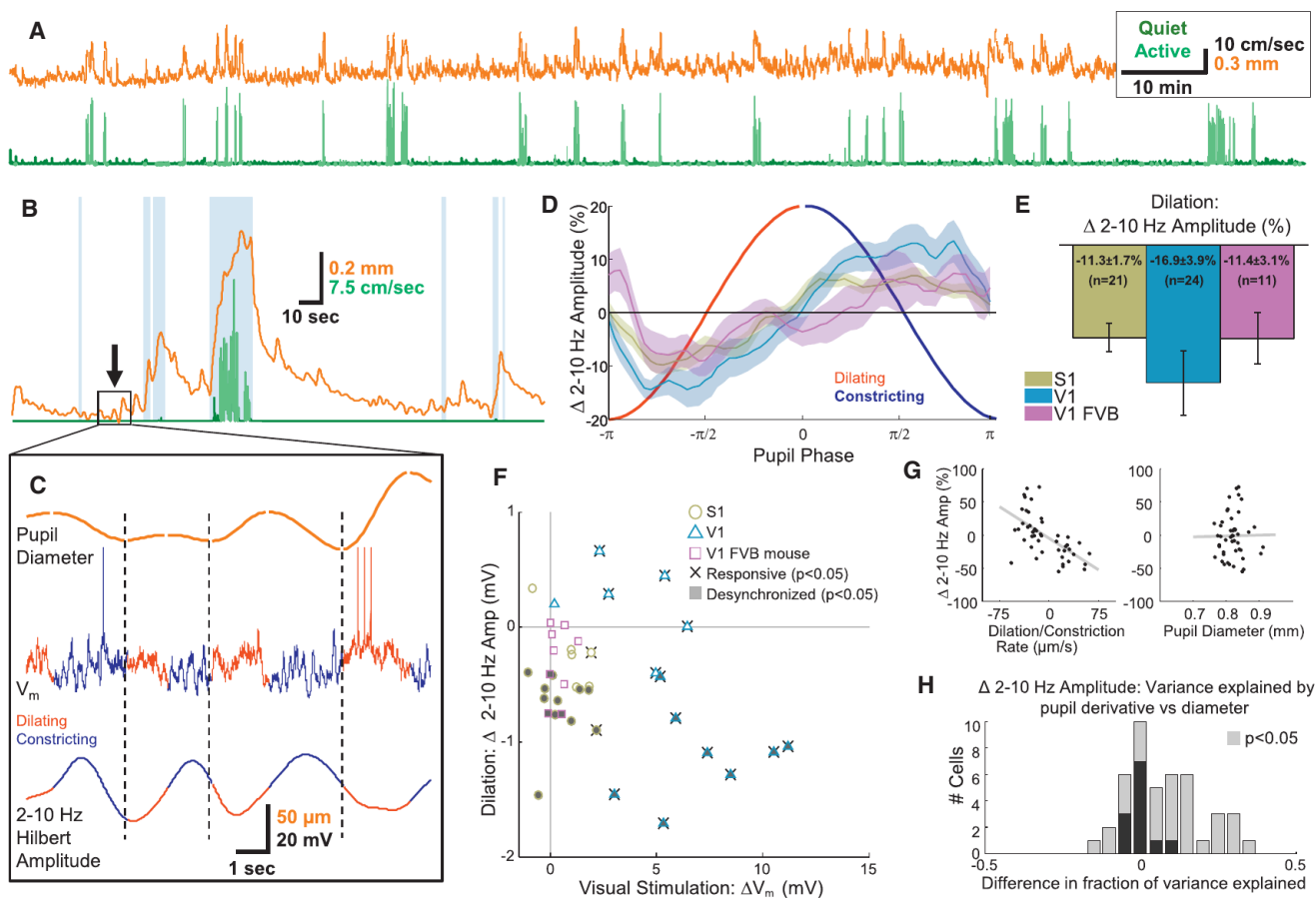


Figure 2. Pupil Diameter Correlates with Cortical State in the Absence of Exploratory Behavior

(A) Concatenated recordings of treadmill speed (running periods in light green, quiet periods in dark green) and pupil diameter (orange) from a single mouse (total time ~ 2.4 hr).

(B) Pupil diameter (orange) around a single active period (running in light green and whisking in light blue background).

(C) Zoomed-in period of quiet wakefulness from rectangle in (B) showing four sequential cycles of pupil dilation (red) and constriction (dark blue) correlated with low-frequency amplitude (separate cycles of dilation and constriction separated by dashed vertical lines).

(D) V_m is desynchronized during dilation and synchronized during constriction of the pupil in S1 (olive), V1 (blue), and V1 of FVB mice (mauve; 64 phase bins from $-\pi$ to π , plots are mean \pm SEM for each bin).

(E) Averages over entire dilation and constriction periods for cells in each area (bar plots are mean \pm SEM across cells, one-way ANOVA across cell groups was not significant $p = 0.53$).

(F) Scatterplot of desynchronization during dilation and visual responsiveness for all cells in each area. Significantly responsive cells are indicated with whiskers; significantly desynchronized cells are indicated with shading.

(G) Linear regression of the rate of change (left) and the absolute value of pupil diameter (right) against percent change in 2–10 Hz amplitude for a single cell.

(H) Stacked histogram of the difference in total variance in 2–10 Hz amplitude explained by pupil derivative and pupil diameter in a two-way ANOVA for each cell. Cells where either factor was significant ($p < 0.05$) are indicated with lighter bars. Overall, variations in cortical state indexed by low-frequency amplitude are more closely tracked by pupil dilation and constriction than by absolute pupil diameter ($p < 0.0001$, t test). See also Figures S2–S4 and Movie S2.

SOM+ Type I and Type II cells were distinct from morphologically identified (spiny) pyramidal cells, which were rarely labeled ($n = 2/56$), presumably due to leaky expression of Cre recombinase (Figure S5). Although the fact that the widely used SST-IRES-Cre line (Taniguchi et al., 2011) labels subpopulations of interneurons with different *in vivo* functional properties has not been previously reported, a recent *in vitro* study using these mice found two electrophysiologically distinct populations of labeled cells in almost the same proportions that we observed here (Hu et al., 2013). Based on these findings, we excluded Type II SOM+ cells in subsequent analyses.

Having confirmed the results of Fu et al. with respect to running, we wondered whether the SOM+/VIP+ cortical circuit might also participate in the state changes indexed by dilation and constriction during quiet wakefulness. Indeed, we found that VIP+ cells were relatively depolarized during dilation (2.1 ± 0.6 mV, $p < 0.05$) while SOM+ cells were hyperpolarized (-0.7 ± 0.3 mV, $p < 0.05$; Wilcoxon signed-rank test for all comparisons; Figures 3D and 3E). Our results support the view that the SOM+/VIP+ circuit is not only recruited during active behavior, but may also play a role in cortical state changes during quiet wakefulness.

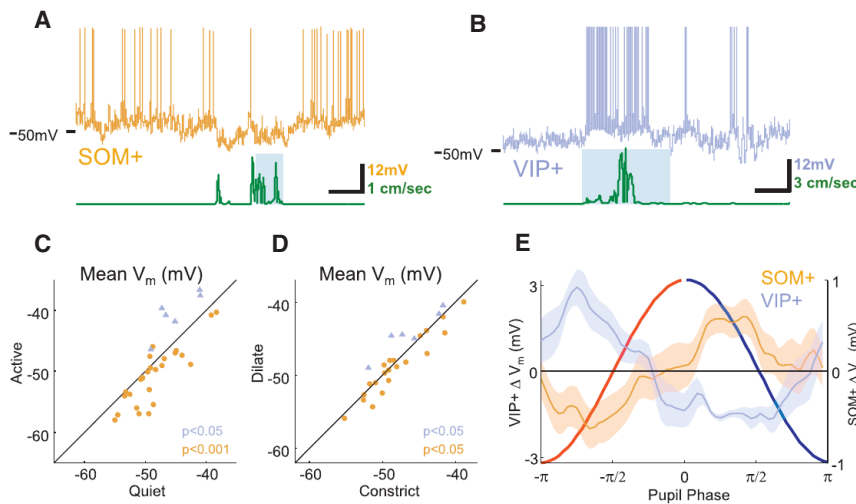


Figure 3. VIP+ Cells Are Excited and SOM+ Cells Are Inhibited during Active Behaviors and during Dilation

(A) Example SOM+ cell (brown) and treadmill (green) trace with whisking epoch as light blue rectangles in background. SOM+ cells are hyperpolarized during locomotion.

(B) Example VIP+ cell (blue) and treadmill (green) trace with whisking epoch as gray background. VIP+ activity is dramatically enhanced during running.

(C) Inhibition of SOM+ and excitation of VIP+ during exploratory behaviors compared to quiet wakefulness.

(D) In quiet wakefulness, SOM+ cells are inhibited and VIP+ cells are excited during dilation compared to constriction.

(E) Phase-binned change in SOM+ and VIP+ V_m showing time course of signature opposition of VIP+ and SOM+ activity over dilating and constricting periods (error bands are SEM).

Visual Encoding Is Improved during Desynchronized States Defined by Pupil Dilation

To determine whether stimulus encoding in V1 is improved during the desynchronized state indexed by pupil dilation, we performed two-photon calcium imaging of populations of layer 2/3 cells loaded with the calcium-sensitive fluorescent indicator Oregon Green BAPTA-1AM while presenting drifting oriented gratings (example site, Figures 4A and 4B; $n = 34$ imaging sites in six mice). We analyzed cells that were tuned for orientation (1,200/3,435 cells significantly tuned; see Experimental Procedures). During exploratory activity (running and whisking), there was a 20% increase in the mean response to preferred direction ($p < 10^{-12}$) and a 19% increase in the mean response to orthogonal directions ($p < 10^{-15}$; $n = 516$ tuned cells in 14 sites with sufficient numbers of visual responses during both active behavior and quiet wakefulness). These changes resulted in a slight decrease in orientation selectivity, but consistent with previous reports (Niell and Stryker, 2010; Polack et al., 2013), this change was not significant (7% decrease in OSI, $p = 0.07$; Figure 4C, error bands are SEM across cells). During quiet wakefulness, with running, whisking, and saccades removed, dilation was associated with a 9% increase in the mean response to preferred direction ($p < 10^{-13}$) and no change (0.6%, $p = 0.47$) in the response to the orthogonal direction, resulting in an enhancement of orientation selectivity (Figures 4D and 4E; 16% increase in OSI, $p < 10^{-6}$). Note that there was no significant difference in the size of the pupil between dilating and constricting trials (Figure S6). During dilation, responses to drifting gratings were also more reliable (Figure 4F; 28% increase in mean variability explained by stimulus conditions, $p < 10^{-15}$; $n = 619$ cells in 22 sites). Although there are a number of caveats that make it difficult to estimate the *absolute* magnitude of noise correlations using calcium imaging data (Cotton et al., 2013), we found that the relative magnitude of correlated activity varied significantly between the two states. There was a decrease in both signal and noise correlations during dilation versus constriction (Figures 4G and 4H; 20% decrease in mean noise correlations, $p < 0.0001$ and 16% decrease in mean signal correlations, $p < 0.01$; $n = 21$ sites,

paired t test used for all comparisons; see Experimental Procedures). In summary, we found that responses to drifting gratings were more selective, more reliable, and less correlated during dilation compared to constriction.

We next asked whether visual encoding of natural stimuli was also enhanced during desynchronized states indexed by pupil dilation. We presented multiple repetitions of short prerecorded movies from a head-mounted camera of a mouse navigating an enriched environment. We performed calcium imaging in V1 ($n = 53$ imaging sites in seven mice). In addition to excluding running and whisking periods, we also removed saccades and any epochs where the eye deviated by more than 10° from its mean position. Correlating neural activity directly with changes in pupil size was not possible in this experiment because differences in brightness across frames elicited reliable dilations and constrictions of the pupil across multiple repetitions of the movie ($r = 0.61$ correlation of pupil size across trials for one example recording session, Figure 5A). To account for the effects of frame-to-frame changes in luminance, we sorted the responses to each 150 ms segment of the movie by the rate of change of pupil diameter and compared the neural responses for the upper and lower quartiles of the rates of change within each time bin (Figure 5B). Here, we assumed that the average change in pupil size over multiple movie repetitions (gray trace in Figure 5B) was due to luminance changes in the stimulus, while the variability around this average (blue and red vertical lines in Figure 5B) reflected the trial-to-trial differences in cortical state. Thus, for each bin, we compared “high” trials, when the pupil was dilating faster than usual (or constricting slower than usual) to “low” trials, when the pupil was dilating slower (or constricting faster) than the average.

Visual responses were enhanced during high trials compared to low trials (example cell in Figure 5C). Consistent with the increased OSI we observed for oriented gratings, responses to preferred frames of the movie were selectively enhanced during high trials compared to low trials (Figures 5D and 5E). Again, the pupil was not larger during high trials than low trials (Figure S6). At the population level, both signal (Figure 5F; $p < 0.001$) and

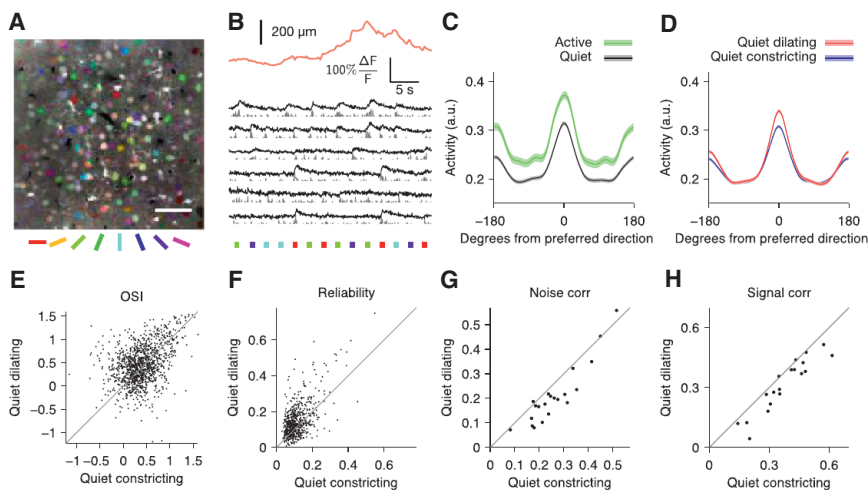


Figure 4. Orientation Tuning Is Enhanced during Pupil Dilation

(A) Mean fluorescence image colored by orientation preferences of individual pixels; scale bar, 50 μm .

(B) Example pupil diameter trace (orange) with simultaneous calcium traces from segmented cells (black) and inferred firing rates (gray). Colored squares indicate the direction of drifting gratings. (C) Average tuning curves aligned to cells' preferred direction for active (running and/or whisking) periods (green) and quiet (black) periods. Peak responses are increased (20%, $p < 10^{-12}$) and orientation selectivity is unchanged (7% decrease, $p = 0.07$). Error bands are SEM computed over cells ($n = 516$).

(D) Average tuning during pupil dilation (red) and constriction (blue) during quiet periods (excluding running and whisking).

(E–H) Orientation selectivity is increased during dilation compared to constriction (16% increase in

mean OSI, $p < 10^{-6}$) (E). Cells also respond more reliably during dilation compared to constriction (28% increase in mean binned R^2 values of stimulus responses of individual cells, $p < 10^{-15}$) (F). Across populations of neurons, mean noise correlations (G) ($p < 10^{-4}$) and signal correlations (H) ($p < 0.01$) are reduced during pupil dilation ($n = 21$ sites). Paired t test for all comparisons. Reliability and correlations are computed on 150 ms bins during stimulus presentations (see Supplemental Experimental Procedures).

noise (Figure 5G; $p < 0.05$) correlations were reduced, and there was an increase in the reliability (Figure 5H; $p < 0.001$) and discriminability (Figure 5I; $p < 0.001$) of responses during high trials compared to low trials (t test for all comparisons). In summary, consistent with the enhancement of responses to drifting gratings during dilation, responses to natural movies were more selective, more reliable, and less correlated during high trials.

DISCUSSION

We performed whole-cell patching and two-photon calcium imaging in awake mice (Bennett et al., 2013; Niell and Stryker, 2010; Polack et al., 2013) and focused our analysis on quiet periods between epochs of running and whisking. During these periods, we observed small spontaneous fluctuations in pupil diameter on a timescale of 1–2 s, which tracked changes in intracellular dynamics of L2/3 neurons in both somatosensory (S1) and visual (V1) cortex. V_m was desynchronized while the pupil was dilating and was dominated by low-frequency oscillations while the pupil was constricting. Dilation was accompanied by activation of VIP+ and inhibition of SOM+ interneurons, a phenomenon that has been shown to be essential to the enhanced visual responses observed during running (Fu et al., 2014). Using two-photon calcium imaging, we found that dilation was associated with an enhancement of visual responses and a reduction in both noise and signal correlations across ensembles of neurons for both gratings and natural stimuli.

For almost half a century, pupillometry has been widely used to index covert changes in attention and effort in humans and nonhuman primates (Gilzenrat et al., 2010; Hess and Polt, 1960, 1964; Iriki et al., 1996; Kahneman, 1973; Kahneman and Beatty, 1966; Kristjansson et al., 2009; Onorati et al., 2013; Wierda et al., 2012). Surprising and provocative stimuli produce a transient increase in pupil size (Bradley et al., 2008; Hess and Polt, 1960, 1964; Libby et al., 1973; Preusschoff et al., 2011), and

pupil dilation preceding stimulus onset is correlated with faster reaction times in psychophysical tasks (Kristjansson et al., 2009). Our results provide evidence of changes in intracellular membrane potential dynamics and neural population activity underlying these psychophysical effects and emphasize the utility of pupil dilation and constriction as a proxy for noninvasively monitoring internal cortical states.

Previous authors have pointed out the analogy between desynchronization and enhanced sensory encoding during attention in primates, and the changes in cortical state during exploratory behaviors in mice (Harris and Thiele, 2011). Our results suggest that this analogy may be extended further, to encompass fluctuations in brain state in mice in the absence of overt behavioral changes. The ability to leverage mouse genetics to study the mechanisms that produce these state changes will be valuable, as will the ability to examine the potential dysregulation of brain state in mouse models of human disease.

Intracellular signatures of cortical activation were linked to pupil dilation across multiple cortical areas, suggesting that the effects we observe reflect a global change in brain state. Given the close relationship between pupil diameter, locus coeruleus activity, and sympathetic tone (Aston-Jones et al., 1999; Bradley et al., 2008; Gilzenrat et al., 2010), our data suggest a role for norepinephrine in the regulation of cortical state. Consistent with this notion, a recent study has implicated norepinephrine in the desynchronization that occurs during running (Polack et al., 2013). However, the potential contribution of other neuromodulators such as acetylcholine (Goard and Dan, 2009; Pinto et al., 2013) is also strongly suggested by the fact that the VIP+ activation during running has been shown to depend on cholinergic input from the diagonal band of Broca (Fu et al., 2014).

Additional mechanisms may also contribute to the state changes we describe here, which differ in at least two important ways from the state associated with exploratory behavior: First, unlike the effects of running, the desynchronization during

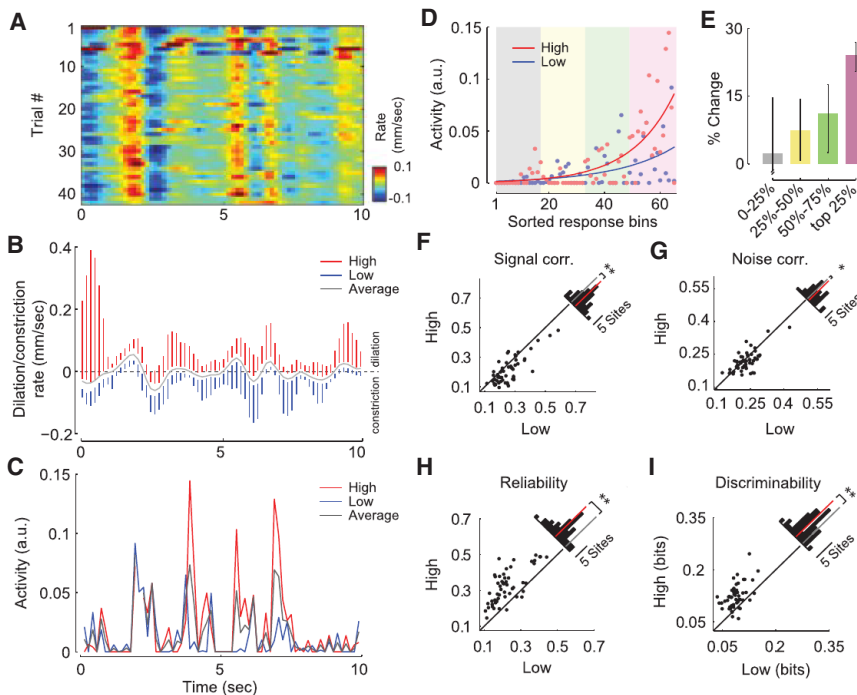


Figure 5. Encoding of Natural Images Is Improved during Pupil Dilation

(A) Pupil dilation/constriction rates across multiple repetitions of a natural movie. (B) Mean (gray) and range in upper and lower quartiles (red and blue, respectively) of the pupil dilation/constriction rate for multiple presentations of a single movie (150 ms bins). Subsequent analyses compare neural responses in the upper quartile of pupil dilation/constriction rates (“high”) to the lower quartile (“low”). (C) Increase in mean activity during high trials compared to low trials for a single cell. (D) For each cell, movie frames are sorted by the mean neural response, not considering pupil dilation and constriction. Responses in high (red dots) and low (blue dots) conditions are fit with an exponential function (solid red and blue lines) to illustrate the selective increase in response to preferred stimuli. (E) Median change in firing rate in high trials compared to low trials ($n = 467$ neurons, 95% confidence intervals) for least preferred (0%–25%), intermediate (25%–50% and 50%–75%), and most-preferred (75%–100%) frames for each cell. Responses to preferred frames are selectively enhanced. (F–I) Mean signal (F) and noise (G) correlations decreased during the high condition, while reliability (H) and discriminability (I) were enhanced. Insets show histograms of absolute change with red bar indicating the mean difference ($n = 53$ sites, $**p < 0.001$, $*p < 0.05$, t test).

dilation is not accompanied by a significant depolarization of V_m . Second, we observe a qualitative difference in the effect of state on orientation tuning. During running, visual responses are enhanced at all orientations, while during dilation, responses at preferred orientations are enhanced without changing responses at orthogonal orientations, resulting in an increase in orientation selectivity. Further work will be necessary to uncover the mechanisms underlying these differences.

It is interesting to consider the potential computational role of continuous fluctuations in state during behaviorally quiescent periods. We speculate that during quiet wakefulness, the cortex may rapidly alternate between two distinct modes of information processing: a desynchronized state characterized by improved representation of feedforward sensory information and a synchronized state dominated by internally generated low-frequency network oscillations. Interestingly, theoretical work has suggested that alternating between bottom-up and top-down processing may be an efficient learning mechanism for the cortex to build a representation of the external world (Hinton, 2010).

EXPERIMENTAL PROCEDURES

All procedures were approved by the Institutional Animal Care and Use Committee (IACUC) of Baylor College of Medicine. Briefly, mice were anesthetized and a 3 mm craniotomy was made over the cortex as previously described (Froudarakis et al., 2014). For calcium imaging experiments, OGB1-AM was injected before sealing the craniotomy with a glass coverslip, which in some cases was prepared with a small (~ 500 μm) hole to allow pipette access. Following surgery, the mouse was placed on a treadmill with its head restrained beneath the microscope objective. Locomotion was detected by treadmill movement, and eye and whisker movements were detected optically. Whole-cell *in vivo* patching was performed using borosilicate patch pipettes (6–10

M Ω) filled with a standard low Cl^- internal solution (Jiang et al., 2013) as well as Alexa 488 or 598 for visualization. Visual stimuli were as follows: Figures 1, 2, and 3, blank screen; Figure 4, full-field square wave gratings (0.04 cycles/degree at 2 Hz, 500 ms trials interleaved with 1 s luminance-matched blanks, 100 repeats \times 8 orientations); Figure 5, natural scene movies collected as previously described (Froudarakis et al., 2014). Calcium imaging was performed using either a standard galvo-galvo (Sutter Instruments) or resonant scanner (Thor Labs) using a Ti-Sapphire laser (Coherent) exciting at either 800 or 1,000 nm and equipped with either a 20 \times (1.0 NA, Olympus) or 25 \times (1.1 NA, Nikon) objective lens. Imaging data were motion-corrected and cell segmentation was manually supervised. A more detailed description of all experimental procedures can be found online in our Supplemental Experimental Procedures.

SUPPLEMENTAL INFORMATION

Supplemental Information includes Supplemental Experimental Procedures, six figures, and two movies and can be found with this article online at <http://dx.doi.org/10.1016/j.neuron.2014.09.033>.

AUTHOR CONTRIBUTIONS

J.R. collected and analyzed patching and calcium imaging data, performed pupil segmentation in all videos, and helped organize results and prepare the manuscript. E.F. helped build the behavioral apparatus and collected and analyzed calcium imaging data with natural movie stimuli. C.R.C. contributed to writing the paper and helped guide analyses. D.Y. created the Data-Joint framework for data organization and analyzed calcium imaging data for oriented gratings. G.H.D. collected data and helped with manuscript revisions. A.S.T. supervised experiments, analysis, and preparation of the manuscript. E.F., C.R.C., and D.Y. contributed equally to this project.

ACKNOWLEDGMENTS

This work was supported by grants P30EY002520, T32EY07001, R01DA028525, DP1EY023176, and DP1OD008301 to A.S.T.; the McKnight

Scholar Award to A.S.T.; the Arnold & Beckman Foundation Young Investigator Award to A.S.T.; grants F30MH095440 and T32GM007330 to C.R.C.; and grant T32EB006350 to C.R.C. and D.Y. We thank Xiaolong Jiang for sharing his expertise in *in vivo* patching; Megan Rech, James Cotton, and Ryan Ash for helpful comments on the manuscript; and Ben Arenkiel for sharing the SST-IRES-Cre mouse line.

Accepted: September 22, 2014

Published: October 22, 2014

REFERENCES

- Aston-Jones, G., Rajkowski, J., and Cohen, J. (1999). Role of locus coeruleus in attention and behavioral flexibility. *Biol. Psychiatry* **46**, 1309–1320.
- Bennett, C., Arroyo, S., and Hestrin, S. (2013). Subthreshold mechanisms underlying state-dependent modulation of visual responses. *Neuron* **80**, 350–357.
- Bradley, M.M., Miccoli, L., Escrig, M.A., and Lang, P.J. (2008). The pupil as a measure of emotional arousal and autonomic activation. *Psychophysiology* **45**, 602–607.
- Chang, B., Hawes, N.L., Hurd, R.E., Davisson, M.T., Nusinowitz, S., and Heckenlively, J.R. (2002). Retinal degeneration mutants in the mouse. *Vision Res.* **42**, 517–525.
- Colten, H.R., and Altevogt, B.M., eds. (2006). *Sleep Disorders and Sleep Deprivation: An Unmet Public Health Problem* (Washington, DC: National Academies Press).
- Cotton, R.J., Froudarakis, E., Storer, P., Saggau, P., and Tolias, A.S. (2013). Three-dimensional mapping of microcircuit correlation structure. *Front Neural Circuits* **7**, 151.
- Crochet, S., and Petersen, C.C.H. (2006). Correlating whisker behavior with membrane potential in barrel cortex of awake mice. *Nat. Neurosci.* **9**, 608–610.
- Froudarakis, E., Berens, P., Ecker, A.S., Cotton, R.J., Sinz, F.H., Yatsenko, D., Saggau, P., Bethge, M., and Tolias, A.S. (2014). Population code in mouse V1 facilitates readout of natural scenes through increased sparseness. *Nat. Neurosci.* **17**, 851–857.
- Fu, Y., Tucciarone, J.M., Espinosa, J.S., Sheng, N., Darcy, D.P., Nicoll, R.A., Huang, Z.J., and Stryker, M.P. (2014). A cortical circuit for gain control by behavioral state. *Cell* **156**, 1139–1152.
- Gentet, L.J., Kremer, Y., Taniguchi, H., Huang, Z.J., Staiger, J.F., and Petersen, C.C.H. (2012). Unique functional properties of somatostatin-expressing GABAergic neurons in mouse barrel cortex. *Nat. Neurosci.* **15**, 607–612.
- Gilzenrat, M.S., Nieuwenhuis, S., Jepma, M., and Cohen, J.D. (2010). Pupil diameter tracks changes in control state predicted by the adaptive gain theory of locus coeruleus function. *Cogn. Affect. Behav. Neurosci.* **10**, 252–269.
- Goard, M., and Dan, Y. (2009). Basal forebrain activation enhances cortical coding of natural scenes. *Nat. Neurosci.* **12**, 1444–1449.
- Gould, I.C., Rushworth, M.F., and Nobre, A.C. (2011). Indexing the graded allocation of visuospatial attention using anticipatory alpha oscillations. *J. Neurophysiol.* **105**, 1318–1326.
- Grant, R.A., Mitchinson, B., and Prescott, T.J. (2012). The development of whisker control in rats in relation to locomotion. *Dev. Psychobiol.* **54**, 151–168.
- Grent-’t-Jong, T., Boehler, C.N., Kenemans, J.L., and Woldorff, M.G. (2011). Differential functional roles of slow-wave and oscillatory- α activity in visual sensory cortex during anticipatory visual-spatial attention. *Cereb. Cortex* **21**, 2204–2216.
- Harris, K.D., and Thiele, A. (2011). Cortical state and attention. *Nat. Rev. Neurosci.* **12**, 509–523.
- Hei, X., Stoelzel, C.R., Zhuang, J., Bereshpolova, Y., Huff, J.M., Alonso, J.M., and Swadlow, H.A. (2014). Directional selective neurons in the awake LGN: response properties and modulation by brain state. *J. Neurophysiol.* **112**, 362–373.
- Hess, E.H., and Polt, J.M. (1960). Pupil size as related to interest value of visual stimuli. *Science* **132**, 349–350.
- Hess, E.H., and Polt, J.M. (1964). Pupil Size in Relation to Mental Activity during Simple Problem-Solving. *Science* **143**, 1190–1192.
- Hinton, G.E. (2010). Learning to represent visual input. *Philos. Trans. R. Soc. Lond. B Biol. Sci.* **365**, 177–184.
- Hu, H., Cavendish, J.Z., and Agmon, A. (2013). Not all that glitters is gold: off-target recombination in the somatostatin-IRES-Cre mouse line labels a subset of fast-spiking interneurons. *Front Neural Circuits* **7**, 195.
- Iriki, A., Tanaka, M., and Iwamura, Y. (1996). Attention-induced neuronal activity in the monkey somatosensory cortex revealed by pupillometrics. *Neurosci. Res.* **25**, 173–181.
- Jiang, X., Wang, G., Lee, A.J., Stornetta, R.L., and Zhu, J.J. (2013). The organization of two new cortical interneuronal circuits. *Nat. Neurosci.* **16**, 210–218.
- Kahneman, D. (1973). *Attention and Effort*. (Englewood Cliffs, NJ: Prentice-Hall Inc.).
- Kahneman, D., and Beatty, J. (1966). Pupil diameter and load on memory. *Science* **154**, 1583–1585.
- Kristjansson, S.D., Stern, J.A., Brown, T.B., and Rohrbaugh, J.W. (2009). Detecting phasic lapses in alertness using pupillometric measures. *Appl. Ergon.* **40**, 978–986.
- Lee, S.-H., and Dan, Y. (2012). Neuromodulation of brain states. *Neuron* **76**, 209–222.
- Libby, W.L., Jr., Lacey, B.C., and Lacey, J.I. (1973). Pupillary and cardiac activity during visual attention. *Psychophysiology* **10**, 270–294.
- Niell, C.M., and Stryker, M.P. (2010). Modulation of visual responses by behavioral state in mouse visual cortex. *Neuron* **65**, 472–479.
- Onorati, F., Barbieri, R., Mauri, M., Russo, V., and Mainardi, L. (2013). Characterization of affective states by pupillary dynamics and autonomic correlates. *Front Neuroeng* **6**, 9.
- Pinto, L., Goard, M.J., Estandian, D., Xu, M., Kwan, A.C., Lee, S.H., Harrison, T.C., Feng, G., and Dan, Y. (2013). Fast modulation of visual perception by basal forebrain cholinergic neurons. *Nat. Neurosci.* **16**, 1857–1863.
- Polack, P.-O., Friedman, J., and Golshani, P. (2013). Cellular mechanisms of brain state-dependent gain modulation in visual cortex. *Nat. Neurosci.* **16**, 1331–1339.
- Poulet, J.F.A., and Petersen, C.C.H. (2008). Internal brain state regulates membrane potential synchrony in barrel cortex of behaving mice. *Nature* **454**, 881–885.
- Preuschhoff, K., ’t Hart, B.M., and Einhäuser, W. (2011). Pupil Dilation Signals Surprise: Evidence for Noradrenaline’s Role in Decision Making. *Front Neurosci* **5**, 115.
- Rohenkohl, G., and Nobre, A.C. (2011). α oscillations related to anticipatory attention follow temporal expectations. *J. Neurosci.* **31**, 14076–14084.
- Taniguchi, H., He, M., Wu, P., Kim, S., Paik, R., Sugino, K., Kvitsiani, D., Fu, Y., Lu, J., Lin, Y., et al. (2011). A resource of Cre driver lines for genetic targeting of GABAergic neurons in cerebral cortex. *Neuron* **71**, 995–1013.
- Wierda, S.M., van Rijn, H., Taatgen, N.A., and Martens, S. (2012). Pupil dilation deconvolution reveals the dynamics of attention at high temporal resolution. *Proc. Natl. Acad. Sci. USA* **109**, 8456–8460.
- Zagha, E., Casale, A.E., Sachdev, R.N., McGinley, M.J., and McCormick, D.A. (2013). Motor cortex feedback influences sensory processing by modulating network state. *Neuron* **79**, 567–578.
- Zhuang, J., Bereshpolova, Y., Stoelzel, C.R., Huff, J.M., Hei, X., Alonso, J.M., and Swadlow, H.A. (2014). Brain state effects on layer 4 of the awake visual cortex. *J. Neurosci.* **34**, 3888–3900.

Distinct Tau Prion Strains Propagate in Cells and Mice and Define Different Tauopathies

David W. Sanders,^{1,4} Sarah K. Kaufman,^{1,4} Sarah L. DeVos,¹ Apurwa M. Sharma,¹ Hilda Mirbaha,¹ Aimin Li,¹ Scarlett J. Barker,¹ Alex C. Foley,³ Julian R. Thorpe,³ Louise C. Serpell,³ Timothy M. Miller,¹ Lea T. Grinberg,² William W. Seeley,² and Marc I. Diamond^{1,*}

¹Department of Neurology, Washington University in St. Louis, St. Louis, MO 63105, USA

²Department of Neurology and Pathology, University of California, San Francisco, San Francisco, CA 94143, USA

³School of Life Sciences, University of Sussex, Falmer BN1 9QG, UK

⁴Co-first author

*Correspondence: diamondm@neuro.wustl.edu

<http://dx.doi.org/10.1016/j.neuron.2014.04.047>

SUMMARY

Prion-like propagation of tau aggregation might underlie the stereotyped progression of neurodegenerative tauopathies. True prions stably maintain unique conformations (“strains”) in vivo that link structure to patterns of pathology. We now find that tau meets this criterion. Stably expressed tau repeat domain indefinitely propagates distinct amyloid conformations in a clonal fashion in culture. Reintroduction of tau from these lines into naive cells reestablishes identical clones. We produced two strains in vitro that induce distinct pathologies in vivo as determined by successive inoculations into three generations of transgenic mice. Immunopurified tau from these mice recreates the original strains in culture. We used the cell system to isolate tau strains from 29 patients with 5 different tauopathies, finding that different diseases are associated with different sets of strains. Tau thus demonstrates essential characteristics of a prion. This might explain the phenotypic diversity of tauopathies and could enable more effective diagnosis and therapy.

INTRODUCTION

Tauopathies are a diverse group of neurodegenerative diseases defined by accumulation of fibrillar deposits of the microtubule-associated protein tau (MAPT) (Lee et al., 2001). Alzheimer’s disease (AD), the most common tauopathy, affects >30 million people worldwide and will afflict >120 million by 2050 (Holtzman et al., 2011). *MAPT* mutations cause dominantly inherited tauopathies (Hutton et al., 1998) and most increase the propensity of tau to form amyloids (Barghorn et al., 2000), which are paracrystalline protein assemblies rich in beta-sheet structure (Bonar et al., 1969). Most tauopathy cases are sporadic, with variable clinical and pathological presentation (Lee et al., 2001).

The prion hypothesis posits that pathological aggregates of the mammalian prion protein (PrP) cause infectious, sporadic,

and familial neurodegenerative diseases (Prusiner, 1998). In contrast, yeast prions are adaptive and confer phenotypic diversity and rapid evolution of new traits in times of stress (True and Lindquist, 2000). Both yeast and mammalian prions form strains, which are encoded by distinct fibrillar structures (Safar et al., 1998; Toyama et al., 2007). Prion strains determine the incubation periods of disease in humans (Kim et al., 2012) and mice (Legname et al., 2006). In addition, human prion strains are thought to underlie clinical symptoms and pathological presentation (Collinge and Clarke, 2007).

The hypothesis that common neurodegenerative diseases such as AD could be caused by a prion-like mechanism was suggested three decades ago (Prusiner, 1984). Recently, however, experimental work on diverse amyloids has generated new interest (Frost and Diamond, 2010; Guo and Lee, 2014). Human neurodegenerative diseases target unique neural networks (Braak and Braak, 1995; Seeley et al., 2009), an observation most parsimoniously explained by the network-based spread of a toxic agent (Raj et al., 2012; Zhou et al., 2012). Prior studies suggest that tau aggregates spread among cells via templated conformational change (Frost et al., 2009a; Holmes et al., 2013). In vivo work supports this model (Clavaguera et al., 2009; de Calignon et al., 2012; Iba et al., 2013; Kim et al., 2010; Liu et al., 2012) as has similar work with other intracellular amyloids such as α -synuclein (Desplats et al., 2009; Luk et al., 2012) and extracellular amyloids including amyloid β (Meyer-Luehmann et al., 2006).

Bona fide prions are defined by propagation of distinct conformational strains in vivo, and prior studies have hinted at prion-like strain properties of non-PrP human amyloids. For example, amyloid β protein forms at least two distinct, self-propagating fibrillar conformations in vitro (Petkova et al., 2005) and in vivo (Lu et al., 2013). Others have demonstrated propagation in vitro of distinct tau (Frost et al., 2009b; Siddiqua and Margittai, 2010) and α -synuclein conformers (Bousset et al., 2013; Guo et al., 2013; Sacino et al., 2013). While provocative, these prior studies have not demonstrated that noninfectious proteopathic seeds act as true prions. Specifically, it has not been shown that distinct conformations or “strains” are capable of transmission into a living cell or organism, propagation through multiple generations, extraction, and reintroduction to naive cells or organisms to replicate the same structural phenotype (Collinge

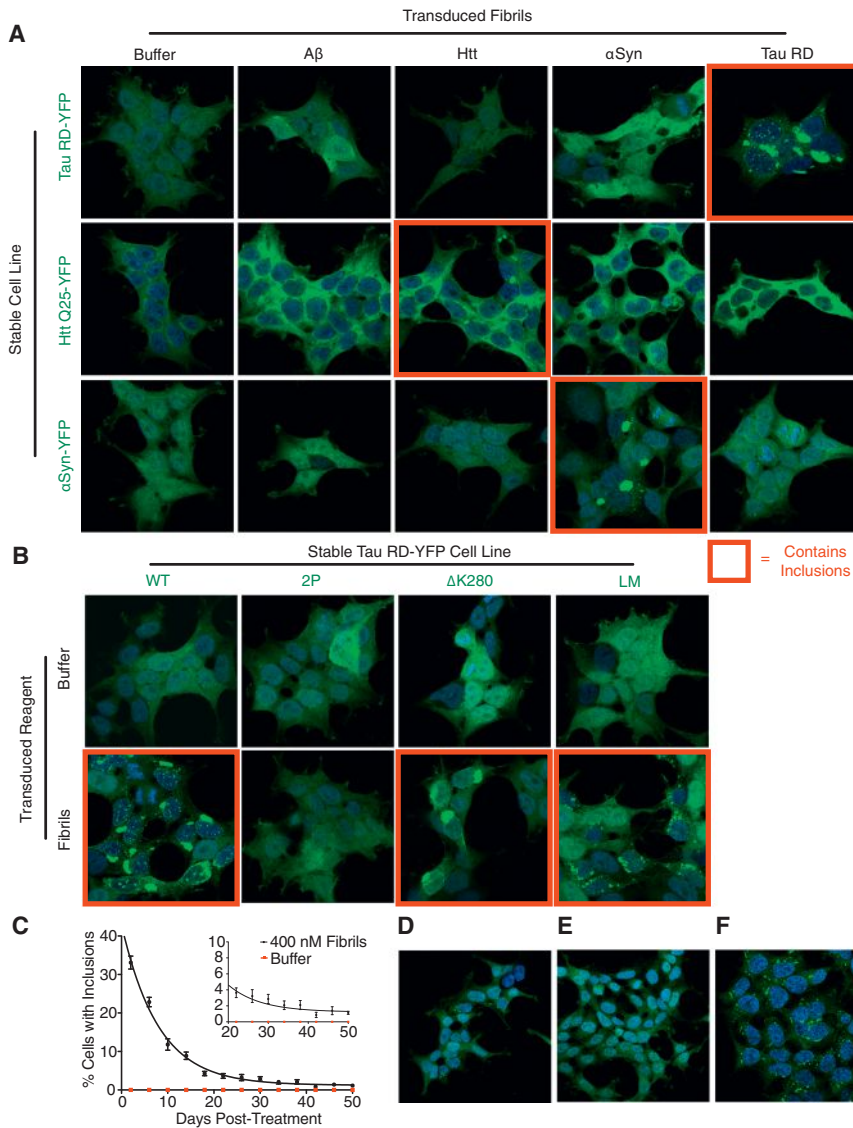


Figure 1. Homotypic Seeding Produces Stably Propagated Tau RD Inclusions

(A) Polyclonal HEK293 lines stably expressing YFP-tagged tau RD, α -synuclein, or htt exon1(Q25) were transduced with buffer, or fibrils of A β , Htt, α -syn, or tau RD. Cells were DAPI-stained on day 6. Only homotypic seeding occurred. See Figure S1A for construct diagrams, Figure S1B for quantification, and Figures S1C and S1D for similar homotypic seeding with full-length (FL) 4R1N tau P301S.

(B) Polyclonal HEK293 lines stably expressing tau RD-YFP with no mutations (WT), Δ K280 (proaggregation), Δ K280/I277P/I308P (2P; anti-aggregation), or P301L/V337M (LM; proaggregation) were transduced with either buffer or tau RD fibrils. Upon fibril transduction, all form inclusions, except for 2P.

(C) Tau RD(LM)-YFP cells transduced with either buffer or tau RD fibrils were passaged every two days. On every other passage, the percentage of cells with inclusions was quantified (n = 10 fields, each with 150+ cells per condition). Inset highlights inclusion-positive cells at later time points. Error bars represent SEM.

(D) At day 50 following exposure to fibrils, inclusion-positive cells were visible.

(E and F) At day 3 following exposure to fibrils, tau RD(LM)-YFP cells were diluted sparsely on coverslips and grown for 8 days. Colonies were either 100% inclusion-negative (E) or 100% inclusion-positive (F).

and Clarke, 2007). This is important not for semantic reasons, but because if prion mechanisms underlie human disease, only stably propagating strains can account for stereotyped clinical presentation and network spread. In this study, we have found that tau acts as a prion by these criteria, and, further, that individual human tauopathies are associated with unique strains.

RESULTS

Homotypic Seeding of Tau Depends on Beta-Sheet Structure

Amino acid sequence disparities impair cross-seeding between PrP moieties from different species, leading to “seeding barriers” (Collinge and Clarke, 2007). To test the fidelity of hetero- versus homotypic seeding for tau, we expressed several amyloidogenic proteins and exposed them to a variety of fibrillar seeds. Prolonged expression of full-length (FL) tau can be toxic to dividing cells. Thus for tau, we expressed the aggregation-

competent core, termed the repeat domain (tau RD; aa 244–372 of the 441 aa FL tau 4R2N) (Wischik et al., 1988). We generated polyclonal HEK293 cell lines stably expressing tau RD-YFP, α -synuclein-YFP, or huntingtin (htt) exon 1(Q25)-YFP (see Figure S1A for construct diagrams). Inclusions did not occur in any line without exposure to exogenous fibrils. However, upon transduction of fibrils (A β [1–42], htt exon 1 N17[Q35], α -synuclein, tau RD) with liposomes, we observed homotypic but not heterotypic seeding for each amyloidogenic protein (Figure 1A; Figure S1B for quantification), consistent with sequence-specific templating. Prior reports have indicated that in certain cases, α -synuclein aggregates can cross-seed FL tau (Giasson et al., 2003; Guo et al., 2013; Waxman and Giasson, 2011). Thus, we tested this for both YFP-tagged and untagged versions of FL tau 4R1N P301S. We observed only homotypic seeding and no cross-seeding of tau by α -synuclein or any other amyloid (Figures S1C and S1D). This is consistent with sequence-specific templating, although we cannot rule out the possibility that different amyloid conformers are capable of heterologous seeding, as has previously been reported (Guo et al., 2013).

Amyloids typically feature a cross beta-sheet conformation (Bonar et al., 1969). We exploited two proline substitutions (I277P/I308P) in tau that block its ability to enter into this

quaternary form (von Bergen et al., 2001) to test whether inclusion formation requires this property. Polyclonal HEK293 cell lines stably expressing tau RD-YFP with no mutations (wild-type, WT), P301L/V337M (LM: proaggregation), Δ K280 (proaggregation), or Δ K280/I277P/I308P (2P: antiaggregation) were transduced with tau RD fibrils. All formed inclusions except tau RD(2P)-YFP, confirming that beta-sheet structure is required for tau RD inclusion formation in our model system (Figure 1B).

Stable Inheritance of Tau RD Aggregates

Seeded htt exon 1 (Ren et al., 2009), Sup35NM (Krammer et al., 2009), SOD1 (Münch et al., 2011), and α -synuclein (Bousset et al., 2013) form persistent intracellular inclusions in cultured cells. We tested this for tau RD. We transduced tau RD fibrils or buffer into polyclonal tau RD(LM)-YFP (hereafter, referred to as tau RD) cells, chosen for their superior ability to be seeded relative to tau RD(WT)-YFP, and quantified the percentage of cells with inclusions on every other passage. Transduced fibrils induced tau RD inclusions that persisted >50 days postexposure (Figure 1C). We hypothesized that the aggregated state was stably inherited because inclusion-containing cells formed local clusters (Figure 1D). To test this, we sparsely diluted fibril-transduced tau RD cells to isolate individual colonies. These were composed of either 100% inclusion-negative (Figure 1E) or 100% inclusion-positive (Figure 1F) cells, indicating stable inheritance of the aggregated state.

Tau RD Propagates Conformationally Distinct Strains

Only prion protein (PrP) (Birkett et al., 2001) and certain fungal prions (e.g., Sup35 [PSI⁺]) (Derkatch et al., 1996) unequivocally propagate distinct conformational states, or strains, in cell culture. To test the ability of tau RD to propagate distinct conformers, we diluted fibril-transduced monoclonal tau RD cells and isolated individual clones that stably propagated inclusions (Figure 2A). Previous work with the Sup35 protein has indicated that inclusion morphology is a proxy for biochemically distinct yeast prion strains in dividing mammalian cells (Krammer et al., 2009). We thus characterized 20 tau RD clones based on inclusion morphology, numbered in order of isolation. Most (Figure S2A) featured small juxtanuclear inclusions with many nuclear speckles, exemplified by clone 9 (Figure 2B). Clone 10 alone propagated a single, large juxtanuclear inclusion (Figure 2B). We confirmed that stably propagated tau RD inclusions were amyloids as clones 9 and 10, but not inclusion-negative clone 1, bound X-34, a Congo red derivative that stains beta-sheet structures (Figure 2C).

To characterize the clones biochemically, we first used semi-denaturing detergent agarose gel electrophoresis (SDD-AGE), a method that differentiates strains based on aggregate size (Kryndushkin et al., 2003). Tau RD species from clone 10 were larger than those propagated by clone 9 (Figure 2D). Thus, the clone 10 fibrils might not be as readily fragmented into smaller species (Tanaka et al., 2006). Next, we used sedimentation analysis to differentiate the strains (Tanaka et al., 2006). Clone 1 had entirely soluble tau RD, whereas clones 9 and 10 had insoluble tau RD (Figure 2E). Clone 10 featured more soluble tau RD than clone 9. To probe for structural differences, we used limited proteolysis as has been used previously for differentiating PrP conformers

(Bessen and Marsh, 1994). Cell lines propagating aggregates (clones 9, 10) featured pronase-resistant species between 10 and 13 kDa, as well as between 20 and 25 kDa in size (Figure 2F). Clone 9 produced a smear between 10 and 13 kDa, whereas clone 10 produced a clear doublet. These studies indicated clear differences in biochemical characteristics of the clones, consistent with distinct strain conformations.

Prion strains often have different seeding efficiencies, which can result in variable incubation times in vivo (Legname et al., 2006). Thus we compared the clones, modifying a preexisting split-luciferase complementation assay (Naik and Piwnicka-Worms, 2007) for use as a tau aggregation sensor (Figure S1A). Clone 1 contained no seeding activity. However, inclusion-containing lines seeded robustly, especially clone 9, which seeded more than clone 10 (Figure 2G). Differences in seeding were not an artifact of cell confluency, as determined by normalizing to cell number in seeding experiments (Figure S2B).

Next, we compared the toxicities of clones 9 and 10. Although clone 9 lysate initially seeded a greater number of cells, these were rapidly eliminated relative to those induced by clone 10 (Figure 2H). Furthermore, cells containing clone 9-derived inclusions grew more slowly than those derived from clone 10 (Figure 2I). Whereas growth rate of nontransfected HEK293 cells was not affected by inoculation with clone 9 lysate, growth of tau RD cells was impaired following the same treatment (Figure S2C). This was not seen for clone 10. Finally, an LDH assay suggested that clone 9 lysate is toxic to tau RD cells relative to a sham treatment (Figure S2D).

A previous study reported that tau from human brain can induce aggresome structures in vitro (Santa-Maria et al., 2012). Thus, we examined the subcellular localization of inclusions associated with clones 9 and 10. Based on antivimentin stains (Figure S2E), electron microscopy (Figure S2F), and anti- γ -tubulin stains (Figure S2G), we conclude that juxtanuclear clone 10 inclusions are canonical aggresomes, unlike the inclusions of clone 9. Intracellular clone 9 inclusions did not colocalize with PML bodies (Figure S2H). Thus, clones 9 and 10 propagate conformationally distinct tau prion strains, with different consequences for the cell. To test the fidelity of strain inheritance, we passaged them continuously for 6 months. Inclusion morphologies (Figure 2J) and limited proteolysis patterns (Figure 2K) associated with clones 9 and 10 were unaltered. Thus, tau RD prion strains are robust, maintaining their phenotypes indefinitely in cell culture.

Transfer of Strain Phenotype to Naive Cells

To rule out an effect of cell background on strain formation, we transduced clone 9 and 10 lysates into naive monoclonal tau RD cells, isolating 6 colonies (A–F) for each (Figure 3A). We evaluated derivative clones (9C was lost in passage) by inclusion morphology (Figure 3B), SDD-AGE (Figure 3C), sedimentation analyses (Figure 3D; Figure S3B), seeding activity (Figure 3E), and limited proteolysis (Figure 3F). In all cases, derivative clones matched their associated progenitors, indicating that tau RD prion strains are encoded by conformation, independent of cell background. Faithful templating into naive cells also occurred after passive addition of lysates to media (Figure S3A), thus indicating that bypassing physiological uptake is not necessary for

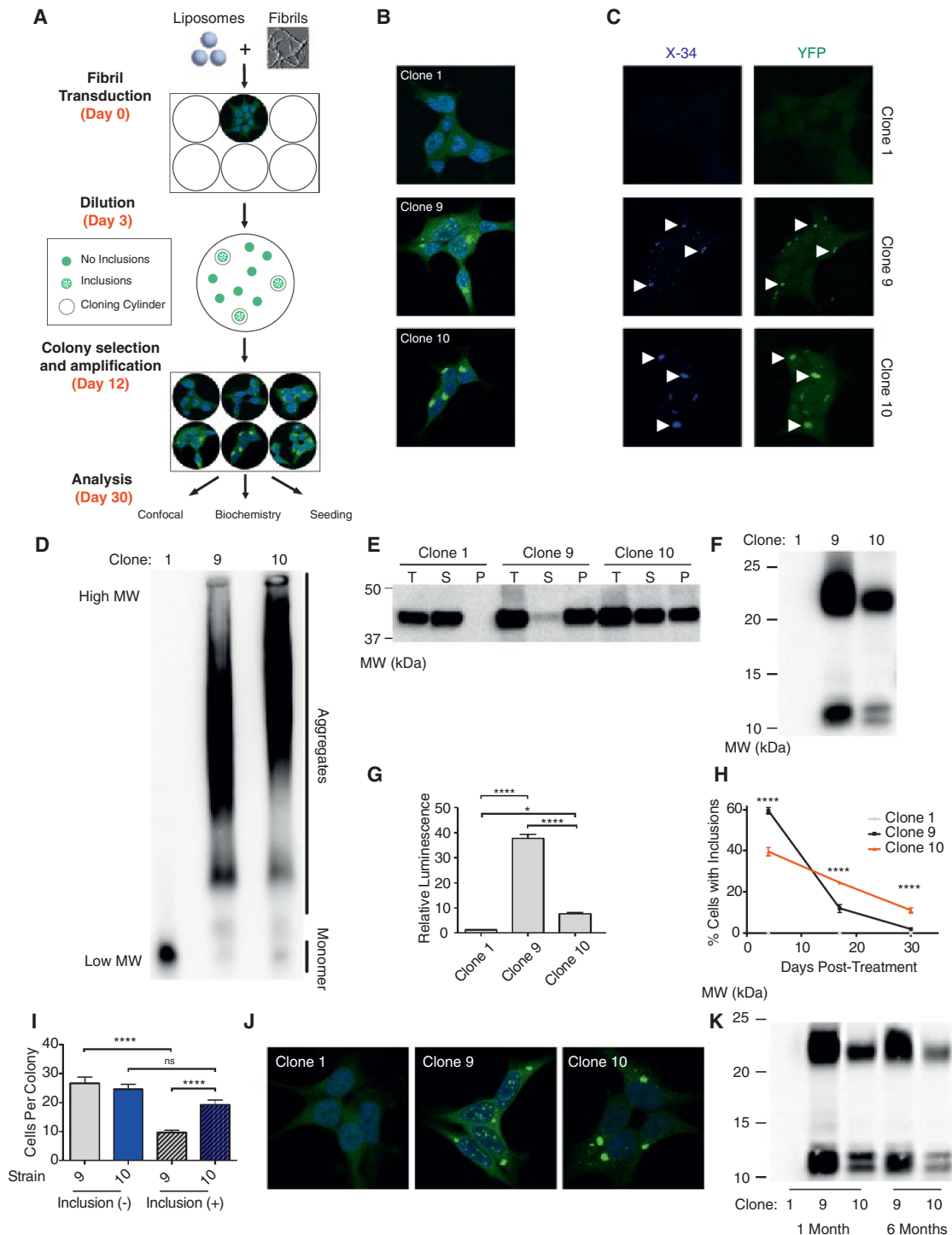


Figure 2. Generation of Stably Inherited Tau RD Prion Strains

(A) A monoclonal HEK293 line stably expressing tau RD(LM)-YFP (hereafter referred to as tau RD) was transduced with tau RD fibrils. At day 3, cells were diluted sparsely in a 10 cm dish. At day 12, inclusion-positive colonies were identified and picked, amplifying to confluency in separate 10 cm dishes. At day 30, cells were replated for confocal analysis or harvested for subsequent experiments.

(B) Confocal analysis of morphologically distinct tau RD prion strains. Clone 1 does not contain inclusions. Clone 9 contains nuclear speckles and a small juxtannuclear inclusion. Clone 10 features one very large juxtannuclear inclusion and no nuclear speckles. See Figure S2A for other clones.

(C) Clones 1, 9, and 10 were stained with X-34, an amyloid dye. X-34 staining is only observed in clone 9 and clone 10, indicating that the propagated aggregates are amyloids.

(legend continued on next page)

templating. With a Tet Off line to control tau RD expression, we demonstrated that the aggregate-positive phenotype can be cured by stopping expression for 7 days and then restarting it (Figures S3C and S3D).

To rule out an artifact of using artificial truncated tau RD and dividing cell model systems, we examined FL tau inclusion formation in primary cortical neurons. Neurons expressing FL tau P301S-YFP formed detergent-resistant inclusions following treatment with clone 9 or 10, but not clone 1 or PBS (Figure 3G). Clone 9 seeded very robustly relative to clone 10 (Figure S3E). Clone 9 lysate created inclusions throughout the soma and processes of neurons with untagged and YFP-tagged FL P301S tau, whereas clone 10 lysate primarily seeded inclusion bodies confined to the soma (Figure 3G; Figures S3F and S3G). Corroborating prior studies (Aoyagi et al., 2007; Miyasaka et al., 2001), we observed a seeding barrier between WT tau and P301 mutants (P301L, P301S). Specifically, aggregates from clones 9 and 10, which feature both the P301L and V337M mutations, never seeded aggregation in neurons expressing FL tau WT-YFP (Figure 3H) and FL tau WT (no tag) (data not shown). This seeding barrier was confirmed to be asymmetric by using a panel of split-luciferase tau RD mutant pairs (Figure S3H), which demonstrated that WT tau RD can seed all forms of RD (WT, P301L, P301S, P301L/V337M), whereas P301 mutants cannot seed WT.

Tau Strains Induce Unique Pathologies in Transgenic Tau P301S Mice

Inoculation of recombinant fibrils into transgenic P301S mice (Yoshiyama et al., 2007), which express a form of mutant tau associated with dominantly inherited tauopathy, rapidly induces pathology within weeks (Iba et al., 2013). Thus, we tested whether tau strains formed in cell culture would have similar effects. We inoculated equivalent amounts of lysate from clones 1, 9, and 10, as well as recombinant tau RD fibrils (RF), bilaterally into the hippocampi of 3-month-old mice (Figure 4A). For all experiments, conditions were gender matched (Table S1). After 3 weeks, RFs induced tangle-like pathology when assessed by AT8 (Figures 4B and 4C), an antibody against FL phospho-tau, as previously reported (Iba et al., 2013). Clones 9 and 10 induced

unique pathologies, whereas clone 1 did not cause any detectable abnormality (Figures 4C and 4D). Whereas clone 9 induced tangle-like inclusions throughout CA1 and CA3, clone 10 induced AT8-positive puncta in mossy fiber tracts (Figure 4D). Staining with MC1, an antibody against conformationally-altered tau (Jicha et al., 1997), confirmed these differences (Figure S4A). X-34, an amyloid dye, primarily recognized clone 9 pathology (Figure S4A), although light staining was observed in CA1 of clone 10-inoculated mice. Pathological differences could not be explained by differences in the amount of total or insoluble tau RD inoculated (Figures S4E and S4F). Injected WT mice never developed pathology (Figure S4B), possibly due to a seeding barrier between inoculated tau RD and WT murine tau (Figure 3H; Figures S3E and S3H).

P301S mice inoculated with clone 10 uniquely accumulated elongated Iba1-positive rod microglia (Figure 4E), which aligned end-to-end parallel to CA1 pyramidal axons (Figure S4C). Such unique coupling of rod microglia has been observed in a rodent traumatic-brain-injury model and might be protective for injured axons (Ziebell et al., 2012). WT mice inoculated with clones 9 and 10 did not feature this pathology, indicating that endogenous human P301S tau is required for this induced microglial phenotype (Figure S4D).

Tau Strains Are Stably Propagated through Multiple Generations in Mice

Prions can be stably passaged *in vivo* (Bruce et al., 1994). Thus, we performed serial inoculation of brain homogenates into naive P301S mice (Figure 5A). Brain homogenate from WT or P301S mice inoculated with clones 1, 9, or 10 (termed generation G0) was inoculated into naive P301S mice (generation G1). After 28 days, brains were collected for histology and biochemistry, and the process was repeated in a second round of P301S mice (generation G2). Immunohistochemistry demonstrated identical pathology for each generation of mice: clone 9 serial propagation induced AT8-positive, tangle-like pathology in CA1 and CA3 regions, whereas clone 10 serial propagation induced AT8-positive puncta in the mossy fiber tracts of the hippocampus (Figures 5B and 5C; Figure S5A). Clone 1 induced no pathology in any generation (Figure 5B; Figure S5B).

(D) SDD-AGE demonstrates that clone 10 features larger aggregates than clone 9.

(E) Sedimentation analysis was performed on clones 1, 9, and 10. Pellet (P) was isolated from supernatant (S) by ultracentrifugation. For clones 9 and 10, supernatant was loaded at a 3:1 ratio to pellet and total (T) to allow clear detection; clone 1, a 1:1 ratio. Clone 1 has all tau RD in the supernatant, whereas clone 9 has almost all tau RD in the pellet. Clone 10 has mixed solubility.

(F) Limited proteolysis (pronase) digests all tau RD in clone 1 but reveals protease-resistant tau RD peptides between 10 and 13 kDa, as well as between 20 and 25 kDa in clone 9 and 10. Unlike clone 9, clone 10 digestion produces a doublet, consistent with a distinct conformation.

(G) A split-luciferase assay reports differential seeding efficiency of tau RD prion strains. A polyclonal HEK293 line expressing both tau RD-CLuc and tau RD-Nluc was transduced with lysate from the three clones. Clone 1 does not seed aggregation. Clone 9 seeds robustly, whereas clone 10 seeds significantly less. Averages of four separate experiments are shown, each read in quadruplicate 48 hr posttransduction (error bars = S.E.M, * = $p < 0.05$, **** = $p < 0.0001$). See Figure S2B for evidence that differences in cell confluency do not account for differences in luminescence.

(H) Inclusion elimination rates differ between clones. After transduction with lysate from clone 9 or 10, the percentage of cells containing inclusions was quantified on days 4, 17, and 30 ($n = 10$ fields, each with 150+ cells per condition). Cells with inclusions derived from clone 9 are eliminated more rapidly from the population. Error bars represent SEM, **** = $p < 0.0001$.

(I) Clone 9-transduced cells grow more slowly. After transduction of stable cells, colonies with inclusions derived from clone 9 have fewer cells than colonies with inclusions derived from clone 10. Colonies without inclusions have identical cell numbers (error bars represent SEM, **** = $p < 0.0001$). See Figure S2C for differences in cell growth rate in tau RD(LM)-HA cells and Figure S2D for LDH toxicity assay in tau RD(LM)-HA background.

(J) Clones 1, 9, and 10 maintain distinctive morphologies after 6 months in culture. See also Figure S2E–S2H for data indicating that juxtannuclear clone 10, but not clone 9, inclusions are aggregates.

(K) Structural characteristics (limited proteolysis digestion patterns) of strains are propagated with high fidelity over 6 months.

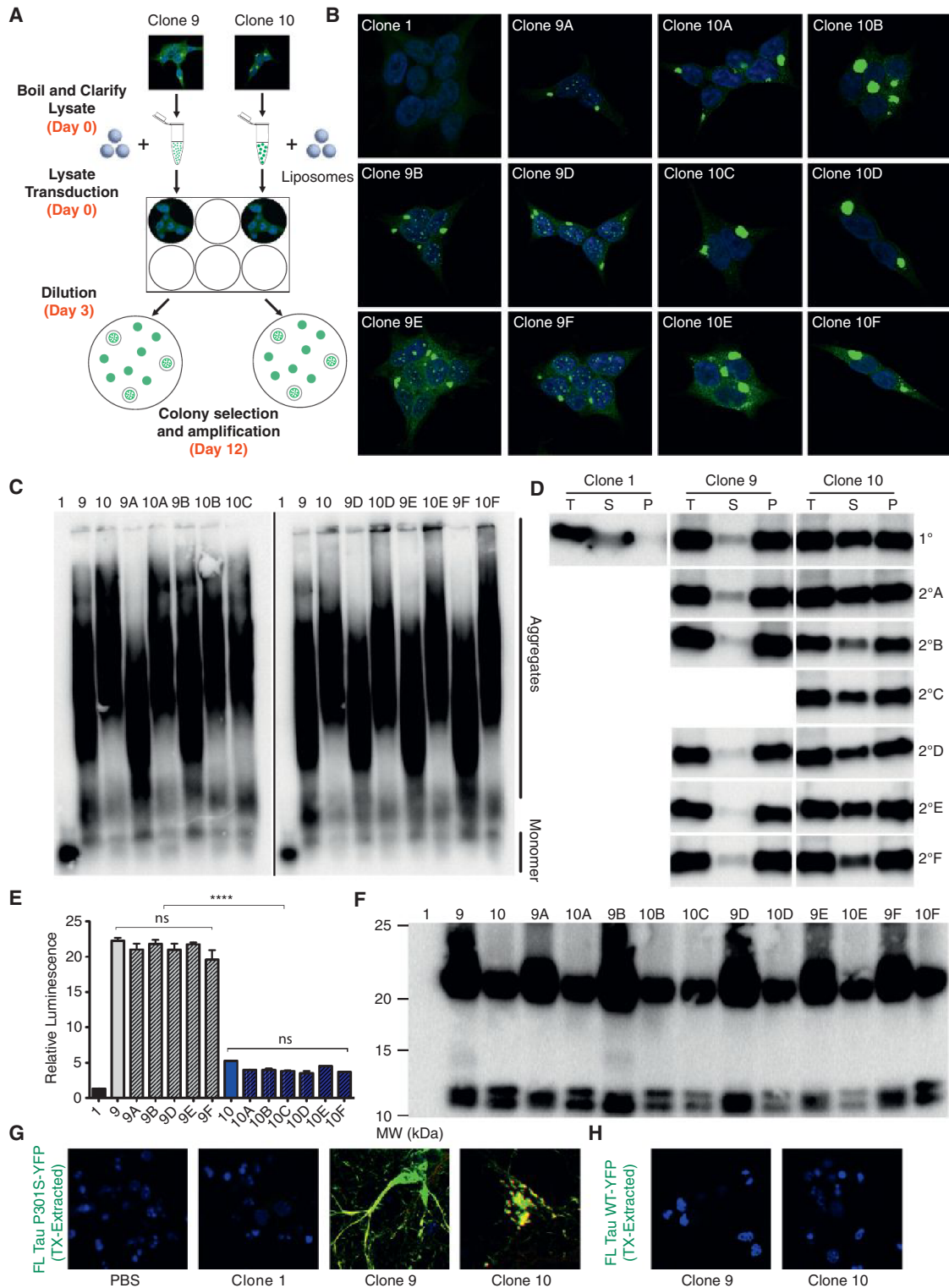


Figure 3. Tau RD Aggregates Transfer Strain Conformations into Naive Cells

(A) Lysates from clones 9 and 10 were transduced into naive tau RD-YFP cells and monoclonal inclusion-containing cells were isolated and amplified. Six secondary clones were generated for each condition, but one (clone 9C) failed to amplify.

(B) Morphologies of primary clones are maintained in secondary cell lines. See also Figure S3A, which demonstrates that this templating of morphology is not dependent on liposome-mediated transduction of lysate.

(legend continued on next page)

Homogenate from WT mice inoculated with the original cell tau strains (G0) did not produce pathology upon passage into P301S mice (Figure S5C). Therefore, pathology observed in G1 and G2 cannot be due to residual tau RD seeds from the original inoculum, and tau prions propagate unique phenotypes for multiple passages *in vivo*.

In Vivo Tau Strains Maintain Phenotypes upon Passage back into Cells

To conclusively test whether tau strains are biochemically stable after passage *in vivo*, we isolated FL P301S tau from microdissected hippocampi of injected mice (G0) by using a monoclonal antibody (HJ8.5) that binds an epitope present in FL tau, but not tau RD (Yanamandra et al., 2013). We assessed seeding activity in G0 samples by split-luciferase complementation and inclusion counts. Only hippocampi from P301S mice (G0) injected with tau RD aggregates contained seeding activity (Figure 6A; Figure S6A). This did not correlate with the amount of immunoprecipitated tau (Figure S6D). WT mouse hippocampi never seeded, regardless of the inoculum. We next tested whether the strains introduced into G0 mice could be reisolated in tau RD cells. Scoring of single colonies based on morphology (containing or lacking nuclear speckles) suggested that strains were unaltered following a single passage through mice (Figures S6B and S6C). To further confirm this, we blindly selected and amplified a single representative colony associated with each mouse. All G0-clone 9 and G0-clone 10 samples recapitulated the morphologies of the original clones 9 and 10 (Figure 6B). Limited proteolysis patterns (Figure 6C) and seeding propensities were also identical (Figure 6D).

Similar experiments were performed following the third passage (G2). Immunoprecipitated (IP) tau from pooled G2-clone 9 and G2-clone 10 homogenates seeded far more strongly than G2-clone 1 homogenates (Figure 6E). Immunoglobulin G (IgG)-precipitated material did not seed (Figure 6E; Figure S6E), and IP tau seeded as strongly as crude homogenate in a split-luciferase assay (Figure S6E). Tau alone thus accounts for the seeding activity reported in these assays.

Next, we introduced IP material from G2 mice into tau RD reporter cells and scored colonies based on morphology prior to isolation of monoclonal lines. G2-clone 9 colonies almost exclusively featured nuclear inclusions, whereas virtually all G2-clone 10 colonies lacked them (Figure S6F). The rare inclusion-positive colonies associated with G2-clone 1 also featured nuclear inclu-

sions, which suggested that some of the G2-clone 10 colonies containing nuclear inclusions could arise from an intrinsic P301S-derived strain. Monoclonal strains ($n = 12$) were blindly selected for each G2 cohort. In all but one case (G2-clone 10D), inclusion morphologies matched that of the original inoculate (Figure 6F; Figure S6G). For both clone 9 and 10 cohorts, 11 of 12 clones matched their parental counterpart based on both limited proteolysis (Figure 6G) and seeding activity (Figure 6H). Intriguingly, the two outliers (G2-clone 9G, G2-clone 10D) had identical proteolysis patterns and seeding ratios, which were unique from those of all other clones. We speculate that these clones result from an intrinsic strain within 4-month-old P301S mice. We conclude that tau prion strains are stable across numerous passages through cells and animals.

Spread of Tau Pathology to Distant, Synaptically Connected Regions

After inoculation with recombinant tau fibrils, pathology can develop in synaptically connected regions (Iba et al., 2013). Our preliminary observations indicated that serial inoculations with clone 9 induced pathology in the ipsilateral entorhinal cortex (EC) (data not shown). To test for spread, we performed a final inoculation (G3) into the left hippocampus of P301S mice. After five weeks, G3-clone 9 mice had AT8-positive pathology in regions that project to or from the hippocampus (Figure 7A) including ipsilateral and contralateral EC, retrosplenial cortex (RSp), and contralateral hippocampus (Figure 7B–7D; Figure S7A) (Andersen, 2007; van Groen et al., 2003). Ipsilateral EC had robust pathology in layers II/III, whereas contralateral EC pathology occurred in deeper cortical layers, suggesting spread along defined anatomical connections (van Groen et al., 2003). Furthermore, pathology was observed in ipsilateral subiculum and dentate gyrus (Figure S7B). In contrast, G3-clone 1 brain did not show AT8-positivity above baseline (Figures 7B and 7D). Overt spread was not observed in G3-clone 10 mice (data not shown), perhaps due to its decreased seeding ability (Figure 2G; Figure S3E). A heatmap summarizes the brain regions with enhanced AT8-positive pathology in G3-clone 9 mice (Figure 7C). These results agree with previous work suggesting that seeded intracellular amyloids spread along discrete neural networks (de Calignon et al., 2012; Iba et al., 2013; Liu et al., 2012; Luk et al., 2012; Zhou et al., 2012). We cannot completely exclude the possibility that this was due to *trans*-synaptic spread of inoculum.

(C) SDD-AGE of lysates from both primary and secondary clones demonstrates similar aggregate sizes in secondary clones relative to the primary ones. A line separates gels run separately.

(D) Sedimentation analysis was performed as described in Figure 2E. Secondary clones feature similar sedimentation patterns to the clones from which they were derived. For original blots, see Figure S3B.

(E) Split-luciferase complementation demonstrates similar seeding efficiencies in secondary lines versus parental lines. Averages of four separate experiments are shown, each read in quadruplicate 48 hr posttransduction of lysate (error bars represent SEM, **** = $p < 0.0001$).

(F) Limited proteolysis shows that all clone 10 derivatives feature a doublet whereas clone 9 derivatives are associated with an unresolvable band between 10 and 13 kDa. Clone 9 derivatives feature a more resistant band between 20 and 25 kDa. See Figures S3C and S3D for reversibility of aggregated state.

(G) Lysates from clones 9 and 10, but not clone 1, induce detergent-resistant FL tau P301S-YFP species, which colocalize with AT8 (red) in primary cortical neurons. Clone 9 induces tangle-like structures throughout the soma and neuritic processes. Clone 10 primarily seeds punctate-like structures in the soma. See Figure S3E for data showing that clone 9 seeds more widespread inclusion formation, Figure S3F for similar results in neurons expressing untagged FL tau P301S, and Figure S3G for images of tangles throughout processes of clone 9-inoculated neurons.

(H) Clone 9 and clone 10 lysates containing tau RD(P301L/V337M)-YFP, do not seed inclusion formation in neurons expressing WT FL tau. For evidence that this is due to an asymmetric seeding barrier between FL tau with and without P301 mutations, see Figure S3H.

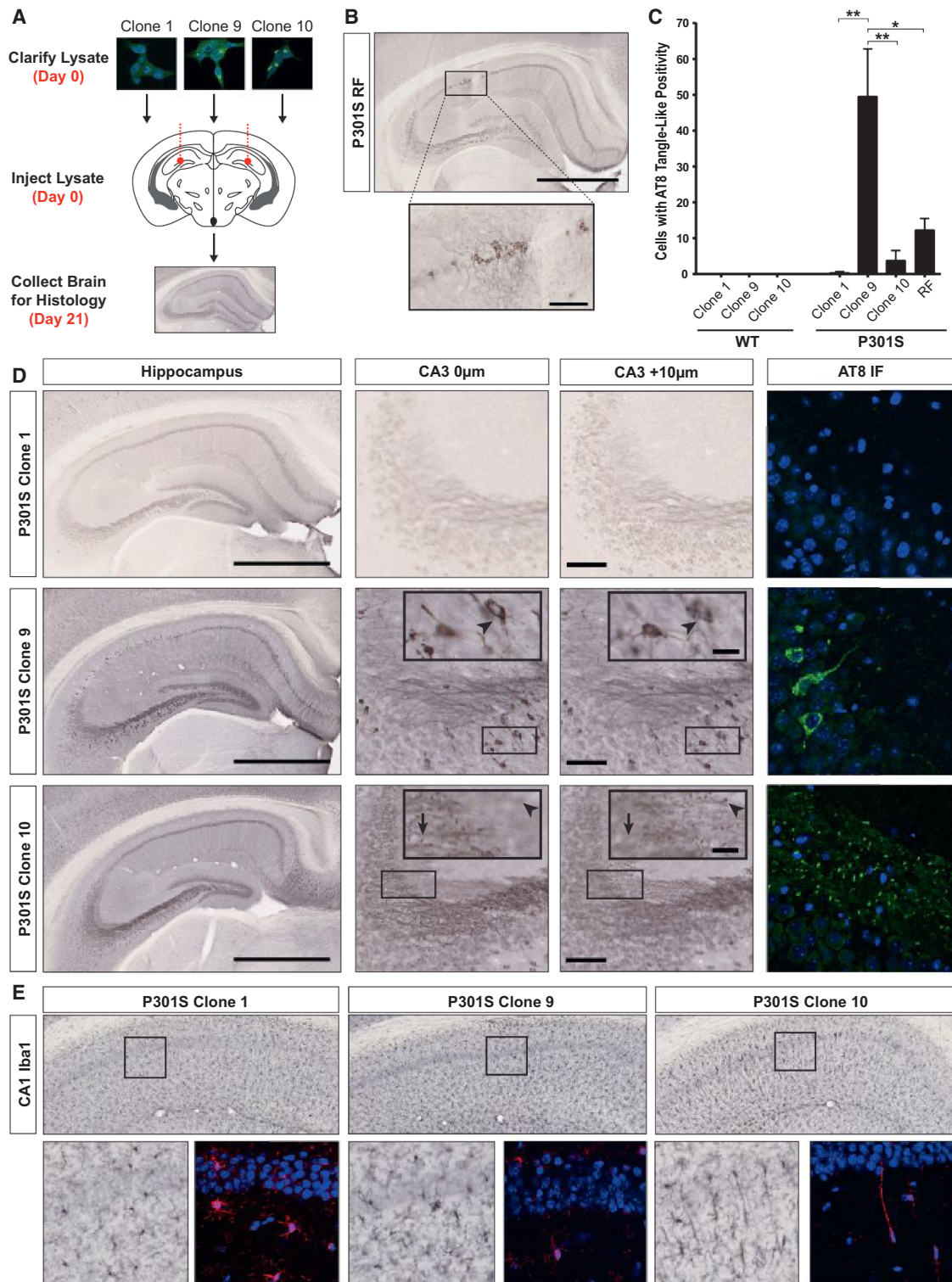


Figure 4. Clone 9 and 10 Induce Unique Tau and Microglia Pathology in P301S Mice

(A) Lysates (10 µg total protein) were injected bilaterally into the hippocampi of 3 month P301S and WT mice. At 21 days postinjection, left hemispheres were collected for histology and right hemispheres for homogenization. See Table S1 for description of mice used in all experiments.

(B) Recombinant tau RD fibrils (RF) induce tangle-like, AT8-positive tau pathology near the injection site in CA1 (scale bars represent hippocampus – 1 mm and inset – 100 µm).

(legend continued on next page)

Intrapatient and Interdisease Phenotypic Diversity in the Tauopathies

It has been hypothesized that conformationally distinct tau prion strains might be associated with individual tauopathies (Clavaguera et al., 2013b; Frost and Diamond, 2010), and a recent study found that inoculation of transgenic human tau mice with brain homogenates from patients with different tauopathies recapitulates certain pathological features of the diseases (Clavaguera et al., 2013a). To examine whether inclusion morphology is a reasonable indicator of distinct strains, we first used our cell model to examine brain homogenates from three individuals with clinically distinct, pathologically verified tauopathies (all patient samples obtained from the Neurodegenerative Disease Brain Bank at UCSF): Alzheimer's disease (AD), corticobasal degeneration (CBD), and argyrophilic grain disease (AGD). We transduced IP or crude (CR) homogenate into the monoclonal Tet Off HEK293 cell line (Figure 8A), used for its relatively high tau RD expression and greater seeding efficacy, and characterized resulting colonies morphologically and biochemically (Figures S8A–S8I). Each brain induced a unique inclusion morphology, independent of the transduction method (IP versus CR) (Figures S8A–S8D). By analyzing three representative clones derived from each brain by sedimentation analysis (Figure S8E), seeding (Figures S8F and S8G), and limited proteolysis (Figures S8H and S8I), we concluded that morphology reliably differentiates biochemically distinct strains. Next, we expanded our analysis to include IP tau from patients with AD (n = 6), AGD (n = 6), CBD (n = 6), Pick's disease (PiD, n = 5), and progressive supranuclear palsy (PSP; n = 6) (Table S2). Excepting PiD, a three-repeat tauopathy, these are predominantly four-repeat (AGD, CBD, PSP) or mixed-repeat (AD) tauopathies that differ in the morphology and distribution of neuronal and glial tau inclusions (Lee et al., 2001). We transduced IP tau from each sample into the monoclonal Tet Off cell line and isolated clones with inclusions (Figure 8A). We identified six morphological phenotypes as follows: (1) no seeding, (2) toxic (all cells with inclusions died and clones could not be isolated), (3) mosaic (unstable prion strain), (4) ordered, (5) disordered, and (6) speckles (Figure 8B). We blindly scored all clones based on tau RD inclusion morphology. This revealed distinct strain compositions across the diseases (Figure 8C). AD patient samples revealed remarkable homogeneity, suggesting a predominant strain. Other disorders revealed interpatient variation. Some patients featured homogeneous strain composition (e.g., certain patients with AGD, PSP), whereas others exhibited considerable heterogeneity. With few exceptions (e.g., AD1–AD4, AGD2, CBD5, PiD3), most patient samples produced two or more strains. The range

of phenotypes associated with single patients suggests a diversity of patient-derived tau prion strains. Because the cell-based strain isolation system can likely amplify only a subset of strains, these data suggest that a disease-associated ensemble or “cloud” of conformations exists within individual patients. Nevertheless, certain tauopathies can be differentiated by their strain composition.

DISCUSSION

Many papers describing “prion-like” behavior of proteins associated with neurodegenerative diseases have been published in the last several years. In the case of tau, fibrils transmit its aggregated state from the outside to the inside of a cell (Frost et al., 2009a; Holmes et al., 2013), suggesting that this mechanism could account for the stereotyped progression of tauopathies. This model of disease was subsequently supported in vivo with reports of *trans*-synaptic spread of pathology (de Calignon et al., 2012; Kim et al., 2010; Liu et al., 2012) and protein-only induction of tau inclusions (Iba et al., 2013). Work with other intracellular amyloids (Desplats et al., 2009; Holmes and Diamond, 2012; Münch et al., 2011; Ren et al., 2009) has suggested that prion-like transmission can explain the progression of many neurodegenerative diseases.

Whether or not various noninfectious amyloids are “true” prions has become a contentious subject of debate. Some define prions as being capable of interorganism transmission of pathology and by the ability to survive freely in the environment (Aguzzi and Rajendran, 2009). To date, there exists no evidence that this definition can be applied to proteins other than PrP. This restrictive definition, based on early research into prion diseases such as kuru and scrapie, potentially ignores a rich biology that mechanistically unites many common diseases. Importantly, we now know that the vast majority of human prion diseases have noninfectious etiology, and that their great phenotypic heterogeneity can be attributed to strains (Collinge and Clarke, 2007). With respect to prion-like intracellular amyloids in humans, recent data indicate that homogenates from distinct tauopathies might reproduce certain pathological features of the diseases in transgenic mice, which is consistent with strain behavior (Clavaguera et al., 2013a). Other studies explicitly suggest the existence of α -synuclein strains, based on the production of different α -synuclein conformers in vitro (Bousset et al., 2013; Guo et al., 2013; Sacino et al., 2013). However, to account for phenotypic diversity at a systems level, a prion strain must replicate with remarkable reliability for extended periods of time. A stringent test of this is to ensure that the strain is stable,

(C) Quantification of tangle-like, AT8-positive cell bodies within the hippocampus (CA1 and CA3) of WT and P301S mice. P301S mice injected with clone 9 lysate have significantly more AT8-positive cell bodies than those injected with clone 1, clone 10, or RF (error bars represent SEM, * = $p < 0.05$, ** = $p < 0.01$). WT mice do not develop pathology after injection.

(D) P301S mice were inoculated with clone 1, clone 9, or clone 10 lysate. Representative whole hippocampus images are shown with the corresponding CA3 z stacks. Arrowheads in clone 9 CA3 insets highlight an AT8-positive cell body that can be seen throughout both z stack images. The arrow and arrowhead in clone 10 CA3 insets each represent a different AT8-positive puncta that is visible in only one z stack plane (scale bars represent hippocampus – 1 mm; CA3 – 100 μ m; CA3 inset and AT8 IF – 25 μ m; n = 3–4 per clone). See Figure S4A for MC1 and X-34 staining, Figure S4B for lack of pathology in inoculated WT mice.

(E) Iba1 staining of microglia in CA1 of inoculated P301S mice indicates that only clone 10 induces the formation of rod microglia, which extend highly polarized processes into CA1. See Figure S4C for columns of rod microglia in these animals and Figure S4D for absence of these microglia in clone 10-inoculated WT animals. See Figure S4E and Figure S4F for data indicating that identical amounts of total and insoluble tau were used in inoculations.

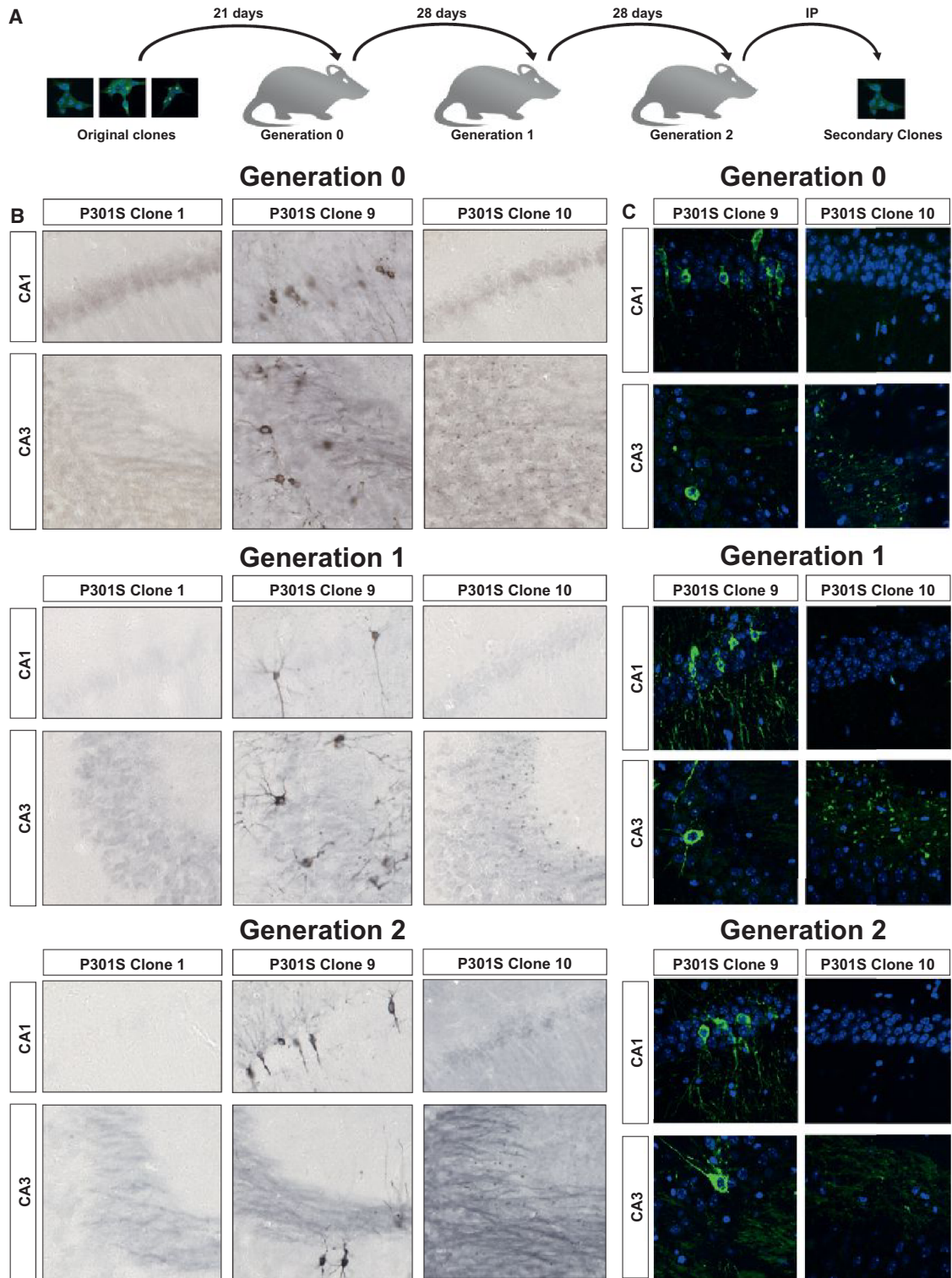


Figure 5. Tau Strains Passage Stably through Multiple Generations of P301S Mice

(A) Lysates (10 μ g protein) were injected bilaterally into the hippocampi of 3-month-old P301S mice (Generation 0/G0). At 21 days postinjection, brains were collected for histology and homogenization. Hippocampal homogenate (10 μ g) was then bilaterally inoculated into a new round of 3-month-old P301S mice (Generation 1/G1) followed by a 28-day incubation before the process was repeated for a new cohort of 3-month-old P301S mice (Generation 2/G2). At G0 and

(legend continued on next page)

isolatable, and replicates its phenotype through living systems with high fidelity (Bruce et al., 1994; Prusiner, 1998). Until now, these characteristics have not been linked to a mammalian protein other than PrP. Based on these criteria, our data strongly suggest that tau should be considered a bona fide prion. Fittingly, we also find that different tauopathies are associated with different strains. This has direct implications for understanding the phenotypic diversity of tauopathies.

Tau as a Prion in Cell Culture and Mice

We began this work by establishing a monoclonal HEK293 cell line that stably expresses the tau repeat domain fused to YFP. In the absence of tau aggregate exposure, these cells propagate only tau RD monomer ("naïve" cells). Induction of aggregation with recombinant fibrils, however, created clonal lines (clone 9 and clone 10) that indefinitely propagate unique aggregate structures, or strains, from mother to daughter cells. These strains differ with respect to inclusion morphology, aggregate size, sedimentation profile, seeding capacity, protease digestion patterns, toxicity, and subcellular localization. Importantly, these properties are cell-independent, because we recreated the strains by protein transfer into naive cells. Furthermore, the distinct inclusion morphologies we observed might represent specific cellular responses to different aggregate conformations, consistent with their unique patterns of compartmentalization. The cell-culture system established here might thus prove useful to detect, propagate, and characterize additional tau prion strains, as well as to understand the cellular mechanisms that govern strain replication, subcellular localization, degradation, and toxicity.

In vivo, we found that strains 9 and 10 induce unique pathological phenotypes in transgenic P301S mice. Moreover, clone 10 lysate uniquely results in the formation of rod-shaped microglia, which indicates that distinct tau conformers initiate different physiological responses in vivo. More remarkably, we report that the morphological phenotypes breed true through multiple generations of mice, a property that is shared with PrP. We recognize that pathological phenotypes can be prone to bias in detection. Thus, we passaged strains back to naive tau RD-YFP cells, conclusively demonstrating the robust inheritance of tau conformations. This data also indicates that the repeat domain is sufficient to encode strains that are unaltered by templating of their structure to FL tau. Therefore, the reported cell model is useful for detecting and propagating physiologically relevant tau prion strains. Finally, using unilateral inoculation of clone 9 lysate, we show that tau aggregation propagates along known anatomical connections, supporting conclusions of previous studies (de Calignon et al., 2012; Iba et al., 2013; Liu et al., 2012). More importantly, however, these cellular and in vivo studies indicate that a mammalian protein amyloid other than PrP templates itself with high fidelity through living systems.

Tau Prion Strains in Human Tauopathy Brains

Knowing that tau acts as a prion in experimental models, we examined whether this concept could explain phenotypic diversity observed in tauopathies. Brain samples from three patients with distinctive tauopathies induced diverse self-propagating tau prion strains in culture. Our initial work with these strains indicated that inclusion morphology is a reliable surrogate for more labor-intensive biochemical characterization. This led us to assess the morphological phenotypes of tau strains derived from numerous patients ($n = 29$) across a spectrum of tauopathies (AD, AGD, CBD, PiD, PSP). Each of the diseases was associated with several cellular inclusion morphologies, although certain diseases (AD, CBD, PiD) are more homogeneous than others (PSP, AGD). It is noteworthy that AD pathology is characteristically more uniform than other tauopathies (Duyckaerts et al., 2009; Feany et al., 1996), and the tau strains isolated from AD brains were by far the most homogeneous. The isolation of multiple conformers from individuals suggests that a tau aggregate ensemble exists within each person, and that standard methodologies (e.g., histopathology, inoculation into mice, protease digestion) will be insufficient for a nuanced understanding of this conformational complexity. Similar to what has been reported for PrP amyloids (Collinge and Clarke, 2007; Li et al., 2010), we speculate that these clouds of tau conformers are prone to selective pressures at the cellular level, which might have implications for therapies that target extracellular tau (Holmes et al., 2013; Yanamandra et al., 2013).

Although we have now succeeded in categorizing multiple distinct strains, the cell-based isolation method can only detect those that successfully template to tau RD-YFP and propagate without overt cellular toxicity. The inability to reselect clone 9 derivatives in the Tet Off background illustrates this problem. On the other extreme, strains that do not propagate with high fidelity might be lost prior to clonal selection. For example, the strains present in several AGD and PiD samples were not stable in cell culture, making detailed characterization of these strains difficult with our model system. Furthermore, it is likely that seeding barriers between tau from patient brain (consisting of various tau isoforms and posttranslationally modified species) and tau RD in cell-culture limits the strains we can detect. Our observation of an asymmetric seeding barrier between P301 mutants and WT tau underscores this limitation, as does recent work indicating similar barriers between three-repeat (3R) and four-repeat (4R) tau (Dinkel et al., 2011). Despite some limitations, the model system presented here has many advantages over standard animal inoculations, because it is less resource-intensive and can parse multiple conformations from a single isolate. Finally, knowledge of the existence of multiple strains in vivo might allow us to characterize them on molecular terms and diagnose patients with much greater precision, possibly by determining structures and conformational

G2, hippocampal homogenates were IP (anti-tau 8.5; epitope = aa 25–30; outside RD region) and inoculated into the original tau RD-YFP line to test the fidelity of strain inheritance (G0 and G2 clones). For each cohort, $n = 3-4$ animals.

(B and C) AT8 staining (DAB = B and immunofluorescence = C) reveals that the morphological phenotypes of phosphorylated tau inclusions breed true through multiple generations of tau P301S mice. See Figure S5A for images of whole hippocampi, Figure S5B for images of clone 1 AT8 immunofluorescence, and Figure S5C for data indicating that strain passage is not due to residual tau RD seeds remaining in diluted inoculate.

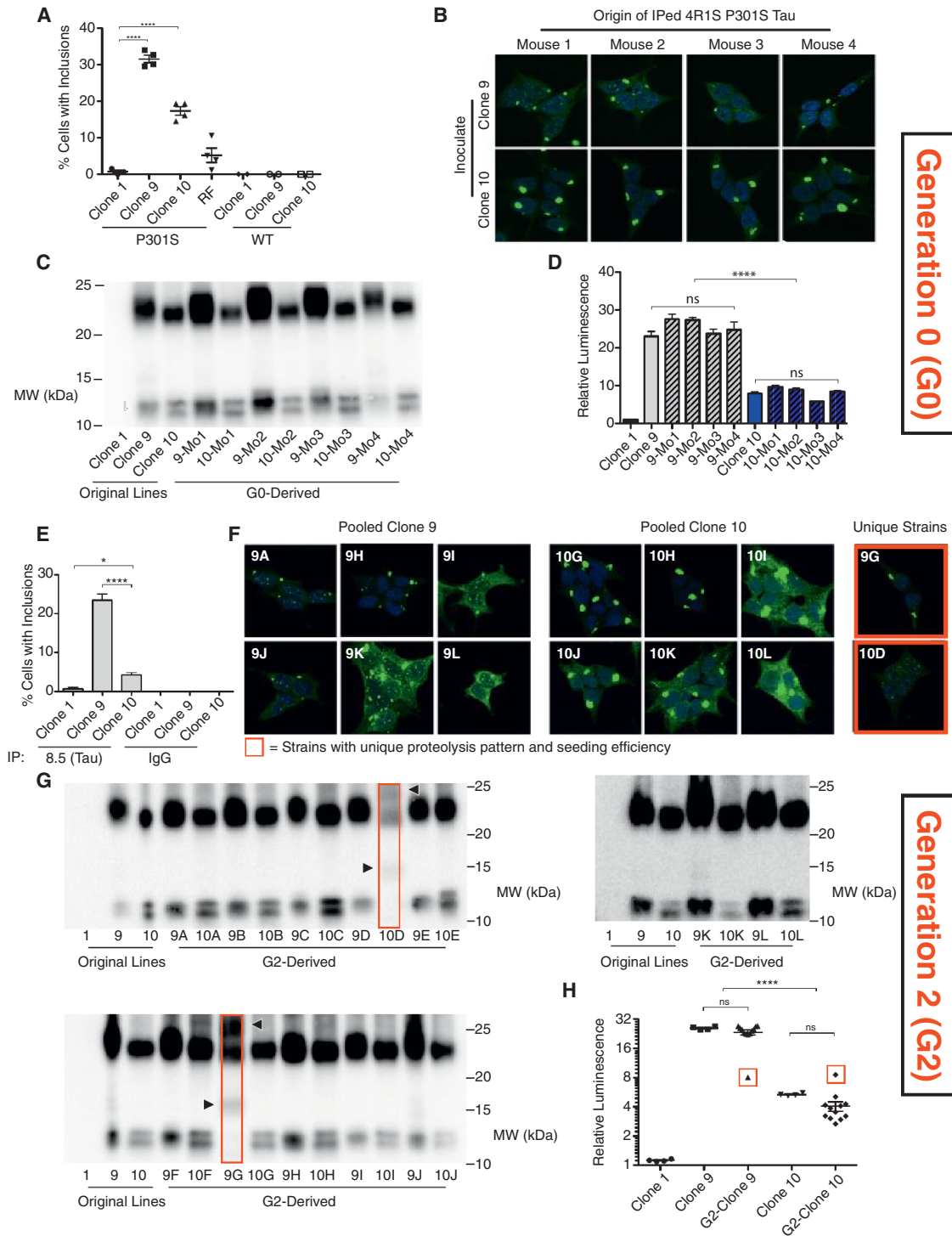


Figure 6. Strains Transfer Faithfully to Cell Culture after Passage through Generation 0 and Generation 2 Mice

(A) IP material was transduced into tau RD-YFP cells prior to passage onto coverslips. At 96 hr, cells were fixed. Only clone 9-, clone 10-, and RF-inoculated mice seed inclusions robustly. WT mouse homogenates never seed aggregation. Ten fields, each with 100+ cells, were analyzed per brain, and averages were collapsed within cohorts (error bars represent SEM, **** = $p < 0.0001$). See also Figure S6A for split-luciferase complementation data. (B) Inclusion morphologies are maintained following passage through P301S mice (G0). IP FL tau from individual P301S mice inoculated with clone 9 or clone 10 was transduced into tau RD-YFP cells, and a single representative clone per mouse was isolated and amplified. All G0-derived clones continue to propagate the original phenotypes. See also Figures S6B and S6C for quantification of colony morphologies prior to monoclonal cell line isolation and Figure S6D for quantification of total IP tau used in G0 experiments.

(legend continued on next page)

epitopes specific to individual diseases. This could help facilitate therapeutic strategies tailored toward the underlying protein pathology.

Expanding the Spectrum of Prion Diseases

Our data, along with cell-culture (Holmes and Diamond, 2012), pathological (Clavaguera et al., 2013b), and imaging (Greicius and Kimmel, 2012) studies are consistent with the model of cell-cell “transmission” of neurodegenerative diseases throughout the nervous system. Our finding of multiple self-propagating conformations in experimental and patient-derived tau preparations suggests that tau should be defined as a prion, because it encodes self-catalyzing conformational information that it propagates indefinitely with high fidelity. Importantly, however, there is no evidence to suggest that AD or other tauopathies are infectious in the classical sense, as they are not known to be communicable between individuals. The infectious property of PrP^{Sc} might reflect its anomalous biochemical stability or expression profile, whereas a host of other cell biological and biophysical properties, especially the ability to encode self-propagating conformers, will more appropriately unify the growing family of “prion-like” proteins. Indeed, the vast majority (>95%) of human prion disease cases appear to be genetic or sporadic, indicating that infectivity should not be a restrictive criterion. We predict that strains associated with distinct clinical phenotypes will also be identified for synucleinopathies and ALS/FTLD spectrum disorders, both of which feature diversity in pathological presentation (Halliday et al., 2011; Van Langenhove et al., 2012). Understanding disparate amyloid neurodegenerative diseases in light of this model should create new possibilities for common diagnostic and therapeutic approaches.

EXPERIMENTAL PROCEDURES

Statistical Analysis

Unless explicitly stated, all statistical analyses used one-way analysis of variance with Bonferroni's multiple comparison test.

Liposome-Mediated Transduction of Fibrils, Lysate, Brain Homogenate

Cell lines were plated at 250,000 cells per well in 12-well plates. Twenty-four hr later, fibrils or lysate were combined with OptiMEM (GIBCO) to a final volume

of 100 μ L. 96 μ L OptiMEM and 4 μ L lipofectamine-2000 (Invitrogen) was then added to a final volume of 200 μ L. After 20 min, liposome preparations were added to cells. Eighteen hr later, cells were replated in wells of a 6-well plate. For more details, see Supplemental Experimental Procedures.

Semidenaturing Detergent Agarose Gel Electrophoresis

SDD-AGE was performed as previously described (Kryndushkin et al., 2003) with minor modifications. Cell pellets lysed in 0.05% Triton X were clarified by sequential centrifugations (500 \times g, 1000 \times g). Low-SDS 1.5% agarose gels were prepared by dissolving agarose in buffer G (20 mM Tris-Base, 200 mM glycine, in ddH₂O) with 0.02% SDS. For each condition, 5 μ g of clarified cell lysate was incubated with 0.02% SDS sample buffer for 7 min prior to loading. SDD-AGE was run in Laemmli buffer (Buffer G with 0.1% SDS). Protein was transferred to Immobilon P (Millipore). Membranes were probed for tau with rabbit polyclonal anti-tau ab64193 (1:4000, AbCam) and counter-probed with goat anti-rabbit HRP (1:4,000, Jackson ImmunoTherapy). For more details, see Supplemental Experimental Procedures.

Sedimentation Analysis

Clarified cell lysate was centrifuged at 100,000 \times g for 1 hr. Supernatant was placed aside and the pellet was washed with 1.5 ml PBS prior to ultracentrifugation at 100,000 \times g for 30 min. The supernatant was aspirated and the pellet was resuspended by boiling in RIPA buffer with 4% SDS and 100 mM DTT. Bradford assay (Bio-Rad) with BSA standard curve was used to normalize all protein concentrations. Samples were run on 4%–15% SDS-PAGE gels (Bio-Rad) and protein was transferred to Immobilon P (Millipore). Membranes were probed for tau as described above. For more details, see Supplemental Experimental Procedures.

Split-Luciferase Complementation Assay

Polyclonal HEK293 cells stably expressing tau RD-Cluc and tau RD-Nluc were plated at 240,000 cells per well in 12-well plates 24 hr prior to cell lysate transduction. Clarified cell lysate was prepared as described above. Cell lysate (20 μ g in 10 μ L volume) was diluted with 90 μ L OptiMEM (GIBCO) and incubated with 96 μ L OptiMEM and 4 μ L lipofectamine-2000 (Invitrogen) for 20 min. Liposome preparations were then added to cells and 18 hr later, cells were replated in quadruplicate in a 96-well plate. Twenty-four hr later, media was aspirated from wells and replaced with luciferin solution (150 μ g/mL D-luciferin potassium salt, Gold Biosciences, in Dulbecco's phosphate-buffered saline, GIBCO). Cells were incubated with luciferin solution for 3 min at 37°C prior to reading luminescence with a Tecan M1000 fluorescence plate reader. For more details, see Supplemental Experimental Procedures.

Protease Digestion

Pronase (Roche) was diluted in PBS to a final concentration of 1 mg/mL and single-use aliquots were stored at -80° C. Clarified cell lysate was prepared

(C) Limited proteolysis reveals that G0 clones feature similar banding patterns to the original parental lines, with G0-clone 10 featuring a doublet between 10–13 kDa (versus smear for G0-clone 9) and a band between 20 and 25 kDa that is slightly smaller than G0-clone 9 bands.

(D) Split-luciferase complementation demonstrates similar seeding efficiencies in G0 clones relative to original parental lines. Averages of four separate experiments are shown, each read in quadruplicate at 48 hr posttransduction of lysate (error bars represent SEM, **** = $p < 0.0001$).

(E) IP material from pooled G2 mice was transduced into naive tau RD-YFP cells prior to passage onto coverslips. At 96 hr, cells were fixed. Seeding of inclusion formation is significantly greater for G2-clone 9 and G2-clone 10 mice than G2-clone 1 mice. G2-clone 1 tau induces inclusions on rare occasions (~1% of cells). Seeding is specific to tau because IgG-precipitated material never seeds. Ten fields, each with 150+ cells, were analyzed per condition (error bars represent SEM, * = $p < 0.05$, **** = $p < 0.0001$). See also Figure S6E for split-luciferase complementation data.

(F) Inclusion morphologies are maintained following passage through three generations of mice. IP full-length tau from pooled G2 homogenates was transduced into tau RD-YFP cells, and 12 clones per cohort were isolated. Representative examples are shown. The two clones boxed in red feature similar limited proteolysis digestion patterns and seeding ratios to each other, which are unique from all 22 other clones. See Figure S6F for quantification of colony morphologies prior to monoclonal cell line isolation and Figure S6G for images of all 24 clones.

(G) Limited proteolysis reveals that G2 clones feature similar banding patterns to their parental lines, with G2-clone 10 featuring a doublet between 10–13 kDa (versus smear for G2-clone 9) and a band between 20 and 25 kDa that is slightly smaller than G2-clone 9 digests. Two clones (boxed in red), one for each cohort, are unique in featuring bands at 15 and 25 kDa.

(H) Split-luciferase complementation demonstrates similar seeding efficiencies in G2 clones relative to original parental lines. Seeding ratios were averaged across clones, each of which was read in quadruplicate at 48 hr posttransduction of lysate (error bars represent SEM, **** = $p < 0.0001$). Boxed in red are two outlier clones (9G and 10D), which also feature unique inclusion morphologies and limited proteolysis digestion patterns.

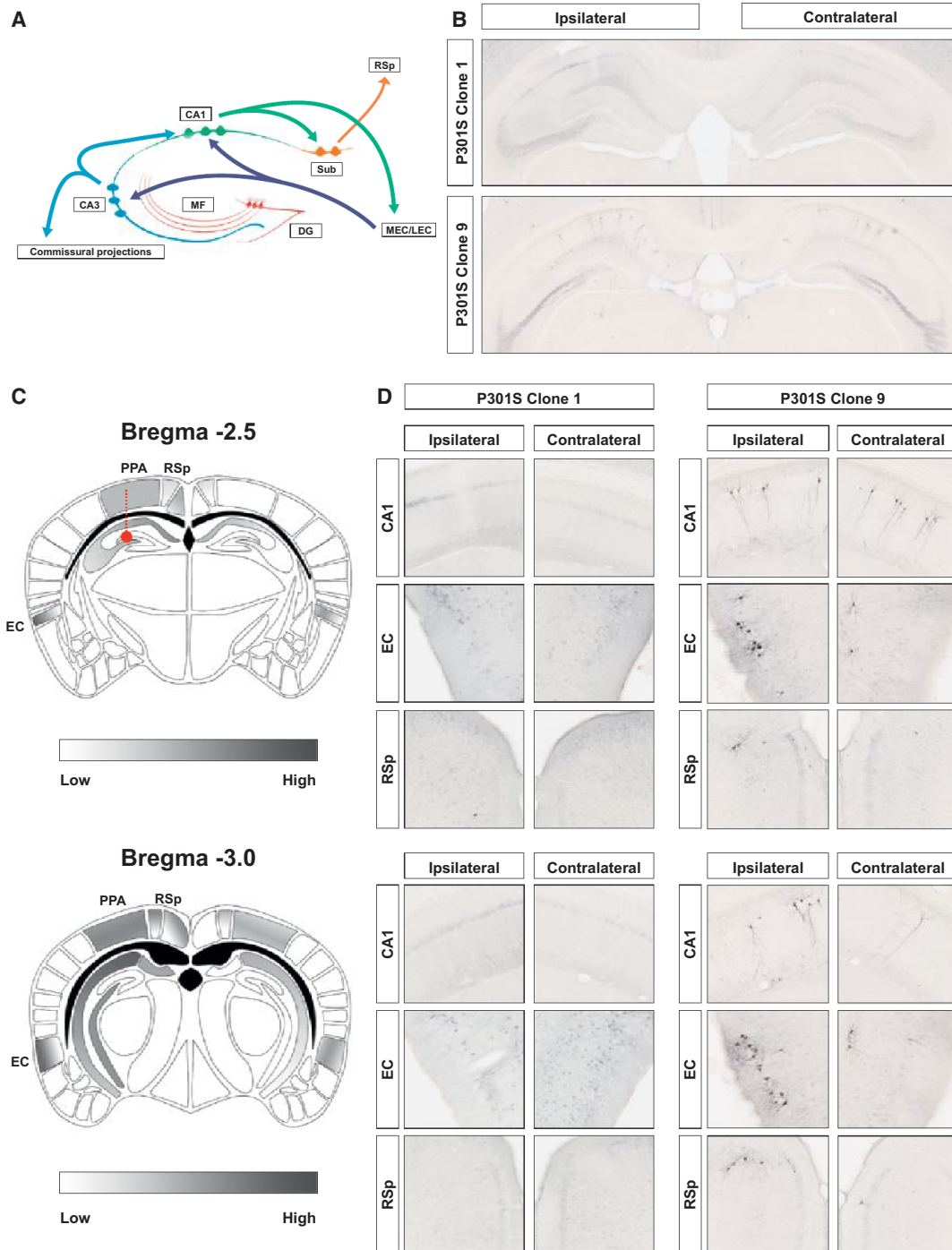


Figure 7. Anterograde and Retrograde Spread of Pathology to Synaptically Connected Regions in Generation 3-clone 9 Mice

(A) Schematic of known projections to and from the hippocampus (DG, dentate gyrus; MEC/LEC, medial and lateral entorhinal cortices; MF, mossy fibers; RSp, retrosplenial cortex; Sub, subiculum).

(B) Representative images of AT8 staining in the hippocampi of G3 mice inoculated with 10 μ g of G2 brain homogenate. Spread of clone 9 pathology to the contralateral hippocampus is evident. See Figure S7A for whole brain slices.

(C) Summary of pathology present in G3-clone 9 mice. Gradient represents semiquantitative analysis of neurofibrillary tangle-like AT8 cell body positivity observed in each region (PPA, posterior parietal association area) both 2.5 and 3.0 mm posterior to bregma.

(D) AT8 histopathology observed in brain regions with known projections to and from the hippocampus. Ipsilateral AT8 pathology is observed in the EC and appears in cortical layers II-III, whereas contralateral pathology is observed in deeper layers of the EC. Pathology is also observed in the retrosplenial cortex, especially ipsilateral to the injection site. See Figure S7B for subiculum and dentate gyrus images.

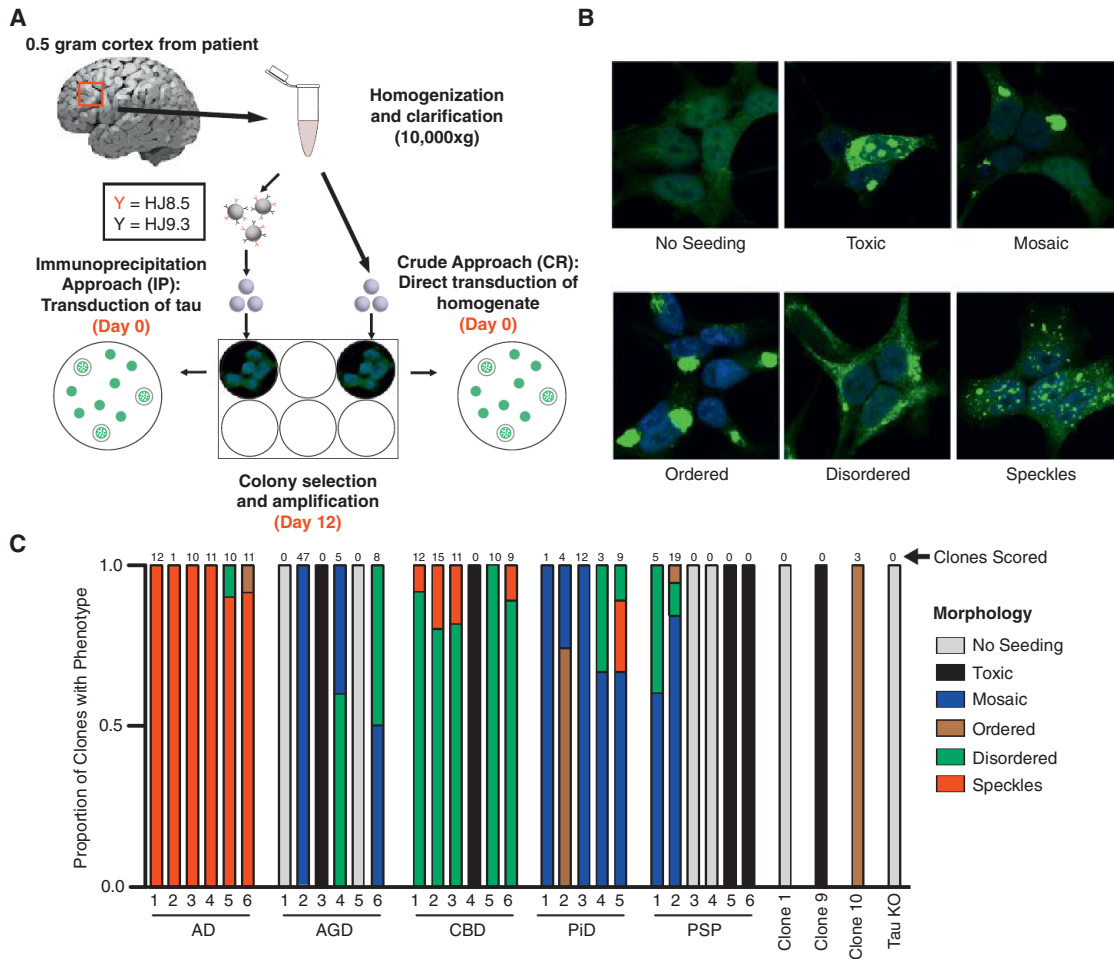


Figure 8. Diverse Tau Prion Strains within Patients and across Diseases

(A) Schematic illustrating methods used to generate patient-derived tau RD prion strains in a monoclonal Tet Off-tau RD-YFP line. See Figure S8 for data indicating that different inclusion morphologies are associated with different biochemical and seeding properties.

(B) Morphological phenotypes associated with tau RD prion strains induced by patient material: no seeding, toxic, mosaic, ordered, disordered, speckles. Representative examples are shown.

(C) IP tau from 29 patient samples (AD, Alzheimer's disease; AGD, argyrophilic grain disease; CBD, corticobasal degeneration; PiD, Pick's disease; PSP, progressive supranuclear palsy) was transduced into tau RD-YFP cells (Tet Off) and as many inclusion-positive clones as could be identified for each patient sample were blindly picked and amplified. Once confluent in 10 cm dishes, morphological phenotypes were scored by a separate blinded experimenter. See Table S2 for numerical values, patient-related information, and tissue origin.

as previously described (see SDD-AGE) and protein concentrations were normalized to 1.7 $\mu\text{g}/\mu\text{L}$. 17 μg (10 μL) of cell lysate was added to 10 μL of pronase at a concentration of 100 $\mu\text{g}/\text{mL}$ (diluted in PBS) for a final volume of 20 μL . Cell lysates were digested at 37°C for one hour. Reactions were quenched by addition of 20 μL 2 \times sample buffer (final SDS concentration of 1%) and boiling for 5 min. Each sample (15 μL) was run on a 10% Bis-Tris NuPAGE gel (Novex by Life Technologies) and protein was transferred to Immobilon P (Millipore). Membranes were probed for tau as described above. For more details, see Supplemental Experimental Procedures.

Animals and Hippocampal Injections

Transgenic mice expressing FL human tau 4R1N P301S under the murine prion promoter (Yoshiyama et al., 2007) were maintained on a B6C3 background. P301S and nontransgenic littermates were anesthetized with isoflurane and were bilaterally injected into the hippocampus (from bregma: -2.5 mm posterior, ± 2 mm lateral, -1.8 mm ventral) with either 2 μL of

5 $\mu\text{g}/\mu\text{L}$ clarified lysate/homogenate or 2 μL of 2.5 $\mu\text{g}/\mu\text{L}$ recombinant tau RD fibrils as previously described (DeVos and Miller, 2013). For all experiments, conditions were gender-matched (Table S1). Unilateral injections were used for G3 spread experiments. All protocols involving animal use were approved by the institutional animal care and use committee at Washington University in St. Louis. For more details, see Supplemental Experimental Procedures.

Histology and Immunohistochemistry

Sections (50 μm) were taken through the entire left hemisphere with a freezing microtome. For DAB stains, brain slices were incubated with indicated antibodies overnight at 4°C. Slices were then counter-stained with the appropriate secondary. Slices were then incubated at room temperature for 30 min with the VECTASTAIN Elite ABC Kit (Vector Labs), followed by DAB development with the DAB Peroxidase Substrate Kit with the optional nickel addition (Vector Labs). Histological images and z stacks were captured with the Olympus Nanozoomer 2.0-HT (Hamamatsu) and analyzed with the NDP viewer software

(Hamamatsu). For immunofluorescence stains, slices were incubated in blocking solution with indicated primary antibody overnight at 4°C, followed by appropriate secondary labeling. For more details, see Supplemental Experimental Procedures.

SUPPLEMENTAL INFORMATION

Supplemental Information includes eight figures, two tables, and Supplemental Experimental Procedures and can be found with this article online at <http://dx.doi.org/10.1016/j.neuron.2014.04.047>.

AUTHOR CONTRIBUTIONS

D.W.S. and S.K.K. contributed equally to this work. D.W.S. performed all cell culture and biochemistry experiments. S.K.K. performed all animal experiments. S.L.D. provided technical assistance and guidance for animal inoculations. A.M.S. aided with biochemistry. H.M. and A.L. contributed unpublished reagents. S.J.B. helped with cell-culture experiments and performed blind scoring. A.C.F., J.R.T., and L.C.S. performed electron microscopy. L.T.G. and W.W.S. analysed and selected human samples. D.W.S., S.K.K., S.L.D., T.M.M., and M.I.D. designed experiments. D.W.S., S.K.K., and M.I.D. analysed results and wrote the manuscript.

ACKNOWLEDGMENTS

We thank John Cirrito, Peter Davies, David Holtzman, Paul Kotzbauer, Jeffrey Milbrandt, and David Piwnica-Worms for reagents. We thank Dorrie Young for help with figures and Jan Bieschke, William Dauer, Jen Dulle, Bess Frost, Brandon Holmes, Suzanne Schindler, Kevin Stein, and Heather True for critiques. Our work was funded by the Tau Consortium, Muscular Dystrophy Association, American Health Assistance Foundation, Ruth K. Broad Foundation, Harrington Discovery Institute, and the NIH (1F31NS086251, D.W.S.; 1R01NS071835, M.I.D.; 1R01NS078398, T.M.M.). This work was supported by the Hope Center Alafi Neuroimaging Lab and a P30 Neuroscience Blueprint Interdisciplinary Center Core award to Washington University (P30NS057105). Human tissue samples were provided by the Neurodegenerative Disease Brain Bank at the University of California, San Francisco, which receives funding support from NIH grants P01AG019724 and P50AG023501, the Consortium for Frontotemporal Dementia Research, and the Tau Consortium. M.I.D. acknowledges a potential conflict of interest in that he is a coinventor of antibodies used in this study (HJ9.3 and HJ8.5) that have been licensed by C2N Diagnostics through an agreement with Washington University in St. Louis.

Accepted: April 15, 2014

Published: May 22, 2014

REFERENCES

- Aguzzi, A., and Rajendran, L. (2009). The transcellular spread of cytosolic amyloids, prions, and prionoids. *Neuron* 64, 783–790.
- Andersen, P. (2007). *The Hippocampus Book*. (Oxford: Oxford University Press).
- Aoyagi, H., Hasegawa, M., and Tamaoka, A. (2007). Fibrillogenic nuclei composed of P301L mutant tau induce elongation of P301L tau but not wild-type tau. *J. Biol. Chem.* 282, 20309–20318.
- Barghorn, S., Zheng-Fischhöfer, Q., Ackmann, M., Biernat, J., von Bergen, M., Mandelkow, E.M., and Mandelkow, E. (2000). Structure, microtubule interactions, and paired helical filament aggregation by tau mutants of frontotemporal dementias. *Biochemistry* 39, 11714–11721.
- Bessen, R.A., and Marsh, R.F. (1994). Distinct PrP properties suggest the molecular basis of strain variation in transmissible mink encephalopathy. *J. Virol.* 68, 7859–7868.
- Birkett, C.R., Hennion, R.M., Bembridge, D.A., Clarke, M.C., Chree, A., Bruce, M.E., and Bostock, C.J. (2001). Scrapie strains maintain biological phenotypes on propagation in a cell line in culture. *EMBO J.* 20, 3351–3358.
- Bonar, L., Cohen, A.S., and Skinner, M.M. (1969). Characterization of the amyloid fibril as a cross-beta protein. *Proc. Soc. Exp. Biol. Med.* 131, 1373–1375.
- Bousset, L., Pieri, L., Ruiz-Arlandis, G., Gath, J., Jensen, P.H., Habenstein, B., Madiona, K., Olieric, V., Böckmann, A., Meier, B.H., and Melki, R. (2013). Structural and functional characterization of two alpha-synuclein strains. *Nat Commun* 4, 2575.
- Braak, H., and Braak, E. (1995). Staging of Alzheimer's disease-related neurofibrillary changes. *Neurobiol. Aging* 16, 271–8–discussion278–84.
- Bruce, M., Chree, A., McConnell, I., Foster, J., Pearson, G., and Fraser, H. (1994). Transmission of bovine spongiform encephalopathy and scrapie to mice: strain variation and the species barrier. *Philos. Trans. R. Soc. Lond. B Biol. Sci.* 343, 405–411.
- Clavaguera, F., Bolmont, T., Crowther, R.A., Abramowski, D., Frank, S., Probst, A., Fraser, G., Stalder, A.K., Beibel, M., Staufienbiel, M., et al. (2009). Transmission and spreading of tauopathy in transgenic mouse brain. *Nat. Cell Biol.* 11, 909–913.
- Clavaguera, F., Akatsu, H., Fraser, G., Crowther, R.A., Frank, S., Hench, J., Probst, A., Winkler, D.T., Reichwald, J., Staufienbiel, M., et al. (2013a). Brain homogenates from human tauopathies induce tau inclusions in mouse brain. *Proc. Natl. Acad. Sci. USA* 110, 9535–9540.
- Clavaguera, F., Lavenir, I., Falcon, B., Frank, S., Goedert, M., and Tolnay, M. (2013b). "Prion-like" templated misfolding in tauopathies. *Brain Pathol.* 23, 342–349.
- Collinge, J., and Clarke, A.R. (2007). A general model of prion strains and their pathogenicity. *Science* 318, 930–936.
- de Calignon, A., Polydoro, M., Suárez-Calvet, M., William, C., Adamowicz, D.H., Kopeikina, K.J., Pittstick, R., Sahara, N., Ashe, K.H., Carlson, G.A., et al. (2012). Propagation of tau pathology in a model of early Alzheimer's disease. *Neuron* 73, 685–697.
- Derkatch, I.L., Chernoff, Y.O., Kushnirov, V.V., Inge-Vechtomov, S.G., and Liebman, S.W. (1996). Genesis and variability of [PSI] prion factors in *Saccharomyces cerevisiae*. *Genetics* 144, 1375–1386.
- Desplats, P., Lee, H.-J., Bae, E.-J., Patrick, C., Rockenstein, E., Crews, L., Spencer, B., Masliah, E., and Lee, S.-J. (2009). Inclusion formation and neuronal cell death through neuron-to-neuron transmission of alpha-synuclein. *Proc. Natl. Acad. Sci. USA* 106, 13010–13015.
- DeVos, S.L., and Miller, T.M. (2013). Direct intraventricular delivery of drugs to the rodent central nervous system. *J. Vis. Exp.* 12, e50326.
- Dinkel, P.D., Siddiqua, A., Huynh, H., Shah, M., and Margittai, M. (2011). Variations in filament conformation dictate seeding barrier between three- and four-repeat tau. *Biochemistry* 50, 4330–4336.
- Duyckaerts, C., Delatour, B., and Potier, M.-C. (2009). Classification and basic pathology of Alzheimer disease. *Acta Neuropathol.* 118, 5–36.
- Feany, M.B., Mattiace, L.A., and Dickson, D.W. (1996). Neuropathologic overlap of progressive supranuclear palsy, Pick's disease and corticobasal degeneration. *J. Neuropathol. Exp. Neurol.* 55, 53–67.
- Frost, B., and Diamond, M.I. (2010). Prion-like mechanisms in neurodegenerative diseases. *Nat. Rev. Neurosci.* 11, 155–159.
- Frost, B., Jacks, R.L., and Diamond, M.I. (2009a). Propagation of tau misfolding from the outside to the inside of a cell. *J. Biol. Chem.* 284, 12845–12852.
- Frost, B., Ollesch, J., Wille, H., and Diamond, M.I. (2009b). Conformational diversity of wild-type Tau fibrils specified by templated conformation change. *J. Biol. Chem.* 284, 3546–3551.
- Giasson, B.I., Forman, M.S., Higuchi, M., Golbe, L.I., Graves, C.L., Kotzbauer, P.T., Trojanowski, J.Q., and Lee, V.M.-Y. (2003). Initiation and synergistic fibrillization of tau and alpha-synuclein. *Science* 300, 636–640.
- Greicius, M.D., and Kimmel, D.L. (2012). Neuroimaging insights into network-based neurodegeneration. *Curr. Opin. Neurol.* 25, 727–734.

- Guo, J.L., Covell, D.J., Daniels, J.P., Iba, M., Stieber, A., Zhang, B., Riddle, D.M., Kwong, L.K., Xu, Y., Trojanowski, J.Q., and Lee, V.M. (2013). Distinct α -synuclein strains differentially promote tau inclusions in neurons. *Cell* **154**, 103–117.
- Guo, J.L., and Lee, V.M. (2014). Cell-to-cell transmission of pathogenic proteins in neurodegenerative diseases. *Nat. Med.* **20**, 130–138.
- Halliday, G.M., Holton, J.L., Revesz, T., and Dickson, D.W. (2011). Neuropathology underlying clinical variability in patients with synucleinopathies. *Acta Neuropathol.* **122**, 187–204.
- Holmes, B.B., and Diamond, M.I. (2012). Cellular mechanisms of protein aggregate propagation. *Curr. Opin. Neurol.* **25**, 721–726.
- Holmes, B.B., DeVos, S.L., Kfoury, N., Li, M., Jacks, R., Yanamandra, K., Ouidja, M.O., Brodsky, F.M., Marasa, J., Bagchi, D.P., et al. (2013). Heparan sulfate proteoglycans mediate internalization and propagation of specific proteopathic seeds. *Proc. Natl. Acad. Sci. USA* **110**, E3138–E3147.
- Holtzman, D.M., Morris, J.C., and Goate, A.M. (2011). Alzheimer's disease: the challenge of the second century. *Sci Transl Med* **3**, 77sr1.
- Hutton, M., Lendon, C.L., Rizzu, P., Baker, M., Froelich, S., Houlden, H., Pickering-Brown, S., Chakraverty, S., Isaacs, A., Grover, A., et al. (1998). Association of missense and 5'-splice-site mutations in tau with the inherited dementia FTDP-17. *Nature* **393**, 702–705.
- Iba, M., Guo, J.L., McBride, J.D., Zhang, B., Trojanowski, J.Q., and Lee, V.M.-Y. (2013). Synthetic tau fibrils mediate transmission of neurofibrillary tangles in a transgenic mouse model of Alzheimer's-like tauopathy. *J. Neurosci.* **33**, 1024–1037.
- Jicha, G.A., Bowser, R., Kazam, I.G., and Davies, P. (1997). Alz-50 and MC-1, a new monoclonal antibody raised to paired helical filaments, recognize conformational epitopes on recombinant tau. *J. Neurosci. Res.* **48**, 128–132.
- Kim, W., Lee, S., Jung, C., Ahmed, A., Lee, G., and Hall, G.F. (2010). Interneuron transfer of human tau between Lamprey central neurons in situ. *J. Alzheimers Dis.* **19**, 647–664.
- Kim, C., Haldiman, T., Surewicz, K., Cohen, Y., Chen, W., Blevins, J., Sy, M.-S., Cohen, M., Kong, Q., Telling, G.C., et al. (2012). Small protease sensitive oligomers of PrP^{Sc} in distinct human prions determine conversion rate of PrP(C). *PLoS Pathog.* **8**, e1002835.
- Krammer, C., Kryndushkin, D., Suhre, M.H., Kremmer, E., Hofmann, A., Pfeifer, A., Scheibel, T., Wickner, R.B., Schätzl, H.M., and Vorberg, I. (2009). The yeast Sup35NM domain propagates as a prion in mammalian cells. *Proc. Natl. Acad. Sci. USA* **106**, 462–467.
- Kryndushkin, D.S., Alexandrov, I.M., Ter-Avanesyan, M.D., and Kushnirov, V.V. (2003). Yeast [PSI⁺] prion aggregates are formed by small Sup35 polymers fragmented by Hsp104. *J. Biol. Chem.* **278**, 49636–49643.
- Lee, V.M., Goedert, M., and Trojanowski, J.Q. (2001). Neurodegenerative tauopathies. *Annu. Rev. Neurosci.* **24**, 1121–1159.
- Legname, G., Nguyen, H.-O.B., Peretz, D., Cohen, F.E., DeArmond, S.J., and Prusiner, S.B. (2006). Continuum of prion protein structures enciphers a multitude of prion isolate-specified phenotypes. *Proc. Natl. Acad. Sci. USA* **103**, 19105–19110.
- Li, J., Browning, S., Mahal, S.P., Oelschlegel, A.M., and Weissmann, C. (2010). Darwinian evolution of prions in cell culture. *Science* **327**, 869–872.
- Liu, L., Drouet, V., Wu, J.W., Witter, M.P., Small, S.A., Clelland, C., and Duff, K. (2012). Trans-synaptic spread of tau pathology in vivo. *PLoS ONE* **7**, e31302.
- Lu, J.-X., Qiang, W., Yau, W.-M., Schwieters, C.D., Meredith, S.C., and Tycko, R. (2013). Molecular structure of β -amyloid fibrils in Alzheimer's disease brain tissue. *Cell* **154**, 1257–1268.
- Luk, K.C., Kehm, V.M., Zhang, B., O'Brien, P., Trojanowski, J.Q., and Lee, V.M.-Y. (2012). Intracerebral inoculation of pathological α -synuclein initiates a rapidly progressive neurodegenerative α -synucleinopathy in mice. *J. Exp. Med.* **209**, 975–986.
- Meyer-Luehmann, M., Coomaraswamy, J., Bolmont, T., Kaeser, S., Schaefer, C., Kilger, E., Neuenschwander, A., Abramowski, D., Frey, P., Jaton, A.L., et al. (2006). Exogenous induction of cerebral beta-amyloidogenesis is governed by agent and host. *Science* **313**, 1781–1784.
- Miyasaka, T., Morishima-Kawashima, M., Ravid, R., Kamphorst, W., Nagashima, K., and Ihara, Y. (2001). Selective deposition of mutant tau in the FTDP-17 brain affected by the P301L mutation. *J. Neuropathol. Exp. Neurol.* **60**, 872–884.
- Münch, C., O'Brien, J., and Bertolotti, A. (2011). Prion-like propagation of mutant superoxide dismutase-1 misfolding in neuronal cells. *Proc. Natl. Acad. Sci. USA* **108**, 3548–3553.
- Naik, S., and Piwnica-Worms, D. (2007). Real-time imaging of beta-catenin dynamics in cells and living mice. *Proc. Natl. Acad. Sci. USA* **104**, 17465–17470.
- Petkova, A.T., Leapman, R.D., Guo, Z., Yau, W.-M., Mattson, M.P., and Tycko, R. (2005). Self-propagating, molecular-level polymorphism in Alzheimer's beta-amyloid fibrils. *Science* **307**, 262–265.
- Prusiner, S.B. (1984). Some speculations about prions, amyloid, and Alzheimer's disease. *N. Engl. J. Med.* **310**, 661–663.
- Prusiner, S.B. (1998). Prions. *Proc. Natl. Acad. Sci. USA* **95**, 13363–13383.
- Raj, A., Kuceyeski, A., and Weiner, M. (2012). A network diffusion model of disease progression in dementia. *Neuron* **73**, 1204–1215.
- Ren, P.-H., Lauckner, J.E., Kachirskaja, I., Heuser, J.E., Melki, R., and Kopito, R.R. (2009). Cytoplasmic penetration and persistent infection of mammalian cells by polyglutamine aggregates. *Nat. Cell Biol.* **11**, 219–225.
- Sacino, A.N., Thomas, M.A., Ceballos-Diaz, C., Cruz, P.E., Rosario, A.M., Lewis, J., Giasson, B.I., and Golde, T.E. (2013). Conformational templating of α -synuclein aggregates in neuronal-glia cultures. *Mol. Neurodegener.* **8**, 17.
- Safar, J., Wille, H., Itri, V., Groth, D., Serban, H., Torchia, M., Cohen, F.E., and Prusiner, S.B. (1998). Eight prion strains have PrP(Sc) molecules with different conformations. *Nat. Med.* **4**, 1157–1165.
- Santa-Maria, I., Varghese, M., Ksiezak-Reding, H., Dzhun, A., Wang, J., and Pasinetti, G.M. (2012). Paired helical filaments from Alzheimer disease brain induce intracellular accumulation of Tau protein in aggresomes. *J. Biol. Chem.* **287**, 20522–20533.
- Seeley, W.W., Crawford, R.K., Zhou, J., Miller, B.L., and Greicius, M.D. (2009). Neurodegenerative diseases target large-scale human brain networks. *Neuron* **62**, 42–52.
- Siddiqua, A., and Margittai, M. (2010). Three- and four-repeat Tau coassemble into heterogeneous filaments: an implication for Alzheimer disease. *J. Biol. Chem.* **285**, 37920–37926.
- Tanaka, M., Collins, S.R., Toyama, B.H., and Weissman, J.S. (2006). The physical basis of how prion conformations determine strain phenotypes. *Nature* **442**, 585–589.
- Toyama, B.H., Kelly, M.J.S., Gross, J.D., and Weissman, J.S. (2007). The structural basis of yeast prion strain variants. *Nature* **449**, 233–237.
- True, H.L., and Lindquist, S.L. (2000). A yeast prion provides a mechanism for genetic variation and phenotypic diversity. *Nature* **407**, 477–483.
- van Groen, T., Miettinen, P., and Kadish, I. (2003). The entorhinal cortex of the mouse: organization of the projection to the hippocampal formation. *Hippocampus* **13**, 133–149.
- Van Langenhove, T., van der Zee, J., and Van Broeckhoven, C. (2012). The molecular basis of the frontotemporal lobar degeneration-amyotrophic lateral sclerosis spectrum. *Ann. Med.* **44**, 817–828.
- von Bergen, M., Barghorn, S., Li, L., Marx, A., Biernat, J., Mandelkow, E.M., and Mandelkow, E. (2001). Mutations of tau protein in frontotemporal dementia promote aggregation of paired helical filaments by enhancing local beta-structure. *J. Biol. Chem.* **276**, 48165–48174.
- Waxman, E.A., and Giasson, B.I. (2011). Induction of intracellular tau aggregation is promoted by α -synuclein seeds and provides novel insights into the hyperphosphorylation of tau. *J. Neurosci.* **31**, 7604–7618.
- Wischik, C.M., Novak, M., Thøgersen, H.C., Edwards, P.C., Runswick, M.J., Jakes, R., Walker, J.E., Milstein, C., Roth, M., and Klug, A. (1988). Isolation

- of a fragment of tau derived from the core of the paired helical filament of Alzheimer disease. *Proc. Natl. Acad. Sci. USA* 85, 4506–4510.
- Yanamandra, K., Kfoury, N., Jiang, H., Mahan, T.E., Ma, S., Maloney, S.E., Wozniak, D.F., Diamond, M.I., and Holtzman, D.M. (2013). Anti-tau antibodies that block tau aggregate seeding in vitro markedly decrease pathology and improve cognition in vivo. *Neuron* 80, 402–414.
- Yoshiyama, Y., Higuchi, M., Zhang, B., Huang, S.-M., Iwata, N., Saido, T.C., Maeda, J., Suhara, T., Trojanowski, J.Q., and Lee, V.M.-Y. (2007). Synapse loss and microglial activation precede tangles in a P301S tauopathy mouse model. *Neuron* 53, 337–351.
- Zhou, J., Gennatas, E.D., Kramer, J.H., Miller, B.L., and Seeley, W.W. (2012). Predicting regional neurodegeneration from the healthy brain functional connectome. *Neuron* 73, 1216–1227.
- Ziebell, J.M., Taylor, S.E., Cao, T., Harrison, J.L., and Lifshitz, J. (2012). Rod microglia: elongation, alignment, and coupling to form trains across the somatosensory cortex after experimental diffuse brain injury. *J. Neuroinflammation* 9, 247.

Loss of mTOR-Dependent Macroautophagy Causes Autistic-like Synaptic Pruning Deficits

Guomei Tang,¹ Kathryn Gudsruk,² Sheng-Han Kuo,¹ Marisa L. Cotrina,^{3,7} Gorazd Rosoklija,^{4,8} Alexander Sosunov,³ Mark S. Sonders,¹ Ellen Kanter,¹ Candace Castagna,¹ Ai Yamamoto,¹ Zhenyu Yue,⁶ Ottavio Arancio,³ Bradley S. Peterson,^{4,8} Frances Champagne,² Andrew J. Dwork,^{3,4,8} James Goldman,³ and David Sulzer^{1,4,5,8,*}

¹Department of Neurology

²Department of Psychology

³Department of Pathology and Cell Biology

⁴Department of Psychiatry

⁵Department of Pharmacology

Columbia University Medical Center, New York, NY 10032, USA

⁶Departments of Neurology and Neuroscience, Friedman Brain Institute, Icahn School of Medicine at Mount Sinai, New York, NY 10029, USA

⁷Center for Translational Neuromedicine, University of Rochester, Rochester, NY 14642, USA

⁸New York State Psychiatric Institute, New York, NY 10032, USA

*Correspondence: ds43@columbia.edu

<http://dx.doi.org/10.1016/j.neuron.2014.07.040>

SUMMARY

Developmental alterations of excitatory synapses are implicated in autism spectrum disorders (ASDs). Here, we report increased dendritic spine density with reduced developmental spine pruning in layer V pyramidal neurons in postmortem ASD temporal lobe. These spine deficits correlate with hyperactivated mTOR and impaired autophagy. In *Tsc2+/-* ASD mice where mTOR is constitutively overactive, we observed postnatal spine pruning defects, blockade of autophagy, and ASD-like social behaviors. The mTOR inhibitor rapamycin corrected ASD-like behaviors and spine pruning defects in *Tsc2+/-* mice, but not in *Atg7^{CKO}* neuronal autophagy-deficient mice or *Tsc2+/-:Atg7^{CKO}* double mutants. Neuronal autophagy furthermore enabled spine elimination with no effects on spine formation. Our findings suggest that mTOR-regulated autophagy is required for developmental spine pruning, and activation of neuronal autophagy corrects synaptic pathology and social behavior deficits in ASD models with hyperactivated mTOR.

INTRODUCTION

Autism spectrum disorders (ASDs) are characterized by impaired social interactions, communication deficits, and repetitive behaviors. Multiple ASD susceptibility genes converge on cellular pathways that intersect at the postsynaptic site of glutamatergic synapses (Bourgeron, 2009; Peça and Feng, 2012), implicating abnormalities in dendritic spines in ASD pathogenesis. Consistently, increased spine density is observed in frontal, temporal, and parietal lobes in ASD brains (Hutsler and Zhang, 2010) and changes in synaptic structure are detected in multiple

ASD model mice (Zoghbi and Bear, 2012). It remains however unclear why spine pathology occurs and how it is associated with the onset and progression of ASD-related symptoms.

Postnatal synaptic development in mammalian cerebral cortex is a dynamic process involving concurrent formation and elimination/pruning (Purves and Lichtman, 1980; Rakic et al., 1986). Synapse formation exceeds pruning at early ages, yielding excessive excitatory synapses essential for the assembly of neural circuits. Synaptic elimination subsequently outpaces formation, resulting in net spine pruning from childhood through adolescence. Consistently, the density of dendritic spines peaks in early childhood and is followed by a steep decline during late childhood and adolescence to adult levels (Penzes et al., 2011), a process that provides selection and maturation of synapses and neural circuits.

While ASDs exhibit striking genetic and clinical heterogeneity, multiple ASD syndromes are caused by mutations in genes that act to inhibit mammalian target of rapamycin (mTOR) kinase, including *Tsc1/Tsc2*, *NF1*, and *Pten* (Bourgeron, 2009). Synaptic mTOR integrates signaling from various ASD synaptic and regulatory proteins, including SHANK3, FMRP, and the glutamate receptors mGluR1/5 (Peça and Feng, 2012; Bourgeron, 2009). Overactive mTOR signaling may produce an excess of synaptic protein synthesis, which could indicate a common mechanism underlying ASD. Synapses, however, must balance protein synthesis and degradation to maintain homeostasis and support plasticity (Bingol and Sheng, 2011). An important means for removing damaged organelles and degrading long-lived or aggregate-prone proteins is macroautophagy (autophagy hereafter), a process downstream of mTOR signaling that involves the formation of autophagosomes to capture and transport cytoplasmic components to lysosomes. The activation of mTOR inhibits autophagy at an early step in autophagosome formation (Kim et al., 2011). In support of a role for autophagy dysregulation in ASD etiology, a recent study identified ASD-associated exonic copy number variation mutations in genes coding for proteins involved in autophagic pathways (Poultney et al., 2013).

Autophagy has been implicated in synaptic remodeling in *C. elegans* (Rowland et al., 2006) and *Drosophila* (Shen and Ganetzky, 2009), but a role in mammalian synaptic development is unexplored. We hypothesized that autophagy remodels synapse maturation downstream of mTOR, and autophagy deficiency downstream of overactivated mTOR contributes to ASD synaptic pathology. We found a higher spine density in basal dendrites of layer V pyramidal neurons in ASD patients than in controls. The increased spine density was associated with a defect in net postnatal spine pruning that was correlated with hyperactivated mTOR and impaired autophagy. Using *Tsc1/2* mutant ASD mice and *Atg7^{CKO}* neuronal autophagy-deficient mice, we found that aberrant autophagy and mTOR hyperactivation underlies ASD-like synaptic pathology and correcting autophagy signaling could normalize developmental dendritic spine pruning defects and social behaviors.

RESULTS

Dendritic Spine Pruning Deficits in ASD Human Brain

We measured dendritic spines of basal dendrites of layer V pyramidal neurons in the superior middle temporal lobe, Brodmann Area 21 (BA21), a region implicated in ASD due to its participation in brain networks involved in social and communicative processes, including language, social and speech perception, auditory and visual processing, and comprehension of intentions (Redcay, 2008; Zahn et al., 2007). Abnormalities in ASD temporal lobe have been confirmed by functional imaging and pathological studies, including disturbed gene transcription profiles (Garbett et al., 2008; Voineagu et al., 2011), increased dendritic spine densities in pyramidal neurons (Hutsler and Zhang, 2010), and reduced functional specialization (Shih et al., 2011).

We compared dendritic spine morphology in ASD patients and controls (demographic data in Table S1 available online) using the Golgi-Kopsch technique. In the adolescent group, only males were examined to exclude effects of hormone status. No correlation was revealed between spine density and potential confounding factors, including postmortem interval (PMI), seizure history, cause of death, brain pH, or tissue storage (Table S2). As in previous studies (Harris et al., 1992), dendritic protrusions with the ratio of head/neck diameter >1 were classified as spines. The spines were characterized by a neck 0.9–3.0 μm long and a spine head diameter of 0.5–2.0 μm (Figures S1A and S1B). The average spine head diameter ($p = 0.519$) and spine length ($p = 0.819$) from individual neurons were similar in ASD patients and controls at all ages examined (Figures S1C and S1D). The mean net spine density per individual was significantly higher in ASD patients than in controls (Figures 1A and 1B: mean \pm SD: 11.32 \pm 1.23 spines/10 μm versus 8.81 \pm 2.77 spines/10 μm , $p = 0.017$, two tailed t test).

Linear regression of spine density with age indicated a substantially greater level of net spine pruning in controls (slope = -0.40 spines/10 $\mu\text{m}/\text{year}$, $R^2 = 0.93$) than in ASD patients (slope = $-0.19/10$ $\mu\text{m}/\text{year}$, $R^2 = 0.55$; difference from linear regression of controls, $F = 9.4$, $p = 0.007$) (Figure 1C). Due to the limited number of brain samples available, we grouped patients and controls into two age categories: childhood (2–9 years) and adolescence (13–20 years) (Figures 1D and 1E). Analysis

revealed profound effects of both disease and age on spine density ($p < 0.001$, two-way ANOVA, effect of disease: $F(1, 16) = 73.11$, $p < 0.001$; effect of age: $F(1, 16) = 145.7$, $p < 0.001$; disease \times age interaction: $F(1, 16) = 28.35$, $p < 0.001$). The spine density was slightly higher in childhood ASD patients than controls (mean \pm SD: 12.32 \pm 0.60 spines/10 μm in ASD cases versus 11.37 \pm 0.68 spines/10 μm in controls) but markedly higher in adolescent ASD patients than controls (10.33 \pm 0.74 spines/10 μm in ASD cases versus 6.24 \pm 0.59 spines/10 μm in controls). From childhood through adolescence, dendritic spines decreased by $\sim 45\%$ in control subjects but only by $\sim 16\%$ in ASD patients (Figure 1E), demonstrating a developmental defect in net spine pruning in ASD.

Disturbed mTOR-Autophagy Signaling and Spine Pruning in ASD

To test the hypothesis that mTOR-autophagy signaling is disturbed in ASD and associated with ASD spine pathology, we performed western blot analysis of phospho-mTOR (p-mTOR), total mTOR (t-mTOR), phospho-S6 (p-S6), total S6 (t-S6), and the autophagosome marker LC3 and p62 (Figures 2A and 2F) in frozen BA21 brain samples from age-, gender-, and PMI- matched ASD patients and controls (demographic data in Table S3). To determine the relationship between mTOR activity and density of dendritic spines, we examined the protein levels of postsynaptic marker PSD95 and the presynaptic protein synapsin I (Figure 2A).

No effects of PMI, cause of death, brain pH, or length of storage on protein levels were detected (Table S2). We observed a decrease in p-mTOR level with age in controls and higher p-mTOR level in ASD patients than in controls at 13–20 years (Figure 2B). We observed similar changes in p-S6, a reporter for mTOR activity (Figure 2C). PSD95 protein level was higher in controls aged 2–10 years than controls aged 13–20 years, consistent with normal developmental spine pruning. This decrease in PSD95 level with age was absent in ASD patients (Figure 2D), consistent with the lower spine pruning in ASD patients. The presynaptic marker synapsin I exhibited a near-significant decrease with age in controls but not in patients (Figure 2E). Levels of p-mTOR were correlated with PSD95 (Figure 2I), indicating that lower mTOR activity is associated with a higher dendritic spine density in children and adolescents.

To determine whether impaired autophagy underlies the spine pruning deficit in human ASD, we characterized basal autophagy in postmortem tissue of the temporal lobe in patients with ASD. The level of LC3-II, a biomarker that indicates the abundance of autophagosomes, was significantly lower in ASD patients than controls throughout childhood and adolescence (Figures 2F and 2G), while the level of p62, a protein substrate for autophagy, was higher in both childhood and adolescent ASD patients than controls (Figures 2F and 2H). These data suggest a low level of basal autophagy in ASD temporal cortex throughout development. LC3-II and p62 protein levels were not correlated with any confounding factor for tissue preservation but were correlated with seizure activity (Table S2), a common feature of ASD.

The impairment in autophagy in ASD patients was confirmed by immunolabel of LC3-positive puncta in BA21 layer V: the cellular area occupied by LC3 puncta and the integrated

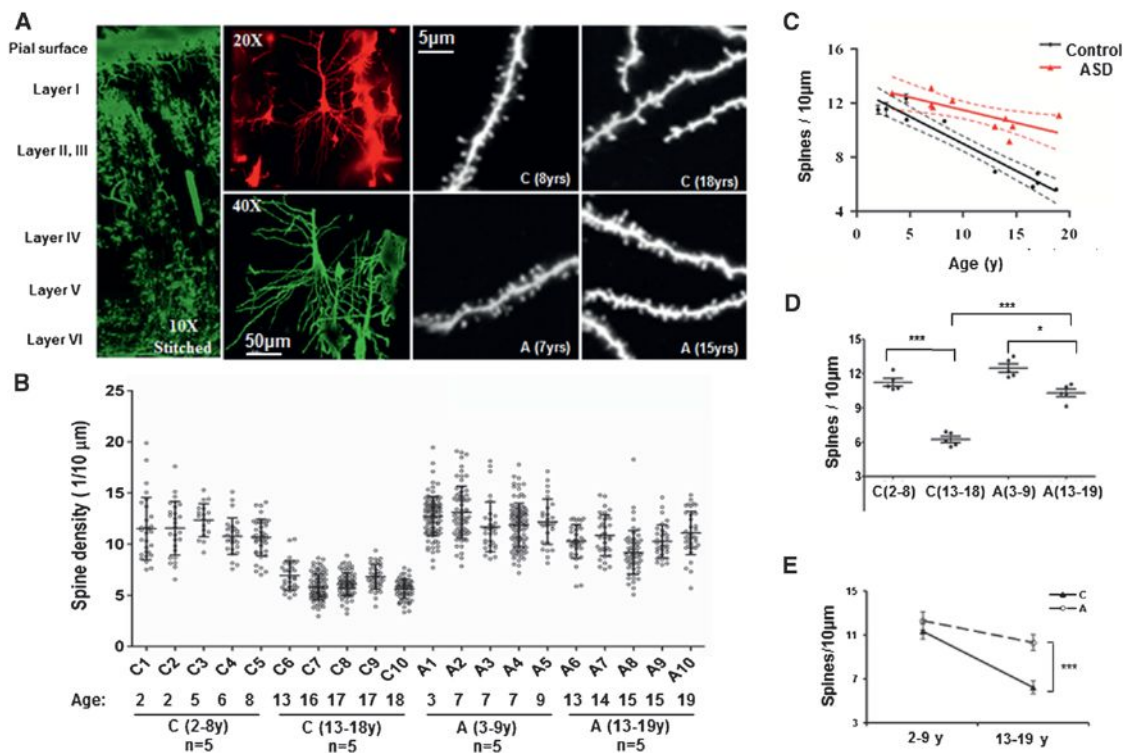


Figure 1. Dendritic Spine Pruning in Temporal Lobe of ASD Patients and Controls

(A) Representative Golgi images for postmortem human temporal lobe (left, 10 \times , stitched from nine separate image stacks), layer V pyramidal neurons with basal dendritic tree (top middle, 20 \times , pseudocolored in red; bottom middle, 40 \times , pseudocolored in green; scale bar, 50 μ m). The right four panels (100 \times ; scale bar, 5 μ m) are representative images of proximal basal dendritic segments from two control subjects (C, aged 8 years and 18 years) and two ASD cases (A, aged 7 years and 15 years).

(B) Distribution of spine density (mean \pm SD) in basal dendrites after the first bifurcation. Age and diagnosis are indicated for each sample. Controls aged 2–8 years [C(2–8 years)]: n = 5; controls aged 13–18 years [C(13–18 years)]: n = 5; ASD cases aged 2–8 years [A(2–8 years)]: n = 5; ASD cases aged 13–18 years [A(13–18 years)]: n = 5. Each point represents the average spine density for each individual neuron measured from each individual.

(C) A linear regression of spine density with age in the control subjects (n = 10) and ASD patients (n = 10). The number of spines per 10 μ m was plotted against the age of each individual. Broken lines indicate 95% confidence intervals.

(D) Spine density (mean \pm SD) for the controls and ASD patients in childhood and adolescence. Each point represents the mean spine density for an individual. Two-way ANOVA, Bonferroni post hoc test. ***p < 0.001, *p < 0.05.

(E) The decrease of spine density with age was greater in the controls than the ASD patients (mean \pm SD). ***p < 0.001.

intensity of LC3 puncta were lower in pyramidal neurons from ASD patients than age-matched controls during both early childhood and adolescence (Figures S1E, S1F, and S1G). Decreased autophagy in cortical neurons was confirmed by the accumulation of autophagy substrates p62 and ubiquitin (Ub) (Figures S1H, S1I, and S1J) and is thus an early feature of ASD. Higher levels of p-mTOR in both control and patients with ASD were strongly associated with lower levels of LC3-II (Figure 2J), suggesting that the lower level of autophagy in ASD patients was attributable to high mTOR activity. Higher LC3-II levels were strongly associated with lower levels of PSD95 (Figure 2K). These data indicate that mTOR-dependent autophagy is negatively correlated with spine density in human brain during childhood and adolescence.

mTOR Dysregulation Causes Spine Pruning Defects in TSC-Deficient Mouse Models of ASD

We then investigated whether mTOR hyperactivation and resulting inhibition of autophagy causes ASD-like dendritic spine pa-

thology in ASD animal models. We focused on mutations in genes encoding tuberous sclerosis complexes TSC1 (hamartin) and TSC2 (tuberin), proteins that form a heterodimer that constitutively inhibits Rheb to inactivate mTOR (Ehninger and Silva, 2011). Mutations in both *Tsc1* and *Tsc2* cause mTOR hyperactivation and ASD-like behaviors in mice (Chévere-Torres et al., 2012; Tsai et al., 2012a; Goorden et al., 2007; Sato et al., 2012).

Tsc2^{+/-} mice however exhibit normal social preference in a three-chamber test (Ehninger et al., 2008; Ehninger et al., 2012) but deficient social interaction in a dyadic reciprocal social test (Sato et al., 2012). This discrepancy in social behaviors could be due to differences in testing protocols, the gender, the age, or genetic background of the testing mice. We thus characterized ASD-like social behaviors in P30–P35 adolescent male *Tsc2*^{+/-} mice maintained in a B6/C57 background. We observed no motor defects or anxiety-like behaviors in open field (Figures S2A–S2F). In the novel object recognition test, *Tsc2*^{+/-} mice spent less time exploring the novel object than their wild-type (WT) littermates, with no difference in time spent

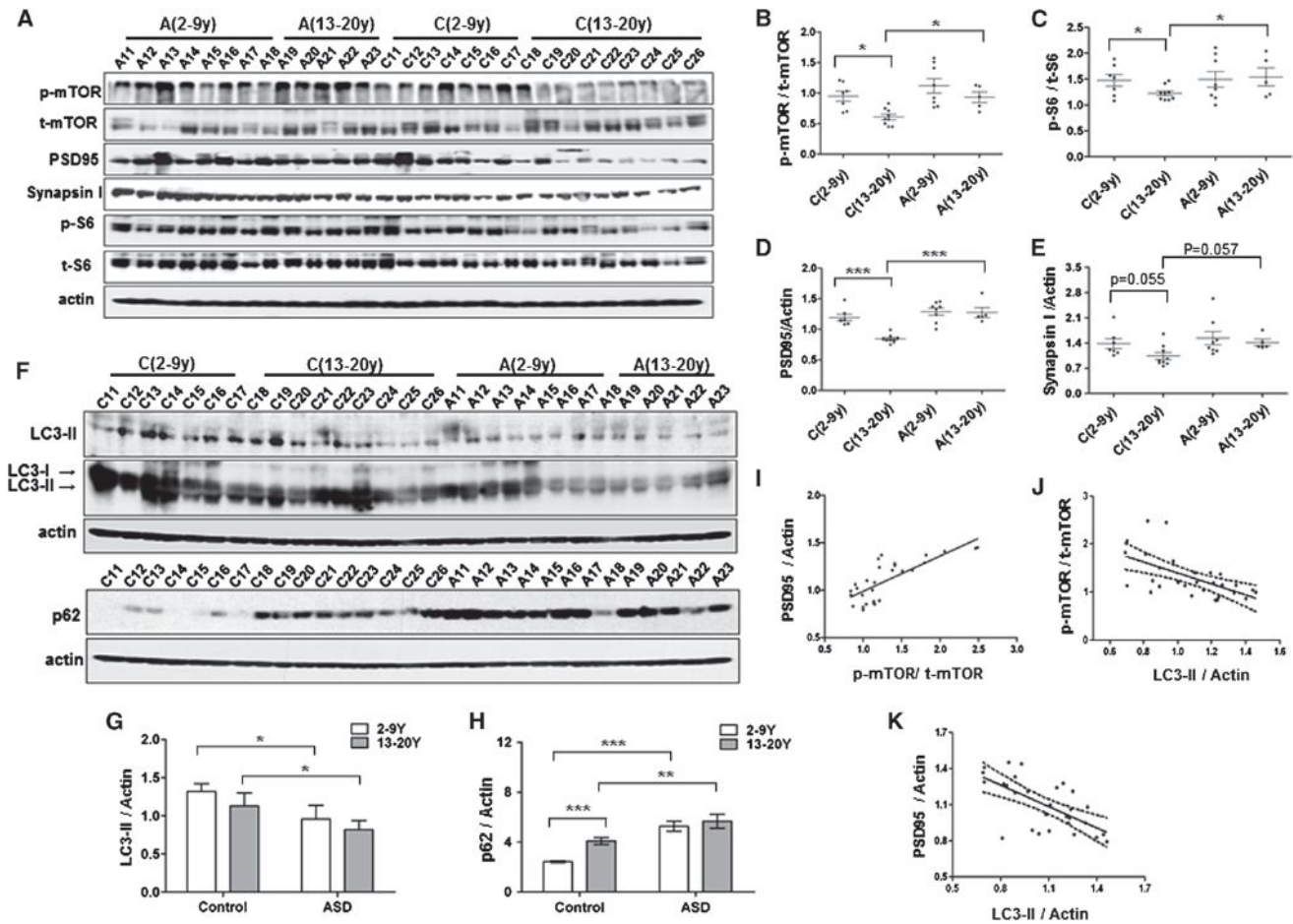


Figure 2. Dysregulated mTOR-Autophagy Signaling and Spine Pruning in ASD Temporal Lobe

(A) Representative western blots of p-mTOR, t-mTOR, p-S6, t-S6, PSD95, and synapsin I in temporal lobe of ASD patients and control subjects aged 2–9 years (ASD, $n = 8$; controls, $n = 7$) and 13–19 years (ASD, $n = 5$; controls, $n = 9$). A, ASD patients; C, controls.

(B–E) The relative density (mean \pm SD) for p-mTOR (B) and p-S6 (C) were normalized to t-mTOR and t-S6, respectively. PSD95 (D) and synapsin I (E) levels were normalized to the relative actin and are presented as scatterplots for ASD patients and controls in two age groups. Each point represents each individual subject. ** $p < 0.01$; *** $p < 0.001$ (two-way ANOVA, Bonferroni's post hoc test).

(F) Western blot of autophagy markers, LC3-II and p62, in temporal lobe of ASD patients and control subjects aged 2–9 years and 13–20 years.

(G) LC3-II levels normalized to actin in controls and patients. ** $p < 0.01$; *** $p < 0.001$ (two-way ANOVA, Bonferroni post hoc test). Mean \pm SD.

(H) p62 levels normalized to actin in controls and patients. ** $p < 0.01$; *** $p < 0.001$ (two-way ANOVA, Bonferroni post hoc test). Mean \pm SD.

(I) Correlation between p-mTOR and PSD95 ($R^2 = 0.598$, $p < 0.001$).

(J) Correlation between p-mTOR and LC3-II in individuals younger than 10 years ($R^2 = 0.347$, $p < 0.0001$), indicating that LC3-II is regulated by mTOR in both ASD patients and controls.

(K) Correlation between LC3-II and PSD95 in individuals younger than 10 years ($R^2 = 0.422$, $p < 0.0001$), suggesting a relationship between synaptic structure protein levels and autophagy.

exploring the familiar object (Figure 3A). *Tsc2*^{+/-} mice, however, did not exhibit ASD-like repetitive behaviors (Figure 3B). Sociability was assessed during a dyadic social interaction with a novel (noncagemate) mouse matched for sex and genotype (see Supplemental Information). *Tsc2*^{+/-} mice spent less time sniffing the stimulus mouse (Figure 3C), indicating impaired social interactions. Social deficits were confirmed using a three-chamber social test. While *Tsc2*^{+/-} mice showed a preference for interacting with a social target compared with nonsocial target (Figure 3D, left), the preference index (the ratio of time sniffing mouse versus nonsocial target) was decreased

(Figure 3D, right). In the social novelty test, *Tsc2*^{+/-} mice spent a similar amount of time sniffing both novel and familiar social targets (Figure 3E, left), with decreased preference index (the ratio of time sniffing a stranger mouse versus a familiar mouse; Figure 3E, right), indicating a reduced preference for social novelty.

The density of dendritic spines in pyramidal neuron basal dendrites of layer V A1/S2 in temporal cortex, which is thought to be analogous to the primate primary auditory cortex (A1) and secondary somatosensory cortex (S2) (Benavides-Piccione et al., 2002), was examined by DiOlistic labeling (Figure 3F). A higher

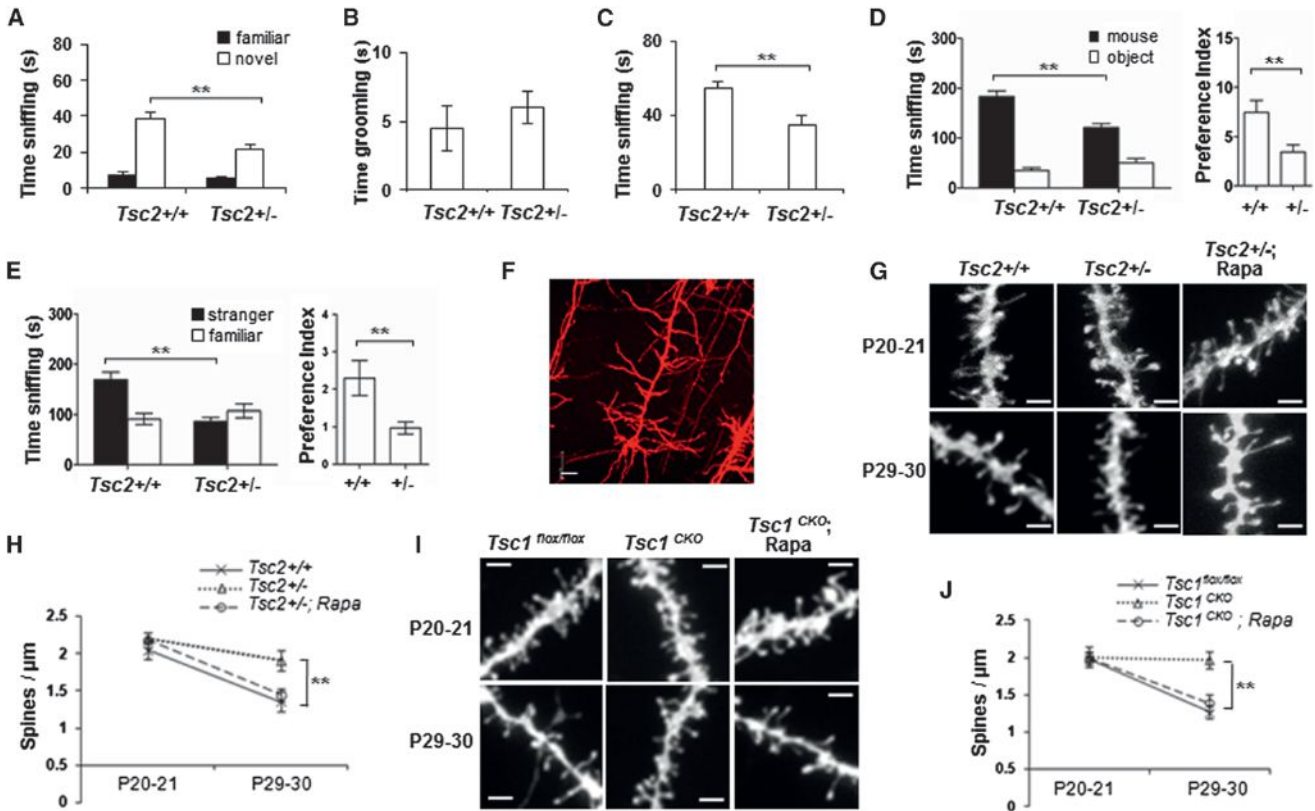


Figure 3. Spine Pruning Defects in *Tsc1/2*-Deficient Cortical Projection Neurons

(A–D) Social behaviors in P30–P33 male adolescent *Tsc2*^{+/-} mice. *Tsc2*^{+/+} WT: n = 15, *Tsc2*^{+/-}: n = 14. Mean ± SEM. (A) Novel object recognition test showing time spent investigating a familiar versus novel object. (B) ASD-like repetitive behavior. (C) Dyadic reciprocal social interaction test showing time spent sniffing a stimulus mouse. (D) Sociability in the three-chamber test showing time spent (left) and preference (right) for sniffing a stimulus mouse or an object.

(E) Social novelty in the three-chamber test showing time spent (left) and preference (right) for sniffing a stranger mouse versus a familiar mouse. Compared to WT, **p < 0.01; *p < 0.05 (unpaired t test). Mean ± SEM.

(F) A confocal image of a Dil-labeled layer V cortical pyramidal neuron. Scale, 20 μm.

(G) Typical confocal images of Dil labeled dendrites in WT, *Tsc2*^{+/-} and rapamycin (Rapa) treated *Tsc2*^{+/-} mice at P19–P20 and P29–P30. Rapamycin was administered at 3 mg/kg/day intraperitoneally from P21 to P28, and the mice were labeled for spine analysis on P29–P30. Scale bar, 2 μm.

(H) Spine pruning in *Tsc2*^{+/-} mice. ** compared with WT at P29–30, p < 0.01 (two-way ANOVA, Bonferroni post hoc test). n = 7–10 mice per group. Mean ± SD.

(I) Representative images of Dil-labeled dendrites from *Tsc1*^{CKO} mutants and *Tsc1*^{flx/flx} controls. Scale bar, 2 μm.

(J) Spine density in *Tsc1*^{flx/flx} and *Tsc1*^{CKO} mice at P19–P20 and P29–P30. ** compared to P29–P30 *Tsc1*^{flx/flx} controls, p < 0.01 (two-way ANOVA, Bonferroni post hoc test). Mean ± SD.

spine density was found in adolescent *Tsc2*^{+/-} mice than in WT (Figures 3G and 3H). The greater spine density in *Tsc2*^{+/-} layer V cortex at P30 was confirmed by increased immunolabel for the presynaptic marker, synaptophysin, and the postsynaptic marker, PSD95 (Figures S2G and S2H). We also observed increased PSD95 and F-actin-labeled puncta along the dendrites of mature *Tsc2*^{+/-} primary neuronal cultures (Figures S2I and S2J).

Net spine pruning normally occurs in mice after the third postnatal week (Zuo et al., 2005), and so we compared spine densities between P19–P20 and P29–P30. If the lack of TSC and hyperactivation of mTOR led to spine overgrowth, an increase in spine density would be expected prior to spine pruning. DiI-olistic labeling revealed similar numbers of spines at P19–P20 in *Tsc2*^{+/-} and WT mice but far more spines in P29–P30 *Tsc2*^{+/-} mice than in WT (Figures 3G and 3H). The soma size

and basal dendritic tree complexity were similar in WT and *Tsc2*^{+/-} mutants (Figure S3A). These results suggest that there is a period of massive spine pruning between the ages of P19–P20 and P29–P30 in WT but a lack of normal pruning in *Tsc2*^{+/-} mice. Inhibition of mTOR by intraperitoneal (i.p.) injection of rapamycin showed no effects in WT controls (Figure S3B) but corrected the pruning defect in *Tsc2*^{+/-} mutants to the control level.

To confirm the effect of the *Tsc* deficiency on dendritic spine pruning, we used a *Tsc1* conditional knockout mouse line (*Tsc1*^{CKO}), in which the *Tsc1* gene was depleted from pyramidal neurons in the forebrain by crossing *Tsc1*^{flx/flx} mice to *CamKII-Cre* mice. As *CamKII* promoter-driven *Cre* recombination begins in layer II–III cortical pyramidal neurons at P19–P20 but is substantial in all cortical layers at P23–P30 (Figure S4A), the level of TSC1 is normal in deep cortical layers at the start of this time window for spine pruning and depleted thereafter (Figures

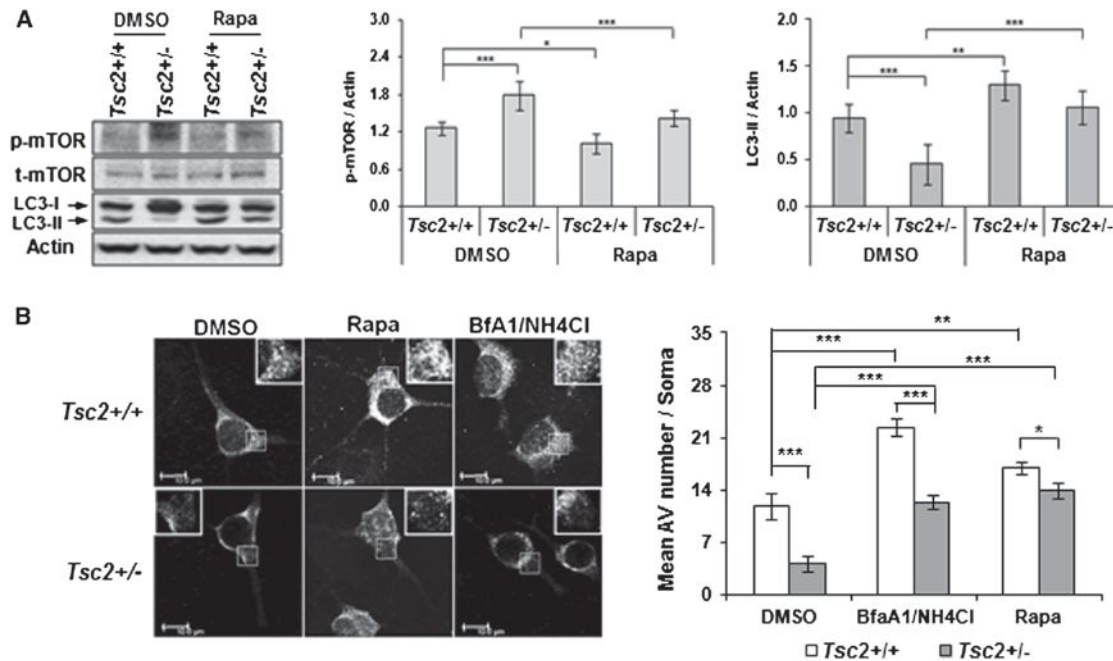


Figure 4. TSC Ablation Downregulates Autophagic Activity and Rapamycin Reconstitutes Normal Autophagy

(A) Western blot analysis of p-mTOR, t-mTOR, and LC3-II in P29 *Tsc2*^{+/-} mouse brain. *Tsc2* WT and *Tsc2*^{+/-} mice were i.p. injected with DMSO vehicle or rapamycin from P20 to P28. Right: quantification of p-mTOR and LC3-II levels. Mean \pm SD. * $p < 0.05$; ** $p < 0.01$; *** $p < 0.001$ (two-way ANOVA, Bonferroni post hoc test). $n = 5-6$ animals per group. *Tsc2*^{+/-} mutant cortex on P29–P30 showed increased p-mTOR levels and decreased levels of LC3-II. Inhibiting mTOR with rapamycin decreased p-mTOR and increased LC3II in both wild-type and mutant lines.

(B) Impaired autophagic flux in *Tsc2*^{+/-}; *GFP-LC3* cortical neurons. Right: mean number of GFP-LC3 puncta per soma of cortical neurons; 8–10 neurons per group in triplicates were analyzed. Scale bar, 10 μ m. * $p < 0.05$; ** $p < 0.01$; *** $p < 0.001$ (two-way ANOVA, Bonferroni post hoc test). Mean \pm SD.

S4B and S4C). This mouse line allows us to model an appropriate developmental period for evaluating roles for cell-autonomous effects of neuronal mTOR in the regulation of developmental spine pruning. At P19–P20, the density of spines in basal dendrites of A1/S2 layer V pyramidal neurons was equivalent for both *Tsc1*^{flax/flax} control and *Tsc1*^{CKO} mice ($p > 0.05$), but spines in control mice were significantly less dense than in *Tsc1*^{CKO} mice at P29–P30 ($p < 0.01$, Figures 3I and 3J). Although soma size was slightly greater (15%) in P29–P30 *Tsc1*^{CKO} pyramidal neurons, the number of primary basal dendrites was similar for control and *Tsc1*^{CKO} mice (Figures S4D, S4E, and S4F). Rapamycin treatment did not affect spine density in *Tsc1*^{flax/flax} control mice (Figure S5B), but corrected spine pruning in *Tsc1*^{CKO} mice to control levels (Figures 3I and 3J), with no effect on basal dendritic branching. Thus, both *Tsc1*^{CKO} and *Tsc2*^{+/-} mutants showed a lack of efficient postnatal spine pruning, indicating that TSC inhibition of mTOR is required for postnatal spine pruning. The effects of TSC1 deletion on spine density in pyramidal neurons at P30 is consistent with those reported in vivo in Purkinje cells (Tsai et al., 2012a).

Autophagy Deficiency in *Tsc2*^{+/-} Mutant Neurons

We then addressed whether autophagy remodels dendritic spines downstream of mTOR. We confirmed suppression of basal autophagy due to mTOR disinhibition in the *Tsc* mutant mouse brain by (1) a decrease in protein levels of LC3-II in *Tsc2*^{+/-} cortex, which was normalized by rapamycin (Figure 4A);

(2) an increase in the level of phospho-S6 (pS6), indicating mTOR hyperactivation, and a reduction in GFP-LC3 puncta, a fluorescent marker for autophagosomes, in cortical pyramidal neurons from *Tsc2*^{+/-}; *GFP-LC3* mice (Figure S5A), indicating impaired autophagy and rapamycin-normalized pS6 levels and numbers of GFP-LC3 puncta; (3) decreased immunolabel for endogenous LC3 in *Tsc2*^{+/-} mutant primary neuronal cultures (Figure S5B); (4) an accumulation of autophagy substrates, including p62 (Komatsu et al., 2007a), lipid droplets, and damaged mitochondria (Martinez-Vicente et al., 2010), in *Tsc2*^{+/-} primary neuronal cultures (Figures S5B, S5C, S5D, and S5E); (5) accumulation of p62- and Ub- positive inclusions in pyramidal neurons in *Tsc1*^{CKO} mouse brain (Figure S5F).

We analyzed autophagy flux in *Tsc2*^{+/-}; *GFP-LC3* neurons in comparison to *Tsc2* WT; *GFP-LC3* neurons (Figure 4B). Cultured primary neurons were treated with bafilomycin (BafA1) and NH₄Cl to inhibit lysosomal hydrolase and block autophagosome-lysosome fusion. We reasoned that if autophagy flux was impaired by mTOR hyperactivation, BafA1/NH₄Cl blockade of lysosomal degradation would produce a lower accumulation of autophagosomes in *Tsc2*^{+/-} neurons than in WT. As expected, there was more accumulation of GFP-LC3 puncta in BafA1/NH₄Cl-treated WT neurons than *Tsc2*^{+/-} neurons, confirming a failure of autophagosome induction in *Tsc2*^{+/-} neurons (Figure 4B). Rapamycin (200 nM, 8 hr) normalized autophagosome formation in *Tsc2*^{+/-} neurons. These findings support the hypothesis that basal neuronal

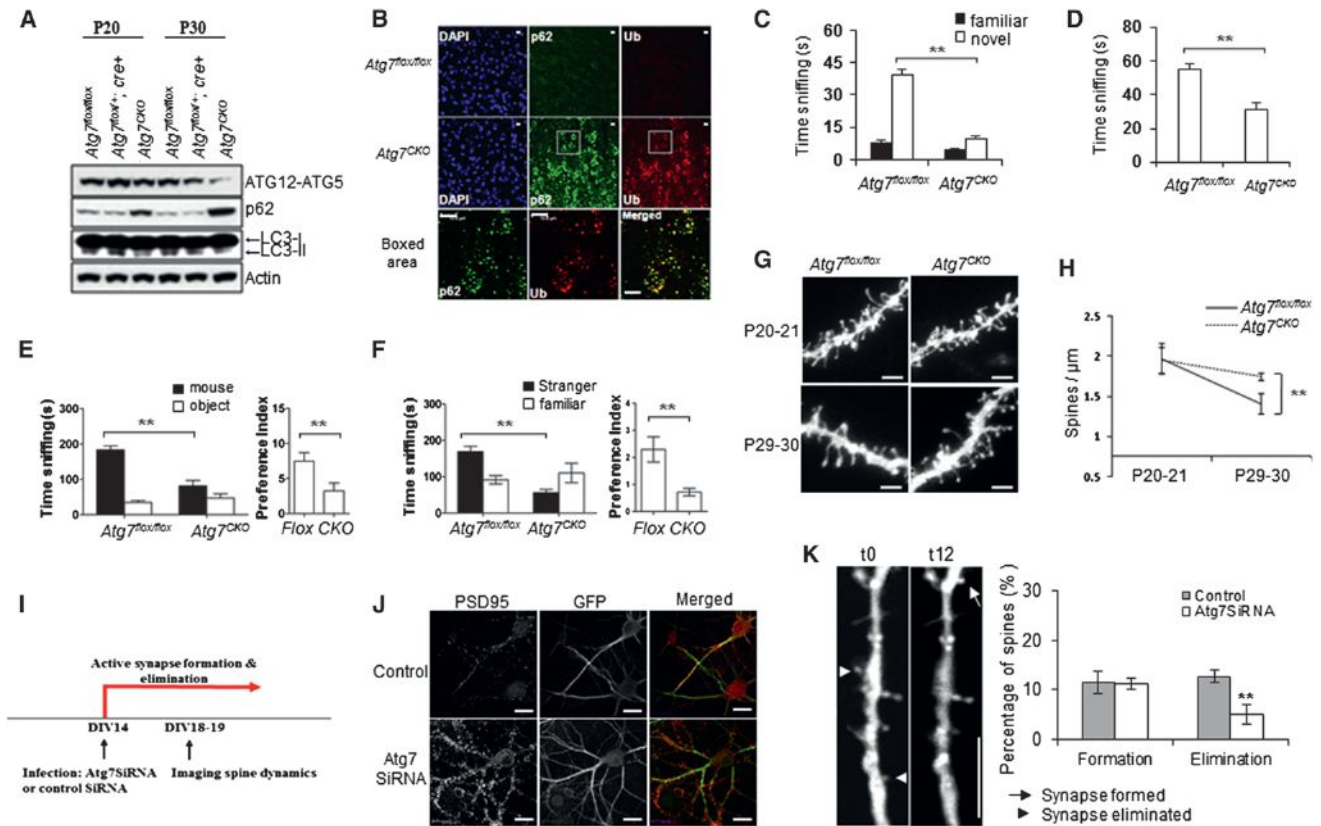


Figure 5. Dendritic Spine Pruning Defects and ASD-like Behaviors in *Atg7^{CKO}* Mice

(A) Western blot analysis of autophagy markers in the *Atg7^{CKO}* cortex. Brain homogenates from P19–P20 and P29–P30 mice were immunoblotted with antibodies against Atg12–Atg5, LC3, and autophagy substrate p62. Data shown are representative of three separate experiments. Loss of autophagy was indicated by a decrease in levels of Atg5–12 conjugation and LC3-II protein, and an increase in p62 protein.

(B) Immunofluorescent labeling of p62 and ubiquitin (Ub) in P30 *Atg7^{CKO}* mouse cortex. Scale bar, 10 μ m.

(C–F) ASD-like social behaviors in *Atg7^{CKO}* mice. *Atg7^{lox/lox}* males, n = 15; *Atg7^{CKO}* males, n = 13. (C) Novel object recognition test showing time spent sniffing a familiar object versus a novel object. (D) Dyadic social interaction test showing the time testing mice spent sniffing a stimulus mouse. ** Compared to *Atg7^{lox/lox}*; p < 0.01; unpaired t test. (E) Sociability in the three-chamber test showing time spent (left) and preference (right) for a stimulus mouse or an object. (F) Social novelty in the three-chamber test showing time spent (left) and preference (right) for sniffing a stranger mouse versus a familiar mouse. Compared to WT, **p < 0.01 (unpaired t test). Mean \pm SEM.

(G) Dendritic segments from *Atg7^{lox/lox}* and *Atg7^{CKO}* pyramidal neurons at P19–P20 and P29–P30. n = 7–10 animals per group. Scale bar, 2 μ m.

(H) Fewer spines were pruned in *Atg7^{CKO}* mice. ** Compared to P29–P30 *Atg7^{lox/lox}*, p < 0.01 (two-way ANOVA, Bonferroni post hoc test). Mean \pm SD.

(I) Timeline of infection and spine analysis.

(J) Cultured control and *Atg7* siRNA lentiviral infected mouse hippocampal neurons at DIV20, visualized by GFP and PSD95 fluorescence. *Atg7* siRNA expressing neurons exhibited more PSD95 puncta than controls. Scale bar, 20 μ m.

(K) Spine formation and elimination in control and *Atg7* siRNA-infected neurons during a 12 hr time window at DIV19–DIV20. Mean \pm SD. Scale bar, 10 μ m.

autophagy is depressed due to mTOR hyperactivation in *Tsc* mutant ASD mouse models.

Autophagy Deficiency Results in ASD-like Social Behaviors and Spine Pruning Defects

To investigate whether neuronal autophagy deficiency produces ASD-like behaviors and dendritic spine pathology, we generated forebrain excitatory neuronal specific autophagy-deficient mice by crossing *Atg7^{lox/lox}* mice to *CamKIIa-cre* mice. *Atg7* is an E1-like activating enzyme required for autophagosome formation (Komatsu et al., 2006). A deficit in autophagy was confirmed by western blot analysis of conjugated ATG5–12, p62, and LC3-II proteins (Figure 5A) and by immunolabel of p62 and ubiquitin

(Ub) (Figures 5B and 6A), proteins that form aggregates after autophagy inhibition (Komatsu et al., 2006, 2007a). At P20 there were no differences in LC3-II and conjugated ATG5–12 levels between genotypes, although p62 levels were higher in *Atg7^{lox/lox};CamKII-Cre (Atg7^{CKO)}* autophagy-deficient mice (Figure 5A). By P30, however, *Atg7^{CKO}* mice exhibited less conjugated ATG5–12 and LC3-II protein and more p62 protein than the *Atg7^{lox/lox}* controls. *Atg7^{CKO}* mice displayed occasional p62/Ub-positive inclusions in pyramidal neurons at P20 and prominent p62/Ub-positive aggregates in layer II–III and layer V–VI pyramidal neurons at P30 (Figure 5B). The results confirm a loss of autophagy between P20 and P30 in cortical pyramidal neurons in *Atg7^{CKO}* mice.

Atg7^{CKO} mice exhibited ASD-like social recognition (Figure 5C) and social interaction deficits similar to those seen in *Tsc2+/-* mutants. During dyadic encounters, they spent less time sniffing stimulus mice than their control littermates (Figure 5D). In the three-chamber test, *Atg7^{CKO}* mice displayed impaired preference for sniffing the social target (Figure 5E) and for social novelty (Figure 5F). However, these mice did not show stereotyped repetitive behaviors, motor defects, or anxiety-like behaviors (Figures S6A–S6G).

We did not observe significant changes in the size of neuronal soma and the number of primary basal dendrites during this developmental period (Figures S6H–S6J). At P19–P20, *Atg7^{CKO}* basal dendrites from layer V A1/S2 pyramidal neurons exhibited a similar number of spines as those in the *Atg7^{flox/flox}* control mice (Figures 5G and 5H). In contrast, by P29–P30 the *Atg7^{CKO}* basal dendrites exhibited more spines than controls. Thus, basal neuronal autophagy is required for normal spine pruning during postnatal development and for the development of normal social behaviors. The pruning defect is unlikely to result from abnormalities in microglia and astrocytes, as we observed no activation of microglia or astrocytes at any age in *Atg7^{CKO}* mice (Figures S6K and S6L).

Autophagy Mediates Spine Elimination in Primary Cultures of Hippocampal Neurons

The increased spine density and reduced spine pruning in *Atg7^{CKO}* mice may result from an increase in synapse formation or a decrease in synapse elimination. Primary cultures of hippocampal neurons have been used as an *in vitro* system to investigate the formation, maturation, and pruning of dendritic spines, in which dendritic spines are formed and pruned during a developmental period similar to that *in vivo* in mouse brain (Orefice et al., 2013; Ko et al., 2011; Papa et al., 1995), with spine density increases between 6–10 days *in vitro* (DIV6–DIV10), peaks at DIV14–DIV21, and decreases after weeks 3 or 4 *in vitro* in neuronal cultures. We thus infected CA1 hippocampal neurons with a lentivirus expressing EGFP-Atg7 siRNA or an EGFP control virus at DIV14–DIV15, a period of active synapse formation and stabilization in cultures. Three to four days after infection, the cultures were fixed and stained for postsynaptic marker PSD95 (Figures 5I and 5J). Neurons expressing Atg7 siRNA exhibited a higher level of PSD95 puncta at DIV19–DIV20 than neurons infected with control virus (Figure 5J), suggesting an increased spine density. We calculated the rate of spine genesis and spine pruning at DIV19–DIV20 during a 12 hr time window. In control neurons infected with viral vector controls, ~12% of spines were formed and ~13% eliminated, indicating equivalent rates of spine formation and elimination that reflect stabilized spine densities (Figure 5K). In contrast, ~12% of spines were formed, but only ~5% of pre-existing spines were pruned in Atg7 siRNA-infected neurons ($p < 0.05$, *t* test). Therefore, Atg7 knockdown produced excessive dendritic spines by inhibiting elimination but exerted no effect on formation.

Autophagy Deficiency Underlies Spine Pruning Defects in *Tsc2+/-* Mice

We then asked whether autophagy deficiency underlies spine pruning defects in *Tsc2+/-* mice. mTOR regulates a number of

downstream biological processes including protein synthesis, autophagy, ribosome biogenesis, and activation of transcription leading to lysosome biogenesis or mitochondrial metabolism. To disentangle autophagy from other downstream effectors of mTOR, we crossed *Tsc2+/-* mice to the *Atg7^{CKO}* mice to produce a *Tsc2+/-:Atg7^{CKO}* double mutant line. We hypothesized that if neuronal autophagy were responsible for spine pruning, rapamycin treatment during the fourth week would reconstitute normal autophagy and pruning in the *Tsc2+/-* mice but would not do so in *Atg7^{CKO}* and *Tsc2+/-:Atg7^{CKO}* double mutant mice.

We observed high levels of p62 and ubiquitin in *Tsc2+/-*, *Atg7^{CKO}*, and *Tsc2+/-:Atg7^{CKO}* double mutant cortices at P30, consistent with a deficit of autophagy between P20 and P30 (Figure 6A). We imaged basal dendrites of layer V A1/S2 pyramidal neurons in all lines at P20 to provide a baseline. We then treated mice from all lines with DMSO vehicle or rapamycin from P21 to P28. On P29, basal dendrites of layer V A1/S2 pyramidal neurons were labeled and analyzed (Figures 6B and 6C). In the DMSO vehicle-treated mice, the percentage of spines pruned between P21 and P29 was 26%; 8%, 3%, and 2% were pruned in the *Atg7^{CKO}*, *Tsc2+/-*, and double mutant mouse lines, respectively, all of which were treated with DMSO vehicle (Figure 6D, two-way ANOVA, Bonferroni's post hoc test; genotype \times treatment interaction: $F(3,16) = 15.38$, $p < 0.001$; effect of treatment: $F(1,16) = 32.16$, $p < 0.001$; effect of genotype: $F(3,16) = 56.17$, $p < 0.001$). Therefore, basal levels of autophagy appeared responsible for ~70% ($[(26 - 8)/26]$) of postnatal spine pruning in control mice. No significant effect of rapamycin on spine pruning in *Atg7^{flox/flox}* control mice was observed. Rapamycin reversed spine pruning defects in *Tsc2+/-* mice to the level of control mice but did not rescue spine pruning in *Atg7^{CKO}* mice or in *Tsc2+/-:Atg7^{CKO}* double mutants, demonstrating that neuronal autophagy is required for spine elimination in *Tsc2+/-* mice. Note that a relatively small fraction ($8\%/26\% = 30\%$) of spine pruning was preserved in *Atg7^{CKO}* mice, indicating that additional mechanisms independent from neuronal autophagy are responsible for the remainder of spine elimination during postnatal development. Consistently, we found that rapamycin rescued spine pruning in *Tsc2+/-:Atg7^{CKO}* mice to this relatively low level of neuronal autophagy-independent pruning.

Rapamycin Normalizes Social Deficits in *Tsc2+/-* Mice but Not in *Atg7* Conditional Knockouts

We next examined whether rapamycin rescued social deficits in *Tsc2+/-* mice, *Atg7^{CKO}* mice, and the double mutants. Sociability and social novelty were tested with the three-chamber testing paradigm as above. DMSO vehicle produced no effect on any mouse line (Figures 3, 5, and 6). *Atg7^{flox/flox}* control mice treated with vehicle preferred to sniff the novel mouse more than the nonsocial object in the sociability test (Figures 6E and 6F) and preferred to sniff the stranger mouse more than the familiar mouse in the social novelty test (Figures 6G and 6H). In contrast, each mutant mouse line displayed impaired preferences for sociability and social novelty.

The preferences of the *Atg7^{flox/flox}* control mice were unaffected by rapamycin. In contrast, rapamycin normalized the sociability and social novelty preferences of the *Tsc2+/-* mice. Rapamycin, however, did not normalize preferences of either

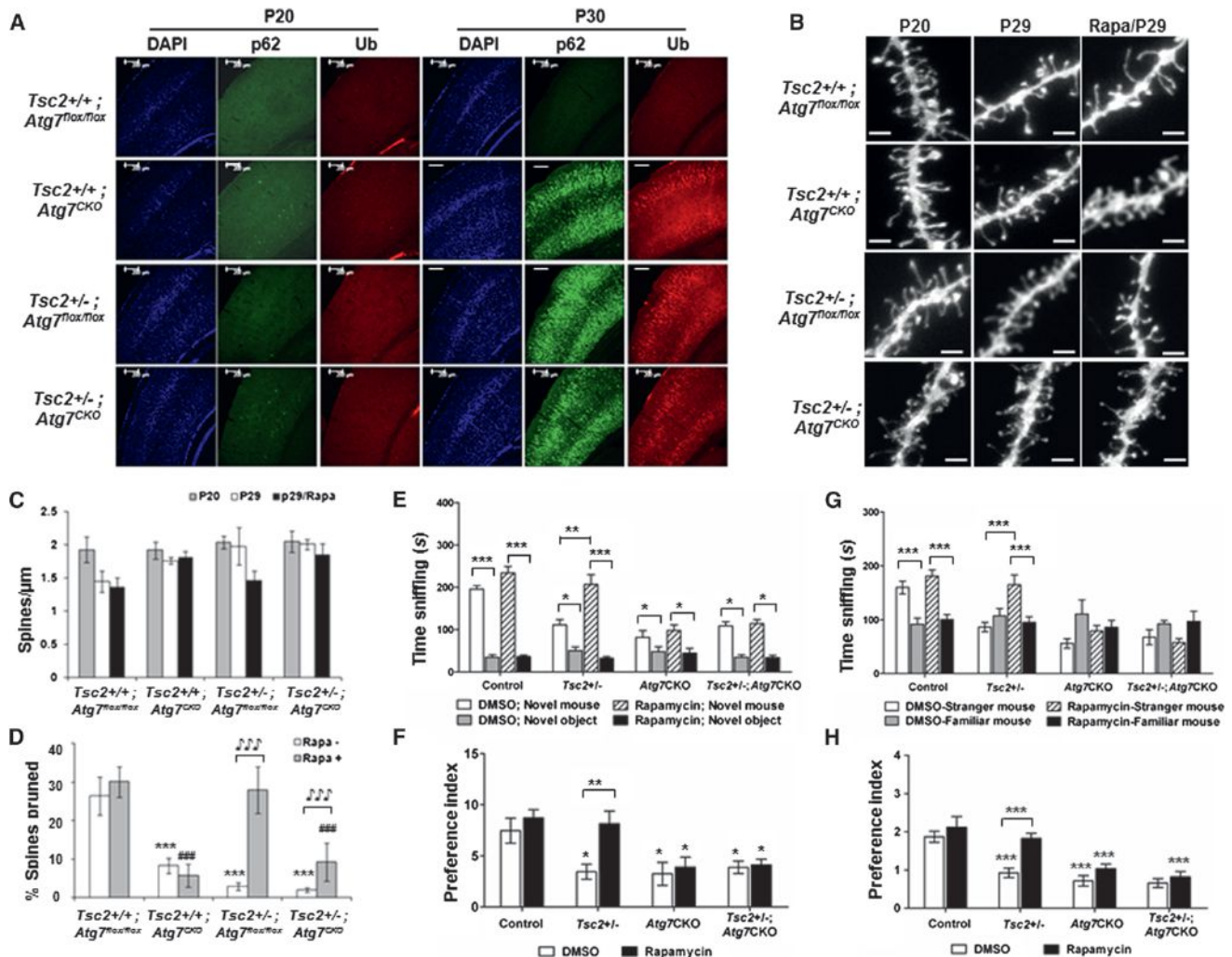


Figure 6. Autophagy Deficiency Underlies Spine Pruning Defects and ASD-like Social Deficits in *Tsc2+/-* Mice

(A) p62- and Ub-positive immunolabeled inclusions in autophagy-deficient neurons. Note that P62⁺ and Ub⁺ inclusions were occasionally present in *Tsc2+/-*, *Atg7^{CKO}*, and *Tsc2+/-; Atg7^{lox/lox}* cortex at p20 but appear in a majority of cortical neurons in these three lines at P30. No p62⁺ and Ub⁺ inclusions were seen in P30 cortical neurons from *Atg7^{lox/lox}* control mice. Scale bar, 200 μ m.

(B–D) Rapamycin normalized dendritic spine pruning in an autophagy-dependent manner. (B) Representative images of dendrites from different mouse lines treated with DMSO vehicle or rapamycin. Scale, 2 μ m. (C) Graphic representation of dendritic spine densities in each condition. Mean \pm SD. (D) Percentage of spines pruned in control and mutant mouse lines. Percentage change in mean spine density (MSD) between P20 and P29 was calculated as: (MSD (P20) – MSD (P29)) / MSD (P20) \times 100%. Rapamycin rescued spine pruning deficits in *Tsc2+/-* mice but not in *Atg7^{CKO}* and had relatively little effect in *Tsc2+/-; Atg7^{CKO}* double mutants. n = 7–10 animals per group. *** Compared to DMSO treated *Atg7^{lox/lox}* controls, p < 0.001; ### Compared to rapamycin treated *Atg7^{lox/lox}* controls, p < 0.001; [^] compared to DMSO vehicle controls, p < 0.001 (two-way ANOVA, Bonferroni post hoc test). Mean \pm SD.

(E–H) Autophagy deficiency blocks the rescue by rapamycin on ASD-like social behaviors in *Tsc2+/-* mice. n = 10–14 animals per group. (E and F) Sociability: DMSO-treated *Tsc2+/-*, *Atg7^{CKO}*, and *Tsc2+/-; Atg7^{CKO}* mice each spent less time sniffing social target versus nonsocial target (E) and exhibited decreased preference (F) for the social target versus nonsocial target. Rapamycin treatment ameliorated impaired sociability in *Tsc2+/-* mice, but not in *Atg7^{CKO}* and *Tsc2+/-; Atg7^{CKO}* mice. (G and H) Social novelty: DMSO-treated *Tsc2+/-*, *Atg7^{CKO}*, and *Tsc2+/-; Atg7^{CKO}* mice all spent less time sniffing novel mice during social novelty test (G) and displayed a decrease in preference for social novelty (H). Rapamycin treatment prevented the loss of preference for social novelty in *Tsc2+/-* mice but not in *Atg7^{CKO}* and *Tsc2+/-; Atg7^{CKO}* mice. *p < 0.05; **p < 0.01; ***p < 0.001 (two-way ANOVA, Bonferroni post hoc test). Mean \pm SEM.

the *Atg7^{CKO}* mice or the double mutants (sociability test, Figure 6F, p < 0.01, two-way ANOVA, Bonferroni's post hoc test; genotype \times treatment interaction: p > 0.05, effect of treatment: F(1,85) = 4.156, p < 0.05; effect of genotype: F(3,85) = 6.775, p < 0.001; social novelty test, Figure 6H, p < 0.01, two-way ANOVA: genotype \times treatment interaction: F(3,85) = 3.085,

p < 0.05; effect of treatment: F(1,85) = 13.02, p < 0.001; effect of genotype: F(3,85) = 25.64, p < 0.001). Thus, rapamycin rescued impaired sociability and social novelty preferences of *Tsc2+/-* mice but did not rescue behaviors in *Atg7^{CKO}* mice in which neuronal autophagy cannot be activated. Note that rapamycin failed to reverse the impaired social behaviors in

Tsc2+/-:Atg7^{CKO} double mutants, although spine pruning deficits were partially reversed.

DISCUSSION

Dendritic Spine Pruning Defect in the ASD Brain

We assessed spine density across development and confirm an increase in basal dendrite spine density in layer V pyramidal neurons in ASD temporal lobe. Layer V pyramidal neurons are the major excitatory neurons that form cortical-cortical and cortical-subcortical projections. Basal dendrites receive excitatory and inhibitory inputs from local sources, and excitatory cell types target this compartment almost exclusively (Spruston, 2008). The increase in basal dendrite spine density suggests an enhanced local excitatory connectivity, a feature of ASD (Belmonte et al., 2004) proposed to cause failure in differentiating signals from noise, prevent development of normal long-range cortical-cortical and cortical-subcortical communications, and underlie neocortical excitation/inhibition imbalance (Sporns et al., 2000; Gogolla et al., 2009).

Note that while signs of ASD can often be detected at 12–18 months, ~82% of ASD diagnoses occur at 4 years or older (<http://www.cdc.gov/ncbddd/autism/data.html>), and CNS tissues from very young ASD patients are extremely rare. As human brain samples from ASD patients cannot be identified prior to diagnosis, pathological analysis cannot determine whether increased spine density precedes symptoms. We therefore relied on correlations among an age range of available pathological specimens, synaptic density, and biochemical markers for analysis. It is remarkable that the only available brain sample suitable for morphological study of a very young diagnosed ASD patient (age = 3 years) displayed a synaptic density higher than any control subject. We find that a defect in net spine pruning was responsible for the abnormally high synaptic densities in childhood and adolescent ASD, an observation confirmed in animal models. A variety of results indicate that this deficit is due in large part to a loss of mTOR-dependent autophagy in neurons. While synapse formation outpaces synapse elimination at young ages, yielding the highest synaptic density in early life, significantly reduced cortical autophagy was also apparent in the youngest diagnosed ASD patient (age = 2 years, frozen tissue), as indicated by low levels of the autophagic vacuole marker LC3-II and increased level of autophagy substrates p62. An ongoing deficiency in autophagy and impaired spine elimination at younger ages would be expected to increase net spine density and interfere with the dynamic turnover of synapses that organizes neural circuits. Interruption of this maturational organization of the brain would lead to a persistence of immature or formation of aberrant circuits in ASD.

The near-linear decrease in spine number from all cases between the ages of 2 to 19 years indicates that spine pruning in temporal lobe occurs over the first two decades and that net loss of synapses is substantially greater in controls than ASD patients. The spine densities declined during the first and second decade by 41% in normal controls but only by 16% in ASD patients, a level independently confirmed by analysis of pre- and postsynaptic markers. This deficit may contribute to abnormalities in cognitive functions that humans acquire in their late child-

hood, teenage, or early adult years, such as the acquisition of executive skills such as reasoning, motivation, judgment, language, and abstract thought (Goda and Davis, 2003; Sternberg and Powell, 1983). Many children diagnosed with ASD reach adolescence and adulthood with functional disability in these skills, in addition to social and communication deficits (Seltzer et al., 2004). The extended duration for normal spine pruning in human brain may provide an opportunity for therapeutic intervention of multiple functional domains associated with ASD after the disease is diagnosed.

While our study examined a single brain region, spine pruning during early postnatal development occurs in cerebral cortex, cerebellum, olfactory bulb, and hippocampus (Purves and Lichtman, 1980; Shinoda et al., 2010). As ASD-related neuropathology involves disruptions in connectivity across the brain, it is likely that additional ASD brain regions may feature spine pruning defects during different periods of synaptic development. Nevertheless, the disorganization of synaptic connectivity in the temporal lobe, a central node in the social brain network (Gotts et al., 2012), may compromise function of a network of anatomically distinct brain regions that underlie global brain dysfunction and ASD-like social deficits (Normand et al., 2013; Tsai et al., 2012a).

mTOR-Regulated Autophagy and ASD Synaptic Pathology

The genetic heterogeneity of ASD encourages the identification of steps that converge on common pathways to produce the clinical syndrome. Dysregulated mTOR signaling has been identified in autism, fragile X syndrome, tuberous sclerosis, neurofibromatosis, and PTEN-mediated macrocephaly (Peça and Feng, 2012; Bourgeron, 2009), each of which features altered dendritic spine densities. mTOR inhibitors, including rapamycin and its analogs, have been examined in clinical trials for treating ASD and neuropsychological deficits in children with TSC (Sahin, 2012).

We find that ASD brains exhibit both disrupted mTOR signaling and synaptic defects. It is highly unlikely that these patients possessed TSC mutations, and so our findings suggest that mTOR signaling provides a common convergent mechanism in ASD. mTOR signaling, however, contributes to protein synthesis required for neuronal survival, development, synaptic plasticity, learning, and memory (Hoeffler and Klann, 2010), and prolonged use of mTOR inhibitors may cause adverse effects (Rodrik-Outmezguine et al., 2011). An important goal is to identify specific signaling pathways downstream of mTOR that may provide more precise targets. For example, a link has been established between eIF4E-dependent translational control downstream of mTOR and ASD-like phenotypes in mouse models (Santini et al., 2013). We provide evidence from postmortem brain that autophagy deficiency, which is a consequence of mTOR overactivation, strongly correlates with ASD dendritic spine pathology. The reduction of mTOR-regulated neuronal autophagy is further consistent with our recent findings of a lack of autophagic mitochondrial turnover in ASD brains (Tang et al., 2013).

We have confirmed in mouse models that inhibition of neuronal autophagy produced ASD-like inhibition of normal

developmental spine pruning and ASD-like behaviors. Pharmacological inhibition of mTOR activity normalized ASD-like spine pruning deficits and ASD-like behaviors in mice largely by activating neuronal autophagy. As these data suggest a direct link between mTOR-regulated autophagy and pruning of synaptic connections during postnatal development, developing targeted means to enhance autophagy downstream of mTOR during development may provide the basis for novel ASD therapeutics.

Autophagy and Spine Pruning

The precise control of synapse pruning could be achieved by multiple signaling systems that converge to eliminate synaptic connections. This could involve the targeted degradation of synaptic components. Recent evidence suggests that neuronal activity decreases dendritic spine number in part through activation of the myocyte enhancer factor 2 (MEF2) transcription factor (Pfeiffer et al., 2010), which promotes ubiquitin-proteasome system (UPS)-dependent degradation of the synaptic scaffolding protein PSD95 (Tsai et al., 2012b). In addition to the UPS, which is primarily responsible for the degradation of short-lived cytosolic proteins, neurons rely on lysosomal-dependent degradation mechanisms for the turnover of long-lived synaptic proteins and damaged organelles. Ablation of autophagy genes *ATG7* or *ATG5* causes neurodegeneration associated with aberrant organelles and ubiquitin-rich inclusions in neuronal cell bodies (Hara et al., 2006; Komatsu et al., 2006), as well as disrupted membrane homeostasis in axon terminals (Komatsu et al., 2007b; Hernandez et al., 2012).

Using an in vitro primary neuronal culture system, we find that autophagy regulates spine elimination but not spine formation during developmental pruning of dendritic spines. Autophagy may remodel dendritic spines by directing internalized postsynaptic membrane neurotransmitter receptors, including GABA-A (Rowland et al., 2006) and AMPAR (Shehata et al., 2012), toward lysosomal degradation. Although autophagy was classically considered an “in-bulk” process, evidence now supports selectivity mediated via recognition of posttranslational modifications by molecules that bind cargo and components of the autophagic machinery. p62 is the most extensively characterized cargo-recognizing molecule and binds preferentially to an ubiquitin linkage (Lys63) on the surface of ubiquitinated protein aggregates, polyubiquitinated proteins, and organelles. In addition, autophagy may degrade proteins that suppress spine elimination, and the loss of autophagy could accumulate proteins that block spine pruning, for example, by releasing translationally suppressed synaptic mRNA for local protein synthesis (Banerjee et al., 2009).

As neuronal autophagy is responsible for ~70% of postnatal net spine elimination, it is likely that basal autophagy regulates spine elimination in cooperation with additional regulatory mechanisms downstream of mTOR, including eIF4E-dependent translational control and neuronal outgrowth (Santini et al., 2013) and other nonneuronal intrinsic regulatory mechanisms including neuroimmune disturbances and astrocyte activation (Garbett et al., 2008; Voineagu et al., 2011; Paolicelli et al., 2011; Schafer et al., 2012; Chung et al., 2013). Defective neuronal autophagy can be induced by infected microglia (Alirezaei et al., 2008),

pointing to the possibility of glial non-cell-autonomous autophagic regulation of spine morphogenesis. In addition, changes in mTOR-autophagy signaling and spine pruning defects may represent a secondary mechanism in response to an imbalance between excitatory and inhibitory neurotransmission, identified in both *Mecp2* mutant mice and *Tsc1*-deficient mice and implicated in ASD-associated stereotypies and social behavioral deficits (Chao et al., 2010; Fu et al., 2012; Yizhar et al., 2011). Altered synaptic function is consistent with our recent finding that chronic lack of neuronal autophagy enhances evoked neurotransmitter release and rate of synaptic recovery (Hernandez et al., 2012).

In summary, we find that many ASD brains exhibit both disrupted mTOR signaling and synaptic defects during childhood and adolescence, suggesting that mTOR signaling may provide a common mechanism involved in ASD synaptic pathology (Sawicka and Zukin, 2012). We further demonstrated that ASD behaviors and synaptic deficits are elicited by altered mTOR signaling via an inhibition of autophagy required for normal developmental spine pruning. The results indicate a direct link between mTOR-autophagy and pruning of synaptic connections during postnatal development and suggest that targeting neuronal autophagy could provide therapeutic benefit.

EXPERIMENTAL PROCEDURES

ASD-like Social Behavioral Tests

Mice were tested for novel object recognition and social interactions, anxiety-like behaviors, exploratory locomotion behaviors, and self-grooming repetitive behavior. Sociability and social novelty were tested in a three-chamber testing paradigm. Procedures were approved by Columbia University IACUC.

Biochemistry, DiOlistic Labeling, Golgi Staining, and Immunohistochemistry

Mouse and human brain tissue were lysed with 1X RIPA buffer supplemented with protease inhibitors and phosphatase inhibitors, and subjected to western blot analysis. Neurons in mouse brain were labeled with Dil using a Helios gene gun system at 120 psi. Fluorescent image stacks were acquired with a Leica multiphoton system. Neuronal morphology in postmortem human brain was analyzed by Golgi-Kopsch technique. Images were reconstructed with Imaris FilamentTracer Module (Bitplane).

Full Methods and associated references are in the Supplemental Information.

SUPPLEMENTAL INFORMATION

Supplemental Information includes Supplemental Experimental Procedures, six figures, and three tables and can be found with this article online at <http://dx.doi.org/10.1016/j.neuron.2014.07.040>.

AUTHOR CONTRIBUTIONS

G.T. and D.S. conceived and designed the study. G.T. and M.L.C. performed and analyzed DiOlistic labeling experiments; K.G. and F.C. designed, performed, and analyzed all behavioral experiments; G.T. and C.B. performed mouse breeding; and E.K. made neuronal cultures. G.T. and A.S. performed biochemistry, Golgi staining, immunolabeling of mouse and human brains, and establishing neuronal cultures. S.H.K. and M.S. performed data analysis. G.R., A.J.D., and J.E.G. supervised brain sample selection, Golgi staining, and data interpretation in human subjects. Z.Y., A.Y., and O.A. assisted with the design of autophagy and behavioral study. G.T., J.E.G., B.S.P., and D.S. wrote the manuscript. All authors read and approved the final version.

ACKNOWLEDGMENTS

This study was supported by the Simons Foundation. Additional support for D.S. is from DOD TSCRP (TS110056) and the Parkinson's Disease and JPB Foundations, for G.T. from NIMH (K01MH096956), for M.L.C. from AHA, for A.J.D. from NIMH (MH64168), for F.C. from NIH (DP2OD001674-01), for O.A. from NIH (NS049442). We thank the Autism Tissue Portal, Harvard Brain Bank, and Maryland NICHD Brain & Tissue Bank for kindly providing us brain tissues for the present study. We thank Ana Maria Cuervo for reagents and valuable advice.

Accepted: July 24, 2014

Published: August 21, 2014

REFERENCES

- Alirezaei, M., Kiosses, W.B., Flynn, C.T., Brady, N.R., and Fox, H.S. (2008). Disruption of neuronal autophagy by infected microglia results in neurodegeneration. *PLoS ONE* 3, e2906.
- Banerjee, S., Neveu, P., and Kosik, K.S. (2009). A coordinated local translational control point at the synapse involving relief from silencing and MOV10 degradation. *Neuron* 64, 871–884.
- Belmonte, M.K., Allen, G., Beckel-Mitchener, A., Boulanger, L.M., Carper, R.A., and Webb, S.J. (2004). Autism and abnormal development of brain connectivity. *J. Neurosci.* 24, 9228–9231.
- Benavides-Piccione, R., Ballesteros-Yáñez, I., DeFelipe, J., and Yuste, R. (2002). Cortical area and species differences in dendritic spine morphology. *J. Neurocytol.* 31, 337–346.
- Bingol, B., and Sheng, M. (2011). Deconstruction for reconstruction: the role of proteolysis in neural plasticity and disease. *Neuron* 69, 22–32.
- Bourgeron, T. (2009). A synaptic trek to autism. *Curr. Opin. Neurobiol.* 19, 231–234.
- Chao, H.T., Chen, H., Samaco, R.C., Xue, M., Chahrouh, M., Yoo, J., Neul, J.L., Gong, S., Lu, H.C., Heintz, N., et al. (2010). Dysfunction in GABA signalling mediates autism-like stereotypies and Rett syndrome phenotypes. *Nature* 468, 263–269.
- Chévere-Torres, I., Maki, J.M., Santini, E., and Klann, E. (2012). Impaired social interactions and motor learning skills in tuberous sclerosis complex model mice expressing a dominant/negative form of tuberin. *Neurobiol. Dis.* 45, 156–164.
- Chung, W.S., Clarke, L.E., Wang, G.X., Stafford, B.K., Sher, A., Chakraborty, C., Joung, J., Foo, L.C., Thompson, A., Chen, C., et al. (2013). Astrocytes mediate synapse elimination through MEGF10 and MERTK pathways. *Nature* 504, 394–400.
- Ehninger, D., and Silva, A.J. (2011). Rapamycin for treating Tuberous sclerosis and Autism spectrum disorders. *Trends Mol. Med.* 17, 78–87.
- Ehninger, D., Han, S., Shilyansky, C., Zhou, Y., Li, W., Kwiatkowski, D.J., Ramesh, V., and Silva, A.J. (2008). Reversal of learning deficits in a *Tsc2*^{+/−} mouse model of tuberous sclerosis. *Nat. Med.* 14, 843–848.
- Ehninger, D., Sano, Y., de Vries, P.J., Dies, K., Franz, D., Geschwind, D.H., Kaur, M., Lee, Y.S., Li, W., Lowe, J.K., et al. (2012). Gestational immune activation and *Tsc2* haploinsufficiency cooperate to disrupt fetal survival and may perturb social behavior in adult mice. *Mol. Psychiatry* 17, 62–70.
- Fu, C., Cawthon, B., Clinkscales, W., Bruce, A., Winzenburger, P., and Ess, K.C. (2012). GABAergic interneuron development and function is modulated by the *Tsc1* gene. *Cereb. Cortex* 22, 2111–2119.
- Garbett, K., Ebert, P.J., Mitchell, A., Lintas, C., Manzi, B., Mirnics, K., and Persico, A.M. (2008). Immune transcriptome alterations in the temporal cortex of subjects with autism. *Neurobiol. Dis.* 30, 303–311.
- Goda, Y., and Davis, G.W. (2003). Mechanisms of synapse assembly and disassembly. *Neuron* 40, 243–264.
- Gogolla, N., Leblanc, J.J., Quast, K.B., Südhof, T.C., Fagiolini, M., and Hensch, T.K. (2009). Common circuit defect of excitatory-inhibitory balance in mouse models of autism. *J. Neurodev. Disord.* 1, 172–181.
- Goorden, S.M., van Woerden, G.M., van der Weerd, L., Cheadle, J.P., and Elgersma, Y. (2007). Cognitive deficits in *Tsc1*^{+/−} mice in the absence of cerebral lesions and seizures. *Ann. Neurol.* 62, 648–655.
- Gotts, S.J., Simmons, W.K., Milbury, L.A., Wallace, G.L., Cox, R.W., and Martin, A. (2012). Fractionation of social brain circuits in autism spectrum disorders. *Brain* 135, 2711–2725.
- Hara, T., Nakamura, K., Matsui, M., Yamamoto, A., Nakahara, Y., Suzuki-Migishima, R., Yokoyama, M., Mishima, K., Saito, I., Okano, H., and Mizushima, N. (2006). Suppression of basal autophagy in neural cells causes neurodegenerative disease in mice. *Nature* 441, 885–889.
- Harris, K.M., Jensen, F.E., and Tsao, B. (1992). Three-dimensional structure of dendritic spines and synapses in rat hippocampus (CA1) at postnatal day 15 and adult ages: implications for the maturation of synaptic physiology and long-term potentiation. *J. Neurosci.* 12, 2685–2705.
- Hernandez, D., Torres, C.A., Setlik, W., Cebrián, C., Mosharov, E.V., Tang, G., Cheng, H.C., Kholodilov, N., Yarygina, O., Burke, R.E., et al. (2012). Regulation of presynaptic neurotransmission by macroautophagy. *Neuron* 74, 277–284.
- Hoeffer, C.A., and Klann, E. (2010). mTOR signaling: at the crossroads of plasticity, memory and disease. *Trends Neurosci.* 33, 67–75.
- Hutsler, J.J., and Zhang, H. (2010). Increased dendritic spine densities on cortical projection neurons in autism spectrum disorders. *Brain Res.* 1309, 83–94.
- Kim, J., Kundu, M., Viollet, B., and Guan, K.L. (2011). AMPK and mTOR regulate autophagy through direct phosphorylation of Ulk1. *Nat. Cell Biol.* 13, 132–141.
- Ko, J., Soler-Llavina, G.J., Fuccillo, M.V., Malenka, R.C., and Südhof, T.C. (2011). Neuroligins/LRRTMs prevent activity- and Ca²⁺/calmodulin-dependent synapse elimination in cultured neurons. *J. Cell Biol.* 194, 323–334.
- Komatsu, M., Waguri, S., Chiba, T., Murata, S., Iwata, J., Tanida, I., Ueno, T., Koike, M., Uchiyama, Y., Kominami, E., and Tanaka, K. (2006). Loss of autophagy in the central nervous system causes neurodegeneration in mice. *Nature* 441, 880–884.
- Komatsu, M., Waguri, S., Koike, M., Sou, Y.S., Ueno, T., Hara, T., Mizushima, N., Iwata, J., Ezaki, J., Murata, S., et al. (2007a). Homeostatic levels of p62 control cytoplasmic inclusion body formation in autophagy-deficient mice. *Cell* 131, 1149–1163.
- Komatsu, M., Wang, Q.J., Holstein, G.R., Friedrich, V.L., Jr., Iwata, J., Kominami, E., Chait, B.T., Tanaka, K., and Yue, Z. (2007b). Essential role for autophagy protein Atg7 in the maintenance of axonal homeostasis and the prevention of axonal degeneration. *Proc. Natl. Acad. Sci. USA* 104, 14489–14494.
- Martinez-Vicente, M., Tallozy, Z., Wong, E., Tang, G., Koga, H., Kaushik, S., de Vries, R., Arias, E., Harris, S., Sulzer, D., and Cuervo, A.M. (2010). Cargo recognition failure is responsible for inefficient autophagy in Huntington's disease. *Nat. Neurosci.* 13, 567–576.
- Normand, E.A., Crandall, S.R., Thorn, C.A., Murphy, E.M., Voelcker, B., Browning, C., Machan, J.T., Moore, C.I., Connors, B.W., and Zervas, M. (2013). Temporal and mosaic *Tsc1* deletion in the developing thalamus disrupts thalamocortical circuitry, neural function, and behavior. *Neuron* 78, 895–909.
- Orefice, L.L., Waterhouse, E.G., Partridge, J.G., Lalchandani, R.R., Vicini, S., and Xu, B. (2013). Distinct roles for somatically and dendritically synthesized brain-derived neurotrophic factor in morphogenesis of dendritic spines. *J. Neurosci.* 33, 11618–11632.
- Paolicelli, R.C., Bolasco, G., Pagani, F., Maggi, L., Scianni, M., Panzanelli, P., Giustetto, M., Ferreira, T.A., Guiducci, E., Dumas, L., et al. (2011). Synaptic pruning by microglia is necessary for normal brain development. *Science* 333, 1456–1458.
- Papa, M., Bundman, M.C., Greenberger, V., and Segal, M. (1995). Morphological analysis of dendritic spine development in primary cultures of hippocampal neurons. *J. Neurosci.* 15, 1–11.
- Peça, J., and Feng, G. (2012). Cellular and synaptic network defects in autism. *Curr. Opin. Neurobiol.* 22, 866–872.

- Penzes, P., Cahill, M.E., Jones, K.A., VanLeeuwen, J.E., and Woolfrey, K.M. (2011). Dendritic spine pathology in neuropsychiatric disorders. *Nat. Neurosci.* *14*, 285–293.
- Pfeiffer, B.E., Zang, T., Wilkerson, J.R., Taniguchi, M., Maksimova, M.A., Smith, L.N., Cowan, C.W., and Huber, K.M. (2010). Fragile X mental retardation protein is required for synapse elimination by the activity-dependent transcription factor MEF2. *Neuron* *66*, 191–197.
- Poultney, C.S., Goldberg, A.P., Drapeau, E., Kou, Y., Harony-Nicolas, H., Kajiwara, Y., De Rubeis, S., Durand, S., Stevens, C., Rehnström, K., et al. (2013). Identification of small exonic CNV from whole-exome sequence data and application to autism spectrum disorder. *Am. J. Hum. Genet.* *93*, 607–619.
- Purves, D., and Lichtman, J.W. (1980). Elimination of synapses in the developing nervous system. *Science* *210*, 153–157.
- Rakic, P., Bourgeois, J.P., Eckenhoff, M.F., Zecevic, N., and Goldman-Rakic, P.S. (1986). Concurrent overproduction of synapses in diverse regions of the primate cerebral cortex. *Science* *232*, 232–235.
- Redcay, E. (2008). The superior temporal sulcus performs a common function for social and speech perception: implications for the emergence of autism. *Neurosci. Biobehav. Rev.* *32*, 123–142.
- Rodrik-Outmezguine, V.S., Chandralapaty, S., Pagano, N.C., Poulikakos, P.I., Scaltriti, M., Moskatel, E., Baselga, J., Guichard, S., and Rosen, N. (2011). mTOR kinase inhibition causes feedback-dependent biphasic regulation of AKT signaling. *Cancer Discov* *1*, 248–259.
- Rowland, A.M., Richmond, J.E., Olsen, J.G., Hall, D.H., and Bamber, B.A. (2006). Presynaptic terminals independently regulate synaptic clustering and autophagy of GABAA receptors in *Caenorhabditis elegans*. *J. Neurosci.* *26*, 1711–1720.
- Sahin, M. (2012). Targeted treatment trials for tuberous sclerosis and autism: no longer a dream. *Curr. Opin. Neurobiol.* *22*, 895–901.
- Santini, E., Huynh, T.N., MacAskill, A.F., Carter, A.G., Pierre, P., Ruggero, D., Kaphzan, H., and Klann, E. (2013). Exaggerated translation causes synaptic and behavioural aberrations associated with autism. *Nature* *493*, 411–415.
- Sato, A., Kasai, S., Kobayashi, T., Takamatsu, Y., Hino, O., Ikeda, K., and Mizuguchi, M. (2012). Rapamycin reverses impaired social interaction in mouse models of tuberous sclerosis complex. *Nat. Commun.* *3*, 1292.
- Sawicka, K., and Zukin, R.S. (2012). Dysregulation of mTOR signaling in neuropsychiatric disorders: therapeutic implications. *Neuropsychopharmacology* *37*, 305–306.
- Schafer, D.P., Lehrman, E.K., Kautzman, A.G., Koyama, R., Mardinly, A.R., Yamasaki, R., Ransohoff, R.M., Greenberg, M.E., Barres, B.A., and Stevens, B. (2012). Microglia sculpt postnatal neural circuits in an activity and complement-dependent manner. *Neuron* *74*, 691–705.
- Seltzer, M.M., Shattuck, P., Abbeduto, L., and Greenberg, J.S. (2004). Trajectory of development in adolescents and adults with autism. *Ment. Retard. Dev. Disabil. Res. Rev.* *10*, 234–247.
- Shehata, M., Matsumura, H., Okubo-Suzuki, R., Ohkawa, N., and Inokuchi, K. (2012). Neuronal stimulation induces autophagy in hippocampal neurons that is involved in AMPA receptor degradation after chemical long-term depression. *J. Neurosci.* *32*, 10413–10422.
- Shen, W., and Ganetzky, B. (2009). Autophagy promotes synapse development in *Drosophila*. *J. Cell Biol.* *187*, 71–79.
- Shih, P., Keehn, B., Oram, J.K., Leyden, K.M., Keown, C.L., and Müller, R.A. (2011). Functional differentiation of posterior superior temporal sulcus in autism: a functional connectivity magnetic resonance imaging study. *Biol. Psychiatry* *70*, 270–277.
- Shinoda, Y., Tanaka, T., Tominaga-Yoshino, K., and Ogura, A. (2010). Persistent synapse loss induced by repetitive LTD in developing rat hippocampal neurons. *PLoS ONE* *5*, e10390.
- Sporns, O., Tononi, G., and Edelman, G.M. (2000). Theoretical neuroanatomy: relating anatomical and functional connectivity in graphs and cortical connection matrices. *Cereb. Cortex* *10*, 127–141.
- Spruston, N. (2008). Pyramidal neurons: dendritic structure and synaptic integration. *Nat. Rev. Neurosci.* *9*, 206–221.
- Sternberg, R.J., and Powell, J.S. (1983). The development of intelligence. In *Handbook of Child Psychology*, 4th Edition, P.H. Mussen, ed. (New York: John Wiley and Sons), pp. 341–419.
- Tang, G., Gutierrez Rios, P., Kuo, S.H., Akman, H.O., Rosoklija, G., Tanji, K., Dwork, A., Schon, E.A., Dimauro, S., Goldman, J., and Sulzer, D. (2013). Mitochondrial abnormalities in temporal lobe of autistic brain. *Neurobiol. Dis.* *54*, 349–361.
- Tsai, P.T., Hull, C., Chu, Y., Greene-Colozzi, E., Sadowski, A.R., Leech, J.M., Steinberg, J., Crawley, J.N., Regehr, W.G., and Sahin, M. (2012a). Autistic-like behaviour and cerebellar dysfunction in Purkinje cell Tsc1 mutant mice. *Nature* *488*, 647–651.
- Tsai, N.P., Wilkerson, J.R., Guo, W., Maksimova, M.A., DeMartino, G.N., Cowan, C.W., and Huber, K.M. (2012b). Multiple autism-linked genes mediate synapse elimination via proteasomal degradation of a synaptic scaffold PSD-95. *Cell* *151*, 1581–1594.
- Voineagu, I., Wang, X., Johnston, P., Lowe, J.K., Tian, Y., Horvath, S., Mill, J., Cantor, R.M., Blencowe, B.J., and Geschwind, D.H. (2011). Transcriptomic analysis of autistic brain reveals convergent molecular pathology. *Nature* *474*, 380–384.
- Yizhar, O., Fenno, L.E., Prigge, M., Schneider, F., Davidson, T.J., O’Shea, D.J., Sohal, V.S., Goshen, I., Finkelstein, J., Paz, J.T., et al. (2011). Neocortical excitation/inhibition balance in information processing and social dysfunction. *Nature* *477*, 171–178.
- Zahn, R., Moll, J., Krueger, F., Huey, E.D., Garrido, G., and Grafman, J. (2007). Social concepts are represented in the superior anterior temporal cortex. *Proc. Natl. Acad. Sci. USA* *104*, 6430–6435.
- Zoghbi, H.Y., and Bear, M.F. (2012). Synaptic dysfunction in neurodevelopmental disorders associated with autism and intellectual disabilities. *Cold Spring Harb. Perspect. Biol.* *4*, a009886.
- Zuo, Y., Yang, G., Kwon, E., and Gan, W.B. (2005). Long-term sensory deprivation prevents dendritic spine loss in primary somatosensory cortex. *Nature* *436*, 261–265.

Increases in Functional Connectivity between Prefrontal Cortex and Striatum during Category Learning

Evan G. Antzoulatos^{1,2,*} and Earl K. Miller^{1,*}

¹The Picower Institute for Learning & Memory, Department of Brain & Cognitive Sciences, Massachusetts Institute of Technology, Cambridge, MA 02139, USA

²Center for Neuroscience, Department of Neurobiology, Physiology and Behavior, University of California, Davis, Davis, CA 95618, USA

*Correspondence: eantzoulatos@ucdavis.edu (E.G.A.), ekmiller@mit.edu (E.K.M.)

<http://dx.doi.org/10.1016/j.neuron.2014.05.005>

SUMMARY

Functional connectivity between the prefrontal cortex (PFC) and striatum (STR) is thought critical for cognition and has been linked to conditions like autism and schizophrenia. We recorded from multiple electrodes in PFC and STR while monkeys acquired new categories. Category learning was accompanied by an increase in beta band synchronization of LFPs between, but not within, the PFC and STR. After learning, different pairs of PFC-STR electrodes showed stronger synchrony for one or the other category, suggesting category-specific functional circuits. This category-specific synchrony was also seen between PFC spikes and STR LFPs, but not the reverse, reflecting the direct monosynaptic connections from the PFC to STR. However, causal connectivity analyses suggested that the polysynaptic connections from STR to the PFC exerted a stronger overall influence. This supports models positing that the basal ganglia “train” the PFC. Category learning may depend on the formation of functional circuits between the PFC and STR.

INTRODUCTION

Anatomical loops between the prefrontal cortex (PFC) and basal ganglia (BG) suggest a close functional relationship, but the nature of their interactions is not yet understood. It is clear that both areas are critical for learning. One hypothesis is that they have different types of plasticity: The BG (in particular the striatum or STR) are thought to rapidly acquire simple information (single associations, decision alternatives, etc.) in piecemeal fashion, while the PFC knits together such details into more elaborate and generalized representations (Daw et al., 2005). Interactions between these mechanisms may explain category learning (Seger and Miller, 2010). The idea is that the STR rapidly forms associations that are then fed through the BG to the PFC (Ashby et al., 2007; Djurfeldt et al., 2001). Iterations allow more gradual changes in synaptic weights in the PFC to detect and store the common features across patterns learned by the BG, thereby

acquiring the categories (Miller and Buschman, 2008; Seger and Miller, 2010).

Support for this comes from human imaging studies showing that both the PFC and STR are engaged during category learning (Reber et al., 1998; Seger et al., 2000; Vogels et al., 2002). Also, computational and neurophysiological studies suggest more rapid changes in the STR than PFC during learning, as if the BG was “training” the cortex (Djurfeldt et al., 2001; Pasupathy and Miller, 2005). We recently provided more direct support in monkeys trained to learn new categories (Antzoulatos and Miller, 2011). There was the predicted reversal: Early in learning, when the associations of a few stimuli could be formed, the STR led; its activity was the earliest predictor of the behavioral choice. But then, as the animals began to truly acquire categories, the PFC became the earliest predictor of the choice.

While such results are certainly suggestive of PFC-BG functional interactions, direct evidence for functional interactions between the PFC and STR is rare. It is possible that these structures are part of different learning systems that work relatively independently. We sought to test for functional connectivity between the PFC and STR by examining synchrony between oscillations of their local field potentials (LFPs) (Friston et al., 2013). Frequency-dependent synchrony between LFPs suggests neural communication and has been observed in perceptual (Hipp et al., 2011), motor (Brovelli et al., 2004), and cognitive tasks (Daich et al., 2013). The functional connectivity between BG and PFC is of particular interest, as the network between them has been implicated in several neurological and psychiatric conditions, such as autism and schizophrenia (Padmanabhan et al., 2013; Uhlhaas and Singer, 2012; Yoon et al., 2013). We found evidence that functional connectivity between the PFC and STR increased as animals acquired new categories.

RESULTS

Learning-Related Enhancement of Synchrony between the PFC and STR

The animals were required to respond to a randomly chosen category exemplar with a saccade to the left or right target (Figure 1A). All exemplars were created de novo each day through distortion of a new pair of prototypes (Figure 1B). Each training session began with a single new exemplar per category, which monkeys learned as specific stimulus-response (SR)

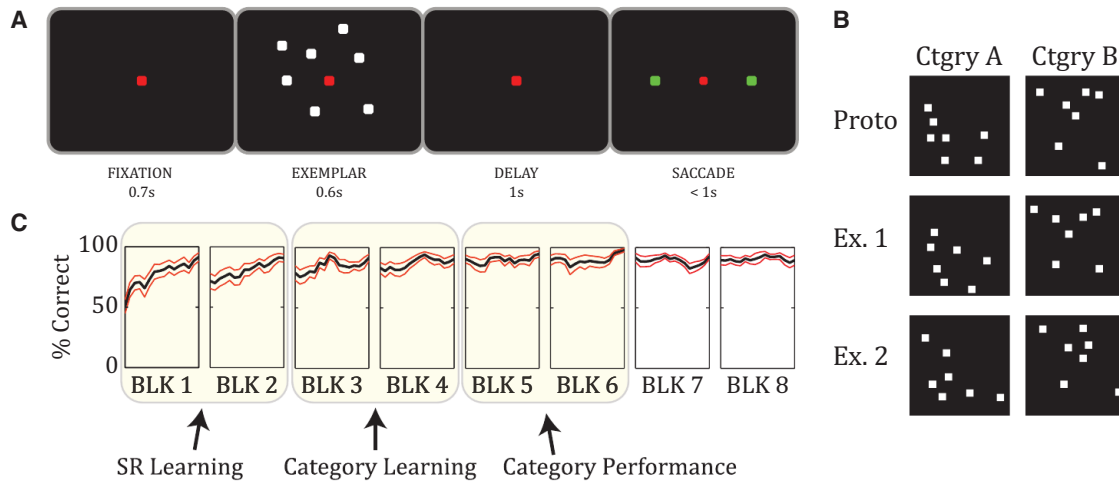


Figure 1. Task Design

(A) The schematic illustrates the time course of a single trial. The animal had to respond to a randomly presented exemplar by choosing between a saccade to the right or left targets (green squares).

(B) Two example categories. New pairs of prototypes (top) were constructed for each recording session. Distortion of each prototype gave rise to hundreds of unique exemplars (only two of which are shown for each category).

(C) Average behavioral performance (% correct) \pm SEM across recording sessions. The animals started by learning a few individual SR associations (SR Learning stage: always the first two blocks). As they progressed through the blocks, they were trained on more and more exemplars (Category Learning stage) until they eventually learned the categories and their behavior stabilized (Category Performance stage). The Category Learning and Category Performance stages are shown for illustration only: the timing of each could vary across recording sessions, based on the animals' performance on each new set of categories. (Adapted from Antzoulatos and Miller, 2011.)

associations (Antzoulatos and Miller, 2011). Then, as learning progressed, more and more exemplars were added. This required animals to learn the categories (or fail), because sooner or later, they would be confronted with too many new exemplars to sustain performance by SR learning alone.

Based on the monkeys' performance, we could distinguish three stages of learning (Antzoulatos and Miller, 2011) (Figure 1C). In stage 1 (SR Learning), monkeys learned the category of (i.e., the correct saccade for) each new exemplar individually. In stage 2 (Category Learning), the monkeys were challenged with many more exemplars but began to perform above chance with new exemplars. This indicates the start of acquisition of category information. In stage 3 (Category Performance), learning of the categories was complete. Behavior remained at asymptote even though monkeys were mainly seeing new exemplars for the first time on most trials. We examined changes in synchrony between the PFC and STR as a function of learning stage.

We first calculated synchrony of LFPs between recording sites in the PFC and STR ($n = 426$ electrode pairs). Each site's LFP signal was decomposed to its frequency components using wavelet analysis (Torrence and Compo, 1998) and then a phase-locking value (PLV) was determined for each pair of simultaneously recorded LFPs (Lachaux et al., 1999). We subtracted out any phase-locking due to external events (e.g., stimulus onset) so that we could isolate true neural synchrony (i.e., the PLV values shown are the difference between observed PLV and surrogate-data PLV) (see Supplemental Experimental Procedures available online). Analysis was focused on two critical task epochs, the last 500 ms of the 600-ms-long exemplar pre-

sentation (exemplar epoch) and the last 500 ms preceding the behavioral response (decision epoch). Similar results were obtained from other trial epochs and using diverse measures of synchrony (i.e., coherence and pairwise phase consistency). We first limited this analysis to correctly performed trials; error trials will be considered further below.

This analysis revealed a peak of PFC-STR synchrony in the beta band (defined as 12–30 Hz) during the exemplar and decision epochs (peak at ~ 20 Hz) (see Figure 2A). After the switch from SR Learning to Category Learning (Stage 1 to 2), there was a significant increase in decision-epoch average beta band PLV between the PFC and STR (Figure 2A, right) (ANOVA, $F(2,1277) = 11.23$, $p = 1.5 \times 10^{-5}$; post hoc comparison: SR Learning PLV less than Category Learning and Category Performance PLV, $p = 0.0005$). Correspondingly, during the decision epoch, there was a learning-related increase in the percentage of pairs of PFC-STR recording sites that showed significant beta band PLV (greater than the 95th percentile of the PLV expected by chance): more pairs showed significant PLV during Category Learning (57.3%, Stage 2) and Category Performance (55.9%, Stage 3) than during SR Learning (42.3%, Stage 1; $p = 0.003$, chi-square test). Learning-related changes in PFC-STR synchrony were limited to the decision epoch. The PFC-STR beta PLV during the exemplar epoch did not significantly increase across learning stages (Figure 2A, left) (ANOVA across stages: $F(2,1277) = 1.06$, $p = 0.35$). Likewise, the number of pairs of PFC-STR recording sites with significant PLV was not different across learning stages for the exemplar epoch (SR Learning: 48.6%; Category Learning: 55.9%; Category Performance: 50.5%; $p = 0.31$, chi-square test). There were also no significant

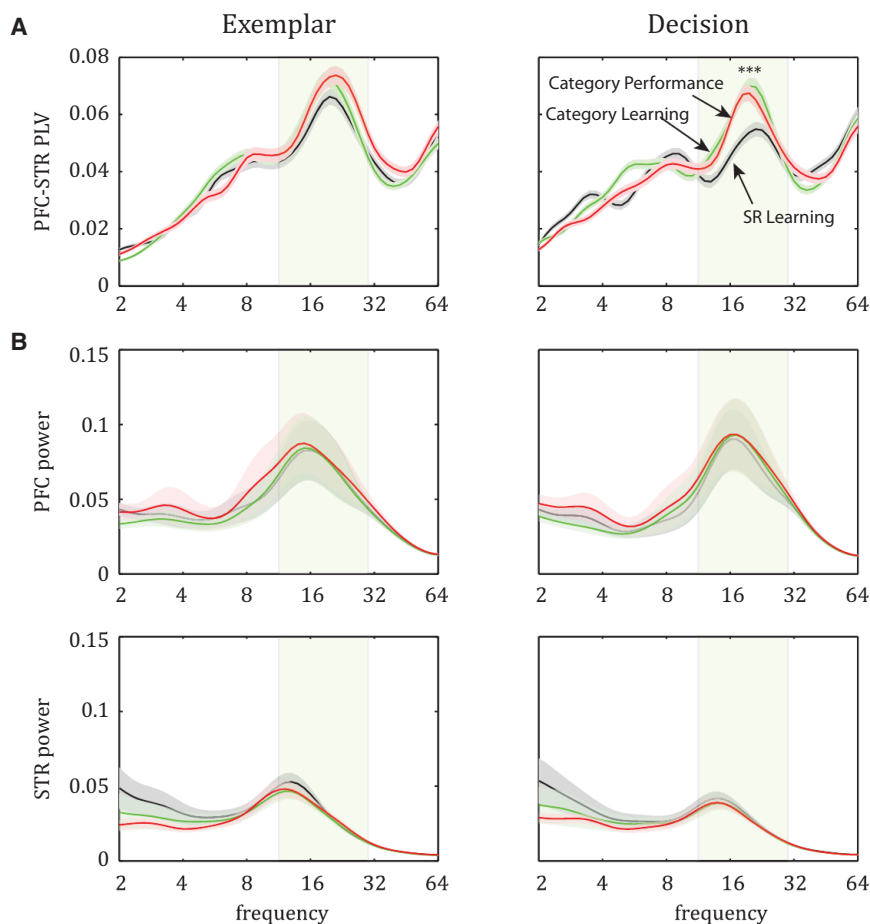


Figure 2. Frequency-Specific Oscillations in PFC and STR during Two Trial Epochs (Exemplar and Decision) Across the Three Stages of Learning

(A) Average PLV \pm SEM as a function of frequency: peak synchrony between PFC and STR beta band oscillations (in this and all figures, shaded rectangle indicates the 12–30 Hz beta band) and learning-induced enhancement of this synchrony during the decision epoch (see also Figures S1 and S2; Table S1).

(B) Average spectral power (\pm SEM) in PFC (top) and STR (bottom) is high at the beta band, but does not change across learning stages.

exemplar epoch $F(2,194) = 0.49$, $p = 0.62$, decision epoch $F(2,194) = 0.18$, $p = 0.82$). This suggests that the learning-related changes in synchrony between the PFC and STR reflected changes in functional connectivity per se rather than just a general change in oscillatory dynamics. Indeed, as we will see next, learning-related changes in synchrony only occurred between the PFC and STR; there was no learning-related change in synchrony within either area.

No Changes in Synchrony within the PFC or STR

The learning-related increase in beta synchrony was limited to interactions between the PFC and STR; there was no

learning-related changes in PLV for baseline activity (middle 500 ms time segment from the 3-s-long intertrial interval; ANOVA: $F(2,1277) = 1.04$, $p = 0.35$) (Figure S2A). The phase relationship between PFC and STR remained stable at 0° phase lag across all trial epochs and learning stages (Figure S2B).

No Changes in Oscillatory Power within the PFC or STR

The learning-related increase in PFC-STR synchrony was independent of changes in oscillatory power (i.e., the synchrony changes were not a by-product of increased oscillations per se). Note that the synchrony measure we employed (PLV) is computed only from the phase of the wave, independently from its amplitude (and thus oscillatory power). However, we also computed the frequency-dependent power of PFC and STR LFPs. To correct for the LFP's power-law decay, power was normalized to $1/\text{frequency}$.

Both PFC ($n = 84$ electrodes) and STR ($n = 65$ electrodes) LFPs displayed a peak in beta (STR LFPs also displayed strong power in the 2–4 Hz delta band) (Figure 2B). Beta power was stronger in the PFC than STR, with a peak at a somewhat higher frequency (peak at 16 Hz versus 13 Hz, respectively) (Figure 2B). However, there was no change in beta oscillatory power across learning stages in either area for either the exemplar or decision epoch (Figure 2B, ANOVA in PFC: exemplar epoch $F(2,251) = 0.004$, $p = 0.99$, decision epoch $F(2,251) = 0.001$, $p = 0.99$; STR:

learning-related change in beta (or any other frequency band) synchrony within either area. We performed the same analyses as above on pairs of recording sites within each area (Figures 3A and S2A). Synchrony between recording sites within the PFC ($n = 240$ electrode pairs) or STR ($n = 141$ electrode pairs) were overall greater than those between PFC and STR (within-STR average PLV was also greater than within-PFC average PLV) with a peak in the beta band (at ~ 20 Hz). However, beta band PLV values within the PFC and STR did not change across learning stages in either the exemplar epoch (ANOVA across stages in beta-specific PLV within PFC: $F(2,719) = 0.05$, $p = 0.95$; within STR: $F(2,422) = 0.23$, $p = 0.79$) (Figure 3A, left) or the decision epoch (within PFC: $F(2,719) = 0.06$, $p = 0.94$; within STR: $F(2,422) = 0.42$, $p = 0.66$) (Figure 3A, right). Decision-epoch PLV within the PFC and within the STR was similar during SR Learning, Category Learning, and Category Performance (only 0.5%–2.12% difference across learning within PFC and 2.2%–4.4% within STR). Compare this to learning-related increases in beta band PLV of around 30% between the PFC and STR (Figure 3B, right).

Decrease in PFC-STR Synchrony during Error Trials

To determine whether the PFC-STR synchrony was related to task performance, we examined PLV from trials in which the monkeys made the incorrect behavioral choice at the end of

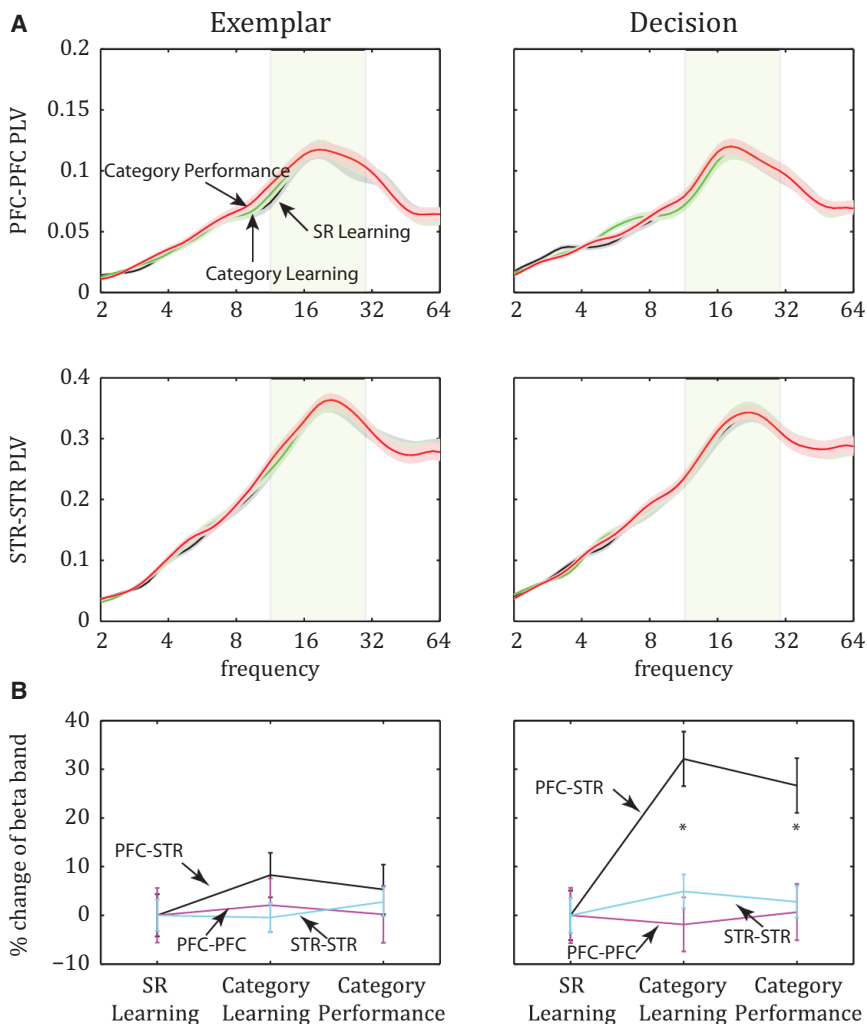


Figure 3. Synchrony between Intrinsic Pairs of Electrodes in PFC and STR

(A) Average PLV (\pm SEM): although intrinsic connectivity peaked at the beta band both in PFC (top) and in STR (bottom), it did not change with learning (see also Figure S2).

(B) The percent increase of synchrony between PFC and STR after the SR Learning stage during the decision epoch (right) was significantly greater than the corresponding change in synchrony of intrinsic PFC pairs (PFC-PFC) and STR pairs (STR-STR) of electrodes. Error bars indicate SEM.

band from SR Learning to Category Learning (15–20 Hz; ANOVA on exemplar epoch d' between SR Learning and Category Learning: $F(1,810) = 54.11$, $p = 4.7 \times 10^{-13}$; during decision epoch: $F(1,810) = 60.97$, $p = 1.8 \times 10^{-14}$). Figure 4B plots the z scores for correct trials subtracted from error trials (i.e., the average z-transformed d'). During the exemplar epoch (Figure 4B, left), note that the scores were significantly above zero in beta for SR Learning (t test for d' relative to zero discrimination: $p = 1.7 \times 10^{-8}$), indicating greater synchrony on error trials and significantly below zero for Category Learning ($p = 2.8 \times 10^{-5}$), indicating greater beta synchrony on correct trials. For the decision epoch (Figure 4B, right), error-correct values were significantly greater than zero for SR Learning, indicating greater beta synchrony on error trials (t test, $p = 3 \times 10^{-21}$). However, during Category Learning, there was no difference in beta synchrony between correct and error trials (i.e., error-correct PLV values did not differ from zero [$p = 0.81$]). Therefore, we see that the shift from SR Learning to Category Learning led to changes in PFC-STR synchrony that depended on trial epoch and task performance. In the exemplar epoch, there was a significant decline of PLV during error trials (Figure 4A, left) but no change in correct trials (Figure 2A, left). In the decision epoch, there was a significant increase of PLV during correct trials (Figure 2A, right) but no change in error trials (Figure 4A, right). Note that the net effect is similar: for both exemplar and decision epochs, the transition from SR Learning to Category Learning preferentially favored the PFC-STR synchrony during correct, relative to erroneous, categorization.

the trial. This analysis was necessarily focused only on the SR Learning and Category Learning stages because the animals' asymptotic performance during Category Performance did not include sufficient error trials for their analysis.

While there was strong beta band synchrony during error trials (Figure 4A), there was no learning-related increase in beta synchrony (PLV), unlike what was seen for correct trials (see above). On the contrary, there was a significant decrease of PFC-STR beta band PLV from SR Learning to Category Learning during the exemplar epoch (Figure 4A, left; ANOVA across stages: $F(1,810) = 28.83$, $p = 10^{-7}$). Synchrony did not change significantly across the two stages in the decision epoch ($F(1,810) = 3.48$, $p = 0.06$; Figure 4A, right).

In order to compare synchrony between correct and error trials, we employed the discrimination index d' , which quantifies the difference between the mean of two sets of trials (i.e., error and correct trials), normalized to their pooled SD (Dayan and Abbott, 2001). This quantity was transformed into a z score, based on 200 random shuffles of the trials between the correct and error groups. The average z-transformed d' indicated a significant decline in error-correct synchrony for the beta

category Learning, there was no difference in beta synchrony between correct and error trials (i.e., error-correct PLV values did not differ from zero [$p = 0.81$]). Therefore, we see that the shift from SR Learning to Category Learning led to changes in PFC-STR synchrony that depended on trial epoch and task performance. In the exemplar epoch, there was a significant decline of PLV during error trials (Figure 4A, left) but no change in correct trials (Figure 2A, left). In the decision epoch, there was a significant increase of PLV during correct trials (Figure 2A, right) but no change in error trials (Figure 4A, right). Note that the net effect is similar: for both exemplar and decision epochs, the transition from SR Learning to Category Learning preferentially favored the PFC-STR synchrony during correct, relative to erroneous, categorization.

Emergence of Category-Specific Patterns of Synchrony between the PFC and STR with Learning

A recent study of PFC LFPs reported rule-specific patterns of beta band synchrony between different recording sites, suggesting that beta synchrony can help form network ensembles for rules (Buschman et al., 2012). We examined whether

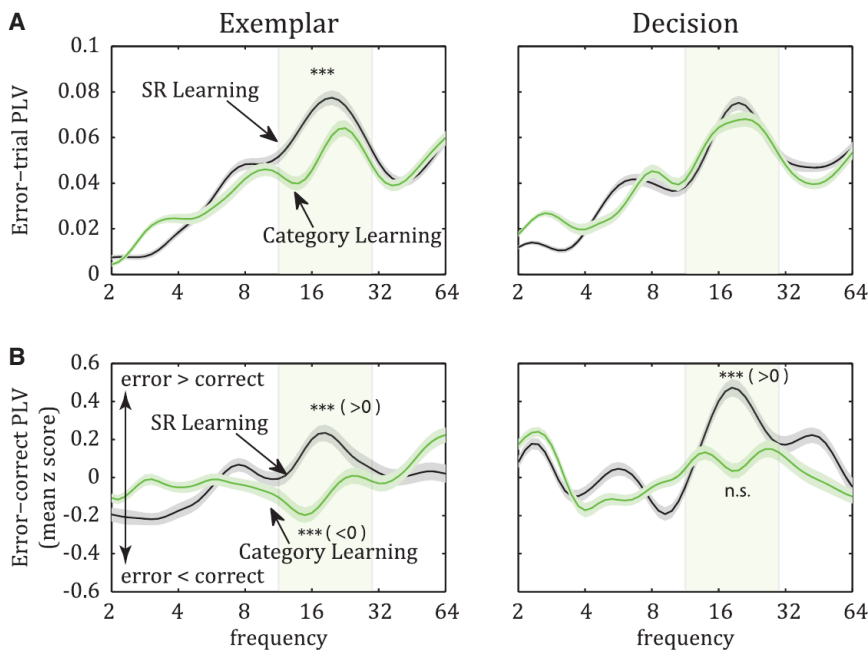


Figure 4. Analyses of PFC-STR Synchrony in Error Trials of SR Learning and Category Learning Stages

(A) Average (\pm SEM) PLV in error trials: in contrast to the increase of beta band synchrony observed in correct trials (Figure 2), synchrony between PFC and STR did not increase across learning stages; rather, it decreased significantly, at least during the exemplar epoch.

(B) The average (\pm SEM) z-transformed difference (d') between error- and correct-trial PLV. During both trial epochs, error trials displayed stronger PFC-STR synchrony than did correct trials in the SR Learning stage, but, in the Category Learning stage, this difference was either eliminated (decision epoch) or reversed (exemplar epoch).

delta band of decision epoch: SR Learning, $p = 0.99$; Category Learning, $p = 0.99$; Category Performance, $p = 5.7 \times 10^{-16}$.

As was seen for the learning-related general increase in beta synchrony, sig-

nificant category-selective synchrony was only seen between the PFC and STR. There was no significant category-selective synchrony within the PFC or STR (t test for selectivity greater than zero: SR Learning stage: exemplar epoch, within PFC $p = 0.99$, within STR $p = 0.99$, decision epoch, PFC $p = 0.14$, STR $p = 0.99$; Category Learning stage: exemplar PFC $p = 0.99$, STR $p = 0.06$, decision PFC $p = 0.99$, STR $p = 0.08$; Category Performance stage: exemplar PFC $p = 0.99$, STR $p = 0.99$, decision PFC $p = 0.27$, STR $p = 0.92$). Thus, it seems that acquisition of the categories is accompanied by development of category-specific patterns of synchrony between, but not within, the PFC and STR.

Significant category-selective beta synchrony (at ~ 14 Hz) during Category Performance was also seen between spikes and LFPs during the exemplar epoch, specifically between PFC multiunit spiking activity (MUA) and STR LFPs (Figure 5B; ANOVA across stages: $F(2,1239) = 19.71$, $p = 3.8 \times 10^{-9}$; post hoc comparisons: selectivity during Category Performance greater than during SR Learning and Category Learning stages, $p = 5 \times 10^{-6}$). This spike-LFP synchrony was significantly greater than that expected by chance during Category Performance (t test: $p = 5.3 \times 10^{-8}$) but not during SR Learning ($p = 0.49$) or Category Learning ($p = 0.90$). Importantly, spike-LFP category-selective synchrony was asymmetric. It was seen between PFC spikes and STR LFPs (above) but not between STR spikes and PFC LFPs at any of the learning stages (Figures 5B and S3A, t test: SR Learning, $p = 0.82$; Category Learning, $p = 0.96$; Category Performance, $p = 0.59$). As was seen for LFP-LFP synchrony, there was no evidence for category-specific spike-LFP synchrony within PFC or STR (Figure S3B; SR Learning stage: PFC $p = 0.96$, STR $p = 0.99$; Category Learning stage: PFC $p = 0.52$, STR $p = 0.86$; Category Performance stage: PFC $p = 0.11$, STR $p = 0.23$). Thus, it seemed that patterns of category-selective synchrony were

category-specific rhythmic networks formed in the process of category learning. For each pair of electrodes, we computed differences in synchrony (PLV) for exemplars from the two categories using the discrimination index d' (described above), as in our previous study of neural activity (Antzoulatos and Miller, 2011). To correct biases of the d' metric due to variable and unequal numbers of trials, and to evaluate its statistical significance, trials were randomly shuffled 200 times between the two categories, thus generating a randomization distribution for the d' quantity, which was then used to z transform each electrode pair's d' . In short, we used this measure to determine whether different electrode pairs showed different levels of synchrony for the two different categories (i.e., category selectivity). Significant category-selective synchrony was observed, but only after the animals had learned the categories. During Category Performance, there was a significant increase of exemplar epoch category-selective synchrony in the beta band (peak at ~ 19 Hz) between the PFC and STR (Figure 5A, left) (ANOVA on category selectivity across learning stages, $F(2,1277) = 21.88$, $p = 4.5 \times 10^{-10}$; post hoc comparisons: selectivity during Category Performance greater than during SR Learning and Category Learning, $p = 5 \times 10^{-7}$). During the decision epoch, there was a significant increase of delta band category selectivity (peak at ~ 3 Hz, Figure 5A, right) ($F(2,1277) = 39.37$, $p = 2.6 \times 10^{-17}$; post hoc comparisons: selectivity during Category Performance greater than during SR Learning and Category Learning: $p = 10^{-11}$). Correspondingly, category-selective PFC-STR synchrony was not different from that expected by chance during the SR Learning or Category Learning stages but was significantly different from chance during Category Performance (t test for selectivity greater than zero in beta band of exemplar epoch: SR Learning, $p = 0.99$; Category Learning, $p = 0.99$; Category Performance, $p = 7.2 \times 10^{-8}$; in

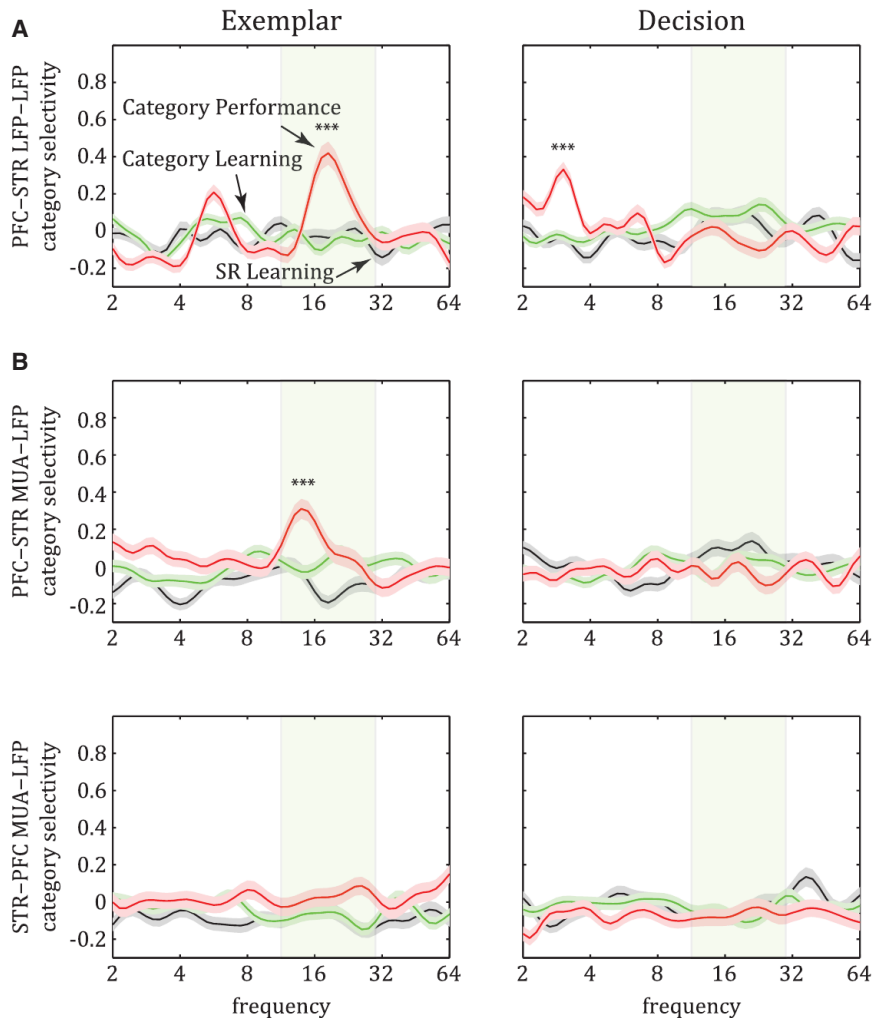


Figure 5. Category Selectivity in the Strength of PFC-STR Synchrony

(A) Synchrony between PFC and STR LFPs (average z-transformed $d' \pm \text{SEM}$) displayed significant category selectivity during the Category Performance stage. Category-specific synchrony was observed at the beta band during the exemplar epoch and at the delta band during the decision epoch.

(B) Similar to the LFP-LFP synchrony above, MUA-LFP synchrony (average z-transformed $d' \pm \text{SEM}$) between PFC-STR (spikes in PFC, LFP in STR; top) also displayed significant category selectivity at the beta band of the exemplar epoch; again, this was evident for the first time during the Category Performance stage. In contrast, the reverse direction (spikes in STR and LFP in PFC; bottom) did not show any category selectivity (see also Figure S3).

STR Exerts Larger Causal Influence on PFC than the Reverse

The measure of synchrony utilized above (PLV) is a measure of functional, not causal, connectivity, because it provides no information on the causal influence of one area on the other. Granger's test of causal connectivity can be used to indicate the degree of influence each area has on another. It evaluates how much of one area's LFP variance can be explained by the other area's LFP variance. Furthermore, this analysis can be performed at the frequency domain to identify causal influence specific to brain rhythms (Friston et al., 2013). Because Granger causality can also be affected

from the PFC to the STR, not the other way around and not within either area.

In our task, each category was uniquely associated with a saccade to the left or the right. Most cortical areas show activity that is biased toward processing of, and actions to, the contralateral hemifield. We therefore sought to determine whether the category-selective synchrony was primarily associated with categories signaling contralateral saccades. While LFP-LFP synchrony was seen for categories associated with both contralateral and ipsilateral saccades, there was a significant bias toward contralateral saccades for delta band category-selective synchrony during the decision epoch, when the monkeys prepared to execute the saccade (63.9% of all electrode pairs preferred contralateral saccades; $p = 0.0001$, chi-square test). By contrast, there was no contralateral or ipsilateral bias for beta band category-selective synchrony during the exemplar epoch (53.5% of all pairs preferred contralateral saccades; $p = 0.16$). Category-specific beta band spike-LFP synchrony between PFC-STR was also not biased for ipsilateral versus contralateral saccades (50.8% of all pairs preferred contralateral saccades; $p = 0.81$).

by areas that provide common input to PFC and STR and/or intervene between the two (e.g., the rest of BG), it is also a more global measure of influence than the spike-LFP synchrony we showed above (which is more sensitive to direct neurophysiological connections between the two areas).

We analyzed the causality between PFC and STR LFPs with a nonparametric variant of the Granger causality test so the results would not hinge on the order of the multivariate autoregressive model that a parametric test would require (Dhamala et al., 2008; Roberts et al., 2013). This analysis revealed that, although both areas had causal influence on each other, STR exerted a significantly stronger causal influence on PFC than PFC on STR (i.e., STR LFPs were better predictors of PFC LFPs rather than the reverse), and this was evident across the largest part of the frequency spectrum (Figure 6A) (e.g., 20 Hz beta band at SR Learning stage, exemplar epoch: t test on magnitude of Granger causality between the two directions: $p = 10^{-45}$; decision epoch: $p = 10^{-41}$). Indeed, most of the PFC-STR electrode pairs showed a stronger influence from STR to the PFC than the other way around (exemplar epoch: 80.8% of all pairs: $p = 0.0001$, chi-square test; decision epoch: 77.2%; $p = 0.0001$). In

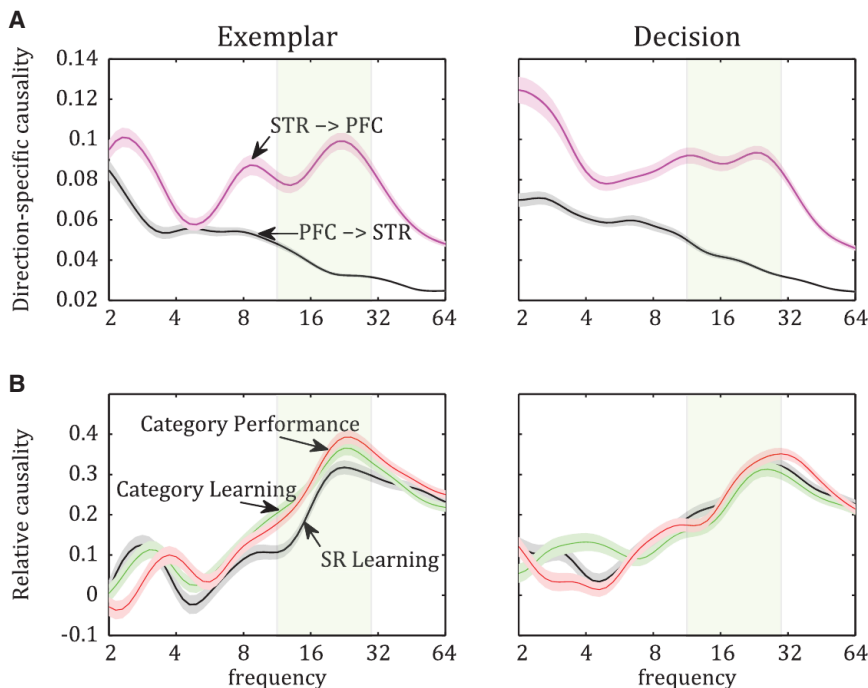


Figure 6. Analyses of Granger Causal Connectivity between PFC and STR

(A) Average Granger connectivity index \pm SEM: the two directions of causal connectivity during the two trial epochs of the SR Learning stage. Striatum exerts stronger influence on the prefrontal LFPs (STR \rightarrow PFC) than the other way around (PFC \rightarrow STR). This difference is seen across the frequency spectrum, but especially at the beta band (shaded rectangle).

(B) Average (\pm SEM) relative causality (STR \rightarrow PFC direction normalized to the PFC \rightarrow STR direction) across learning stages. In contrast to the robust enhancement of functional connectivity at the beta band (20 Hz) with learning (Figure 2), causal connectivity did not increase significantly, suggesting that the relative influence of one area on the other did not change.

addition to their difference in magnitude of causal connectivity, the two areas also differed in the spectral profile of their causal influence on one another: PFC had the strongest influence on the low frequencies of STR LFPs (e.g., delta band), whereas STR displayed clear peak influence on both the delta and beta bands of the prefrontal LFPs (Figure 6A).

In order to evaluate learning-induced changes in the relative causal connectivity between PFC and STR, we computed a composite causality index from both directions (PFC \rightarrow STR and STR \rightarrow PFC) for each learning stage and trial epoch: $(A-B)/(A+B)$, wherein A is STR \rightarrow PFC causality and B is PFC \rightarrow STR causality. There was little change in the direction of influence between the PFC and STR (Figure 6B) and no significant change in the 20 Hz beta band that displayed the aforementioned synchrony changes (ANOVA on causality of exemplar epoch across stages of learning: $F(2,1277) = 2.49$, $p = 0.08$; decision epoch: $F(2,1277) = 1.37$, $p = 0.25$). This suggests that the relative weight of one area's influence on the other did not change as a result of learning. Thus, while the analysis on category-selective spike-LFP synchrony (above) suggested a one-way PFC-STR synchrony, consistent with the monosynaptic connections from the PFC to STR, it appears that the polysynaptic connections from the STR back to the PFC had a greater influence on the PFC oscillations.

DISCUSSION

We found that category learning was accompanied by increased synchronization between, but not within, the PFC and striatum. Synchrony is thought to play a role in establishing functional circuitry (Engel et al., 2001; Fries, 2005; Miller and Buschman, 2013; Uhlhaas et al., 2009). Supporting this, we found that once the categories were learned, different pairs of PFC-STR

recording sites showed increased synchrony for one or the other category, suggesting functional circuits for mapping category representations in the PFC to the appropriate motor program in the BG. Spike-LFP synchrony did suggest that the category-specific synchrony was, in fact, asymmetric between the PFC and STR, reflecting the asymmetric monosynaptic projections between them. However, causal connectivity analysis suggested that the polysynaptic projections from the STR back to the PFC exerted a greater influence. This is consistent with models positing that the STR (through the BG) continually "trains" the PFC (Antzoulatos and Miller, 2011; Ashby et al., 2007; Djurfeldt et al., 2001; Houk and Wise, 1995; Miller and Buschman, 2008; Pasupathy and Miller, 2005; Seger and Miller, 2010).

The learning-related increases in PFC-STR synchrony seemed functional. First, they were not simply due to an overall increase in oscillatory power. Second, they were only seen during the trial and not in baseline activity. Third, they were specific to synchrony between the areas; there were no synchrony changes within PFC or STR. Finally, error trials (incorrect choices) did not display the same increase in beta synchrony that correct trials did. Curiously, error trials during SR Learning displayed stronger PFC-STR beta synchrony than did correct trials. This reversed once the animals advanced to Category Learning. SR learning is well known to rely on the BG (Packard and Knowlton, 2002), and striatal neurons display rapid acquisition of SR associations (Antzoulatos and Miller, 2011; Pasupathy and Miller, 2005). It is possible that stronger error trial beta synchrony between the STR and PFC interfered with the ability of STR to map the stimulus to the correct motor response during SR Learning. Indeed, excessive synchrony of cortex-BG networks is seen during Parkinsonian motor symptoms (Hammond et al., 2007; Marreiros et al., 2012).

Learning-related effects in the beta band are consistent with prior observations that beta band (12–30 Hz) oscillations are prominent in frontal cortex (Puig and Miller, 2012; Siegel et al., 2009) while gamma band oscillations predominate in posterior

cortex (Fries, 2009), that cortical beta versus gamma are associated with top-down (feedback) versus bottom-up (feedforward) processing (Buschman and Miller, 2007; Engel and Fries, 2010), and beta band oscillations synchronize striatal neurons in monkeys performing oculomotor tasks (Courtemanche et al., 2003). It should be noted that “beta band” may include more than one type of oscillation with distinct neurophysiological mechanisms and functions (Cannon et al., 2013). Indeed, the different results from this study showed peaks at different frequencies within the beta band. A dissection of the contributions of different beta sub-bands was beyond the scope of our study.

The learning-related changes in PFC-STR synchrony parallel the changes in category learning-related changes in single-neuron activity previously seen in this data set (Antzoulatos and Miller, 2011). During SR Learning, STR spiking activity was an earlier predictor of the corresponding saccade than the PFC. However, when monkeys advanced to Category Learning, PFC neurons began predicting the saccade associated with each category before the STR. One result of this was that PFC and STR neurons showed more overlap of their task-related spiking activity during and after Category Learning, relative to SR Learning. This overlap was in the decision epoch, just before the behavioral response. This is when we also first observed the learning-related increase in PFC-STR beta synchrony.

Category-selective beta synchrony could serve to communicate the categorical decision from the PFC to the STR. It occurred well before the motor response, during exemplar presentation, and did not show a contralateral motor bias. By contrast, category-specific delta synchrony occurred when the monkeys were about to make their motor response, and it was contralaterally biased. This could reflect recruitment of PFC and striatum in a larger network for motor acts. Low frequency oscillations (like delta and theta) have been associated with long-range synchronization among spatially diverse systems in the context of decision making, attention, and memory (Haegens et al., 2011; Schroeder and Lakatos, 2009; Watrous et al., 2013). Delta band synchronization (at least in visual cortex) is also observed during eye movements (Bosman et al., 2009; Ito et al., 2013). It should be noted that an emergence of category selectivity in the absence of a change in general synchrony suggests that synchrony during the preferred category increases, while synchrony during the nonpreferred category decreases, thus offsetting each other when synchrony across all trials is computed.

Dopamine may play a role in learning-related changes in synchrony. It mediates plasticity of excitatory corticostriatal connections. Because the phasic dopamine release that signals reward-prediction errors induces long-term potentiation of active cortical synapses onto medium spiny striatal neurons of the direct pathway (Gerfen and Surmeier, 2011; Lerner and Kreitzer, 2011)—i.e., the pathway that closes the PFC-BG-thalamus-PFC loop—it may also be responsible for increasing the synchronization between PFC and STR. Although dopamine is also known to affect the activity of prefrontal neurons during SR learning (Puig and Miller, 2012) and working memory (Arnsten et al., 2012), it is thought to be of less consequence for cortico-cortical than for corticostriatal synapses (Ashby et al., 2007; Miller and Buschman, 2008). This may be why we found that

corticostriatal synchrony was enhanced while corticocortical synchrony was not. It is also possible that corticocortical (and striatostriatal) connections require more experience for functional circuitry to be established. Rule-specific beta synchronization within the PFC has been observed (Buschman et al., 2012), but it was for highly familiar rules and not during new learning, as in this study.

The lack of learning-related changes in synchrony within the PFC and STR was in contrast to changes between them. Although we cannot exclude a ceiling effect for intrinsic synchrony, it is unlikely. The PFC-PFC synchrony was weaker than STR-STR synchrony, and yet it did not change with learning. Interestingly, the lateral connections between the STR medium spiny neurons are sparse, with high failure rate (Plenz, 2003). The stronger intrinsic STR synchrony, therefore, may arise from a common signal external to the STR, such as the substantia nigra pars compacta (SNpc): its dopaminergic neurons fire spikes at highly regular intervals and could have pacemaking functions (Surmeier et al., 2005). Recent studies have also suggested that striatal synchrony can be regulated by the subthalamic nucleus (Marreiros et al., 2012).

We found that the STR had a stronger net influence on the PFC than PFC on STR. This causal influence may be task dependent. In a stimulus-stimulus association task, the PFC was reported to exert larger causal influence on STR, consistent with their monosynaptic connections (Ma et al., 2013). However, the BG is indeed thought to exert a strong influence on frontal cortex (Ashby et al., 2007; Seger, 2008). The globus pallidus (which receives direct projections from the STR) affects the timing and presumably strength of thalamocortical communication (Goldberg et al., 2013) and also sends monosynaptic feedback signals to STR (Gerfen and Surmeier, 2011; Lerner and Kreitzer, 2011). The dopaminergic projection from SNpc is denser (i.e., presumably stronger) to STR than to the PFC (Lynd-Balta and Haber, 1994). Any of these signals, therefore, could shape both the PFC but mostly the STR rhythms, thus making the STR LFPs better predictors of PFC signals. The greater causal influence of the STR on the PFC is consistent with the hypothesis that STR learns about individual exemplars and then, via the rest of the BG, “trains” their categories in the PFC (Antzoulatos and Miller, 2011; Pasupathy and Miller, 2005; Seger and Miller, 2010). However, this process is continual and recursive: once the categories are learned, they can be fed into the STR for further learning, which may explain why, after learning, we found category-specific synchrony from the PFC to the STR.

EXPERIMENTAL PROCEDURES

Animals

Data were acquired from two adult female macaque monkeys, maintained in accordance with the National Institutes of Health guidelines and the policies of the Massachusetts Institute of Technology Committee for Animal Care.

Task

The details of the task have been presented previously (Antzoulatos and Miller, 2011). Briefly, the animals initiated a trial by fixating on a central target. While the animals maintained fixation, a randomly chosen category exemplar from either category was presented for 0.6 s. Trials from both categories were randomly interleaved throughout the session. One second after the exemplar

display offset, two saccade targets appeared on the left and right of the center of fixation, and the animal had to make a single, direct saccade to the correct target for reward. Category exemplars were random 7-dot constellations, generated through distortion of the corresponding prototype (Figure 1).

Neurophysiology

Simultaneous recordings from PFC and STR were performed using multielectrode arrays, lowered at different PFC and STR sites every day. LFPs were decomposed to their individual frequency components using wavelet analysis. Functional connectivity (i.e., frequency-specific synchrony) between pairs of LFP signals was computed as a PLV over two 500 ms trial epochs: the exemplar epoch (last 500 ms of exemplar display) and the decision epoch (last 500 ms before the animals' saccade). PLV computes the circular mean of a sample of phase differences (phase lags) and varies between 0 (when all phase lags are uniformly distributed across 360 degrees) and 1 (when all phase lags are concentrated at a single phase). Similar results on synchrony were obtained when we computed coherence or pairwise phase consistency. For differences in synchrony between two sets of trials (e.g., correct versus error, or category A versus B), we used the same selectivity metric (discrimination index d') we employed previously (Antzoulatos and Miller, 2011). To correct for sampling bias, we randomly shuffled the trials between the two sets 200 times, thus generating a randomization distribution that was used as surrogate data. The observed d' values were subsequently transformed into z scores based on the surrogate data set and averaged across the population of electrode pairs. Finally, causal connectivity analyses relied on a nonparametric Granger test, which evaluates the degree to which signal A can predict (i.e., explain the variance of) the frequency-specific oscillations of signal B. All computations were done using MATLAB (see Supplemental Information for more details).

SUPPLEMENTAL INFORMATION

Supplemental Information includes three figures, one table, and Supplemental Experimental Procedures and can be found with this article online at <http://dx.doi.org/10.1016/j.neuron.2014.05.005>.

ACKNOWLEDGMENTS

The authors thank B. Gray, S. Koopman, and D. Ouellette for technical assistance; S. Brincat, J. Donoghue, S. Kornblith, R. Loonis, M. Lundqvist, M. Moazami, V. Puig, J. Rose, J. Roy, and M. Silver for helpful discussions; and M. Wickerski for comments on the manuscript. This work was funded by the National Institute of Mental Health (5R01MH065252-12) and the Picower Foundation.

Accepted: May 1, 2014

Published: June 12, 2014

REFERENCES

- Antzoulatos, E.G., and Miller, E.K. (2011). Differences between neural activity in prefrontal cortex and striatum during learning of novel abstract categories. *Neuron* 71, 243–249.
- Arnsten, A.F., Wang, M.J., and Paspalas, C.D. (2012). Neuromodulation of thought: flexibilities and vulnerabilities in prefrontal cortical network synapses. *Neuron* 76, 223–239.
- Ashby, F.G., Ennis, J.M., and Spiering, B.J. (2007). A neurobiological theory of automaticity in perceptual categorization. *Psychol. Rev.* 114, 632–656.
- Bosman, C.A., Womelsdorf, T., Desimone, R., and Fries, P. (2009). A micro-saccadic rhythm modulates gamma-band synchronization and behavior. *J. Neurosci.* 29, 9471–9480.
- Brovelli, A., Ding, M., Ledberg, A., Chen, Y., Nakamura, R., and Bressler, S.L. (2004). Beta oscillations in a large-scale sensorimotor cortical network: directional influences revealed by Granger causality. *Proc. Natl. Acad. Sci. USA* 101, 9849–9854.
- Buschman, T.J., and Miller, E.K. (2007). Top-down versus bottom-up control of attention in the prefrontal and posterior parietal cortices. *Science* 315, 1860–1862.
- Buschman, T.J., Denovellis, E.L., Diogo, C., Bullock, D., and Miller, E.K. (2012). Synchronous oscillatory neural ensembles for rules in the prefrontal cortex. *Neuron* 76, 838–846.
- Cannon, J., McCarthy, M.M., Lee, S., Lee, J., Borgers, C., Whittington, M.A., and Kopell, N. (2013). Neurosystems: brain rhythms and cognitive processing. *Eur. J. Neurosci.* 39, 705–719.
- Courtemanche, R., Fujii, N., and Graybiel, A.M. (2003). Synchronous, focally modulated beta-band oscillations characterize local field potential activity in the striatum of awake behaving monkeys. *J. Neurosci.* 23, 11741–11752.
- Daitch, A.L., Sharma, M., Roland, J.L., Astafiev, S.V., Bundy, D.T., Gaona, C.M., Snyder, A.Z., Shulman, G.L., Leuthardt, E.C., and Corbetta, M. (2013). Frequency-specific mechanism links human brain networks for spatial attention. *Proc. Natl. Acad. Sci. USA* 110, 19585–19590.
- Daw, N.D., Niv, Y., and Dayan, P. (2005). Uncertainty-based competition between prefrontal and dorsolateral striatal systems for behavioral control. *Nat. Neurosci.* 8, 1704–1711.
- Dayan, P., and Abbott, L.F. (2001). *Theoretical Neuroscience*. (Cambridge: The MIT Press).
- Dhamala, M., Rangarajan, G., and Ding, M. (2008). Analyzing information flow in brain networks with nonparametric Granger causality. *Neuroimage* 41, 354–362.
- Djurfeldt, M., Ekeberg, O., and Graybiel, A.M. (2001). Cortex-Basal Ganglia Interaction and Attractor States. *Neurocomputing* 38–40, 573–579.
- Engel, A.K., and Fries, P. (2010). Beta-band oscillations—signalling the status quo? *Curr. Opin. Neurobiol.* 20, 156–165.
- Engel, A.K., Fries, P., and Singer, W. (2001). Dynamic predictions: oscillations and synchrony in top-down processing. *Nat. Rev. Neurosci.* 2, 704–716.
- Fries, P. (2005). A mechanism for cognitive dynamics: neuronal communication through neuronal coherence. *Trends Cogn. Sci.* 9, 474–480.
- Fries, P. (2009). Neuronal gamma-band synchronization as a fundamental process in cortical computation. *Annu. Rev. Neurosci.* 32, 209–224.
- Friston, K., Moran, R., and Seth, A.K. (2013). Analysing connectivity with Granger causality and dynamic causal modelling. *Curr. Opin. Neurobiol.* 23, 172–178.
- Gerfen, C.R., and Surmeier, D.J. (2011). Modulation of striatal projection systems by dopamine. *Annu. Rev. Neurosci.* 34, 441–466.
- Goldberg, J.H., Farries, M.A., and Fee, M.S. (2013). Basal ganglia output to the thalamus: still a paradox. *Trends Neurosci.* 36, 695–705.
- Haegens, S., Nacher, V., Hernández, A., Luna, R., Jensen, O., and Romo, R. (2011). Beta oscillations in the monkey sensorimotor network reflect somatosensory decision making. *Proc. Natl. Acad. Sci. USA* 108, 10708–10713.
- Hammond, C., Bergman, H., and Brown, P. (2007). Pathological synchronization in Parkinson's disease: networks, models and treatments. *Trends Neurosci.* 30, 357–364.
- Hipp, J.F., Engel, A.K., and Siegel, M. (2011). Oscillatory synchronization in large-scale cortical networks predicts perception. *Neuron* 69, 387–396.
- Houk, J.C., and Wise, S.P. (1995). Distributed modular architectures linking basal ganglia, cerebellum, and cerebral cortex: their role in planning and controlling action. *Cereb. Cortex* 5, 95–110.
- Ito, J., Maldonado, P., and Grün, S. (2013). Cross-frequency interaction of the eye-movement related LFP signals in V1 of freely viewing monkeys. *Front Syst Neurosci* 7, 1.
- Lachaux, J.P., Rodriguez, E., Martinerie, J., and Varela, F.J. (1999). Measuring phase synchrony in brain signals. *Hum. Brain Mapp.* 8, 194–208.
- Lerner, T.N., and Kreitzer, A.C. (2011). Neuromodulatory control of striatal plasticity and behavior. *Curr. Opin. Neurobiol.* 21, 322–327.
- Lynd-Balta, E., and Haber, S.N. (1994). The organization of midbrain projections to the ventral striatum in the primate. *Neuroscience* 59, 609–623.
- Ma, C., Pan, X., Wang, R., and Sakagami, M. (2013). Estimating causal interaction between prefrontal cortex and striatum by transfer entropy. *Cogn Neurodyn* 7, 253–261.

- Marreiros, A.C., Cagnan, H., Moran, R.J., Friston, K.J., and Brown, P. (2012). Basal ganglia-cortical interactions in Parkinsonian patients. *Neuroimage* 66C, 301–310.
- Miller, E.K., and Buschman, T.J. (2008). Rules through recursion: How interactions between the frontal cortex and basal ganglia may build abstract, complex rules from concrete, simple ones. In *Neuroscience of Rule-Guided Behavior*, S.A. Bunge and J.D. Wallis, eds. (New York: Oxford University Press).
- Miller, E.K., and Buschman, T.J. (2013). Cortical circuits for the control of attention. *Curr. Opin. Neurobiol.* 23, 216–222.
- Packard, M.G., and Knowlton, B.J. (2002). Learning and memory functions of the Basal Ganglia. *Annu. Rev. Neurosci.* 25, 563–593.
- Padmanabhan, A., Lynn, A., Foran, W., Luna, B., and O’Hearn, K. (2013). Age related changes in striatal resting state functional connectivity in autism. *Front Hum Neurosci* 7, 814.
- Pasupathy, A., and Miller, E.K. (2005). Different time courses of learning-related activity in the prefrontal cortex and striatum. *Nature* 433, 873–876.
- Plenz, D. (2003). When inhibition goes incognito: feedback interaction between spiny projection neurons in striatal function. *Trends Neurosci.* 26, 436–443.
- Puig, M.V., and Miller, E.K. (2012). The role of prefrontal dopamine D1 receptors in the neural mechanisms of associative learning. *Neuron* 74, 874–886.
- Reber, P.J., Stark, C.E., and Squire, L.R. (1998). Cortical areas supporting category learning identified using functional MRI. *Proc. Natl. Acad. Sci. USA* 95, 747–750.
- Roberts, M.J., Lowet, E., Brunet, N.M., Ter Wal, M., Tiesinga, P., Fries, P., and De Weerd, P. (2013). Robust gamma coherence between macaque V1 and V2 by dynamic frequency matching. *Neuron* 78, 523–536.
- Schroeder, C.E., and Lakatos, P. (2009). Low-frequency neuronal oscillations as instruments of sensory selection. *Trends Neurosci.* 32, 9–18.
- Seger, C.A. (2008). How do the basal ganglia contribute to categorization? Their roles in generalization, response selection, and learning via feedback. *Neurosci. Biobehav. Rev.* 32, 265–278.
- Seger, C.A., and Miller, E.K. (2010). Category learning in the brain. *Annu. Rev. Neurosci.* 33, 203–219.
- Seger, C.A., Poldrack, R.A., Prabhakaran, V., Zhao, M., Glover, G.H., and Gabrieli, J.D. (2000). Hemispheric asymmetries and individual differences in visual concept learning as measured by functional MRI. *Neuropsychologia* 38, 1316–1324.
- Siegel, M., Warden, M.R., and Miller, E.K. (2009). Phase-dependent neuronal coding of objects in short-term memory. *Proc. Natl. Acad. Sci. USA* 106, 21341–21346.
- Surmeier, D.J., Mercer, J.N., and Chan, C.S. (2005). Autonomous pacemakers in the basal ganglia: who needs excitatory synapses anyway? *Curr. Opin. Neurobiol.* 15, 312–318.
- Torrence, C., and Compo, G.P. (1998). A Practical Guide to Wavelet Analysis. *Bull. Am. Meteorol. Soc.* 79, 61–78.
- Uhlhaas, P.J., and Singer, W. (2012). Neuronal dynamics and neuropsychiatric disorders: toward a translational paradigm for dysfunctional large-scale networks. *Neuron* 75, 963–980.
- Uhlhaas, P.J., Pipa, G., Lima, B., Melloni, L., Neunenschwander, S., Nikolić, D., and Singer, W. (2009). Neural synchrony in cortical networks: history, concept and current status. *Front Integr Neurosci* 3, 17.
- Vogels, R., Sary, G., Dupont, P., and Orban, G.A. (2002). Human brain regions involved in visual categorization. *Neuroimage* 16, 401–414.
- Watrout, A.J., Tandon, N., Conner, C.R., Pieters, T., and Ekstrom, A.D. (2013). Frequency-specific network connectivity increases underlie accurate spatio-temporal memory retrieval. *Nat. Neurosci.* 16, 349–356.
- Yoon, J.H., Minzenberg, M.J., Raouf, S., D’Esposito, M., and Carter, C.S. (2013). Impaired prefrontal-basal ganglia functional connectivity and substantia nigra hyperactivity in schizophrenia. *Biol. Psychiatry* 74, 122–129.

States of Curiosity Modulate Hippocampus-Dependent Learning via the Dopaminergic Circuit

Matthias J. Gruber,^{1,*} Bernard D. Gelman,¹ and Charan Ranganath^{1,2}

¹Center for Neuroscience, University of California at Davis, Davis, CA 95618, USA

²Department of Psychology, University of California at Davis, Davis, CA 95616, USA

*Correspondence: mjgruber@ucdavis.edu

<http://dx.doi.org/10.1016/j.neuron.2014.08.060>

SUMMARY

People find it easier to learn about topics that interest them, but little is known about the mechanisms by which intrinsic motivational states affect learning. We used functional magnetic resonance imaging to investigate how curiosity (intrinsic motivation to learn) influences memory. In both immediate and one-day-delayed memory tests, participants showed improved memory for information that they were curious about and for incidental material learned during states of high curiosity. Functional magnetic resonance imaging results revealed that activity in the midbrain and the nucleus accumbens was enhanced during states of high curiosity. Importantly, individual variability in curiosity-driven memory benefits for incidental material was supported by anticipatory activity in the midbrain and hippocampus and by functional connectivity between these regions. These findings suggest a link between the mechanisms supporting extrinsic reward motivation and intrinsic curiosity and highlight the importance of stimulating curiosity to create more effective learning experiences.

INTRODUCTION

In a typical day, most of the events that a person experiences will be forgotten. What differentiates those occasions that are successfully remembered? It is clear that learning is influenced by the characteristics of particular stimuli and how they are processed. Much less is known about whether, in addition to such stimulus-related processing, particular motivational states can also influence the likelihood of memory formation and later consolidation processes. Consistent with this possibility, recent evidence suggests that neural activity in the midbrain (i.e., the substantia nigra/ventral tegmental area complex [SN/VTA]) along with hippocampal activity during anticipation of a reward can influence memory formation for a preceding (Wittmann et al., 2005) or subsequent stimulus (Adcock et al., 2006; Wolosin et al., 2012). In addition, it has been shown that increased functional connectivity between the SN/VTA and hippocampus

supports reward-related memory benefits (Adcock et al., 2006; Wolosin et al., 2012).

In real-life situations, learning is often self-motivated, driven by intrinsic curiosity in a particular topic, rather than by external reward (Berlyne, 1966; Reeve and Reeve, 1996; Ryan and Deci, 2000). Little is known about how intrinsic motivation affects brain activity and learning, but an initial study by Kang et al. (2009) provided important clues. In this study, the authors found that curiosity to learn the answers to trivia questions was associated with enhanced activation in the caudate nucleus. In a separate behavioral study, Kang and colleagues found that, after an 11- to 16-day retention period, participants were better able to recall answers to questions that they were highly curious about.

The results of Kang et al. (2009) raise important questions about the mechanisms by which intrinsic motivation can modulate brain activity and memory performance, and the degree to which intrinsic motivation influences memory in a manner similar to extrinsic motivation. Here, we used functional magnetic resonance imaging (fMRI) to address three critical questions: (1) Is curiosity associated with activity in key brain regions that are responsive to extrinsic motivation? (2) What are the neural mechanisms that promote the influence of curiosity on learning? (3) Most importantly, does a curious state enhance learning of incidental material, and if so, what are the brain areas that support curiosity-related memory benefits?

First, each participant rated his/her curiosity to learn the answer to a series of trivia questions (see Figure 1A for an example). Next, they were scanned during encoding of the answers to these questions, along with a set of neutral, unrelated face stimuli (Figure 1B). Each trial commenced with presentation of a selected trivia question, and the participant anticipated the associated answer during a 14 s delay. During this anticipation period, the participant incidentally encoded a face. After the scan session, participants performed a surprise recognition memory test for the faces that were presented during the anticipation period, followed by a memory test for the answers to the trivia questions. The critical analyses focused on activity that preceded the presentation of the face or the trivia answer, which we interpret to reflect anticipatory states of high or low curiosity.

For the fMRI analyses, we focused our hypotheses on three major regions of interest (ROIs)—the SN/VTA, the nucleus accumbens, and the hippocampus. These three regions show high intrinsic functional connectivity (Kahn and Shohamy,

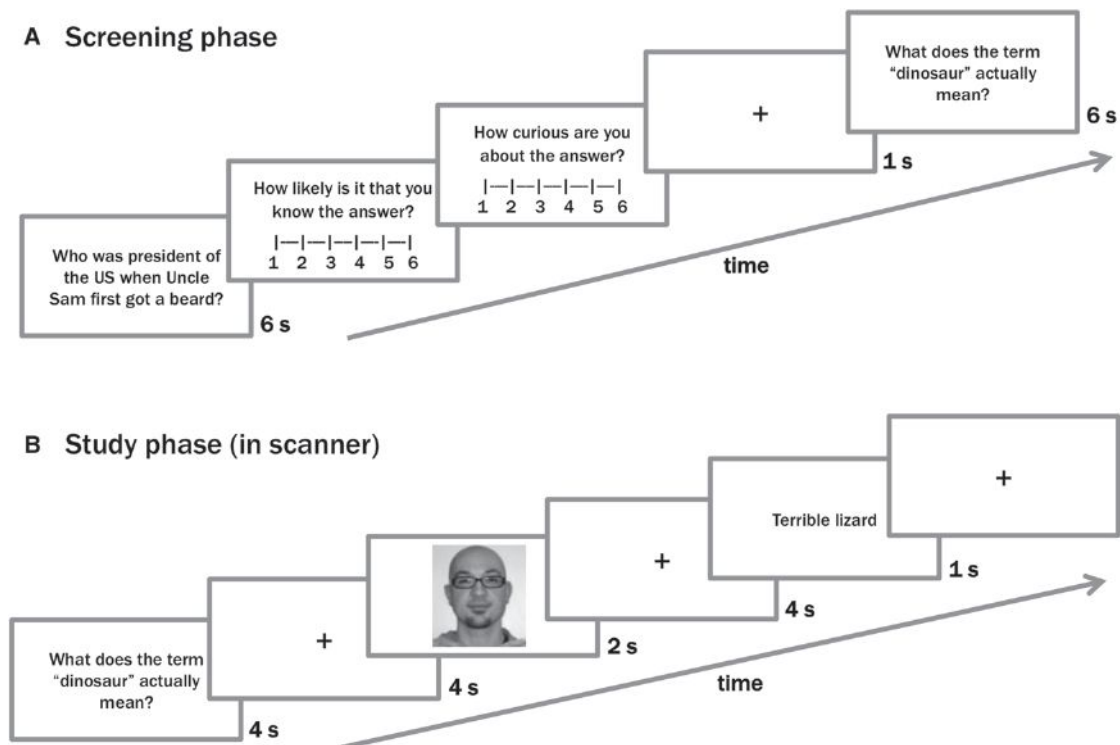


Figure 1. Example Trials from Screening and Study Phases

(A) Screening phase: for each trial, participants rated how likely they knew the answer to a trivia question and how curious they were to learn the answer. Questions associated with high and low curiosity, for which participants did not know the answer, were used for the next phase. Answers were not presented in this phase.

(B) Study phase (performed in the MRI scanner): For each trial, a selected trivia question was presented and the participant anticipated presentation of the answer. During this anticipation period, participants were required to make an incidental judgment to a face (shown as color image in the experiment). Following the study phase, participants completed memory tests (not shown) on both the trivia answers and the faces that were studied in the scanner.

2013) and have been hypothesized to comprise a functional loop in the service of learning (Düzel et al., 2010; Lisman and Grace, 2005; Lisman et al., 2011). According to these views, the SN/VTA (particularly, the VTA) modulates learning of salient information in the hippocampus via enhanced dopamine release, whereas the nucleus accumbens incorporates additional information related to novelty and goal relevance into this functional circuit. Although the hippocampal-VTA loop theory has primarily been used to explain effects of stimulus-related salience on learning, we predicted that the same circuit might also mediate effects of intrinsic motivational states. Accordingly, we used the NeuroSynth tool (Yarkoni et al., 2011) to conduct a meta-analysis based on 329 studies of reward processing to identify voxels within the three regions that are reliably recruited during extrinsic motivational states (see the Experimental Procedures; Figure S1 available online). If curiosity indeed relies on similar brain mechanisms as extrinsic reward motivation, we would expect that activity in these ROIs to be modulated by curiosity. In turn, curiosity-driven memory benefits should be supported by increased activity in the ROIs. Finally, based on work suggesting that extrinsic salience promotes stable memories by enhancing the late stage of long-term potentiation (LTP), we hypothesized

that curiosity-driven memory benefits should persist even after a 1-day retention delay.

RESULTS

What Are the Brain Areas that Support Curiosity?

Our first analyses identified brain areas that are recruited during states of high curiosity. Based on studies of extrinsic reward anticipation (Adcock et al., 2006; Knutson et al., 2001), we hypothesized that activity in the SN/VTA and nucleus accumbens should be enhanced during states of high curiosity. We were less certain about effects of curiosity in the hippocampal ROI, as it is unclear from prior studies whether hippocampal activity is generally reward-sensitive or if it more specifically reflects motivational influences on learning (Shohamy and Adcock, 2010). To quantify the positive relationship between curiosity and brain activity (cf. Kang et al., 2009), we ran an analysis testing for parametric modulation of activation during each trial as a function of curiosity ratings (see Experimental Procedures for details). Because of directed hypotheses, we performed one-tailed t tests (note that this is the approach routinely used in voxel-based fMRI analyses). As we did not have strong predictions about whether effects would be seen in the left or right hemispheres, we

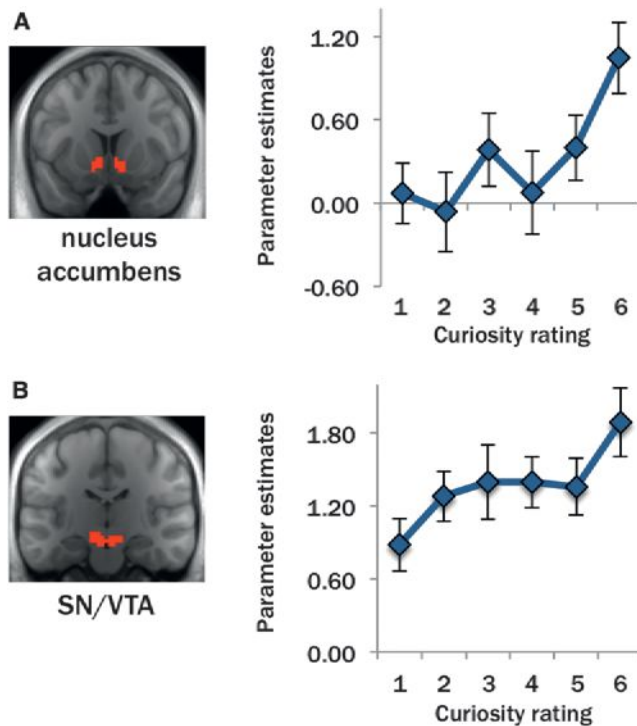


Figure 2. Curiosity-Modulated Activity in the Dopaminergic Circuit
Curiosity ratings were associated with activity increases in the bilateral nucleus accumbens ROI (A) and left SN/VTA ROI (B). On the left, ROIs are shown in red on the average, normalized anatomical image in our group of participants. On the right, to depict the effects modeled by the parametric modulation analysis, mean BOLD parameter estimates related to the onset of the trivia questions are plotted on the y axis against the curiosity rating given during the screening phase on the x axis. Error bars represent ± 1 SEM.

corrected for multiple comparisons across hemispheres by using a Bonferroni-adjusted alpha level of 0.025 per analysis.

During presentation of trivia questions (when curiosity was elicited), activity in the bilateral nucleus accumbens (left: $t_{(18)} = 3.16$, $p = 0.003$; right: $t_{(18)} = 2.60$, $p = 0.009$) and the left SN/VTA (left: $t_{(18)} = 2.23$, $p = 0.020$; right: $t_{(18)} = 1.52$, $p = 0.073$) increased linearly with curiosity ratings (Figures 2A and 2B). In contrast, no significant modulation was seen in these regions during presentation of trivia answers, when curiosity was satisfied (left and right nucleus accumbens: $t_{(18)} = 0.54$, and $t_{(18)} = 0.73$, respectively; left and right SN/VTA: $t_{(18)} = 0.23$ and $t_{(18)} = -0.06$, respectively; $p > 0.05$). Activity in the hippocampal ROIs was not significantly modulated by curiosity during presentation of trivia questions (left: $t_{(18)} = 0.31$; right: $t_{(18)} = -0.28$; $p > 0.05$) or answers (left: $t_{(18)} = -0.61$; right: $t_{(18)} = -0.43$; $p > 0.05$).

In addition to the parametric modulation analysis, we also performed a simpler analysis in which we directly contrasted activation following the presentation of questions associated with high (4–6) and low (1–3) curiosity ratings. Consistent with findings from the parametric modulation analyses, we found significantly increased question-related activation for high compared to low curiosity conditions in the left SN/VTA (left: $t_{(18)} = 2.53$, $p = 0.010$; right: $t_{(18)} = 0.95$, $p = 0.177$), and

similar trends in the bilateral nucleus accumbens that did not exceed the Bonferroni-corrected threshold (left: $t_{(18)} = 2.05$, $p = 0.027$; right: $t_{(18)} = 1.70$, $p = 0.053$). Again, no significant effects were seen in the hippocampal ROIs (left: $t_{(18)} = -0.91$; right: $t_{(18)} = -0.68$; $p > 0.05$). As in the parametric modulation analysis, no significant effects of curiosity were seen during presentation of the trivia answers (left nucleus accumbens: $t_{(18)} = 1.68$, $p = 0.055$; all other ROIs: t values ≤ 1.22 , $p > 0.05$).

To characterize activation outside of the a priori ROIs and enable comparison to prior fMRI studies of motivation (e.g., Kang et al., 2009; Knutson et al., 2001), we performed whole-brain, voxel-based analyses testing for parametric modulation of activity following presentation of trivia questions as a function of curiosity. This analysis revealed suprathreshold clusters of the bilateral striatum (i.e., dorsal and ventral), left inferior frontal gyrus, left superior gyrus, and the cerebellum (for details, see Table S1 and Figure S2). These results are highly consistent with the work of Kang et al. (2009), who also showed curiosity-related activation in the dorsal striatum, inferior frontal gyrus, and superior frontal gyrus.

In summary, the results described above suggest that curiosity modulates activity in the nucleus accumbens and SN/VTA, along with a possible set of SN/VTA afferents across the striatum and prefrontal cortex.

How Does Curiosity Benefit Learning of Interesting Material?

We next investigated the effect of curiosity on learning. We first compared recall rates for answers to trivia questions associated with high and low curiosity. Participants recalled significantly more answers to high-curiosity questions compared to low-curiosity questions (70.6% SE = ± 2.60 versus 54.1% SE = ± 3.04 ; $t_{(17)} = 5.64$, $p < 0.001$; Figure 3A), replicating earlier findings (Kang et al., 2009).

Based on studies of extrinsic motivation on memory (Adcock et al., 2006; Wittmann et al., 2005; Wolosin et al., 2012), we hypothesized that activation in the nucleus accumbens, SN/VTA, and hippocampus evoked by presentation of high-curiosity trivia questions (i.e., the point at which participants began to anticipate the answer) would be predictive of successful recall of the answers to those questions in the postscan memory test. Within each ROI, we analyzed activity evoked by high- and low-curiosity trivia questions depending on whether the associated trivia answers were later recalled or forgotten (see Figure 3B). In the nucleus accumbens, significant Curiosity \times Memory interactions were observed (left: $F_{(1,17)} = 6.75$, $p = 0.019$; right: $F_{(1,17)} = 8.56$, $p = 0.009$; Figure 3C, left), revealing that activity during anticipation of trivia answers predicted later memory for high-curiosity (left: $t_{(17)} = 2.23$, $p = 0.020$; right: $t_{(17)} = 2.79$, $p = 0.006$), but not low-curiosity trivia answers (left: $t_{(17)} = -0.80$; right: $t_{(17)} = -1.15$, $p > 0.05$). Activity in the SN/VTA was predictive of successful memory formation in both curiosity conditions (main effect memory: left: $F_{(1,17)} = 7.17$, $p = 0.016$; right: $F_{(1,17)} = 6.46$, $p = 0.021$; Figure 3C, middle), and no significant interactions were observed (left: $F_{(1,17)} = 0.06$, $p = 0.810$; right: $F_{(1,17)} = 0.48$, $p = 0.496$). Findings for the hippocampus paralleled those for the nucleus accumbens, exhibiting a trend for a Curiosity \times Memory interaction in the right hippocampus ($F_{(1,17)} = 5.25$,

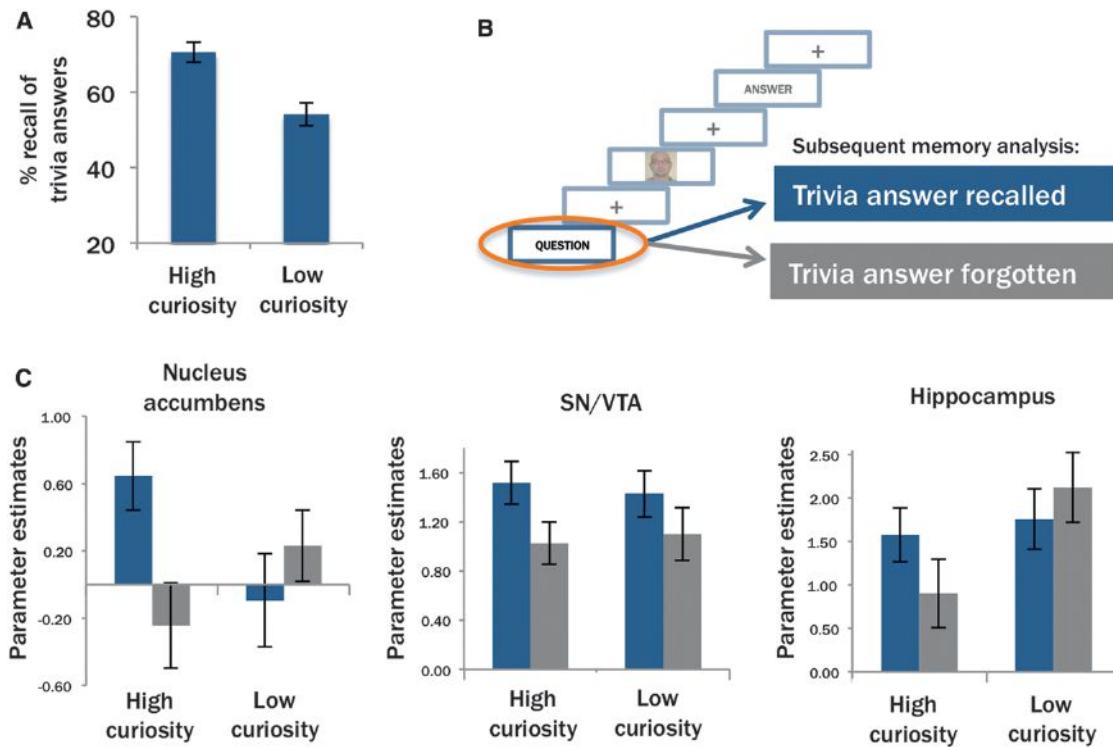


Figure 3. Curiosity Benefits Learning of Trivia Answers via the Nucleus Accumbens and Hippocampus

(A) Recall was higher for answers to high-curiosity trivia questions than for answers to low-curiosity trivia questions.

(B) Brain activity elicited by the onset of each trivia question was analyzed according to whether the associated answer was recalled in the postscan memory test. These analyses therefore tested the relationship between activation prior to the processing of trivia answers and successful encoding of those answers.

(C) Anticipatory brain activity (across-participant mean BOLD parameter estimates) in our three ROIs sorted by curiosity ratings and memory for the trivia answer. In the bilateral nucleus accumbens (left), activation evoked by the trivia question was increased for high-curiosity questions whose answers were later recalled compared to all remaining conditions. In the bilateral SN/VTA (middle), question-elicited activation was enhanced for later recalled compared to later forgotten answers independent of curiosity. In the right hippocampus (right), question-evoked activation predicted later memory performance only for trivia answers associated with high curiosity. Error bars represent ± 1 SEM.

$p = 0.035$; Figure 3C, right), but not in the left hippocampus ($F_{(1,17)} = 2.01$, $p = 0.175$). Further analyses showed that activity during anticipation of trivia answers predicted later memory on high-curiosity trials in the right hippocampus ($t_{(17)} = 2.12$, $p = 0.0247$), with a similar effect in the left hippocampus that did not exceed the Bonferroni-corrected threshold ($t_{(17)} = 2.04$, $p = 0.029$). No subsequent memory effect was evident on low-curiosity trials (left: $t_{(17)} = 0.00$; right: $t_{(17)} = -1.37$; $p > 0.05$).

Analyses of activity directly evoked by the trivia answers revealed subsequent memory effects that did not differentiate between high- and low-curiosity conditions (see Supplemental Information and Figure S3), consistent with results from fMRI studies of stimulus-related encoding activity (Paller and Wagner, 2002). Thus, the results indicate that curiosity-driven memory benefits were driven by anticipatory activity, rather than activity elicited during processing of interesting trivia answers (cf. Adcock et al., 2006).

How Does a Curious State Modulate Learning of Incidental Items?

Our next analyses focused on incidental learning of faces presented during states of high or low curiosity. We predicted that

neural processes that are elicited by the presentation of a high-curiosity question would enhance incidental learning of faces that were presented during this period. Consistent with this prediction, recognition performance was higher for faces that were encoded during states of high curiosity ($Pr = 42.4\%$ [hits – false alarms], $SE = \pm 2.68$) than for faces encoded during low curiosity trials ($Pr = 38.2\%$, $SE = \pm 2.37$; $t_{(18)} = 1.97$, $p = 0.032$; Figure 4A). This small, but significant effect is in line with the idea that a curious state can benefit learning of incidental information.

We then tested whether activity in our ROIs during states of high curiosity (i.e., question-evoked activity) supports the memory benefits for faces that were incidentally encoded during high- compared to low-curiosity states. We did not, however, find significant interactions between curiosity and memory or main effects of memory in the ROIs (all F values ≤ 2.01 , $p \geq 0.173$), possibly due to high intersubject variability in behavioral effects of curiosity on face encoding. Stimulus-related activity was predictive of successful memory formation, but this effect was independent of whether a face was presented during high or low curiosity states (see Supplemental Information).

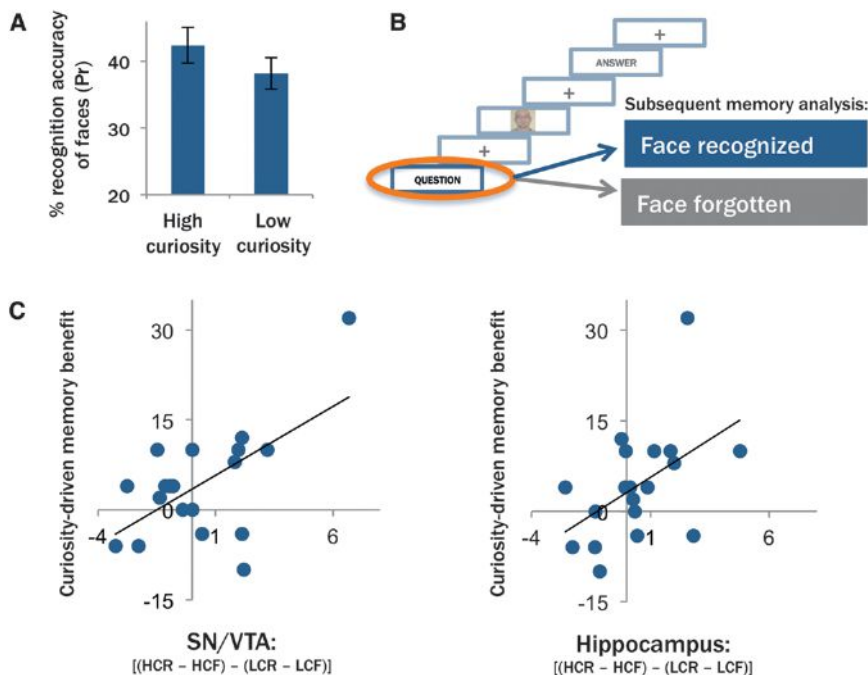


Figure 4. Enhanced Incidental Learning of Faces Encoded during States of High Curiosity

(A) Recognition discriminability (Pr values) was higher for faces presented during states of high curiosity compared to low-curiosity trials.

(B) Brain activity elicited by onset of each trivia question was analyzed based on whether the face that was subsequently presented on the same trial was recognized or forgotten on the postscan face recognition test.

(C) The neural interaction between anticipatory curiosity and memory was highly correlated with the curiosity-driven memory benefit for neutral faces. The scatter plots show significant, positive correlations between the intersubject variability in the curiosity-driven memory benefit (plotted on the y axis) and in activity for the bilateral SN/VTA (left) and the right hippocampus (right). Each data point represents one participant. HCR/HCF, high-curiosity recognized/forgotten; LCR/LCF, low-curiosity recognized/forgotten. Error bars represent ± 1 SEM.

Given the large intersubject variability in curiosity-driven memory benefits for incidentally presented faces, we investigated whether this variability might be driven by interindividual variations in activation during states of high curiosity. That is, if a curious state promotes learning of incidental information via activity in our ROIs, we might expect that those participants who exhibited the largest activation increase during states of high curiosity would show the largest memory benefits for neutral faces. As with the earlier analyses, this analysis was again performed on fMRI data during anticipation of answers to trivia questions (and therefore prior to face encoding; see Figure 4B).

To test this prediction, we computed the Pearson product moment correlation between the curiosity-driven memory benefit for faces (i.e., the difference in recognition memory performance between faces presented on high- versus low-curiosity trials) and the neural interaction between curiosity and subsequent memory (i.e., [subsequently recognized – forgotten faces on high-curiosity trials] – [subsequently recognized – forgotten faces on low-curiosity trials]). Results revealed strong relationships between the behavioral effect of curious states on subsequent memory for faces and curiosity-driven activation increases during anticipation of trivia answers in the bilateral SN/VTA (left: $r = 0.618$, $p = 0.002$; right: $r = 0.537$, $p = 0.009$) and right hippocampus (right: $r = 0.493$, $p = 0.016$; see Figure 4C). Correlations were not significant for the left hippocampus ($r = 0.176$, $p = 0.236$) or nucleus accumbens (left: $r = -0.189$; right: $r = -0.108$; $p > 0.05$). To confirm that correlations were not driven by extreme values, we repeated these analyses using Spearman's rank order correlation coefficient, which is robust to outliers. These analyses revealed a similar pattern of results, such that the neural interaction between curiosity and memory showed a trend for a positive correlation with curiosity-driven

memory benefits for faces in the bilateral SN/VTA (left: $r = 0.384$, $p = 0.052$; right: $r = 0.393$, $p = 0.048$) and right hippocampus ROI (left: $r = 0.149$, $p = 0.272$; right: $r = 0.447$, $p = 0.028$), but not in the bilateral nucleus accumbens (left: $r = -0.154$; right: $r = 0.084$; $p > 0.05$). A further mediation analysis revealed that the relationship between hippocampal memory-predicting activity and curiosity-driven memory benefits was mediated by midbrain memory-predicting activity (see Supplemental Experimental Procedures and Figure S4). Importantly, the correlations described above were solely driven by neural memory-predicting effects on high curiosity trials (left SN/VTA: Pearson's $r = 0.760$, $p = 0.001$; Spearman's $r = 0.588$, $p = 0.004$; right SN/VTA: Pearson's $r = 0.710$, $p < 0.001$; Spearman's $r = 0.638$, $p = 0.002$; right hippocampus: Pearson's $r = 0.504$, $p = 0.014$; Spearman's $r = 0.371$, $p = 0.059$; see Figure S5). No significant relationships were observed between the behavioral curiosity-driven memory benefit and memory-predicting activity in the low-curiosity condition (all Pearson's and Spearman's r values ≤ -0.107 , $p > 0.05$).

Given that between-individual variations in activity in the SN/VTA and hippocampus predicted memory benefits for unrelated, neutral faces, it is reasonable to speculate that these relationships were driven by functional connectivity between the two regions (Adcock et al., 2006; Wolosin et al., 2012). We therefore performed psychophysiological interaction analyses (PPI) to investigate whether the SN/VTA ROIs (i.e., seed region) show increased functional correlations with the hippocampus ROIs during successful, as compared with unsuccessful incidental encoding of faces. We performed separate PPI analyses for the high- and low-curiosity conditions targeting the critical time period following onset of the trivia question (for details, see Experimental Procedures). Results revealed a positive correlation between curiosity-driven memory benefits for faces and

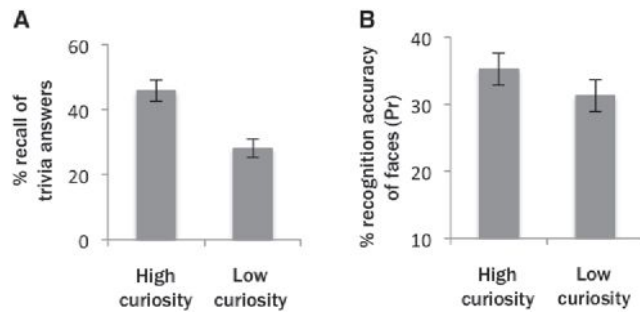


Figure 5. Follow-Up Behavioral Experiment Replicates Curiosity-Driven Memory Benefits for Interesting and Incidental Material over a 1-Day Retention Interval

(A) Participants recalled more answers to high-curiosity trivia questions than answers to low-curiosity questions.

(B) Participants showed higher rates of confident recognition for faces that were encoded during states of high curiosity than for faces encoded on low-curiosity trials. Error bars represent ± 1 SEM.

the magnitude of memory-predicting enhanced functional connectivity between the left SN/VTA and left hippocampus. Although the Pearson's r value ($r = 0.432$, $p = 0.032$) did not reach the Bonferroni-corrected significance threshold, the correlation was significant when calculated with Spearman's rank order correlation coefficient ($r = 0.4768$, $p = 0.020$). In contrast, we did not find significant correlations with memory benefits for faces in the low-curiosity condition (Pearson's $r = 0.134$, Spearman's $r = -0.005$, $p > 0.05$). Additional analyses on functional connectivity between the right SN/VTA and right hippocampus did not reveal any significant findings.

In summary, the findings suggest that individual differences in activity in the SN/VTA and hippocampus, and functional connectivity between the two regions accounted for between-individual variability in incidental face encoding during states of high curiosity.

Do Curiosity-Driven Memory Benefits for Incidental Events Persist after a Long Delay?

Behavioral results from the fMRI study revealed that curiosity influenced memory for trivia answers and for incidentally encoded faces. On average, the interval between initial encoding of an item and presentation of that item at test was around 53 min (range, 20–85 min) for faces and 70 min (range, 40–100 min) for trivia answers, though the interval varied across items and also across subjects. This time frame is consistent with the possibility that LTP was enhanced for stimuli presented on high-curiosity trials. If LTP was enhanced for stimuli on high-curiosity trials, then we would expect that curiosity-related memory benefits should extend across longer retention intervals. Accordingly, in a second, behavioral experiment, we tested whether curiosity-driven memory benefits would be evident after a 1 day delay between study and test (for details, see Experimental Procedures). Results of this experiment replicated the behavioral findings of the fMRI experiment. Recall of trivia answers to high-curiosity questions was higher than recall of answers to low-curiosity questions (45.9% SE = ± 3.35 versus

28.1% SE = ± 2.84 ; $t_{(26)} = 11.11$, $p < 0.001$; Figure 5A), consistent with the findings of Kang et al. (2009) and the findings of our fMRI study. Results also replicated the small, but reliable recognition advantage for faces that were presented during high-curiosity states, although this finding was specific to confidently recognized faces. The rate of confidently recognized faces was significantly higher for faces encoded during high-curiosity states than for faces encoded during low-curiosity states (Pr = 35.2% SE = ± 2.39 versus Pr = 31.2% SE = ± 2.38 ; $t_{(27)} = 2.44$, $p = 0.011$; Figure 5B), whereas the difference was not significant for overall hit rates (Pr = 39.6% SE = ± 2.76 versus Pr = 38.0% SE = ± 2.68 ; $t_{(27)} = 0.96$, $p = 0.173$; see also Table S3 for the full pattern of memory responses). These findings are consistent with the idea that curiosity can influence memory consolidation of interesting material and incidental material encoded during high-curiosity states.

DISCUSSION

The goal of the present study was to examine how intrinsic motivation benefits learning of interesting and incidental information. Behavioral results from two studies revealed that states of high curiosity enhance not only learning of interesting information, but also learning of incidental material. Imaging results demonstrated that these learning benefits are related to anticipatory brain activity in the mesolimbic dopaminergic circuit including the hippocampus. In particular, curiosity-driven memory benefits for incidental material were supported by activity in the SN/VTA and the hippocampus and by increased midbrain-hippocampus functional connectivity. Importantly, the effects of curiosity on memory for incidental material were correlated with activity in the SN/VTA prior to the encoding event, accounting for more than half of the behavioral variance in incidental encoding during high-curiosity states. These findings are consistent with the idea that curiosity enhances learning, at least in part, through increased dopaminergic modulation of hippocampal activity.

Parallels between Intrinsic and Extrinsic Motivation

The current findings complement results from a study on the neurocognitive mechanisms of curiosity by Kang et al. (2009). Both our whole-brain analyses and their results demonstrated that curiosity to learn answers to trivia questions was associated with increased activation in focal clusters in the ventrolateral prefrontal cortex and dorsal striatum. Using regions identified from a synthesis of published fMRI studies of reward, we additionally demonstrated that the specific ventral striatum and midbrain regions that were consistently recruited during reward anticipation also show increased activity during anticipation of interesting information (c.f. Knutson et al., 2001; O'Doherty et al., 2002). Results from the behavioral study conducted by Kang et al. (2009), like our study, also demonstrated that curiosity influences memory for trivia answers even across long retention intervals.

One major difference between Kang et al.'s (2009) study and the present study is that Kang et al. investigated how curiosity interacts with prior knowledge, whereas our study investigated how curiosity influences new learning. In their study, participants

guessed answers to the questions and activity during the answer was contrasted between trials associated with correct and incorrect guesses. Activation in the midbrain, putamen, and the medial temporal lobe was enhanced for incorrectly guessed answers, if the participant was curious about the answer, leading the authors to conclude that the effect was driven by a reward prediction error. In contrast, the present study revealed that activation in the midbrain and nucleus accumbens was enhanced during anticipation of answers, but not during the presentation of the answer itself. Thus, our findings speak more to the influences of a curious state on memory, rather than to the phasic reinforcing influence of satisfying one's curiosity.

Given that activity in the midbrain and nucleus accumbens has been reliably linked to presentation of reward, the fact that we did not see curiosity-related modulation of responses in these areas to trivia answers might seem surprising. However, we note that responses to external reward in the dopaminergic circuit scale with reward prediction errors and value (Dayan and Balleine, 2002; Schultz, 2013). In the present study, we could not assess the extent to which answers to trivia questions satisfied participants' curiosity, and it is likely that this variance contributed to variability in SN/VTA activity during presentation of the answers. Consistent with this explanation, Kang et al. (2009) found responses to trivia answers that resembled reward prediction errors.

Dopaminergic Mechanisms of Motivated Memory

Although we cannot make strong conclusions about whether fMRI signals in the midbrain and nucleus accumbens in our study reflect increased release of dopamine, there is reason to believe that dopamine might have played an important role. First, recent evidence indicates that blood oxygen level-dependent (BOLD) fMRI signals in the dopaminergic midbrain and nucleus accumbens are positively correlated with dopamine release in the striatum (Knutson and Gibbs, 2007; Schott et al., 2008). Second, our whole-brain analyses confirmed that curious states were associated with relatively restricted activation in regions that are thought to be targets of midbrain dopaminergic nuclei (Haber and Fudge, 1997). Third, as we describe below, the findings linking activity in the SN/VTA and hippocampus to memory formation during curious states strongly parallel theoretical accounts and findings in rodents showing that dopaminergic activity can modulate hippocampus-dependent learning (for reviews, see Düzel et al., 2010; Lisman and Grace, 2005; Lisman et al., 2011; Shohamy and Adcock, 2010).

It has been shown that dopamine stimulates local protein synthesis in the dendrites of hippocampal neurons, which in turn is necessary for the late phase of LTP (e.g., Smith et al., 2005). Blockade of D1 receptors, in turn, can inhibit hippocampal synaptic plasticity (e.g., Frey et al., 1990; O'Carroll and Morris, 2004). Accordingly, several models (Frey and Morris, 1998; Lisman and Grace, 2005; Lisman et al., 2011; Redondo and Morris, 2011; Shohamy and Adcock, 2010) propose that stabilization of learning-induced hippocampal plasticity depends on dopaminergic neuromodulation, in addition to synaptic activity. Critically, research has indicated that weak learning events can elicit LTP if they are preceded by events that upregulate dopaminergic activity (Wang et al., 2010). Thus, dopaminergic activity might

influence encoding "not only of specific salient events, but also the contexts in which they occur" (Shohamy and Adcock, 2010, p. 470).

The present results are consistent with this proposal, in that anticipatory activity in the hippocampal-VTA circuit was related to subsequent memory for trivia answers and for temporally contiguous faces. These increases in BOLD signal could have been driven by increased dopaminergic input to the hippocampus during anticipation of the answer (Shohamy and Adcock, 2010). If so, then dopaminergic activity during states of high curiosity might have "rescued" memories for incidentally encoded faces that would otherwise be forgotten (Lisman et al., 2011; Redondo and Morris, 2011). This result is in line with recent studies showing similar memory enhancements on temporally contiguous information with extrinsic reward (Murty and Adcock, 2013; Mather and Schoeke, 2011; Murayama and Kitagami, 2014). In addition, activity that predicted curiosity-driven memory benefits for interesting and incidental material was the activity during the anticipatory state, which is also consistent with findings from reward-motivated learning (Adcock et al., 2006; Gruber and Otten, 2010; Gruber et al., 2013; Murty and Adcock, 2013). Collectively, these findings suggest that both intrinsic and extrinsic motivational states can modulate memory formation.

If the effects of curiosity on learning were driven, at least in part, by dopaminergic modulation of hippocampal activity, it would imply a specific effect of curiosity on the late phase of LTP. The lower bound of the timescale for late LTP is not clear, but the retention intervals tested here are potentially consistent with such a mechanism. In the first experiment, memory was tested almost 1 hour after its initial encoding (on average, 53 min for each face, 70 min for each trivia answer). Importantly, we replicated the curiosity-driven memory benefits with a 1 day retention interval, which is definitely consistent with the timescale of late LTP. The findings are therefore in line with the idea that curiosity influenced memory for trivia answers and incidental memory for faces via dopaminergic facilitation of hippocampal LTP.

Different Roles of the Dopaminergic Circuit for Intentional and Incidental Learning

Although curiosity enhanced encoding of both trivia answers and incidentally presented faces, our results revealed some differences between effects of curiosity on intentional and incidental learning. Anticipatory activation in the nucleus accumbens predicted later memory performance only for high-curiosity trivia answers, whereas activation in the SN/VTA was related to memory for high- and low-curiosity trivia answers and to faces incidentally encoded during states of high curiosity. We did not predict this difference between the nucleus accumbens and SN/VTA, but we speculate that this may reflect different roles for the accumbens and SN/VTA in intentional and incidental encoding. Anticipatory activity in the nucleus accumbens may set the stage for encoding of upcoming information that is goal relevant. In contrast, anticipatory activity in the midbrain may promote memory for goal-relevant information, temporally contiguous goal-irrelevant information (e.g., faces shown during high-curiosity trials), and other information that is somehow salient but irrelevant to current goals (e.g., subsequently

remembered answers to low-curiosity trivia questions). This account is admittedly speculative, but it aligns with models (Goto and Grace, 2008; Lisman and Grace, 2005; Scimeca and Badre, 2012) proposing that the VTA signals salience, whereas the nucleus accumbens integrates information about salience from the VTA with information about goal relevance conveyed by the prefrontal cortex.

Future Directions

Further research is needed to explore the relationship between extrinsic and intrinsic motivation. Although there is reason to think that they share common mechanisms, they might also interact in counterintuitive ways. For instance, behavioral studies have shown that extrinsic reward can undermine intrinsic motivation (for a review, see Deci et al., 1999), an effect that has been linked to decreased activation in the striatum and prefrontal cortex (Murayama et al., 2010). Furthermore, Murayama and Kuhbandner (2011) demonstrated that the effects of extrinsic reward and curiosity on memory encoding are not additive. In their study, extrinsic reward was associated with enhanced memory for uninteresting trivia answers, but reward did not improve memory for answers of questions that participants were highly curious about. These findings suggest that it would be useful to directly assess interactions between intrinsic and extrinsic motivational processes in relation to dopaminergic activity and learning.

Another important question concerns the cognitive processes that are influenced by intrinsic motivation. One possibility is that curiosity was associated with increased arousal or attentional processes. Although this is certainly possible, we do not believe that the relationship between curiosity and memory can be solely attributed to increased attentional processing. Behavioral studies have revealed direct influences of reward motivation on memory that cannot be explained by attentional processes *per se* (Wittmann et al., 2011). Consistent with this idea, the effects of curiosity identified in the whole-brain analyses bore little resemblance to the frontoparietal networks seen in whole-brain analyses of anticipatory attention (cf. Corbetta and Shulman, 2002). Furthermore, an attentional account would predict that curiosity should enhance intentional encoding of trivia answers but impair incidental encoding of faces as these faces were irrelevant to the questions that stimulated participants' curiosity. It is conceivable that the encoding task, which required participants to rate the faces for potential knowledge of the trivia answers, made the faces seem relevant. However, participants knew that the faces did not correspond to people who would actually provide an answer, and, irrespective of the rating, the answer was always presented only a few seconds after the face. Thus, the faces were more likely to be seen as distracters that were not relevant to satisfying their curiosity. Accordingly, the fact that we found enhanced memory for faces on high-curiosity trials is not obviously consistent with a purely attentional account. Nonetheless, further research is needed to more extensively characterize how states of curiosity affect attentional and mnemonic processing.

Perhaps the most interesting finding to emerge from these experiments is that states of curiosity enhance encoding of temporally contiguous, but otherwise incidental information.

These effects were relatively subtle, but reliable across experiments. Additionally, the high intersubject variability in this effect was related to variability in hippocampal and midbrain activity and to functional connectivity between the two regions. Findings of high intersubject variability are common in studies that investigate the influence of the dopaminergic circuit on learning in both animals (Flagel et al., 2011) and humans (Krebs et al., 2009; Wimmer and Shohamy, 2012; Zald et al., 2008). Further research is needed to better understand the sources of this intersubject variability, which might reflect different genotypes, personality traits, or other influences on motivation and/or dopaminergic function.

Implications

The present findings have potential implications for understanding memory deficits in the elderly and in patients with psychiatric and neurological disorders that affect dopaminergic transmission (Chowdhury et al., 2013; Düzel et al., 2010; Goto and Grace, 2008; Lisman et al., 2011). We found that curiosity had large and long-lasting effects on memory for interesting information. Although effects on memory for incidental information were more subtle, it should be noted that our trivia question paradigm might only weakly approximate the effects of an individual's idiosyncratic interests and motivation to learn. If anything, it is likely that our results may be underestimating the effects of curiosity on learning in daily life.

Given that healthy aging and several neurological and psychiatric disorders are associated with changes in dopaminergic function, it is possible that these conditions affect memory, in part, through changes in intrinsic motivation to learn. In addition, the results are pertinent to learning in educational and occupational settings. For example, our findings suggest that, in addition to optimizing instructional methods, stimulating curiosity ahead of knowledge acquisition could enhance learning success (Lisman et al., 2011). Furthermore, teaching of detailed material that may not be of broad interest might be best done in the context of instruction on topics that students are highly motivated to learn.

EXPERIMENTAL PROCEDURES

The details about the participants, stimulus material, and the presentation are presented in the Supplemental Experimental Procedures. The UC Davis Institutional Review Board approved both experiments.

Task Procedures

In both experiments, participants underwent a four-stage paradigm with (1) a screening phase, (2) a study phase, (3) a surprise recognition test phase for incidental items (i.e., faces), and (4) a surprise recall test for trivia answers presented during the study phase. The delay between the study phase and the first memory test was on average 20 min in the fMRI experiment and 1 day (22.5 hr) in the follow-up behavioral experiment. There were no other differences with respect to task procedures between both experiments.

Screening Phase

Because the level of curiosity elicited by different trivia questions is likely to vary between participants, we used participants' ratings to sort trivia questions into participant-specific high- and low-curiosity categories (56 questions each). Trivia questions were randomly selected from a pool of 375 trivia questions and were consecutively presented. After the presentation of a trivia question, participants had to give two self-paced ratings on 6-point scales

(see Figure 1A). First, they had to rate how confident they were that they knew the answer to a trivia question (extremes of scale: 1 = “I am confident that I do not know the answer” and 6 = “I am confident that I know the answer”). Second, participants rated their level of curiosity about the answer to a trivia question (extremes of scale: 1 = “I am not interested at all in the answer” and 6 = “I am very much interested in the answer”). If participants did not indicate that they knew the answer to a trivia question (i.e., they did not give a 6 point response on the answer confidence rating), trivia questions with response points 1–3 on the curiosity rating were allocated to the low-curiosity condition and response points 4–6 to the high-curiosity condition. The screening phase lasted until 56 trivia questions were allocated for each curiosity condition. On average (min–max), participants gave a high curiosity rating on 85 (range, 56–173) and a low curiosity rating on 58 (range, 56–68) trivia questions.

Study Phase

In the subsequent study phase that took place in an MRI scanner for the fMRI experiment, the selected 112 trivia questions were presented along with the associated answers (see Figure 1B). A trial started with the presentation of a trivia question, followed by an anticipation period that preceded the presentation of the associated trivia answer. Six of the 56 trials (~10%) in each condition were catch trials to ensure participants’ attention throughout the scanning session. In these trials, the letter string “xxxxx” was presented instead of the trivia answer. During the anticipation period, a cross-hair was presented that was replaced by an image of an emotionally neutral face (incidental item) during the middle of the anticipation period. During the presentation of the face, participants had to give a yes/ no response as to whether this particular person would be knowledgeable about the trivia topic and could help them figure out the answer. “Yes” responses were given with the right index finger and “no” responses with the right middle finger on an MRI-compatible response box in the fMRI experiment and on a computer keyboard for the behavioral experiment. This encoding judgment was used to ensure that faces were likely to be encoded with a similar level of attention across both curiosity conditions. The study phase was divided into four scanning runs (9 min each).

Recognition Memory Test for Incidental Items

Approximately 20 min (fMRI experiment) or 22.5 hr (behavioral experiment) after the end of the study phase, a surprise recognition memory test for the faces was administered. All 112 faces from the study phase and 56 new faces were randomly presented. Participants made confidence judgments on whether they thought the face was presented during the study phase or was not presented earlier (i.e., “confident new,” “unconfident new,” “unconfident old,” and “confident old”). Participants were encouraged to try to give a response as accurately and quickly as possible.

Recall Test for Trivia Answers

After the recognition memory test for faces, participants were given a list with all trivia questions from the study phase in random order. Participants were encouraged to take approximately 20 min to write down the correct answers without guessing any answers.

Behavioral Analyses

To assess whether memory improved for the high compared to the low curiosity condition and whether memory was above chance, we performed one-tailed paired-sample *t* tests. Catch trials were not included in any analyses.

fMRI Methods

fMRI Acquisition

We used a 3T Siemens Skyra scanner with a 32-channel phased array head coil to acquire anatomical and functional MRI images. A multiband Echo-Planar Imaging sequence was used to acquire whole brain T_2^* -weighted images (repetition time = 1.22 s, echo time = 24 ms; 38 slices per volume; multiband factor = 2; voxel size = 3 mm isotropic) with 441 volumes for each of the four scanning runs. In addition, a T_1 -weighted MP-RAGE with whole brain coverage was acquired. Inside the head coil, the participant’s head was padded to restrict excessive motion. Stimuli were displayed on a mirror attached to the head coil above the participant’s eyes. During the scanning, the participant’s eyes were monitored by the experimenter via an eye tracker to ensure that the participant attended to all stimuli.

fMRI Preprocessing

The functional and anatomical images were preprocessed and analyzed using the SPM8 software (The Wellcome Trust Centre for Neuroimaging, London, UK). The functional images were first realigned and then coregistered to the anatomical images. Anatomical images were segmented into gray and white matter images and imported into DARTEL to create a template anatomical image that was specific to the participants in this study. We then used DARTEL to normalize functional and anatomical images into MNI space. Functional images were spatially smoothed with a 6 mm full-width half-maximum Gaussian kernel. The ART repair toolbox (<http://cibsr.stanford.edu/tools/human-brain-project/artrepair-software.html>) was used to identify individual scans that showed abrupt movements (spikes).

fMRI Analyses

General linear models (GLMs) were estimated by modeling BOLD signal changes using a stick function (0 s duration) to model the onset of the particular events. We convolved these stick functions with a canonical hemodynamic response function and included motion covariates to account for motion-related noise in the data (i.e., three rigid-body translation and three rigid-body rotation parameters and additional spike regressors for scans that were identified by the ART repair toolbox). Catch trials were modeled separately for all event onsets and were not included in any analyses.

Regions-of-Interest Approach

We focused our analyses on three ROIs: the SN/VTA, the nucleus accumbens, and the hippocampus. First, the SN/VTA ROI was derived from a probabilistic mask based on magnetization transfer images (Guitart-Masip et al., 2011) containing the whole SN/VTA complex. Second, the nucleus accumbens ROI was traced on the mean anatomical images according to accepted guidelines (Haber and Knutson, 2010; Center for Morphometric Analyses, Massachusetts General Hospital, Charlestown, MA, USA; <http://www.cma.mgh.harvard.edu/>). Third, the hippocampus ROI was derived from the hippocampal mask from the SPM Anatomy Toolbox (Amunts et al., 2005). To have a sensitive measure within these anatomical ROIs we conducted a meta-analysis using the NeuroSynth tool (<http://neurosynth.org/>; Yarkoni et al., 2011). We performed a term-based search on “reward” that included 329 studies (retrieved July 2, 2013) and generated a reverse inference mask (i.e., probability of the term “reward” given the observed activation). The reverse inference mask was chosen because of its increased selectivity in brain activation related to the search term (Yarkoni et al., 2011). We then inclusively masked this functional “reward” mask with our three anatomical masks. Figure S1 shows the resulting ROIs that indicate the overlap between the functional “reward” mask and the anatomical masks. Using this approach, the SN/VTA ROI potentially captured the whole VTA and parts of the SN, the nucleus accumbens ROI was used as a whole, and the hippocampus ROI was restricted to clusters in the hippocampal head and body. Importantly, our reward-sensitive hippocampus ROI overlapped with a hippocampal region that shows high functional connectivity with the VTA and the nucleus accumbens (Kahn and Shohamy, 2013). Analyses are based on activity in the left and right hemisphere separately.

Curiosity-Related Activation

The first GLM tested whether curiosity ratings parametrically modulated activity in our ROIs. Separate regressors were used for onsets of the trivia questions, faces, and trivia answers. The analyses of interest were the onsets of the trivia questions and answers (i.e., when curiosity was elicited and satisfied). That is, for each participant, activation in response to the question was modeled with one regressor modeling mean activation across all trials, and a mean-centered parametric modulation regressor whose magnitude scaled linearly with curiosity ratings given for the question during the screening phase. Because we hypothesized that activity in our ROIs might linearly increase with curiosity ratings, fMRI beta estimates were entered into one-tailed one-sample *t* tests and tested against the value 0 (i.e., per ROI and events of interest). Because we did not have strong predictions about laterality, tests for left and right hemisphere ROIs were evaluated using a Bonferroni-corrected threshold of 0.025 per analysis. For additional whole brain analyses, we used 3DClustSim (Cox, 1996; http://afni.nimh.nih.gov/pub/dist/doc/program_help/3dClustSim.html) to determine a cluster correction of $p < 0.05$ for the

whole brain ($p < 0.005$ and $k = 65$ voxels using a gray matter mask based on the subjects' mean anatomical image).

Activation Predicting Later Recall of Trivia Answers

The second GLM modeled activation depending on later memory performance for trivia answers. Event onsets for trivia questions, faces, and trivia answers were modeled according to trials in which trivia answers were later correctly recalled or forgotten. All regressors were further separated into the low- (curiosity ratings 1–3 during the screening phase) and high-curiosity condition (curiosity ratings 4–6; for trial numbers, see Supplemental Information). Our main analyses of interest targeted the onset of the trivia questions (when a curious state was elicited). We hypothesized that our ROIs would support learning of interesting—but not uninteresting—material via increased activity for later recalled compared to later forgotten trivia answers. Importantly, we hypothesized such memory-predicting activity at the time interval when curiosity was elicited (i.e., at the time of trivia questions; see Figure 3B). We therefore performed a 2×2 repeated-measures ANOVA with the factors curiosity (high/ low) and memory (recalled/ forgotten). If an interaction was present, paired-sample one-tailed t tests were performed on memory-predicting activity in both curiosity conditions separately. In addition to activity elicited by trivia questions, we hypothesized that stimulus-related activity (i.e., during the actual learning of trivia answers) should also predict later recall of trivia answers (see Figure S3A). ANOVAs on stimulus-related activity in our ROIs were performed in the same way as the analyses for activity elicited by trivia questions.

Activation Predicting Later Recognition of Faces

The third GLM modeled activity depending on later memory performance of faces that were presented during the anticipation phase. As in the previous GLMs, all event onsets for trivia questions, faces, and trivia answers were modeled separately, but in this GLM separate regressors were used according to whether a face in a given trial was later correctly recognized (i.e., a “confident old” or “unconfident old” response) or forgotten (i.e., a “confident new” or “unconfident new” response; for trial numbers, see Supplemental Information). Regressors were further separated into both curiosity conditions. Our main analyses of interest again targeted the time when curiosity was elicited (i.e., at the time of the trivia questions). This way, we could ask how memory benefits for incidental stimuli (i.e., faces) that were presented during states of high compared to low curiosity would be supported by activity in our ROIs (see Figure 4B). To test whether memory for neutral faces was supported by question-evoked activity, ANOVAs were performed using an identical approach as for the analyses concerning memory for trivia answers. In addition, we performed Pearson's and Spearman's correlations to investigate relationships between participants' behavioral curiosity-driven memory benefit for faces (i.e., recognition accuracy for faces: high- – low-curiosity condition) and the neural interaction between curiosity and subsequent memory (i.e., [high-curiosity condition: faces recognized – forgotten] – [low-curiosity condition: faces recognized – forgotten]).

Functional Connectivity Analyses

PPI analyses were performed to investigate how functional connectivity between the SN/VTA and hippocampus ROIs predicted memory benefits for incidental, unrelated faces. PPI general linear models included the raw time course of a seed region (i.e., the physiological term; here: the left or right SN/VTA ROI), the onsets of either high- or low-curiosity questions convolved with an HRF (i.e., the psychological term; contrasting trials with later recognized [1] and later forgotten faces [–1]), the critical interaction term (i.e., physiological term multiplied by the unconvolved psychological term), and movement-related regressors. For each participant, we then extracted the PPI beta weights from the hippocampal ROI on the same hemisphere as the SN/VTA seed region. We performed correlations between individual PPI beta weights and individual memory benefits for faces to investigate how individual variability in the strength of connectivity between seed region and ROIs predicted memory benefits for faces.

SUPPLEMENTAL INFORMATION

Supplemental Information includes Supplemental Experimental Procedures, five figures, and three tables, and can be found with this article online at <http://dx.doi.org/10.1016/j.neuron.2014.08.060>.

AUTHOR CONTRIBUTIONS

M.J.G. and C.R. designed the experiment, B.D.G. and M.J.G. collected the data, M.J.G. analyzed the data, and M.J.G. and C.R. wrote the manuscript.

ACKNOWLEDGMENTS

We thank each of the reviewers for their helpful suggestions and comments. We also thank Mason Oliver for help with the data collection; Manoj Doss and Maria Montchal for help with creating the stimuli; and Brian Wiltgen, Mariam Aly, Eva Bauch, Laura Libby, and Maureen Ritchey for comments on earlier versions of the manuscript. This work was supported by NIH grant 1R01MH083734, a Guggenheim Fellowship, a Parke-Davis Exchange Fellowship from the University of Cambridge, and a Visiting Professorship from the Leverhulme Trust awarded to C.R. and a postdoctoral fellowship from the German Academic Exchange Service (Deutscher Akademischer Austausch Dienst) to M.J.G. The content is solely the responsibility of the authors and does not necessarily represent the official views of the NIH.

Accepted: August 29, 2014

Published: October 2, 2014

REFERENCES

- Adcock, R.A., Thangavel, A., Whitfield-Gabrieli, S., Knutson, B., and Gabrieli, J.D.E. (2006). Reward-motivated learning: mesolimbic activation precedes memory formation. *Neuron* 50, 507–517.
- Amunts, K., Kedo, O., Kindler, M., Pieperhoff, P., Mohlberg, H., Shah, N.J., Habel, U., Schneider, F., and Zilles, K. (2005). Cytoarchitectonic mapping of the human amygdala, hippocampal region and entorhinal cortex: intersubject variability and probability maps. *Anat. Embryol. (Berl.)* 210, 343–352.
- Berlyne, D.E. (1966). Curiosity and exploration. *Science* 153, 25–33.
- Chowdhury, R., Guitart-Masip, M., Lambert, C., Dayan, P., Huys, Q., Düzel, E., and Dolan, R.J. (2013). Dopamine restores reward prediction errors in old age. *Nat. Neurosci.* 16, 648–653.
- Corbetta, M., and Shulman, G.L. (2002). Control of goal-directed and stimulus-driven attention in the brain. *Nat. Rev. Neurosci.* 3, 201–215.
- Cox, R.W. (1996). AFNI: software for analysis and visualization of functional magnetic resonance neuroimages. *Comput. Biomed. Res.* 29, 162–173.
- Dayan, P., and Balleine, B.W. (2002). Reward, motivation, and reinforcement learning. *Neuron* 36, 285–298.
- Deci, E.L., Koestner, R., and Ryan, R.M. (1999). A meta-analytic review of experiments examining the effects of extrinsic rewards on intrinsic motivation. *Psychol. Bull.* 125, 627–668, discussion 692–700.
- Düzel, E., Bunzeck, N., Guitart-Masip, M., and Düzel, S. (2010). Novelty-related motivation of anticipation and exploration by dopamine (NOMAD): implications for healthy aging. *Neurosci. Biobehav. Rev.* 34, 660–669.
- Flagel, S.B., Clark, J.J., Robinson, T.E., Mayo, L., Czuj, A., Willuhn, I., Akers, C.A., Clinton, S.M., Phillips, P.E.M., and Akil, H. (2011). A selective role for dopamine in stimulus-reward learning. *Nature* 469, 53–57.
- Frey, U., and Morris, R.G. (1998). Synaptic tagging: implications for late maintenance of hippocampal long-term potentiation. *Trends Neurosci.* 21, 181–188.
- Frey, U., Schroeder, H., and Matthies, H. (1990). Dopaminergic antagonists prevent long-term maintenance of posttetanic LTP in the CA1 region of rat hippocampal slices. *Brain Res.* 522, 69–75.
- Goto, Y., and Grace, A.A. (2008). Limbic and cortical information processing in the nucleus accumbens. *Trends Neurosci.* 31, 552–558.
- Gruber, M.J., and Otten, L.J. (2010). Voluntary control over prestimulus activity related to encoding. *J. Neurosci.* 30, 9793–9800.
- Gruber, M.J., Watrous, A.J., Ekstrom, A.D., Ranganath, C., and Otten, L.J. (2013). Expected reward modulates encoding-related theta activity before an event. *Neuroimage* 64, 68–74.

- Guitart-Masip, M., Fuentemilla, L., Bach, D.R., Huys, Q.J.M., Dayan, P., Dolan, R.J., and Düzel, E. (2011). Action dominates valence in anticipatory representations in the human striatum and dopaminergic midbrain. *J. Neurosci.* *31*, 7867–7875.
- Haber, S.N., and Fudge, J.L. (1997). The primate substantia nigra and VTA: integrative circuitry and function. *Crit. Rev. Neurobiol.* *11*, 323–342.
- Haber, S.N., and Knutson, B. (2010). The reward circuit: linking primate anatomy and human imaging. *Neuropsychopharmacology* *35*, 4–26.
- Kahn, I., and Shohamy, D. (2013). Intrinsic connectivity between the hippocampus, nucleus accumbens, and ventral tegmental area in humans. *Hippocampus* *23*, 187–192.
- Kang, M.J., Hsu, M., Krajchich, I.M., Loewenstein, G., McClure, S.M., Wang, J.T.-Y., and Camerer, C.F. (2009). The wick in the candle of learning: epistemic curiosity activates reward circuitry and enhances memory. *Psychol. Sci.* *20*, 963–973.
- Knutson, B., and Gibbs, S.E.B. (2007). Linking nucleus accumbens dopamine and blood oxygenation. *Psychopharmacology (Berl.)* *191*, 813–822.
- Knutson, B., Adams, C.M., Fong, G.W., and Hommer, D. (2001). Anticipation of increasing monetary reward selectively recruits nucleus accumbens. *J. Neurosci.* *21*, RC159.
- Krebs, R.M., Schott, B.H., and Düzel, E. (2009). Personality traits are differentially associated with patterns of reward and novelty processing in the human substantia nigra/ventral tegmental area. *Biol. Psychiatry* *65*, 103–110.
- Lisman, J.E., and Grace, A.A. (2005). The hippocampal-VTA loop: controlling the entry of information into long-term memory. *Neuron* *46*, 703–713.
- Lisman, J., Grace, A.A., and Düzel, E. (2011). A neoHebbian framework for episodic memory; role of dopamine-dependent late LTP. *Trends Neurosci.* *34*, 536–547.
- Mather, M., and Schoeke, A. (2011). Positive outcomes enhance incidental learning for both younger and older adults. *Front Neurosci* *5*, 129.
- Murayama, K., and Kitagami, S. (2014). Consolidation power of extrinsic rewards: reward cues enhance long-term memory for irrelevant past events. *J. Exp. Psychol. Gen.* *143*, 15–20.
- Murayama, K., and Kuhbandner, C. (2011). Money enhances memory consolidation—but only for boring material. *Cognition* *119*, 120–124.
- Murayama, K., Matsumoto, M., Izuma, K., and Matsumoto, K. (2010). Neural basis of the undermining effect of monetary reward on intrinsic motivation. *Proc. Natl. Acad. Sci. USA* *107*, 20911–20916.
- Murty, V.P., and Adcock, R.A. (2013). Enriched Encoding: Reward Motivation Organizes Cortical Networks for Hippocampal Detection of Unexpected Events. *Cereb. Cortex*.
- O'Carroll, C.M., and Morris, R.G.M. (2004). Heterosynaptic co-activation of glutamatergic and dopaminergic afferents is required to induce persistent long-term potentiation. *Neuropharmacology* *47*, 324–332.
- O'Doherty, J.P., Deichmann, R., Critchley, H.D., and Dolan, R.J. (2002). Neural responses during anticipation of a primary taste reward. *Neuron* *33*, 815–826.
- Paller, K.A., and Wagner, A.D. (2002). Observing the transformation of experience into memory. *Trends Cogn. Sci.* *6*, 93–102.
- Redondo, R.L., and Morris, R.G.M. (2011). Making memories last: the synaptic tagging and capture hypothesis. *Nat. Rev. Neurosci.* *12*, 17–30.
- Reeve, J., and Reeve, J.M. (1996). *Motivating others: Nurturing inner motivational resources.* (Boston, MA: Allyn and Bacon).
- Ryan, R.M., and Deci, E.L. (2000). *Intrinsic and Extrinsic Motivations: Classic Definitions and New Directions.* *Contemp. Educ. Psychol.* *25*, 54–67.
- Schott, B.H., Minuzzi, L., Krebs, R.M., Elmenhorst, D., Lang, M., Winz, O.H., Seidenbecher, C.I., Coenen, H.H., Heinze, H.-J., Zilles, K., et al. (2008). Mesolimbic functional magnetic resonance imaging activations during reward anticipation correlate with reward-related ventral striatal dopamine release. *J. Neurosci.* *28*, 14311–14319.
- Schultz, W. (2013). Updating dopamine reward signals. *Curr. Opin. Neurobiol.* *23*, 229–238.
- Scimeca, J.M., and Badre, D. (2012). Striatal contributions to declarative memory retrieval. *Neuron* *75*, 380–392.
- Shohamy, D., and Adcock, R.A. (2010). Dopamine and adaptive memory. *Trends Cogn. Sci.* *14*, 464–472.
- Smith, W.B., Starck, S.R., Roberts, R.W., and Schuman, E.M. (2005). Dopaminergic stimulation of local protein synthesis enhances surface expression of GluR1 and synaptic transmission in hippocampal neurons. *Neuron* *45*, 765–779.
- Wang, S.-H., Redondo, R.L., and Morris, R.G.M. (2010). Relevance of synaptic tagging and capture to the persistence of long-term potentiation and everyday spatial memory. *Proc. Natl. Acad. Sci. USA* *107*, 19537–19542.
- Wimmer, G.E., and Shohamy, D. (2012). Preference by association: how memory mechanisms in the hippocampus bias decisions. *Science* *338*, 270–273.
- Wittmann, B.C., Schott, B.H., Guderian, S., Frey, J.U., Heinze, H.-J., and Düzel, E. (2005). Reward-related fMRI activation of dopaminergic midbrain is associated with enhanced hippocampus-dependent long-term memory formation. *Neuron* *45*, 459–467.
- Wittmann, B.C., Dolan, R.J., and Düzel, E. (2011). Behavioral specifications of reward-associated long-term memory enhancement in humans. *Learn. Mem.* *18*, 296–300.
- Wolosin, S.M., Zeithamova, D., and Preston, A.R. (2012). Reward modulation of hippocampal subfield activation during successful associative encoding and retrieval. *J. Cogn. Neurosci.* *24*, 1532–1547.
- Yarkoni, T., Poldrack, R.A., Nichols, T.E., Van Essen, D.C., and Wager, T.D. (2011). Large-scale automated synthesis of human functional neuroimaging data. *Nat. Methods* *8*, 665–670.
- Zald, D.H., Cowan, R.L., Riccardi, P., Baldwin, R.M., Ansari, M.S., Li, R., Shelby, E.S., Smith, C.E., McHugo, M., and Kessler, R.M. (2008). Midbrain dopamine receptor availability is inversely associated with novelty-seeking traits in humans. *J. Neurosci.* *28*, 14372–14378.

Supported by:



Even more ways to access Cell Press journals



App Features:

- Available to subscribers at no additional charge
- Free 30-day trial to all 30 Cell Press journals
- Interactive reading experience
- Browse abstracts and full-text articles
- Download now, read later
- Make article notes
- Share with your friends and colleagues
- Now on the iPhone, iPad, Android tablet and Android phone



Download the app at
cell.com/mobile

CellPress

New from Garland Science

PRINCIPLES OF NEUROBIOLOGY

LIQUN LUO

Stanford University, USA

P **principles of Neurobiology** presents the major concepts of neuroscience with an emphasis on how we know what we know. The text is organized around a series of key experiments to illustrate how scientific progress is made and helps upper-level undergraduate and graduate students discover the relevant primary literature. Written by a single author in a clear and consistent writing style, each topic builds in complexity from electrophysiology to molecular genetics to systems level in a highly integrative approach.

- Integrates molecular, cellular, circuit, systems, and behavioral approaches within each subject.
- Written in a consistent and engaging style, with many cross-chapter references to further integrate concepts across chapters.
- Covers important topics of modern neurobiology with sufficient depth to represent the frontiers of research.
- The descriptions of key experiments, the figures with data from original literature, and the references to primary papers provide a rich resource for students to understand and utilize primary research.
- Contains many examples of the use of diverse animal models in research, including many from invertebrates.

Visit us at Booth 153 at the Society for Neuroscience meeting in Chicago.

To purchase in the U.S., Canada and Latin America, please contact:

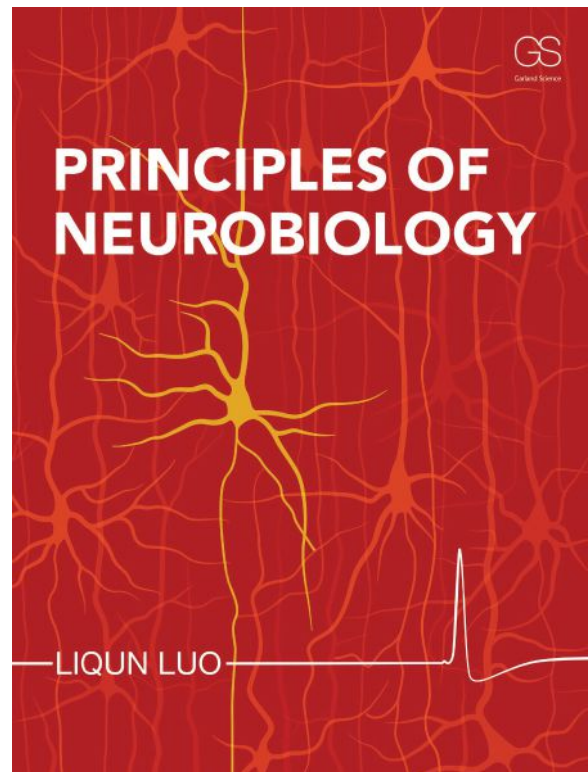
Taylor & Francis • 7625 Empire Drive • Florence, KY 41042

Call toll-free: 1-800-634-7064 • Call international: 561-361-6000 x 6418

Fax toll-free: 1-800-248-4724 • Fax international: 561-361-6075

E-mail: orders@taylorandfrancis.com

To apply for an examination copy for course consideration, write to science@garland.com.



CONTENTS

1. An Invitation to Neurobiology
2. Signaling within Neurons
3. Signaling across Synapses
4. Vision
5. Wiring of the Visual System
6. Olfaction, Taste, Audition, and Somatosensation
7. Wiring of the Nervous System
8. Motor and Regulatory Systems
9. Sexual Behavior
10. Memory, Learning, and Synaptic Plasticity
11. Brain Disorders
12. Evolution of the Nervous System
13. Ways of Exploring

A sample chapter and detailed table of contents are available at garlandscience.com/neurobiology.

GS Garland Science
Taylor & Francis Group

Issues with your tissues? Process all your slides in a SNAP for streamlined IHC.

Variability – it's the challenge you face in traditional immunohistochemistry (IHC) experiments. If you're handling slides manually, using pipettes, dipping and pouring, you risk slide-to-slide process variability, which may affect your results.

Experience a controlled vacuum force that removes solutions evenly from all your slides at once – in seconds.

Experience minimal slide handling, with blocking, washing, antibody and staining solutions contacting your tissues in self-contained reservoirs.

The SNAP i.d.® 2.0 system has been delighting Western blot users for years. Now we've applied its power to IHC.



Enhance your research with
the SNAP i.d.® 2.0 system.
www.emdmillipore.com/IHC

EMD Millipore is a division of Merck KGaA, Darmstadt, Germany



ORCA-Flash4.0 V2

DISCOVER THE BREAKTHROUGH

**The first sCMOS camera with 82% peak Quantum Efficiency.
Available NOW from Hamamatsu.**

Scientific breakthroughs rarely come from giant steps. Rather, it's a continuous progression of small steps and astute application of those differences that enables advances. From its introduction the ORCA-Flash4.0 has challenged the status quo of imaging and has undergone a series of useful enhancements. The most recent is perhaps the most exciting; a notable increase in the ability to detect photons. If you have not yet experienced the ORCA-Flash4.0 V2 sCMOS, now is the time.

What breakthrough will you make with your extra photons?

HAMAMATSU

PHOTON IS OUR BUSINESS

908-231-0960 <http://bit.ly/FlashV2>